Karlsruhe Institute of Technology (KIT)

Karlsruhe Institute of Technology

GPS Stochastic Modelling

Signal Quality Measures and ARMA Processes

Inaugural dissertation

for the fulfilment of the requirements
for the academic degree of

Doctor of Engineering (Dr.-Ing.)

Accepted by
the Department of Civil Engineering,
Geo and Environmental Sciences of the
Karlsruhe Institute of Technology

Submitted by

Dipl.-Ing. Xiaoguang Luo

from Baoji, Shaanxi, P.R. China

Karlsruhe 2012

"There is one thing even more vital to science than intelligent methods; and that is, the sincere desire to find out the truth, whatever it may be."

Charles Sanders Peirce (1839 - 1914)
American mathematician and logician

Parts of this thesis have been published in the following journal and proceedings articles:

Luo, X., Mayer, M., and Heck, B. (2011). On the probability distribution of GNSS carrier phase observations. *GPS Solutions*, 15(4):369–379. doi:10.1007/s10291-010-0196-2.

Luo, X., Mayer, M., and Heck, B. (2011). Verification of ARMA identification for modelling temporal correlations of GNSS observations using the ARMASA toolbox. *Studia Geophysica et Geodaetica*, 55(3):537–556. doi:10.1007/s11200-011-0033-2.

Luo, X., Mayer, M., and Heck, B. (2009). Improving the stochastic model of GNSS observations by means of SNR-based weighting. In: Sideris, M. G. (ed.), *Observing our Changing Earth*, Proceedings of the 2007 IAG General Assembly, Perugia, Italy, July 2-13, 2007, IAG Symposia, Vol. 133, Springer-Verlag, Berlin Heidelberg, pp. 725–734. doi:10.1007/978-3-540-85426-5_83.

Luo, X., Mayer, M., and Heck, B. (2008). Erweiterung des stochastischen Modells von GNSS-Beobachtungen unter Verwendung der Signalqualität. *Zeitschrift für Geodäsie, Geoinformatik und Landmanagement (ZfV)*, 133(2):98–107.

Supervisor's Foreword

The Global Positioning System (GPS) has become an efficient tool for a wide range of applications. However, when analysing GPS data, the stochastic model characterising the precision and correlations of GPS observations is usually simplified and incomplete. Extending the GPS stochastic model is the goal of this thesis, using signal-to-noise ratio (SNR) measurements and time series analysis of observation residuals.

First, this work proposes a novel SNR-based observation weighting model, which sufficiently copes with weak signals, multipath effects, and atmospheric variations. Its employment in high-precision, static relative positioning significantly improves the results of ambiguity resolution, troposphere parameter estimation, and site coordinate determination. Next, applying auto-regressive moving average (ARMA) processes, the temporal correlation of GPS observation noise is investigated in a mathematically rigorous manner. The outcomes are statistically valid and physically interpretable, showing the influences of multipath effects, satellite geometry, and atmospheric conditions.

This study is a milestone and a key step towards a realistic GPS stochastic model and provides an excellent example of statistical verification and physical interpretation of results. Furthermore, this work includes a comprehensive description of different methods, which are applicable to various other data sets. Last but not least, this thesis gives an up-to-date overview of the GPS error effects and an illustrative description of the stochastic components.

July 6, 2012

Prof. Dr.-Ing. habil. Dr. h.c. Bernhard Heck

Abstract

When using the least-squares method to process Global Positioning System (GPS) observations, reliable parameter estimates and realistic accuracy measures can only be obtained if both the functional and stochastic models are properly defined. In comparison to the continuously improved functional model, the stochastic model characterising the statistical properties of GPS observations is still incomplete. Its main deficiencies arise from unrealistic observation weighting and neglecting physical correlations between GPS measurements. In many GPS software products, a simplified elevation-dependent weighting model is implemented, which is inappropriate for observations strongly affected by multipath, signal diffraction, and atmospheric effects. The physical correlations can be subdivided into temporal, spatial, and cross correlations, describing observation dependencies over time, in space, and between frequencies, respectively.

On the basis of a realistic assessment of observation quality and temporal correlation, this thesis extends the GPS stochastic model using signal-to-noise ratio (SNR) measurements and residual time series from least-squares evaluations. Being superior to the commonly employed elevation-dependent weighting scheme, the proposed SNR-based approach realistically handles low-elevation observations and sufficiently characterises the variations in observation quality due to multipath effects and atmospheric conditions. The residual-based temporal correlation modelling essentially consists of two steps. First, by performing Vondrák filtering and sidereal stacking, a residual decomposition is carried out for noise extraction. Next, the obtained noise component is modelled by means of autoregressive moving average (ARMA) processes. The results of the residual decomposition and ARMA modelling are verified by applying continuous wavelet transforms and suitable statistical hypothesis tests.

For static relative positioning on a regional scale, the employment of the SNR-based observation weighting model improves the success rate of ambiguity resolution by about 10%, the standard deviations of site-specific troposphere parameters by about 20%, and the estimates of station coordinates by up to the cm- or even dm-level. Analysing representative residuals from relative and precise point positioning (PPP), the noise's temporal correlation is found to be statistically significant and can be efficiently described by the automatically identified ARMA models. Both the temporal correlation characteristics and the results of ARMA modelling are considerably influenced by satellite geometry, atmospheric conditions, and multipath effects. By considering freely available surface meteorological data, the enhancements achieved by the SNR-based observation weighting, as well as the outcomes from the residual-based temporal correlation modelling are physically interpretable. Using the statistically verified ARMA models to describe the physically interpretable temporal correlations, the extended PPP stochastic model clearly reflects the impacts of multipath effects and atmospheric variations.

Zusammenfassung

Werden die Daten des Globalen Positionierungssystems (GPS) durch eine Ausgleichung nach der Methode der kleinsten Quadrate ausgewertet, sind zuverlässige Parameterschätzwerte und realistische Genauigkeitsmaße nur dann zu erhalten, wenn sowohl das funktionale als auch das stochastische Modell zutreffend definiert sind. Im Vergleich zum stetig verbesserten funktionalen Modell ist das stochastische Modell, das die statistischen Eigenschaften von GPS-Beobachtungen charakterisiert, immer noch unvollständig. Seine Unzulänglichkeiten sind zum einen auf die unrealistische Beobachtungsgewichtung und zum anderen auf die Vernachlässigung der physikalischen Korrelationen zwischen den Beobachtungen zurückzuführen. In vielen GPS-Auswerteprogrammen ist ein vereinfachtes elevationsabhängiges Gewichtsmodell implementiert. Es ist ungegeigt für Beobachtungen, die stark von Mehrwegeeffekten, Signalbeugungen und atmosphärischen Einflüssen beeinträchtiget werden. Physikalische Korrelationen können in zeitliche, räumliche und Kreuzkorrelationen untergliedert werden, die die Beobachtungsabhängigkeiten über die Zeit, im Raum und zwischen Frequenzen beschreiben.

Auf Basis einer realitätsnahen Beurteilung der Beobachtungsqualität und zeitlicher Korrelationen wird in dieser Arbeit das stochastische Modell von GPS-Beobachtungen unter Verwendung von gemessenen Signal-Rausch-Verhältnissen (engl.: signal-to-noise ratio; SNR) und basierend auf der Analyse von Residuenzeitreihen aus der Ausgleichung nach kleinsten Quadraten erweitert. Im Vergleich zum häufig verwendeten elevationsabhängigen Gewichtsmodell ist der vorgeschlagene, auf SNR beruhende Ansatz für die Gewichtung der GPS-Messungen insbesondere in niedrigen Elevationen besser geeignet. Außerdem ermöglicht dieser Ansatz eine adäquate Berücksichtigung variierender Beobachtungsqualitäten aufgrund von Mehrwegeeffekten und atmosphärischen Bedingungen. Die residuenbasierte Modellierung zeitlicher Korrelationen besteht im Wesentlichen aus zwei Schritten. Zur Rauschextraktion wird zunächst eine Residuendekomposition mit Hilfe des Vondrák-Filters und eines siderischen Stacking-Verfahrens durchgeführt, um die verbleibenden systematischen Effekte zu beseitigen. Anschließend wird die erhaltene Rauschkomponente anhand von AutoRegressiven Moving Average (ARMA) Prozessen modelliert. Die Ergebnisse der Residuendekomposition und ARMA-Modellierung werden mittels kontinuierlicher Wavelet-Transformation und geeigneter statistischer Tests überprüft.

Wird das SNR-basierte Gewichtsmodell für statische relative Positionierung in regionalen Netzen eingesetzt, führt es zu einer Zunahme der gelösten Phasenmehrdeutigkeiten um ca. 10%, zu einer Reduktion der Standardabweichungen der geschätzten stationsspezifischen Troposphärenparameter um ca. 20% sowie zu einer Änderung der ermittelten Stationskoordinaten im Zentimeter- oder sogar Dezimeterbereich. Auf Basis von repräsentativen Residuenzeitreihen aus relativer und präziser Einzelpunktpositionierung (engl.: precise point positioning; PPP) können statistisch signifikante zeitliche Korrelationen in der Rauschkomponente festgestellt und durch automatisch identifizierte ARMA-Modelle effizient beschrieben werden. Sowohl die Charakteristika der zeitlichen Korrelationen als auch die Ergebnisse der ARMA-Modellierung werden von Satellitengeometrie, Atmosphärenbedingungen und Mehrwegeeffekten deutlich beeinflusst. Unter Berücksichtigung von frei verfügbaren meteorologischen Oberflächendaten sind die aus der SNR-basierten Beobachtungsgewichtung resultierenden Verbesserungen sowie die aus der residuenbasierten Korrelationsmodellierung erhaltenen Ergebnisse physikalisch interpretierbar. Werden die statistisch gesicherten ARMA-Modelle zur Beschreibung der physikalisch interpretierbaren zeitlichen Korrelationen herangezogen, reflektiert das erweiterte stochastische Modell bei PPP eindeutig die Einflüsse von Mehrwegeeffekten und atmosphärischen Bedingungen.

Contents

Chapter 1

Introduction

1.1 Problem statement

The Global Positioning System (GPS), being one of the Global Navigation Satellite Systems (GNSS), serves as an efficient tool for a wide range of geodetic applications in the industrial, commercial, cadastral, and scientific research sectors. The rising demands for accurate positions and realistic quality measures require continuous improvements, not only in hardware developments, but also in the mathematical models applied in GPS data analysis. Using the least-squares (LS) method for GPS data processing, the mathematical models consist of functional and stochastic components. While the functional model formulates the mathematical relationship between GPS measurements and unknown parameters, the stochastic model describes the observations' precisions and correlations, generally expressed by the main- and off-diagonal elements of a variance-covariance matrix (VCM), respectively. For accurate parameter estimates and realistic quality measures, both the functional and stochastic models must be properly defined.

Over the past few decades, the functional model of GPS observations has been investigated in considerable detail (Seeber, 2003; Xu, 2007; Hofmann-Wellenhof et al., 2008). Nevertheless, it still contains deficiencies in terms of modelling site-specific multipath effects and atmospheric propagation delays, particularly when using low-elevation data. In comparison to the advanced functional model, the stochastic model is still under development and represents a controversial research topic. The main deficiencies of the current stochastic model arise from unrealistic observation weighting and the neglect of physical correlations between GPS measurements.

Assuming azimuthal symmetry, elevation-dependent weighting models are commonly used in GPS software products (Euler and Goad, 1991; Han, 1997; King and Bock, 2002, chap. 5, p. 9; Dach et al., 2007a, p. 144). Such geometry-related weighting schemes require a strong relationship between observation quality and satellite elevation angle, and become inefficient for high-precision applications when including GPS data severely affected by multipath effects, signal diffraction, receiver characteristics, and variable atmosphere. Moreover, GPS measurements are physically correlated over time, in space, and between different frequencies, known as temporal, spatial, and cross correlations, respectively. These dependencies are generally neglected in the stochastic model, resulting in a diagonal VCM structure. As found in different studies, any misspecification of the stochastic model will inevitably produce unreliable parameter estimates and over-optimistic accuracy measures (El-Rabbany, 1994, p. 21; Tiberius and Kenselaar, 2000; El-Rabbany and Kleusberg, 2003; Howind, 2005, p. 30; Schön and Brunner, 2008b).

1.2 State of the art

In order to exploit the potential of low-elevation observations in GPS parameter estimation, signal quality measures such as signal-to-noise ratio (SNR) are used to enable a more realistic assessment of observation quality under non-ideal observational conditions. Different SNR-based weighting models haven been developed, not only in an analytical manner based on the formula provided by Langley (1997) (Brunner et al., 1999; Hartinger and Brunner, 1999; Wieser and Brunner, 2000), but also in an empirical way by directly using SNR measurements (Mayer, 2006,

p. 62; Luo et al., 2008a,d). Relying upon LS residuals of redundant GPS observations, realistic VCM can be estimated by means of rigorous statistical methods such as variance component estimation (VCE) (Satirapod et al., 2002; Tiberius and Kenselaar, 2003; Bischoff et al., 2005, 2006; Amiri-Simkooei, 2007; Li et al., 2008; Teunissen and Amiri-Simkooei, 2008; Amiri-Simkooei et al., 2009; Li et al., 2011). Studies comparing these indicators for GPS observation quality, i.e., satellite elevation angle, SNR, and LS residuals, can be found in Collins and Langley (1999), Satirapod and Wang (2000), and Satirapod and Luansang (2008).

In addition to VCE, physical correlations of GPS observations can be modelled using other techniques, for example, auto- and cross-correlation functions (El-Rabbany, 1994, p. 34; Howind et al., 1999; Tiberius et al., 1999; Bona, 2000; Borre and Tiberius, 2000; El-Rabbany and Kleusberg, 2003; Howind, 2005, p. 57; Leandro and Santos, 2007), stochastic processes (Wang et al., 2002; Teusch, 2006; Luo et al., 2011b, 2012b), and atmospheric turbulence theory (Schön and Brunner, 2008a,b). In fact, as found in various studies, a realistic stochastic model turns out to play an important role in ambiguity resolution (Teunissen, 2000; Wang et al., 2002; Luo et al., 2008a,d), troposphere parameter estimation (Jin and Park, 2005; Luo et al., 2008c; Lo et al., 2009; Jin et al., 2010; Zhu et al., 2010), and site coordinate determination (Howind, 2005, p. 93; Jin et al., 2005; Mayer, 2006, p. 193; Lo et al., 2009; Schön and Brunner, 2008b). For more detailed reviews of previous work on SNR-based observation weighting and temporal correlation modelling, the reader is referred to sections 5.2 and 7.1, respectively.

Despite the successful attempts mentioned above, there are still a number of open questions. For example, a SNR-based weighting scheme using the formula given by Langley (1997) ignores any contribution to the noise characteristics from local oscillators and is only valid for relatively strong signals (Collins and Langley, 1999, p. 4). This motivates empirical SNR-based weighting models that are capable of dealing with weak signals and handling manufacture-dependent SNR measures. Within the context of residual-based correlation modelling, there exists a strong need for additional research on a reliable extraction and characterisation of the observation noise as well as a rigorous statistical evaluation and physical interpretation of the results.

1.3 Objectives of this thesis

The main objective of this thesis is to extend the GPS stochastic model by means of SNR-based observation weighting and residual-based temporal correlation modelling. The specific objectives of this work can be formulated as follows:

- The development of an empirical SNR-based weighting model and its implemented into the Bernese GPS Software 5.0 (Dach et al., 2007a). The effects of the SNR-based weighting scheme on LS adjustment results are investigated with respect to phase ambiguity resolution, troposphere parameter estimation, and site coordinate determination.

- The extraction of the noise component of GPS observation residuals and its characterisation by means of autoregressive moving average (ARMA) processes. The results of the residual-based temporal correlation modelling are statistically verified, physically interpreted, and experimentally used to extend the GPS stochastic model.

Representative case studies in both relative and precise point positioning (PPP) are carried out to verify the efficiency of the proposed methods and the applied software packages. In addition to GPS observations, freely available surface meteorological data are incorporated, allowing for a physically reasonable interpretation of the results.

1.4 Outline of the thesis

This thesis is structured as follows:

Chapter 2 gives a brief introduction to the mathematical methods that are employed in this thesis, such as LS adjustment in linear models, time series analysis, statistical hypothesis tests, and wavelet transforms. For a better understanding of time series modelling and wavelet transforms, representative examples are presented. The description of the statistical tests focuses on their core characteristics and relative strengths and weaknesses in practical use.

Chapter 3 reviews the mathematical models for PPP and relative positioning, along with some general background information about GPS. Furthermore, an overview of the error sources limiting the performance of GPS positioning is provided, with a special emphasis on their effects in the measurement and solution domains.

Chapter 4 describes the data sets and GPS processing strategies for both PPP and relative positioning. The data include not only static GPS observations from the German SA*POS*®network[1], but also freely available DWD[2] surface meteorological measurements.

Chapter 5 deals with the realisation of an empirical SNR-based weighting model and its implementation into the Bernese GPS Software 5.0 (Dach et al., 2007a). Moreover, its advantages in appropriately handling low-quality measurements of weak signals as well as in sufficiently capturing multipath and atmospheric variations are demonstrated.

Chapter 6 presents the effects of the SNR-based weighting model on GPS short- and long-term relative positioning, considering phase ambiguity resolution, troposphere parameter estimation, and coordinate determination. Making use of the surface meteorological data, these effects are analysed for physical causes.

Chapter 7 introduces a residual decomposition approach for noise extraction and gives a theoretical insight into ARMA modelling for noise characterisation. While the decomposition procedure is accomplished by performing Vondrák filtering and sidereal stacking, the ARMA modelling is carried out using the freely available MATLAB® Toolbox ARMASA (Broersen, 2006, chap. 9).

Chapter 8 discusses the results of the residual-based temporal correlation modelling in view of satellite geometry, atmospheric conditions, and multipath impact. The efficiency of residual decomposition and ARMA modelling is verified by applying continuous wavelet transforms and the hypothesis tests outlined in chapter 2. The statistically valid ARMA model estimates are then used to extend the PPP stochastic model.

Finally, chapter 9 summaries the most important findings from this work and provides recommendations for future research.

---

[1]Satellite Positioning Service of the German State Survey
[2]German Meteorological Service (Deutscher Wetterdienst)

Chapter 2

Mathematical Background

In this chapter the basic background of the mathematical methods applied throughout this thesis is described. Since the classical least-squares (LS) adjustment method has been widely used in GPS data processing, section 2.1 outlines the concept of LS parameter estimation in linear models. Afterwards, some fundamental ideas behind time series analysis are presented in section 2.2. Of particular importance are the so-called autoregressive moving average (ARMA) processes which hold great potential for modelling the temporal correlation behaviour of GPS observation noise. Section 2.3 summarises the core characteristics as well as the strengths and weaknesses of the employed statistical hypothesis tests. In view of practical applications, appendix A provides the quantiles of the distributions of the test statistics for usual significance levels. Finally, section 2.4 gives a brief introduction to wavelet transforms, serving within the framework of this thesis as a time-frequency analysis tool for the visual verification of the residual-based temporal correlation modelling presented in chapters 7 and 8.

2.1 Parameter estimation in linear models

On the basis of the detailed discussion given by Amiri-Simkooei (2007, sect. 2.1), this section outlines the theory of LS adjustment in an inconsistent linear model of observation equations, where the inconsistency arises from errors and uncertainty in the observations. Within the context of finding certain optimum estimators for unknown parameters, two methods, namely weighted LS estimation and best linear unbiased estimation are briefly described. More information about this topic is available in standard textbooks on adjustment theory, such as Grafarend and Schaffrin (1993), Caspary and Wichmann (1994), Koch (1999), and Niemeier (2008).

2.1.1 Estimators and optimisation criteria

Let $\underline{l}$ be an n-dimensional random vector whose randomness is expressed by its probability density function (PDF) $f_l(l|\boldsymbol{x})$, where $\boldsymbol{x}$ denotes a u-dimensional non-random vector of unknown parameters. Using an observed vector $\boldsymbol{l}$ as a realisation of $\underline{l}$ with the PDF $f_l(l|\boldsymbol{x})$, an estimate $\hat{\boldsymbol{x}}$ of $\boldsymbol{x}$ can be obtained by determining a function $G : \mathbb{R}^n \mapsto \mathbb{R}^u$ with $\hat{\boldsymbol{x}} = G(\boldsymbol{l})$. Applying G to $\underline{l}$, the resulting vector $\underline{\hat{\boldsymbol{x}}} = G(\underline{l})$ is called an estimator for $\boldsymbol{x}$. $\underline{\hat{\boldsymbol{x}}}$ is random and has its own PDF, where $\hat{\boldsymbol{x}}$ represents a realisation of $\underline{\hat{\boldsymbol{x}}}$. The difference $\underline{\hat{\boldsymbol{\epsilon}}} = \underline{\hat{\boldsymbol{x}}} - \boldsymbol{x}$ is referred to as the estimation error. Since $\underline{\hat{\boldsymbol{x}}}$ depends on the selected function G, the estimation error $\hat{\boldsymbol{\epsilon}}$ also depends on G. In order to find an optimum function G that minimises $\underline{\hat{\boldsymbol{\epsilon}}}$, there exist different kinds of criteria such as unbiasedness, minimum variance, and maximum likelihood. Table 2.1 provides these optimisation criteria with the associated mathematical formulations.

Table 2.1: Criteria used to find optimum estimators for unknown parameters

Criterion	Measure	Mathematical fomulation
Unbiasedness	Bias of estimator	$E(\underline{\hat{\boldsymbol{\epsilon}}}) = E(\underline{\hat{\boldsymbol{x}}}) - \boldsymbol{x} = 0$
Minimum variance	Mean squared error	$\mathrm{MSE} = E(\|\underline{\hat{\boldsymbol{x}}} - \boldsymbol{x}\|^2) \to \min$
Maximum likelihood	Probability value	$P(\|\underline{\hat{\boldsymbol{x}}} - \boldsymbol{x}\|^2 \le r^2) \to \max$

Based on the first moment of the distribution of $\hat{\underline{x}}$, the unbiasedness criterion indicates that the mean estimation error $\mathrm{E}(\hat{\underline{\epsilon}})$ is equal to zero for all $\boldsymbol{x}$, where $\mathrm{E}(\cdot)$ is the expectation operator. The minimum variance condition also accounts for the second moment of the distribution of $\hat{\underline{x}}$ and requires the minimum mean squared error (MSE), where $\|\cdot\|$ denotes the norm of a vector. The maximum likelihood (ML) criterion makes use of the probability $P(\cdot)$ that the estimator $\hat{\underline{x}}$ is located within a hyperspherical region centred at $\boldsymbol{x}$ with a given radius r. The estimator with the highest probability is preferred.

2.1.2 Weighted least-squares estimation

The simplest approach for estimating $\boldsymbol{x}$ requires information about the first moment of the distribution of $\underline{l}$. Since the PDF $f_l(\boldsymbol{l}|\boldsymbol{x})$ depends on the vector of unknown parameters $\boldsymbol{x}$, the mean of $\underline{l}$ also depends on $\boldsymbol{x}$. The relation between $\mathrm{E}(\underline{l})$ and $\boldsymbol{x}$ is assumed to be known and can be represented by a mapping function $\boldsymbol{A} : \mathbb{R}^u \mapsto \mathbb{R}^n$. In the linear(ised) case, $\boldsymbol{A}$ is an $n \times u$ matrix. If $n > u = \mathrm{rank}(\boldsymbol{A})$, indicating redundant measurements, the linear system of equations in the form $\boldsymbol{l} \approx \boldsymbol{A}\boldsymbol{x}$ is overdetermined with a redundancy of $m = n - u$ and inconsistent due to intrinsic errors and uncertainties in the observations. As is well known, an inconsistent linear equation system has no solution $\boldsymbol{x}$ being able to reproduce $\boldsymbol{l}$. To make the system consistent, an n-dimensional observation error vector $\boldsymbol{e}$ is introduced such that $\boldsymbol{l} = \boldsymbol{A}\boldsymbol{x} + \boldsymbol{e}$ holds. This consistent linear equation system is called the linear model of observation equations:

$$\mathrm{E}(\underline{l}) = \boldsymbol{A}\boldsymbol{x}, \quad \boldsymbol{W}, \quad \text{or} \quad \mathrm{D}(\underline{l}) = \boldsymbol{C}_{ll} = \sigma_0^2 \boldsymbol{Q}_{ll}, \tag{2.1}$$

where

$\underline{l}$: n-dimensional vector of stochastic observables,
$\boldsymbol{A}$: $n \times u$ design matrix,
$\boldsymbol{x}$: u-dimensional vector of unknown parameters,
$\boldsymbol{W}$: $n \times n$ weight matrix,
$\boldsymbol{C}_{ll}$: $n \times n$ variance-covariance matrix (VCM),
$\boldsymbol{Q}_{ll}$: $n \times n$ cofactor matrix,
σ_0^2 :   a priori variance factor (variance of unit weight).

The design matrix $\boldsymbol{A}$ is assumed to be of full column rank, i.e., $\mathrm{rank}(\boldsymbol{A}) = u \leq n$. The matrices $\boldsymbol{W}$, $\boldsymbol{C}_{ll}$, and $\boldsymbol{Q}_{ll}$ are symmetric and positive-definite, where $\mathrm{D}(\cdot)$ denotes the dispersion operator. The parametric form of the linear model given by equation (2.1) is referred to as a Gauss-Markov model if $\underline{l}$ is normally distributed with $\underline{l} \sim \mathcal{N}(\boldsymbol{A}\boldsymbol{x}, \boldsymbol{C}_{ll})$.

The introduction of the error vector $\boldsymbol{e}$ solves the problem of inconsistency, but leads to an underdetermined system with $u + n$ unknowns in a total set of n equations. In this case, there are an infinite number of possible solutions for $\boldsymbol{x}$ and $\boldsymbol{e}$. It seems reasonable to select from the infinitely many solutions the most appropriate one with which the resulting $\boldsymbol{A}\boldsymbol{x}$ is as close as possible to the observation vector $\boldsymbol{l}$. This suggests that the squared weighted norm of $\boldsymbol{e}$, i.e.,

$$\|\boldsymbol{e}\|_W^2 = \boldsymbol{e}^T \boldsymbol{W} \boldsymbol{e} = (\boldsymbol{l} - \boldsymbol{A}\boldsymbol{x})^T \boldsymbol{W} (\boldsymbol{l} - \boldsymbol{A}\boldsymbol{x}) \tag{2.2}$$

has to be minimised, where $\|\cdot\|$ denotes the norm of a vector, and the weight matrix $\boldsymbol{W}$ is symmetric and positive-definite. According to equation (2.2), the weighted LS solution for the linear model of observation equations is given by

$$\hat{\boldsymbol{x}} = \arg \min_{\boldsymbol{x} \in \mathbb{R}^u} (\boldsymbol{l} - \boldsymbol{A}\boldsymbol{x})^T \boldsymbol{W} (\boldsymbol{l} - \boldsymbol{A}\boldsymbol{x}). \tag{2.3}$$

The difference $\hat{e} = l - A\hat{x}$ is known as the weighted least-squares error vector and its squared weighted norm $\|\hat{e}\|_W^2$ is a scalar measure for the inconsistency of the linear system. Considering the properties of matrix transposition, $\|\hat{e}\|_W^2$ can be reformulated as

$$\|\hat{e}\|_W^2 = (l - A\hat{x})^T W (l - A\hat{x}) = l^T W l - 2\hat{x}^T A^T W l + \hat{x}^T A^T W A \hat{x}. \tag{2.4}$$

Setting the derivative of equation (2.4) with respect to $\hat{x}$

$$\frac{\partial \|\hat{e}\|_W^2}{\partial \hat{x}} = -2A^T W l + 2A^T W A \hat{x} \tag{2.5}$$

to zero, the weighted LS estimate of x is obtained as

$$\hat{x} = G(l) = \left(A^T W A\right)^{-1} A^T W l. \tag{2.6}$$

If the columns of A are linearly independent, the second-order derivative, given by

$$\frac{\partial^2 \|\hat{e}\|_W^2}{\partial \hat{x} \partial \hat{x}^T} = 2A^T W A, \tag{2.7}$$

is positive definite. Therefore, a minimum for $\|\hat{e}\|_W^2$ has been found. Applying the function $G : \mathbb{R}^n \mapsto \mathbb{R}^u$ to the random vector $\underline{l}$, the weighted least-squares estimator (WLSE) for x is

$$\underline{\hat{x}} = G(\underline{l}) = \left(A^T W A\right)^{-1} A^T W \underline{l} = H\underline{l}. \tag{2.8}$$

From $\underline{\hat{l}} = A\underline{\hat{x}}$ and $\underline{\hat{e}} = \underline{l} - \underline{\hat{l}}$, the LS estimators for the observable and error vectors can be derived as follows:

$$\underline{\hat{l}} = A \left(A^T W A\right)^{-1} A^T W \underline{l} = P_A \underline{l}, \tag{2.9}$$

$$\underline{\hat{e}} = \underline{l} - \underline{\hat{l}} = (I_n - P_A) \underline{l} = P_A^{\perp} \underline{l}, \tag{2.10}$$

where P_A and $P_A^{\perp}$ define two orthogonal projectors. P_A projects onto the range space of A (i.e., $\mathcal{R}(A)$) along its orthogonal complement (i.e., $\mathcal{R}(A)^{\perp}$), while $P_A^{\perp}$ projects onto $\mathcal{R}(A)^{\perp}$ along $\mathcal{R}(A)$. Substituting $\underline{\hat{e}}$ into equation (2.2) or $\underline{\hat{x}}$ into equation (2.4), the squared weighted norm of the errors measuring the inconsistency of the linear system is written as

$$\|\underline{\hat{e}}\|_W^2 = \underline{\hat{e}}^T W \underline{\hat{e}} = \underline{l}^T W \underline{l} - \underline{l}^T W A \left(A^T W A\right)^{-1} A^T W \underline{l}. \tag{2.11}$$

Under the assumption that the expectation of $\underline{e}$ is equal to zero, i.e., $\mathrm{E}(\underline{e}) = 0$, the WLSE $\underline{\hat{x}}$ for x represents a linear unbiased estimator (LUE) due to

$$\mathrm{E}(\underline{\hat{x}}) = \left(A^T W A\right)^{-1} A^T W \cdot \mathrm{E}(\underline{l}) = \left(A^T W A\right)^{-1} A^T W A \cdot x = x. \tag{2.12}$$

Furthermore, this unbiasedness is independent from the choice of the weight matrix W. The unbiased properties of $\underline{\hat{l}}$ and $\underline{\hat{e}}$ are given by

$$\mathrm{E}(\underline{\hat{l}}) = \mathrm{E}(A\underline{\hat{x}}) = A\mathrm{E}(\underline{\hat{x}}) = Ax = \mathrm{E}(\underline{l}), \quad \mathrm{E}(\underline{\hat{e}}) = \mathrm{E}(\underline{l} - \underline{\hat{l}}) = 0 = \mathrm{E}(\underline{e}). \tag{2.13}$$

Since x is a non-random vector in $\underline{l} = Ax + \underline{e}$, the vector of observables $\underline{l}$ and the error vector $\underline{e}$ exhibit the same statistical properties. Assuming that the variance-covariance matrix (VCM) of $\underline{l}$, i.e., C_{ll}, is known, the covariance matrices of $\underline{\hat{x}}$, $\underline{\hat{l}}$, and $\underline{\hat{e}}$ can be derived by applying the variance-covariance propagation law to equations (2.8), (2.9), and (2.10) as

$$C_{\hat{x}\hat{x}} = H C_{ll} H^T, \quad C_{\hat{l}\hat{l}} = P_A C_{ll} P_A^T, \quad C_{\hat{e}\hat{e}} = P_A^{\perp} C_{ll} P_A^{\perp T}. \tag{2.14}$$

Obviously, the statistical properties of the estimators directly depend on the observables' VCM C_{ll} and weight matrix W. If $\underline{l}$ follows a normal distribution, i.e., $\underline{l} \sim \mathcal{N}(Ax, C_{ll})$, then the random vectors $\underline{\hat{x}}$, $\underline{\hat{l}}$, and $\underline{\hat{e}}$ are also normally distributed:

$$\underline{\hat{x}} \sim \mathcal{N}(x, C_{\hat{x}\hat{x}}), \quad \underline{\hat{l}} \sim \mathcal{N}(Ax, C_{\hat{l}\hat{l}}), \quad \underline{\hat{e}} \sim \mathcal{N}(0, C_{\hat{e}\hat{e}}), \tag{2.15}$$

since they are all linear functions of $\underline{l}$. Unlike $\underline{\hat{x}}$ and $\underline{\hat{l}}$, the PDF of $\underline{\hat{e}}$ is completely known once C_{ll} is specified. The quality of the WLSE can be assessed using

$$\mathrm{MSE} = \mathrm{E}(\|\underline{\hat{x}} - x\|^2) = \mathrm{E}(\|\underline{\hat{x}} - \mathrm{E}(\underline{\hat{x}})\|^2) + \mathrm{E}(\|x - \mathrm{E}(\underline{\hat{x}})\|^2), \tag{2.16}$$

which measures the magnitude of the estimation error $\underline{\hat{\varepsilon}} = \underline{\hat{x}} - x$. The first summand in equation (2.16) is the trace of $C_{\hat{x}\hat{x}}$ denoted as $\mathrm{tr}(C_{\hat{x}\hat{x}})$, and the second summand disappears due to the unbiasedness of $\underline{\hat{x}}$ (see equation (2.12)). Since $C_{\hat{x}\hat{x}}$ depends on the weight matrix W included in H (see equation (2.8)), the MSE of the unbiased WLSE also depends on W. Therefore, it is necessary to find the optimum weight matrix that minimises the MSE.

In summary, table 2.2 gives an overview of the dependencies in the weighted LS estimation. The unbiasedness property of the WLSE depends neither on the distribution of $\underline{l}$ nor on the choice of W and C_{ll}. In addition, full knowledge of the observables' probability distribution is not required for computing $\underline{\hat{x}}$, $\underline{\hat{l}}$, $\underline{\hat{e}}$ and the associated covariance matrices. However, in order to obtain accurate parameter estimates and realistic quality measures, an appropriate specification of the weight and covariance matrices turns out to be an essential issue.

Table 2.2: Overview of the dependencies in the weighted LS estimation

Estimator and statistical property	Dependency on		Related equation
	Distribution of $\underline{l}$	W or C_{ll}	
$\underline{\hat{x}}$, $\underline{\hat{l}}$, $\underline{\hat{e}}$	No	Yes	(2.8), (2.9), (2.10)
$C_{\hat{x}\hat{x}}$, $C_{\hat{l}\hat{l}}$, $C_{\hat{e}\hat{e}}$	No	Yes	(2.14)
Distribution of $\underline{\hat{x}}$, $\underline{\hat{l}}$, $\underline{\hat{e}}$	Yes	Yes	(2.15)
Unbiasedness of WLSE	No	No	(2.12), (2.13)
Squared norm $\|\underline{\hat{e}}\|_W^2$	No	Yes	(2.11)
Mean squared error	No	Yes	(2.16)

2.1.3 Best linear unbiased estimation

The weighted LS estimation only represents an approach for solving an inconsistent linear equation system and does not account for the optimisation criteria presented in table 2.1. A reasonable choice of an optimum WLSE is the one that minimises the MSE, or the trace of $C_{\hat{x}\hat{x}}$ ($\mathrm{tr}(C_{\hat{x}\hat{x}})$) in the case of LUE (see equation (2.16)). The WLSE possessing the smallest MSE of all LUE is referred to as the best linear unbiased estimator (BLUE). If the cofactor matrix Q_{ll} is available, the BLUE is obtained by taking the weight matrix W to be the inverse of Q_{ll}, i.e., $W = Q_{ll}^{-1}$. As a result, the BLUE solutions for x, $\underline{l}$, and $\underline{e}$ in equation $\underline{l} = Ax + \underline{e}$ are derived as

$$\underline{\hat{x}} = \left(A^T Q_{ll}^{-1} A\right)^{-1} A^T Q_{ll}^{-1} \underline{l} = H\underline{l}, \quad \underline{\hat{l}} = P_A \underline{l}, \quad \underline{\hat{e}} = P_A^{\perp} \underline{l}, \tag{2.17}$$

where the orthogonal projectors P_A and $P_A^{\perp}$ are

$$P_A = A \left(A^T Q_{ll}^{-1} A\right)^{-1} A^T Q_{ll}^{-1}, \quad P_A^{\perp} = I_n - P_A. \tag{2.18}$$

Substituting $\boldsymbol{H}$ from equation (2.17) as well as $\boldsymbol{P_A}$ and $\boldsymbol{P_A^\perp}$ from equation (2.18) into equation (2.14), the resulting covariance matrices of $\hat{\underline{\boldsymbol{x}}}$, $\hat{\underline{\boldsymbol{l}}}$, and $\hat{\underline{\boldsymbol{e}}}$ are

$$C_{\hat{x}\hat{x}} = \sigma_0^2 \left(\boldsymbol{A}^T \boldsymbol{Q}_{ll}^{-1} \boldsymbol{A} \right)^{-1}, \quad C_{\hat{l}\hat{l}} = \boldsymbol{P_A} C_{ll}, \quad C_{\hat{e}\hat{e}} = \boldsymbol{P_A^\perp} C_{ll}. \tag{2.19}$$

The minimum $\mathrm{tr}(\boldsymbol{C}_{\hat{x}\hat{x}})$ indicates that the BLUE is a minimum variance linear unbiased estimator. This property is also independent of the distribution of $\underline{\boldsymbol{l}}$. Setting $\boldsymbol{W}$ equal to $\boldsymbol{Q}_{ll}^{-1}$ in equation (2.11), the squared weighted norm of the errors becomes

$$\|\hat{\underline{\boldsymbol{e}}}\|_{Q_{ll}^{-1}}^2 = \hat{\underline{\boldsymbol{e}}}^T \boldsymbol{Q}_{ll}^{-1} \boldsymbol{e} = \underline{\boldsymbol{l}}^T \boldsymbol{Q}_{ll}^{-1} \underline{\boldsymbol{l}} - \underline{\boldsymbol{l}}^T \boldsymbol{Q}_{ll}^{-1} \boldsymbol{A} \left(\boldsymbol{A}^T \boldsymbol{Q}_{ll}^{-1} \boldsymbol{A} \right)^{-1} \boldsymbol{A}^T \boldsymbol{Q}_{ll}^{-1} \underline{\boldsymbol{l}}. \tag{2.20}$$

In the weighted LS estimation, the weight matrix $\boldsymbol{W}$ plays the role of a metric tensor in a vector space. The specification of $\boldsymbol{W} = \boldsymbol{Q}_{ll}^{-1}$ for the BLUE allows some geometric interpretations of the covariance matrix in the vector space. For example, if all observables are uncorrelated with each other, the standard basis vectors of the vector space are orthogonal. In other words, uncorrelated observables indicate basis vectors having no projection on each other. If all observables have additionally unit variances, the basis vectors are orthonormal. Thus, the minimum distance in the vector space required for the WLSE ($\|\hat{\underline{\boldsymbol{e}}}\|_W^2 \to \min$) corresponds to the minimum variance in the stochastic space required for the BLUE ($\mathrm{tr}(\boldsymbol{C}_{\hat{x}\hat{x}}) \to \min$) (Amiri-Simkooei, 2007, p. 10).

2.2 Time series analysis

A time series is a set of observations x_t, each of which is recorded at a specific time t. A discrete time series is one in which the set T of times at which observations are made is a discrete set, while a continuous time series is obtained when observations are recorded over some continuous time interval (Brockwell and Davis, 2002, p. 1, 2). The main objective of time series analysis consists in identifying the nature of phenomena represented by sequences of observations (the aim to which this thesis is primarily devoted) and predicting future values of the time series variables. For these purposes, the determination of an appropriate time series model from the given data plays an important role in time series analysis.

This section describes the widely used classical decomposition model and the class of autoregressive moving average (ARMA) models which provide a general framework for studying stationary processes. In addition to the theoretical discussion, a practical example is presented to illustrate the general approach followed in this thesis to time series modelling. A more detailed discussion of the algorithms introduced in this section can be found, for example, in Kendall and Ord (1990), Brockwell and Davis (2002), Broersen (2006), and Box et al. (2008).

2.2.1 Classical decomposition model

In general, the first step in time series analysis is to plot the data for visual inspection. If discontinuities are present in the time series, for instance, a sudden change of level, it may be advisable to break the series into more homogenous segments. Furthermore, if outlying observations exit, they should be detected and discarded on the basis of appropriately specified outlier criteria. Inspection of a time series graph also allows the representation of the observations $\{y_1, \ldots, y_n\}$ as a realisation of the classical decomposition model given by

$$Y_t = m_t + s_t + X_t, \quad t \in \mathbb{N}, \tag{2.21}$$

where m_t is known as the trend component which varies slowly over time and does not repeat within the time range captured by the data, s_t is the seasonal component which may have a formally similar nature and repeats itself in systematic intervals over time, and X_t is a random noise component which usually complicates the identification of the deterministic components m_t and s_t (Brockwell and Davis, 2002, p. 23).

Sometimes it is necessary to apply transformations to $\{Y_t\}$ in order to obtain $\{X_t\}$ which exhibits approximately consistent variability over time. For a systematic account of a general class of variance-stabilising transformations, the reader is referred to Box and Cox (1964). A commonly used Box-Cox transformation f_λ is defined as

$$f_\lambda(y_t) = \begin{cases} \lambda^{-1}(y_t^\lambda - 1), & y_t \geq 0 \text{ and } \lambda > 0, \\ \ln(y_t), & y_t > 0 \text{ and } \lambda = 0, \end{cases} \tag{2.22}$$

where λ values between 0 and 1.5 are reasonable. In practice, if a Box-Cox transformation is necessary, either f_0 or $f_{0.5}$ is adequate in most cases. f_0 is particularly suitable for positive data whose standard deviation increases linearly with level (Brockwell and Davis, 2002, p. 188, 399). Since the work of Box and Cox (1964), many modifications of the Box-Cox transformation have been carried out, for example, by Manly (1976), John and Draper (1980), Bickel and Doksum (1981), and Yeo and Johnson (2000). The modified Box-Cox transformations can accommodate negative y_t values and bring the distribution of the power-transformed data closer to a Gaussian normal distribution.

To remove the trend (m_t) and seasonality (s_t) terms, there are two general approaches. One is to model m_t and s_t, and then to subtract them from the data. The other is to eliminate m_t and s_t by differencing the series $\{Y_t\}$. To identify and model the trend component in the observed data, two methods are commonly used in practice, namely fitting a function and smoothing. Monotonous (consistently increasing or decreasing) trends can be adequately approximated by a linear, polynomial, or exponential function, where the unknown parameters can be estimated by means of LS regression (Chatterjee and Hadi, 2006). In the case that the trending behaviour cannot be sufficiently characterised by a global function, smoothing and filtering techniques can be applied. The most common approaches are, for example,

- (weighted) moving average (Velleman and Hoaglin, 1981, p. 167),

- Savitzky-Golay filter (Savitzky and Golay, 1964),

- (robust) local regression (Cleveland, 1979; Cleveland and Devlin, 1988),

- exponential smoothing (Holt, 2004; Hyndman et al., 2008), and

- finite impulse response filter (IEEE, 1979; Shenoi, 2006, chap. 5).

Since the mathematical principles of the above-mentioned methods are well documented in the literature on time series analysis and signal processing (Brockwell and Davis, 2002, chap. 1), they are not repeated in this thesis. Moreover, such methods for trend determination have been implemented in statistical analysis software such as the MATLAB$^{®}$ Curve Fitting Toolbox$^{\text{TM}}$ and the free software R (Crawley, 2007; `www.r-project.org`). In the following text, the estimated trend component is denoted as $\hat{m}_t$.

In addition to trends, many time series are affected by seasonally varying factors which can be described by a periodic component s_t with a period of d, satisfying $s_{t-d} = s_t$ and $\sum_{j=1}^{d} s_j = 0$. In the absence of a trend, i.e., $y_t - \hat{m}_t$, two commonly applied approaches to determining the seasonal component are the empirical averaging method (EAM) and analytical harmonic regression (Brockwell and Davis, 2002, p. 13, 31). For each $k = 1, \ldots, d$, the average w_k of the differences $\{(y_{k+id} - \hat{m}_{k+id}), i \in \mathbb{Z}_0^+, k + id \leq n\}$ can be computed. Since these average differences do not necessarily sum to zero, the seasonal component is estimated as

$$\hat{s}_k = w_k - \frac{1}{d} \sum_{i=1}^{d} w_i, \quad k = 1, \ldots, d, \tag{2.23}$$

and $\hat{s}_k = \hat{s}_{k-d}$ for $k > d$. Another convenient choice for modelling s_t is to use the sum of harmonics given by

$$s_t = a_0 + \sum_{j=1}^{k} [a_j \cos(\lambda_j t) + b_j \sin(\lambda_j t)], \tag{2.24}$$

where $a_0, a_1, \ldots, a_k$ and $b_1, \ldots, b_k$ are unknown coefficients, and $\lambda_1, \ldots, \lambda_k$ are fixed frequencies, each being some integer multiple of $2\pi/d$. These unknown coefficients can be estimated by means of a LS regression on the detrended data $y_t - \hat{m}_t$. In case no information about d is available, an analysis in the frequency domain, for example, with the help of Fourier or wavelet transforms, is necessary to determine the period d and the number of harmonics k. Instead of modelling the systematic components, another approach directly eliminates the trend and seasonal terms by repeatedly applying differencing operators to $\{Y_t\}$ (Brockwell and Davis, 2002, p. 29). The lag-1 difference operator Δ is defined as

$$\Delta Y_t = Y_t - Y_{t-1} = (1 - r)Y_t, \tag{2.25}$$

where r is the backward shift operator, i.e., $r^s Y_t = Y_{t-s}$. Using Δ to detrend a linear function $m_t = c_0 + c_1 t$ results in a constant $\Delta m_t = c_0 + c_1 t - (c_0 + c_1(t - 1)) = c_1$. Analogously, any polynomial trend of degree k can be reduced to a constant by k times use of Δ (Δ^k). In the absence of seasonality, i.e., $Y_t = m_t + X_t$, where $m_t = \sum_{i=0}^{k} c_i t^i$, the application of Δ^k gives

$$\Delta^k Y_t = k! \, c_k + \Delta^k X_t. \tag{2.26}$$

Considering the fact that many slowly-changing functions can be well approximated by a low-degree polynomial on an interval of finite length, the order k of differencing required in practice is quite small, being often one or two. If the data has a seasonal component of period d, the lag-d differencing operator

$$\Delta_d Y_t = Y_t - Y_{t-d} = (1 - r^d)Y_t \tag{2.27}$$

can be used to eliminate the seasonality. Applying Δ_d to the model $Y_t = m_t + s_t + X_t$,

$$\Delta_d Y_t = m_t - m_{t-d} + X_t - X_{t-d} \tag{2.28}$$

represents a decomposition of $\Delta_d Y_t$ into a trend $(m_t - m_{t-d})$ and a noise term $(X_t - X_{t-d})$. The remaining trend $m_t - m_{t-d}$ can be eliminated using a power of the differencing operator Δ. Although the systematic terms m_t and s_t can be effectively eliminated by differencing, certain statistical properties of the original noise component X_t such as temporal correlation behaviour, cannot be retrieved from the differenced noise given in equations (2.26) and (2.28). Accordingly, trend and seasonality removal by repeatedly differencing is particularly applicable when predicting future values of time series variables Y_t. Moreover, differencing introduces additional mathematical correlations which must be taken into account when making statistical inferences by means of hypothesis tests (Howind, 2005, p. 45; Bischoff et al., 2006).

In summary, the particular method chosen for handling trend and seasonality depends on the objective of the time series analysis as well as on the availability of physical background information which may help one understand the apparent systematic variability. The performance of the employed detrending and deseasonalisation approaches directly affects the statistical properties of the noise component ($x_t = y_t - \hat{m}_t - \hat{s}_t$). For example, while analysing representative residual time series of GPS phase observations, Luo et al. (2009) investigated the influences of different smoothing and filtering techniques on the noise's temporal correlation behaviour. The most significant decorrelation effect is found after applying the exponential smoothing. In contrast, a higher degree of local regression results in negatively autocorrelated noise.

2.2.2 (Partial) Autocorrelation function

After removing the deterministic trend and seasonal components, the remaining noise component is supposed to represent a stationary time series. Loosely speaking, a discrete time series $\{X_t, t \in \mathbb{N}\}$ with $\mathrm{E}(X_t^2) < \infty$ is considered to be stationary if it has statistical properties similar to those of the time-shifted series $\{X_{t+h}\}$ for each $h \in \mathbb{Z}$. Strict stationarity of a time series is defined by the condition that $(X_1, \ldots, X_n)$ and $(X_{1+h}, \ldots, X_{n+h})$ have the same joint distributions for all integers h and $n > 0$. A weaker form of stationarity, known as weak stationarity, simply requires that the mean and the covariance functions of $\{X_t\}$, i.e.,

$$\mu_X(t) = \mathrm{E}(X_t) \tag{2.29}$$

and

$$\gamma_X(t + h, t) = \mathrm{Cov}(X_{t+h}, X_t) = \mathrm{E}\left\{[X_{t+h} - \mu_X(t+h)]\,[X_t - \mu_X(t)]\right\} \tag{2.30}$$

do not vary with respect to time t for each $h \in \mathbb{Z}$, indicating that

$$\mathrm{E}(X_t) = \mu_0 \tag{2.31}$$

and

$$\gamma_X(t + h, t) := \mathrm{Cov}(X_{t+h}, X_t) = \mathrm{Cov}(X_h, X_0) =: \gamma_X(h), \tag{2.32}$$

where $\gamma_X(\cdot)$ is referred to as the autocovariance function (ACVF) and $\gamma_X(h)$ as its value at lag h. $\gamma_X(h)$ depends only on the time distance (or lag) h between two observables and is an even function, i.e., $\gamma_X(-h) = \gamma_X(h)$. If $\{X_t\}$ is strictly stationary and $\mathrm{E}(X_t^2) < \infty$ for all t, then $\{X_t\}$ is also weakly stationary. For the sake of brevity, the term stationary used in this thesis means weakly stationary, unless it is specified otherwise. Setting $h = 0$ in equation (2.32), the variance function of a stationary time series is equal to a constant:

$$\mathrm{Var}(X_t) = \mathrm{Cov}(X_t, X_t) = \mathrm{Cov}(X_0, X_0) = \mathrm{Var}(X_0) = \gamma_X(0). \tag{2.33}$$

Relying upon the ACVF of $\{X_t\}$, the associated autocorrelation function (ACF) at lag h is

$$\rho_X(h) := \frac{\gamma_X(h)}{\gamma_X(0)} = \mathrm{Cor}(X_{t+h}, X_t). \tag{2.34}$$

The ACF is symmetrical about the origin where it attains its maximum value of one. Most physical processes have an ACF decreasing in absolute value with an increasing lag. This means that the relation between X_t at a short temporal distance is stronger than that over a longer distance. Rapidly decaying ACF values as $|h|$ increases indicate short-term dependency, while slowly decaying ACF values suggest the presence of long-term dependency.

In practical problems, one may not start directly with a model, but with observed time series data $\{x_1, x_2, \ldots, x_n\}$. To assess the degree of dependence in the observations and to select an appropriate time series model to describe it, one important tool is the sample ACF of the data.

Assuming that $\{x_t\}$ is a realisation of a stationary time series $\{X_t\}$, the sample ACF of $\{x_t\}$ represents an estimate of the ACF of $\{X_t\}$. Based on the definition of the sample ACVF

$$\hat{\gamma}(h) := \frac{1}{n} \sum_{t=1}^{n-|h|} (x_{t+|h|} - \bar{x})(x_t - \bar{x}), \quad -n < h < n, \tag{2.35}$$

the sample ACF is given by

$$\hat{\rho}(h) := \frac{\hat{\gamma}(h)}{\hat{\gamma}(0)}, \quad -n < h < n, \tag{2.36}$$

where $\bar{x} = \frac{1}{n} \sum_{t=1}^{n} x_t$ is the sample mean (Brockwell and Davis, 2002, p. 19). Both estimates $\hat{\gamma}(h)$ and $\hat{\rho}(h)$ are biased even if the denominator n is replaced by $n - |h|$ in equation (2.35). However, using $n - |h|$ instead of n, the sample covariance matrix

$$\hat{\mathbf{\Gamma}}_n := [\hat{\gamma}(i-j)]_{i,j=1}^n = \begin{pmatrix} \hat{\gamma}(0) & \hat{\gamma}(1) & \cdots & \hat{\gamma}(n-1) \\ \hat{\gamma}(1) & \hat{\gamma}(0) & \cdots & \hat{\gamma}(n-2) \\ \vdots & \vdots & \vdots & \vdots \\ \hat{\gamma}(n-1) & \hat{\gamma}(n-2) & \cdots & \hat{\gamma}(0) \end{pmatrix} \tag{2.37}$$

and the associated correlation matrix $\hat{\mathbf{P}}_n = \hat{\mathbf{\Gamma}}_n / \hat{\gamma}(0)$ may not be positive-semidefinite (Brockwell and Davis, 2002, p. 60). Therefore, in this thesis, $\hat{\gamma}(h)$ and $\hat{\rho}(h)$ are calculated using equations (2.35) and (2.36). For $|h|$ values that are slightly smaller than n, $\hat{\gamma}(h)$ and $\hat{\rho}(h)$ are unreliable, since there are only a few pairs $(x_{t+|h|}, x_t)$ available. As a useful guide, n should be at least about 50 and $h \leq n/3$ (Box and Jenkins, 1976, p. 33; Brockwell and Davis, 2002, p. 404).

The sample ACF plays an important role in identifying time series models and assessing the degree of correlation, where the distributional properties of $\hat{\rho}(h)$ are assumed to be known. The probability distribution of $\hat{\rho}(h)$ can be asymptotically approximated by a multivariate normal distribution, i.e.,

$$\hat{\boldsymbol{\rho}}_h \longrightarrow \mathcal{N}(\boldsymbol{\rho}_h, \frac{1}{n}\mathbf{\Sigma}), \tag{2.38}$$

where $\hat{\boldsymbol{\rho}}_h = [\hat{\rho}(1), \ldots, \hat{\rho}(h)]^T$, $\boldsymbol{\rho}_h = [\rho(1), \ldots, \rho(h)]^T$, and $\mathbf{\Sigma}$ is the VCM of $\boldsymbol{\rho}_h$. The (i, j) element of $\mathbf{\Sigma}$ can be computed using Bartlett's formula (Brockwell and Davis, 2002, p. 61)

$$\sigma_{ij} = \sum_{h=1}^{\infty} [\rho(h+i) + \rho(h-i) - 2\rho(i)\rho(h)] \cdot [\rho(h+j) + \rho(h-j) - 2\rho(j)\rho(h)]. \tag{2.39}$$

If $\{X_t\}$ is a sequence of independent and identically distributed (iid) random variables, each with zero mean and variance σ_X^2, indicated by the notation $\{X_t\} \sim \text{IID}(0, \sigma_X^2)$, then $\rho(h) = 0$ for $h > 0$ and $\rho(h) = 1$ for $h = 0$. Applying Bartlett's formula to $\{X_t\}$, $\sigma_{ij} \neq 0$ only if $i = j$. Asymptotically, $\hat{\rho}(1), \ldots, \hat{\rho}(h)$ represent iid normal random variables with zero mean and variance n^{-1} (see equation (2.38)). This is usually used to calculate the confidence bounds for sample ACF, making statistical inferences on uncorrelatedness.

The partial correlation primarily contributes to model identification for the observed data. Loosely speaking, it can be interpreted as the difference between the autocorrelation coefficient at a certain lag and its extrapolation from the lower-order correlations (Broersen, 2006, p. 90). The partial autocorrelation function (PACF) of a stationary time series $\{X_t\}$ is the function $\alpha(\cdot)$ defined by the equations

$$\alpha(0) = 1 \quad \text{and} \quad \alpha(h) = \phi_{hh}, \quad h \geq 1, \tag{2.40}$$

where ϕ_{hh} is the last element of $\boldsymbol{\phi}_h = \boldsymbol{\Gamma}_h^{-1}\boldsymbol{\gamma}_h$ with $\boldsymbol{\Gamma}_h = [\gamma(i-j)]_{i,j=1}^h$ and $\boldsymbol{\gamma}_h = [\gamma(1),\ldots,\gamma(h)]^T$. For a set of observations $\{x_1,\ldots,x_n\}$ with $x_i \neq x_j$, the sample PACF is given by

$$\hat{\alpha}(0) = 1 \quad \text{and} \quad \hat{\alpha}(h) = \hat{\phi}_{hh}, \quad h \geq 1, \tag{2.41}$$

where $\hat{\phi}_{hh}$ is the last component of $\hat{\boldsymbol{\phi}}_h = \hat{\boldsymbol{\Gamma}}_h^{-1}\hat{\boldsymbol{\gamma}}_h$ (Brockwell and Davis, 2002, p. 95).

2.2.3 Autoregressive moving average (ARMA) processes

As an important parametric family of stationary models, autoregressive moving average (ARMA) processes play a key role in analysing time series data. According to Brockwell and Davis (2002, p. 83), a large class of autocovariance functions that asymptotically converge to zero can be well approximated by the autocovariance function of an appropriately identified ARMA model. Moreover, the linear structure of ARMA processes leads to a substantial simplification of the general methods for linear prediction. This section provides a brief introduction to ARMA processes, along with some of their core characteristics.

The time series $\{X_t\}$ is an ARMA(p,q) process if $\{X_t\}$ is stationary and

$$X_t + \sum_{i=1}^{p} a_i X_{t-i} = Z_t + \sum_{j=1}^{q} b_j Z_{t-j}, \quad t \in \mathbb{N} \tag{2.42}$$

holds for each time index t. Thereby, $\{Z_t\}$ is a white noise (WN) process representing a sequence of uncorrelated random variables, each with zero mean and variance σ_Z^2. Such a process is indicated by the notation $\{Z_t\} \sim \text{WN}(0, \sigma_Z^2)$ (Broersen, 2006, p. 74). The pair (p,q) denotes the order of the ARMA process. The terms $\{a_1, a_2, \ldots, a_p\}$ and $\{b_1, b_2, \ldots, b_q\}$ are the model coefficients. If $q = 0$, $\{X_t\}$ is an autoregressive process of order p, i.e., AR(p):

$$X_t = -\sum_{i=1}^{p} a_i X_{t-i} + Z_t, \quad t \in \mathbb{N}, \tag{2.43}$$

and if $p = 0$, a moving average process of order q, i.e., MA(q):

$$X_t = \sum_{j=1}^{q} b_j Z_{t-j} + Z_t, \quad t \in \mathbb{N}. \tag{2.44}$$

It is more convenient to write equation (2.42) in the concise form as

$$A_p(r)X_t = B_q(r)Z_t, \quad t \in \mathbb{N}, \tag{2.45}$$

where $A_p(r)$ and $B_q(r)$ are the pth- and q^{th}-degree characteristic polynomials expressed as

$$A_p(r) = 1 + a_1 r + \cdots + a_p r^p, \tag{2.46}$$

$$B_q(r) = 1 + b_1 r + \cdots + b_q r^q, \tag{2.47}$$

and r is the backward shift operator defined by $r^s X_t = X_{t-s}$ for arbitrary $s \in \mathbb{N}$ (see equation (2.25)). A unique stationary solution of equation (2.42) exists if and only if $A_p(r) \neq 0$ for all $r \in \mathbb{C}$ with $|r| = 1$. This means, among other things, that the AR characteristic equation $A_p(r) = 0$ has no unit root. An ARMA(p,q) process $\{X_t\}$ is called causal (invertible) if $A_p(r) \neq 0$ $(B_q(r) \neq 0)$ for all $r \in \mathbb{C}$ with $|r| \leq 1$, indicating that the zeros of $A_p(r)$ $(B_q(r))$ are strictly outside the unit circle in the complex number domain.

Note that causality and invertibility are properties not of $\{X_t\}$ alone, but rather of the relationship between $\{X_t\}$ and $\{Z_t\}$. If $\{X_t\}$ is an ARMA(p,q) process defined by $A_p(r)X_t = B_q(r)Z_t$, where $B_q(r) \neq 0$ for $|r| = 1$, then it is always possible to find polynomials $\tilde{A}_p(r)$ and $\tilde{B}_q(r)$, as well as a WN sequence $\{Z_t^*\}$, such that $\tilde{A}_p(r)X_t = \tilde{B}_q(r)Z_t^*$ represents a causal and invertible ARMA(p,q) process. However, the new WN sequence $\{Z_t^*\}$ is not necessarily iid unless $\{Z_t\}$ is Gaussian (Brockwell and Davis, 1991, p. 127; Brockwell and Davis, 2002, p. 88).

A generalisation of the ARMA class is provided by the autoregressive integrated moving average (ARIMA) processes which incorporate a wide range of non-stationary time series. If k is a non-negative integer, then $\{Y_t\}$ is an ARIMA(p,k,q) process if the differenced process $(1-r)^k Y_t$ is a causal ARMA(p,q) process, where r is the backward shift operator, and $(1-r)^k = \Delta^k$ denotes k times application of the lag-1 difference Δ (see equation (2.25)). This definition means that $\{Y_t\}$ satisfies a difference equation of the form

$$A_p^*(r)Y_t = A_p(r)(1-r)^k Y_t = B_q(r)Z(t), \quad \{Z_t\} \sim \text{WN}(0, \sigma_Z^2), \tag{2.48}$$

where $A_p(r)$ and $B_q(r)$ are the characteristic polynomials of order p and q, respectively, and $A_p(r) \neq 0$ for all $|r| \leq 1$ (causality). The polynomial $A_p^*(r)$ has a zero of order k at $r = 1$, indicating the presence of a unit root and non-stationarity. Therefore, the process $\{Y_t\}$ is stationary if and only if $k = 0$. In this case, the ARIMA(p,k,q) process is reduced to an ARMA(p,q) process. Since non-stationary components can be efficiently eliminated by differencing, the differenced observations can be modelled and predicted based on the theory of ARMA processes. Taking advantage of the data-based removal of non-stationarity, ARIMA processes are often used in forecasting applications (Brockwell and Davis, 2002, chap. 6).

Once a causal and invertible ARMA(p,q) process is uniquely defined by equation (2.42), the associated model ACVF can be computed. Two methods are briefly described in the following text. The first one solves a set of homogenous linear difference equations (Brockwell and Davis, 2002, p. 90), while the second determines the ACVF of an ARMA process as a convolution of the separate autocovariances of the AR and MA components (Broersen, 2006, p. 74).

First Method. For a causal ARMA(p,q) process $\{X_t\}$, there exist constants $\{\psi_j\}$ such that

$$X_t = \sum_{j=0}^{\infty} \psi_j Z_{t-j} = \Psi(r)Z_t, \quad \forall t, \tag{2.49}$$

where $\sum_{j=0}^{\infty} |\psi_j| < \infty$ and $\Psi(r) = \sum_{j=0}^{\infty} \psi_j r^j$ (Brockwell and Davis, 2002, p. 85). Regarding equations (2.45) and (2.49), $\{\psi_j\}$ can be determined based on the relation $\Psi(r) = B_q(r)/A_p(r)$, or equivalently by the identity

$$(1 + a_1 r + \cdots + a_p r^p)(\psi_0 + \psi_1 r + \cdots) = 1 + b_1 r + \cdots + b_q r^q. \tag{2.50}$$

Comparing the coefficients of r^j yields

$$\psi_j + \sum_{k=1}^{p} a_k \psi_{j-k} = b_j, \quad j = 0, 1, \ldots, \tag{2.51}$$

where $b_0 := 1$, $b_j := 0$ for $j > q$, and $\psi_j := 0$ for $j < 0$. Substituting the ARMA coefficients $\{a_1, a_2, \ldots, a_p\}$ and $\{b_1, b_2, \ldots, b_q\}$ into equation (2.51), the constants $\{\psi_j\}$ can be calculated successively. Multiplying each side of the ARMA(p,q) process

$$X_t + a_1 X_{t-1} + \cdots + a_p X_{t-p} = Z_t + b_1 Z_{t-1} + \cdots + b_q Z_{t-q} \tag{2.52}$$

by $X_{t-k} = \sum_{j=0}^{\infty} \psi_j Z_{t-k-j}$, $k = 0, 1, 2, \ldots$, and taking expectations on each side, it follows that

$$\gamma_X(k) + a_1 \gamma_X(k-1) + \cdots + a_p \gamma_X(k-p) = \sigma_Z^2 \sum_{j=0}^{\infty} b_{k+j} \psi_j, \quad 0 \le k < m, \tag{2.53}$$

$$\gamma_X(k) + a_1 \gamma_X(k-1) + \cdots + a_p \gamma_X(k-p) = 0, \quad k \ge m, \tag{2.54}$$

where $m = \max(p, q+1)$, $\psi_j := 0$ for $j < 0$, $b_0 = 1$, and $b_j := 0$ for $j \notin \{0, \ldots, q\}$ (Brockwell and Davis, 2002, p. 90; Broersen, 2006, p. 77). Equation (2.54) represents a set of homogenous linear difference equations with constant coefficients, and the solution has the form

$$\gamma_X(h) = \beta_1 \xi_1^{-h} + \beta_2 \xi_2^{-h} + \cdots + \beta_p \xi_p^{-h}, \quad h \ge m - p, \tag{2.55}$$

where $\xi_1, \ldots, \xi_p$ are the roots of the characteristic equation $A_p(r) = 0$ (see equation (2.46)), and $\beta_1, \ldots, \beta_p$ are arbitrary constants (Brockwell and Davis, 1991, sect. 3.6). Substituting the solution (2.55) into equation (2.53), the constants $\beta_1, \ldots, \beta_p$ and the $m - p$ autocovariances $\gamma_X(h)$ with $0 \le h < m - p$ can be uniquely determined by solving a set of m linear equations. Substituting the determined $\beta_1, \ldots, \beta_p$ into equation (2.55), the autocovariances $\gamma_X(h)$ are obtained for $h \ge m - p$. Once the ACVF of the ARMA(p, q) process is known, the corresponding ACF and PACF can be computed using equations (2.34) and (2.40), respectively.

Second Method. This approach considers an ARMA(p, q) process as a combination of an AR(p) process $\{V_t\}$ and a MA(q) process $\{X_t\}$, i.e.,

$$A_p(r) V_t = Z_t, \quad X_t = B_q(r) V_t. \tag{2.56}$$

Multiplying both sides of the AR(p) equation by V_{t-k}

$$(V_t + a_1 V_{t-1} + \cdots + a_p V_{t-p}) \cdot V_{t-k} = Z_t \cdot V_{t-k}, \tag{2.57}$$

and taking expectations on each side yields

$$\gamma_V(0) \left[1 + a_1 \rho_V(1) + \cdots + a_p \rho_V(p) \right] = \sigma_Z^2, \quad k = 0, \tag{2.58}$$

$$\rho_V(k) + a_1 \rho_V(k-1) + \cdots + a_p \rho_V(k-p) = 0, \quad k \ge 1. \tag{2.59}$$

After solving the linear equation system resulting from equation (2.59), the autocorrelation coefficients $\rho_V(1), \ldots, \rho_V(p)$ can be uniquely determined (Broersen, 2006, sect. 4.4.3). Next, they are substituted into equation (2.58) to calculate the variance $\gamma_V(0)$. For an arbitrary k, the autocovariance $\gamma_V(k)$ can be computed by $\gamma_V(k) = \gamma_V(0)\rho_V(k)$, where $\rho_V(k)$ is successively derived using equation (2.59).

Considering the second part of equation (2.56), the input process $\{V_t\}$ is an autoregressive process and no longer a white noise. Therefore, the convenient approach for computing the ACVF of a MA(q) process provided by Brockwell and Davis (2002, p. 89) cannot be applied. Multiplying each side of the MA(q) process by X_{t-k}

$$X_t \cdot X_{t-k} = (V_t + b_1 V_{t-1} + \cdots + b_q V_{t-q}) \cdot X_{t-k}, \tag{2.60}$$

and taking expectations on each side, it follows that

$$\begin{aligned}
\gamma_X(k) &= \mathrm{E}(X_t X_{t-k}) \\
&= \mathrm{E}\left[(V_t + b_1 V_{t-1} + \cdots + b_q V_{t-q})(V_{t-k} + b_1 V_{t-k-1} + \cdots + b_q V_{t-k-q}) \right].
\end{aligned} \tag{2.61}$$

Making use of the associated covariances, equation (2.61) can be written as

$$
\gamma_X(k) = (1 \; b_1 \; \cdots \; b_q)
\begin{pmatrix}
\gamma_V(k) & \gamma_V(k+1) & \cdots & \gamma_V(k+q) \\
\gamma_V(k-1) & \gamma_V(k) & \cdots & \gamma_V(k+q-1) \\
\vdots & \vdots & \vdots & \vdots \\
\gamma_V(k-q) & \gamma_V(k-q+1) & \cdots & \gamma_V(k)
\end{pmatrix}
\begin{pmatrix}
1 \\
b_1 \\
\vdots \\
b_q
\end{pmatrix},
\tag{2.62}
$$

or in a more compact form as

$$
\gamma_X(k) = \sum_{m=-q}^{q} \left(\gamma_V(k+m) \sum_{j=0}^{q} b_j \, b_{j+|m|} \right), \quad \forall k.
\tag{2.63}
$$

Obviously, the ACVF of an ARMA(p,q) process $\{X_t\}$ can be calculated as a convolution of the autoregressive ACVF $\gamma_V(k)$ with the sum of products of the MA coefficients (Broersen, 2006, p. 75). Based on the ACVF of $\{X_t\}$, the corresponding ACF and PACF can be easily derived.

2.2.4 An example of the classical decomposition model

To demonstrate the general approach to time series modelling, an example of the classical decomposition model is presented in this section. Figure 2.1(a) shows the monthly sales (in kiloliters) of red wine by Australian winemakers from January 1980 to December 1990. Given a set of n observations available at uniformly spaced time intervals, the time axis is usually rescaled in such a way that the set of times T becomes the set of integers $\{1, 2, \ldots, n\}$. In this example, T has a total of 11 years $\times$ 12 months $= 132$ elements. The graph illustrates that the sales have an upward trend and a seasonal pattern with a peak in July and a trough in January. Furthermore, the seasonal and noise fluctuations seem to increase with time. This appearance suggests a preliminary data transformation, for example, using the Box-Cox transformation given by equation (2.22). In figure 2.1(b), the transformed data obtained by setting $\lambda = 0$ exhibit considerably more homogenous variability along the upward trend, and can thus be more appropriately described by a classical decomposition model than the original data. Since the transformed observations appear to increase at a roughly linear rate, a parametric trend model of the form $m_t = a_0 + a_1 t$ is estimated by means of the ordinary LS (OLS) regression.

(a) Original data y_t 　　　　　　　　　　(b) Transformed data $f_\lambda(y_t)$ and linear trend $\hat{m}_t$
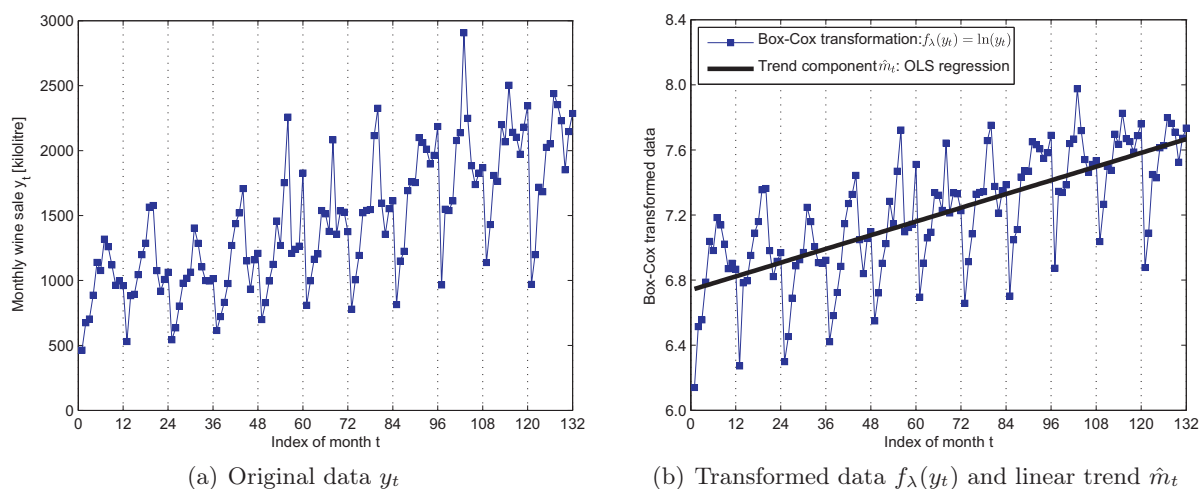
Figure 2.1: Monthly Australian red wine sales from January 1980 to December 1990 with Box-Cox transformation and linear trend estimation (Brockwell and Davis, 2002, p. 2)

After subtracting the estimated linear trend $\hat{m}_t$ from the Box-Cox transformed data, figure 2.2 displays the seasonal component determined by applying the empirical averaging method (EAM; see equation (2.23)) and analytical harmonic regression (see equation (2.24)). The regression order and all fixed frequencies are determined by performing a spectral analysis (see figure 2.2(b)), where the normalised frequency axis, normally ranging from 0 Hz to the Nyquist frequency of 0.5 Hz, is converted into times per year by multiplying the frequencies by 12 months. The unknown parameters in the harmonic regression model, i.e., $a_0, a_1, \ldots, a_k$ and $b_1, \ldots, b_k$ in equation (2.24), are estimated using the OLS method.

As can be seen from figure 2.2(a), the empirical approach EAM turns out to be an efficient method for determining the seasonal component in the detrended data. Comparing the results from the harmonic regressions shown in figures 2.2(c) and (d), the higher-order harmonic with $k = 4$ enables a more accurate characterisation of the seasonal behaviour and the resulting curve is rather similar to that from the empirical averaging. The reason for the relatively poor fit using the first-order harmonic with $k = 1$ can be found in the amplitude spectrum of the detrended data visualised in figure 2.2(b). Obviously, the total energy of the signal cannot be sufficiently approximated by considering only the most significant frequency of once per year (i.e., period $d = 12$ months). From this comparison, it can be concluded that although sometimes the dominant period is quite visible in the time domain, a spectral analysis of the detrended data is strongly advisable for a more reasonable specification of the order of harmonics.

(a) Empirical averaging method (EAM)

(b) Amplitude spectrum of the detrended data

(c) Harmonic regression with $k = 1$

(d) Harmonic regression with $k = 4$
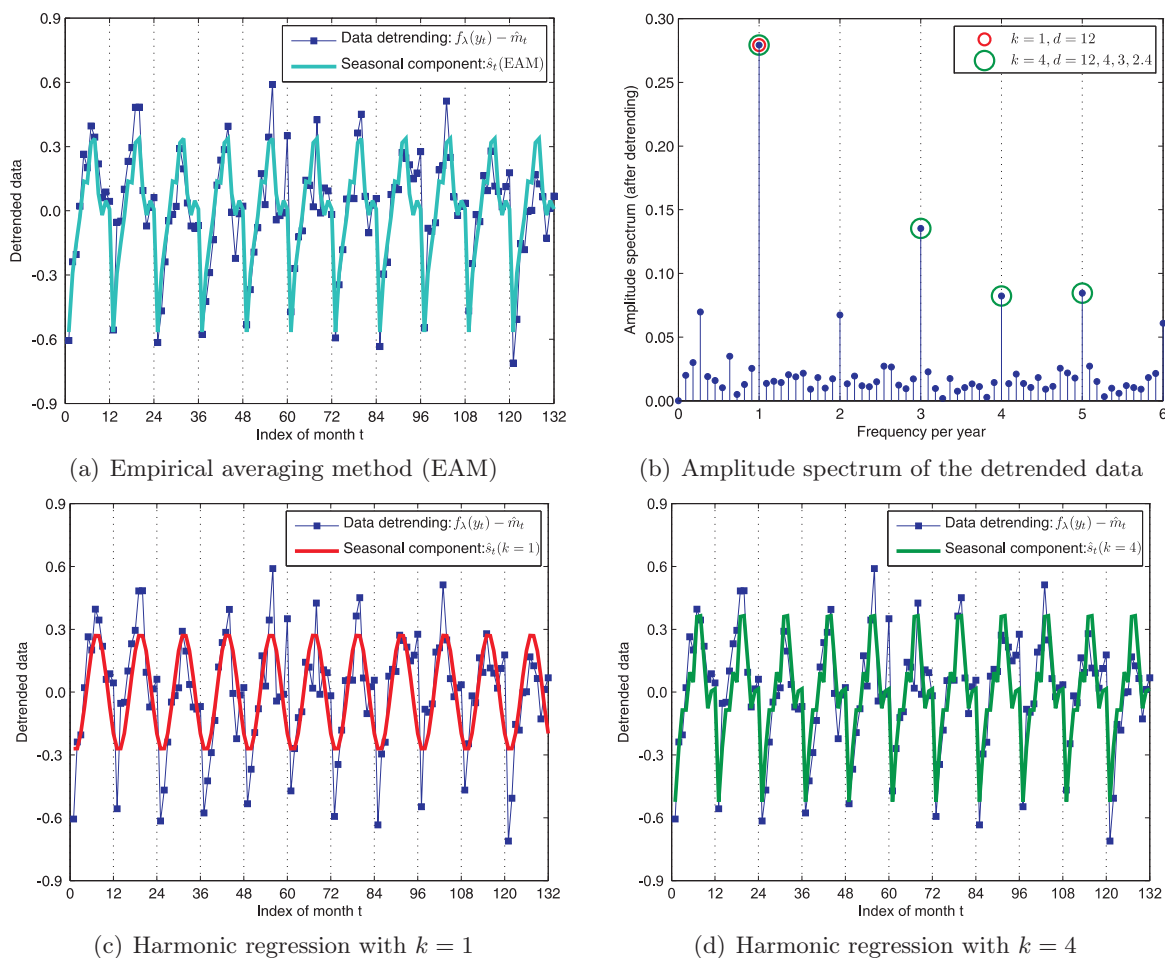
Figure 2.2: Determination of the seasonal component $\hat{s}_t$ of the time series shown in figure 2.1 by applying empirical averaging and harmonic regressions (see equations (2.23) and (2.24))

After removing the seasonal component $\hat{s}_t$ determined using different techniques, the resulting noise series and the associated amplitude spectra are depicted in figure 2.3. Due to the better performance of the EAM and fourth-order harmonic regression, the corresponding noise series are more homogenous and exhibit smaller variation ranges. Examining figure 2.3(b), the frequencies that have not been considered in the course of harmonic regression illustrate significant noise amplitude spectra. Furthermore, the advantages of the empirical averaging over the harmonic regression are clearly visible at the frequencies of twice and six times per year. In addition to the annual and sub-annual periodicities, the first significant peak in figure 2.3(b) at a frequency (period) of about 0.27 times per year (3.7 years) indicates a long-periodic signal, which may be attributed to an artefact without a realistic background (Fischer et al., 2011).

(a) Noise time series   (b) Noise amplitude spectrum
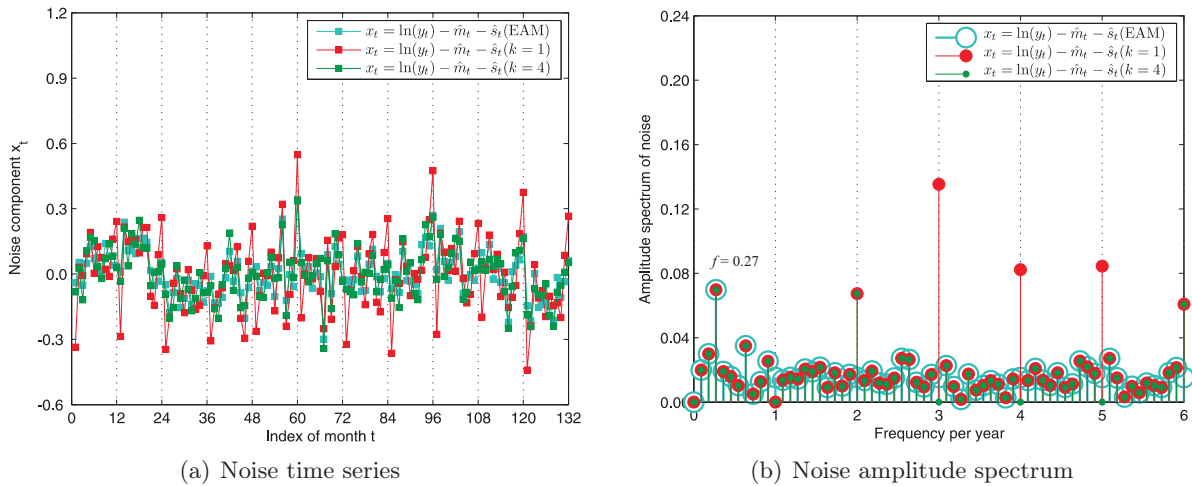
Figure 2.3: Noise component after applying linear detrending and different deseasonalisation methods to the time series shown in figure 2.1

Although ACF and PACF are defined for stationary time series (Brockwell and Davis, 2002, p. 16), their empirical versions are often used in practice even if the data do not fulfil the stationarity conditions given by equations (2.31) and (2.32). To illustrate the difficulties in the interpretation of the correlation behaviour caused by the systematic components, figure 2.4 compares the sample ACF and PACF of the Box-Cox transformed, linearly detrended, and differently deseasonlised (noise) data. In terms of the maximum lag value, Brockwell and Davis (2002, p. 404) noted that the sample ACF and PACF are good estimates of the ACF and PACF of a stationary process for lags up to about one third of the sample size, i.e., $h_{\max} = 132/3 = 44$.

As the graphs show, the trend and seasonal components have a significant impact on the temporal correlation structure represented by the sample ACF and PACF. A sample ACF which is positive and very slowly decaying implies that the data may have a trend (see the Box-Cox transformed data in figure 2.4(a)). A sample ACF with very slowly damped periodicity suggests the presence of a periodic seasonal component (see the linearly detrended data in figure 2.4(a)). In comparison to the sample ACF, the sample PACF depicted in figure 2.4(b) appears to be primarily affected by the seasonal component. In this example, the better performance of the EAM technique in modelling seasonality is verified by the lower variations in the corresponding noise's sample ACF and PACF. The dashed horizontal lines in the figures are the confidence bounds $\pm 1.96/\sqrt{n}$. If the data series represents a realisation of an iid sequence, approximately 95% of the sample autocorrelations should lie within these bounds (see equation (2.38)). Large or frequent excursions from the bounds indicate significant dependencies in the data. Under the assumption that the trend and seasonal components have been sufficiently reduced, the remaining noise can be modelled by means of ARMA processes.

(a) Sample ACF   (b) Sample PACF
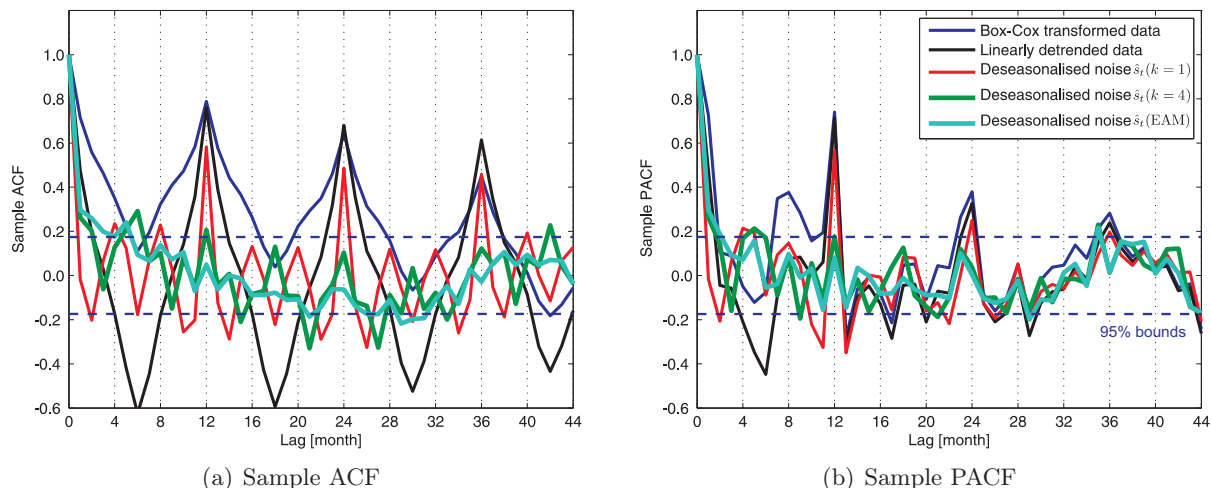
Figure 2.4: Comparison of the sample ACF and PACF of the Box-Cox transformed, linearly detrended, and differently deseasonlised (noise) data for the data set shown in figure 2.1

The determination of a well-fitting ARMA(p,q) model to represent a stationary times series involves a number of interrelated problems, such as the choice between AR(p), MA(q), and ARMA(p,q) processes, the selection of the order parameters p and q, as well as the estimation of the model coefficients $\{a_1, a_2, \ldots, a_p\}$, $\{b_1, b_2, \ldots, b_q\}$, and the WN variance σ_Z^2. The solutions to these problems will be discussed in section 7.3. The appropriateness of the fitted ARMA model can be assessed by means of suitable hypothesis tests. Once a time series model has been properly identified and statistically verified, it can then be used to enhance our understanding of the underlying mechanisms that generate the time series data.

2.3 Statistical hypothesis tests

In this thesis, the efficiency of the residual-based temporal correlation modelling is statistically evaluated by means of various hypothesis tests for normality, trend, stationarity, and uncorrelatedness. The description of the applied test methods in this section focuses on their main characteristics as well as relative strengths and weaknesses in practical use. Prior to this, the basic theory of hypothesis testing is briefly outlined.

2.3.1 Hypothesis testing

A statistical hypothesis is a statement about a population parameter which may or may not be true. The best way to find out whether a statistical hypothesis is true or not would be to examine the entire population. Since this is often impractical, a random sample from the population is usually used to verify the consistency of the sample data with the statistical hypothesis. There are two complementary statements in a hypothesis testing problem: the null hypothesis and the alternative hypothesis. They are denoted by $\mathcal{H}_0 : \theta \in \Theta_0$ and $\mathcal{H}_1 : \theta \in \Theta_0^c$, respectively, where θ is the population parameter, and Θ_0 is some subset of the parameter space with its complement Θ_0^c. $\mathcal{H}_0$ usually represents the hypothesis that sample observations result purely by chance, while $\mathcal{H}_1$ is the hypothesis that sample observations are influenced by some non-random factor. A hypothesis is referred to as a simple hypothesis if the population distribution is completely known, and a composite one if some of the characteristic parameters of the population distribution are left unspecified. The concept of simple and composite hypotheses applies to both $\mathcal{H}_0$ and $\mathcal{H}_1$.

Hypothesis testing, also known as confirmatory data analysis in contrast to exploratory data analysis, is a formal process to decide whether to reject a null hypothesis based on sample data. A hypothesis test is typically specified by a test statistic $T := f(\{X_1, \ldots, X_n\}) = f(\boldsymbol{X})$ that represents a function of the random sample $\{X_1, \ldots, X_n\}$. The choice of a test statistic depends not only on the assumed probability model, but also on the hypotheses under consideration. From the observed data $\boldsymbol{x} = \{x_1, \ldots, x_n\}$, a realisation of T, i.e., $t = f(\boldsymbol{x})$, can be calculated. Under $\mathcal{H}_0$ the probability distribution of T can be analytically derived or asymptotically approximated. It partitions all possible values of T into a rejection region (R) and a complementary non-rejection region (R^c). These regions are defined by considering the significance level at which the test is carried out, and whether the test is one-sided or two-sided.

In the case of simple hypotheses, the significance level, usually denoted by the Greek symbol α, is the probability that the test incorrectly rejects the null hypothesis (i.e., Type I error, see table 2.3). It is set by the investigator in consideration of its consequence on the test decision. That is, one specifies α to be as small as possible to protect the null hypothesis and to prevent, as far as possible, the investigator from inadvertently making false claims. Usually, the significance level is chosen to be 1%, 5%, or 10%. A one-sided (two-sided) statistical hypothesis test means that R is on only one side (both sides) of the probability distribution of T. The choice between a one-sided and a two-sided test is determined by the purpose of the investigation. Based on the calculated test statistic $t = f(\boldsymbol{x})$ and the rejection region R, the decision rule is to reject $\mathcal{H}_0$ at a significance level of α if t is located in R, and to fail to reject $\mathcal{H}_0$ otherwise.

In addition to the decision rule based on t and R, the so-called p-value that measures the strength of evidence in support of a null hypothesis is often used to make a test decision. Assuming that $\mathcal{H}_0$ is true (i.e., $\theta \in \Theta_0$), the p-value represents the probability of obtaining a test statistic as large as or larger than t by chance alone. Mathematically, it can be expressed as

$$p(\boldsymbol{x}) = \sup_{\theta \in \Theta_0} P_\theta(T \geq t). \tag{2.64}$$

The smaller the p-value, the stronger the evidence for rejecting $\mathcal{H}_0$. If the p-value is smaller than the specified significance level α, the null hypothesis has to be rejected. In comparison to the region-based decision rule, a p-value reports the test results on a more continuous scale, rather than a dichotomous choice "Reject $\mathcal{H}_0$" or "Do not reject $\mathcal{H}_0$".

It is important to note the philosophical difference between "acceptance" and "failure to reject". The "failure to reject" terminology emphasises the fact that $\mathcal{H}_0$ is assumed to be true from the start of the test, since the data are not sufficiently persuasive to prefer $\mathcal{H}_1$ over $\mathcal{H}_0$. The expression "acceptance" indicates that $\mathcal{H}_0$ has been proved to be true simply because it cannot be rejected by the data. This is a logical fallacy known as "argumentum ad ignorantiam", asserting that a proposition is necessarily true because it has not been proven false (or vice versa; Casella and Berger, 2002, p. 374). Therefore, the phrase "failure to reject" is used in this thesis for the case that $\mathcal{H}_0$ cannot be rejected at the specified significance level.

In deciding whether to reject $\mathcal{H}_0$, a hypothesis test of $\mathcal{H}_0 : \theta \in \Theta_0$ versus $\mathcal{H}_1 : \theta \in \Theta_0^c$ may be subject to one of two types of errors. A Type I error is committed if the test incorrectly decides to reject $\mathcal{H}_0$ in spite of $\theta \in \Theta_0$. The corresponding probability can be written as $P_\theta(\theta \in \Theta_0 \wedge T \in R)$. On the other hand, if $\theta \in \Theta_0^c$, but the test decides not to reject $\mathcal{H}_0$, a Type II error is made and the associated probability is

$$P_\theta(\theta \in \Theta_0^c \wedge T \in R^c) = 1 - P_\theta(\theta \in \Theta_0^c \wedge T \in R). \tag{2.65}$$

Obviously, all the probabilistic information about the test with respect to the rejection region R is included in

$$P_\theta(T \in R) = \begin{cases} P_\theta(\theta \in \Theta_0 \wedge T \in R) = \alpha \\ 1 - P_\theta(\theta \in \Theta_0^c \wedge T \in R^c) = \beta. \end{cases} \quad (2.66)$$

On the basis of equation (2.66), the power function of a hypothesis test with rejection region R is a function of θ defined by $\zeta(\theta) = P_\theta(T \in R)$. The ideal power value is 0 for all $\theta \in \Theta_0$ (i.e., $\alpha = 0$) and 1 for all $\theta \in \Theta_0^c$ (i.e., $\beta = 1$). The former indicates that $\mathcal{H}_0$ is never erroneously rejected and the latter implies that $\mathcal{H}_1$ is permanently correctly identified. However, these ideal situations cannot be reached in reality. A good hypothesis test has a power function near 0 for most $\theta \in \Theta_0$ and near 1 for most $\theta \in \Theta_0^c$. The two types of errors committed in hypothesis testing are summarised in table 2.3.

Table 2.3: Two types of errors committed in hypothesis testing

Test decision	Actual condition	
	$\mathcal{H}_0$ **is true** $(\theta \in \Theta_0)$	$\mathcal{H}_1$ **is true** $(\theta \in \Theta_0^c)$
Failure to reject $\mathcal{H}_0$ $(T \in R^c)$	Correct decision $P_\theta(\theta \in \Theta_0 \wedge T \in R^c) = 1 - \alpha$	Type II error $P_\theta(\theta \in \Theta_0^c \wedge T \in R^c) = 1 - \beta$
Reject $\mathcal{H}_0$ $(T \in R)$	Type I error $P_\theta(\theta \in \Theta_0 \wedge T \in R) = \alpha$ (significance level)	Correct decision $P_\theta(\theta \in \Theta_0^c \wedge T \in R) = \beta$

Considering a class $\mathcal{C}$ of statistical tests for verifying $\mathcal{H}_0 : \theta \in \Theta_0$ versus $\mathcal{H}_1 : \theta \in \Theta_0^c$, a test with power function $\zeta^*(\theta)$ is called the uniformly most powerful (UMP) test at significance level α_0 if $\zeta^*(\theta) \leq \alpha_0$ for all $\theta \in \Theta_0$ and $\zeta^*(\theta) \geq \zeta(\theta)$ for all $\theta \in \Theta_0^c$, where $\zeta(\theta)$ is the power function of a test in class $\mathcal{C}$. For example, according to the Neyman-Pearson lemma (Lehmann and Romano, 2005, p. 59), the simple likelihood-ratio test is UMP when comparing the fit of two models (Amiri-Simkooei, 2007, p. 13). Moreover, it is worth mentioning that a UMP test may not exist, particularly for two-sided alternative hypotheses.

2.3.2 Tests for normality

If the noise component $\{X_t\}$ resulting from the classical decomposition model represents a Gaussian process, i.e., all of its joint distributions are normal, then stronger conclusions can be drawn when fitting a time series model to the data (Brockwell and Davis, 2002, p. 38). This section begins by specifying the null and alternative normality hypotheses. After that, four test methods based on different principles are briefly outlined, allowing one to verify whether it is reasonable to assume that observations from an iid sequence are Gaussian.

The null hypothesis states that the sample $\{x_1, \ldots, x_n\}$ from an iid process $\{X_t\} \sim \text{IID}(\mu_X, \sigma_X^2)$, $t = 1, \ldots, n$, follows a normal distribution with mean μ_X and variance σ_X^2. Taking the iid property of $\{X_t\}$ into account, $\{x_1, \ldots, x_n\}$ can be interpreted as n independent realisations of a normally distributed random variable $X \sim \mathcal{N}(\mu_X, \sigma_X^2)$. Therefore, the null hypothesis $\mathcal{H}_0$ and the complementary alternative hypothesis $\mathcal{H}_1$ can be formulated as

$$\mathcal{H}_0 : F(x) = F_0(x) = \Phi(x, \mu_X, \sigma_X^2), \quad \mathcal{H}_1 : F(x) \neq F_0(x), \quad (2.67)$$

where $F(x)$ denotes the cumulative distribution function (CDF) of X. The empirical CDF $F_n(x)$ represents an estimate of $F(x)$ and is given by

$$F_n : \mathbb{R} \to [0, 1], \quad x \to F_n(x) = \sum_{x_i \leq x} h(x_i), \quad i = 1, \dots, n, \tag{2.68}$$

where $h(x_i)$ is the relative frequency of x_i. According to the strong law of large numbers, $F_n(x)$ converges almost surely to $F(x)$ for all fixed x and $n \to \infty$ (Casella and Berger, 2002, p. 235). Therefore, $F_n(x)$ represents a consistent and unbiased estimate of $F(x)$.

The Jarque-Bera (JB) test assesses deviations from a normal distribution using the sample skewness and kurtosis, also known as the third and fourth standardised moments, respectively. In Jarque and Bera (1987), the test statistic T_{JB} is defined as

$$T_{JB} = \frac{n}{6} \left[g_1^2 + \frac{(g_2 - 3)^2}{4} \right], \quad g_1 = \frac{m_3}{m_2^{3/2}}, \quad g_2 = \frac{m_4}{m_2^2}, \tag{2.69}$$

where g_1 is the sample skewness, g_2 is the sample kurtosis, and m_r is the r-th central sample moment given by $m_r = \frac{1}{n} \sum_{i=1}^{n} (x_i - \bar{x})^r$, with $\bar{x}$ denoting the arithmetical mean. Asymptotically, T_{JB} follows a chi-square distribution with two degrees of freedom (i.e., $T_{JB} \to \chi_2^2$). The null hypothesis of normality is rejected at a significance level of α if $T_{JB} > \chi_{2;1-\alpha}^2$.

As is well known, the sample moments are very sensitive to outliers. Accordingly, T_{JB} is sensitive to extreme observations as well. Using a robust measure of variance, Gel and Gastwirth (2008) suggested an advanced JB test which is more resistant to outliers and delivers equal or higher statistical power than the standard JB test. In addition, the chi-square distribution approximation of T_{JB} is poorly suited for small sample sizes. This leads to a high probability of wrongly rejecting $\mathcal{H}_0$ (Type I error, see table 2.3). For sample sizes $n < 2000$, the MATLAB® Statistics Toolbox™ (MST) uses critical values computed by means of Monte-Carlo simulations.

The chi-square (CS) test, also referred to as Pearson's chi-square goodness-of-fit test (Plackett, 1983), verifies whether the frequency distribution of an observed sample is consistent with the assumed theoretical one (Lehmann and Romano, 2005, chap. 14). The computation of the chi-square test statistic

$$T_{CS} = \sum_{k=1}^{m} \frac{(O_k - E_k)^2}{E_k} \tag{2.70}$$

is performed by grouping the data into m bins first and then evaluating the observed (O_k) and the expected counts (E_k) for those bins. E_k is calculated using $E_k = n[F_0(c_u) - F_0(c_l)]$, where c_u and c_l are the upper and lower boundaries of class k, respectively. Asymptotically, T_{CS} follows a chi-square distribution with $(m - u)$ degrees of freedom (i.e., $T_{CS} \to \chi_{m-u}^2$), where u is the number of unknown parameters characterising the hypothesised distribution plus one (e.g., $u = 3$ for a normal distribution). $\mathcal{H}_0$ is rejected at a significance level of α if $T_{CS} > \chi_{m-3;1-\alpha}^2$.

The CS test can be applied to both discrete (e.g., binomial, Poisson) and continuous distributions. However, T_{CS} is sensitive to the choice of bins. According to Reißmann (1980, p. 359), m between 10 and 15 with a bin width of approximately $s/2$ (s: sample standard deviation) seems to be a reasonable choice in practice. Moreover, the expected counts E_k in each bin should not be less than 5. Therefore, the CS test requires a sufficiently large sample size for reliable test results.

The Lilliefors (LF) test is based on a single distance measure defined as the supremum of the absolute difference between the empirical (F_n) and theoretical CDF (F_0) (Lilliefors, 1967):

$$T_{LF} = \sup_{1 \leq i \leq n} |F_n(x_i) - F_0(x_i)|. \tag{2.71}$$

The LF test is particularly suitable for composite hypotheses, where the location and shape parameters (e.g., mean, variance) are not fully specified, but are estimated from data. For small sample sizes ($n \leq 30$), Lilliefors (1967, p. 400) provided critical values $C_{LF,1-\alpha}$ for T_{LF} at different significance levels (see table A.3). In the case of $n > 30$, $C_{LF,1-\alpha}$ can be obtained by analytical approximation or Monte-Carlo simulations, as implemented in the MST. $\mathcal{H}_0$ is rejected at a significance level of α if $T_{LF} > C_{LF,1-\alpha}$. Additional information about the LF test is available in Conover (1999, p. 443) and Abdi and Molin (2007).

Making use of the identical test statistic as the LF test, the Kolmogorov-Smirnov (KS) test is applicable for simple hypotheses, where the theoretical CDF has been predetermined or completely specified (Chakravarti et al., 1967, p. 392-394). Employing the KS test to verify the composite normality hypothesis of representative GPS observation residuals, Luo et al. (2011a) found a large rate of erroneous non-rejection of $\mathcal{H}_0$ (Type II error, see table 2.3).

The Anderson-Darling (AD) test uses a weighted (higher weight to the tails) overall distance measure between the empirical and theoretical CDF to verify if a sample of data comes from a population with the hypothesised distribution (Anderson and Darling, 1952). The AD test statistic is defined as

$$T_{AD} = -n - \sum_{i=1}^{n} \frac{(2i-1)}{n} \left\{ \ln F_0(y_i) + \ln\left[1 - F_0(y_{n+1-i})\right]\right\}, \tag{2.72}$$

where y_i are the sorted data in ascending order. Applying the AD test for normal distribution, y_i can be replaced by $(x_i - \bar{x})/s$ ($\bar{x}$, s: sample mean and standard deviation) and F_0 by the CDF of the standard normal distribution $\mathcal{N}(0,1)$, where x_i are also sorted in ascending order. Considering the modified test statistic

$$T_{AD}^* = \left(1 + \frac{0.75}{n} + \frac{2.25}{n^2}\right) T_{AD}, \tag{2.73}$$

adjusted with respect to sample size n, the critical values $C_{AD,1-\alpha}$ for the composite hypothesis of normality are available in Stephens (1986, table 4.9) for different significance levels. $\mathcal{H}_0$ is rejected at a significance level of α if $T_{AD}^* > C_{AD,1-\alpha}$.

Although the AD test is restricted to continuous distributions, Stephens (1974) found that T_{AD} is one of the best empirical CDF statistics for detecting most departures from normality. Moreover, the AD test incorporates the assumed distribution into the calculation of critical values. This results in the advantage of enabling more sensitive tests, but the disadvantage of computing individual critical values for each kind of distribution to be tested.

2.3.3 Tests for trend

Within the framework of classical decomposition (see section 2.2.1), a slowly changing trend component has to be estimated and removed before finding a satisfactory time series model for the noise component. The performance of the detrending procedure can be verified by means of hypothesis tests for trend. Furthermore, the results of trend tests help specify parameters

when applying the unit root tests for stationarity (see section 2.3.4). Two non-parametric trend tests are employed in this thesis to verify the null hypothesis $\mathcal{H}_0$ that there is no trend in the realisation of an iid sequence $\{x_1, \ldots, x_n\}$ against the alternative hypothesis $\mathcal{H}_1$ that a monotonic trend is present. Additional trend tests with examples can be found in Gilbert (1987, chap. 16), Hipel and McLeod (1994, chap. 23), and Hartung et al. (2005, chap. 4).

The Cox-Stuart (CT) test relies upon the simple principle that a data series exhibits an upward (downward) trend if the earlier observations tend to be smaller (larger) than the later ones (Cox and Stuart, 1955). The test statistic T_{CT} is defined as the number of positive differences y_i, given by

$$y_i = x_{i+m} - x_i, \quad i = \begin{cases} 1, \ldots, m & m = n/2, & \text{if } n \text{ is even,} \\ 1, \ldots, m-1 & m = (n+1)/2, & \text{if } n \text{ is odd.} \end{cases} \tag{2.74}$$

In fact, T_{CT} follows a binomial distribution $T_{CT} \sim Bin(L, p)$ with $p = 1/2$, where L denotes the number of non-zero y_i. If $L < 20$, the test decision can be made based on the q-quantile of the binomial distribution $B_{L, p; q}$, i.e., $\mathcal{H}_0$ is rejected at a significance level of α if $T_{CT} < B_{L, p; \alpha/2}$ or $T_{CT} > B_{L, p; 1-\alpha/2}$. For large L values (e.g., $L \geq 20$), the modified test statistic

$$Z_{CT} = \frac{T_{CT} - L/2}{\sqrt{L}/2} \tag{2.75}$$

follows asymptotically the standard normal distribution $\mathcal{N}(0, 1)$ and can be used to make the test decision (Hartung et al., 2005, p. 242). This modification can be easily derived by approximating the binomial distribution $Bin(L, p)$ by the normal distribution $\mathcal{N}(Lp, Lp(1-p))$, where $p = 1/2$. In general, this approximation improves as L increases and is more appropriate when p is not close to 0 or 1 (Box et al., 1978, p. 130). $\mathcal{H}_0$ is rejected at a significance level of α if $|Z_{CT}| > z_{1-\alpha/2}$, where z_q denotes the q-quantile of the standard normal distribution.

The Mann-Kendall (MK) test originates from the non-parametric test for randomness proposed by Mann (1945), which constitutes a particular application of Kendall's test for correlation between two measured quantities (Kendall, 1975). The MK test evaluates the observed data as an ordered time series, and each observation is compared to all subsequent values. Under the null hypothesis of a trend-free $\boldsymbol{x}$, the MK test statistic is

$$T_{MK} = \sum_{k=1}^{n-1} \sum_{j=k+1}^{n} \text{sgn}(x_j - x_k), \quad \text{sgn}(x) = \begin{cases} +1, & x > 0, \\ 0, & x = 0, \\ -1, & x < 0, \end{cases} \tag{2.76}$$

where $\text{sgn}(x)$ is the signum function of a real number x (Hartung et al., 2005, p. 249). A very large positive value of T_{MK} indicates that there exists an upward trend in which the observations increase with time. On the other hand, a very low negative value of T_{MK} means that a downward trend is present. For small sample sizes ($n \leq 40$), the q quantile of the Kendall's K-statistic $K_{n; q}$ can be used as the critical value for T_{MK}. $\mathcal{H}_0$ is rejected at a significance level of α if $T_{MK} < -K_{n; 1-\alpha/2}$ or $T_{MK} > K_{n; 1-\alpha/2}$. These quantile values are elaborately tabulated for different significance levels by Hollander and Wolfe (1999, p. 724–731). In the case of large n, the transformed test statistic

$$Z_{MK} = \frac{T_{MK}}{\sqrt{n(n-1)(2n+5)/18}} \tag{2.77}$$

follows asympototically the standard normal distribution (Hartung et al., 2005, p. 250). If Z_{MK} is significantly different from zero, for example, fulfilling $|Z_{MK}| > z_{1-\alpha/2}$, $\mathcal{H}_0$ is rejected at a significance level of α, suggesting the existence of a monotonic trend.

An attractive feature of the non-parametric trend tests is that they are distribution-free in the sense that the data to be tested do not need to conform to any particular distribution. However, several limitations should be kept in mind. For example, these tests are incapable of accounting for the magnitude of the data or the temporal variations in the data (e.g., changes in slope). Moreover, the slowly varying trend component should not repeat within the time range captured by the data. In the presence of seasonality, the so-called (correlated) seasonal MK tests can be applied (Hipel and McLeod, 1994, p. 866–871).

2.3.4 Tests for stationarity

The trend tests introduced above provide information on the presence of trends, but not on their types. According to the physical nature and causes, trend signals in time series data can be classified into deterministic and stochastic trends. Deterministic trends are regulated by time and imply the fact that all deviations from the long-run equilibrium path are only temporary. In contrast, stochastic trends are caused by cumulated shocks which have persistent effects over time. In this case, the deviations from the trending path will hardly return. Accordingly, these kinds of shocks are called permanent in contrast to the transitory shocks inducing deterministic trends (Kirchgässner and Wolters, 2008, p. 191).

A time series that is stationary around a deterministic trend is called trend-stationary, while a non-stationary time series due to stochastic trends that becomes stationary after applying serial difference operators is called difference-stationary (see equation (2.25)). Whether a time series is trend- or difference-stationary is not only important for selecting an appropriate detrending technique, but also has a considerable impact on the associated physical interpretation of the trend signals. Table 2.4 presents the consequences of trend handling using regression and differencing. Generally, the influence of spurious regression is more serious than erroneously applying difference operators to trend-stationary time series (see section 2.2.1).

Table 2.4: Consequences of handling trend signals by means of regression and differencing

Trend handling	True type of trend	
	Deterministic (trend-stationary)	Stochastic (difference-stationary)
Regression	Ok, eventually autocorrelated noise	Spurious regression, biased estimator
Differencing	Autocorrelated noise	Ok, eventually autocorrelated noise

Two unit root tests for stationarity are used in this thesis. The augmented Dickey-Fuller (ADF) test verifies difference-stationarity and looks for autoregressive (AR) unit roots. The Kwiatkowski-Phillips-Schmidt-Shin (KPSS) test examines trend-stationarity and is based on moving average (MA) unit roots. By testing both AR and MA unit roots, one may distinguish series that appear to be difference-stationary, trend-stationary, and series for which the data or the test methods are not sufficiently informative to make a decision whether they are stationary or not. This section gives a brief introduction to the ADF and KPSS tests. For a more detailed discussion of unit root testing, see, for example, Stock (1994, chap. 46), Maddala and Kim (1998), Phillips and Xiao (1998), and Brockwell and Davis (2002, sect. 6.3).

The augmented Dickey-Fuller (ADF) test is based on the existence and uniqueness property of an ARMA(p, q) process, i.e., the pth-degree autoregressive characteristic equation $A_p(r) = 0$ given by equation (2.46) has no unit root (Said and Dickey, 1984). Assuming that the stochastic dynamics in the data can be sufficiently described by an ARMA process, the regression model of the ADF test, verifying the null hypothesis $\mathcal{H}_0$ that $\{x_t\}$ is difference-stationary against the alternative hypothesis $\mathcal{H}_1$ that $\{x_t\}$ is trend-stationary, is formulated as

$$x_t = c + \delta t + \phi x_{t-1} + \sum_{j=1}^{l-1} \vartheta_j \Delta x_{t-j} + z_t, \tag{2.78}$$

where c and δ capture the deterministic trend, and the $(l-1)$ difference terms Δx_{t-j} approximate the ARMA structure of the residuals. Neglecting the deterministic trend $c + \delta t$, the presentability of an ARMA process by the ADF regression model is mathematically proved in appendix B.1. If the truncation lag l is set to a too small value, the remaining serial (or temporal) correlations in regression residuals will bias the test. If l is too large, then the power of the ADF test will suffer. Ng and Perron (1995) proposed a data-based procedure for selecting appropriate truncation lags. At first, the test regression is performed with a maximum lag value $l = l_{max}$, such as the one recommended by Schwert (1989):

$$l_{\max} = \left\lfloor 12 \cdot \left(\frac{n}{100}\right)^{1/4} \right\rfloor, \tag{2.79}$$

where $\lfloor x \rfloor$ denotes the integer part of x. Then, the significance of the coefficient of the last lagged difference is assessed by applying the t-statistic. If this coefficient is statistically significant, the unit root test is carried out. Otherwise, the lag value l is reduced by one and the procedure is repeated. The truncation lag determined in this manner leads to a stable size (i.e., probability of incorrectly rejecting $\mathcal{H}_0$, Type I error, see table 2.3) and a minimum power loss. The test statistic of the ADF test

$$T_{ADF} = t_{\phi=1} = \frac{\hat{\phi} - 1}{SE(\hat{\phi})} \tag{2.80}$$

is computed based on the OLS estimates of equation (2.78), where $SE(\hat{\phi})$ denotes the standard error of $\hat{\phi}$. The asymptotical distribution of T_{ADF} is referred to as the Dickey-Fuller (DF) distribution, which does not have a closed-form representation (Dickey and Fuller, 1979). The PDF of the DF distribution is slightly left-skewed and is located on the left side of Student's t-distribution. For a range of sample sizes and usual significance levels, critical values for T_{ADF} have been derived using Monte Carlo simulations (MATLAB$^\circledR$ Econometrics Toolbox$^{\text{TM}}$, MET). Furthermore, MacKinnon (1996) suggested response surface algorithms that enable the determination of critical and p-values for an arbitrary sample size. The ADF test is a one-sided left-tailed test, indicating that $\mathcal{H}_0$ is rejected at a significance level of α if $T_{ADF} < DF_\alpha$, where DF_α is the α-quantile of the DF distribution. It is worth mentioning that under $\mathcal{H}_0$, the asymptotic distribution of T_{ADF} is affected by the presence of the deterministic terms c and δ in equation (2.78), but not by their values. The modelling of a deterministic trend in the ADF test decreases the critical values and test power (see tables A.7 and A.8).

In addition to the ADF test, the Phillips-Perron (PP) test is also used to detect autoregressive unit roots (Phillips and Perron, 1988). Asymptotically, these two tests are equivalent, but they may differ substantially in finite samples due to the different handling of serial correlations in the test regression. If the ARMA representation of the lag-1 difference of $\{x_t\}$ (i.e., $\{\Delta x_t\}$) has a large and negative MA component, then the ADF and PP tests illustrate severe size distortion with a large rate of Type I error, where the PP test is more size-distorted than the ADF test (Schwert, 1989). Furthermore, the ADF and PP tests have low power against trend-stationary

alternatives which are close to being difference-stationary (e.g., stationary persistent processes). To achieve maximum power against highly persistent alternatives, the efficient autoregressive unit root tests proposed by Elliott et al. (1996) and Ng and Perron (2001) can be applied.

The Kwiatkowski-Phillips-Schmidt-Shin (KPSS) test suggested by Kwiatkowski et al. (1992) makes use of the fact that the serial difference of a causal and invertible $ARMA(p, q)$ process results in a non-invertible $ARMA(p, q + 1)$ model, and the associated MA characteristic equation is supposed to have a unit root (Brockwell and Davis, 2002, p. 196). This is known as overdifferencing, i.e., one erroneously considers the time series as difference-stationary while it is actually trend-stationary. The KPSS test has the regression model

$$y_t = c + \delta t + u_t + x_t, \quad u_t = u_{t-1} + z_t, \quad z_t \sim \text{WN}(0, \sigma_z^2), \tag{2.81}$$

where $c + \delta t$ describes the deterministic trend, $\{u_t\}$ represents a pure random walk with innovation variance σ_z^2, and $\{x_t\}$ denotes a stationary error. The null hypothesis of trend-stationary $\{y_t\}$ is formulated as $\mathcal{H}_0 : \sigma_z^2 = 0$, indicating that $\{u_t\}$ must be a constant. The alternative hypothesis of difference-stationary $\{y_t\}$ is expressed as $\mathcal{H}_1 : \sigma_z^2 > 0$. Although it is not explicitly apparent, $\mathcal{H}_0$ implies a MA unit root in the ARMA representation of $\{\Delta y_t\}$, which is mathematically illustrated in appendix B.2. Assuming that $\{x_t\}$ satisfies the (strong mixing) regularity conditions of Phillips and Perron (1988, p. 336) or the linear process conditions of Phillips and Solo (1992), the KPSS test statistic is the modified Lagrange multiplier

$$T_{KPSS} = \left(n^{-2} \sum_{t=1}^{n} \hat{S}_t^2 \right) / \hat{\lambda}^2 \tag{2.82}$$

with

$$\hat{S}_t = \sum_{i=1}^{t} \hat{x}_i, \quad t = 1, 2, \ldots, n \tag{2.83}$$

and

$$\hat{\lambda}^2 = \frac{1}{n} \sum_{t=1}^{n} \hat{x}_t^2 + \frac{2}{n} \sum_{j=1}^{l} \omega_{jl} \sum_{t=j+1}^{n} \hat{x}_t \hat{x}_{t-j}. \tag{2.84}$$

$\hat{S}_t$ denotes a partial sum process of the residual $\{\hat{x}_t\}$ resulting from an OLS regression of $\{y_t\}$ on $c + \delta t$, and $\hat{\lambda}^2$ is a consistent estimate of the long-run variance of $\{x_t\}$ using $\{\hat{x}_t\}$ (Perron, 1988). For the consistency of $\hat{\lambda}^2$, the truncation lag $l = O(n^{1/2})$ will usually be satisfactory under both the null (Andrew, 1991) and the alternative hypothesis (Kwiatkowski et al., 1992). The term ω_{jl} in equation (2.84) is a weight function corresponding to the choice of a spectral window in the frequency domain. Newey and West (1987) used the Bartlett window which ensures non-negativity of $\hat{\lambda}^2$ values. Under the null hypothesis that $\{y_t\}$ is trend-stationary, Kwiatkowski et al. (1992) showed that T_{KPSS} converges to a function of a standard Brownian motion that depends on the form of the deterministic terms (i.e., $c \neq 0$ and $\delta = 0$, $c \neq 0$ and $\delta \neq 0$), but not on their numerical values. Critical values for T_{KPSS} must be derived by means of simulation methods. The KPSS test is a one-sided right-tailed test so that $\mathcal{H}_0$ is rejected at a significance level of α if $T_{KPSS} > C_{KPSS,1-\alpha}$, where the $(1 - \alpha)$ quantiles of the asymptotical distribution of T_{KPSS} can be found in Nabeya and Tanaka (1988) and Kwiatkowski et al. (1992).

On the basis of numerous AR(1) simulations, Kwiatkowski et al. (1992) empirically investigated the size and power of the KPSS test for different sample sizes n and truncation lags l. It was found that the KPSS test rejects $\mathcal{H}_0$ (trend-stationary) too often for positively correlated data and too seldom for negatively correlated data. Furthermore, in the presence of realistic amounts of autocorrelation, using large truncation lags will mitigate the size distortion on the one hand, and decrease the test power on the other.

2.3.5 Tests for uncorrelatedness

To assess the significance of the temporal correlation in the extracted noise (i.e., residuals obtained either by estimating and subtracting the trend and seasonal components or by applying difference operators), four test methods are used in this thesis to verify the null hypothesis $\mathcal{H}_0$ that the noise data are realisations of uncorrelated random variables. If $\mathcal{H}_0$ cannot be rejected at the specified significance level, then there is no further time series modelling necessary. Otherwise, to characterise the dependence in the noise sequence, an appropriate stationary time series model can be found, for example, during the course of ARMA modelling (see section 7.3). Moreover, the appropriateness of the fitted ARMA(p, q) model can be examined by testing the uncorrelatedness of the ARMA residuals. The applied tests make use of the so-called von Neumann ratio, sample ACF, and properties of empirical spectral density. For more detailed information about uncorrelatedness tests, see, for example, Teusch (2006, chap. 6).

The von Neumann ratio (VNR) is defined as the ratio of the mean square successive difference to the sample variance, i.e.,

$$VNR := \frac{\frac{1}{n-1}\sum_{j=2}^{n}(x_j - x_{j-1})^2}{\frac{1}{n}\sum_{j=1}^{n}(x_j - \bar{x})^2} = \frac{n}{n-1}T, \quad \bar{x} = \frac{1}{n}\sum_{j=1}^{n}x_j, \tag{2.85}$$

and was suggested by von Neumann (1941, 1942) and Young (1941) as a test statistic for evaluating independence of observations $\{x_1, \ldots, x_n\}$ of a stationary Gaussian time series. The VNR is approximately 2 for a WN process and 0 (4) for a strongly positively (negatively) correlated process (Teusch, 2006, p. 100). For sample sizes ranging from 4 to 60, the critical values for the lower level of VNR $C_{n;\alpha/2}$ are tabulated in Hart (1942). Since the distribution of VNR is symmetric about $2n/(n-1)$ (von Neumann, 1941), the critical values for the upper level $C_{n;1-\alpha/2}$ can be easily derived. However, the upper limits are rarely of practical use, since large VNR values indicate strong negative correlations and alternatively varying time series data which normally arise from artificial observations (Hart, 1942). The null hypothesis of uncorrelatedness is rejected at a significance level of α if $VNR < C_{n;\alpha/2}$ or $VNR > C_{n;1-\alpha/2}$. For larger sample sizes ($n > 60$), Bingham and Nelson (1981) suggested a modified test statistic

$$T_{VNR} = \frac{(n+1)^{1/2}\tilde{\epsilon}}{(1-\tilde{\epsilon}^2)^{1/2}}, \quad \tilde{\epsilon} = \left(\frac{n^2-1}{n^2-4}\right)^{1/2}\epsilon, \quad \epsilon = 1 - \frac{T}{2}, \tag{2.86}$$

where T is given in equation (2.85), and T_{VNR} follows approximately Student's t-distribution with $n+1$ degrees of freedom. Comparing the quantile values derived based on this approximation with those computed by numerical integration of a differential equation of von Neumann (1941), four decimal accuracy is obtained for $n \geq 15$. Using this modified test statistic, the null hypothesis of uncorrelatedness is rejected at a significance level of α if $|T_{VNR}| > t_{n+1;1-\alpha/2}$.

The portmanteau test proposed by Box and Pierce (1970) uses the test statistic

$$T_{BP} = n\sum_{j=1}^{h}\hat{\rho}^2(j), \tag{2.87}$$

where $\hat{\rho}(j)$ denotes the sample ACF at lag j, and h is the number of lags considered in the test statistic (see equation (2.36)). If $\{x_1, x_2, \ldots, x_n\}$ is a realisation of an iid sequence with finite variance, based on the asymptotical probability distribution of sample ACF given in equation (2.38), T_{BP} represents the sum of squares of independent random variables $\sqrt{n}\hat{\rho}(j)$, $j = 1, \ldots, h$, each of which follows the standard normal distribution. Therefore, T_{BP} is approximately chi-squared

distributed with h degrees of freedom. A large value of T_{BP} indicates that the sample autocorrelations of the data are too high to be a sample of an uncorrelated sequence. In this thesis, a refined version of the portmanteau test proposed by Ljung and Box (1978) is applied. The test statistic is

$$T_{LB} = n(n+2) \sum_{j=1}^{h} \hat{\rho}^2(j)/(n-j) \tag{2.88}$$

whose distribution is better approximated by the chi-square distribution with h degrees of freedom. For the truncation lag h, a value between 10 and 30 seems to be sufficient (Ljung and Box, 1978). For example, the default value for h is $\min(20, n-1)$ in the MST, and 12 in the TSA (time series analysis) package of the software R (Crawley, 2007). The null hypothesis of uncorrelatedness is rejected at level α if $T_{LB} > \chi^2_{h;1-\alpha}$, where $\chi^2_{h;1-\alpha}$ is the $(1-\alpha)$ quantile of the chi-squared distribution with h degrees of freedom. Another portmanteau test can be found in McLeod and Li (1983), where the sample autocorrelations of the data are replaced by the sample autocorrelations of the squared data (Brockwell and Davis, 2002, p. 36).

The Kolmogorov-Smirnov (KV) test for uncorrelatedness is based on the maximum distance between the empirical and theoretical spectral distribution functions of a stationary process (Teusch, 2006, p. 103). The spectral density and distribution functions used in frequency-domain analysis are closely related to the ACF used in time-domain analysis (Chatfield, 2004, chap. 6). Under the null hypothesis of uncorrelatedness, the KV test statistic given by

$$T_{KV} = \max_{z \in [0,1]} \left| \frac{\sqrt{2n}}{\pi} \sum_{h=1}^{n-1} \hat{\rho}(h) \frac{\sin(\pi z \cdot h)}{h} \right| \tag{2.89}$$

follows asymptotically the Kolmogorov distribution (Kolmogorov, 1933, 1941; Feller, 1948). The mathematical derivation of T_{KV} is briefly described in appendix B.3. Using the $(1-\alpha)$ quantile of the Kolmogorov distribution $K_{1-\alpha}$, for example, provided by Kolmogorov (1941) and Teusch (2006, p. 104), the null hypothesis of uncorrelated observations is rejected at a significance level of α if $T_{KV} > K_{1-\alpha}$. In addition to the tabulated $K_{1-\alpha}$ values for usual significance levels, the critical value for an arbitrary α can be computed using the routine kolminv, which is freely available in MATLAB® Central. Marsaglia et al. (2003) wrote a C program that efficiently computes the Kolmogorov distribution with 13-15 digit accuracy for $2 \le n \le 16000$.

The Cramér-von Mises (CM) test measures the overall distance between the empirical and theoretical spectral distribution functions of a stationary process (Teusch, 2006, p. 104). Being continuous on a closed interval, the spectral distribution functions are quadratically integrable. Instead of the maximum absolute deviation in the spectral distribution, the CM test uses

$$T_{CM} = \int_0^1 \left[\frac{\sqrt{2n}}{\pi} \sum_{h=1}^{n-1} \hat{\rho}(h) \frac{\sin(\pi z \cdot h)}{h} \right]^2 dz \tag{2.90}$$

as the test statistic. The distribution of T_{CM} converges weakly to that of $\int_0^1 B_0^2(z)dz$, where $B_0(z)$ denotes the Brownian bridge. The critical values for different significance levels $C_{1-\alpha}$ can be found in Anderson and Darling (1952, table 1). The CM test is a one-sided right-tailed test, meaning that the null hypothesis of uncorrelatedness is rejected at a significance level of α if $T_{CM} > C_{1-\alpha}$. Note that the Cramér-von Mises criterion can also be used to judge the goodness of fit of a probability distribution. More detailed information about this application is available in Anderson and Darling (1952), Anderson (1962), and Teusch (2006, p. 113).

2.4 Wavelet transforms

In this thesis, wavelet transforms serve as a time-frequency analysis tool for visual inspection and interpretation of the results from the residual-based temporal correlation modelling (see sections 8.1.7 and 8.2.7). In comparison to conventional Fourier transform which assumes that the signal to be processed has temporal or spatial invariant statistical properties, analysing a given function or a time series by means of wavelets has advantages in simultaneously examining signal characteristics in both the time and frequency domains, in conveniently representing functions with discontinuities and sharp peaks, as well as in accurately deconstructing and reconstructing finite, non-periodic or non-stationary signals. This section provides some basic background to wavelets and wavelet transforms. Taking simulated times series as an example, the temporal variations are mapped into spectra using the MATLAB® Wavelet Toolbox™ (MWT).

There are a variety of textbooks on wavelet theory and its application. The reader who is primarily interested in the mathematical background of wavelet transforms is referred to Daubechies (1992) and Holschneider (1995), which contain strong theoretical components and foundations for the most current applications of wavelets. A large number of examples in terms of mathematical, physical, and engineering contexts are available in Debnath (2001). Typical applications of wavelets in geodesy and geodynamics are presented in Keller (2004), along with the fundamentals of Fourier analysis and wavelet theory. Trauth (2007, sect. 5.8) provides easy-to-understand examples and illustrates how to perform wavelet transforms using the MWT.

2.4.1 Wavelets and Morlet wavelet

In 1982, Jean Morlet, in collaboration with a group of French engineers, first used the French word "ondelette", meaning "small wave", which was transferred to English by translating "onde" into "wave", giving "wavelet". Wavelets are small packages of wave-like oscillations that approach zero at both ends (i.e., local support). Morlet et al. (1982) introduced the idea of wavelets as a family of functions constructed by translating and dilating a single function known as the "mother wavelet" $\psi(t)$:

$$\psi_{a,b}(t) = \frac{1}{\sqrt{a}} \psi\left(\frac{t-b}{a}\right), \quad a \in \mathbb{R}^+, b \in \mathbb{R}, \tag{2.91}$$

where a denotes the scale (or dilation) parameter which measures the degree of compression, and b is the translation parameter which determines the time location of the wavelet. In the case of $0 < a < 1$, the wavelet $\psi_{a,b}(t)$ is the compressed version of the mother wavelet and corresponds to high frequencies. On the other hand, if $a > 1$, $\psi_{a,b}(t)$ has a larger time width than $\psi(t)$ and corresponds to low frequencies.

The resolution of wavelets at different scales varies in the time and frequency domains as governed by Heisenberg's uncertainty principle which states that the more precisely the position is determined, the less precisely the momentum is known in this instant, and vice versa (Heisenberg, 1927). For large scale values, the resolution is coarse in the time domain, but fine in the frequency domain. Conversely, as the scale decreases, the resolution in the time domain becomes finer while that in the frequency domain becomes coarser (Debnath, 2001, p. 12). One important property of a wavelet is the so-called admissibility, formulated by

$$0 < C_\psi = 2\pi \int_{-\infty}^{+\infty} \frac{\left|\hat{\psi}(\omega)\right|^2}{|\omega|} d\omega < \infty, \tag{2.92}$$

where $\hat{\psi}(\omega)$ denotes the Fourier transform of the mother wavelet $\psi(t)$ (Debnath, 2001, p. 14). From equation (2.92) it follows immediately that

$$\hat{\psi}(\omega = 0) = 0 \Longleftrightarrow (2\pi)^{-1/2} \int_{-\infty}^{+\infty} \psi(t)dt = 0, \tag{2.93}$$

indicating that $\psi(t)$ must be an oscillatory function with zero mean (Holschneider, 1995, p. 4; Keller, 2004, p. 31). Moreover, equation (2.92) imposes a restriction on the rate of decay of $|\hat{\psi}(\omega)|^2$ and is needed for the inverse of the continuous wavelet transform (see section 2.4.2).

Many kinds of mother wavelets have been well documented in the literature, for example, the Haar wavelet that is considered as the first known wavelet (Haar, 1910), the Morlet wavelet (Goupillaud et al., 1984), and the Daubechies wavelets (Daubechies, 1992). One of the most frequently used wavelet is the Morlet wavelet, which was first employed in geophysical exploration (Grossmann and Morlet, 1985) and was at the origin of the development of wavelet analysis. The Morlet wavelet, also referred to as Morlet's Gaussian wavelet, is obtained by shifting a Gaussian function in Fourier space

$$\psi_M(t) = \pi^{-1/4} e^{i\omega_0 t} e^{-t^2/2}, \tag{2.94}$$

$$\hat{\psi}_M(\omega) = \pi^{-1/4} e^{-(\omega-\omega_0)^2/2}, \tag{2.95}$$

where $e^{i\omega_0 t} = \cos(\omega_0 t) + i\sin(\omega_0 t)$ is Euler's formula, and ω_0 is the wavenumber giving the number of oscillations within the wavelet itself (Torrence and Compo, 1998, table 1). Strictly speaking, the Morlet wavelet is not a wavelet, since it does not satisfy the admissibility condition given by equation (2.92). In particular, its Fourier transform does not vanish at $\omega = 0$, i.e.,

$$\hat{\psi}_M(0) = \pi^{-1/4} e^{-\omega_0^2/2} \neq 0. \tag{2.96}$$

However, $\hat{\psi}_M(0)$ is numerically negligibly small if $\omega_0 > 0$ is large enough (e.g., $\omega_0 \geq 5$, Holschneider, 1995, p. 31). For different wavenumbers ω_0, figure 2.5 depicts examples of the Morlet wavelet, along with the associated Fourier transforms. Obviously, for $\omega_0 = 2$, equation (2.93) is not fulfilled due to $\hat{\psi}_M(0) \approx 0.1 \neq 0$, while for $\omega_0 = 6$, $\hat{\psi}_M(0)$ is insignificantly different from zero and the corresponding wavelet $\psi_M(t)$ sufficiently satisfies the admissibility condition.

(a) Morlet wavelet $\psi_M(t)$ (real part)   (b) Fourier transform of $\psi_M(t)$ ($\hat{\psi}_M(\omega)$)
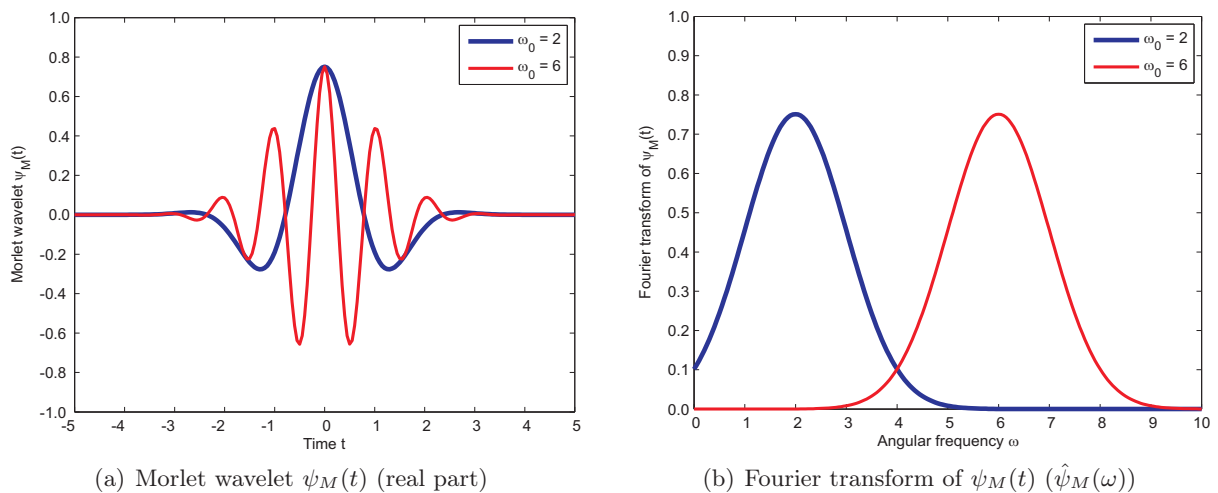
Figure 2.5: Comparison of Morlet wavelets and the associated Fourier transforms using different wavenumbers ω_0 (see equations (2.94) and (2.95))

2.4.2 Continuous wavelet transform

A wavelet transform represents a function by wavelets and can be classified into continuous and discrete wavelet transforms, CWT and DWT, respectively. The CWT operates over each possible scale and translation parameter, while the DWT is performed using a specific subset of scale and translation values. The CWT of a function $f(t) \in L^p(\mathbb{R})$, $1 \leq p < \infty$, is defined as

$$\mathscr{W}_\psi[f](a,b) = (f, \psi_{a,b}) = \int_{-\infty}^{+\infty} f(t)\psi_{a,b}^*(t)dt = \frac{1}{\sqrt{a}} \int_{-\infty}^{+\infty} f(t)\psi^*\left(\frac{t-b}{a}\right)dt, \quad (2.97)$$

where $L^p(\mathbb{R})$ is the vector space of all complex-valued p^{th}-power Lebesgue integrable functions defined on $\mathbb{R}$, and ψ^* is the complex conjugate of ψ defined on the open time and scale real (b,a) half plane (Holschneider, 1995, p. 5; Debnath, 2001, p. 12; Trauth, 2007, p. 115). The numbers $\mathscr{W}_\psi[f](a,b)$ are called wavelet coefficients of $f(t)$ with respect to the mother wavelet $\psi(t)$. Normally, the output $\mathscr{W}_\psi[f](a,b)$ is a real valued function except when the mother wavelet is complex. The power spectrum from the CWT can be expressed by $|\mathscr{W}_\psi[f](a,b)|^2$. Like the Fourier transform, the CWT is also linear. Unlike the Fourier transform, the CWT is not a single transform, but any transform obtained in this way. The inverse wavelet transform can be defined such that the original function $f(t)$ can be reconstructed by means of

$$f(t) = C_\psi^{-1} \int_{-\infty}^{+\infty} \int_{-\infty}^{+\infty} \mathscr{W}_\psi[f](a,b)\psi_{a,b}(t)(a^{-2}da)db, \quad (2.98)$$

provided that C_ψ satisfies the admissibility condition given by equation (2.92). Using the MWT to perform the CWT analysis in practice, the wavelet coefficients are the sums of the signal $f(t)$ multiplied by scaled and shifted versions of the mother wavelet over all time. This process produces $\mathscr{W}_\psi[f](a,b)$ as a function of scale a and position b within a total of five steps, schematically illustrated in figure 2.6.

1. Select a mother wavelet $\psi(t)$ and compare it to a start section of the signal $f(t)$.

2. Compute the correlation C between the wavelet and this signal section, where the C values depend on the shape of the chosen wavelet (see figure 2.6(a)). If both the signal and wavelet energies are equal to one, C can be interpreted as a correlation coefficient.

3. Shift the wavelet rightwards by parameter b and repeat steps 1 and 2 until the whole signal has been covered (see figure 2.6(b)).

4. Scale the wavelet using parameter a and repeat steps 1 through 3 (see figure 2.6(c)).

5. Repeat steps 1 through 4 for all scales.

(a) Steps 1 and 2   (b) Step 3   (c) Step 4
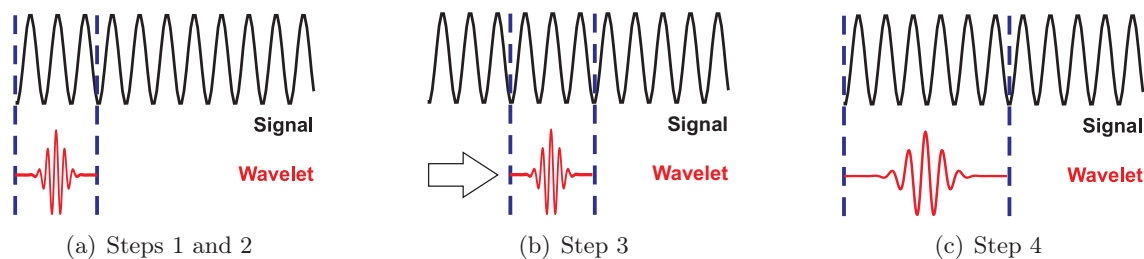
Figure 2.6: A five-step CWT procedure implemented in the MATLAB® Wavelet Toolbox™ (MWT)

After all five steps have been accomplished, the coefficients produced at different scales and sections constitute the results of a regression of the signal $f(t)$ on the wavelets $\psi_{a,b}(t)$. Based on the centre frequency F_m of the mother wavelet $\psi(t)$, the pseudo-frequency F_a corresponding to the scale a can be computed using

$$F_a = \frac{F_m}{a \cdot \Delta t},\tag{2.99}$$

where Δt is the sampling period. The basic idea behind the centre frequency determination is to associate a given mother wavelet with a purely periodic signal of frequency F_m. Thereby, the frequency that maximises $|\hat{\psi}(\omega)|$ turns out to be a reasonable choice for F_m, where $\hat{\psi}(\omega)$ is the Fourier transform of the mother wavelet $\psi(t)$. Taking the real-valued Morlet wavelet $\psi_M(t) = \pi^{-1/4} e^{-t^2/2} \cos(5t)$ with $\omega_0 = 5$ as an example, i.e., substituting $e^{i\omega_0 t} = \cos(5t)$ into equation (2.94), figure 2.7 illustrates the results of the wavelet approximation and centre frequency determination. As can be seen from the plots, the main lobe of the Morlet wavelet is sufficiently approximated by the purely periodic signal at the determined centre frequency.

(a) Morlet wavelet approximation   (b) Centre frequency determination
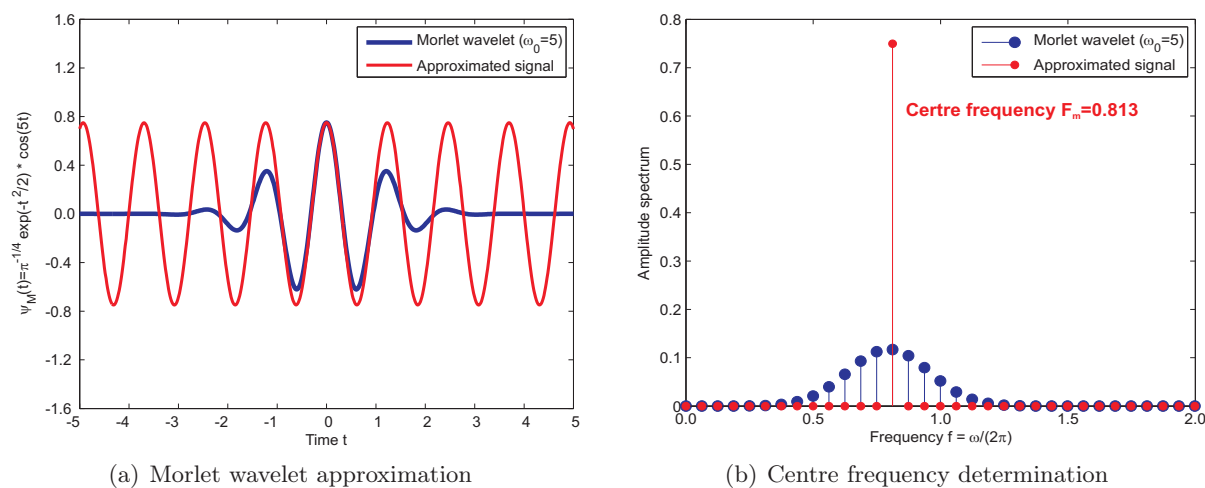
Figure 2.7: Example of centre frequency determination for the real-valued Morlet wavelet with a wavenumber of $\omega_0 = 5$ (see equations (2.94) and (2.95))

The results of a CWT is usually visualised by means of so-called scalograms which communicate the time-frequency localisation property of wavelet transforms. The x-axis of a wavelet scalogram represents position along the signal (or time t), the y-axis represents scale (a) or converted pseudo-frequency (F_a, see equation (2.99)), and the colour at each (x, y) point represents the magnitude of the wavelet coefficient. Analysing a simulated signal with temporally varying periods in section 2.4.4, the resulting continuous wavelet scalogram is compared with the one from a discrete wavelet transform (see figure 2.10).

2.4.3 Discrete wavelet transform

Calculating the wavelet coefficients at each possible scale a and position b is a computationally time-consuming task. Therefore, in practical applications involving fast numerical algorithms, the CWT can be performed at discrete grid points being a subset of the whole family of scales and positions. To do this, discrete wavelets are defined by replacing a with a_0^m ($a_0 \neq 0, 1$), b with $nb_0 a_0^m$ ($b_0 \neq 0$), leading to

$$\psi_{m,n}(t) = \frac{1}{\sqrt{a}} \psi\left(\frac{t-b}{a}\right) = \frac{1}{a_0^{m/2}} \psi\left(\frac{t}{a_0^m} - nb_0\right),\tag{2.100}$$

where m and n are integers. Accordingly, the DWT of a function $f(t)$ is defined as

$$\mathscr{W}_\psi[f](m,n) = (f, \psi_{m,n}) = \int_{-\infty}^{+\infty} f(t)\psi_{m,n}^*(t)dt, \qquad (2.101)$$

where $\psi_{m,n}(t)$ is given by equation (2.100). Generally, there is no guarantee that the original function $f(t)$ can be reconstructed from its discrete wavelet coefficients $\mathscr{W}_\psi[f](m,n)$. If the discrete lattice has a very fine mesh, the reconstruction of $f(t)$ is still possible. In the case of a coarse mesh, the wavelet coefficients may not contain sufficient information for the determination of $f(t)$ from these coefficients. If the function $f(t)$ belongs to the Hilbert space $L^2(\mathbb{R})$ (Debnath and Mikusinski, 2005, p. 99), and the wavelets form an orthonormal basis (Debnath, 2001, p. 14, 73), then $f(t)$ can be completely reconstructed by its discrete wavelet coefficients using

$$f(t) = \sum_{m,n=-\infty}^{+\infty} \mathscr{W}_\psi[f](m,n)\psi_{m,n}(t). \qquad (2.102)$$

In terms of choosing an appropriate subset of scales and positions, the dyadic scheme based on powers of two enables an efficient analysis and sufficient accuracy. To implement this scheme in computing the DWT, Mallat (1989) proposed a filter-based algorithm which is actually a classical approach in the signal processing community, known as a two-channel subband coder using conjugate quadrature filters or quadrature mirror filters. Mallat's algorithm for the DWT represents a multiple-level signal decomposition and allows for a fast wavelet transform (FWT). The basic principle of this algorithm is schematically shown in figure 2.8.
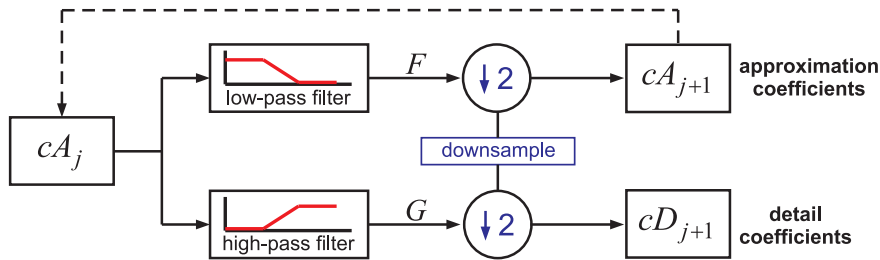
Figure 2.8: Discrete wavelet transform using multiple-level decomposition

Given a signal S of length n, the DWT consists of a maximum of $\lfloor \log_2 n \rfloor$ stages or levels, where $\lfloor x \rfloor$ denotes the integer part of x. S can be decomposed into approximations and details; the former are the high-scale and low-frequency components, while the latter are the low-scale and high-frequency signals. At the initialisation level with $j = 0$ and $cA_0 = S$, two sets of coefficients, namely approximation coefficients cA_1 and detail coefficients cD_1 are obtained by convolving S with a low-pass and a high-pass filter, respectively. The selection of the filters depends on the used mother wavelet. Assuming that the length of each filter is equal to $2N$, the resulting signals F and G are of length $n + 2N - 1$, indicating that the data volume is increased to about twice as much as that of the original signal. Therefore, a power-of-two downsampling is applied to F and G so that the coefficients cA_1 and cD_1 are of length $\lfloor (n-1)/2 + N \rfloor$.

This decomposition process can be iterated, i.e., the approximation coefficients cA_1 can be further separated into cA_2 and cD_2 by replacing cA_0 by cA_1. In doing so, the signal S is broken down into many lower resolution components and has the structure $(cA_j, cD_j, \ldots, cD_1)$ at level j. In practice, the iterative decomposition can proceed until the individual details consist of a single sample. An appropriate number of levels can be selected based on the signal characteristics or a suitable optimisation criterion such as the minimum-entropy criterion proposed by Coifman and Wickerhauser (1992). The computation cost of the FWT is the convolution carried out in

each of the filters. Since the number of data samples in the convolution is halved after each downsampling step, the total computational complexity is

$$O(n + \frac{n}{2} + \frac{n}{4} + \frac{n}{8} + \cdots + 1) = O(n), \tag{2.103}$$

meaning that the FWT algorithm has a linear complexity. The results of a DWT can also be visualised by scalograms, where the x-axis represents time or position along the signal, the y-axis represents a stage or level, and the colour at each (x, y) point represents the absolute values of the detail coefficients.

2.4.4 An example of wavelet transforms

Following the basic wavelet theory, examples are presented in this section to illustrate the advantages of wavelet transforms over Fourier transforms, as well as the differences between the CWT and DWT. For these purposes, a simple sine signal S_p of length 1000 is simulated, where the first and second half of S_p have different periods of 250 s and 100 s, respectively. Adding an upward linear trend to S_p results in S_d. Figure 2.9 shows the signals S_p and S_d with the associated amplitude spectra computed using the fast Fourier transform (FFT).

(a) Periodic sine signal	(b) Amplitude spectrum
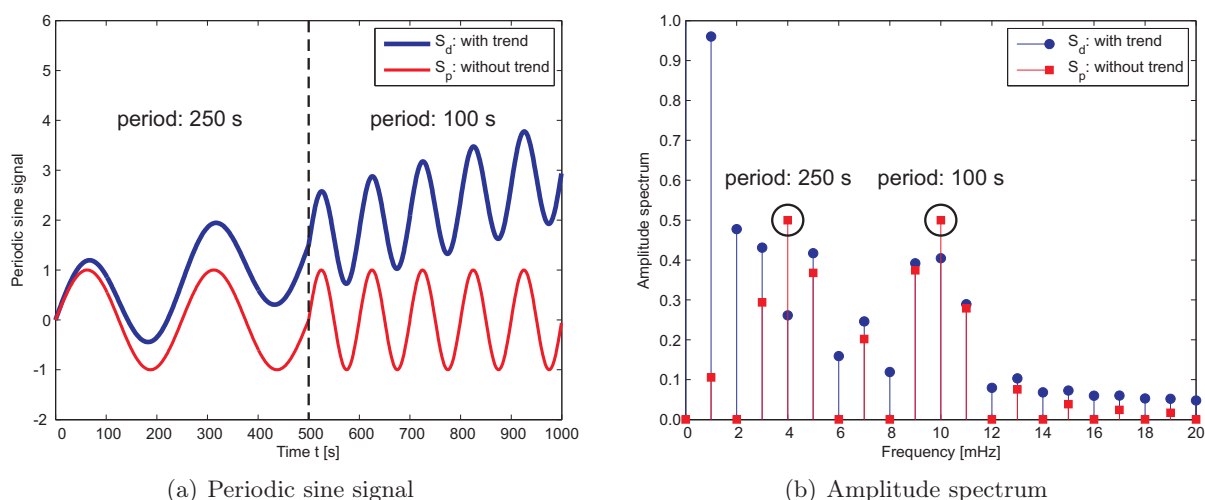
Figure 2.9: Examples of periodic sine signals with the associated results of Fourier transforms

As figure 2.9(b) depicts, in the absence of the linear trend, the periods of S_p can be determined by means of a Fourier transform. However, if the data exhibit a non-stationary trending behaviour, the Fourier analysis does not deliver the correct frequencies (periods). Therefore, a reliable FFT-based identification of periodic components requires an appropriate trend detection and removal at the preliminary stage of time series analysis. In addition, despite the correct periods detected for S_p, information about the time at which the sine signal's period changes is still lacking. These deficiencies of the conventional Fourier approach are absent when performing wavelet transforms. Figure 2.10 compares the scalograms resulting from the CWT and DWT of S_d (i.e., sine signal with trend). For the CWT, the real-valued Morlet wavelet shown in figure 2.7 is used. For the DWT, a symlet of order 6 is chosen which is similar to the applied Morlet wavelet with respect to the centre frequency and symmetry properties in the time domain. Symlets are nearly symmetrical wavelets modified by Daubechies with improved symmetry (Daubechies, 1992, p. 198–199). The y-axis of the CWT scalogram represents the pseudo-frequencies converted from scales (see equation (2.99)). Taking the signal length of 1000 into account, the maximum level visualised in the DWT scalogram is equal to $\lfloor \log_2 1000 \rfloor = 9$ (see section 2.4.3).

(a) CWT (Morlet wavelet with $\omega_0 = 5$)

(b) DWT (Daubechies symlet of order 6)
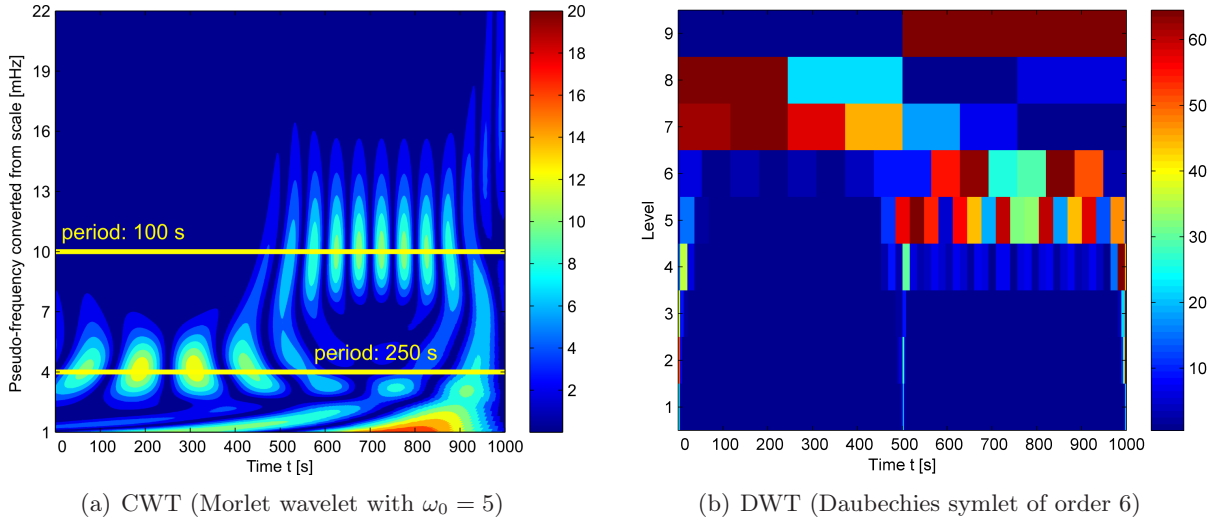
Figure 2.10: Comparison of the scalograms resulting from the continuous and discrete wavelet transforms of the trending signal S_d (see figure 2.9)

Being localised in both the time and frequency domains, the CWT scalogram exhibits not only the correct frequencies of 4 and 10 mHz, corresponding to periods of 250 and 100 s, but also the time $t = 500$ s at which the change in the signal's period takes place. All of these results are obtained in the presence of the linear trend which is also visible at the bottom of the CWT scalogram around a frequency of 1 mHz. Furthermore, according to the temporally increasing absolute wavelet coefficients, the visibility of the linear trend also increases with time. The DWT scalogram represents the absolute detail coefficients which are converted to a colour scale ranging between 0 and 64. In comparison to the continuous wavelet scalogram, the discrete one appears to be more difficult to interpret, particularly with respect to frequency determination. Nevertheless, the main temporal variation patterns and the moment of the frequency change can still be discerned in the DWT scalogram, for example, by comparing the levels 6 and 7. Comparing figures 2.9(a) and 2.10(b) with each other, the signal period (frequency) captured by the symlet wavelets increases (decreases) with level. From this comparison between the CWT and DWT scalograms it can be concluded that the CWT analysis gains in ease of readability, but loses in terms of computational efficiency. Moreover, the CWT is advisable for the purpose of signal interpretation, while the DWT can be used for signal reconstruction.

As demonstrated above, the main difference between Fourier and wavelet transforms is that wavelets are localised in both the time (via translations) and frequency (via dilations) domains, while the standard Fourier transform is only localised in the frequency domain. Performing the Fourier transform on a sliding window of length T, known as windowed Fourier transform (WFT; Mallat, 2009, sect. 4.2), the time-frequency localisation can be achieved by investigating all multiples of T^{-1} between T^{-1} and the Nyquist frequency $(2\Delta t)^{-1}$ at each time step, where Δt denotes the sampling period. However, Kaiser (1994, chap. 2) pointed out that the WFT method is neither accurate nor efficient in practice. The inaccuracy arises from the aliasing of the high- and low-frequencies which are not included in the frequency range of the time window. The inefficiency in turn is attributed to a possible large number $(T/(2\Delta t))$ of frequencies that must be analysed at each time step. An additional difficulty in the practical application of the WFT method is to determine the most appropriate window length. In view of computational efficiency, conducting the FWT by means of the multiple-level decomposition technique, schematically shown in figure 2.8, the total complexity is reduced to $O(n)$ (see equation (2.103)) as compared to $O(n \log_2 n)$ of the conventional FFT (Buttkus, 2000, p. 76).

Taking advantage of the time-frequency localisation property, wavelets have been used for pattern recognition in geoscientific applications, for example, the characterisation of temporally varying features of polar motion, the extraction of fault scarps in bathymetric data from the seafloor, and the detection of cycle slips in GPS observations (Keller, 2004, sect. 3.1). Furthermore, wavelet transforms can be used as a spectral microscope to approximate mathematical functions, in particular those with discontinuities and sharp spikes (Mallat, 2009, chap. 9). For instance, transients in acoustics and audio signals usually need substantially fewer wavelets than sine-cosine terms to achieve a comparable approximation. This property of wavelet transforms has been exploited in data compression, such as the image coding system JPEG 2000, which enables a smaller compression loss than the original JPEG standard based on discrete cosine transforms (Keller, 2004, p. 173; Mallat, 2009, p. 523).

Chapter 3

Mathematical Models for GPS Positioning

In this chapter, section 3.1 provides a brief introduction to the Global Positioning System (GPS). Next, sections 3.2 and 3.3 describe the mathematical models for GPS absolute and relative positioning, respectively. The mathematical models of GPS observations consist of a functional and a stochastic component. In contrast to the continuously improved functional model, the stochastic model characterising the statistical properties of GPS measurements is still a controversial research topic. Here the functional model is discussed with a special focus on the error sources considerably affecting GPS positioning quality, while the stochastic model is presented with respect to observation weighting and correlation structure.

For a more detailed discussion on the theory and applications of GPS, there exist a variety of textbooks with different emphases. El-Rabbany (2006) offers professionals and practitioners a non-mathematical explanation of how GPS works and a wide range of its applications. A detailed description of GPS signal structure can be found, for example, in Kaplan and Hegarty (2006, chaps. 4, 5). Textbooks such as Teunissen and Kleusberg (1998) and Xu (2007) provide a deep theoretical insight into the mathematical models for GPS data processing, while Hofmann-Wellenhof et al. (2008) introduce the theory and practice of the Global Navigation Satellite Systems (GNSS), including the Russian system GLONASS, the European system Galileo, as well as additional global, regional, and augmentation systems in a more generic sense. Considering the innovative characteristics, services, and potential applications anticipated in the next generation of GNSS, Prasad and Ruggieri (2005) examine the advanced architectures paving the way for the future integration of different satellite-based navigation systems. Within the context of network-aided GPS positioning, Leick (2003, chaps. 4, 8) presents a comprehensive treatment of least-squares (LS) adjustment methods and data quality control techniques using minimum constraints, reliability measures, and procedures for outlier detection. By bringing the two fields of GNSS technology and environmental studies, Awange (2012) provides a simplified presentation of the concepts of GNSS and its applications to environmental monitoring.

3.1 Global Positioning System (GPS)

GPS is a satellite-based navigation system allowing the determination of the positions of observation sites on land or at sea, in the air or in space, by means of artificial satellites. It was developed by the U.S. Department of Defence in the early 1970s as the next generation replacement to the first satellite-based navigation system, TRANSIT, which made use of Doppler shift measurements in the early 1960s. Within the framework of the TIMATION (TIMe/navigATION) program instigated in 1964, two satellites, known as NTS I & II (navigation technology satellite), were launched in 1974 and 1977, respectively. These were the first satellites equipped with atomic clocks, a rubidium (Rb) and caesium (Cs) one, respectively, and as such could be considered as prototypes of the later GPS satellites. In February 1978, the first GPS satellite was successfully launched. This section briefly outlines the main characteristics of GPS, including its reference and time systems, segments, as well as signals and observations. The readers who are interested in the evolution of satellite-based navigation are referred to Guier and Weiffenbach (1997), Prasad and Ruggieri (2005, sect. 1.2), Ashkenazi (2006), Hofmann-Wellenhof et al. (2008, sect. 9.1), and Parkinson and Powers (2010).

3.1.1 Reference and time systems

The official GPS terrestrial reference system is the three-dimensional and Earth-centred World Geodetic System 1984 (WGS84), which was originally realised by the coordinates of about 1500 terrestrial sites derived from the TRANSIT Doppler observations. Associated with the refined WGS84 (G1150, Merrigan et al., 2002), a geocentric ellipsoid of revolution is defined by semi-major axis, flattening, Earth's angular velocity, and geocentric gravitational constant. With respect to ITRF2008 (International Terrestrial Reference Frame), the current WGS84 frame shows systematic differences of the order of 1 cm (Karabatić, 2011, p. 12). Moreover, the WGS84 is the reference system for the GPS broadcast ephemerides (Görres, 2010b). The system time of GPS is related to the atomic time system and referenced to coordinated universal time (UTC). However, in contrast to UTC, GPS time (GPST) is not corrected to match the Earth's rotation rate. This means that while at the GPS standard epoch, i.e., 00:00:00 UTC on January 6, 1980, UTC and GPST were coincident with each other, since January 1, 2009, 00:00:00 UTC, GPST is ahead of UTC by exactly 15 s. In addition, considering the current offset of 19 s between GPST and international atomic time (TAI), it follows that

$$\text{GPST} = \text{UTC} + 15 \text{ s} \quad \text{and} \quad \text{GPST} = \text{TAI} - 19 \text{ s}. \tag{3.1}$$

Therefore, TAI and UTC currently differ by an integer number of 34 s. This difference will become 35 s after July 1, 2012, 00:00:00 UTC, since a positive leap second will be introduced at the end of June 2012 (Bulletin C43-IERS, 2012). The actual integer offsets are reported by the International Bureau of Weights and Measures (BIPM[1]). Starting from the Julian date (JD) of the GPS standard epoch JD_0=2444244.5, the system time of GPS in terms of GPS week (GW) and day of week (DOW) can be calculated using

$$\text{GW} = \text{INT} \left[(\text{JD} - \text{JD}_0)/7 \right] \quad \text{and} \quad \text{DOW} = \text{MOD} \left[(\text{INT}(\text{JD}+0.5), 7 \right], \tag{3.2}$$

where INT and MOD are the integer and modulo operators, respectively. A DOW value of 0 means Monday, 1 means Tuesday, and so on. Taking the epoch J2012.0 (i.e., January 1, 2012, 00:00:00 UTC) as an example, where JD = 2455927.5, the GW and DOW are equal to 1669 and 6 (Sunday), respectively (Hofmann-Wellenhof et al., 2008, p. 25, 315).

3.1.2 GPS segments

GPS is comprised of three segments: the space, control, and user segments. The present space segment consists of nominally 24 operational satellites deployed in six evenly spaced orbital planes in near-circular orbits (i.e., an elliptical shape with a maximum eccentricity of about 0.01; El-Rabbany, 2006, p. 2) with an inclination of 55° and four active satellites in each orbital plane (see figure 3.1(a)). The semi-major axis of a GPS orbit is nearly 26560 km, indicating a satellite altitude of about 20200 km above the Earth's surface (Langley, 1991b). The revolution period of a GPS satellite is approximately half a sidereal day, i.e., around 11 h 58 min. Hence, for the same location, the satellite configuration repeats in universal time about 4 min earlier each day (Seeber, 2003, p. 213). The initial operational capability (IOC) was officially announced in December 1993, meaning that 24 satellites were available to be used for navigation. The full operational capability (FOC) was achieved in July 1995, implying that the satellite constellation was tested for operational military performance (Hofmann-Wellenhof et al., 2008, p. 310). With the full constellation geometry, the space segment provides global coverage with 4 to 8 simultaneously observable satellites above an elevation angle of 15° at any time of day. Decreasing the elevation mask to 5°, 12 satellites will be occasionally visible (Hofmann-Wellenhof et al., 2008, p. 323).

---

[1]`ftp://ftp2.bipm.org/pub/tai/scale/UTCGPSGLO/utcgpsglo10.ar`

Since 1978, different types of GPS satellites have been launched, such as the Block I (no longer in service), Block II, Block IIA (A: advanced), Block IIR (R: replenishment), Block IIR-M (M: modernised), and Block IIF (F: follow-on) satellites. During the course of the GPS modernisation, the future generation Block III satellites will be launched in 2014, and are expected to carry GPS into 2030 and beyond. In figures 3.1(b)-(f), the different generations of GPS satellites are shown. Table 3.1 lists some selected features of these satellite categories, where SVN denotes the satellite vehicle number (Prasad and Ruggieri, 2005, p. 6, 121).

(a) GPS constellation   (b) Block I   (c) Block II/IIA

(d) Block IIR/IIR-M   (e) Block IIF   (f) Future Block III
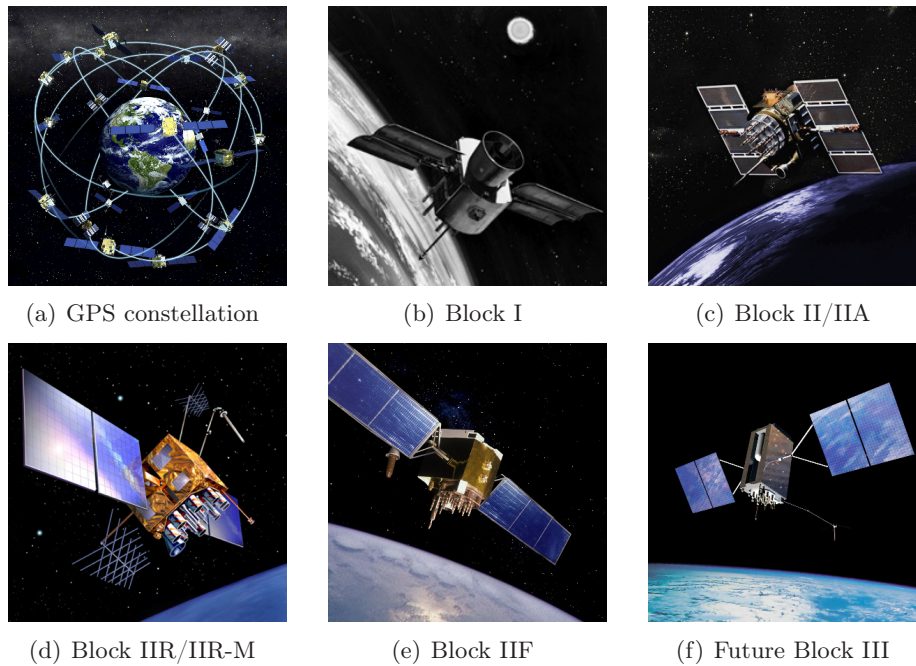
Figure 3.1: GPS constellation and the different generations of GPS satellites (image sources: (a) NOAA, (b) Aerospace Corporation, (c), (d), (f) `www.gps.gov`, (e) `www.navigadget.com`)

Table 3.1: Selected characteristic features of the different GPS satellite categories

Satellite category	Launches during	SVN[1]	Inclination (degree)	Atomic clock	Design life (year)
Block I	1978-1985	01-11 (07)	63	1 Cs+2 Rb	4.5
Block II	1989-1990	13-21		2 Cs+2 Rb	7.5
Block IIA	1990-1997	22-40	55		
Block IIR	1997-2004	41-61 (42)		3 Rb	10
Block IIR-M	2005-2009				
Block IIF	2010-2011	62, 63		2 Cs+1 Rb	12.7

[1] Unsuccessful launches are provided in brackets.

The Block I satellites, whose orbital planes had an inclination of 63°, were built mainly for experimental purposes. Today, none of the original Block I satellites are in operation, the last being taken out of service in November 1995. Considering the 4.5-year design life of the Block I satellites, it is remarkable that some of them were operational for more than 10 years. The orbital planes of the Block II/IIA satellites are inclined at 55° to the equator. Being an advanced version of Block II, Block IIA satellites are equipped with mutual communication capability and have a larger storage capacity, increased from 14 to 180 days. While the Block I satellite signals were fully accessible to civilian users, some Block II satellite signals are restricted in view of U.S.

national security purposes. The Block IIR/IIR-M satellites are equipped with enhanced facilities for communication and intersatellite tracking. In addition, an improved antenna panel was developed for the last four Block IIR and all of the Block IIR-M satellites to increase the power of the received GPS signals. The Block IIR-M satellites transmit the new military M-code on the carrier frequencies L1 and L2 as well as the new civil L2C-code on L2, enabling an ionospheric correction for code signals. The Block IIF satellites emit a third civil signal called L5, along with the L2C- and the M-code previously introduced into Block IIR-M. The L5 signal is expected to be more robust and to have a higher signal power level. The future Block III satellites will deliver significant improvements over the current GPS space vehicles, including a new international civil signal L1C, and high-powered, anti-jamming M-code with full Earth coverage for military users. The first Block III satellite is scheduled to be launched in 2014 (Prasad and Ruggieri, 2005, p. 123). For a more detailed description of the GPS satellite generations, see, for example, Prasad and Ruggieri (2005, p. 120), El-Rabbany (2006, p. 5, 16), Hofmann-Wellenhof et al. (2008, p. 323, 340), and Marquis and Riggs (2010). Further information about launch dates, orbital position, and satellite status is available on the web site of the United States Naval Observatory (USNO, http://tycho.usno.navy.mil/gpscurr.html).

The GPS control segment is composed of a master control station (MCS) located in Colorado Springs, 12 worldwide distributed tracking (monitoring) stations, and 4 ground antennas (Prasad and Ruggieri, 2005, p. 123). The main tasks of the control segment are the collection of GPS observations at the unmanned tracking stations, determination and prediction of satellite orbits, clocks, and other parameters at the MCS, and the uploading of navigation data to the GPS satellites. In addition, the MCS is responsible for monitoring the GPS system's integrity. During satellite maintenance or outages, the MCS sets the status of a satellite to unhealthy. Scheduled satellite maintenance or outages are reported in the so-called NANU (notice advisory to NAVSTAR users) message provided by the U.S. Coast Guard Navigation Centre (www.navcen.uscg.gov). For more information about the GPS control segment, the reader is referred to Prasad and Ruggieri (2005, sects. 3.2.2, 6.3) and Hofmann-Wellenhof et al. (2008, sect. 9.4.2).

The GPS user segment can be subdivided into three groups: (1) user categories including all military and civilian users, as well as authorised and unauthorised users, (2) receiver types characterised by the type of observables and the number of tracked frequencies, depending on the application of concern, and (3) various services providing system status information and GPS products for positioning at different accuracy levels (Hofmann-Wellenhof et al., 2008, p. 7).

3.1.3 GPS signals

Each GPS satellite transmits a microwave L-band radio signal composed of carrier frequencies modulated by ranging codes and a navigation message. The first operational GPS satellites (Block II, IIA, and IIR) emit navigation signals on the carrier frequencies L1 and L2, while the modernised satellites (Block IIR-M, IIF, and III) transmit a third civil frequency L5 and several new ranging codes on different carrier links. An overview of the available signals is given in table 3.2 (Prasad and Ruggieri, 2005, p. 121; Hofmann-Wellenhof et al., 2008, p. 329).

The C/A-code (C/A: coarse/acquisition), which is only modulated onto the L1 carrier, is a stream of 1023 binary digits (i.e., zeros and ones, known as bits or chips) that repeats itself every millisecond. This indicates a bit duration of approximately 1 μs and a chip length of about 300 m. The relatively short code duration allows for fast signal acquisition, but makes the C/A-code susceptible to interference. Having been designed in particular to fulfil commercial needs, the new civil L2C-code consists of the L2CM-code (M: moderate length) and a 75 times longer L2CL-code (L: long length). It shows improved cross-correlation performance and enables

the correction of ionospheric effects (Fontana et al., 2001). These benefits will be available to users if the majority of the GPS satellites are L2C capable (Dixon, 2005). The FOC with 24 L2C-transmitting satellites may be achieved in 2015 (Prasad and Ruggieri, 2005, p. 120). To meet the requirements of safety-of-life applications, two ranging codes will be transmitted on L5, which are referred to as L5I- and L5Q-code. The L5I-code (I: in-phase) is modulated with a navigation message, while the L5Q-code (Q: quadraphase) is used as a pilot channel. In order to reduce the narrowband interference effect, both L5I and L5Q are additionally modulated with low-frequency secondary codes possessing lengths of 10 and 20 chips, respectively. The resulting codes are 10 and 20 times longer than the C/A-code and exhibit advanced autocorrelation and cross-correlation properties that allow better inference resistance in combination with the higher signal power. A constellation of 24 L5-emitting satellites may be achieved in 2019 (Prasad and Ruggieri, 2005, p. 121). The L1C-code, including a data channel L1CD and a pilot channel L1CP, will be the fourth civil signal and will provide high interoperability with Galileo's E1 signal. By applying the multiplexing binary offset carrier (MBOC) modulation technique, more power is added to the higher frequencies to improve the tracking performance (Hein et al., 2006; Hofmann-Wellenhof et al., 2008, p. 83, 336).

Table 3.2: Signal availability of the operational and future GPS satellites

Carrier	L1				L2			L5
Modulated code	C/A	P/Y	M	C	C	P/Y	M	C
Block II/IIA/IIR	X	X				X		
Block IIR-M	X	X	X		X	X	X	
Block IIF	X	X	X		X	X	X	X
Block III	X	X	X	X	X	X	X	X
Frequency [MHz]	$f_1 = 1575.42$				$f_2 = 1227.60$			$f_5 = 1176.45$
Wavelengh [cm]	$\lambda_1 = 19.0$				$\lambda_2 = 24.4$			$\lambda_5 = 25.5$

The P-code (P: precision), which is modulated onto both the L1 and L2 carriers, has been designed primarily for military purposes. It has a very long stream of about $2.35 \cdot 10^{14}$ chips and repeats itself every 38 weeks, implying a chip length of about 30 m. Due to the extremely long code length, the P-code is very difficult to directly acquire if no a priori information is available, such as accurate clock corrections, coordinate estimates, and satellite ephemerides. Therefore, the C/A-code is used by military receivers for a coarse acquisition, and then the receiver locks onto the P-code for higher performance. The main properties of the new military M-code modulated onto the L1 and L2 carriers are the improved anti-jamming and navigation performance, higher security using new cryptography algorithms, and the possibility of higher transmission power. Furthermore, being superior to the P-code, a direct acquisition of the M-code is possible (Hofmann-Wellenhof et al., 2008, p. 333, 335).

For the initial series of GPS satellites (Block II, IIA, and IIR), the navigation message is added to the P- and C/A-code, and thus is available on both the L1 and L2 carriers. It contains, along with other information, the model (a quadratic polynomial) parameters for satellite clock corrections, the satellite health status, the broadcast ephemerides, the satellite almanac, and error correction data (e.g., for ionospheric effects). Of particular importance is the part known as the hand-over word (HOW) that helps the receiver achieve a rapid lock to the transmitted part of the long P-code. For the modernised GPS satellites (Block IIR-M, IIF, and III), the navigation message is added to the L2CM-, L5I-, and L1CD-code. A new military navigation message with efficient data structure and improved security and system integrity has been specified to be modulated onto the M-code (El-Rabbany, 2006, p. 15; Hofmann-Wellenhof et al., 2008, p. 339).

Since GPS is a military system, two techniques, known as selective availability (SA) and anti-spoofing (AS), have been implemented to limit the accuracy for unauthorised users. The SA is realised by degrading the satellite clock (δ-process) and manipulating the satellite ephemerides (ϵ-process). The δ-process is carried out by dithering the fundamental frequency of the satellite clock, while the ϵ-process truncates the orbit information in the navigation message so that the satellite positions cannot be accurately determined. The effect of the δ-process can be eliminated by differencing observations from one satellite to two receivers. The SA was activated on March 25, 1990 and turned off on May 2, 2000. Nevertheless, both processes may be retained and reactivated due to a growing awareness of the potential misuse of GPS and the increasing hybridisation of navigation approaches, which reduces the dependency on GPS as the sole navigation provider (Kelly, 2006). The AS has the purpose to prevent unauthorised users from getting access to the P-code, and to "spoof", or mislead, a receiver. The encrypted code is called Y-code. In doing so, adversaries could neither jam the satellite signal using ground-based transmitters, nor spoof military GPS receivers by transmitting a false P-code from a satellite. The time periods during which the AS was activated can be found in Steigenberger (2009, p. 15).

3.1.4 GPS observations

GPS observations include code pseudo-range measurements in the unit meter, carrier-phase measurements in the unit cycle, Doppler measurements in the unit Hertz, and signal strengths in the unit decibel Hertz or in manufacturer-specific units (see section 5.1). After the activation of the AS, manufactures of dual-frequency GPS receivers have developed different methods to recover the P-code and the L2 carrier. Nowadays, most receivers apply two approaches known as cross-correlation and Z-Tracking$^{\text{TM}}$ (Ashjaee and Lorenz, 1992; Hofmann-Wellenhof et al., 2008, p. 101, 102). Both techniques completely recover the L2 carrier, but at a degraded signal strength. The degradation is even higher when applying the cross-correlation method. The achievement of the FOC with the modernised GPS satellites (Block IIR-M, IIF, and III) will make the use of these signal-recovering techniques unnecessary (El-Rabbany, 2006, p. 19).

The pseudo-range derived from code observations represents a distance measure between the antenna centre of the GPS receiver and the antenna centre of the GPS satellite by determining the signal travel time in space. Since the satellite and receiver clocks are not perfectly synchronised with each other, the measured range is distorted by the clock synchronisation error, along with other effects and biases. As a rule of thumb, the precision of a code pseudo-range is about 1% of the chip length. Accordingly, the civil C/A-code (precise P-code) has a precision of 3 m (0.3 m) (Hofmann-Wellenhof et al., 2008, p. 106). Another way to measure the distance between receiver and satellite is to sum up the number of full carrier cycles plus the fractional part, and then multiply that by the carrier wavelength (see table 3.2). After a GPS receiver is switched on, it is capable of keeping track of phase changes, while the satellite-specific initial number of complete cycles is still unknown, or ambiguous. As long as no signal loss occurs, this phase ambiguity remains unchanged over time. The GPS phase can be measured to better than 0.01 cycles, indicating a precision of about 2 mm (Hofmann-Wellenhof et al., 2008, p. 108).

The Doppler shift represents the difference between the received satellite frequency and the stable frequency emitted by the satellite. Since this difference is linearly dependent on the radial relative velocity of the satellite with respect to the receiver, it can be used to determine the receiver velocity in real time and is thus important for navigation. Furthermore, the Doppler shift contributes to integer ambiguity resolution in kinematic surveying and may be used as an additional independent observable for point positioning. For a more detailed discussion of Doppler shift and its geodetic applications, see, for example, Leick (1995, sect. 8.3.6.1), El-Rabbany (2006, p. 24), and Hofmann-Wellenhof et al. (2008, p. 59, 108).

3.1.5 Linear combinations

Based on the code pseudo-range and carrier-phase measurements on two frequencies, for example, L1 and L2, linear combinations of observations can be formed which possess new preferable properties for different purposes. Taking the phase observations Φ_1 and Φ_2 in the unit meter for example, the resulting linear combination (LC) Φ_i is defined as

$$\Phi_i = k_{1,i} \cdot \Phi_1 + k_{2,i} \cdot \Phi_2, \tag{3.3}$$

where $k_{1,i}$ and $k_{2,i}$ are real-valued coefficients (see table 3.3). If $n_{R,1}^s$ and $n_{R,2}^s$ are the initial phase ambiguities of Φ_1 and Φ_2 relating to receiver R and satellite s, the ambiguity term of the linear combination is

$$n_{R,i}^s = \underbrace{\frac{k_{1,i} \cdot \lambda_1}{\lambda_i}}_{\alpha_{1,i}} n_{R,1}^s + \underbrace{\frac{k_{2,i} \cdot \lambda_2}{\lambda_i}}_{\alpha_{2,i}} n_{R,2}^s, \tag{3.4}$$

where λ_1 and λ_2 can be found in table 3.2, and λ_i is the effective wavelength of the linear combination. For $n_{R,i}^s$ to be an integer, $\alpha_{1,i}$ and $\alpha_{2,i}$ defined in equation (3.4) must also be integers. On the basis of $\alpha_{1,i}$ and $\alpha_{2,i}$, the coefficients $k_{1,i}$ and $k_{2,i}$ can be expressed by

$$k_{1,i} = \lambda_i \frac{\alpha_{1,i}}{\lambda_1}, \quad k_{2,i} = \lambda_i \frac{\alpha_{2,i}}{\lambda_2}. \tag{3.5}$$

This means that using $k_{1,i}$ and $k_{2,i}$ to compute a linear combination in metric units implicitly converts Φ_1 and Φ_2 into cycles by Φ_1/λ_1 and Φ_2/λ_2 before combining them. Imposing the constraint of unchanged satellite-receiver distance, i.e., $k_{1,i} + k_{2,i} = 1$ (Collins, 1999), the wavelength λ_i and frequency f_i of the linear combination Φ_i can be derived using equation (3.5) and the generic relationship $\lambda = c/f$ as

$$\lambda_i = \frac{\lambda_1 \lambda_2}{\alpha_{2,i} \cdot \lambda_1 + \alpha_{1,i} \cdot \lambda_2}, \quad f_i = \alpha_{1,i} \cdot f_1 + \alpha_{2,i} \cdot f_2, \tag{3.6}$$

where c is the speed of light in a vacuum, and f_1 and f_2 are given in table 3.2. Assuming that the observations on L1 and L2 are uncorrelated and have the same noise level σ_1, the noise of the linear combination is obtained by applying the variance propagation law as

$$\sigma_i = \sigma_1 \cdot \sqrt{k_{1,i}^2 + k_{2,i}^2}. \tag{3.7}$$

Different linear combinations are formed in the practice of GPS data analysis, such as the wide-lane LC (LC5), the ionosphere-free LC (LC3), the geometry-free LC (LC4), and the Melbourne-Wübbena LC (LC6). In table 3.3, the main properties of these commonly used phase linear combinations are summarised, where ION_i denotes the ionospheric amplification factor with respect to Φ_1 in metric units (Collins, 1999; Seeber, 2003, p. 263; Howind, 2005, p. 24; Dach et al., 2007a, p. 42; Wildt, 2007, p. 61).

Due to a large wavelength of 86.2 cm, the LC5 is particularly suitable for ambiguity resolution. The LC3 has the advantage of sufficient elimination of the first-order ionospheric effect, but the disadvantages of the noise level being increased by a factor of 3 compared to L1 and the extremely small wavelength of 6 mm which makes a direct ambiguity resolution impossible (Dach et al., 2007a, p. 40). Therefore, an indirect two-step ambiguity resolution strategy is employed. On the basis of the LC5, the wide-lane integer ambiguities are first determined. Next, the resolved LC5 ambiguities are introduced into an ionosphere-free (LC3) solution to evaluate the ambiguities in narrow-lane cycles with a wavelength of $c/(f_1 + f_2) \approx 11$ cm (Hofmann-Wellenhof et al., 2008, p. 112). This strategy is able to resolve ambiguities for baselines of up to several

hundred kilometres (Dach et al., 2007a, p. 181, 182). Being independent of receiver and satellite clocks, and of the associated geometry (i.e., satellite orbits and site coordinates), the LC4 mainly contains the ionospheric effects and the non-integer ambiguity terms (Steigenberger, 2009, p. 18). Therefore, this linear combination is particularly suitable for estimating ionospheric models.

Table 3.3: Commonly used phase linear combinations based on L1 and L2

LC	$k_{1,i}$	$k_{2,i}$	$\alpha_{1,i}$	$\alpha_{2,i}$	λ_i [m]	σ_i/σ_1	ION_i
L1	1	0	1	0	0.190	1	1
L2	0	1	0	1	0.244	1	1.65
LC5	$\frac{f_1}{f_1-f_2}=4.53$	$\frac{-f_2}{f_1-f_2}=-3.53$	1	-1	0.862	5.74	1.28
LC3	$\frac{f_1^2}{f_1^2-f_2^2}=2.55$	$\frac{-f_1^2}{f_1^2-f_2^2}=-1.55$	77	-60	0.006^1	2.98	0
LC4	1	-1	-60	77	–	1.41	0.65

[1] See, e.g., Wanninger (2000, p. 15)

Independently described by Melbourne (1985) and Wübbena (1985), the LC6 linear combination is the difference between the carrier-phase wide-lane and the pseudo-code narrow-lane combinations (Seeber, 2003, p. 263, 265):

$$\mathrm{LC6} = \frac{1}{f_1 - f_2}(f_1\Phi_1 - f_2\Phi_2) - \frac{1}{f_1 + f_2}(f_1 P_1 + f_2 P_2). \tag{3.8}$$

It also has a wavelength of 86.2 cm and eliminates the effects of geometry, clocks, the ionosphere, and the troposphere. Along with good P-code data, providing a precision less than 1 m, the LC6 can be used to resolve the wide-lane ambiguities for very long baselines of up to 6000 km and to check observations for cycle slips (i.e., discontinuities in the carrier-phase measurements by an integer number of cycles due to temporary interruptions of the GPS signals). In addition, the noise level of the LC6 is reduced by nearly 30% compared to that of P_1 and P_2 (Dach et al., 2007a, p. 41, 42, 182).

Considering the modernised triple-frequency GPS, the number of possible linear combinations will be drastically increased. Han and Rizos (1999) proposed several three-carrier combinations with larger effective wavelengths and lower noise amplifications. Odijk (2003) derived ionosphere-free combinations for which direct integer ambiguity resolution is possible. In the case of triple-frequency, different ambiguity resolution algorithms are already available, for example, the three carrier ambiguity resolution (TCAR; Forssell et al., 1997; Vollath et al., 1998), the cascade integer resolution (CIR; Hatch et al., 2000; De Jonge et al., 2000), and the least-squares ambiguity decorrelation adjustment (LAMBDA; Teunissen, 1995; Teunissen et al., 2002). Subdividing all possible phase linear combinations based on L1, L2, and L5 into a wide-lane, an intermediate-lane, and a narrow-lane region, Cocard et al. (2008) performed a systematic investigation of optimum three-carrier combinations with respect to effective wavelength, noise amplification, and ionospheric sensitivity. The most interesting results are summarised in table 3.4, where the subscript 3 denotes the third frequency L5 (see table 3.2). To calculate the phase noise factor and the first-order ionospheric scale factor in metric units, Feng (2008) provided

$$\frac{\sigma_i}{\sigma_1} = \left[\frac{(\alpha_{1,i} \cdot f_1)^2 + (\alpha_{2,i} \cdot f_2)^2 + (\alpha_{3,i} \cdot f_5)^2}{(\alpha_{1,i} \cdot f_1 + \alpha_{2,i} \cdot f_2 + \alpha_{3,i} \cdot f_5)^2}\right]^{1/2}, \tag{3.9}$$

$$\mathrm{ION}_i = \frac{f_1^2(\alpha_{1,i}/f_1 + \alpha_{2,i}/f_2 + \alpha_{3,i}/f_5)}{\alpha_{1,i} \cdot f_1 + \alpha_{2,i} \cdot f_2 + \alpha_{3,i} \cdot f_5}, \tag{3.10}$$

where the carrier-phase measurements on all three frequencies are assumed to be mutually uncorrelated and identical in variance, i.e., $\sigma_1 = \sigma_2 = \sigma_5$.

Table 3.4: Important phase linear combinations using three frequencies
(λ_i: Cocard et al. (2008); σ_i/σ_1, ION_i: equations (3.9) and (3.10))

Linear combination (LC)	$\alpha_{1,i}$	$\alpha_{2,i}$	$\alpha_{3,i}$	λ_i [m]	σ_i/σ_1	ION_i
Wide-lane region (75 cm $\leq \lambda_i <$ 29.31 m)	1	0	−1	0.751	**4.93**	−1.34
	1	−6	5	3.256	103.80	**−0.07**
	0	1	−1	5.861	33.24	−1.72
	−1	8	−7	**29.305**	1262.30	−16.52
Intermediate-lane region (19 cm $\leq \lambda_i <$ 75 cm)	1	−1	1	0.197	1.52	1.09
	1	−2	2	0.204	2.54	1.19
	0	2	−1	0.235	2.13	1.51
Narrow-lane region (10 cm $\leq \lambda_i <$ 19 cm)	4	0	−3	0.108	**2.61**	−0.01
	0	24	−23	**0.125**	16.64	0.00

In the wide-lane region, there exists no linear combination which is completely insensitive to the ionosphere and provides an acceptably low noise amplification factor at the same time. The combination ($\alpha_{1,i} = 1, \alpha_{2,i} = 0, \alpha_{3,i} = -1$) has the lowest phase noise factor, while $(1, -6, 5)$ is the most insensitive to the ionosphere. The extra wide-lane $(0, 1, -1)$ has been the straightforward choice in all TCAR approaches. A potentially interesting combination is $(-1, 8, -7)$, resulting in a large wavelength of 29.31 m. The intermediate-lane combinations exhibit low-noise properties and a comparable ionospheric impact as on L1. To fulfil the requirement of little ionospheric influence, narrow-lane combinations can be formed. Regarding both the noise and ionospheric amplification factors, $(4, 0, -3)$ turns out to be a promising choice. The wavelength of the triple-carrier ionosphere-free linear combination $(0, 24, -23)$ amounts to about 12.5 cm, which is significantly larger than that of the corresponding double-carrier combination $(77, -60)$ (see table 3.3). Within the context of GNSS (GPS/Galileo/Compass), additional useful combinations, as well as their characteristics and applications, are presented in Feng (2008).

3.2 Precise Point Positioning (PPP)

Relying upon the principle of trilateration (Langley, 1991a), simultaneously measured distances between a GPS receiver and four satellites are needed to determine the receiver's position in a three-dimensional space, along with the receiver clock synchronisation error. In this section, the basic concept of precise point positioning (PPP) is described, including the associated mathematical models and error effects. A deeper insight into PPP can be obtained from Zumberge et al. (1997), Witchayangkoon (2000), and Bisnath and Gao (2009).

3.2.1 Introduction

Representing a modern positioning technique at the cm-level precision, PPP makes use of undifferenced dual-frequency pseudo-range and carrier-phase measurements, as well as accurate satellite orbit and clock products, provided, for example, by the International GNSS Service (IGS; Moore, 2007). Thereby, the first-order ionospheric effect is eliminated by means of the ionosphere-free linear combination LC3 (see table 3.3). Other factors limiting the achievable positioning accuracy are either estimated as additional unknown parameters (e.g., receiver clock error, tropospheric delay) or accounted for by employing available sufficiently accurate models (e.g., antenna correction models, geophysical models). The PPP technique should not be confused with the code-based single point positioning (SPP) method, which uses the navigation message and achieves a positioning accuracy at the metre level (El-Rabbany, 2006, sect. 5.1).

Due to the use of the LC3 and the fact that the non-integer receiver- and satellite-dependent uncalibrated phase delays (UPD) are absorbed by the real-valued ambiguity estimates (Geng et al., 2010), it turns out to be a difficult task in PPP to resolve integer ambiguities adequately to access the full GPS carrier-phase accuracy. As a result, long observation periods are generally required in PPP applications. Using observations on a daily basis, static PPP is able to achieve a positioning accuracy of several millimetres (Kouba and Héroux, 2001). Recent studies presented in Heßelbarth (2009) showed that hourly position estimates can reach sub-decimetre accuracy, while an observation interval of 4 hours provides a positioning accuracy at the centimetre level. In addition, the incorporation of the 30-second instead of the 5-minute satellite clocks and the GLONASS observations leads to improved coordinate accuracy and reduced convergence time, particularly in kinematic applications (Wanninger and Heßelbarth, 2009).

Using data from a network consisting of about 100 globally and homogeneously distributed reference sites, the Jet Propulsion Laboratory (JPL) generates for commercial applications real-time products with an accuracy of 15-20 cm for orbits and 0.5 ns for clocks (`www.gdgps.net`). Benefiting from these real-time products with a sampling interval of 1 s and a latency of about 5 s, Gao and Chen (2004) showed in a static control survey that all coordinate components converge to the centimetre level within 20 min. In vehicle and airborne kinematic experiments, cm-level accuracy can be achieved after about 30 min. Moreover, the high potential of the PPP-based real-time determination of atmospheric water vapour was demonstrated. To overcome the limitations of PPP, such as long convergence time and the need for dual-frequency measurements, Wübbena et al. (2005) proposed the PPP-RTK (real time kinematic) network solution which enables the use of single-frequency receivers by providing ionospheric corrections, and improves the positioning accuracy and convergence time ($10 \ldots 50$ s) by solving integer ambiguities. Recent studies have revealed that integer ambiguity resolution in PPP is possible if the non-integer term UPD can be precisely determined based on a network of reference sites (Laurichesse and Mercier, 2007; Collins, 2008; Ge et al., 2008). Geng et al. (2009, 2010) found that reliable ambiguity resolution can be achieved for an observation period of 1 h. Nevertheless, over 3 hours of data are still required to obtain sub-centimetre accuracy for the vertical component.

The PPP-related services can be subdivided into data, processing, and positioning services. During the course of becoming a true GNSS service, the IGS will provide consistent GNSS products, in particular clock corrections with enhanced accuracy and temporal resolution (Springer and Dach, 2010). As a temporary solution, Heßelbarth and Wanninger (2008) suggested an interpolation technique for clock data with poor temporal resolutions. For post-processing and near real-time applications, diverse PPP online services have become convenient tools to obtain position solutions in national or global reference frames. For example, the Canadian Spatial Reference System-PPP (CSRS-PPP) online service enables worldwide point positioning with a latency of 90 min and an accuracy of centimetre or sub-decimetre level, depending on user dynamics (Tétreault et al., 2005; Ghoddousi-Fard and Dare, 2006; Mireault et al., 2008). Fuhrmann et al. (2010, chap. 6) compared four currently available online PPP services with respect to processing strategies, parameter estimation, and residual properties. Applying the so-called state-space concept (Mueller, 1994; Kee, 1996), different global commercial services, such as OmniSTAR introduced by the Fugro company (Heister et al., 2009, 2010), StarFire developed by John Deere and Company (Dixon, 2006), and Global Differential GPS (GDGPS) operated by JPL (Bar-Sever et al., 2004), are available for real-time PPP. Assuming optimum receiving conditions, dm-level kinematic positioning accuracy is achievable using dual-frequency receivers (Kechine et al., 2003; Dixon, 2006; Heister et al., 2010). While a momentary interruption of the correction signal can be easily handled, the loss of GPS signals results in significant accuracy degradation and requires reinitialisation (Heunecke and Heister, 2010).

3.2.2 Functional model

The functional model of GPS observations formulates the mathematical relationship between the measured satellite-receiver distances and the unknown parameters such as site coordinates. For static PPP, the simplified observation equation of the LC3 measurements from receiver R and satellite j is

$$\Phi_{R,3}^j = \rho_R^j + c \cdot (\delta t_R - \delta t^j) + T_R^j + \lambda_3 \cdot B_{R,3}^j + \epsilon_{R,3}^j, \tag{3.11}$$

where

ρ_R^j :   geometrical range between receiver R and satellite j in m,
c :   speed of light in a vacuum in m/s,
δt_R :   receiver clock offset from the GPS time in s,
δt^j :   satellite clock offset from the GPS time in s,
T_R^j :   tropospheric signal path delay in m,
λ_3 :   wavelength of the LC3 measurement in m,
$B_{R,3}^j$:   non-integer phase ambiguity of the LC3 measurement in cycles,
$\epsilon_{R,3}^j$:   random noise of the LC3 measurement in m.

The range ρ_R^j represents the Euclidean distance between the three-dimensional satellite position (X^j, Y^j, Z^j) at the transmission epoch and the receiver position (X_R, Y_R, Z_R) at the reception epoch, given by

$$\rho_R^j = \sqrt{(X^j - X_R)^2 + (Y^j - Y_R)^2 + (Z^j - Z_R)^2}. \tag{3.12}$$

The tropospheric slant path delay (SPD) T_R^j can be expressed as a product of the zenith path delay (ZPD) T_R and the mapping function (MF) $m_R^{z_i}$ that relates the ZPD to the SPD at a zenith distance of z_i. Hopfield (1969) showed the possibility of separating the SPD into a predominant and well-behaved dry (d) part and a complementary and volatile wet (w) part. The dry delay term can be accurately determined on the basis of air density (Davis et al., 1985), while the wet part is very difficult to handle due to atmospheric water vapour being highly variable in time and space. According to Rothacher (1992, p. 83), the total SPD can be expressed as

$$T_R^j = T_{R,d} \cdot m_{R,d}^{z_j} + T_{R,w} \cdot m_{R,w}^{z_j}, \tag{3.13}$$

where $T_{R,d}$ is the zenith dry delay (ZDD), $T_{R,w}$ is the zenith wet delay (ZWD), and $m_{R,d}$ and $m_{R,w}$ are the associated mapping functions. Under the assumption of hydrostatic equilibrium, the ZDD can be determined at the millimetre accuracy level using ground pressure measurements and is thus considered to be known. In contrast, the ZWD must be estimated based on GPS data. Substituting equation (3.13) into (3.11) and introducing satellite orbit (X^j, Y^j, Z^j) and clock (δt^j) products, for example, those provided by the IGS, equation (3.11) becomes

$$l_{R,3}^j = \rho_R^j + c \cdot \delta t_R + T_{R,w} \cdot m_{R,w}^{z_j} + \lambda_3 \cdot B_{R,3}^j + \epsilon_{R,3}^j. \tag{3.14}$$

The vector of unknown parameters is

$$\boldsymbol{x} = (X_R, Y_R, Z_R, \delta t_R, T_{R,w}, B_{R,3}^j)^T, \quad j = 1, \ldots, n_s, \tag{3.15}$$

where n_s denotes the total number of the satellites observed by receiver R. Regarding all $l_{R,3}^j$ as a realisation of the vector of stochastic observables $\underline{l}_{\boldsymbol{Z3}}$ and assuming zero-mean random measurement noise, i.e., $\mathrm{E}(\underline{\epsilon}_{R,3}^j) = 0$, the functional model of static PPP is

$$\mathrm{E}(\underline{l}_{\boldsymbol{Z3}}) = \mathbf{F}(\boldsymbol{x}) = \rho_R^j + c \cdot \delta t_R + T_{R,w} \cdot m_{R,w}^{z_j} + \lambda_3 \cdot B_{R,3}^j, \tag{3.16}$$

where $\mathrm{E}(\cdot)$ is the expectation operator. Obviously, equation (3.12) is non-linear. Therefore, a linearisation of $\mathbf{F}(\boldsymbol{x})$ using the Taylor series expansion around the a priori parameter values $\boldsymbol{x}_0$ results in

$$\mathbf{F}(\boldsymbol{x}) = \mathbf{F}(\boldsymbol{x}_0) + \frac{\partial \mathbf{F}(\boldsymbol{x})}{\partial \boldsymbol{x}}(\boldsymbol{x} - \boldsymbol{x}_0) + \cdots . \qquad (3.17)$$

The linearised model of the observation equations has the matrix form

$$\boldsymbol{A} \cdot \boldsymbol{\Delta}\hat{\boldsymbol{x}} = \Delta l_{\boldsymbol{Z3}} + \boldsymbol{v}, \qquad (3.18)$$

where $\boldsymbol{A}$ is the design matrix, $\boldsymbol{\Delta}\hat{\boldsymbol{x}}$ is the estimated vector of the reduced parameters (i.e., $\boldsymbol{\Delta x} = \boldsymbol{x} - \boldsymbol{x}_0$), $\boldsymbol{\Delta l_{Z3}}$ is the vector of reduced observations (i.e., $\boldsymbol{\Delta l_{Z3}} = l_{Z3} - \mathbf{F}(\boldsymbol{x}_0)$), and $\boldsymbol{v}$ is the vector of residuals. As indicated by equation (3.17), the design matrix $\boldsymbol{A}$ is formed by the partial derivatives of $\mathbf{F}(\boldsymbol{x})$ with respect to the unknown parameters, i.e.,

$$\boldsymbol{A} = \left[\frac{\partial \mathbf{F}(\boldsymbol{x})}{\partial X_R}, \frac{\partial \mathbf{F}(\boldsymbol{x})}{\partial Y_R}, \frac{\partial \mathbf{F}(\boldsymbol{x})}{\partial Z_R}, \frac{\partial \mathbf{F}(\boldsymbol{x})}{\partial \delta t_R}, \frac{\partial \mathbf{F}(\boldsymbol{x})}{\partial T_{R,w}}, \frac{\partial \mathbf{F}(\boldsymbol{x})}{B_{R,3}^j} \right]_{j=1\ldots n_s}^{\boldsymbol{x}=\boldsymbol{x}_0}, \qquad (3.19)$$

where

$$\frac{\partial \mathbf{F}(\boldsymbol{x})}{\partial X_R} = \frac{X_R - X^j}{\rho_R^j}, \quad \frac{\partial \mathbf{F}(\boldsymbol{x})}{\partial Y_R} = \frac{Y_R - Y^j}{\rho_R^j}, \quad \frac{\partial \mathbf{F}(\boldsymbol{x})}{\partial Z_R} = \frac{Z_R - Z^j}{\rho_R^j}, \qquad (3.20)$$

$$\frac{\partial \mathbf{F}(\boldsymbol{x})}{\partial \delta t_R} = c, \quad \frac{\partial \mathbf{F}(\boldsymbol{x})}{\partial T_{R,w}} = m_{R,w}^{z_j}, \quad \frac{\partial \mathbf{F}(\boldsymbol{x})}{\partial B_{R,3}^j} = 0 \text{ or } \lambda_3.$$

Taking the weight matrix $\boldsymbol{W_{Z3}}$ to be the inverse of the cofactor matrix $\boldsymbol{Q_{Z3}}$ of the LC3 observations, i.e., $\boldsymbol{W_{Z3}} = \boldsymbol{Q_{Z3}^{-1}}$, the best linear unbiased estimate of $\boldsymbol{\Delta x}$ is obtained by means of equation (2.17) as

$$\boldsymbol{\Delta}\hat{\boldsymbol{x}} = \underbrace{(\boldsymbol{A}^T \boldsymbol{W_{Z3}} \boldsymbol{A})^{-1} \boldsymbol{A}^T \boldsymbol{W_{Z3}}}_{\boldsymbol{H}} \Delta l_{\boldsymbol{Z3}}. \qquad (3.21)$$

The final estimate of the parameter vector $\boldsymbol{x}$ is therefore

$$\hat{\boldsymbol{x}} = \boldsymbol{x}_0 + \boldsymbol{\Delta}\hat{\boldsymbol{x}}, \qquad (3.22)$$

and the associated variance-covariance matrix (VCM) can be derived by applying the variance-covariance propagation law to equation (3.21) as

$$\boldsymbol{C}_{\hat{\boldsymbol{x}}\hat{\boldsymbol{x}}} = \sigma_0^2 \cdot \boldsymbol{H} \boldsymbol{Q_{Z3}} \boldsymbol{H}^T = \sigma_0^2 \cdot (\boldsymbol{A}^T \boldsymbol{W_{Z3}} \boldsymbol{A})^{-1}. \qquad (3.23)$$

The a posteriori variance of unit weight $\hat{\sigma}_0^2$ represents an estimate of σ_0^2 and can be computed from the weighted sum of squared residuals and $(n - u)$ degrees of freedom:

$$\hat{\sigma}_0^2 = \frac{\boldsymbol{v}^T \boldsymbol{W_{Z3}} \boldsymbol{v}}{n - u}, \qquad (3.24)$$

where n is the number of observations, and u is the number of unknown parameters. Using equation (3.18), the vector of least-squares residuals $\boldsymbol{v}$ is calculated as

$$\boldsymbol{v} = \boldsymbol{A} \cdot \boldsymbol{\Delta}\hat{\boldsymbol{x}} - \Delta l_{\boldsymbol{Z3}}. \qquad (3.25)$$

It is important to note that the formal VCM of the estimated unknown parameters $\boldsymbol{C}_{\hat{\boldsymbol{x}}\hat{\boldsymbol{x}}}$ is usually over-optimistic due to the unrealistic assumption that GPS observations are physically uncorrelated (see section 3.2.4). For a more detailed discussion of the (simplified) functional model of PPP, the reader is referred to Teunissen and Kleusberg (1998, p. 187–230), Hofmann-Wellenhof et al. (2008, p. 166, 254), and Kouba (2009).

3.2.3 Error sources and effects

Section 3.2.2 only presented the simplified functional model for point positioning using dual-frequency carrier-phase observations. To exploit the full accuracy potential of PPP, additional correction terms or models are necessary to account for the satellite-specific, atmospheric, site-specific, site displacement, and relativistic effects. This section provides an overview of these error sources, with a particular focus on their influences in the measurement and solution domains. The effects to be discussed in the following text are summarised in table 3.5.

Table 3.5: Error effects limiting the precise point positioning (PPP) quality

Satellite-specific effects	Satellite orbit and clock products
	Satellite antenna models
	Satellite phase wind-up effect[1]
	Satellite hardware delay
Atmospheric effects	Ionospheric effects
	Tropospheric effects
Site-specific effects	Multipath effects
	Receiver antenna models
	Receiver hardware delay
Site displacement effects	Effects of the solid Earth tides
	Ocean loading displacement
	Deformation due to polar motion
	Sub-daily variations of the ERP[2]
	Atmospheric pressure loading
	Further loading displacements
Relativistic effects	Effects on the equation of motion
	Shapiro (gravitational) time delay
	Effects on satellite clocks
	Effects on receiver clocks

[1] Also known as phase polarisation effect (Steigenberger, 2009, p. 35)
[2] Earth rotation parameters, i.e., pole coordinates (x_p, y_p) and UT1−UTC

Satellite-specific effects

Satellite orbit and clock products. Over the past 15 years, the precision of the IGS final orbit products has improved from about 30 cm to about 2 cm. Furthermore, the IGS rapid combined products, which are generated using fewer tracking stations and with faster delivery times (17-41 h latency), are now more precise than the best analysis centre's (AC) final solution. For the GPS satellites, the largest uncertainty in the orbit determination is due to the solar radiation pressure which can be considered by estimating the so-called dynamical parameters in an enhanced orbit model, for example, the one implemented in the Bernese GPS Software 5.0 (Beutler et al., 1994; Dach et al., 2007a, p. 31, 32). Being consistent with the orbit precision, the current IGS final clock solutions are estimated to be precise at the 0.1 ns level. After removing the small biases, the satellite clocks produced by different AC agree with standard deviations of 0.03-0.07 ns or 1-2 cm (`http://acc.igs.org`). Within the framework of the IGS Real-Time Pilot Project, real-time GNSS clock products with a precision of 0.5 ns will be available to users via Internet and other economical data streaming technologies. At the moment of writing, clock corrections for the GLONASS satellites are provided by the Information-Analytical Centre (IAC) and the European Space Operations Centre (ESOC) with a sampling interval of 5 min and 30 s, respectively. A comparison of the GLONASS clock products from both AC showed an agreement at the 0.08 ns level (Springer and Dach, 2010).

Satellite antenna models. The necessity for correcting the separation between the GPS satellite centre of mass (COM) and the antenna phase centre (APC) arises from the fact that the force models for satellite orbit determination refer to the satellite COM, while the measurements are related to the APC. Starting from November 5, 2006 (GW 1400), the IGS convention applies the so-called absolute phase centre model igs05 (igs05_wwww.atx[2], wwww: GPS week of the latest update), including the satellite-specific z-offsets with an accuracy of several centimetres and the block-specific, nadir-dependent phase centre variations (PCV) with a precision at the sub-millimetre level (Schmid et al., 2007). The PCV of the individual satellites within one block type are quite similar, while large differences of up to 70 cm are present in the z-offsets within the Block II/IIA satellites. The GPS satellite-specific z-offsets vary from 0.5 to 2.65 m, and the block-specific PCV values reach up to about 1 cm (Karabatić, 2011, p. 25, 26). For the horizontal satellite antenna phase centre offsets (PCO), i.e., x- and y-offsets, the block-specific values provided by the satellite manufacture are used in igs05. In the case of PPP, the neglect of the satellite PCO may cause systematic errors of several centimetres in the horizontal components and up to 10 cm in the vertical component, whereas the non-consideration of the satellite PCV leads to a maximum error of 1 mm in the vertical component (Heßelbarth, 2009).

Satellite phase wind-up effect. The phase wind-up effect occurs due to changes in the mutual orientation of the transmitting satellite and the receiving antenna. For a static receiver, its antenna remains oriented towards a fixed reference direction (usually north), while the GPS satellite antennas undergo rapid rotations of up to one revolution within less than half an hour when passing the subsolar point (the so-called noon turn with the Sun-satellite-Earth constellation) and after leaving the Earth's shadow (the so-called midnight turn with the Sun-Earth-satellite constellation). Since about 1994, most of the IGS AC employ the phase wind-up correction model proposed by Wu et al. (1993), which is only applicable to static receivers. Beyerle (2009) generalised this model for arbitrary receiver antenna orientations and pointed out the necessity of the phase wind-up correction in GPS reflectometry. This satellite-specific effect is significant for PPP when fixing the IGS satellite orbits and clocks, as it can reach up to one half of the wave length and result in dm-level position errors (Kouba, 2009). For a detailed discussion on the theoretical background of this phenomenon, see, for example, Tetewsky and Mullen (1997). Practical correction models for the receiver phase wind-up effect during kinematic PPP are presented in Le and Tiberius (2006).

Satellite hardware delay. The hardware delays in the satellite and receiver electronics lead to non-integer ambiguities and cause biases between the code signals on L1 and L2, also known as inter-frequency biases. Since the hardware delays are fully correlated with the clock parameters, the resulting biases can only be determined in a differential way as differential code biases (DCB; Steigenberger, 2009, p. 16). The inter-frequency P1P2-DCB can be obtained from a global ionosphere analysis and vary from -5 to 8 ns for the GPS satellites. The biases between the two types of L1 code measurements, referred to as the intra-frequency P1C1-DCB, can be computed within a global clock analysis using the LC3. The magnitude of the P1C1-DCB is approximately one third of the P1P2-DCB, ranging between -2 and 2 ns. As shown in Dach et al. (2007a, p. 281, 282), the satellite-specific DCB values are rather stable over time. The inter-frequency biases play an important role in the determination of absolute ionosphere parameters from dual-frequency (raw or smoothed) code measurements (Newby, 1992; Rideout and Coster, 2006). The intra-frequency biases must be considered when estimating satellite clocks or solving ambiguities using code observations, for example, by means of the Melbourne-Wübbena linear combination LC6 (see equation (3.8); Dach et al., 2007a, p. 182).

---

[2]`ftp://igscb.jpl.nasa.gov/igscb/station/general/pcv_archive`

Atmospheric effects

Ionospheric effects. Extending from an altitude of about 50 km to about 1000 km, the ionosphere speeds up the propagation of carrier-phase beyond the speed of light, while it slows down pseudo-code by the same amount. Since the ionosphere is a dispersive medium for microwaves, the resulting delay is frequency-dependent. More precisely, the lower the frequency is, the larger the delay will be. The ionospheric delay is proportional to the total electron content (TEC) along the GPS signal path, which in turn depends on the time of day/year, the 11-year solar cycle, and the geographical location (El-Rabbany, 2006, p. 53). The maximum ionospheric delay appears in the region about 10°-15° north and south of the geomagnetic equator where the Earth's magnetic field is horizontal. The use of the LC3 eliminates the first-order (99.9%) ionospheric effect reaching up to 150 m at low elevation angles during the ionospheric maximum. The second-order delay may cause a range bias of up to 4 cm at a satellite elevation angle of 10°, while the magnitude of the third-order effect is about 1 to 4 mm (Steigenberger, 2009, p. 26). Analysing the second-order ionospheric delay, Elsobeiey and El-Rabbany (2011) showed that its effects on GPS satellite orbit and clock reach up to 2 cm and 0.067 ns (i.e., a range error of 2 cm), respectively. Moreover, the consideration of the second-order effect, along with advanced tropospheric models, can improve the PPP coordinate solution by 3 mm and reduce the convergence time by 15%. Further information about the higher-order ionospheric effects and their impact on GPS parameter estimates can be found in Bassiri and Hajj (1993), Kedar et al. (2003), Fritsche et al. (2005), Hernández-Pajares et al. (2007), and Pireaux et al. (2010).

Tropospheric effects. The troposphere is the lowest part of the Earth's atmosphere and reaches up to 20 km at the equator and 7 km at the poles. It contains about 80% of the atmospheric mass and 99% of the water vapour. Unlike the ionosphere, the troposphere is electrically neutral and a non-dispersive medium for radio frequencies below 15 GHz (Hofmann-Wellenhof et al., 2008, p. 128). As a result, it delays the GPS phase and code measurements identically. The tropospheric delay is minimal at the tropospheric zenith and is equal to about 2.4 m at sea level. Subdividing the total zenith path delay (ZPD) into a dry (ZDD) and a wet (ZWD) component, the ZDD amounts to about 90% of the ZPD and increases by a factor of 10 at an elevation angle of 5°. For more accurate weather forecasts and a better understanding of the Earth's climate system, the tropospheric wet delay has been exploited to reconstruct high-resolution atmospheric water vapour fields at global and regional scales (Bevis et al., 1992, 1994; Businger et al., 1996; Ware et al., 1997; Alber et al., 2000; Baltink et al., 2002; Troller, 2004; Troller et al., 2006; Bender and Raabe, 2007; Luo et al., 2007a,b; Morland and Mätzler, 2007; Bender et al., 2008; Luo et al., 2008b; Lutz, 2009; Fuhrmann et al., 2010; Bender et al., 2011a,b; Karabatić, 2011). As can be seen from equation (3.13), high-quality ZDD and accurate MF are essential for a reliable ZWD determination, particularly when including low-elevation GPS data.

The ZDD derived based on pressure level data from numerical weather models (NWM) provided, for example, by the European Centre for Medium-Range Weather Forecasts (ECMWF; Woods, 2006), is temporally variable and delivers a more realistic a priori mode than that obtained using the standard atmosphere (STDAMT; NOAA/NASA/USAF, 1976). Steigenberger (2009, p. 23) showed cm-level biases between the ZDD computed using the STDATM and the ECMWF data, where the maximum bias of 19 cm was found in Antarctica. In the case that neither near-ground meteorological measurements nor representative weather model data are available for the GPS site, Luo et al. (2012a) proposed a height-dependent correction model for the ZDD calculated on the basis of the STDATM. By incorporating freely available regional surface meteorological data, this approach significantly reduces the mean bias in the a priori ZDD from several centimetres to about 5 mm. This correction model has been experimentally applied to regional water vapour determination using PPP (Fuhrmann et al., 2010, sect. 8.1).

Up-to-date tropospheric mapping functions mainly have the continued fraction form proposed by Marini (1972), which was later modified by Herring (1992) and Niell (1996). The Niell mapping function (NMF; Niell, 1996), derived based on radiosonde data, has the main advantage that the function value only depends on the day of year and the site location, but the disadvantages of low temporal/spatial (1 day/15° in latitude) resolution and the neglect of short-term variations of several hours to days (Niell, 2001). Furthermore, the dry NMF unrealistically assumes the same seasonal behaviour of the southern and northern hemispheres.

Recent mapping functions, such as the isobaric mapping function (IMF; Niell, 2000) and the Vienna mapping function (VMF1; Boehm et al., 2006b), rely upon the NWM and have an improved temporal resolution of 6 h. The IMF inputs include the latitude and height of the station, the height of the 200 hpa pressure level, and the ratio of the wet delay along a geometric path at an elevation angle of 3° to the zenith wet delay. The VMF1 was developed by direct ray tracing through the ECMWF weather model. Using the VMF1 instead of the NMF in GPS data analysis, Boehm et al. (2006b) found significant station height changes by up to 1 cm and precision improvements between 3 mm and 1 cm. Applying a spherical harmonic expansion up to degree and order 9 to the VMF1 parameters on a global grid, the global mapping function (GMF; Boehm et al., 2006a) represents an easy-to-implement and consistent version of the VMF1. Although the GMF is less accurate than the VMF1 in terms of modelling short-term variations, it provides more reliable height estimates than the NMF. For an elevation angle of 3°, biases of about 0.1 between the dry NMF and GMF are shown in Steigenberger (2009, p. 24). Together with the global pressure and temperature model (GPT; Boehm et al., 2007), the GMF is particularly applicable if the VMF1 is not implemented or the surface meteorological data are not available. In addition to the mapping functions in the form of continued fraction, Saha et al. (2010) proposed a new dry Tropo-Chi MF by modifying the analytical solution of the Chapman grazing incident (Chi) function. Using the Tropo-Chi function instead of the dry NMF or GMF, the vertical position error was reduced by up to about 1 cm in the Indian region.

If low-elevation data are included, the azimuthal asymmetry of the tropospheric delay at an observation site should be considered by additionally estimating horizontal troposphere gradients. These parameters describe a tilting of the tropospheric zenith (i.e., the direction with the minimal tropospheric delay) with respect to the geometrical zenith. For an elevation cut-off angle of 10°, Fuhrmann et al. (2010, p. 62) obtained meaningful and interpretable horizontal troposphere gradients from static PPP at a regional scale. A more detailed discussion of tropospheric gradients can be found in Meindl et al. (2004) and Dach et al. (2007a, sect. 11.4.3).

Site-specific effects

Multipath effects. Being a major error source of cm-level positioning, multipath effects distort the original GPS signals through interference with diffused and specularly reflected signals, primarily at the receiver antenna. The phase multipath error can reach a quarter of a cycle, that is about 4.8 cm for the L1 and 6.1 cm for the L2 carrier (Hofmann-Wellenhof et al., 2008, p. 157). However, this value may increase when using phase linear combinations, for example, the maximum multipath error for the LC3 is 21.7 cm (Wildt, 2007, p. 61). The site-specific multipath effects can be subdivided into a near-field and a far-field component. Far-field effects show short-periodic properties (up to half an hour; Seeber, 2003, p. 317) and can be averaged out over a long observation period (e.g., several hours). In contrast, near-field effects have non-zero mean and exhibit long-periodic characteristics (up to several hours; Wübbena et al., 2006a). They can be determined during the course of the robot-based absolute antenna calibration (Wübbena et al., 2006b, 2011). Purely from geometry, it is obvious that signals received from low (high) satellite elevations are more susceptible to the far-field (near-field) multipath.

A straightforward option for multipath reduction is to avoid, as far as possible, reflecting objects in the vicinity of the receiver antenna. Further methods for multipath mitigation can be classified as follows: (1) antenna-based attenuation (e.g., improving the antenna gain pattern by choke rings, taking advantage of the right-handed signal polarisation, and using absorbent antenna ground planes), (2) improved receiver architecture (e.g., employing the Gated Correlator, the advanced Strobe Correlator, and the enhanced MEDLL[3]; Ray, 2006), and (3) advanced signal and data processing (e.g., exploring the signal-to-noise ratio, smoothing carrier-phases, and performing stacking and filtering techniques). For more information about multipath mitigation, see, for example, Dißner (2007, sect. 3.1.7) and Hofmann-Wellenhof et al. (2008, sect. 5.6.3).

Receiver antenna models. For a receiver antenna, the antenna phase centre (APC) at which the GPS signal is received does not necessarily coincide with the antenna geometrical (mechanical) centre. The antenna PCO is the difference between the mean electrical APC and the antenna reference point (ARP) that is defined by the IGS convention as the intersection of the vertical antenna axis of symmetry with the bottom of the antenna. As demonstrated by Hofmann-Wellenhof et al. (2008, p. 150, 154), the location of the mean APC is a function of the elevation cut-off angle. The deviation between the APC of an individual phase measurement and the mean APC is known as the antenna PCV, which is frequency-dependent and varies with elevation, azimuth, and intensity of the observed signal. The PCO can reach up to 10 cm, while the PCV values are usually smaller than 2 cm for geodetic antennas (Zeimetz and Kuhlmann, 2006). The magnitude of range errors caused by the receiver antenna PCO and PCV depends on the antenna type and is typically of the order of a few centimetres (El-Rabbany, 2006, p. 50).

For unchanged receiver antennas, the effects of the PCO and PCV are essentially stable, providing the prerequisite for antenna calibration. Three major calibration methods are available: (1) relative field calibration using data collected on short baselines (Mader, 1999), (2) absolute field calibration, where the GPS antenna is rotated and tilted by a high-precision robot (Wübbena et al., 2000), and (3) absolute calibration performed in an anechoic chamber (Zeimetz and Kuhlmann, 2006). The relative method determines the PCO and PCV with respect to a reference antenna (e.g., AOAD/M_T choke ring antenna). Generally, PCV values down to an elevation angle of $10°$ are determined due to the higher noise level of low-elevation data. Allowing for an enhanced error separation and bias removal, the absolute methods calibrate each antenna individually and provide elevation- and azimuth-dependent PCV down to $0°$. The calibration accuracy represents the deviations between repeated calibrations using the same antenna and method, but under different observational conditions, and is better than 1 mm for elevation angles above $10°$ and about 1-2 mm below $10°$ (Zeimetz and Kuhlmann, 2006; Görres, 2010a). The converted robot calibration values with respect to the AOAD/M_T antenna are found to be very consistent with the relative IGS values at the 1-2 mm level (Rothacher, 2001). The two absolute calibration methods agree with each other at the level of 1-2 mm (Görres et al., 2006; Zeimetz and Kuhlmann, 2008). Using the IGS orbit and clock products in PPP, the applied receiver antenna models should conform to the current IGS convention (Kouba, 2009).

Receiver hardware delay. By convention, the IGS precise satellite clock corrections must be consistent with the P1 and P2 observables. Since the clock analysis is performed on the basis of the LC3, each clock correction contains the ionosphere-free linear combination of the unknown P1 and P2 code biases. In order to be fully consistent with the satellite clock information, the code tracking data must be corrected depending on the receiver type with respect to the code registration, such as P1/P2 receivers observing C1, P1, P2 (e.g., Ashtech Z18, Javad, Topcon), C1/X2 cross-correlation receivers (e.g., Rogue, Trimble 4000), and C1/P2 receivers (e.g., recent Leica and Trimble receiver models). Otherwise, the receiver clock and position solutions may be

---

[3]multipath estimating delay lock loop

degraded. It should be noted that certain GNSS receivers cannot be uniquely attributed to one of the classes mentioned above. For example, the Trimble NetR5 behaves like a C1/P2 receiver for GPS and like a P1/P2 receiver for GLONASS (Dach et al., 2007a, p. 279, 282). By an agreed convention, no P1P2-DCB corrections are applied in any IGS AC analysis. Therefore, such DCB calibrations are not necessary when using the LC3 of P1/P2 code data or when the IGS clock products are held fixed or constrained in dual frequency PPP (Kouba, 2009). Nevertheless, the pseudo-code observations from C1/X2 and C1/P2 receivers must be corrected for the P1C1-DCB to achieve full consistency with P1/P2 data, or precise satellite clock information (Dach et al., 2007a, p. 283).

Site displacement effects

Effects of the solid Earth tides. The solid Earth tides describe the elastic response of the Earth's crust to the external tide-generating potential of the Sun and the Moon. They result in permanent and periodic site displacements in the radial and transverse directions. The radial component of the permanent tidal effect amounts to about -12 cm at the poles and about 6 cm at the equator. Adding this effect to the "conventional tide-free" position (e.g., ITRF), one obtains the so-called "mean tide" position (Petit and Luzum, 2010, p. 108).

The periodic site displacements which can be subdivided into long-periodic, diurnal, and semi-diurnal movements are typically described by spherical harmonics in terms of the Love and Shida numbers (Mathews et al., 1997). The values of these numbers depend on the site's latitude and the tidal frequency. According to the current IERS Conventions 2010 (Petit and Luzum, 2010, p. 103), the periodic site displacement vector is computed by means of a two-step procedure. The first step considers the degree 2 and degree 3 tides using the respective nominal values of the Love and Shida numbers. For the degree 3 tides, only the Moon's contribution, causing a radial displacement of up to 1.7 mm, needs to be taken into account. The second step accounts for the frequency-dependent deviations of the Love and Shida numbers from their nominal values as well as the out-of-phase contribution from the zonal tides.

Comparing the solid Earth tide models specified in the IERS Conventions 1992 and 2003, Watson et al. (2006) found aliased annual and semi-annual signals in the time series of height differences. The signal amplitudes increase as a function of latitude, amounting to 0.4 mm at the equator and 2 mm at the geographical poles. Furthermore, mm-level differences with a dominant diurnal frequency were detected in the zenith path delay (ZPD) estimates. This indicates that the choice of the solid Earth tide model is an important issue for an accurate ZPD evaluation, and thus may contribute to the error budget in the PPP-based water vapour determination.

Ocean loading displacement. The ocean loading effects on the underlying crust originate from the ocean tides and are dominated by diurnal and semi-diurnal periods. In comparison to the solid Earth tides, the ocean tide loading is more localised and the resulting site displacements are almost one order of magnitude smaller, reaching up to several centimetres in the vertical component. In addition, the non-tidal ocean loading effect caused by varying sea surface height and changing density in the water column results in mm-level vertical site displacements for coastline stations (Karabatić, 2011, p. 33; Williams and Penna, 2011). For cm-level kinematic or short-term (several hours) static PPP along coastal regions, the ocean loading effects must be taken into account. When performing static PPP on a daily basis, where troposphere and clock estimates are required, ocean loading corrections must also be included, unless the station is more than 1000 km away from the nearest coastline (Kouba, 2009). Otherwise, the ocean loading effects will map into the solutions for troposphere parameters and receiver clocks (Dragert et al., 2000). The neglect of ocean loading displacement may lead to station height errors of up to 5 cm

(Heßelbarth, 2009). In the current IERS Conventions 2010 (Petit and Luzum, 2010, p. 109), the ocean loading displacement is characterised by site-dependent tidal coefficients. Since 2007, most IGS AC apply the ocean loading corrections considering the sub-daily centre of mass (COM) tidal variations when generating their orbit and clock products (Ray and Griffiths, 2008; Kouba, 2009). Therefore, using the IGS products in a PPP solution, the ocean loading corrections should not include the COM motion.

Deformation due to polar motion. Polar motion describes the changes in the Earth's rotation axis relative to the Earth's crust as viewed from an Earth-fixed reference system (e.g., ITRF). It also causes periodic site displacements of up to several centimetres due to the resulting variations in the Earth's centrifugal potential. Unlike the solid Earth tides and the ocean loading effects, the pole tides do not average to nearly zero over 24 hours, and have predominantly Chandler ($\sim$435 days) and annual periods (Torge, 2001, p. 34). Considering the fact that the pole coordinates amount to 0.8 arcsec at most, the maximum site displacements due to polar motion can reach about 25 mm in the radial and 7 mm in the horizontal directions (Petit and Luzum, 2010, p. 116). Using the second degree tidal Love and Shida numbers, most IGS AC apply the pole tide corrections when generating their orbit and clock products (Kouba, 2009).

Sub-daily variations of the ERP. The sub-daily variations of the Earth rotation parameters (ERP), i.e., pole coordinates (x_p, y_p) and $UT1 - UTC$, are dominated by diurnal and sub-diurnal periods of ocean tide origin, and can reach up to 3 cm on the Earth's surface (Kouba, 2009). Much like the ocean tide loading, the sub-daily ERP variations average out to nearly zero over a period of 24 h. Nevertheless, for short-term PPP, sub-daily ERP corrections are still required to achieve sub-centimetre positioning precision. This arises from the fact that the sub-daily ERP variations are not included in the current IERS Conventions 2010 (Petit and Luzum, 2010, p. 50, 52), while they have been considered in all IGS solutions since June 30, 1996 (Héroux and Kouba, 2001). In particular, the instantaneous sub-daily ERP must be added to the tide-free IERS ERP values prior to all transformations between the ITRF and the ICRF (International Celestial Reference Frame). As Kouba (2002b) showed, an inconsistent application of the sub-daily ERP model by the IGS AC can result in significant orbit differences exceeding the 5 cm level. Moreover, the neglect of the sub-daily ERP variations in short-term PPP may introduce errors of more than 1 cm in the position, ZPD, and receiver clock estimates.

Atmospheric pressure loading. The atmospheric pressure loading (APL) can be explained as the displacements of the Earth's crust due to the temporal variations in the geographic distribution of atmospheric mass. The APL can displace the positions of geodetic sites by as much as 10 to 25 mm vertically and one-third to one-tenth of this magnitude horizontally, particularly in the continental medium- and high-latitude regions where the largest pressure variations prevail (van Dam et al., 1994; Mangiarotti et al., 2001; Brondeel and Willems, 2003; Rodrigues, 2007). Like the ocean loading, the APL can also be separated into a tidal and a non-tidal part, where the non-tidal component plays a dominant role (Karabatić, 2011, p. 33).

The geophysical approach for modelling the APL convolves Green's function (Farrell, 1972) with a global pressure field provided by the ECMWF or by the NCEP (National Centres for Environmental Prediction) operational analyses. The ocean's response to the APL is modelled as an inverted barometer (Sun et al., 1995; Petrov and Boy, 2004). This geophysical approach, however, suffers from the availability of a global pressure data set with a minimum latency of 24 h, the low temporal and spatial resolution of the pressure data itself, as well as uncertainties in Green's function and in the ocean response model (McCarthy and Petit, 2004, p. 85). The APL corrections resulting from the geophysical model can be used to adjust site coordinates, to correct original observations (Tregoning and van Dam, 2005), and to estimate regression coefficients by

fitting local pressure variations (van Dam et al., 1994; Kaniuth and Vetter, 2006). The current IERS Conventions 2010 suggest the S_1-S_2 APL tidal model (RP03) derived from the ECMWF operational global surface pressure fields with a spatial resolution of 1.125°. The diurnal (S_1) and semi-diurnal (S_2) atmospheric tides exhibit amplitudes of up to 1.5 mm in the equatorial regions. Assuming that the oceans respond to the APL as the solid Earth, the three-dimensional surface displacements can be determined using the elastic Green's functions. Gridded values of the predicted surface displacements from the RP03 model are available online[4]. In fact, corrections for the vertical displacement are usually sufficient (Petit and Luzum, 2010, p. 112).

Recent studies presented in Dach et al. (2010) showed the advantages of applying the APL corrections at the GPS observation level as well as their impacts on geodetic datum definition and precise orbit determination. According to Steigenberger et al. (2009), parts of the APL-induced deformation may be absorbed by the troposphere modelling when using the GPT together with the GMF. This can be prevented by applying the ECMWF-derived a priori ZDD and the VMF1 so that the complete APL effect remains in the site coordinate estimates. At the time of writing, APL displacements have not been considered in the IGS products. However, in order to improve the quality of GPS data analysis, the IGS AC are required to apply the APL corrections, for example, by means of the RP03 model.

Further loading displacements. Further loading effects due to changes in snow and ice cover, soil moisture and groundwater, as well as in ocean-bottom pressure, also contribute to site displacements. Nominally, they have a comparable or smaller magnitude than the APL. However, at seasonal time scales, hydrological loads may cause larger surface displacements than air pressure, reaching up to 30 mm in the vertical component (Blewitt et al., 2001; Schuh et al., 2004). Models for non-tidal motions associated with changing environmental loads are still under development. Thus, they are not included in the current IERS Conventions 2010 (Petit and Luzum, 2010, p. 99). Since the unmodelled loading effects remain as signals in the geodetic time series results, they can be extracted in post-analysis studies, for example, based on long-term (several years) GPS coordinate time series and GRACE (Gravity Recovery And Climate Experiment) surface load estimates (Tregoning et al., 2009).

Relativistic effects

Effects on the equation of motion. The major acceleration correction to the equation of motion, known as the Schwarzschild term, is due to the general relativistic curvature of space-time caused by the Earth's gravity field. In the case of GPS, it can reach up to $3 \cdot 10^{-10}$ ms^{-2} (Zhu and Groten, 1988). The much smaller effects of the de Sitter precession ($2 \cdot 10^{-11}$ ms^{-2}) and the Lense-Thirring precession ($1 \cdot 10^{-12}$ ms^{-2}) can be neglected (Steigenberger, 2009, p. 36). While the Schwarzschild term primarily results in a secular shift in the argument of perigee, the Lense-Thirring and de Sitter effects cause precessions of the orbital plane. Within the context of orbit determination, the neglect of the Schwarzschild term may lead to an apparent reduction of the orbit radius by 4 mm for circular orbits at all heights (Petit and Luzum, 2010, p. 156).

Shapiro (gravitational) time delay. The Shapiro time delay, in this case, describes the increased propagation time of GPS signals due to the space-time curvature induced by the Earth's gravity field. The propagation correction to obtain the Euclidean distance depends on the geometry between the station, the satellite, and the geocentre, amounting to a maximum of about 19 mm. Note that this maximum only applies to absolute point positioning (Zhu and Groten, 1988; Hofmann-Wellenhof et al., 2008, p. 145).

---

[4]`http://geophy.uni.lu/ggfc-atmosphere/tide-loading-calculator.html`

Effects on satellite clocks. By convention, the relativistic effects on satellite clocks are sub-divided into a constant and a periodic component. The constant part is attributed to both general and specific relativity caused by the gravitational potential differences and the mean satellite velocity, respectively. This component can be compensated by shifting the nominal frequency ($f_0 = 10.23$ MHz) of all GPS satellite frequency standards by a constant clock rate of $\Delta f / f_0 = -4.4647 \cdot 10^{-10}$ (ICD-GPS-200C, 1993, p. 11), which indicates that the standard clock in orbit will run faster by 38.575 μs/day. More specifically, the general relativistic time gain due to the satellite's altitude is about 45.6 μs/day, while the special relativistic time loss because of the satellite's orbital speed is about 7.2 μs/day (Mungan, 2006). Based on empirical analyses of the IGS final combined clock products, Kouba (2002a) found that the differences in the constant part are quite insignificant from satellite to satellite (i.e., about 0.01 μs/day). Taking the different mean orbit altitudes of the GPS satellites into consideration, the actual relativistic frequency offset for an individual satellite can differ from the constant clock shift by up to 10^{-13} (Petit and Luzum, 2010, p. 154).

The periodic part is primarily due to the eccentricity of the satellite's orbit. The amplitude of the periodic correction is proportional to the orbit eccentricity e_o, amounting to about $2.29 \cdot e_o$ μs. For GPS orbits, e_o can reach up to 0.02, leading to a maximum clock correction of 46 ns (Kouba, 2002a; Petit and Luzum, 2010, p. 154). This conventional periodic correction given in ICD-GPS-200C (1993) has been applied by the IGS for its official GPS and GLONASS clock products, which, however, can introduce small clock rate errors of up to about 0.2 ns/day, as well as periodic errors with amplitudes of about 0.1 and 0.2 ns, and periods of about 6 hours and 14 days, respectively. These small relativistic error effects are caused by the gravity field oblateness term J_2 and will become more significant for the future GPS and Galileo satellites which are equipped with better frequency standards. While the small clock rates and the 14-day periodic errors are completely absorbed into the daily clock rates, the 6-hour periodic effects necessitate frequent clock estimation and distribution (e.g., hourly; Kouba, 2004).

Effects on receiver clocks. The Sagnac effect describes a relativistic effect on the receiver clock induced by the Earth's rotation while the GPS signal propagates from the satellite to the receiver. It can lead to a relative frequency shift of $\Delta f / f_0 = 10^{-12}$, corresponding to a clock error of 10 ns or 3 m after 3 h (Hofmann-Wellenhof et al., 2008, p. 147). The Sagnac effect is generally corrected by the receiver software, and a detailed description of the correction model is provided by Marmet (2000). For more information about relativity in GPS, see, for example, Ashby (2002), Kouba (2002a, 2004), and Petit and Luzum (2010, chap. 10).

3.2.4 Stochastic model

In addition to the functional model defining the mathematical relationship between GPS measurements and the unknown parameters, the stochastic model describing the observations' statistical properties is also needed for a least-squares (LS) evaluation. The stochastic model is generally expressed by a variance-covariance matrix (VCM) that characterises the observations' precisions and correlations by the main and off-diagonal elements, respectively (Tiberius et al., 1999). To obtain the best linear unbiased parameter estimates, the inverse of the cofactor matrix $\boldsymbol{Q_{ll}}$ should be used as the weight matrix $\boldsymbol{W}$ in the LS algorithm (see section 2.1.3). As presented in table 2.2, the stochastic model affects not only the estimates, but also the accuracy measures of the unknown parameters such as phase ambiguities (Teunissen et al., 1998; Teunissen, 2000; Wang et al., 2002; Luo et al., 2008a,d), site coordinates (Howind et al., 1999; Jin et al., 2005; Schön and Brunner, 2008b), and troposphere parameters (Jin and Park, 2005; Luo et al., 2008a,c,d). A realistic accuracy assessment plays a key role in quality control and integrity monitoring (Teunissen, 1998; Kim and Langley, 2001; Wieser and Brunner, 2002).

In contrast to the functional model, which has been intensively investigated by accounting for a majority of the error sources and effects discussed in section 3.2.3, the commonly used stochastic model (VCM) still exhibits deficiencies arising from unrealistic observation weighting (variances) and the neglect of physical correlations between GPS measurements (covariances). The physical correlations can be subdivided into temporal, spatial, and cross correlations that describe observational dependencies over time, in space, and between frequencies, respectively. In order to achieve a better understanding of each constituent of the stochastic model, figure 3.2 displays schematically the structure of a fully populated VCM C_Z of the original GPS phase observations from one station (R) to four satellites (j, k, l, r) at two epochs (t_1, t_2).
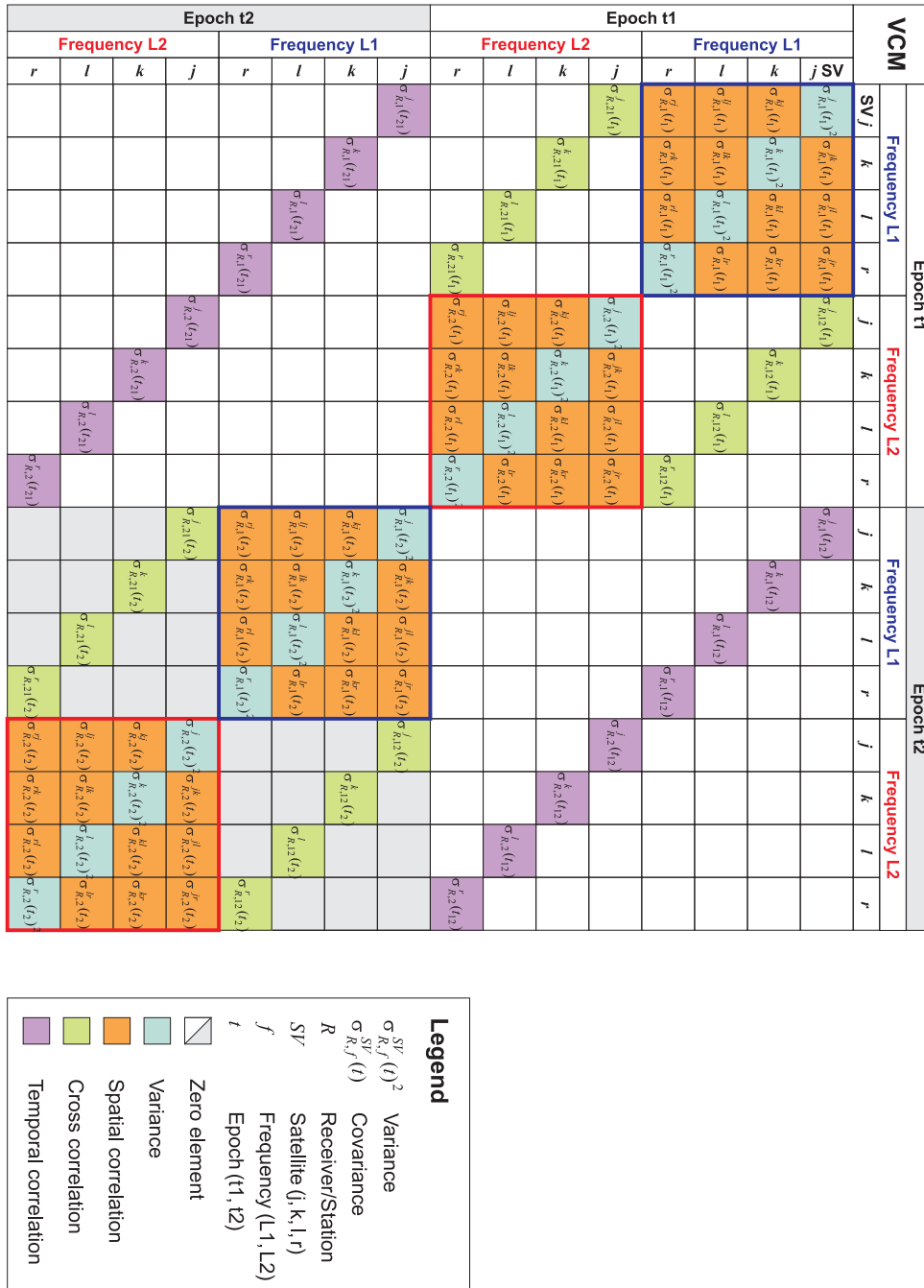

Figure 3.2: Schematic presentation of a fully populated variance-covariance matrix (VCM) C_Z of the original undifferenced phase observations in PPP (SV: space vehicle)

The main diagonal elements of the VCM characterise the observation quality and are different from each other with respect to satellite, frequency, and epoch, i.e.,

$$\left[\sigma_{R,1}^{j}(t_1)\right]^2 \neq \left[\sigma_{R,1}^{k}(t_1)\right]^2, \quad \left[\sigma_{R,1}^{j}(t_1)\right]^2 \neq \left[\sigma_{R,2}^{j}(t_1)\right]^2, \quad \left[\sigma_{R,1}^{j}(t_1)\right]^2 \neq \left[\sigma_{R,1}^{j}(t_2)\right]^2. \quad (3.26)$$

The off-diagonal elements represent the different types of physical correlations, where the so-called inter-physical correlations, including more than one correlating component (e.g., $\sigma_{R,12}^{jk}(t_1)$, $\sigma_{R,1}^{jk}(t_{12})$, $\sigma_{R,12}^{j}(t_{12})$), are assumed to be absent. Using a simplified VCM, for example, only containing the diagonal elements of variances, will result in biased parameter estimates and over-optimistic formal accuracy measures (El-Rabbany, 1994, p. 21; Howind, 2005, p. 30). In the following text, the main properties of the stochastic components are described.

Variance

The variance of an individual GPS observation σ^2 can be obtained based on the a priori variance factor σ_0^2 and the associated weight w using $\sigma^2 = \sigma_0^2/w$ (Hofmann-Wellenhof et al., 2008, p. 239). The necessity of appropriate observation weighting arises from the fact that the GPS measurements from different satellites at different epochs cannot have the same precision (e.g., due to different atmospheric effects). A precise observation should have a higher weight (or lower variance) and contribute more to the parameter estimation than an imprecise one. In statistical inferences and quality control processes, improper weights may cause outliers to remain undetected and truly high-quality observations to be rejected, leading to a considerable loss of accuracy in spite of highly redundant observations. However, in the practice of GPS data analysis, a realistic observation weighting turns out to be a difficult task due to various unmodelled factors such as tracking loop characteristics, receiver and antenna hardware properties, signal strength, receiver dynamics, multipath and atmospheric effects, and so forth (Wieser, 2007).

The simplest weighting scheme assigns an identical weight of $w = 1$ to all observations of the same type recorded by the same receiver. Under the assumption of uncorrelated GPS measurements, the VCM represents a scaled identity matrix. Due to the unrealistic assumptions of uncorrelatedness and homoscedasticity (i.e., homogeneity of variance), this simplified stochastic model is inadequate for high-precision GPS applications, particularly when including low-elevation observations (Luo et al., 2007c; Wieser, 2007; Satirapod and Luansang, 2008). The commonly applied variance model for GPS phase observations, other than a scaled identity matrix, uses the satellite elevation angle as an indicator for observation quality. The basic idea behind the elevation-dependent weighting concept is that observations at lower elevation angles suffer more strongly from atmospheric and multipath effects, hence are more noisy than those from higher elevation angles. Table 3.6 summarises some commonly used elevation-dependent variance models and the associated weight functions derived with respect to the geometrically optimum observation from the zenith direction. By specifying representative model parameters, these weight functions and the corresponding cofactor values ($q = 1/w$) are compared in figure 3.3.

Table 3.6: Commonly used variance functions depending on satellite elevation angle e

Notation	Variance function	σ_0^2 ($e = 90°$)	Weight function
CSC1	$\sigma^2 = \sigma_0^2/[2\sin(e)]$ if $e < 30°$ $\sigma^2 = \sigma_0^2$ $\quad\quad$ if $e \geq 30°$	σ_0^2	$w = \dfrac{\sigma_0^2}{\sigma^2}$
CSC2	$\sigma^2 = a^2 + b^2/\sin^2(e)$	$a^2 + b^2$	
CSC3	$\sigma^2 = [c + d/\sin(e)]^2$	$(c + d)^2$	
EXP	$\sigma^2 = [m + n \cdot \exp(-e/e_0)]^2$	$[m + n \cdot \exp(-90°/e_0)]^2$	

(a) Weight value w

(b) Cofactor value $q = 1/w$
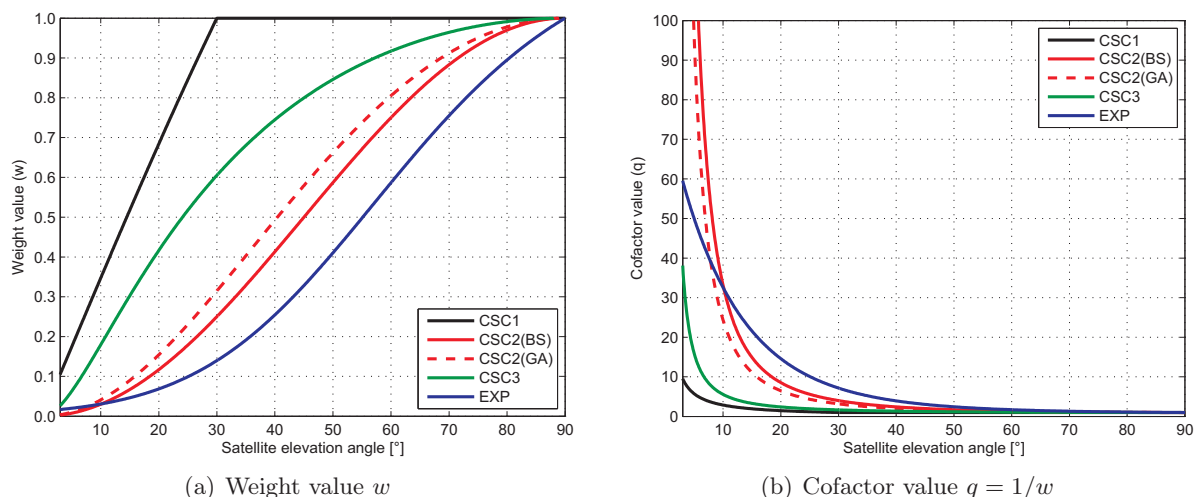
Figure 3.3: Comparison of the commonly used elevation-dependent weight and cofactor functions presented in table 3.6 (CSC2(BS): $a = 0$ mm, $b = 1$ mm, Dach et al., 2007a, p. 144; CSC2(GA): $a = 4.3$ mm, $b = 7$ mm, King and Bock, 2002, chap. 5, p. 9, 12; CSC3: $c = 5$ cm, $d = 2$ cm, Ray and Griffiths, 2008; EXP: $m = 0.3$ cm, $n = 2.6$ cm, $e_0 = 20°$, Han, 1997)

Comparing the weight and cofactor values shown in figure 3.3, particularly for low satellite elevation angles between 3° and 10°, these elevation-dependent weight functions can be categorised into three groups: (1) CSC2 strongly downweighting low-elevation observations, (2) CSC1 and CSC3 producing significantly higher weights at low elevation angles, and (3) EXP appearing to be a compromise between (1) and (2). For elevation angles larger than about 55°, the maximum difference in the cofactor values is below one. The variance function CSC2(BS) has been implemented in the Bernese GPS Software 5.0 (Dach et al., 2007a, p. 144), while the variance model CSC2(GA) is available in the GAMIT GPS data analysis package (King and Bock, 2002, chap. 5, p. 9). The CSC1 and CSC3 are employed by the IGS analysis centres (AC) GFZ (Geo-ForschungsZentrum, Potsdam, Germany) and NGS (National Geodetic Survey, NOAA, USA), respectively. A detailed overview of the observation weighting schemes used by the IGS AC is provided by Ray and Griffiths (2008). In comparison to the widely used cosecant (CSC) construction, the exponential variance function EXP proposed by Euler and Goad (1991) has the advantage of non-singularity in $e = 0°$. The model parameters m, n, and e_0 (see table 3.6) can be determined depending on the receiver and observation types.

The elevation-dependent variance models assume a strong correlation between the satellite elevation angle and GPS signal quality. They become inefficient for observations which are strongly affected by multipath effects, signal diffraction, and receiver characteristics. For measurements collected under non-ideal observational conditions, direct signal quality measures such as signal-to-noise ratio (SNR; see section 5.1) are more appropriate to assess the quality of GPS observations. In addition, since SNR values are generally available on both L1 and L2, the SNR-based variance models account for the frequency-related differences in observation quality. Langley (1997) showed the large potential of SNR as a key parameter in analysing GPS receiver performance and provided a SNR-based variance model for phase observations. In section 5.2, this variance model will be discussed in more detail.

Instead of properly specifying σ_0 and w, the variance of an individual GPS observation can be determined using variance component estimation (VCE), for example, by means of the MINQUE (minimum norm quadratic unbiased estimation) procedure (Rao, 1970, 1971). While the elevation-dependent and SNR-based variance models use the observed information before a LS adjustment is performed, the VCE is carried out based on the residuals obtained from a LS

evaluation. The basic assumption is that the LS residuals represent the same statistical properties as the true errors if the observation period is long enough to remove all systematic effects. Comprehensive details of employing the VCE technique to estimate variance-covariance components of GPS observations can be found in Wang et al. (1998), Satirapod et al. (2002), Tiberius and Kenselaar (2003), Amiri-Simkooei (2007), Li et al. (2008), Amiri-Simkooei et al. (2009), and Li et al. (2011). Moreover, Bischoff et al. (2005, 2006) provided test methods to statistically verify the hypothesis of heterogeneous variances, and estimation procedures to determine the values of variances. For GPS PPP, Satirapod and Luansang (2008) compared the MINQUE method with a scaled identity matrix and an elevation-dependent variance model of the cosecant construction. Thereby, the stochastic model estimated using the MINQUE method produced the most accurate coordinate estimates in both the horizontal and vertical components.

Covariance

The covariances are the off-diagonal elements of the VCM and represent the different kinds of physical correlations between GPS observations, such as the spatial correlation between different channels (e.g., $\rho_{R,1}^{jk}(t_1)$), the cross correlation between the L1 and L2 carriers (e.g., $\rho_{R,12}^{j}(t_1)$), and the temporal correlation between different epochs (e.g., $\rho_{R,1}^{j}(t_{12})$). On the basis of the covariances, the corresponding correlation coefficients quantifying the observational dependencies in space, between frequencies, and over time can be expressed as

$$\rho_{R,1}^{jk}(t_1) = \frac{\sigma_{R,1}^{jk}(t_1)}{\sigma_{R,1}^{j}(t_1) \cdot \sigma_{R,1}^{k}(t_1)}, \quad \rho_{R,12}^{j}(t_1) = \frac{\sigma_{R,12}^{j}(t_1)}{\sigma_{R,1}^{j}(t_1) \cdot \sigma_{R,2}^{j}(t_1)}, \quad \rho_{R,1}^{j}(t_{12}) = \frac{\sigma_{R,1}^{j}(t_{12})}{\sigma_{R,1}^{j}(t_1) \cdot \sigma_{R,1}^{j}(t_2)}.$$

(3.27)

Usually, the physical correlations are not considered in the stochastic model of GPS observations. The spatial correlation between the observations from one site to different satellites or from different sites to one satellite within one epoch is due to the similar observational conditions for these measurements. In fact, this kind of correlation makes the differencing technique applied in relative positioning effective in mitigating error effects (see section 3.3.3). Intuitively, observations being spatially close to each other are more strongly correlated than those with a large spatial distance. Applying the VCE method to residuals from a zero-baseline, Tiberius and Kenselaar (2003) detected insignificant spatial correlation coefficients of the order of −0.1-0.1, which cannot be directly transferred into PPP.

Analysing time series of the LS residuals on L1 and L2, Tiberius et al. (1999) found considerable positive correlation between the L1 and L2 phase observations, particularly for the C1/X2 cross-correlation receivers. The detected cross-correlation coefficients range between 0.3 and 0.7, depending on the receiver type. The correlation between code and phase observations seems negligible (see also Bona, 2000). Using the VCE technique, these results were verified by Tiberius and Kenselaar (2003). Recent LS-VCE studies such as Amiri-Simkooei et al. (2009) showed significant positive correlations of up to 0.8 between the L1 and L2 phase observations.

Since the residual systematic errors change slowly over time, temporal correlation may exist between the observations from one site to the same satellite at different epochs. The temporal correlation behaviour of GPS observations depends not only on the satellite geometry, but also on the prevailing atmospheric conditions (e.g., wind speed and direction; Schön and Brunner, 2008a), the site-specific effects (e.g., multipath impact; Amiri-Simkooei and Tiberius, 2007; Nahavandchi and Joodaki, 2010), and the receiver characteristics (e.g., signal smoothing and filtering; Tiberius et al., 1999; Amiri-Simkooei and Tiberius, 2007). The larger the temporal separation distance is, the weaker the temporal correlation will be. Applying atmospheric turbulence theory to GPS

carrier-phase data, Schön and Brunner (2008b) determined temporal correlation lengths of about 300-600 s for GPS double-difference observations. Smaller correlation lengths can be expected in the case of PPP, since the double differencing procedure may increase the correlation time of GPS phase observations (Nahavandchi and Joodaki, 2010).

Variance-covariance propagation

The weight matrix W_Z derived from the VCM C_Z of the original phase observations Φ_Z, as shown in figure 3.2, cannot be directly substituted into equation (3.21) for W_{Z3} of the LC3 measurements Φ_{Z3}. Relying upon the linear relationship between Φ_Z and Φ_{Z3} formulated by the matrix D_Z, the VCM of Φ_{Z3}, which is denoted as C_{Z3}, can be obtained by applying the variance-covariance propagation law to C_Z as

$$\Phi_{Z3} = D_Z \cdot \Phi_Z, \quad C_{Z3} = D_Z \cdot C_Z \cdot D_Z^T. \tag{3.28}$$

In fact, the matrix D_Z expresses the ionosphere-free linear combination LC3 in a matrix form and contains predominantly zero elements and the real-valued LC3 coefficients $k_{1,3}$ and $k_{2,3}$ (see equation (3.3) and table 3.3). According to the variance-covariance structure shown in figure 3.2, figure 3.4 displays the construction of Φ_Z, D_Z, and Φ_{Z3}. The matrix C_{Z3} computed using equation (3.28) represents a fully populated VCM for the LC3 observations. The corresponding weight matrix W_{Z3} can be calculated as $W_{Z3} = (C_{Z3}/\sigma_3^2)^{-1}$, where σ_3 is given by equation (3.7). Then, W_{Z3} is used to estimate the unknown parameters in a LS adjustment, along with the LC3 observation vector Φ_{Z3} and the design matrix A (see equation (3.19)).

Vector and matrix	Epoch t1								Epoch t2								LC3 observation vector	
	Frequency L1				Frequency L2				Frequency L1				Frequency L2					
	j	k	l	r	j	k	l	r	j	k	l	r	j	k	l	r		
Φ_Z^T	$j_{R,1}(t_1)$	$k_{R,1}(t_1)$	$l_{R,1}(t_1)$	$r_{R,1}(t_1)$	$j_{R,2}(t_1)$	$k_{R,2}(t_1)$	$l_{R,2}(t_1)$	$r_{R,2}(t_1)$	$j_{R,1}(t_2)$	$k_{R,1}(t_2)$	$l_{R,1}(t_2)$	$r_{R,1}(t_2)$	$j_{R,2}(t_2)$	$k_{R,2}(t_2)$	$l_{R,2}(t_2)$	$r_{R,2}(t_2)$	Φ_{Z3}	
D_Z	$k_{1,3}$				$k_{2,3}$												Epoch t1 — j SV	$\Phi_{R,3}^j(t_1)$
		$k_{1,3}$				$k_{2,3}$											k	$\Phi_{R,3}^k(t_1)$
			$k_{1,3}$				$k_{2,3}$										l	$\Phi_{R,3}^l(t_1)$
				$k_{1,3}$				$k_{2,3}$									r	$\Phi_{R,3}^r(t_1)$
									$k_{1,3}$				$k_{2,3}$				Epoch t2 — j	$\Phi_{R,3}^j(t_2)$
										$k_{1,3}$				$k_{2,3}$			k	$\Phi_{R,3}^k(t_2)$
											$k_{1,3}$				$k_{2,3}$		l	$\Phi_{R,3}^l(t_2)$
												$k_{1,3}$				$k_{2,3}$	r	$\Phi_{R,3}^r(t_2)$

Figure 3.4: Construction of Φ_Z, D_Z, and Φ_{Z3} corresponding to the VCM illustrated in figure 3.2

Benefiting from the continuously improved orbit and clock products, PPP has become a powerful technique with a promising future during the course of GNSS evolution. To exploit its full accuracy potential, numerous studies have been carried out aiming at ambiguity resolution, the integration of PPP with RTK and INS (inertial navigation system), and the incorporation of precise atmospheric models (Bisnath and Gao, 2009). In contrast, little attention has been paid to the stochastic model which undoubtedly plays a key role in outlier detection and integrity monitoring. Focusing on the temporal correlation of GPS observation noise, chapters 7 and 8 will extend the PPP stochastic model in a mathematically rigorous manner.

3.3 Relative positioning

Relative positioning employs at least two receivers simultaneously tracking the same satellites to determine the coordinates of an unknown point relative to a reference site with precisely known coordinates. Benefiting from the differencing technique, relative positioning generally provides a higher accuracy than autonomous positioning. Since the principle and the functional model of relative positioning are well documented in GPS literature (Hofmann-Wellenhof et al., 2008, sect. 6.3), this section gives a more detailed discussion of the error effects and the stochastic model with respect to its structure, derivation, and differences from that of PPP.

3.3.1 Introduction

For relative positioning, a minimum of four visible satellites is required at both the reference site and the remote site with unknown position. Assuming that GPS observations are sufficiently simultaneous (Wanninger, 2000, p. 11), single-, double-, and triple-differences can be formed between receivers, satellites, and epochs. The terminus single-difference used in this thesis involves two receivers and one satellite. This kind of single-difference eliminates the satellite clock bias and hardware delay. In addition, atmospheric and orbit errors are reduced, particularly for short baselines. Nevertheless, the ambiguities of single-differences are still non-integer values due to the generally unequal receiver hardware delays. Double-differences are obtained by subtracting two single-differences referring to the same baseline. The elimination of the receiver clock biases is the main reason why double-differences are preferably used. Since both the satellite and receiver hardware delays are cancelled, the double-differenced phase ambiguities have the integer property. Triple-differences, resulting from differencing double-differences between two epochs, can be used to eliminate the time-invariant ambiguities, provided that the receivers did not loose lock within this time interval. The triple-difference solution serves as an important reference for cycle slip detection. Tropospheric effects, which usually do not change rapidly with time, are considerably reduced on the triple-difference level, while this is not the case for ionospheric effects, which may show very rapid temporal variations, particularly in the high northern and southern latitudes (Dach et al., 2007a, p. 39, 116). Mathematical formulations for the differenced phase equations can be found in Hofmann-Wellenhof et al. (2008, sect. 6.3.2).

Relative positioning can be performed in both static and kinematic modes, where the static relative positioning with phase measurements is currently the most accurate satellite-based positioning technique. Depending on the baseline length, the expected accuracy using geodetic-type receivers is normally 5 mm + 0.5 ppm for the horizontal components and 5 mm + 1 ppm for the vertical component, where ppm stands for parts per million. For short baselines of up to 20 km, ambiguity resolution is a key issue to ensure high-performance positioning. In this case, it is recommended to resolve L1 and L2 ambiguities directly (Dach et al., 2007a, p. 182). For long baselines of up to several hundreds of kilometres or more, the ionosphere-free linear combination LC3 should be used along with the precise orbit product (El-Rabbany, 2006, p. 73).

The kinematic relative positioning can be subdivided into the post-processed kinematic (PPK) and real time kinematic (RTK). The PPK method starts with a process known as receiver initialisation, where the initial integer ambiguities are first determined. Once the initialisation has been successfully accomplished, cm-level positioning accuracy can be achieved. The coordinates of the unknown points are obtained by post-processing the collected data. In an RTK operation, the initial ambiguities are resolved almost instantaneously using the so-called on-the-fly ambiguity resolution technique (Hofmann-Wellenhof et al., 2008, p. 217). Establishing data communication (e.g., VHF or UHF radio, cellular telephone), the base receiver measurements and coordinates

are transmitted to the rover receiver whose built-in software processes the collected GPS data to obtain the rover's coordinates in real-time. The expected RTK positioning accuracy using geodetic-type receivers is 1 cm + 1 ppm horizontally and 2 cm + 1 ppm vertically. Under the same conditions, the positioning quality of the RTK method is slightly degraded in comparison to that of the PPK method. This is mainly due to the latency occurring at preparing and transmitting the base data, which necessitates data extrapolation to mach the time tag of the rover receiver measurements (El-Rabbany, 2006, p. 76, 77).

To achieve rapid and reliable ambiguity resolution, the maximum baseline length in a single-base RTK positioning should not exceed 20 km. This limitation is due to the distance-dependent biases such as orbit errors and signal refraction in the atmosphere (see section 3.3.3). However, these errors can be accurately modelled based on the observations from an array of GPS reference sites (Wanninger, 2000, chap. 4; Dai et al., 2001; Fotopoulos and Cannon, 2001). This leads to an extension of the RTK positioning from a single base to a multi-base technique. Moreover, continuously operating reference station networks, for example, the German Satellite Positioning Service (SA*POS*®; Stronk and Wegener, 2005), have been established to provide network RTK positioning services using the master-auxiliary concept (MAC; Brown et al., 2006), area correction parameters (FKP; Wanninger, 2002), and virtual reference stations (VRS; Wanninger, 2003). More information about the principles, limitations, and future challenges of network RTK is provided by Rizos (2003) and Wanninger (2004, 2006). Additional GPS relative positioning modes, such as rapid static and stop-and-go, can be found in El-Rabbany (2006, chap. 5).

3.3.2 Functional model

The functional model of relative positioning describes the mathematical relationship between double-differenced observations and the unknown parameters. Under the assumption of equal frequency $f = f^j = f^k$ for the satellite signals, which is the case for GPS by applying the code division multiple access (CDMA) technique, the simplified observation equation of phase double-differences relating to receivers A and B, satellites j and k, and frequency f is

$$\Phi_{AB,f}^{jk} = \rho_{AB}^{jk} + \lambda_f \cdot N_{AB,f}^{jk} + \epsilon_{AB,f}^{jk}, \tag{3.29}$$

where

ρ_{AB}^{jk}	:	double-difference of the geometrical ranges in m,
λ_f	:	wavelength of the carrier in m,
$N_{AB,f}^{jk}$	:	integer double-difference phase ambiguity in cycles,
$\epsilon_{AB,f}^{jk}$	:	random noise of the double-difference in m.

Such a simplification is valid for short baselines under ideal observational conditions (Wanninger, 2000, p. 12). The term ρ_{AB}^{jk} contains the geometry and can be decomposed as

$$\rho_{AB}^{jk} = \rho_{AB}^{k} - \rho_{AB}^{j} = \rho_{B}^{k} - \rho_{A}^{k} - \rho_{B}^{j} + \rho_{A}^{j}. \tag{3.30}$$

Substituting equation (3.30) into (3.29), the simplified observation equation becomes

$$l_{AB,f}^{jk} = \rho_{B}^{k} - \rho_{A}^{k} - \rho_{B}^{j} + \rho_{A}^{j} + \lambda_f \cdot N_{AB,f}^{jk} + \epsilon_{AB,f}^{jk}. \tag{3.31}$$

In the case of relative positioning, the coordinates of the reference site (e.g., site A) are precisely known. Accordingly, the vector of unknown parameters consists of the coordinates of the rover site B and all double-difference ambiguities, i.e.,

$$\boldsymbol{x} = (X_B, Y_B, Z_B, N_{AB,f}^{i})^T, \quad i = 1, \ldots, m_{sp}, \tag{3.32}$$

where m_{sp} denotes the number of the formed satellite pairs. Regarding all $l_{AB,f}^{jk}$ as a realisation of the vector of stochastic double-difference observables $\underline{\boldsymbol{l}_D}$ and assuming zero-mean random observation noise, the functional model of static relative positioning reads

$$\mathrm{E}(\underline{\boldsymbol{l}_D}) = \mathbf{F}(\boldsymbol{x}) = \rho_B^k - \rho_A^k - \rho_B^j + \rho_A^j + \lambda_f \cdot N_{AB,f}^{jk}. \tag{3.33}$$

The expansion of equation (3.33) into a Taylor series with respect to the approximate position of the rover site B (X_{B0}, Y_{B0}, Z_{B0}) leads to the linearised model of observation equations in the matrix form $\boldsymbol{A} \cdot \boldsymbol{\Delta\hat{x}} = \boldsymbol{\Delta l_D} + \boldsymbol{v}$. According to Hofmann-Wellenhof et al. (2008, p. 255), the design matrix $\boldsymbol{A}$ can be written as

$$\boldsymbol{A} = \left[\frac{\partial \mathbf{F}(\boldsymbol{x})}{\partial X_B}, \frac{\partial \mathbf{F}(\boldsymbol{x})}{\partial Y_B}, \frac{\partial \mathbf{F}(\boldsymbol{x})}{\partial Z_B}, \frac{\partial \mathbf{F}(\boldsymbol{x})}{N_{AB,f}^i} \right]_{i=1,\ldots,m_{sp}}^{\boldsymbol{x}=\boldsymbol{x}_0}, \tag{3.34}$$

where

$$\frac{\partial \mathbf{F}(\boldsymbol{x})}{\partial X_B} = \frac{X_B - X^k}{\rho_B^k} - \frac{X_B - X^j}{\rho_B^j}, \quad \frac{\partial \mathbf{F}(\boldsymbol{x})}{\partial Y_B} = \frac{Y_B - Y^k}{\rho_B^k} - \frac{Y_B - Y^j}{\rho_B^j}, \tag{3.35}$$

$$\frac{\partial \mathbf{F}(\boldsymbol{x})}{\partial Z_B} = \frac{Z_B - Z^k}{\rho_B^k} - \frac{Z_B - Z^j}{\rho_B^j}, \quad \frac{\partial \mathbf{F}(\boldsymbol{x})}{\partial N_{AB,f}^i} = 0 \text{ or } \lambda_f.$$

The vector of reduced parameters $\boldsymbol{\Delta x}$ can be expressed as

$$\boldsymbol{\Delta x} = \boldsymbol{x} - \boldsymbol{x}_0 = (\Delta X_B, \Delta Y_B, \Delta Z_B, N_{AB,f}^i)^T, \quad i = 1, \ldots, m_{sp}. \tag{3.36}$$

From equation (3.33), the reduced observation for $l_{AB,f}^{jk}$ is

$$\Delta l_{AB,f}^{jk} = l_{AB,f}^{jk} - \mathbf{F}(\boldsymbol{x}_0) = l_{AB,f}^{jk} - \rho_{B0}^k + \rho_A^k + \rho_{B0}^j - \rho_A^j, \tag{3.37}$$

where the position of the reference site A is assumed to be known, and the approximate $N_{AB,f}^{jk}$ is equal to zero (cf. equations (3.32) and (3.36)). Once the design matrix $\boldsymbol{A}$, the vector of reduced double-difference observations $\boldsymbol{\Delta l_D}$, and the corresponding weight matrix $\boldsymbol{W_D}$ are available, the parameter estimate $\hat{\boldsymbol{x}} = \boldsymbol{x}_0 + \boldsymbol{\Delta\hat{x}}$ and the associated VCM $\boldsymbol{C_{\hat{x}\hat{x}}}$ can be obtained from a LS adjustment. Initially, the LS ambiguity estimates are float values. The fixing of the ambiguities to their integer values, known as ambiguity resolution, fully exploits the high accuracy of the phase observations and significantly improves the quality of the parameter estimates. A detailed discussion of different ambiguity resolution algorithms is provided by Hofmann-Wellenhof et al. (2008, sect. 7.2). For geodetic-type dual-frequency receivers, the optimum ambiguity resolution strategy primarily depends on the availability of high-quality code measurements on both carriers, as well as on the baseline and session length (Dach et al., 2007a, p. 180).

3.3.3 Error sources and effects

For relative positioning using baselines, it seems reasonable to classify the error sources into distance-dependent and site-specific (distance-independent) effects. Depending on the baseline length, the spatially correlated errors, such as ionospheric and tropospheric refraction, will be reduced by differencing. In contrast, site-specific effects, for example, multipath, are individual for each station and may even be amplified when forming differences between observations (Schön, 2010). Moreover, some effects can be completely neglected for cm-level relative positioning and baselines less than 100 km, but must be taken into account when processing long baselines (e.g., more than 500 km). This section briefly describes the effects of the error sources in the solution domain, with an emphasis on the distance-dependent factors. In table 3.7, the relevant error effects limiting the relative positioning quality are listed.

Table 3.7: Error effects limiting the relative positioning quality

Distance-dependent effects	Satellite orbit errors
	Ionospheric effects
	Tropospheric effects
Site-specific effects	Multipath effects
	Receiver antenna models
Other relevant effects	Satellite antenna models
	Satellite phase wind-up effect
	Site displacement effects
	Relativistic effects

Distance-dependent effects

Satellite orbit errors. For the influence of the unmodelled satellite orbit errors on the station coordinate estimates, a handy rule of thumb is available in Dach et al. (2007a, p. 24), giving the error in baseline length Δl as a function of the error in satellite orbit ΔO as

$$\Delta l \approx \frac{l}{d} \cdot \Delta O, \tag{3.38}$$

where l is the baseline length in km, and $d \approx 25000$ km is the approximate distance between the satellite system and the survey area. Substituting the current accuracy specifications of the IGS products for GPS satellite orbits into equation (3.38), the resulting errors in baseline length are presented in table 3.8. Obviously, for regional networks consisting of baselines shorter than 500 km, the expected errors in baseline length due to inaccurate satellite orbits are below 1 mm if the IGS ultra-rapid, rapid, or final orbit products are used. Furthermore, satellite orbit errors may cause apparent network rotations (Beutler et al., 1989).

Table 3.8: Approximate errors in baseline length (Δl) using different IGS products for GPS satellite orbits (see equation (3.38), unit: mm)

Baseline length [km]	Accuracy of the IGS orbit product [mm][1]			
	Broadcast	Ultra-rapid (P)[2]	Ultra-rapid (O)[2]	Rapid & Final
	1000	**50**	**30**	**25**
10	0.4	0.0	0.0	0.0
100	4.0	0.2	0.1	0.1
500	20.0	1.0	0.6	0.5
1000	40.0	2.0	1.2	1.0

[1] `http://igscb.jpl.nasa.gov/components/prods.html`
[2] P: predicted part, O: observed part

Ionospheric effects. An erroneous estimate of the ionospheric total electron content (TEC) affects single-frequency relative positioning primarily in the form of a scale error. For the maximum zenith angle $z_{max} = 80°$ on a medium-latitude site, an underestimation of the TEC by 10 TECU (1 TECU $= 10^{16}$ electrons/m^2) leads to a decrease in baseline length of 0.7 ppm (i.e., $l = 100$ km $\rightarrow \Delta l = 7$ cm; Santerre, 1989, p. 108). The magnitude of this scale effect depends on the site location, solar activity, and occurrence of sudden ionospheric disturbances. Using the ionosphere-free linear combination LC3, the ionospheric effects can be largely reduced. However, the employment of the LC3 has the disadvantages of complicated ambiguity resolution as well as increased multipath effects and observation noise. Therefore, for baselines of up to several kilometres, the LC3 is not recommended and single-frequency relative positioning is even preferred

for coordinate estimation (Wanninger, 2000, p. 19). If dual-frequency observations are available, ionosphere models can be determined using the geometry-free linear combination LC4 on the zero- or double-difference level. Local and regional ionosphere models can be derived by applying two-dimensional Taylor series expansions, while continental and global ionosphere maps can be generated with the help of spherical harmonic expansions (Dach et al., 2007a, chap. 12).

Tropospheric effects. According to Beutler et al. (1988), the troposphere biases in relative positioning can be subdivided into an absolute and a relative component. The absolute troposphere biases are caused by errors arising from tropospheric refraction which are common to both endpoints of a baseline. They mainly produce scale errors in the estimated baseline lengths. The relative troposphere biases are due to errors of tropospheric refraction at one endpoint of a baseline relative to the other. They primarily induce errors in the estimated station heights. Assuming uniformly distributed satellites above the observing sites, the impact of an absolute (ΔT_a^0) and a relative troposphere bias in the zenith direction (ΔT_r^0) can be calculated as

$$\frac{\Delta l}{l} = \frac{\Delta T_a^0}{R_E \cdot \cos(z_{max})}, \quad \Delta h = \frac{\Delta T_r^0}{\cos(z_{max})}, \tag{3.39}$$

where $R_E \approx 6371$ km is the Earth's radius, Δl is the error in baseline length, and Δh is the bias in station height. For $z_{max} = 80°$ or an elevation cut-off angle of $10°$, equation (3.39) implies that an absolute troposphere bias of 7 cm causes a scale bias of 0.06 ppm (i.e., $l = 100$ km $\rightarrow \Delta l = 6$ mm), whereas a relative troposphere bias of 1 mm already leads to an error of approximately 6 mm in the estimated station height. Note that relative troposphere errors are much more important for local and regional applications. Table 3.9 provides more numerical examples of the biases caused by the atmospheric effects in relative positioning.

Table 3.9: Examples of biases in baseline length (Δl) and station height (Δh) induced by atmospheric effects (see equation (3.39), unit: m)

Baseline length [km]	Ionosphere (Δl)	Troposphere (Δl)		Troposphere (Δh)	
	10 TECU (0.7 ppm)	$\Delta T_a^0 = 0.1$ m		$\Delta T_r^0 = 0.01$ m	
	$z_{max} = 80°$	$z_{max} = 80°$	$z_{max} = 87°$	$z_{max} = 80°$	$z_{max} = 87°$
10	0.007	0.001	0.009	0.058	0.191
100	0.070	0.009	0.087		
500	0.350	0.045	0.437		
1000	0.700	0.090	0.874		

In comparison to the satellite orbit errors, the atmospheric effects reach orders of magnitude above the noise level of GPS phase observations and play a dominant role in the error budget of relative positioning. Due to the fact that the tropospheric refraction originates from the lowest part of the Earth's atmosphere (99% below 10 km) whereas the ionospheric shell height is about 400 km, the tropospheric effects are more site-specific and can be accounted for by estimating site-specific troposphere parameters and gradients in GPS data processing. However, using differenced observations in relative positioning, the resulting troposphere solutions may be biased by a constant offset, particularly for local and regional networks (i.e., $l < 500$ km; Kouba, 2009). To achieve the absolute level, an external tropospheric calibration is required, for example, by means of PPP or the IGS combined troposphere products (Byun and Bar-Sever, 2009). Furthermore, the strong correlation between the zenith tropospheric delay and station height estimates can be considerably reduced by lowering the elevation cut-off angle. Appropriate handling of low-elevation observations requires advanced mapping functions (e.g., GMF, VMF1) on the one hand, and improved stochastic models (e.g., observation weighting) on the other.

Site-specific effects

Multipath effects. For precise relative positioning with short baselines, multipath represents the major systematic error source and its impact on carrier-phases should generally not exceed about 1 cm under good satellite geometry over a reasonably long observation period. Nevertheless, a simple change of the receiver antenna height may increase the multipath effects and deteriorate the positioning results (Hofmann-Wellenhof et al., 2008, p. 155). In addition to the techniques employed in antenna and receiver design, different data-processing approaches have been proposed for multipath mitigation, such as wavelet algorithms (Xia and Liu, 2001; Souza and Monico, 2004; Satirapod and Rizos, 2005; Zhong et al., 2008; Wu et al., 2009), SNR-based methods (Bilich, 2006; Bilich and Larson, 2007; Bilich et al., 2008; Rost and Wanninger, 2009, 2010; Rost, 2011), sidereal filtering (Zheng et al., 2005; Ragheb et al., 2007; Zhong et al., 2010; Lau, 2012), and least mean square adaptive filters (Ge et al., 2000; Weinbach et al., 2009; Liu et al., 2011). Analysing the temporal characteristics of multipath errors by means of auto-covariance functions, Nahavandchi and Joodaki (2010) modelled multipath effects stochastically. Making use of the site environment information, for example, represented by a georeferenced 3D site digital model, Fan and Ding (2006) employed the electromagnetic modelling technique to determine GPS phase multipath signals and visualised their propagations in an urban 3D model. The variety of multipath mitigation methods indicates that a generally valid and applicable multipath model is still lacking, which is mainly attributed to its strong time- and location-dependent properties. For rapid static survey applications, longer observation periods are advisable in the presence of strong multipath interference.

Receiver antenna models. In short-baseline relative positioning using the same antenna type and orientation, phase centre corrections only insignificantly affect the coordinate estimates, because the satellite signals are received under the almost identical azimuth and elevation angles. Nonetheless, if different antenna types are used at either end of a baseline, receiver antenna models must be considered in accordance with the current IGS convention. For long-baseline solutions, even using the same antenna type, calibration effects will not cancel out due to the non-negligible differences in satellite geometry caused by the Earth's curvature. These effects increase if site-specific troposphere parameters are estimated (Menge et al., 1998). Analysing a baseline of about 100 km with elevation-dependent relative and absolute receiver antenna models, Mader (2001) reported height biases varying from several millimetres to several centimetres. Furthermore, the use of radome calibrations may influence the height component by more than 1 cm. Differences between individual antennas of the same antenna type may induce discontinuities in GPS coordinate time series. This can be handled either by individual absolute antenna calibrations (e.g., chamber and robot calibration; Steigenberger, 2009, p. 151–153), or by relative calibrations with respect to an absolutely calibrated antenna.

Other relevant effects

Satellite antenna models. For cm-level relative positioning and baselines of less than 100 km, the influence of phase centre models of GPS satellite antennas can be safely neglected (Kouba, 2009). However, the only use of absolute receiver antenna corrections was found to produce a global reference frame which differs from the results achieved with very long baseline interferometry (VLBI) and satellite laser ranging (SLR) by about 15 ppb (part per billion). This corresponds to a height variation of about 10 cm for all global sites (Rothacher, 2001; Schmid and Rothacher, 2003; Zhu et al., 2003). This scale problem was solved by additionally considering absolute satellite antenna PCO and PCV which have been successively estimated by fixing the absolute receiver antenna models and the terrestrial scale (Schmid et al., 2007). Note that all satellite antenna model parameters refer to the LC3, while an absolute receiver antenna calibration (e.g.,

robot-based) delivers phase centre corrections for L1 and L2. The use of absolute instead of relative receiver and satellite antenna models in GPS global solutions leads to decreased dependency of parameter estimates on the elevation cut-off angle (Schmid et al., 2005), improved orbit consistency, reduced biases in troposphere parameters, and vertical (horizontal) coordinate changes of up to about 2 cm (1 cm) (Schmid et al., 2007; Steigenberger, 2009, sect. 9.2). For the switch from ITRF05 to ITRF08, Dach et al. (2011) performed an update of the absolute IGS antenna phase centre model by a GLONASS extension of the reprocessed GPS-only products (Steigenberger, 2009). The differences between the GPS- and GLONASS-specific receiver antenna PCV amount to 10 mm for the LC3. This update considerably affects site coordinates by up to 5 mm and most benefits GLONASS-only rapid static or kinematic solutions. Due to the antenna assembly and power supply, the satellite antenna PCV are actually azimuth-dependent (Czopek and Shollenberger, 1993) and may cause changes in the horizontal components by up to about 1 cm (Steigenberger, 2009, p. 149). However, this dependency is not considered in the current IGS phase centre model igs08 (Schmid, 2010).

Satellite phase wind-up effect. In general, the satellite phase wind-up correction can be neglected for double-difference positioning on baselines or networks spanning up to a few hundred kilometres (Kouba, 2009). However, for very long baselines (e.g., 4000 km), this correction term has been shown to amount to 4 cm (Wu et al., 1993; Steigenberger, 2009, p. 35). The receiver phase wind-up effect is fully absorbed into station clock solutions or eliminated during the course of double differencing (Le and Tiberius, 2006; Kouba, 2009).

Site displacement effects. Since the site displacement effects discussed in section 3.2.3 are nearly the same over large areas, they almost cancel out in relative positioning over short baselines (i.e., $l < 100$ km), and thus need not be considered. However, for baselines of more than 500 km, the site displacement corrections must be computed and added to the regularised[5] ITRF coordinates to obtain the instantaneous position (Kouba, 2009).

Relativistic effects. In terms of relativistic effects, the dynamic component (Schwarzschild term) and the Shapiro time delay which impact on satellite orbits and signal propagation, respectively, cannot be eliminated by differencing and cause errors of up to 0.001 ppm in positioning (i.e., 7 mm for a baseline of 7000 km; Zhu and Groten, 1988). Therefore, they should be considered in high-accuracy applications, for example, when generating satellite orbit products (Dach et al., 2007a, p. 92). The influence on the satellite clock is completely cancelled out in the between-station differences, and is harmless for relative positioning (Zhu and Groten, 1988).

3.3.4 Stochastic model

Since a double-difference is composed of four zero-differences, the stochastic model of relative positioning is more complex than that of PPP, particularly with regard to correlation type and structure. Instead of a description of the individual stochastic components, as is done for PPP, this section focuses on the mathematical correlation occurring during the course of double differencing, as well as on the variance-covariance structure and propagation. Finally, different approaches for completing and improving the stochastic model in relative positioning, especially with respect to modelling physical correlations, are briefly summarised.

---

[5]The purpose of introducing a regularised (conventional tide-free) position is to remove high-frequency time variations which are mainly caused by geophysical phenomena, in order to obtain a position with more regular time variations (Petit and Luzum, 2010, p. 34).

Mathematical correlation

If double-differenced observations are analysed, the so-called mathematical correlations between the differenced measurements must be taken into account, because the same original observation may be involved in different observation differences (Beutler et al., 1987). As shown by Santos et al. (1997), a proper modelling of mathematical correlations results in more accurate baseline lengths and more realistic formal errors of the estimated position differences. Nowadays, this type of correlation has been successfully considered in both baseline and network solutions using high-end GPS analysis software, for example, the Bernese GPS Software 5.0 (Dach et al., 2007a, p. 146). To gain a better understanding of how the mathematical correlation originates, let $\mathbf{\Phi_Z}$, $\mathbf{\Phi_S}$, and $\mathbf{\Phi_D}$ be the zero-, single-, and double-difference phase observation vector relating to two receivers (A, B) and four satellites (j, k, l, r) observed at the same epoch:

$$\mathbf{\Phi_Z} = (\Phi_A^j, \Phi_A^k, \Phi_A^l, \Phi_A^r, \Phi_B^j, \Phi_B^k, \Phi_B^l, \Phi_B^r)^T, \tag{3.40}$$

$$\mathbf{\Phi_S} = (\Phi_{AB}^j, \Phi_{AB}^k, \Phi_{AB}^l, \Phi_{AB}^r)^T, \quad \mathbf{\Phi_D} = (\Phi_{AB}^{jk}, \Phi_{AB}^{jl}, \Phi_{AB}^{jr})^T,$$

where the double- and single-differences are formed as

$$\Phi_{AB}^{jk} = \Phi_{AB}^k - \Phi_{AB}^j = (\Phi_B^k - \Phi_A^k) - (\Phi_B^j - \Phi_A^j). \tag{3.41}$$

The single- and double-differences can be computed from the matrix-vector relation

$$\mathbf{\Phi_S} = \mathbf{D_Z} \cdot \mathbf{\Phi_Z}, \quad \mathbf{\Phi_D} = \mathbf{D_S} \cdot \mathbf{\Phi_S}, \tag{3.42}$$

where $\mathbf{D_Z}$ and $\mathbf{D_S}$ are

$$\mathbf{D_Z} = \begin{pmatrix} -1 & 0 & 0 & 0 & 1 & 0 & 0 & 0 \\ 0 & -1 & 0 & 0 & 0 & 1 & 0 & 0 \\ 0 & 0 & -1 & 0 & 0 & 0 & 1 & 0 \\ 0 & 0 & 0 & -1 & 0 & 0 & 0 & 1 \end{pmatrix}, \quad \mathbf{D_S} = \begin{pmatrix} -1 & 1 & 0 & 0 \\ -1 & 0 & 1 & 0 \\ -1 & 0 & 0 & 1 \end{pmatrix} \tag{3.43}$$

with j chosen as the reference satellite for double differencing. Assuming that the observation errors of $\mathbf{\Phi_Z}$ are mutually uncorrelated and exhibit a random behaviour following a normal distribution with expectation zero and variance σ_1^2, then the VCM of $\mathbf{\Phi_Z}$, $\mathbf{\Phi_S}$, and $\mathbf{\Phi_D}$ are

$$\mathbf{C_Z} = \sigma_1^2 \cdot \mathbf{I}, \quad \mathbf{C_S} = \mathbf{D_Z} \cdot \mathbf{C_Z} \cdot \mathbf{D_Z^T}, \quad \mathbf{C_D} = \mathbf{D_S} \cdot \mathbf{C_S} \cdot \mathbf{D_S^T}, \tag{3.44}$$

where $\mathbf{I}$ is a 8×8 identity matrix, and the matrices $\mathbf{C_S}$ and $\mathbf{C_D}$ are derived by means of the variance-covariance propagation law. Substituting equation (3.43) into (3.44) yields

$$\mathbf{C_S} = \sigma_1^2 \cdot \begin{pmatrix} 2 & 0 & 0 & 0 \\ 0 & 2 & 0 & 0 \\ 0 & 0 & 2 & 0 \\ 0 & 0 & 0 & 2 \end{pmatrix} = 2\sigma_1^2 \cdot \begin{pmatrix} 1 & 0 & 0 & 0 \\ 0 & 1 & 0 & 0 \\ 0 & 0 & 1 & 0 \\ 0 & 0 & 0 & 1 \end{pmatrix}, \tag{3.45}$$

$$\mathbf{C_D} = 2\sigma_1^2 \cdot \begin{pmatrix} 2 & 1 & 1 \\ 1 & 2 & 1 \\ 1 & 1 & 2 \end{pmatrix} = 4\sigma_1^2 \cdot \begin{pmatrix} 1 & 0.5 & 0.5 \\ 0.5 & 1 & 0.5 \\ 0.5 & 0.5 & 1 \end{pmatrix}. \tag{3.46}$$

The results clearly show that the single-differences are mathematically uncorrelated, while a mathematical correlation is present in the double-differences, with a correlation coefficient of 0.5. The derivations of mathematical correlations in double-differenced network solutions and in triple-differences are well documented in Hofmann-Wellenhof et al. (2008, p. 181, 259).

Variance-covariance structure and propagation

Equations (3.43) and (3.44) indicate that the mathematical correlation introduced by double differencing is maintained when applying the variance-covariance propagation law to the VCM $\boldsymbol{C_Z}$ of the original undifferenced phase observation vector $\boldsymbol{\Phi_Z}$. Therefore, the structures of $\boldsymbol{C_Z}$, $\boldsymbol{D_Z}$, and $\boldsymbol{D_S}$ are essential for appropriately defining the stochastic model in relative positioning. Taking the temporal, spatial, and cross correlations into account, figure 3.5 illustrates schematically the construction of a fully populated VCM of $\boldsymbol{\Phi_Z}$ relating to two stations (A, B), four satellites (j, k, l, r), and two epochs (t_1, t_2).

Under the assumption that the inter-physical correlations with more than one correlating component are absent (see section 3.2.4), figure 3.5 primarily displays the covariance structure due to correlations with respect to satellite, station, frequency, and epoch. While the spatial correlation in PPP exists only between observations from one receiver to different satellites, it is also present between observations from one satellite to different stations in relative positioning (see the black dashed line frames in figure 3.5). Intuitively, observations from short baselines are more strongly correlated in space than those from long baselines. The cross and temporal correlation structures shown in figure 3.5 represent an extension of figure 3.2 for two sites.

Regarding equation (3.42), it seems reasonable to accomplish the whole differencing process in a single step using

$$\boldsymbol{\Phi_D} = \boldsymbol{D_{SZ}} \cdot \boldsymbol{\Phi_Z}, \quad \boldsymbol{D_{SZ}} = \boldsymbol{D_S} \cdot \boldsymbol{D_Z}. \tag{3.47}$$

Applying equation (3.47) to the numerical example given in equation (3.43), the resulting matrix $\boldsymbol{D_{SZ}}$ is equal to

$$\boldsymbol{D_{SZ}} = \begin{pmatrix} 1 & -1 & 0 & 0 & -1 & 1 & 0 & 0 \\ 1 & 0 & -1 & 0 & -1 & 0 & 1 & 0 \\ 1 & 0 & 0 & -1 & -1 & 0 & 0 & 1 \end{pmatrix}, \tag{3.48}$$

where the number of columns (rows) of $\boldsymbol{D_{SZ}}$ corresponds to the number of zero-differences (double-differences). Instead of showing the structures of $\boldsymbol{D_Z}$ and $\boldsymbol{D_S}$ individually, figure 3.6 visualises the construction of $\boldsymbol{D_{SZ}}$ for deriving the LC3 double-difference observations $\boldsymbol{\Phi_{D3}}$ from $\boldsymbol{\Phi_Z}$ whose VCM is illustrated in figure 3.5. For the sake of simplicity, in this example, $\boldsymbol{D_{SZ}}$ has the same structure at different epochs t_1 and t_2. Depending on the satellite geometry and the choice of the reference satellite, the construction of $\boldsymbol{D_{SZ}}$ may differ from one epoch to another. Although $\boldsymbol{D_{SZ}}$ is presented for the LC3 double-differences, it can be applied to other linear combinations using the corresponding coefficients given in table 3.3. Based on the matrices $\boldsymbol{C_Z}$ and $\boldsymbol{D_{SZ}}$ depicted in figures 3.5 and 3.6, respectively, the VCM of $\boldsymbol{\Phi_{D3}}$ can be determined by applying the variance-covariance propagation law to equation (3.47) as

$$\boldsymbol{C_{D3}} = \boldsymbol{D_{SZ}} \cdot \boldsymbol{C_Z} \cdot \boldsymbol{D_{SZ}^T}. \tag{3.49}$$

The associated weight matrix $\boldsymbol{W_{D3}}$ can be computed as $\boldsymbol{W_{D3}} = \left(\boldsymbol{C_{D3}}/\sigma_3^2\right)^{-1}$, where σ_3 in relative positioning is equal to

$$\sigma_3 = 2\sigma_1 \cdot \sqrt{k_{1,3}^2 + k_{2,3}^2} \tag{3.50}$$

with the coefficients $k_{1,3}$ and $k_{2,3}$ provided in table 3.3 (see also Howind, 2005, p. 29). Using the fully-populated weight matrix $\boldsymbol{W_{D3}}$ together with the LC3 double-difference observation vector $\boldsymbol{\Phi_{D3}}$ and the design matrix $\boldsymbol{A}$ given in equation (3.34), a LS adjustment can be performed to estimate the unknown parameters such as site coordinates and phase ambiguities. Additional discussion of the VCM structure in relative positioning is available in Howind et al. (1999).
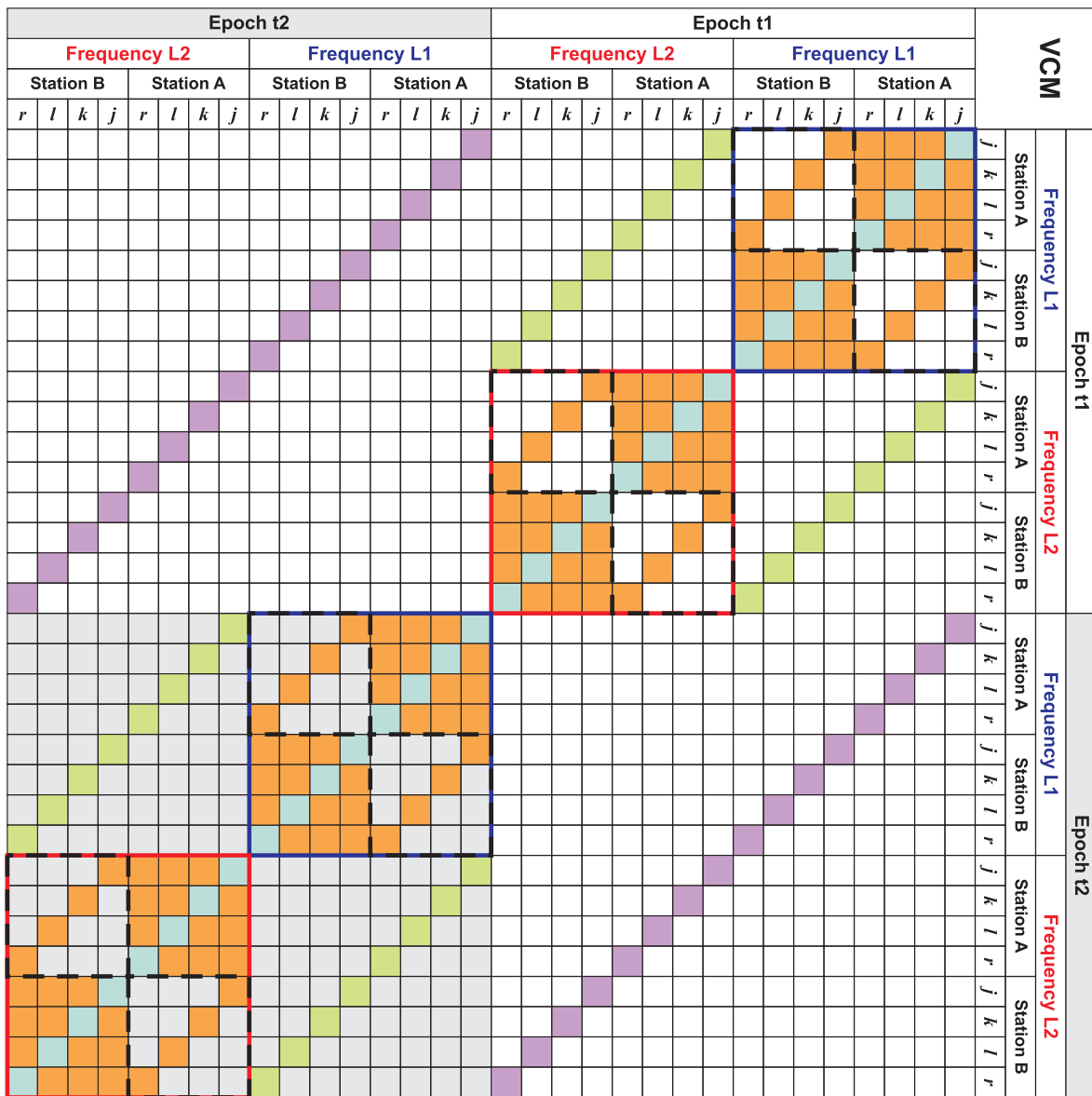
Figure 3.5: Schematical presentation of a fully populated variance-covariance matrix (VCM) C_Z of the original undifferenced phase observations in relative positioning (cf. figure 3.2)

Figure 3.6: Construction of $\boldsymbol{\Phi}_Z$, $\boldsymbol{D_{SZ}}$, and $\boldsymbol{\Phi_{D3}}$ corresponding to the VCM shown in figure 3.5

Improved stochastic models of GPS observations

Up to now, different methods have been proposed to improve the stochastic model of GPS observations in relative positioning. Table 3.10 provides an overview of these methods with respect to variance and covariance modelling. While the elevation-dependent and SNR-based variance (or observation weighting) schemes are usually applied to the original undifferenced measurements, the VCE technique is often performed based on the residuals of differenced observations from zero and ultra-short baselines. Moreover, the VEC method has been successfully employed to study the covariance structure of GPS observations and receiver noise characteristics (Tiberius and Kenselaar, 2003; Amiri-Simkooei and Tiberius, 2007; Li et al., 2008; Amiri-Simkooei et al., 2009; Li et al., 2011). Analysing time series of observation residuals, the temporal and spatial correlations haven been investigated by means of ACF, CCF, and ARMA processes (Bona, 2000; Wang et al., 2002; Howind, 2005, p. 57; Leandro and Santos, 2007; Luo et al., 2012b). In addition to the mathematical approaches, the application of ATT enables a better understanding of the physical processes that correlate and decorrelate GPS phase observations (Schön and Brunner, 2008a,b). It is worth mentioning that among all the listed techniques, VCE is the only one employed to characterise all stochastic components.

In this thesis, an empirical SNR-based observation weighting model is developed and its effects on GPS relative positioning are investigated with respect to ambiguity resolution, troposphere parameter estimation, and site coordinate determination. Furthermore, based on residual decomposition and ARMA modelling, a mathematically rigorous temporal correlation analysis is carried out and the results are statistically verified, physically interpreted, and experimentally used to extend the PPP stochastic model. Representative GPS data and freely available surface meteorological information are incorporated into three case studies which will be described in the next chapter, along with the applied GPS data processing strategies.

Table 3.10: Approaches for completing and improving the stochastic model of GPS observations

Stochastic component		Modelling methods						
		ELV[1]	SNR[2]	VCE[3]	ACF[4]	ARMA[5]	CCF[6]	ATT[7]
Variance (observation weighting)		X	X	X				X
Covariance	Spatial correlation			X		X	X	X
	Cross correlation			X		X	X	
	Temporal correlation			X	X	X		X

[1] ELV: satellite elevation angle
[2] SNR: signal-to-noise ratio
[3] VCE: variance component estimation
[4] ACF: autocorrelation function
[5] ARMA: autoregressive moving average
[6] CCF: cross-correlation function
[7] ATT: atmospheric turbulence theory

Chapter 4

# Data and GPS Processing Strategies

This chapter describes the data and GPS processing strategies used to evaluate the efficiency of the signal-to-noise ratio (SNR)-based observation weighting and the residual-based temporal correlation modelling, which will be presented in chapters 5 and 7, respectively. In addition to representative GPS measurements, freely available surface meteorological data are incorporated, enabling a physically reasonable interpretation of the results. Section 4.1 gives an overview of the selected meteorological and GPS sites, along with the baselines formed for the case studies of relative positioning. After that, sections 4.2 and 4.3 offer more detailed information about the data characteristics and GPS processing strategies applied for relative positioning and precise point positioning (PPP). The GPS data are analysed using the Bernese GPS Software 5.0, where deeper insights into the algorithms are provided by Dach et al. (2007a).

4.1 Selecting sites and forming baselines

To verify the advantages of an improved stochastic model in high-accuracy GPS positioning (Howind et al., 1999; Özlüdemir, 2004; Jin et al., 2005) and tropospheric modelling (Jin and Park, 2005; Luo et al., 2008a,c,d; Jin et al., 2010), representative GPS observations from the German SA*POS*®(Satellite Positioning Service of the German State Survey) network are used. The investigation area is located in the Upper Rhine Graben (URG) region, which is a seismically active area in southwest Germany (Knöpfler et al., 2010; Mayer et al., 2012). The GPS data are chosen by considering the sampling interval, observation period, and data quality (e.g., site-specific multipath effects). Apart from GPS observations, freely available surface meteorological data from DWD (German Meteorological Service) stations, such as air pressure, temperature, relative humidity, and precipitation, are used to characterise the near-ground atmospheric conditions during the periods for which GPS data are processed. Figure 4.1(a) depicts the locations of the selected GPS and meteorological sites, while figure 4.1(b) shows the formed baselines and single points to be analysed within the following three case studies:

- Case study 1: long-term relative positioning,

- Case study 2: short-term relative positioning,

- Case study 3: long-term precise point positioning.

Case studies 1 and 2 are carried out to evaluate the performance of the SNR-based observation weighting model (see chapter 6), while the residual time series from case studies 2 and 3 are used to examine the temporal correlation properties of GPS observations (see chapter 8). More detailed information about the site characteristics is provided in table 4.1, where the multipath classification in case study 1 follows Mayer et al. (2004). For case studies 2 and 3, the phase multipath effects are investigated using the post-processing software WaSoft/Multipath (Wanninger and Wildt, 1997; Wanninger and May, 2000). Some results of the multipath analyses will be discussed in sections 4.2.3 and 4.3.2. As figure 4.1(a) illustrates, a total of six DWD meteorological sites are chosen, which almost cover the whole investigation area. Some properties of the meteorological stations are presented in table 4.2.

(a) GPS and meteorological sites
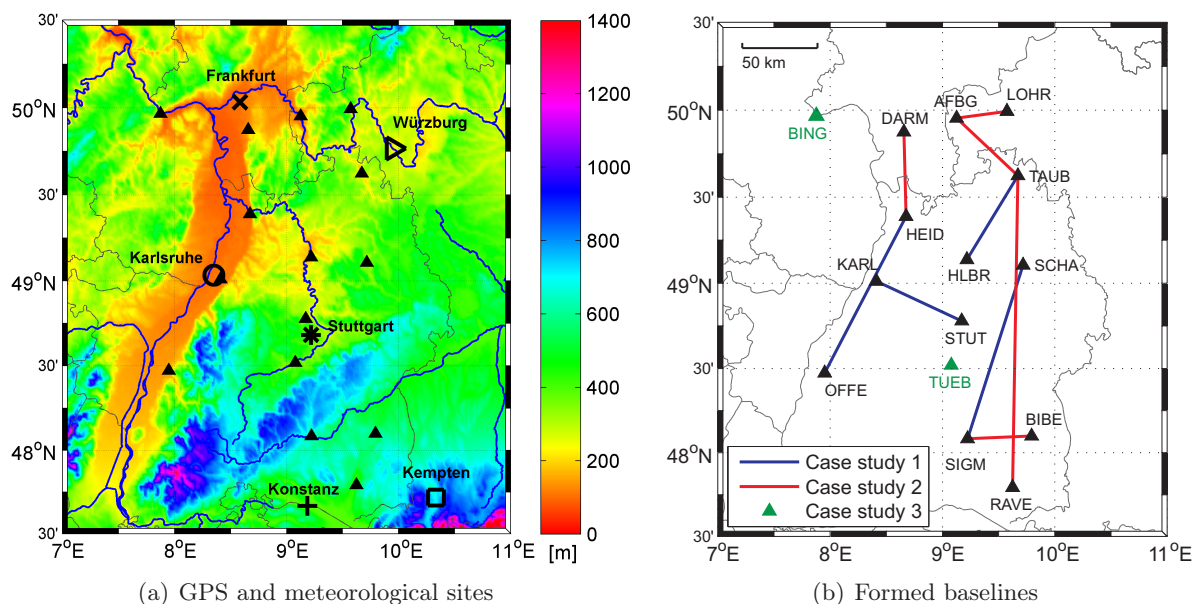
(b) Formed baselines

Figure 4.1: Selected SA*POS*®sites (filled triangle), DWD meteorological stations (multiplication sign, right point triangle, circle, asterisk, plus sign, square), and formed baselines (relief model of the Earth's surface: ETOPO1; Amante and Eakins, 2009)

Table 4.1: Characteristics of the selected SA*POS*®sites used for GPS data processing (MP: multipath)

Station name	Station ID	Lon. [°]	Lat. [°]	Height[1] [m]	Antenna type	Receiver type	MP impact
Case study 1: long-term relative positioning							
Karlsruhe	KARL	8.411	49.011	182.89	TRM29659	Trimble 4000SSI	medium
Stuttgart	STUT	9.171	48.779	341.00	TRM23903	Trimble 4000SSI	strong
Heilbronn	HLBR	9.218	49.138	234.77	LEIAT503	Leica SR520	weak
Tauberbischofsheim	TAUB	9.671	49.624	247.33	LEIAT503	Leica SR520	weak
Offenburg	OFFE	7.951	48.473	233.48	LEIAT503	Leica SR520	strong
Heidelberg	HEID	8.675	49.389	168.82	LEIAT303	Leica SR520	strong
Sigmaringen	SIGM	9.224	48.084	645.28	LEIAT503	Leica SR520	weak
Schwäbisch Hall	SCHA	9.718	49.106	433.03	LEIAT503	Leica SR520	weak
Case study 2: short-term relative positioning							
Heidelberg	HEID	8.675	49.389	168.82	LEIAT303[2]	Leica SR520	medium
Darmstadt	DARM	8.657	49.875	223.94	TRM55971[3]	Trimble NetR5	strong
Ravensburg	RAVE	9.624	47.793	503.96	LEIAT503[2]	Leica SR520	weak
Tauberbischofsheim	TAUB	9.671	49.624	247.33	LEIAT503[2]	Leica SR520	weak
Aschaffenburg	AFBG	9.126	49.954	173.49	TRM29659[4]	Trimble 4700	weak
Lohr	LOHR	9.573	49.994	225.23	TRM29659[4]	Trimble 4700	weak
Sigmaringen	SIGM	9.224	48.084	645.28	LEIAT503[2]	Leica SR520	weak
Biberach	BIBE	9.793	48.100	599.30	LEIAT503[2]	Leica SR520	weak
Case study 3: long-term PPP							
Bingen	BING	7.877	49.968	262.83	LEIAT504	Leica GRX1200PRO	strong
Tübingen	TUEB	9.078	48.519	382.19	TRM59800	Trimble NetR5	weak

[1] WGS84 ellipsoidal height
[2] Leica antenna radome: LEIC
[3] Trimble antenna radome: TZGD
[4] Trimble antenna radome: TCWD

Table 4.2: Characteristics of the selected DWD meteorological stations

Station name	Station ID	Lon. [°]	Lat. [°]	Height[1][m]	Since
Frankfurt	FRAN	8.583	50.033	112	1949
Karlsruhe	KARL	8.350	49.033	112	1876
Würzburg	WUER	9.950	49.767	268	1901
Stuttgart	STUT	9.217	48.683	371	1953
Konstanz	KONS	9.183	47.667	443	1972
Kempten	KEMP	10.333	47.717	705	1952

[1] Height above mean sea level

The DWD surface meteorological data are available online[1] free of charge. They can be downloaded in the collective standard format KL2000 and have a temporal resolution of 6 h. Meteorological observations such as air pressure (P), temperature (T), and relative humidity (RH), are registered at 6:50, 12:50, and 18:50 in Central European Time (CET), while precipitation (or rain fall RF) is measured for the CET time intervals 18:50 (previous day)-6:50, 6:50-12:50, and 12:50-18:50. Based on the relationship between CET and UTC, i.e., CET = UTC + 1 h, as well as the small difference of 15 s between GPS time (GPST) and UTC compared to the 6-hour temporal resolution (see equation (3.1)), the DWD meteorological data P, T, and RH can be considered to be approximately related to 6 h, 12 h, and 18 h in UTC or in GPST. Accordingly, they are denoted as MET_6, MET_{12}, and MET_{18}, respectively, where MET is a generic notation for the meteorological parameters.

In addition to the measurements registered at the three aforementioned time points, a daily mean value MET_m is also available for P, T, and RH, which is derived from more than 21 hourly observations or the measurements at 0 h, 6 h, 12 h, and 18 h in UTC. Therefore, using the daily mean value MET_m and the observations MET_6, MET_{12}, MET_{18}, the unavailable P, T, and RH at 0 h UTC (MET_0) can be calculated as

$$MET_0 = 4MET_m - MET_6 - MET_{12} - MET_{18}. \tag{4.1}$$

The validity and reasonability of the obtained MET_0 are verified, for example, by considering the possible ranges of the meteorological parameters. If the computed RH_0 is slightly larger than 100%, it is simply corrected to 100%. In section 4.2.2, some examples will be shown to demonstrate the applicability of equation (4.1) to the MET_0 reconstruction. While describing the individual case studies, the meteorological data will be presented in more detail. Apart from P, T, RH, and RF, additional meteorological parameters such as wind speed and direction, are also available, which may be interesting for modelling physical correlations of GPS observations based on atmospheric turbulence theory (Schön and Brunner, 2008a).

As figure 4.1(b) shows, for the case studies of relative positioning, a total of nine baselines are formed with respect to baseline length, antenna-receiver combination, and multipath impact. More detailed information about the baseline characteristics is given in table 4.3. In each case study, there exist baselines of comparable lengths, but with significantly different site-specific multipath impact, for example, OFHE and SISC in case study 1, and HEDA and TAAF in case study 2. The shortest and longest baselines are AFLO and RATA, reaching about 32 and 204 km, respectively. The absolute height differences between the two endpoints of a baseline range from 12.56 (HLTA) to 256.63 m (RATA).

---

[1] Available at `www.dwd.de` → Services A-Z → Free Meteorological Information

Table 4.3: Characteristics of the formed baselines (see figure 4.1(b))

Baseline	From	To	Length [km]	$|\Delta H|$ [m]	Multipath
Case study 1: long-term relative positioning					
KAST	KARL	STUT	61.4	158.11	strong
HLTA	HLBR	TAUB	63.2	12.56	weak
OFHE	OFFE	HEID	114.8	64.66	strong
SISC	SIGM	SCHA	119.4	212.25	weak
Case study 2: short-term relative positioning					
AFLO	AFBG	LOHR	32.4	51.74	weak
SIBI	SIGM	BIBE	42.5	45.98	weak
TAAF	TAUB	AFBG	53.7	73.84	weak
HEDA	HEID	DARM	54.1	55.12	strong
RATA	RAVE	TAUB	203.7	256.63	weak

4.2 Relative positioning processing strategies

This section focuses on the GPS processing strategies used for static relative positioning. Following a general description of the processing steps with the Bernese GPS Software 5.0, the more important specifications of the GPS data analysis are provided for the long- and short-term case studies. Furthermore, the DWD surface meteorological data and the results of the multipath analyses using the software WaSoft/Multipath are shown and discussed.

4.2.1 Processing steps

Using the Bernese GPS Software 5.0, the relative GPS positioning performed in this thesis follows the data processing strategies that have been developed and refined during the previous research projects undertaken at the Geodetic Institute of KIT (GIK), such as improved stochastic modelling of GPS phase observations (Howind, 2005), high-accuracy coordinate and velocity estimation in the Antarctic Peninsula (Mayer et al., 2000; Mayer, 2006), and extended GPS-based determination of high-resolution atmospheric water vapour fields (Luo et al., 2007a). The GPS baseline data analysis with the Bernese Software mainly consists of three steps: data preparation, data preprocessing, and parameter estimation, schematically illustrated in figure 4.2. In the following text, only the key issues in each data processing step are described. For a more detailed discussion of the `software routines`, the mathematical algorithms, and the parameter settings, the reader is referred to Dach et al. (2007a,b).

Following the campaign initialisation, which includes data collection, session definition, and site specification, the a priori station coordinates for the observation epoch can be obtained either by linearly extrapolating the coordinates from a reference epoch based on the velocity information with the program `COOVEL`, or by directly performing PPP (`PPP.PCF`) as described by Dach et al. (2007a, sect. 20.4.1). The former is usually used to derive the a priori coordinates for reference sites (e.g., IGS sites in ITRF), while the latter can be applied to new sites. The subsequent orbit part consists of the preparation of the Earth orientation parameters (EOP[2]) and the satellite ephemerides. A set of five EOP such as the pole coordinates (x_p, y_p), the difference UT1 − UTC, and the Celestial pole offsets $(d\psi, d\epsilon)$, describe the irregularities of the Earth's rotation and are

---

[2]The Earth orientation parameters (EOP) include the Earth rotation parameters (ERP) which comprise the pole coordinates (x_p, y_p) and the difference UT1 − UTC (Dach et al., 2007a, p. 85).

required for the transformation from the Earth-fixed ITRF to the space-fixed ICRF or vice versa. The program `POLUPD` transforms the EOP files from the IGS or IERS format into the Bernese format. In this thesis, only the precise ephemerides in the SP3 format are used, which represent the satellite obits as earth-fixed, geocentric positions tabulated every 15 min. Making use of the EOP, the program `PRETAB` converts the satellite positions from the earth-fixed system to the inertial system J2000.0, resulting in the intermediate tabular orbit files. Afterwards, the program `ORBGEN` performs a numerical integration of the equations of motion, and the outcomes are epoch-wise satellite positions in the binary standard orbit format with an internal consistency of about 1 cm with respect to the 15-minute tabular positions (Dach et al., 2007a, p. 95). The standard orbit and the EOP together define the satellite positions in the terrestrial reference frame. In the last step of data preparation, the RINEX (Receiver Independent Exchange Format) observation files are imported into the Bernese format by means of the program `RXOBV3`, where numerous checks on the RINEX header information are carried out.
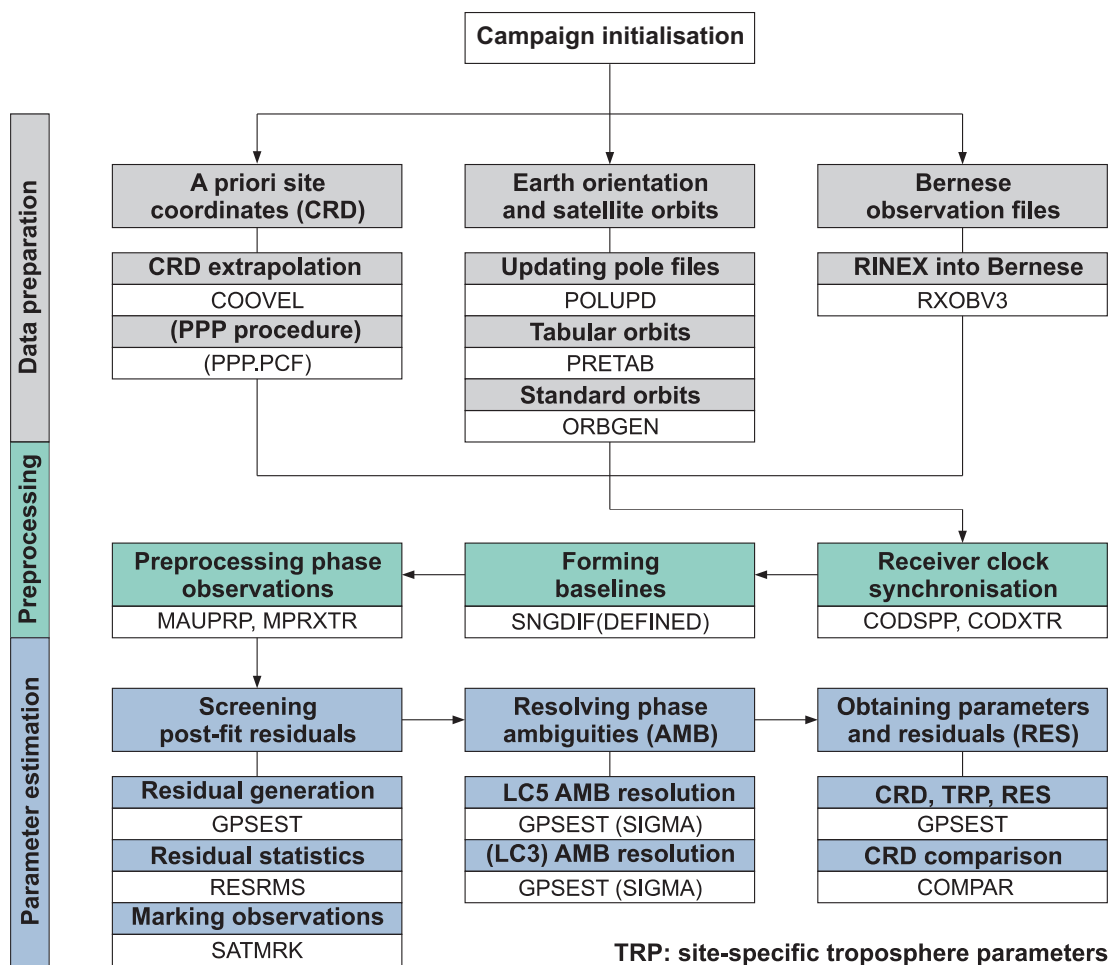
Figure 4.2: Processing steps of the GPS baseline data analysis with the Bernese GPS Software 5.0

The data preprocessing step starts with the code-based receiver clock synchronisation which computes the corrections for the receiver clocks with respect to GPS time (i.e., δt_R in equation (3.11)). Even for a double-difference data analysis, this must be accomplished in order to accurately determine the geometric distance between satellite and receiver (Dach et al., 2007a, p. 38, 39). Applying the least-squares (LS) method, the program `CODSPP` processes zero-difference code measurements (usually the ionosphere-free linear combination LC3) epoch by epoch and produces δt_R with an accuracy of less than 1 μs (Dach et al., 2007a, p. 108). Apart from the receiver clock synchronisation, `CODSPP` can be used to estimate the receiver coordinates at metre

level accuracy, provided that P-code measurements are available without selective availability (see section 3.1.3). The program `CODXTR` extracts the `CODSPP` output and provides a short summary of the code-based point positioning and data screening results. The program `SNGDIF` forms baselines from zero-difference observation files, where different strategies are available concerning the number of observations (`OBS-MAX`), the baseline length (`SHORTEST`), the network structure (`STAR`), and the baseline predefinition (`DEFINED`). The last named strategy is applied in this thesis, forming the predefined baselines shown in figure 4.1(b). In the case of relative positioning, the program `MAUPRP` works with baseline observation files. It marks low-quality observations (e.g., low-elevation data, epochs with unpaired observations, short periods of measurements), identifies significant outliers, detects cycle slips, and introduces multiple phase ambiguities, if the size of the cycle slip cannot be estimated reliably. Moreover, an epoch-difference (triple-difference) solution is performed which represents an approximation of the final solution and serves as the reference for the automatic cycle slip detection. For a successful phase preprocessing, the root mean square error of the epoch-difference solution should be less than 2 cm (Dach et al., 2007a, p. 124), and the coordinate differences, i.e., estimated − a priori, are expected to be less than about 0.5 m (Dach et al., 2007b, p. 34). The program `MPRXTR` extracts the most important information from the `MAUPRP` output and generates a summary of the baseline length, the epoch-difference solution, and the cycle slip detection.

The task of parameter estimation is primarily fulfilled by the program `GPSEST` using the LS adjustment method. Its first run for the purpose of data quality assessment produces an ambiguity-free (float ambiguity) LC3 solution based on all available observations. Although the unknown parameters, such as station coordinates (CRD) and site-specific troposphere parameters (TRP), are estimated within this run, only the normalised residuals (see section 7.2.1) are saved, which are then analysed by the program `RESRMS`. This analysis provides an overview of the data quality and generates an edit information file, containing the epochs of the outlying residuals. Using this file, the program `SATMRK` marks the corresponding measurements in the observation files. Due to the medium baseline lengths between 32 and 204 km (see table 4.3), a two-step ambiguity resolution strategy suggested by Dach et al. (2007a, p. 182) is employed in this thesis. Since good a priori station coordinates are available, the wide-lane (LC5) ambiguities are first resolved by fixing all site coordinates and by incorporating the ionosphere model provided by the Centre for Orbit Determination in Europe (CODE). After that, the resolved LC5 ambiguities are introduced to perform a narrow-lane ambiguity resolution using the LC3 phase observations (see section 3.1.5). Because of the small wavelength, the estimation of the site-specific troposphere parameters is highly recommended (Dach et al., 2007a, p. 181). In both ambiguity resolution steps, the `SIGMA`-dependent algorithm is applied (Dach et al., 2007a, sect. 8.3.3). Introducing the resolved ambiguities as known quantities, the last run of `GPSEST` produces the final parameter estimates (CRD, TRP) and the normalised double-difference residuals (RES) for temporal correlation modelling. The main purpose of the program `COMPAR` is to calculate the mean station coordinates from a list of input coordinate files and the associated repeatability.

4.2.2 A long-term case study

Within the case study of long-term relative positioning, daily (24 h) SA*POS*®data sets are processed in the static mode. In contrast to other experiments, for example, those presented by Hartinger and Brunner (1999) in which mainly short baselines (6 m, 153 m, 938 m) were analysed, the average baseline length in this case study amounts to more than 100 km (see table 4.3). The use of longer baselines enables in particular a more realistic examination of the effects of the observation weighting model on the zenith tropospheric delay estimates. Following the processing steps described in section 4.2.1, the GPS data analysis is performed on a daily basis, where some of the important specifications are listed in table 4.4.

Table 4.4: Important specifications of the GPS data analysis within the long-term relative positioning case study

Geodetic datum	ITRF2000, epoch 1997.0 (Altamimi et al., 2002)
Processing time interval	DOY2004:186-193, daily solution
GPS observation data	15-second phase double-differences
Observation weighting model	CSC2(BS) (i.e., $\sin^2(e)$, see figure 3.3)
	SNR-based (i.e., EMPSNR2, see section 5.3)
Elevation cut-off angle	$3°$ and $10°$, with screening post-fit residuals
EOP/satellite orbits	Final IGS products (24 h/15 min)
Ionosphere model	Precise CODE products
Troposphere a priori model	Saastamoinen model (Saastamoinen, 1973)
Tropospheric mapping function	Niell mapping functions (dry, wet; Niell, 1996)
Time span for troposphere parameters	2 h (Dach et al., 2007a, p. 251)
Phase ambiguity resolution	`SIGMA`-dependent strategy (LC5, LC3)
Satellite antenna correction	Relative calibration
Receiver antenna correction	Individual absolute calibration

Figure 4.3 depicts the box plots of the observed meteorological parameters $MET_{6,12,18}$ and the MET_0 computed using equation (4.1). All P_0 and T_0 values are located within the $1.5 \cdot \text{IQR}$ (interquartile range) of the lower and upper quartiles, which are given on the bottom left of the corresponding box plots. Due to the strong altitude dependency of air pressure, the obtained P_0 values cover the whole range of the pressure observations, while the T_0 values are concentrated, as expected, in the lower half of the temperature measurements. In contrast to T_0, the calculated RH_0 are predominantly in the upper half of the RH observations, with 6 out of 48 values exceeding the maximum possible RH of 100%. As the bar plot illustrates, these 6 values are very close to the upper limit, making a simple correction to 100% applicable.
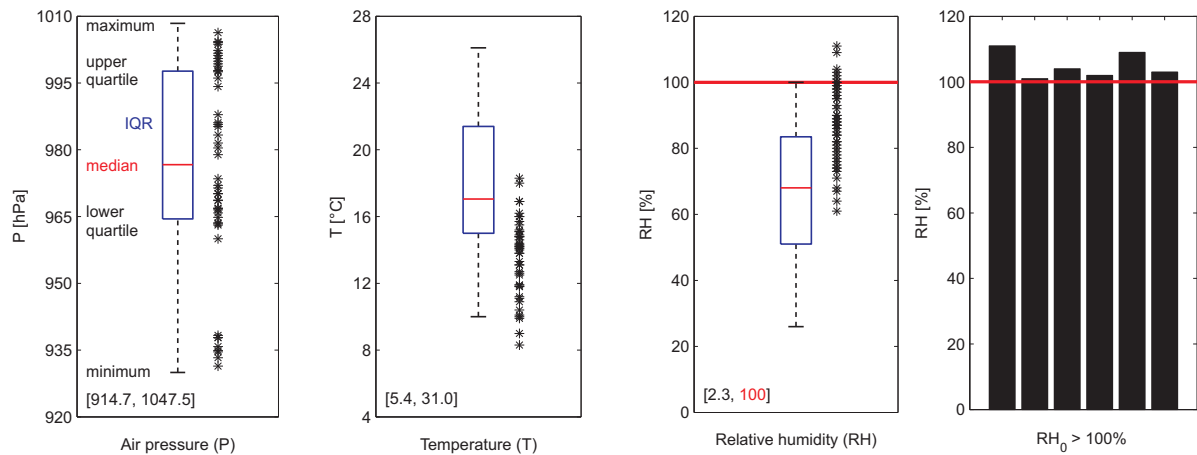
Figure 4.3: Calculated meteorological parameters MET_0 based on the daily mean MET_m and the observations MET_6, MET_{12}, and MET_{18} (see equation (4.1))

In figure 4.4, the incorporated DWD surface meteorological data are plotted for the whole investigation period of case study 1. The P values shown in figure 4.4(a) illustrate the temporally variable atmospheric conditions and the strong height dependency of air pressure (cf. table 4.2). The T and RH data clearly display diurnal variation patterns, where RH increases (decreases) with decreasing (increasing) T. This explains the opposite general tendency in the computed

RH_0 and T_0 values presented in figure 4.3. Furthermore, RH appears to be more spatially variable and site-dependent than T. Comparing the T and RH curves between the northern, middle, and southern areas, obvious differences in the near-ground atmospheric conditions are detectable, for example, on day 188. The lower T and higher RH values in the southern area, see, for instance, KEMP and KONS, evidently correspond to the increased amount of precipitation depicted in figure 4.4(d). High rain fall is registered by all DWD sites on days 190 and 191, where the weather front seems to move from the northwest towards the southeast.

(a) Air pressure P [hPa]

(b) Temperature T [°C]

(c) Relative humidity RH [%]

(d) Rain fall RF [mm]
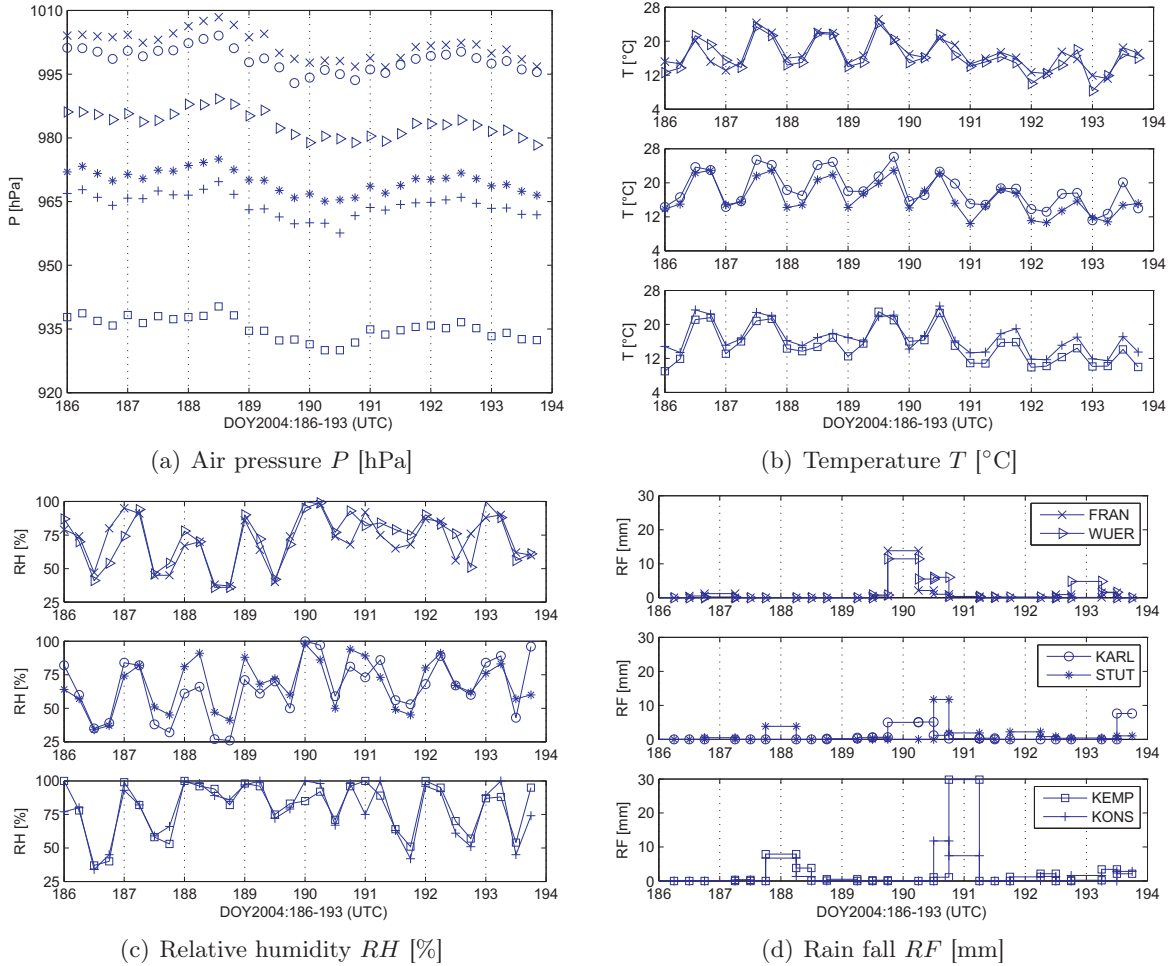
Figure 4.4: Freely available DWD surface meteorological data used to characterise the near-ground atmospheric conditions during the investigation period of case study 1 (DOY2004:186-193)

4.2.3 A short-term case study

For static GPS positioning on a daily basis, the site coordinate estimates may not significantly benefit from a realistic observation weighting model which is more appropriate for dealing with low-elevation and low-quality measurements. Therefore, another case study of short-term (3 h) relative positioning is carried out using 21 days (DOY2007:161-181) of 1-second SA*POS*®data[3]. The 3-hour time interval is selected based on the distribution of satellite elevation angles. Taking the GPS data from the SA*POS*®site Kitzingen on day 175 as an example, figure 4.5 shows the box plots and histograms of the hourly satellite elevation angles. The maximum median elevation angle is found between 10 and 11 h, and the associated histogram illustrates a relatively uniform

---

[3] Alternatively, one may analyse GPS data in the kinematic mode, where the station coordinates are estimated epoch-wise. This technique is not applied in this thesis, but should be considered in future research.

distribution. A low median elevation angle with a small interquartile range is detected between 17 and 18 h, indicating a strong concentration of low-elevation observations, as displayed in the corresponding histogram. Together with the neighbouring two hours 15-17 h in which the GPS data are also dominated by low-elevation measurements, the final 3-hour processing time interval is chosen to be 15-18 h. In addition to the site Kitzingen located in the northeast of the investigation area, satellite elevation angles from more SA*POS*®sites (e.g., Muttenz located in the southwest) are analysed in an analogous manner, yielding very similar conclusions. Furthermore, by neglecting the processing step "screening post-fit residuals" shown in figure 4.2, low-quality data are included in this case study.

(a) Box plots of the hourly satellite elevation angles   (b) Histograms associated with the selected hours
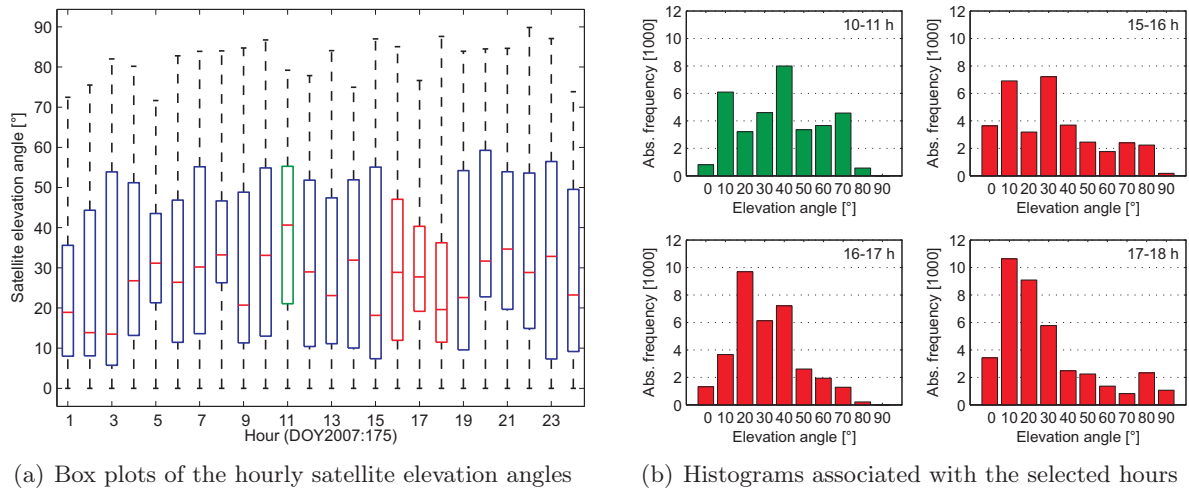
Figure 4.5: Selecting the processing time interval for the case study of short-term relative positioning based on the distribution of satellite elevation angles (SA*POS*®site: Kitzingen, 24-hour observation data, DOY2007:175, sampling interval: 1 s)

To assess the multipath impact of the SA*POS*®sites, the northern and southern sub-networks are created, with sizes of about 100 km. Using the software WaSoft/Multipath (Wanninger and Wildt, 1997; Wanninger and May, 2000), the 21 days of GPS data are analysed on a daily basis, where the original 1-second observations are resampled every 60 s to reduce the computational burden. The northern sub-network includes, among others, the sites AFBG, LOHR, HEID, TAUB, and DARM, while BIBE, SIGM, and RAVE are included in the southern sub-network. Based on the results of daily multipath analyses, figure 4.6 shows examples of mean multipath plots, illustrating weak, medium, and strong site-specific multipath effects.

(a) BIBE: weak multipath   (b) HEID: medium multipath   (c) DARM: strong multipath
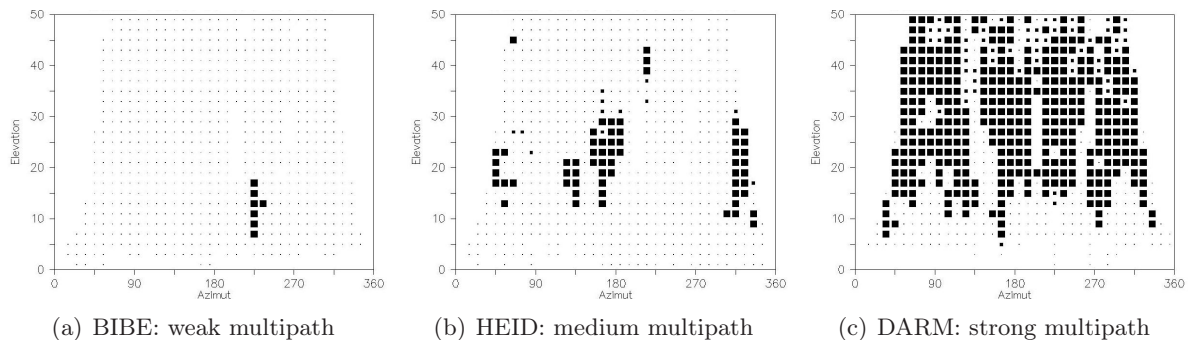
Figure 4.6: Examples of mean multipath plots generated using the software WaSoft/Multipath (DOY2007:171-181, sampling interval: 60 s; plots provided by A. Knöpfler)

In addition to the mean results, the daily multipath plots for the site HEID are presented in figure C.1. The apparent day-to-day variations are mainly due to the variable atmospheric conditions which either introduce changes to the site multipath environments or cannot be sufficiently described by the applied atmospheric models, and thus are erroneously considered as multipath signals. In the latter case, assuming that the residual atmospheric effects are random, it seems more appropriate to use the mean multipath plots than those resulting from the daily solutions. Apart from the graphic multipath characterisation, the software WaSoft/Multipath also delivers the so-called multipath index (MPI) which allows numerical analyses of multipath impact. Comparing the MPI of the sites simultaneously processed in the same network, a higher MPI indicates stronger multipath effects. For the investigation period of case study 2, figure 4.7 displays the MPI of the selected SA*POS*®sites obtained by analysing the northern and southern sub-networks. For BIBE, HEID, and DARM, the associated MPI values correspond fairly well to the mean multipath plots illustrated in figure 4.6. Moreover, the LOHR-related MPI curve exhibits significant increases on days 171, 172, and 173, which is in fact due to the low-quality GPS data contaminated by numerous observation gaps and short periods of measurements. This will be discussed in more detail when analysing the influence of the SNR-based observation weighting model on site coordinate estimates (see section 6.2.4).

(a) Northern sub-network   (b) Southern sub-network
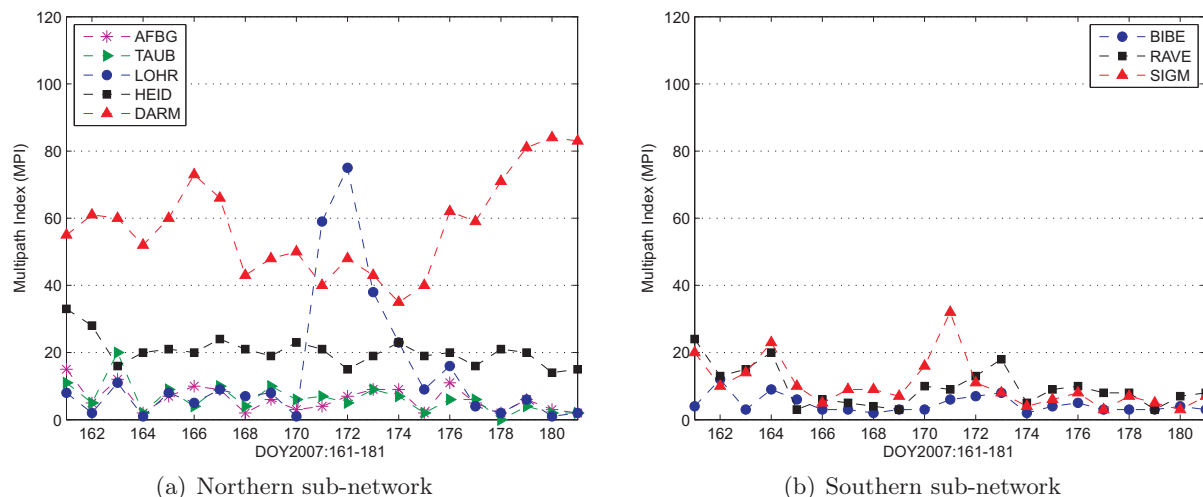
Figure 4.7: Site multipath index (MPI) provided by the software WaSoft/Multipath (DOY2007:161-181, sampling interval: 60 s)

Except for the processing step "screening post-fit residuals", the GPS data analysis scheme shown in figure 4.2 is also applied to the short-term relative positioning. However, considering the short data sampling interval of 1 s, some parameter settings, particularly in the step of data preprocessing using the program `MAUPRP`, must be adapted for reliable observation check, cycle slip detection, and outlier rejection. An elevation cut-off angle of 3° is specified for this case study. Due to the short processing time interval of 3 h, the site-specific troposphere parameters are estimated every 15 min. Such a time span was empirically determined by analysing 1-hour GPS data with different time windows of 5, 10, 15, 30, and 60 min. Thereby, the 15-minute variant appeared to be a good compromise between sufficient troposphere characterisation and precise parameter estimation. Examples within this context will be presented in section 6.2.3. For the investigation period of this case study, the IGS absolute phase centre model is readily available which includes satellite-specific z-offsets and block-specific phase centre variations (see section 3.2.3). The use of the absolute phase centre model improves the consistency between the satellite and receiver antenna corrections. Table 4.5 lists some important specifications of the GPS data analysis carried out within case study 2.

Table 4.5: Important specifications of the GPS data analysis within the short-term relative positioning case study

Geodetic datum	ETRS89, epoch 1989.0 (Boucher and Altamimi, 1992)
Processing time interval	DOY2007:161-181, 15-18 h (GPS time)
GPS observation data	1-second phase double-differences
Observation weighting model	CSC2(BS) (i.e., $\sin^2(e)$, see figure 3.3)
	SNR-based (i.e., EMPSNR2, see section 5.3)
Elevation cut-off angle	$3°$, *without* screening post-fit residuals
EOP/satellite orbits	Final IGS products (24 h/15 min)
Ionosphere model	Precise CODE products
Troposphere a priori model	Saastamoinen model (Saastamoinen, 1973)
Tropospheric mapping function	Niell mapping functions (dry, wet; Niell, 1996)
Time span for troposphere parameters	15 min (empirically determined, see section 6.2.3)
Phase ambiguity resolution	`SIGMA`-dependent strategy (LC5, LC3)
Satellite antenna correction	IGS absolute antenna model (Schmid et al., 2007)
Receiver antenna correction	Individual absolute calibration

(a) Air pressure P [hPa]

(b) Temperature T [°C]

(c) Relative humidity RH [%]

(d) Rain fall RF [mm]
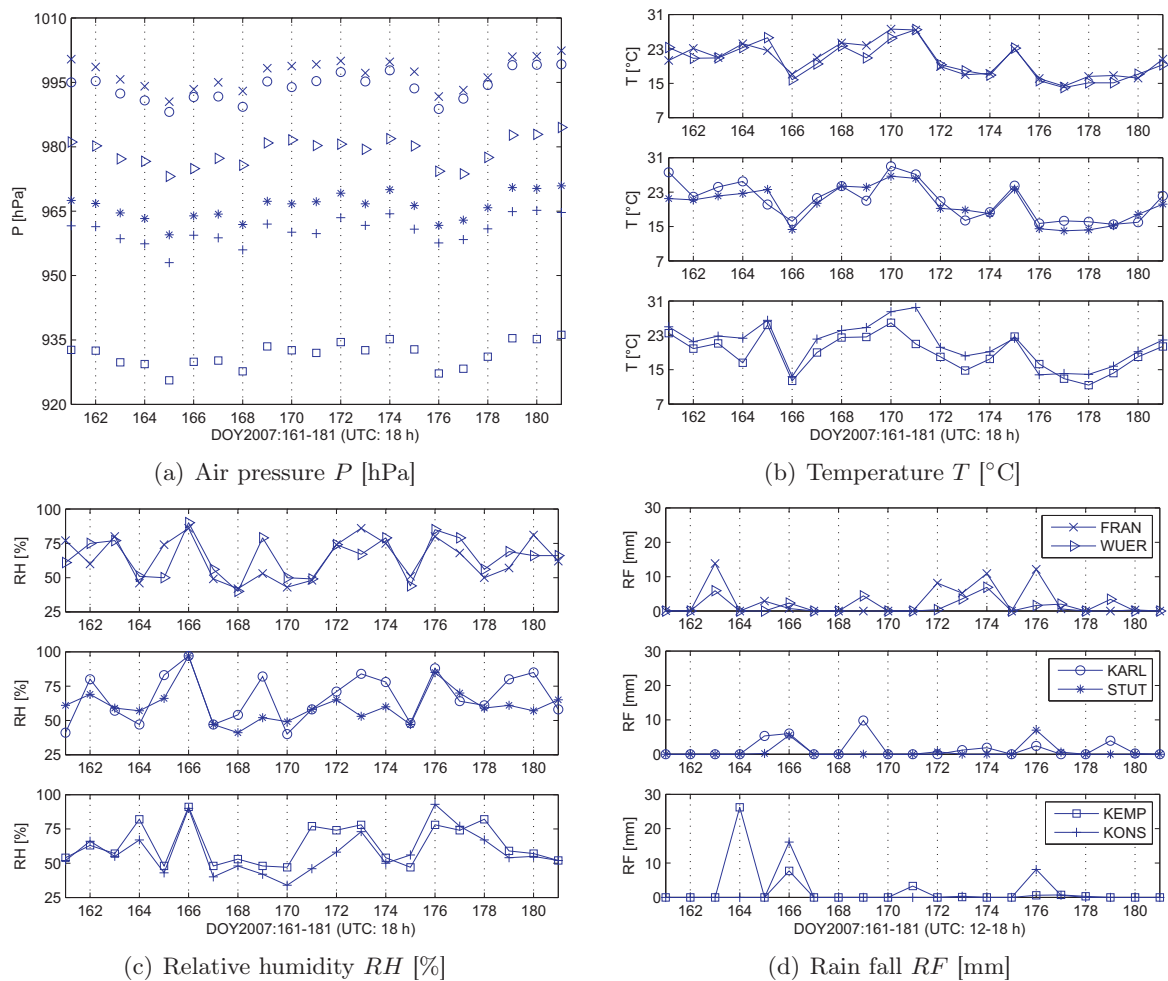
Figure 4.8: Freely available DWD surface meteorological data for the investigation period of case study 2 (DOY2007:161-181, P, T, RH: 18 h UTC, RF: 12-18 h UTC)

Considering the time interval of the daily GPS data analysis, i.e., 15-18 h in GPS time, the P, T, RH observations at 18 h UTC and the RF measurements covering 12-18 h UTC are incorporated into this case study to characterise the near-ground atmospheric conditions. As figure 4.8 shows, temporally and spatially variable atmospheric conditions prevail during the period of investigation. Regarding the whole investigation area, larger amounts of precipitation are registered on days 166 and 176, with lower T and higher RH values. On day 164 the southern area seems to be more humid, while on day 169 higher RH and RF are observed in the northern and middle areas. Such freely available surface meteorological information is particularly helpful for a physically reasonable interpretation of the GPS processing results.

4.3 PPP processing strategies

Like section 4.2, this section first gives an overview of the processing steps of the PPP data analysis using the Bernese GPS Software 5.0. After that, some important parameter settings of the GPS data processing are presented for a long-term case study. Additional information about the site-specific multipath effects and the near-ground atmospheric conditions during the period of investigation is also provided.

4.3.1 Processing steps

The PPP data analysis is performed within the framework of Fuhrmann et al. (2010), where the standard PPP processing control file (`PPP.PCF`) from Dach et al. (2007a, sect. 20.4.1) is slightly modified to enable more reliable outlier detection and troposphere parameter estimation. Table 4.6 gives an overview of the PPP data processing flow using the Bernese GPS Software 5.0, where the modifications are marked in bold. In the following text, only some modified processing steps are described, with a particular emphasis on their purposes and advantages over the standard ones. For a more detailed description of the PPP data analysis, the reader is referred to Dach et al. (2007a, sect. 20.4.1) and Fuhrmann et al. (2010, chap. 5).

In the standard PPP data processing flow, the program `RNXSMT` is used to screen code and phase observations for outliers and cycle slips, and to smooth the code data with the phase measurements. However, the main disadvantage of processing phase observations with `RNXSMT` is that the phase data can only be cleaned with the code measurement accuracy (Dach et al., 2007a, p. 102). Furthermore, applying the smoothed code observations to receiver clock synchronisation, Fuhrmann et al. (2010, p. 55) found strong variations in the estimated receiver clock errors between 10^{-7} and 10^{-5} s, which disappear when using the original pseudo-code observations. Therefore, instead of the smoothed code data, the original code measurements are processed by the program `CODSPP`. In place of `RNXSMT`, the program `MAUPRP` is employed for more sophisticated outlier and cycle slip detection, where high-rate satellite clock products (accuracy < 0.1 ns, with same sampling interval as the data) are necessary (Dach et al., 2007a, p. 116).

For high-precision zenith tropospheric delays, Fuhrmann et al. (2010, sect. 5.3.2) proposed an improved approach that combines two sets of site-specific troposphere parameters (TRP) estimated with a constant time offset. Taking a TRP time span of 2 h as an example, two parameter sets with a time shift of 1 h, i.e., TRP at $0, 2, 4, \ldots$ h and TRP at $1, 3, 5, \ldots$ h, are merged to obtain the final TRP estimates which have a temporal resolution of 1 h and standard deviations being comparable to those derived using a time window of 2 h. Such a simple combination in the parameter domain provides a practical solution to the problem of achieving temporally sufficient troposphere characterisation and statistically reliable parameter estimation.

Table 4.6: Processing steps of the modified PPP data analysis with the Bernese GPS Software 5.0 (Dach et al., 2007a, sect. 20.4.1; Fuhrmann et al., 2010, p. 48)

Script/Program	Purpose in the PPP data analysis
	Copy required files
PPPCOP	Putting the required files from the local data source into the campaign directories
	Prepare pole, satellite orbit, and clock information
POLUPD	Transforming the EOP files from the IGS or IERS format into the Bernese format
PRETAB	Converting the SP3 orbits (Earth-fixed frame) into the tabular orbits (inertial frame)
ORBGEN	Integrating the equations of motion to produce the binary Bernese standard orbits
CCRNXC	Converting the clock files from the RINEX format into the Bernese format
	Convert, synchronise, and preprocess observation data
RNXGRA	Giving an overview of the observed satellites, involved sites and their performance
RXOBV3	Creating the Bernese observation files and checking the RINEX header information
CRDMERGE	Setting the geodetic datum and the coordinate reference epoch to a common value
CODSPP	Synchronising receiver clocks, estimating coordinates, and detecting outliers
CODXTR	Producing a CODSPP summary of outliers, missing orbits and clocks, etc.
MAUPRP	Preprocessing the phase data (marking observations, detecting outliers and cycle slips)
	Compute PPP solutions (parameter estimation)
PPPEDT	Screening the phase observation data and computing PPP solutions
GPSEST(1)	Saving the LC3 normalised residuals for data screening
RESRMS(2)	Screening the residual files and detecting outliers
SATMRK(3)	Marking the corresponding outliers in the observation files
ITERATION	Running steps (1)-(3) iteratively with decreasing limits for outlier detection
GPSEST(4)	Estimating parameters using the cleaned data and saving normal equations
ADDNEQ	Generating PPP result files for each station in the Bernese and external formats
GPSXTR	Producing a GPSEST(4) summary of the PPP solution and data cleaning
PPPCHK	Producing residual statistics before and after data screening
RESRMS	Generating residual statistics before screening (i.e., the first run of GPSEST(1))
RESRMS	Generating residual statistics after screening (i.e., GPSEST(4))
RESCHK	Creating statistics for residual screening
GPSEST	Saving the LC3 normalised residuals for temporal correlation modelling
RESFMT	Converting the residual files from the binary format into the ASCII format
CRDMERGE	Merging the site-specific coordinate files into one coordinate file
ADDNEQ2	Generating a combined normal equation file containing all stations
	Generate summaries and clean directories
PPPSUM	Generating a summary of the whole PPP data analysis
PPPDEL	Deleting the superfluous output files created during the PPP processing

4.3.2 A long-term case study

Within the long-term PPP case study, 10 days (DOY2008:275-284) of 24-hour SA*POS*®data are analysed according to the processing flowchart presented in table 4.6. The resulting zero-difference residual time series are used later to study the temporal correlation behaviour of GPS observations. Benefiting from the use of zero-differences in PPP, the residual signal components can be reasonably interpreted (see section 7.2), and the noise's temporal correlations, modelled by means of autoregressive moving average processes (see section 7.3), may give a realistic picture of the statistical properties of GPS observations. Moreover, based on zero-difference residuals

including one site and one satellite, the effects of satellite geometry and site environments on the noise's temporal correlation can be investigated in a more sophisticated manner than using double-difference residuals, which involve two sites and two satellites. Table 4.7 provides some important information about the long-term PPP data analysis.

Table 4.7: Important parameter specifications of the long-term PPP data analysis

Geodetic datum	IGS05, epoch 2000.0 (Ferland, 2006)
Processing time interval	DOY2008:275-284, daily solution
GPS observation data	30-second phase zero-differences (LC3)
Observation weighting model	CSC2(BS) (i.e., $\sin^2(e)$, see figure 3.3)
Elevation cut-off angle	$10°$, with screening post-fit residuals
EOP/satellite orbits/clocks	Final CODE products (24 h/15 min/30 s)
Troposphere a priori model	Saastamoinen model (Saastamoinen, 1973)
Tropospheric mapping function	Niell mapping functions (dry, wet; Niell, 1996)
Time span for troposphere parameters	30 min, combination of 1-hour solutions
	(Fuhrmann et al., 2010, p. 59)
Time span for troposphere gradients	24 h (Dach et al., 2007a, p. 249)
Phase ambiguity resolution	Float ambiguity estimates (unresolved)
Satellite antenna correction	IGS absolute antenna model (Schmid et al., 2007)
Receiver antenna correction	Individual absolute calibration

For the case study of long-term PPP, two SA*POS*®sites, Tübingen (TUEB) and Bingen (BING), are selected, which differ from each other significantly in view of multipath impact. Figure 4.9 shows the site images and examples of the associated mean multipath plots. The GPS antenna at TUEB is established on the roof of a building and is relatively free of signal interruption. In contrast, the antenna at BING is installed on a mast and has numerous multipath reflectors in its surrounding areas. Although the GPS data sets used to generate the multipath plots do not coincide with the investigation period of this case study, i.e., DOY2008:275-284, these plots are capable of providing an impression of the different multipath situations, since no antenna replacements have taken place at both sites during the period from DOY2008:275 to DOY2009:181. Applying an advanced residual stacking technique using congruent cells, Fuhrmann et al. (2010, p. 120) verified the different multipath impacts between TUEB and BING for the processing time interval of this case study. Additional plots illustrating the strong multipath environments of BING can be found in Knöpfler et al. (2010).

(a) TUEB: weak multipath (DOY2009:174-181)   (b) BING: strong multipath (DOY2009:172-179)
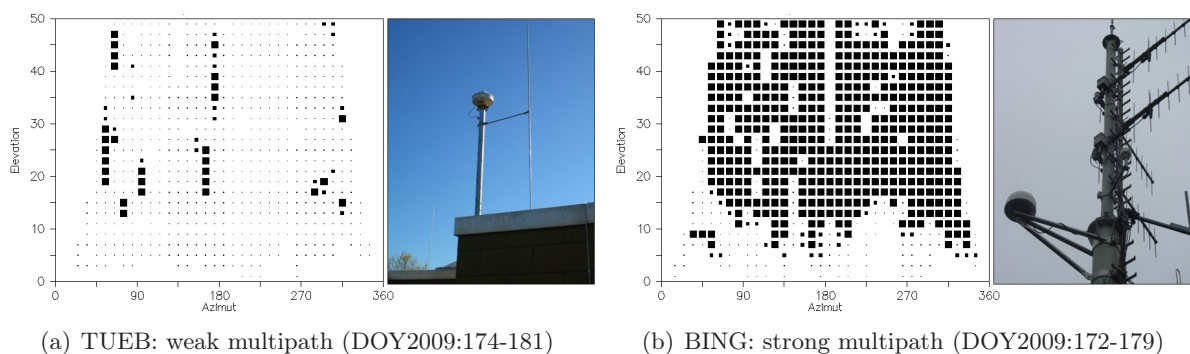
Figure 4.9: Site images and mean multipath plots of the SA*POS*®sites Tübingen (TUEB) and Bingen (BING) (plots provided by A. Knöpfler, current site images available at `www.sapos.de`)

Although in this thesis the long-term PPP case study does not focus on troposphere parameter estimation, the available DWD surface meteorological data are incorporated to enable a physical interpretation of the results from the residual-based temporal correlation analysis (see chapters 7 and 8). The consideration of meteorological information within this context is reasonable, since, on the one hand, the remaining tropospheric effects exist in the observation residuals, while on the other, the temporal correlation properties of GPS observations depend not only on the satellite geometry, but also on the prevailing atmospheric conditions (Schön and Brunner, 2008a).

Figure 4.10 depicts the DWD surface meteorological data for the investigation period, where the MET_0 values are also computed using equation (4.1). The pressure measurements (P) clearly illustrate an increasing trend, while the temperature observations (T) initially decrease during the period DOY2008:275-278, and then increase on day 279 to a relatively constant level. Large amounts of rain fall are registered on days 276, 280, and 281. Taking the locations of the selected SA*POS*®sites BING and TUEB into account, meteorological data from the nearest respective DWD stations FRAN and STUT should be particularly considered (see figure 4.1).

(a) Air pressure P [hPa]

(b) Temperature T [°C]

(c) Relative humidity RH [%]

(d) Rain fall RF [mm]
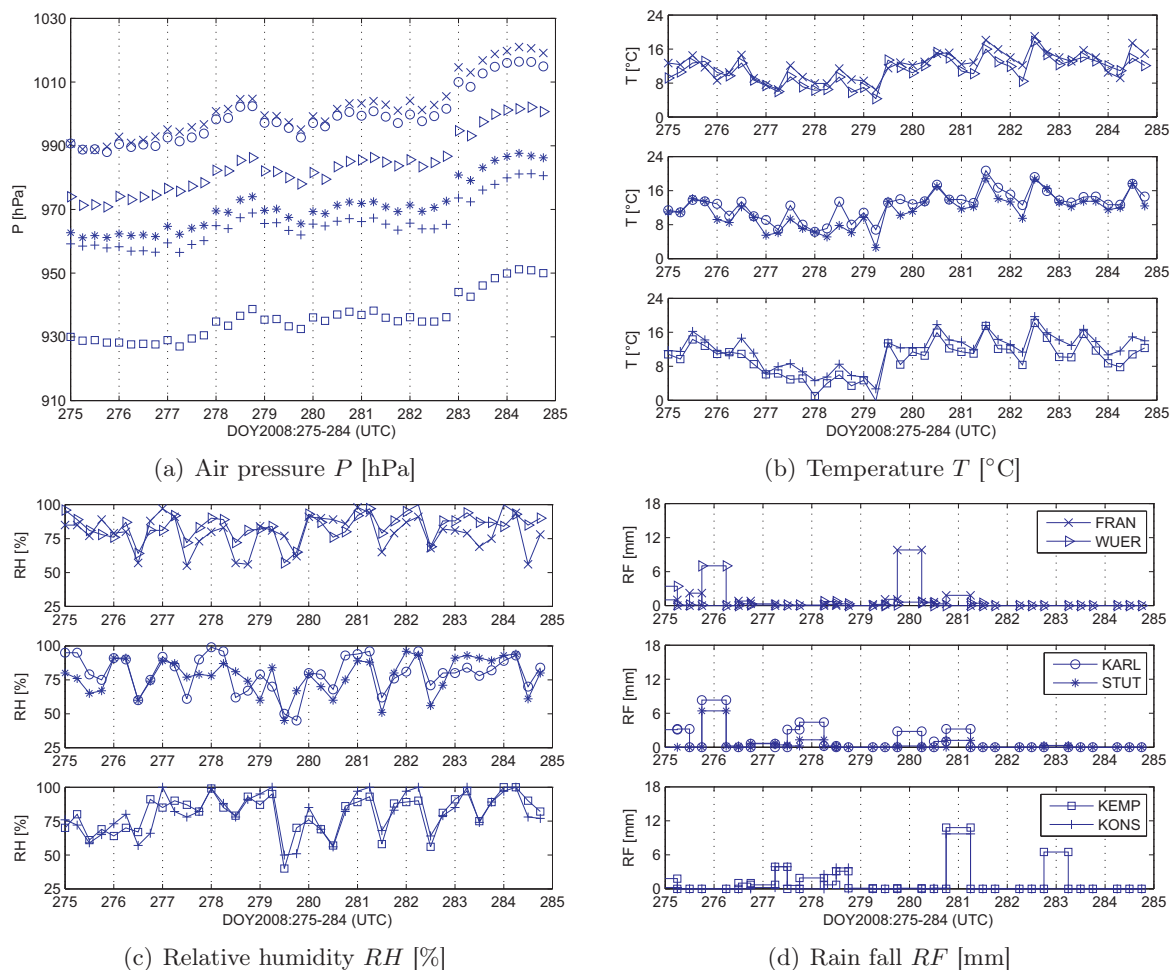
Figure 4.10: Freely available DWD surface meteorological data for the investigation period of case study 3 (DOY2008:275-284)

Chapter 5

Observation Weighting Using Signal Quality Measures

In addition to pseudo-range and carrier-phase measurements, a modern geodetic-type GPS receiver also records signal-to-noise ratio (SNR) data. Relying upon signal quality measures, the heteroscedasticity (i.e., inhomogeneity of variances) of GPS phase observations can be more realistically described than using the satellite elevation angle. Section 5.1 gives a brief introduction to SNR and numerical examples of how various factors affect its characterisation. Next, in section 5.2, different SNR-based weighting schemes are reviewed, with a particular focus on their strengths and weaknesses. Section 5.3 presents an empirical SNR-based weighting model and its implementation into the Bernese GPS Software 5.0. The proposed approach is compared with the commonly applied elevation-dependent weighting scheme and two other SNR-based alternatives. Finally, in section 5.4, the main properties of the novel SNR-based weighting model are summarised from both theoretical and practical points of view.

5.1 Signal-to-noise ratio (SNR)

The notation SNR represents a generic term for signal quality, and is defined as the ratio of signal power S in watts (W) to noise power N in W, measured at the same time and place in a circuit. The signal and noise power can be estimated during the synchronisation (or correlation) between the received and replica signals (Butsch and Kipka, 2004). The main part of noise originates from the receiver electronics (e.g., thermal noise created by the inevitable motion of electrons within any conductor or semiconductor) and the electromagnetic radiation from the sky, ground, and objects in the antenna's vicinity. Thermal noise is generally assumed to be uncorrelated (white) noise with a Gaussian distribution (Langley, 1997). Obviously, the larger the $SNR = S/N$ value, the better the signal quality.

Normally, SNR measurements are obtained using the signal power S_{corr} and noise power N_{corr} of the modulated signal at the correlator output (i.e., $SNR = S/N = S_{corr}/N_{corr}$). However, to assess the quality of a received GPS signal, the so-called carrier-to-noise ratio ($CNR = C/N$) is preferred, which makes use of the signal power C_{ant} and noise power N_{ant} of the unmodulated carrier at the receiving antenna (i.e., $CNR = C/N = C_{ant}/N_{ant}$; Ward et al., 2006, p. 185). From the receiver antenna to correlator output, GPS signals may be amplified by a factor of about 10^{10}, so that S_{corr} is significantly larger than C_{ant} (Butsch and Kipka, 2004). Nevertheless, according to the fact that the signal and noise powers are amplified by approximately the same factor, S_{corr}/N_{corr} and C_{ant}/N_{ant} are almost identical, i.e.,

$$CNR := \frac{C}{N} = \frac{C_{ant}}{N_{ant}} \approx \frac{S_{corr}}{N_{corr}} = \frac{S}{N} =: SNR. \qquad (5.1)$$

For GPS signals, S is several magnitudes lager than N. Therefore, SNR values are usually expressed in terms of the logarithmic decibel (dB) scale by

$$SNR\,[\text{dB}] = 10 \cdot \log_{10}(SNR). \qquad (5.2)$$

In addition, noise power N can be written as the product of noise power density N_0 and loop bandwidth B_L (Misra and Enge, 2006, p. 403):

$$N\,[\mathrm{W}] = N_0\,[\mathrm{W/Hz}] \cdot B_L\,[\mathrm{Hz}]\,, \tag{5.3}$$

where B_L is commonly the same on L1 and L2 for GPS receivers (Lau and Mok, 1999). Substituting equation (5.3) into (5.1), SNR is normalised to a specific bandwidth of 1 Hz, and equation (5.2) becomes

$$
\begin{aligned}
SNR\,[\mathrm{dB}] &= 10 \cdot \log_{10} \frac{S}{N_0 \cdot B_L} = 10 \cdot \log_{10}(\frac{S}{N_0}) - 10 \cdot \log_{10}(B_L) \\
&= SNR0\,[\mathrm{dBHz}] - B_L\,[\mathrm{dBHz}]\,,
\end{aligned}
\tag{5.4}
$$

where $SNR0$ (or S/N_0) is called signal-to-noise power density ratio. $SNR0$ plays a key role in analysing GPS receiver performance, and is directly related to the precision of pseudo-range and carrier-phase observations (Langley, 1997). For moderate to strong signals, the corresponding $SNR0$ should be larger than 35 dBHz (Hofmann-Wellenhof et al., 2008, p. 86). Most high-end GPS receivers deliver $SNR0$ of up to 50 dBHz. Using the minimum received signal strength of $S = -160$ dBW and a typical value for noise power density of $N_0 = -204$ dBW/Hz (IS-GPS-200E, 2010, p. 15), a nominal $SNR0$ of 44 dBHz is obtained.

In fact, $SNR0$ measurements are affected by various factors, for example, (1) the antenna gain of the transmitting satellite, and thus by the satellite type, (2) polarisation errors, (3) the size of solar panels and batteries, (4) changes in path (spreading) loss due to the varying satellite-receiver distance, (5) variations in atmospheric attenuation and receiver antenna gain patterns, depending on the elevation angle and azimuth of the arriving signal, and (6) signal power losses in preamplifier, antenna cable, and receiver subsystems. Furthermore, the noise level may be slightly increased by the signals from other simultaneously observed satellites (Langley, 1997). Table 5.1 provides numerical examples of signal power losses, transmitter and receiver antenna gains, and the typical noise characterisation of a GPS receiver (Misra and Enge, 2006, chap. 10).

Taking the C/A-code on L1 as an example, a GPS satellite transmits a signal power of about 27 W, corresponding to $P_S = 10 \cdot \log_{10}(27) = 14.3$ dBW. This power level is derived from GPS specifications, and typical GPS satellites broadcast 2 to 4 dB more power (3 dB: twice as powerful; Misra and Enge, 2006, p. 395). Assuming that the GPS signals were transmitted in all directions, path loss describes the spreading of the total signal energy over the entire surface area of the sphere, which is centred on the satellite. The path loss can be expressed by $L_P = 4\pi R^2$, where R is the satellite-receiver distance, computed based on the satellite elevation angle e and approximate values of the Earth's and orbital radii, $R_E = 6371$ km and $R_S = 26560$ km, respectively. For a satellite in the zenith direction, i.e., $e = 90°$ and $R = R_S - R_E = 20189$ km, the resulting L_P is 157.1 dBm^2, corresponding to a power attenuation of about $2.0 \times 10^{-16}/\mathrm{m}^2$. Since a GPS satellite focuses its signal energy towards the Earth, satellite antenna gain (or concentration factor) characterises the amplification of the signal power in a certain direction with respect to an isotropic antenna. Assuming that the satellite is capable of concentrating its radiated power within the beam angle completely, the satellite antenna gain G_S can be determined as the ratio of the area of the whole sphere to the area of a spherical cap:

$$G_S(\alpha) = \frac{4\pi R^2}{\pi(R\sqrt{2 - 2\cos\alpha})^2} = \frac{2}{1 - \cos\alpha}\,, \tag{5.5}$$

where α is the satellite nadir angle and can be calculated using e, R_E, and R_S. For $e = 0°$, α reaches a maximum of about 13.9°. In effect, the GPS signal beam has a wider spread of

$\alpha = \pm 21.3°$. As a consequence, the maximum satellite antenna gain may be more realistically approximated by $G_S(21.3°) = 14.7$ dB (see equation (5.5)). Moreover, due to the additional power loss in the satellite antenna and the compensation for the larger distance to those areas at the edge of the Earth, the actual satellite antenna gain is less than 14.7 dB, and is about 2 dB higher for $\alpha = \pm 13.9°(e = 0°)$ than along the so-called bore sight with $\alpha = \pm 0°(e = 90°)$ (Misra and Enge, 2006, p. 397). As an example, for a satellite at zenith with $\alpha = \pm 0°$, the effective radiated power is equal to $P_S + G_S = 14.3$ dBW + 10.2 dB = 24.5 dBW = 282 W.

Within the context of atmospheric loss, L_A, oxygen is the dominant source of signal power attenuation at L-band. However, for elevation angles exceeding 40°, the atmospheric loss approaches 0.035 dB, and thus can be safely neglected. Other phenomena, such as atmospheric turbulence and water vapour, may sometimes cause additional losses (Betz, 2010). Considering the worst-case scenario, L_A is specified to 2 dB for $e = 5°$ (Mehaffey, 2011). For a moderate elevation angle and near zenith at which higher received signal power is expected, a representative value of $L_A = 0.5$ dB is used (GPS-SPS-SS, 1995, p. 18). Combining the above-introduced factors that impact upon the transmitted signal power, the received power density PD_R is given by

$$PD_R\,\left[\text{dBW/m}^2\right] = P_S\,\left[\text{dBW}\right] + G_S\,\left[\text{dB}\right] - L_P\,\left[\text{dBm}^2\right] - L_A\,\left[\text{dB}\right]. \qquad (5.6)$$

Table 5.1: Typical values for signal power losses, transmitter and receiver antenna gains, and noise characterisation of a GPS receiver (Misra and Enge, 2006, tables 10.1-10.4)

Signal characterisation	Notation	Unit	$e = 5°$	$e = 40°$	$e = 90°$
Power (satellite antenna input)	P_S	dBW			14.3
Satellite-antenna distance	R	km	25235	22013	20189
Path (spreading) loss	L_P	dBm^2	159.0	157.8	157.1
Satellite nadir angle	α	degree	± 13.8	± 10.6	± 0
Satellite antenna gain	G_S	dB	12.1	12.9	10.2
Atmospheric loss	L_A	dB	2.0	0.5	0.5
Received power density	PD_R	dBW/m^2	-134.6	-131.1	-133.1
Effective area of an IRA[1]	$A_R(IRA)$	dBm^2			-25.4
Received power for an IRA	$P_R(IRA)$	dBW	-160.0	-156.5	-158.5
Receiver antenna gain	$G_R(IRA)$	dB	-4	2	4
Noise characterisation	**Notation**	**Unit**	**Bef. LNA[2]**	**LNA**	**Aft. LNA**
Power gain	G_i	dB	-1	20	-10
Power loss (1/gain)	L_i	dB	1	-20	10
Noise figure	F_i	dB	1	3	10
Power (C/A-code signal)	**Notation**	**Unit**	$e = 5°$	$e = 40°$	$e = 90°$
Received signal power	S	dBW	-164.0	-154.5	-154.5
Noise power density	N_0	dBW/Hz	-201	-201	-201
Power density ratio	$SNR0$	dBHz	37.0	46.5	46.5
Signal-to-noise (power) ratio	SNR	dB	-36.0 4.0 34.0	$B_L = 20$ MHz 2 KHz 2 Hz	-26.5 13.5 43.5

[1] IRA: isotropic receiver antenna
[2] LNA: low noise amplifier

The received signal power is the product of the received power density in the incident signal field PD_R and the receiver antenna effective area, denoted as A_R. This term measures the antenna's ability to capture the power in a field incident to a certain direction. It can be calculated based on the receiver antenna gain, G_R, which characterises the antenna's ability to focus transmitted

power in a certain direction:

$$A_R = \frac{\lambda^2}{4\pi}G_R, \quad \lambda = \frac{c}{f}, \tag{5.7}$$

where λ is the wavelength of the signal, c is the speed of light in a vacuum, and f is the frequency of the signal (Jordan and Balmain, 1968, p. 377). An isotropic receiver antenna (IRA) is equally sensitive to signals from any direction and has unit gain, indicating $G_R(IRA) = 1$ and $A_R(IRA) = \lambda^2/(4\pi)$. Taking the L1 carrier with a wavelength of about 19 cm as an example, the corresponding $A_R(IRA)$ is equal to $2.87 \times 10^{-3}\mathrm{m}^2 = -25.4$ dBm^2. Assuming that the receiver antenna gain $G_R(IRA)$ is given relative to an isotropic antenna, the received signal power is

$$S\,[\mathrm{dBW}] = \underbrace{PD_R\left[\mathrm{dBW/m}^2\right] + A_R(IRA)\left[\mathrm{dBm}^2\right]}_{P_R(IRA)[\mathrm{dBW}]} + G_R(IRA)\,[\mathrm{dB}]. \tag{5.8}$$

As shown by Misra and Enge (2006, p. 400) and IS-GPS-200E (2010, p. 45), the received C/A-code signal level depends on the satellite elevation angle. As e varies from 5° to 90° (zenith), $P_R(IRA)$ first increases to its maximum of -156.3 dBW at an elevation angle of about 45°, and then decreases. Such a variation pattern can also be expected in the received signal power S, since for most civilian GPS receiver antennas, $G_R(IRA)$ decreases slowly from about 4 dB at $e = 90°$ to -4 dB at $e = 5°$ (Misra and Enge, 2006, p. 401).

The factors that influence the noise power level include the thermal noise generated in the receiver, natural noise from sources outside the receiver, reflected signals (e.g., multipath), signals from other simultaneously observed GPS satellites, and the interfering signals from systems other than GPS. Within the context of noise analysis, it is convenient to treat a GPS receiver as a cascade of components (or subsystems), each of which can be characterised by its power gain G_i and noise figure F_i. While some components, for example, low noise amplifier (LNA), amplify the signal power, some subsystems, such as cables and connectors before and after the LNA, attenuate signals and have gain values less than one (i.e., $G_i < 1$). These components with negative G_i values in dB are termed passive. The resulting power loss converts into heat and introduces thermal noise. Noise figure F_i describes the degradation of $SNR0$ as the signal passes through each receiver component. If there is no internal noise, i.e., $F_i = 1$, then the $SNR0$ at the output of the subsystem i is identical with that at the input. For a passive component, F_i is equal to the power loss L_i, which represents the inverse of G_i. The component before the LNA consists of a low-loss filter that removes signals outside the GPS band, and a short (low-loss) cable that connects the antenna to the LNA (Hofmann-Wellenhof et al., 2008, p. 88). For this part, a low power loss of 1 dB is specified in table 5.1. The LNA is also designed for high gain and low noise, having a typical gain (noise figure) of 20 dB (3 dB). Due to the following more complex filtering and converting steps, the part after the LNA has a significantly higher power loss of 10 dB. Using these noise characteristics, the noise power density N_0 can be determined (Misra and Enge, 2006, p. 409). For a typical GPS receiver, N_0 is of the order of -201 to -204 dBW/Hz (Hofmann-Wellenhof et al., 2008, p. 86). On the basis of S and N_0, the resulting $SNR0$ values vary from 37.0 to 46.5 dBHz for satellites at low and high elevation angles, respectively.

The bandwidth B_L of a GPS receiver is wider for the components near the antenna, and becomes narrower as the signal processing proceeds. For instance, the earliest filters in the receiver front end have bandwidths of tens of megahertz. If $B_L = 20$ MHz $= 73$ dBHz, the signal power is 26.5 to 36 dB weaker than the noise power, indicating that the GPS signal is below the noise floor. As the processing develops, however, the bandwidth decreases. For a bandwidth of 2 Hz (Langley, 1997), the GPS signal is about 34.0 to 43.5 dB above the noise floor (see table 5.1). The technique of increasing signal power by decreasing bandwidth is known as despreading, which is performed by correlators contained in the delay lock loops (Misra and Enge, 2006, sect. 10.5).

Depending on the satellite elevation angle, figure 5.1 shows examples of daily $SNR0$ measurements and the associated box plots for a Leica antenna-receiver combination. In figure 5.1(a), the $SNR0$ values illustrate a strong elevation dependence, with low-quality (i.e., $SNR0 < 35$ dBHz; see figure 5.6) observations concentrating within the range of $e < 20°$. The staircase-shaped structure of the $SNR0$ values arises from both the resolution of signal quality registration and the derivation of $SNR0$ from the raw observation data (Mayer, 2006, p. 63). In comparison to L1, the $SNR0$ values on L2 exhibit a larger minimum (L1: 32 dBHz, L2: 36 dBHz) and a narrower variation range (L1: 19 dBHz, L2: 15 dBHz). These can be easily observed by comparing the sample minima and interquartile ranges (IQR) of the box plots (see figure 5.1(b)). Moreover, the L2 $SNR0$ achieves a maximum of 51 dBHz at an elevation angle of about 40° and maintains it for $e > 50°$, while the L1 $SNR0$ approaches its maximum at about $e = 50°$ and varies within 6 dBHz for higher elevation angles. Applying elevation-dependent observation weighting models (e.g., $\sin^2(e)$), these frequency-related characteristics of signal quality are simply ignored. However, they can be considered by incorporating frequency-dependent signal quality measures into the observation weighting procedure.

| (a) $SNR0$ values on L1 and L2 | (b) Box plots of the $SNR0$ values |
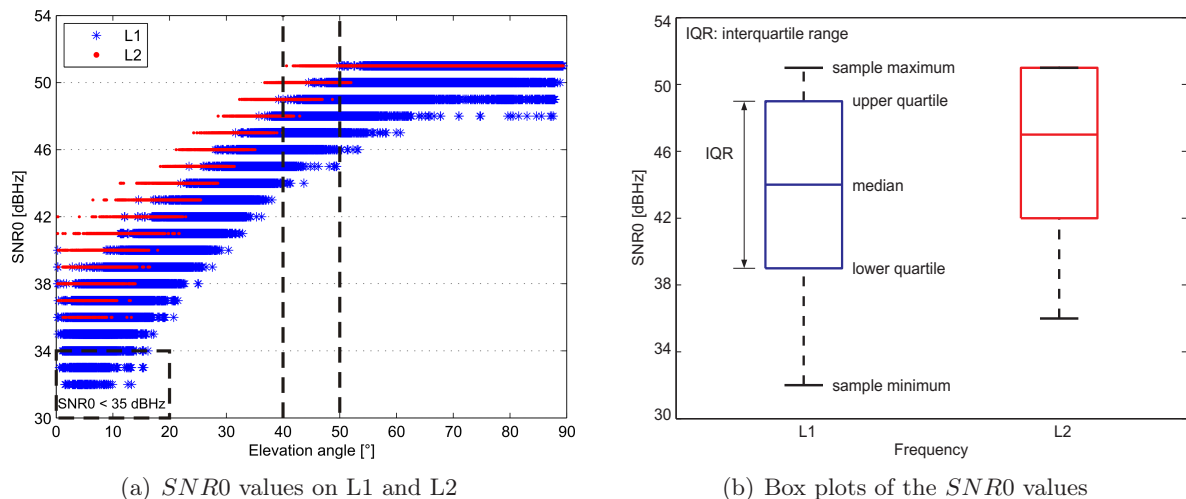
Figure 5.1: Example of $SNR0$ values in dBHz (SA*POS*®site: RAVE, weak multipath, receiver: Leica SR520, antenna: LEIAT503, DOY2004:186; see table 4.1)

Geodetic-type GPS receivers usually provide SNR in dB or $SNR0$ in dBHz. However, sometimes the so-called arbitrary manufacturer (mystery) units (AMU), also known as signal-to-noise counts (SNC), are used to assess the quality of GPS signals (e.g., Trimble 4000SSI receivers). These values are obtained by integrating the output of a signal correlator, and can vary from receiver to receiver due to the differences in receiver bandwidth and in integration time. To keep the consistency across a product line, AMU values are scaled to match a measurement over a bandwidth of 1 kHz. This particular bandwidth is chosen due to the fact that the integration time of a majority of early receivers is 1 ms, corresponding to an effective bandwidth of 1 kHz (Trimble, 1999). Applying the manufacturer-specific formula

$$SNR0\,[\text{dBHz}] = 27 + 20 \cdot \log_{10}(AMU), \tag{5.9}$$

AMU values, for example, from a Trimble 4000SSI receiver, can be converted into $SNR0$. Note that the converted $SNR0$ only represents an approximation, and biases of up to 3 dBHz are possible, particularly for small AMU values at low elevation angles, where the conversion tends to be considerably non-linear (Butsch and Kipka, 2004). Figure 5.2 depicts the conversion equation (5.9), along with some satellite- and site-related results for an antenna-receiver combination from the Trimble 4000 series products. Apart from the conversion function itself, figure 5.2(a)

also illustrates the variation in $SNR0$ due to an error of 1 AMU, derived by applying the error propagation law to eq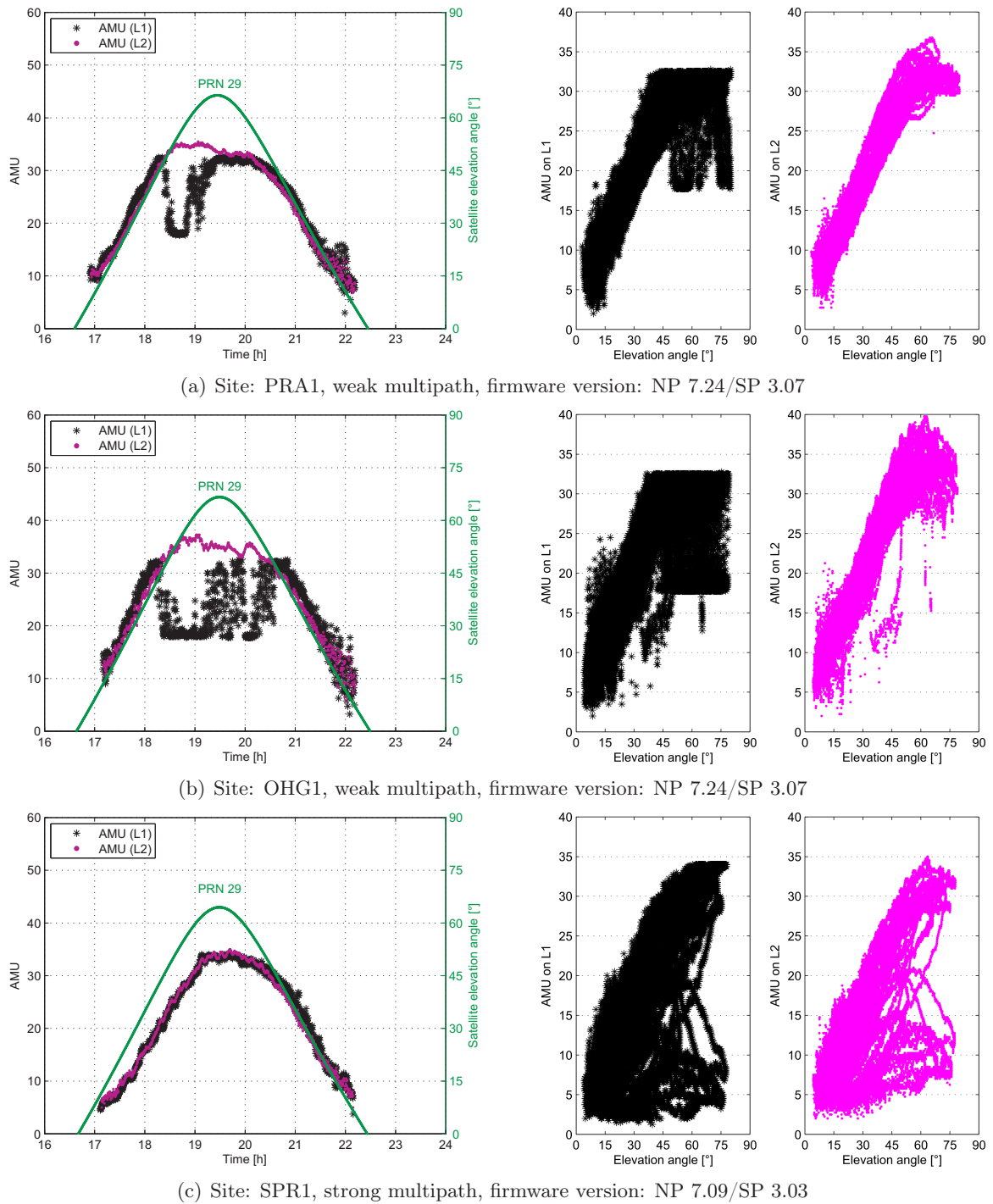uation (5.9). For $AMU < 10$, the conversion exhibits a significantly non-linear behaviour, leading to errors that are considerably larger than 1 dBHz. In figure 5.2(b), the AMU and the converted $SNR0$ values are displayed for a specific satellite, where the elevation angles are obtained from the GPS navigation message file. The conversion from AMU into $SNR0$ causes an obvious offset and a slight compression of the variation range. In spite of the strong correlation between the signal quality measure and the satellite elevation angle, the maximum AMU (or $SNR0$) is reached not at the maximum elevation angle of about 66°, but at about 50°. This coincides with the variation pattern of the received signal power and implies the unrealistic assumption generally made by elevation-dependent weighting models, namely, the larger the satellite elevation angle, the better the observation quality, and the smaller the observation variance. Regarding the items listed in table 5.1 under "signal characterisation", this assumption is true for path loss, atmospheric loss, and receiver antenna gain, but not valid for satellite antenna gain. Considering all observed satellites, figure 5.2(c) plots the original AMU and the converted $SNR0$ versus satellite elevation angle. The offset and compression effects observed in figure 5.2(b) are clearly visible. The large dispersion in signal quality, especially for $e > 50°$, is attributed to the near-ground installation of the GPS antenna (Mayer, 2006, p. 45). The box plots shown in figure 5.2(d) provide an excellent illustration of the changes due to the conversion from AMU into $SNR0$, namely the increased medians and decreased IQR.

(a) Conversion function (equation (5.9))

(b) Satellite-related results (PRN 03)

(c) Site-related results

(d) Box plots of the AMU and $SNR0$ values
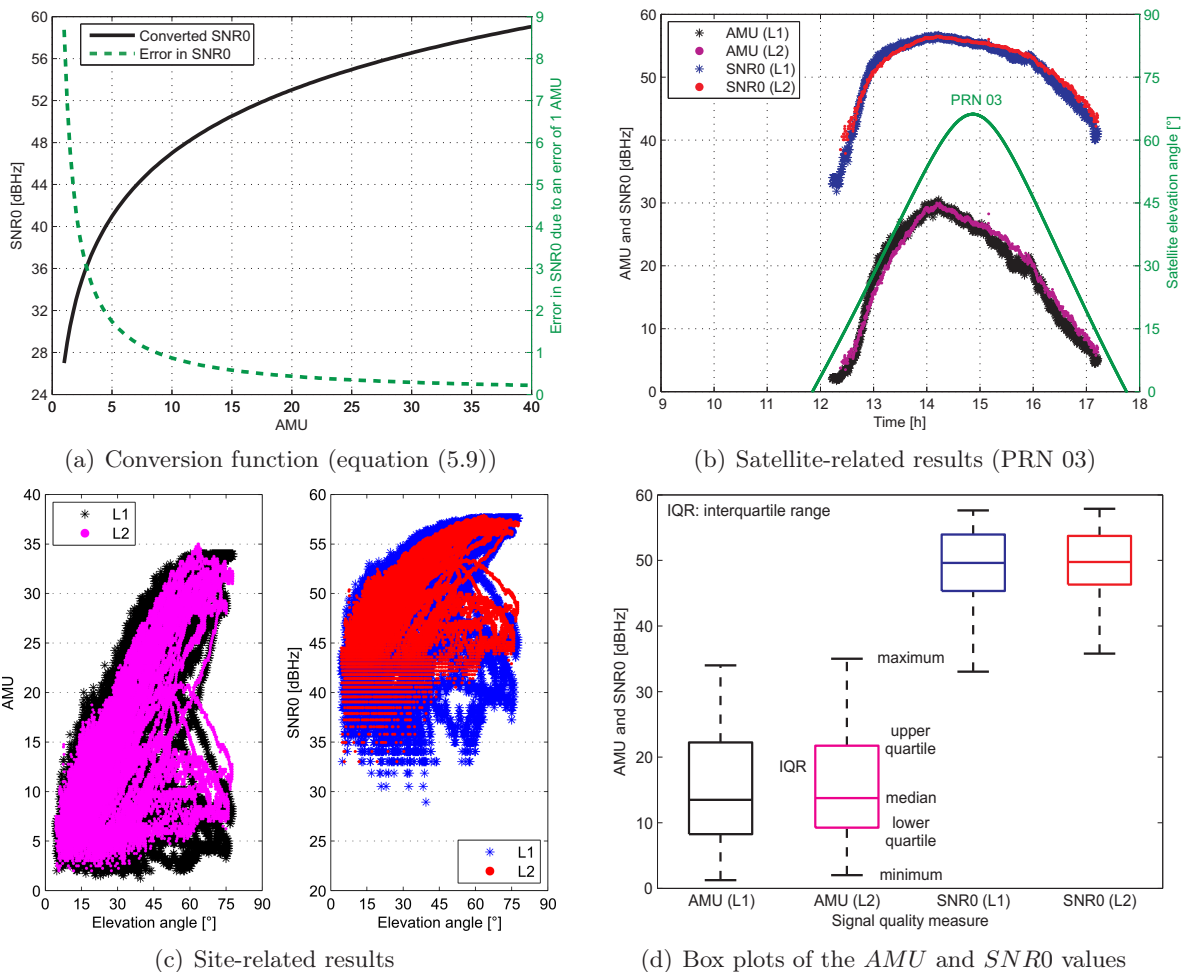
Figure 5.2: Examples of AMU and converted $SNR0$ values in dBHz (site: SPR1, strong multipath, receiver: Trimble 4000SSI, antenna: Trimble 4000ST L1/L2 GEO; Mayer, 2006, p. 44)

Provided that SNR can be accurately recovered by the receiver, it turns out to be a more realistic quality indicator for GPS observations than the satellite elevation angle. However, due to receiver firmware problems, sudden drops in SNR may occur for high-elevation satellites, even when regarding the same receiver type (Satirapod and Wang, 2000). Figure 5.3 illustrates this problem using *AMU* values from the same satellite, which is simultaneously observed at three sites that have different multipath effects, but the same antenna-receiver combination. In

(a) Site: PRA1, weak multipath, firmware version: NP 7.24/SP 3.07

(b) Site: OHG1, weak multipath, firmware version: NP 7.24/SP 3.07

(c) Site: SPR1, strong multipath, firmware version: NP 7.09/SP 3.03

Figure 5.3: Comparison of satellite- and site-related *AMU* values with respect to multipath impact and receiver firmware (satellite: PRN 29, receiver: Trimble 4000SSI, antenna: Trimble 4000ST L1/L2 GEO, site multipath specification: Mayer, 2006, p. 44)

this example, obvious sudden drops are present in the PRA1- and OHG1-related *AMU* values, while they are completely absent for the site SPR1 where the same antenna-receiver combination is used, but with a different firmware version. This emphasises the importance of the information about firmware updates when performing SNR-based data analyses. Furthermore, the site-specific *AMU* presentation in figure 5.3(c) corresponds to the multipath specification provided by Mayer (2006, p. 44), indicating the potential of SNR in multipath modelling.

5.2 Review of previous work

Although the potential merits of using signal quality measures as a weighting scheme were outlined by Talbot (1988), it appears that more intensive investigations and comprehensive applications of this quality indicator for GPS phase observations have only been carried out after Langley (1997) published a direct relationship between the phase variance $\sigma_{\Phi_i}^2$ in m^2 and the signal-to-noise power density ratio $SNR0_i$ in dBHz as

$$\sigma_{\Phi_i}^2 = B_L \cdot \left(\frac{\lambda_i}{2\pi}\right)^2 \cdot 10^{-\left(\frac{SNR0_i}{10}\right)} = C_i \cdot 10^{-\left(\frac{SNR0_i}{10}\right)}, \qquad (5.10)$$

where the subscript i denotes the carrier frequency (e.g., L1 for $i = 1$). The factor C_i in m^{2}Hz depends on the carrier tracking loop bandwidth B_L in Hz and a quadratic term which is related to the wavelength λ_i in m. Using representative loop bandwidths of 5, 10, and 15 Hz for GPS (Braasch and van Dierendonck, 1999), figure 5.4 depicts the phase standard deviation σ_{Φ_i}, derived by means of equation (5.10). In the case that $B_L = 15$ Hz, the L1 (L2) phase standard deviation decreases from 3.7 (4.7) mm to about 0.2 mm as $SNR0$ increases from 30 to 55 dBHz. Obviously, the phase error is inversely proportional to signal strength, and is directly proportional to the loop bandwidth and wavelength.
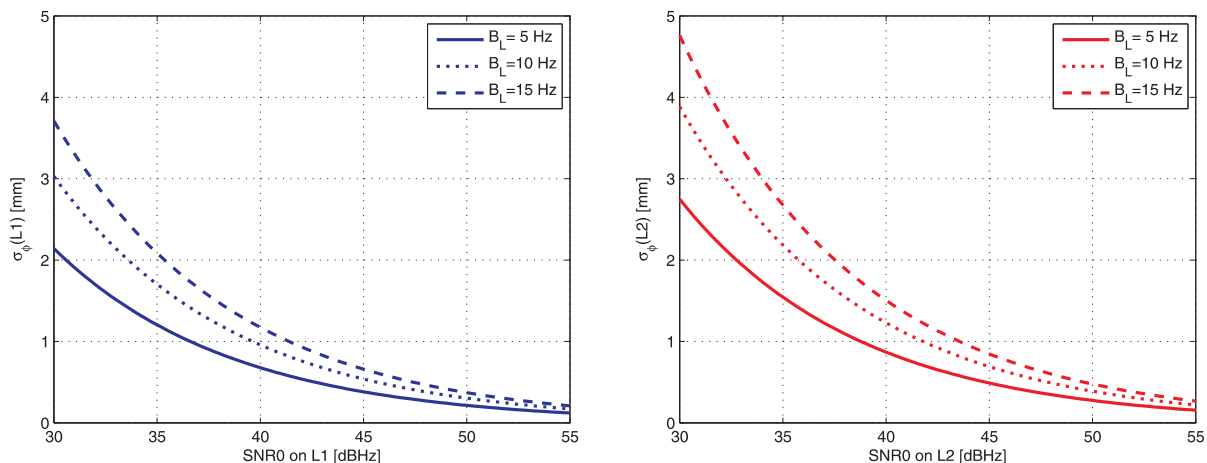
Figure 5.4: Illustration of the phase standard deviations derived by means of the SNR-based variance equation (5.10) (left: L1 with $\lambda_1 = 19.0$ cm, right: L2 with $\lambda_2 = 24.4$ cm; see table 3.2)

Analysing equation (5.10) and figure 5.4, one may attempt to improve the noise performance by narrowing the loop bandwidth. However, B_L must be wide enough to be able to follow the receiver dynamics. A tracking loop with a narrow bandwidth may have problems dealing with rapid phase variations. For most static applications, a bandwidth of 2 Hz or less can be used to derive the phase variance (Langley, 1997). Instead of specifying a typical B_L value, Hartinger and Brunner (1999) developed the SIGMA-ϵ model, where the factor C_i is determined based on double-difference residual and $SNR0$ variances, depending upon the receiver and antenna

types. By analysing multiple data sets, C_1 is estimated to be approximately 1.6×10^{-2} m^{2}Hz. Experimental studies using baselines of up to about 1 km have showed that by applying appropriate observation weights, the SIGMA-ϵ model enables the use of low-elevation data with a cut-off angle of 7.5°. This overcomes the problem of poor satellite geometry and improves the performance of parameter estimation. To illustrate the differences between the commonly used elevation-dependent and SNR-based variance models, i.e., $\sigma_i^2/\sin^2(e)$ and equation (5.10), respectively, figure 5.5 compares the phase standard deviations σ_{Φ_i} and observation weights w_{Φ_i}, which are computed using the elevation angles and $SNR0$ values shown in figure 5.1(a). Thereby, σ_1 and σ_2 are equal to 1 mm and 1.3 mm, respectively (Dach et al., 2007a, p. 144). The frequency-related C_i is calculated in such a way that $\sigma_{\Phi_i} = \sigma_i$ holds for the best observation with the maximum $SNR0_i$ (here 51 dBHz).

(a) L1 phase standard deviations σ_{Φ_1} (mm)

(b) L2 phase standard deviations σ_{Φ_2} (mm)

(c) L1 weight values w_{Φ_1} (unitless)

(d) L2 weight values w_{Φ_2} (unitless)
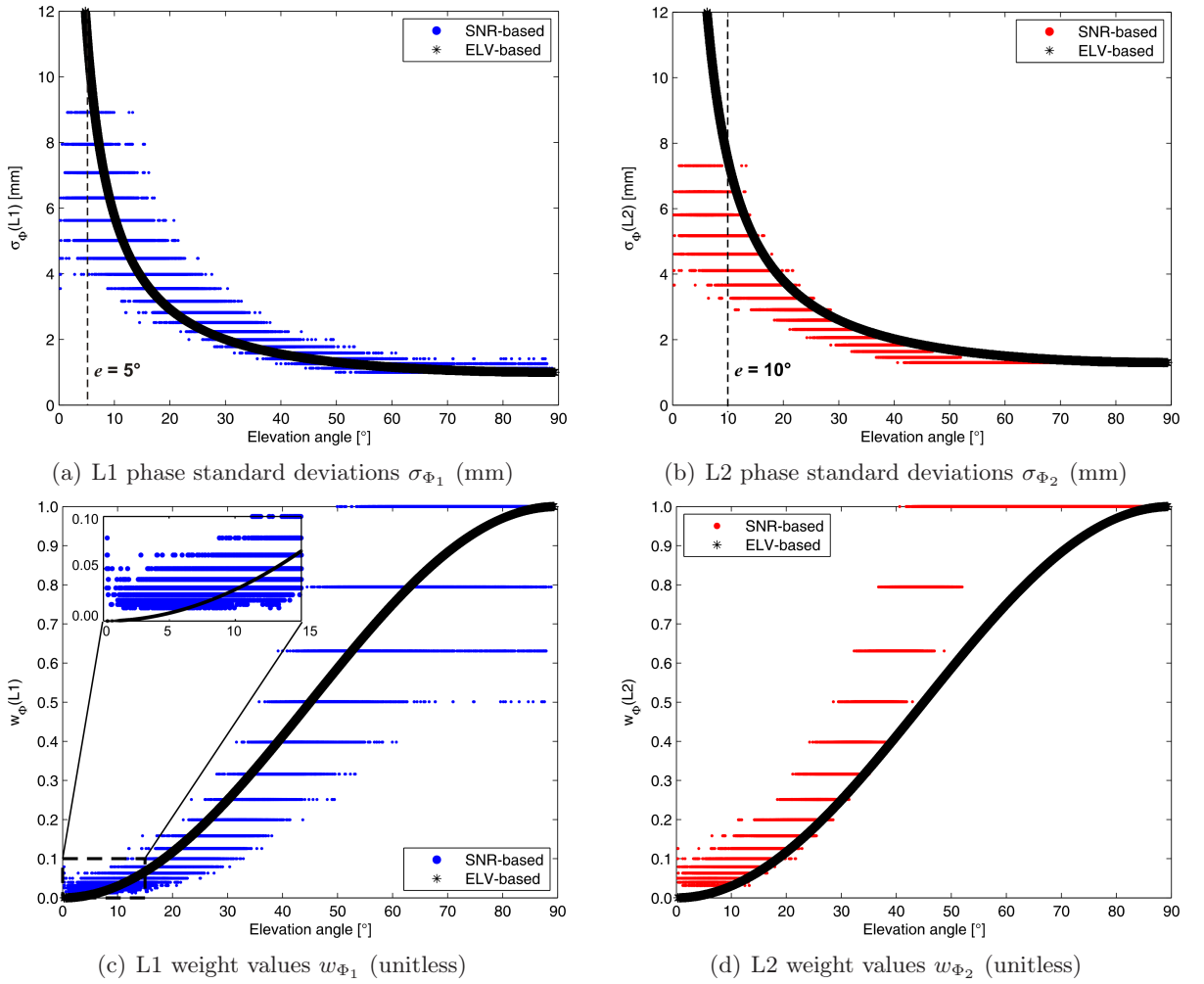
Figure 5.5: Phase standard deviations and observation weights derived using the elevation-dependent ($\sigma_i^2/\sin^2(e)$) and SNR-based (equation (5.10)) variance models ($\sigma_1 = 1$ mm, $\sigma_2 = 1.3$ mm, $SNR0_i$ from figure 5.1(a), $C_1 \approx 0.126$ m^{2}Hz, $C_2 \approx 0.213$ m^{2}Hz, $w_{\Phi_i} = \sigma_i^2/\sigma_{\Phi_i}^2$)

As figures 5.5(a) and (c) show, for L1 observations at satellite elevation angles above 5°, both variance models coincide fairly well in this example. The elevation-dependent weights are obviously equal to $\sin^2(e)$, while the SNR-based ones are computed using $\sigma_i^2/\sigma_{\Phi_i}^2$. Considering low-elevation observations, for example, at an elevation angle of 3°, the SNR-based phase standard deviations σ_{Φ_1} vary between 4 and 9 mm, while the elevation-dependent ones amount to about 2 cm. As the elevation angle further decreases, σ_{Φ_1} increases rapidly to about 6 cm for $e = 1°$. In contrast to L1, the elevation-dependent variance model appears to be incapable of

realistically characterising the observation quality on L2. Throughout the whole range of elevation angles, particularly for $e < 10°$, it provides considerably larger σ_{Φ_2} (see figure 5.5(b)) and smaller w_{Φ_2} (see figure 5.5(d)) than the SNR-based approach, indicating an underestimation of the L2 observations in the LS parameter adjustment. Moreover, this model comparison produces an important message that a frequency-related observation weighting is possible when using signal quality measures instead of the satellite elevation angle. In fact, only considering parameter estimates, it is not even necessary to choose a suitable receiver bandwidth B_L or to estimate a realistic model parameter C_i, since the term C_i only changes the a priori variance factor (Collins and Langley, 1999, p. 26). Nevertheless, in the interest of quality control, parameter constraining, and relative weighting of observation groups, B_L and C_i should be carefully specified.

Although the variance model given by equation (5.10) allows for a more realistic quality assessment of GPS observations, it ignores any contribution to the phase noise from the local oscillator, and thus is only suitable for relatively strong signals well above the tracking threshold of the receiver (Collins and Langley, 1999, p. 4). However, under real observational conditions, signal distortions occur, for example, due to multipath and diffraction. To achieve a realistic SNR-based error characterisation of GPS phase observations without the a priori knowledge about the receiver environment, Brunner et al. (1999) developed the SIGMA-Δ model that automatically computes the phase noise based on the measured $SNR0$ and a $SNR0$ template for a certain antenna type. Such a template is defined by the highest $SNR0$ value at a certain satellite elevation angle. Applying the SIGMA-Δ model in static and kinematic GPS surveys, the positioning errors caused by signal diffraction can be reduced by about 50%-85%.

Wieser and Brunner (2000) verified the effectiveness of estimating the actual phase observation noise in the SIGMA-ϵ model, as well as the appropriateness of using SNR as an indicator for signal distortions in the SIGMA-Δ model. In addition, the limitations of the SNR-based weighting schemes were demonstrated, particularly in the presence of strong multipath effects. To overcome these limitations, the SIGMA-ϵ model was extended by applying robust estimation methods (e.g., the Danish method) and by incorporating residual information into multipath and diffraction handling. The extended weighting model showed good performance in identifying and removing biases, where its efficiency mainly depends on the redundancy of the observation data and the evaluation of the residual covariance matrix. In this context, the epoch-wise data analysis strategy, commonly implemented in GPS processing software, is questionable. If all epochs are simultaneously processed, the temporal (inter-epoch) correlations must be taken into account. Satirapod and Wang (2000) compared the two quality indicators, SNR and satellite elevation angle, and concluded that SNR generally represents a more realistic quality measure, but both of them do not always reflect reality.

In order to mitigate multipath and interference in GPS relative positioning in engineering surveying, Lau and Mok (1999) suggested the CALMS (combined AFM and LSM method with SNR weighting) approach, which combines the ambiguity function method (AFM; Mader, 1992) and the SNR-weighted least-squares method (LSM). Thereby, the double-difference weight matrix is multiplied by a SNR cofactor matrix, resulting in the final weight matrix for the LS adjustment. Employing this SNR-weighted LS algorithm in short-baseline (<10 km) applications, improved positioning accuracy was reported when using 1 min of GPS data (6 epochs) collected in a strong multipath environment. Since the multipath error is reduced by means of an advanced stochastic model, a long observation period for averaging out multipath is not required.

Taking advantage of other favourable properties of SNR, for instance, being sensitive to carrier-phase multipath and reflecting changes in the multipath environment, Bilich and Larson (2007) developed a method to map the temporally variable amplitude and frequency content of various

multipath constituents by applying the continuous wavelet transform (see section 2.4.2) to SNR time series. Using representative continuously operating GPS sites from geodetic networks, it was concluded that near-field multipath, associated with high satellite elevation angles, does not significantly contribute to positioning errors, while the impact of far-field multipath, particularly that caused by topographic features, seems to be more serious than previously believed. If multipath signals are not correctly understood and sufficiently modelled, they may be mistaken for seismic waves in applications of GPS seismology. Based on the theory that the time-evolving property of multipath leads to equal-frequency, but out-of-phase oscillations in carrier-phase and SNR, Bilich et al. (2008) proposed the combined wavelet-ALS algorithm for modelling GPS phase multipath error, where the model parameters, such as the amplitude and relative phase, are estimated by means of an adaptive LS (ALS) method. Applying this approach to short-baseline (11-17 m) network solutions using GPS data collected from a large salt flat (Salar de Uyuni), multipath signals with periods between 200 and 2000 s can be successfully detected and sufficiently reduced. It was shown that a reduction in phase residual noise of up to 20% is achievable for static positioning, and an improvement of 1-7 dB in spectral power at multipath periods is possible for kinematic positioning. In spite of considerable enhancements, the suggested algorithm still has difficulties in extracting multipath amplitude and phase information from SNR time series, and is restricted to simple multipath environments.

According to the same relationship between carrier-phase multipath error and SNR, Rost and Wanninger (2009) derived a simplified multipath correction model for GPS static positioning and single dominant reflectors. It requires a SNR resolution of at least 0.25 dBHz, and mainly considers the multipath relative phase, as well as the ratio of the composite and direct signal amplitudes. Using GPS data from a short baseline of 10 m, established on a parking lot, it was verified that the SNR-based multipath corrections only depend on antenna height and satellite elevation angle due to the large horizontal reflector. Applying the correction values to the phase observations, both the double-difference residuals and single-epoch coordinate estimates are improved by almost 25%. In Rost and Wanninger (2010), this model was used to correct the GNSS (GPS/GLONASS) data from the continuously operating reference stations (CORS) of the German SA*POS*®sub-network of Saxony-Anhalt. Comparing the LC3 single-epoch coordinate standard deviation before and after applying the multipath corrections, both amelioration of up to 13% and deterioration of up to −6.5% are observed in the height and horizontal components, respectively. If the model assumption of one well-defined horizontal reflector is fulfilled, a large portion of the phase multipath effects can be removed. Nonetheless, the proposed method is not generally applicable for multipath mitigation.

Enabling a more realistic assessment of GPS observation quality, SNR-based variance (or weighting) models are preferable for GPS data analysis, particularly when including observations from low-elevation satellites. However, the performance of the variance model given by equation (5.10) strongly depends on how well the generally unknown loop bandwidth B_L is specified. Furthermore, as mentioned above, such a variance model ignores the contribution of the local oscillator to the phase noise. By individually estimating the factor C_i for different antenna and receiver types, the SIGMA-ϵ model is capable of considering site-specific environments and antenna-receiver characteristics. Nevertheless, it still has the disadvantage of being only strictly suitable for relatively strong signals, which are well above the tracking threshold of the receiver (Collins and Langley, 1999, p. 4). To overcome these drawbacks of this analytical SNR-based variance model, an empirical SNR-based weighting scheme is developed in this thesis, which also accounts for site-specific effects and antenna-receiver characteristics. Due to the unrealistic assumptions of the SNR-based multipath modelling, a sidereal stacking technique is employed in this work, which makes use of multiple consecutive days of residual time series (see section 7.2.5).

5.3 SNR-based weighting model

In this section, an empirical SNR-based weighting model is presented. Following a detailed description of its realisation and contribution to the GPS stochastic model, its advantages are demonstrated in comparison to other analytical and empirical approaches using SNR or the satellite elevation angle. Next, the model implementation into the Bernese GPS Software 5.0 is briefly discussed. Finally, the key properties of the proposed SNR-based weighting scheme are summarised considering different aspects, emphasising its strengths in GPS data analysis.

5.3.1 Model realisation

The empirical SNR-based weighting model relies upon a simple and intuitive principle that the best GPS observations with the largest SNR should obtain the maximum weight of one. The weights for other measurements depend on the minimum-related ratios of the corresponding SNR values to the maximum SNR. To ensure the comparability between various SNR realisations (see section 5.1), the signal quality measures should be available as $SNR0$ in dBHz, or can be converted into $SNR0$, where external information from receiver manufacturers, such as SNR unit and computation, may be necessary. Using observation data in the RINEX format, for example, Version 2.10, SNR measurements are reported as observable types S1 and S2, and represent the raw signal strengths as provided by the receiver for L1 and L2 phase observations (Gurtner, 2002, sect. 0.4). The current RINEX Version 3.00 requires that the raw signal strengths should be stored in dBHz if possible, where the raw SNR values are obtained at the correlator output without attempting to recover any correlation loss. In addition, a new header record `SIGNAL STRENGTH UNIT` is available, providing the unit of the signal quality measurements (Gurtner and Estey, 2007, p. 10, 28). The raw signal strength in dBHz can be expressed as a scale of 1-9 (1: very weak, ..., 9: very strong) by means of

$$SNR_{rnx} = \min\{\max\left[\text{INT}(SNR0/6), 1\right], 9\},\tag{5.11}$$

resulting in the so-called RINEX signal strength indicator (Gurtner and Estey, 2007, sect. 5.7). A SNR_{rnx} of 5 corresponds to a $SNR0$ of about 35 dBHz, and is the threshold for average signal quality. If SNR_{rnx} is equal to zero, the associated $SNR0$ is unknown or not present. Figure 5.6 shows the SNR projection given by equation (5.11) in graphic and tabular form. Obviously, the transform from $SNR0$ into SNR_{rnx} can be considered to be linear.

SNR0 [dBHz]	SNRrnx
< 12	1
12-17	2
18-23	3
24-29	4
30-35	5
36-41	6
42-47	7
48-53	8
≥ 54	9
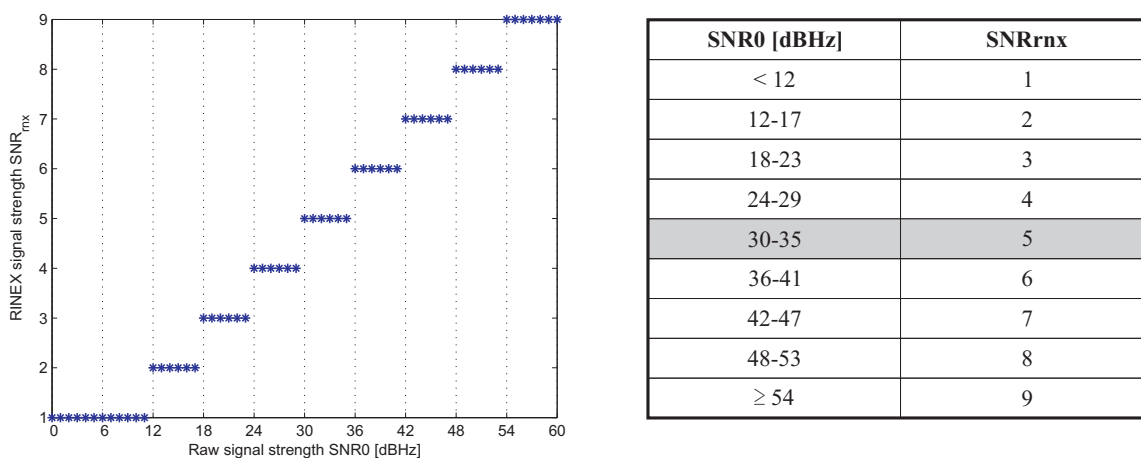
Figure 5.6: Projection of the raw signal strength $SNR0$ in dBHz into the RINEX signal strength indicator SNR_{rnx} (Gurtner and Estey, 2007, table 7; see equation (5.11)).

Although signal quality data can be stored in the unique unit dBHz, differences in $SNR0$ are still present due to receiver characteristics (e.g., hardware, receiver firmware) and site-specific effects (e.g., multipath). The corresponding variations in observation quality should be considered in the SNR-based weighting model to achieve a more realistic noise assessment of GPS phase measurements. Keeping this aspect in mind, an empirical SNR-based observation weighting scheme is realised in two steps, schematically shown in figure 5.7 for GPS relative positioning.
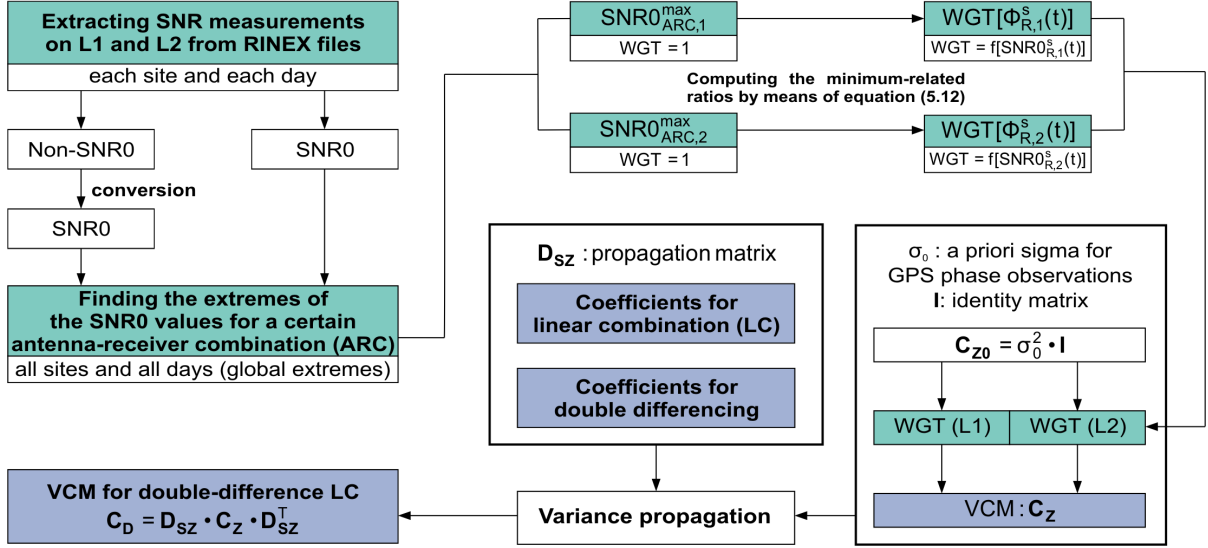
Figure 5.7: An empirical SNR-based observation weighting scheme and its contribution to the stochastic model in GPS relative positioning (WGT: weight, VCM: variance-covariance matrix), after Luo et al. (2008a,d)

In the first step, signal quality measurements are extracted from the RINEX observation files, where missing SNR data are marked by zero. As an alternative to the self-programmed routine, SNR values can be conveniently obtained for each satellite by applying the `cf2ps` program (Hilla, 2002) to the TEQC plot files (Estey and Meertens, 1999). If the extracted SNR quantities are not $SNR0$ in dBHz (e.g., AMU, SNR in dB), they are converted into $SNR0$ based on the information provided by receiver manufactures. Once the SNR data are aligned to a comparable level, for each antenna-receiver combination (ARC) being present in the network, the frequency-dependent minimum and maximum $SNR0$ values, denoted as $SNR0_{ARC,i}^{min}$ and $SNR0_{ARC,i}^{max}$, respectively, are searched over the entire observation period. This procedure guarantees that the found extreme signal strengths are representative with respect to the site's environments, atmospheric variations, as well as antenna and receiver characteristics. The zero-valued SNR data due to missing observations are excluded from the minimum search procedure. In order to avoid the situation where the found global extremes are actually outliers, for each ARC, statistical analysis of $SNR0$ is performed by means of box plots, as demonstrated in figure 5.1(b).

Following the first step in which the SNR measurements are homogenised and the global references for low- and high-quality observations are found, the second step produces individual weights for each L1 and L2 phase observation by calculating the minimum-related ratio between the actual and the corresponding maximum $SNR0$. Considering the phase observation $\Phi_{R,i}^{s}(t)$, which is related to receiver R, satellite s, frequency i, and epoch t, the corresponding SNR-based weight is computed as

$$w\left[\Phi_{R,i}^{s}(t)\right] = f\left[SNR0_{R,i}^{s}(t)\right] = \left[a + (1-a) \cdot \left(\frac{SNR0_{R,i}^{s}(t) - SNR0_{ARC,i}^{min}}{SNR0_{ARC,i}^{max} - SNR0_{ARC,i}^{min}}\right)\right]^{2}, \quad (5.12)$$

where the parameter a is introduced to avoid the singularity problem of the cofactor $q = w^{-1}$ in the case that $SNR0_{R,i}^s(t) = SNR0_{ARC,i}^{min}$. To fulfil the precondition $f(SNR0_{ARC,i}^{max}) = 1$, a factor of $(1 - a)$ is multiplied to the minimum-related ratio. For representative $SNR0$ values between 10 and 55 dBHz (see figure 5.6), figure 5.8 illustrates the weights and cofactors derived from equation (5.12) using different specifications for a. As a decreases from 0.1 to 0.01, one can discern an overall downweighting effect, with decreased weights and increased cofactors, particularly for low-quality signals. By considering figures 5.5(a) and (c), $a = \sin 5° \approx 0.1$ is used in this thesis to reduce the downweighting effect on low-quality observations of weak signals.
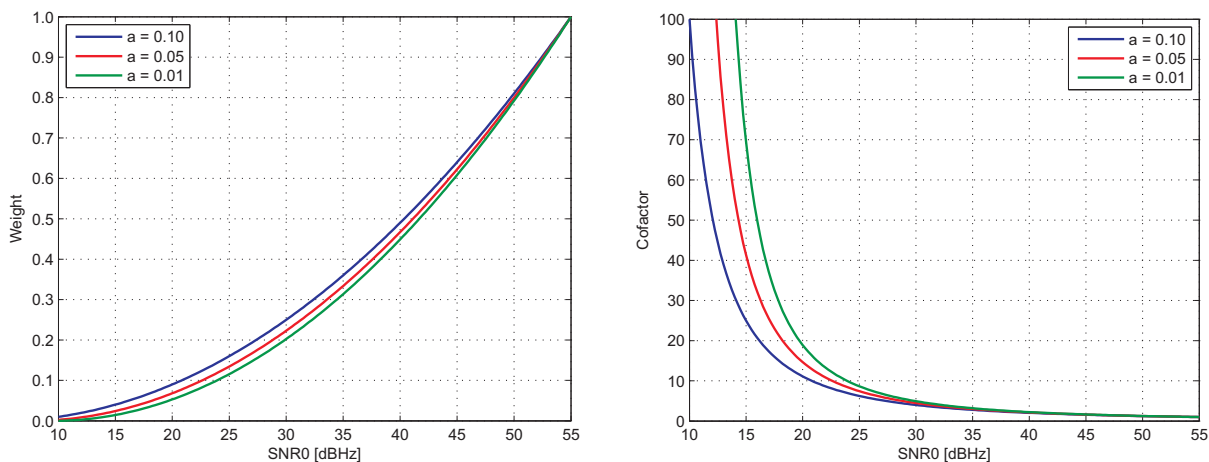

Figure 5.8: Influence of the model parameter a in equation (5.12) on the SNR-based weight and cofactor values ($SNR0_{ARC,i}^{min} = 10$ dBHz, $SNR0_{ARC,i}^{max} = 55$ dBHz)

The SNR-based weights computed using equation (5.12) improve the scaled identity matrix, which is denoted as $\boldsymbol{C_{Z0}}$ in figure 5.7, to the variance-covariance matrix (VCM) $\boldsymbol{C_Z}$ with different diagonal elements. Next, $\boldsymbol{C_Z}$, the VCM of zero-differences, is propagated by considering the propagation matrix $\boldsymbol{D_{SZ}}$, which contains the coefficients for linear combination and double differencing (see figure 3.6). The resulting VCM of double-differences $\boldsymbol{C_D}$ is then used for the LS parameter estimation. Although in this thesis the empirical SNR-based weighting model is only applied to GPS relative positioning, it can be easily adapted to precise point positioning (PPP) by neglecting the variance propagation step with respect to double differencing.

5.3.2 Model comparison

In this section, the suggested SNR-based weighting model (EMPSNR2) is compared with different alternatives, such as the analytical approach (ANLSNR) given by equation (5.10), another empirical method (EMPSNR1) proposed by Mayer (2006, p. 62), and the commonly used elevation-dependent weighing function $\sin^2(e)$, denoted as CSC2(BS) in figure 3.3.

For $SNR0$ varying from 10 and 35 to 55 dBHz, figure 5.9 compares the weight and cofactor values produced by ANLSNR and EMPSNR2, where the ANLSNR-related weights are computed with respect to the maximum $SNR0$. As Collins and Langley (1999, p. 4) noted, the analytical model ANLSNR is only suitable for relatively strong signals (i.e., $SNR0 > 35$ dBHz), while the empirical approach EMPSNR2 is also able to deliver reasonable weights for relatively weak signals (i.e., $SNR0 \leq 35$ dBHz). This indicates a better performance of EMPSNR2 for both low- and high-quality GPS measurements. Furthermore, when decreasing the $SNR0$ range from $[10, 55]$ to $[35, 55]$, the differences between ANLSNR and EMPSNR2 also decrease.
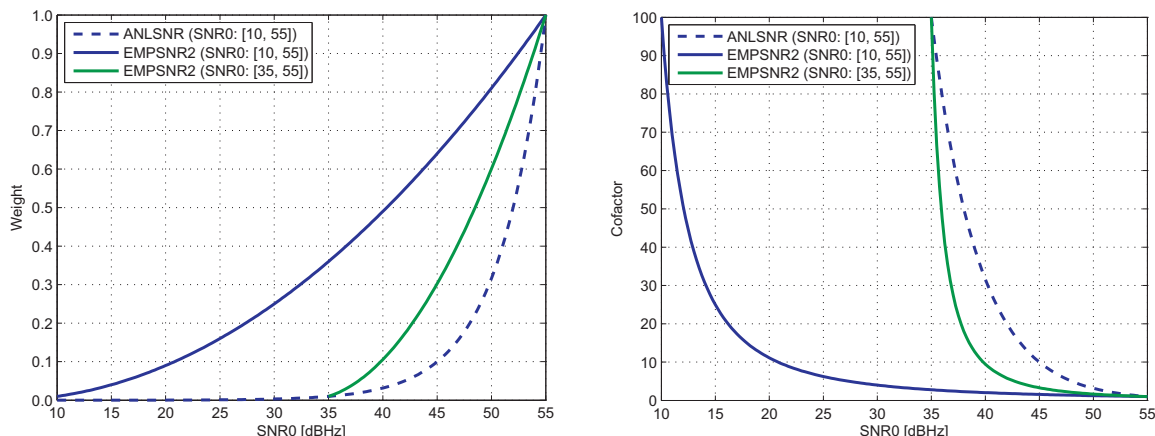
Figure 5.9: Comparison of the weight and cofactor values produced by the observation weighting models ANLSNR and EMPSNR2 (ANLSNR: $w_{\Phi_i} = \sigma^2_{\Phi_i}(SNR0_i^{\max} = 55 \text{ dBHz})/\sigma^2_{\Phi_i}(SNR0_i)$, see equation (5.10); EMPSNR2: $a = 0.1$, see equation (5.12))

Analysing GPS data from the densification network of the Antarctic Peninsula, Mayer (2006, sect. 5.4.2) computed SNR-based observation weights empirically by simply dividing the signal quality measurements by the maximum found during an observation campaign. This approach assumes a homogenous antenna-receiver combination within a survey campaign, and delivers almost azimuth-independent weights between 0.1 and 0.3 for low-elevation (i.e., $e < 20°$) data. For GPS measurements from medium- and high-elevation satellites, the corresponding weights are generally larger than 0.5 (Mayer, 2006, p. 62, 67). Figure 5.10 illustrates the weights and cofactors produced by EMPSNR1 and EMPSNR2. From figure 5.10, one can easily discern that EMPSNR1 always produces larger weights than EMPSNR2, particularly for the narrower $SNR0$ variation range [35, 55]. Overweighting low-quality observations leads to small cofactor values, and thus overestimates the contribution of low-quality data to the LS parameter estimation.
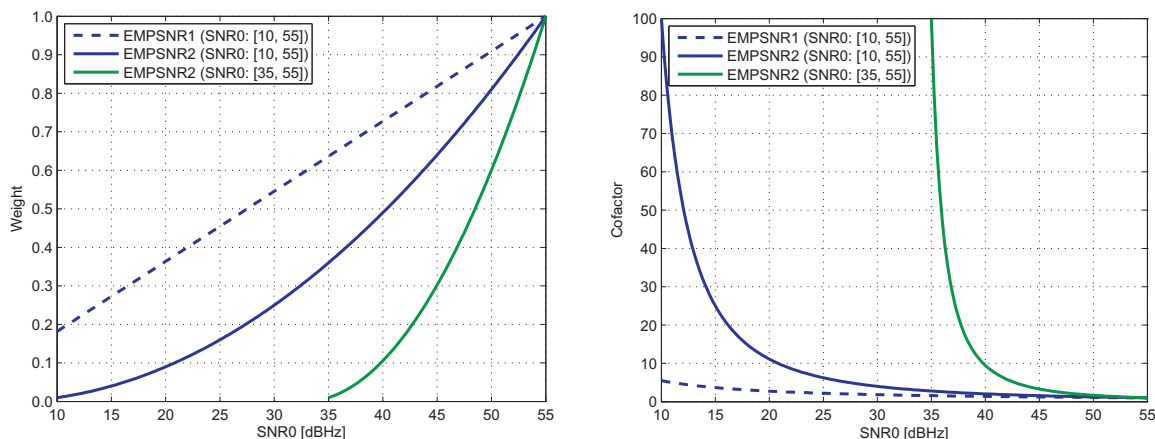
Figure 5.10: Comparison of the weight and cofactor values produced by the empirical observation weighting models EMPSNR1 and EMPSNR2 (EMPSNR1: $w_{\Phi_i} = SNR0_i/SNR0_i^{\max}$, Mayer, 2006, sect. 5.4.2; EMPSNR2: $a = 0.1$, see equation (5.12))

Taking the $SNR0$ data shown in figure 5.1(a) as an example, figure 5.11 compares the empirically derived observation weights depending on the satellite elevation angle. If EMPSNR1 is applied, observations from $e < 20°$ already maintain considerably large weights of about 0.7, which attenuates the qualitative difference between an average and a good observation. This kind of overweighting effect is considerably reduced by means of the proposed EMPSNR2. Thereby, low-elevation observations obtain more realistic weights of up to about 0.4. Therefore,

the application of EMPSNR2 seems to achieve a balance between appropriately downweighting low-quality observations and effectively improving the satellite geometry by incorporating low-elevation measurements into the parameter adjustment.

(a) Weighting model: EMPSNR1   (b) Weighting model: EMPSNR2
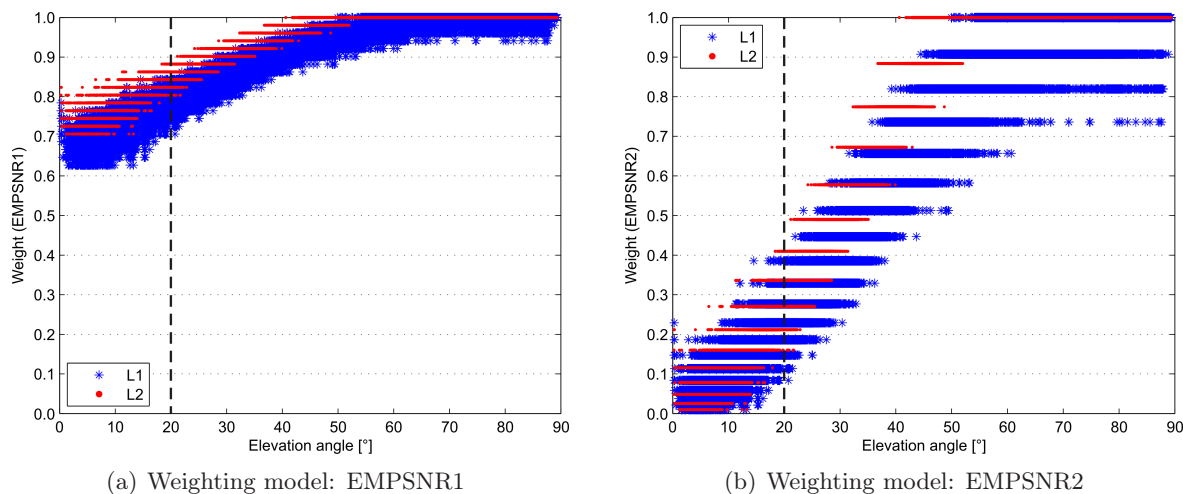
Figure 5.11: Empirical weights derived using the $SNR0$ measurements shown in figure 5.1(a)

The commonly used elevation-dependent variance models presented in table 3.6 depend on the cosecant function of the satellite elevation angle, i.e., $1/\sin(e)$, which actually represents a first-order approximation of the tropospheric mapping function. The underlying theory is that the tropospheric delay error increases towards the horizon, as does the amount of noise inherent to GPS observations. Therefore, the variance of phase noise is assumed to be directly proportional to the squared value of $1/\sin(e)$ (Collins and Langley, 1999, p. 1). Figure 5.12 compares the empirical SNR-based weighting model EMPSNR2 with the elevation-dependent weighting scheme CSC2(BS) (i.e., $\sin^2(e)$; Dach et al., 2007a, p. 144), with respect to observation data volume, antenna-receiver combination, and site-specific multipath impact.

Comparing the weight values for the site RAVE on a daily basis, figure 5.12(a) shows the advantage of EMPSNR2 in attenuating observation downweighting effects over the whole elevation range. Moreover, the differences in observation quality between L1 and L2 become more obvious for $e > 20°$, and they cannot be accounted for by means of CSC2(BS), but by applying EMPSNR2 (see also figure 5.11(b)). In this example, the $SNR0$ values on the L2 carrier frequency range between 36 and 51 dBHz, and are well above the tracking threshold of 35 dBHz (see figures 5.1(b) and 5.6). Accordingly, similar results are also obtained using the analytical approach ANLSNR (see figures 5.5(d) and 5.9).

In addition to long-term (24 h) GPS measurements, short-term static observations are also used for model comparison. Although the weight values presented in figures 5.12(b-d) are related to a 1-hour time interval, the antenna-receiver-specific $SNR0$ extremes are determined based on representative data sets. Despite the different data volumes and receiver firmware versions, the variation patterns of the SNR-based weights shown in figure 5.12(b) are quite similar to those displayed in figure 5.12(a). This demonstrates the potential of EMPSNR2 in short-term static applications if reliable $SNR0$ extremes are available, for example, in the case of CORS.

For the same observation period, a similar degree of multipath impact, but another antenna-receiver combination, figure 5.12(c) illustrates SNR-based weights with considerably different patterns when compared to figure 5.12(b). The antenna-receiver-specific handling, which is realised in EMPSNR2, contributes to the maintenance of instrumental characteristics, although
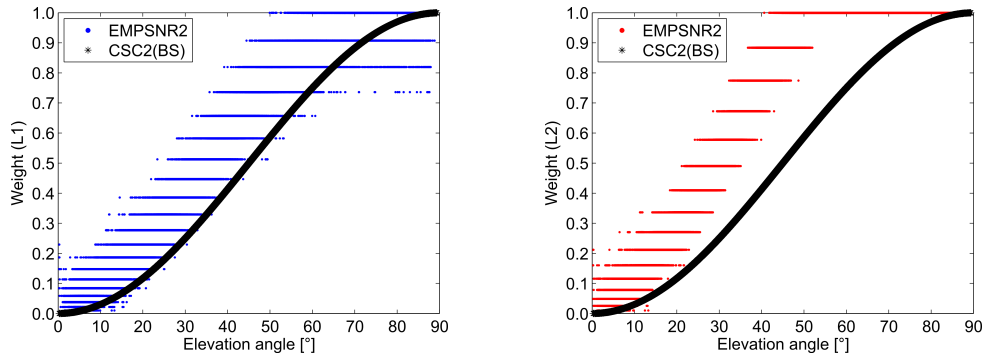
(a) Site: RAVE, weak multipath, 24-hour observation data, sampling interval: 15 s, receiver: Leica SR520, antenna: LEIAT503, firmware version: 4.01
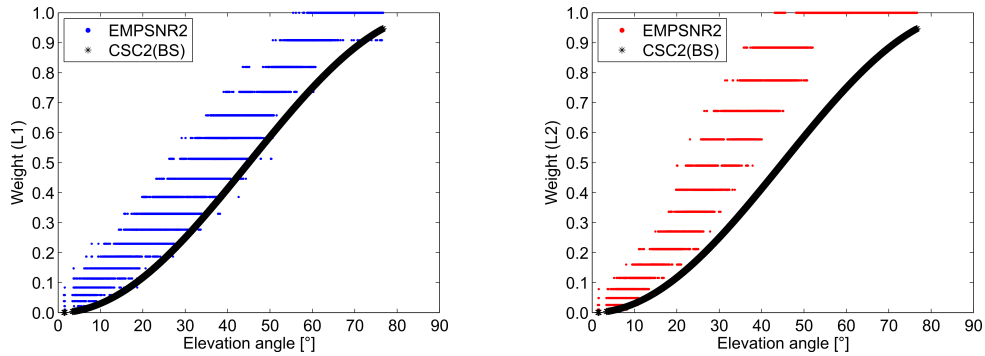
(b) Site: RAVE, weak multipath, 1-hour observation data, sampling interval: 1 s, receiver: Leica SR520, antenna: LEIAT503, firmware version: 4.1
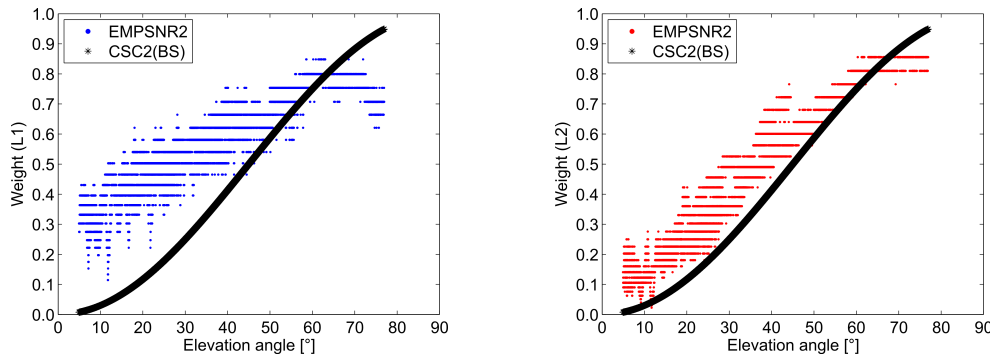
(c) Site: GZBG, weak multipath, 1-hour observation data, sampling interval: 1 s, receiver: Trimble NetR5, antenna: TRM55971.00 TZGD, firmware version: Nav 3.20/Boot 3.10
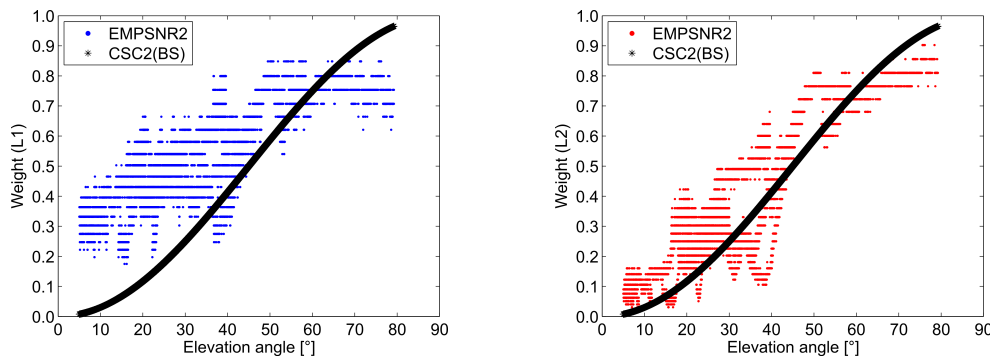
(d) Site: DARM, strong multipath, 1-hour observation data, sampling interval: 1 s, receiver: Trimble NetR5, antenna: TRM55971.00 TZGD, firmware version: Nav 3.30/Boot 3.10

Figure 5.12: Comparison of the observation weights produced by CSC2(BS) and EMPSNR2 considering different aspects (a: DOY2004:186, b-d: DOY2007:161, 17-18 h, GPS time)

both the Leica and Trimble receivers deliver $SNR0$ in dBHz (Landau, 2006b). Furthermore, the elevation-dependent weighting model CSC2(BS) seems to produce more serious downweighting effect on the L1 (L2) observations from the Trimble (Leica) receiver at low (high) elevation angles. In figure 5.12(d), the SNR-based and elevation-dependent weights are compared for the site DARM, which has the same antenna-receiver combination as the site GZBG, but a stronger multipath impact (see figure 4.6(c)). This can be well captured by means of EMPSNR2 due to the fact that the frequency and amplitude content of SNR data are directly related to carrier-phase multipath errors (Bilich et al., 2008).

Another advantage of EMPSNR2 over CSC2(BS) is that SNR measurements respond to environmental variations, while GPS satellite elevation angles observed at the same site repeat with an approximate period of one mean sidereal day. As a result, SNR-based weights reflect changes in observation quality induced by variable atmospheric conditions, while elevation-dependent weights completely ignore these day-to-day variations, and thus produce an unrealistic mapping of observation quality. To demonstrate this benefit from EMPSNR2, figure 5.13 takes the site DARM as an example and compares the 1-hour L2 weights on three consecutive days (DOY2007:179-181). By considering an approximate repeat time of the GPS constellation of one mean sidereal day (i.e., 23 h 56 min 4 s; see section 7.2.5), the observation weights are determined under an almost identical satellite geometry, as illustrated in figure 5.13(a).

(a) Repeating satellite geometry

(b) Weight values on day 179

(c) Weight values on day 180

(d) Weight values on day 181
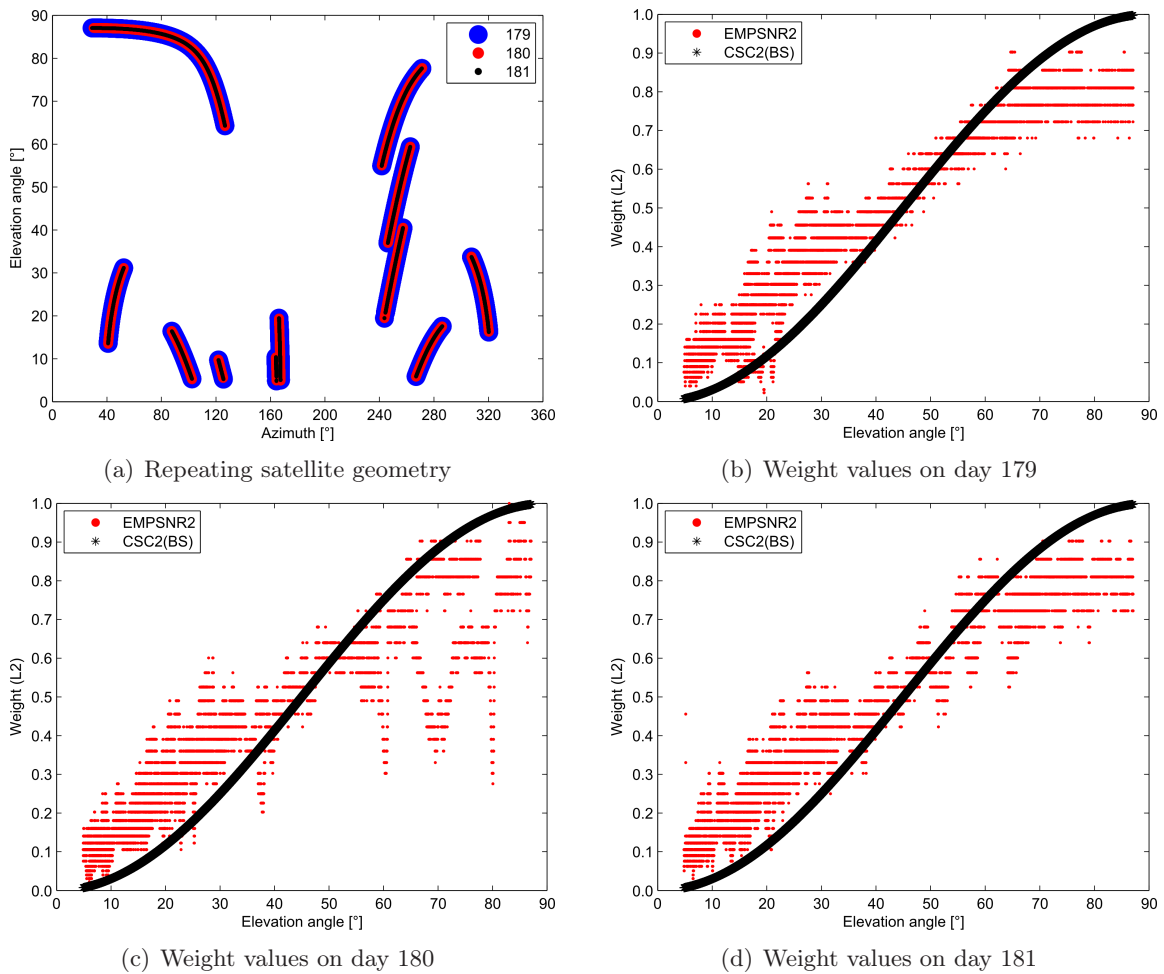
Figure 5.13: Comparison of the 1-hour L2 observation weights produced by CSC2(BS) and EMPSNR2 under an almost identical satellite geometry on three consecutive days (site: DARM, strong multipath, DOY2007:179-181, 17-18 h, GPS time, sampling interval: 1 s)

For elevation angles around $20°$ as well as between $50°$ and $70°$, figures 5.13(b) and (d) exhibit minor, but visible differences in the L2 weights between days 179 and 181. On day 180, large variations are present, particularly at high elevation angles (see figure 5.13(c)). Taking the strong multipath environment of the site DARM into account, these day-to-day variations may be attributed to the changes in site reflection properties, which are caused by variable atmospheric conditions (see *RH* at FRAN in figure 4.8(c)). In contrast, due to the repeating satellite geometry, the elevation-dependent weights are identical on different days.

The above model comparison emphasises the advantages of the proposed SNR-based weighting scheme EMPSNR2 in downweighting reduction, overweighting prevention, and in realistic characterisation of GPS observation quality. In order to exploit these benefits in GPS data analysis and to improve the performance of parameter estimation, EMPSNR2 is experimentally implemented into the Bernese GPS Software 5.0 (Dach et al., 2007a).

5.3.3 Model implementation

The implementation of the empirical SNR-based weighting model consists of two parts, namely weight calculation and weight application, schematically shown in figure 5.14. According to the flowchart presented in figure 5.7, the computation of the frequency-related observation weights is performed in MATLAB. As a result, for each site in each session, a weight file (`WGT`) is generated, which contains the epochs in GPS time, satellite PRN (pseudo random noise) numbers, and the weights for L1 and L2 phase observations. The `WGT` files are located in an additional campaign directory named as `SNR` (i.e., `${P}/MYCAMP/SNR/*.WGT`).
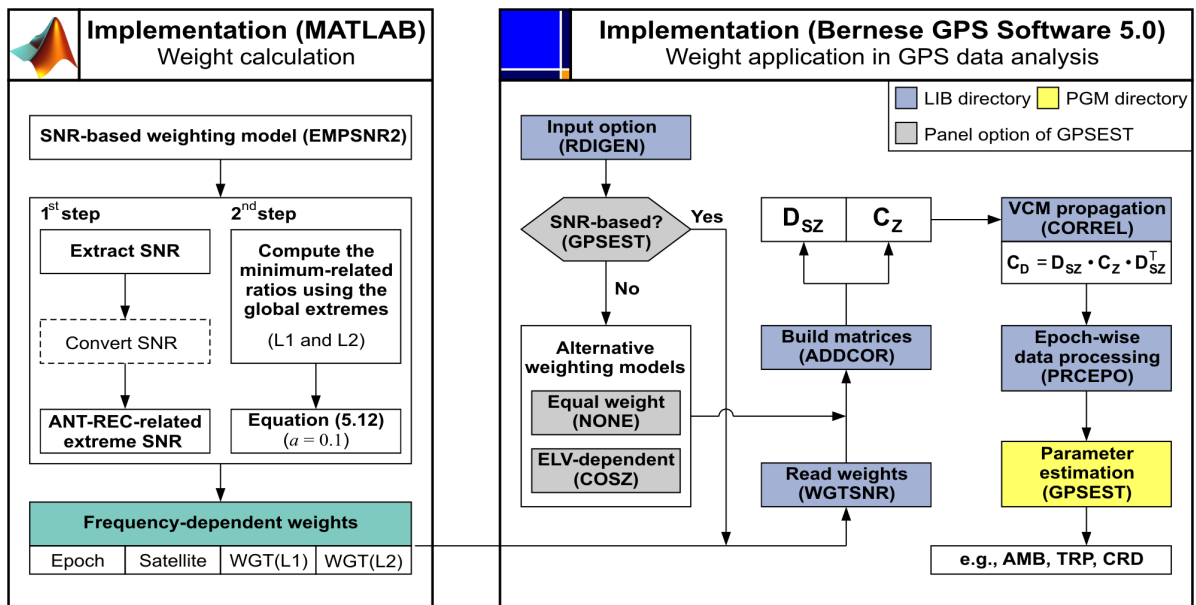
Figure 5.14: Implementation of EMPSNR2 into the Bernese GPS Software 5.0 for relative positioning

At the preliminary stage of the implementation of EMPSNR2 into the Bernese GPS Software 5.0, the input panel of the main program `GPSEST`, located in the user-specific directory (`${U}/PAN/GPSEST.INP`), is modified by adding another observation weighting option `SNR` to the already existing models `NONE` (i.e., equal weight with $w = 1$) and `COSZ` (i.e., elevation-dependent weight with $w = \sin^2(e)$). To connect the extended weighting option to the related Fortran routines, a new `keyValue` must be specified in the subroutine `RDIGEN`, which is located in the library directory (`${C}/LIB`) and has the task of reading general input options for `GPSEST` (`${C}/PGM`).

If the SNR-based weighting model is chosen for parameter estimation, observation weights are read from the WGT files by the self-written subroutine WGTSNR, which is also located in the LIB directory. Otherwise, one of the standard weighting models (NONE or COSZ) is applied.

After importing the observation weights, the VCM of zero-differences C_Z is constructed by the subroutine ADDCOR. The building of the propagation matrix D_{SZ} is not affected by a change in the observation weighting model, since its structure only depends on the coefficients for the applied linear combination and double differencing (see figure 3.6). Once C_Z and D_{SZ} are available, the VCM of double-differences C_D can be derived by applying the variance-covariance propagation law to C_Z, which is accomplished by the subroutine CORREL (see figure 5.7 for C_Z, D_{SZ}, and C_D). Benefiting from the more realistic SNR-based observation weights, such an advanced stochastic model enhances the epoch-wise data processing performed by the subroutine PRCEPO. The main program GPSEST calls PRCEPO and estimates the unknown parameters, such as phase ambiguities (AMB), site-specific troposphere parameters (TRP), and station coordinates (CRD). Improvements in the parameter estimates will reflect the superior performance of the proposed SNR-based weighing model in comparison to the standard elevation-dependent one.

For the residual-based temporal correlation modelling to be presented in chapter 7, double-difference residuals are saved, along with the corresponding time stamps and information about satellite geometry. The necessary modifications were first made in the Bernese GPS Software 4.2 by Howind (2005), and then adapted to the Version 5.0 by Luo et al. (2007a, p. 27).

5.4 Concluding remarks

Being a more realistic quality indicator for GPS phase observations, the signal-to-noise ratio (SNR) holds great potential for improving the stochastic model in GPS data analysis. This chapter introduced an empirical SNR-based observation weighting model EMPSNR2, which relies upon a minimum-related scaling of representative signal quality measurements. In view of downweighting effect reduction and realistic quality assessments, EMPSNR2 appears to be superior to the analytical approach ANLSNR proposed by Langley (1997), as well as to the commonly used elevation-dependent weighting scheme CSC2(BS) (i.e., $\sin^2(e)$). In this thesis, EMPSNR2 has been experimentally implemented into the Bernese GPS Software 5.0, and its advantages over CSC2(BS) in GPS relative positioning will be presented in the next chapter. Table 5.2 compares the key properties of CSC2(BS) and EMPSNR2 considering different aspects.

Table 5.2: Comparing the key properties of the elevation-dependent and SNR-based weighting models

Aspect	**CSC2(BS)**: $\sin^2(e)$	**EMPSNR2**: equation (5.12)
Quality indicator	Indirect: satellite elvation angle (e)	Direct: signal quality measures (SNR)
Model principle	Squared value of the tropospheric MF[1]	Antenna-receiver-specific scaling of SNR
Application area	Kinematic, short- and long-term static positioning	short- and long-term static positioning (e.g., in the case of CORS[2])
Degree of reality	Low, affected by site-specific effects and variable atmospheric conditions	High, due to the sensitivity of SNR to different quality limiting factors
Individual weights for L1 and L2	Impossible, due to the same satellite elevation angle for both frequencies	Possible, due to the individual SNR registration for each frequency
Downweighting	Possible over the whole elevation range	Considerably reduced
Complexity	Simple, low computational burden	Complex, high computational burden

[1] MF: mapping function
[2] CORS: continuously operating reference stations

Chapter 6

Results of SNR-based Observation Weighting

Analysing the relative positioning case studies described in section 4.2, this chapter presents the effects of the SNR-based observation weighting model EMPSNR2 on GPS baseline solutions using the Bernese GPS Software 5.0. Thereby, three important aspects, namely ambiguity resolution, troposphere parameter estimation, and coordinate determination, are taken into account. Being structured in a similar way, sections 6.1 and 6.2 first compare the weight values, then the adjustment results obtained by means of the commonly used elevation-dependent weighting scheme CSC2(BS) and the proposed SNR-based EMPSNR2. Section 6.3 summarises the main findings from the case studies, providing a realistic picture of the advantages of EMPSNR2.

6.1 Case study 1: long-term relative positioning

The long-term relative positioning case study is carried out to determine the effects of the SNR-based weighting model on daily GPS baseline solutions, which represent a typical scenario for a wide range of geodetic applications, such as long-term deformation analysis and reference frame realisation. This section begins with a discussion of the antenna-receiver-specific SNR extremes, playing a key role in the computation of observation weights (see figure 5.7). Next, for different elevation cut-off angles of 10° and 3° (see table 4.4), the impacts of the SNR-based weighting on GPS parameter estimation are demonstrated using representative examples.

6.1.1 SNR extremes and observation weights

As described in section 5.3.1, the frequency-related extremes of the signal-to-noise power density ratio $SNR0$ in dBHz are found for each antenna-receiver combination (ARC) by considering all available non-zero measurements over the entire investigation period. These extremes are substituted into equation (5.12) to derive the SNR-based weights for GPS phase observations. Obviously, the quality of the detected minimum and maximum is essential for realistic weight specification and reliable parameter estimation. Considering the four ARC applied in this case study (see table 4.1), table 6.1 provides the SNR extremes on L1 and L2. While the Leica equipment delivers identical extreme values, the L1 minima from the Trimble instruments exhibit a difference of about 9 dBHz. This may be explained by the differences in antenna performance (TRM23903: Trimble Permanent L1/L2; TRM29659: Trimble D/M choke ring antenna) and site-specific multipath impact (see table 4.1; Mayer et al., 2004).

Table 6.1: Antenna-receiver-specific SNR extremes used for computing the SNR-based observation weights in case study 1 ($SNR0$ in dBHz)

ARC	Antenna	Receiver	Min/Max (L1)	Min/Max (L2)
1	TRM29659	Trimble 4000SSI	**30.38**/57.38	32.27/57.43
2	TRM23903	Trimble 4000SSI	**21.39**/57.38	32.27/58.28
3	LEIAT503	Leica SR520	32/51	36/51
4	LEIAT303	Leica SR520	32/51	36/51

Another difference between the $SNR0$ associated with the Leica and Trimble instruments is that the former are directly extracted from the RINEX observation files, while the latter are converted from signal-to-noise power ratio SNR in dB (see section 5.1). Instead of using equation (5.4) by specifying an appropriate value for loop bandwidth B_L, manufacturer-specific formulas for the Trimble 4000 series receivers are applied, which establish relationships between SNR in dB, AMU (arbitrary manufacturer units), and $SNR0$ in dBHz (Trimble, 1999). First, the SNR values are converted into AMU units by means of (Landau, 2006a)

$$SNR_1 \,[\text{dB}] = 10 \cdot \log_{10}(230 \cdot AMU_1^2), \tag{6.1}$$

$$SNR_2 \,[\text{dB}] = 10 \cdot \log_{10}\left[50 \cdot (AMU_2 - 5)^2\right], \tag{6.2}$$

where the subscripts 1 and 2 denote the carrier frequencies L1 and L2, respectively. Next, the resulting AMU can be easily converted into $SNR0$ using equation (5.9). For a reasonable range of AMU units, figure 6.1(a) illustrates equations (5.9), (6.1), and (6.2), which are involved in this two-step conversion process. Obviously, the transform from SNR_2 into AMU_2 has a singularity at $AMU_2 = 5$ and is not unique for $SNR_2 < 31$ dB. To solve this ambiguity problem, the corresponding SNR_1 is compared with a reference of 37.6 dB, derived by substituting $AMU_1 = 5$ into equation (6.1). If the SNR_1 to be converted is smaller (larger) than this threshold, then the AMU_2 solution for the corresponding SNR_2 is located on the left (right) hand side relative to $AMU_2 = 5$. Taking $SNR_2 = 17$ dB as an example, different AMU_2 of 4 and 6 are obtained for SNR_1 of 36 and 40 dB, respectively. Considering the entire period of investigation, figure 6.1(b) presents the results of SNR conversion for the SA*POS*®site KARL, which is equipped with the Trimble instruments denoted as ARC1 in table 6.1. The difference in the sample medians of SNR_1 and SNR_2 coincides with the offset between the associated conversion curves shown in figure 6.1(a). After transforming SNR into AMU and $SNR0$, this difference is considerably reduced, and the resulting box plots illustrate similar characteristics to those depicted in figure 5.2(d), indicating the appropriateness of the employed conversion approach.

(a) Conversion between signal quality measures   (b) Example of SNR conversion
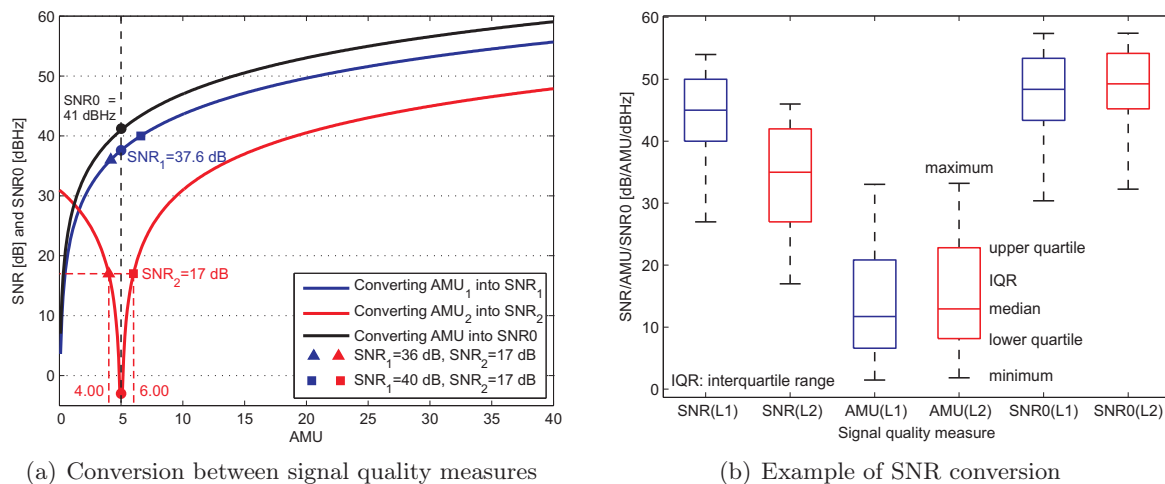
Figure 6.1: Conversion of SNR into $SNR0$ for a Trimble 4000SSI receiver using the manufacturer-specific formulas (5.9), (6.1), and (6.2) (SA*POS*®site: KARL, DOY2004:186-193)

For the sake of completeness, figure 6.2 shows the box plots of the $SNR0$ measurements which are directly extracted from the RINEX observation files. Despite the different antenna types between ARC3 and ARC4 (see table 6.1), these plots illustrate comparable statistical characteristics of the $SNR0$ data. Apart from the SA*POS*®sites used for GPS data processing in this case study, additional stations with the same ARC are considered in order to obtain more reliable and representative SNR extremes.

(a) ARC3 (10 sites, 4.1×10^6 $SNR0$ samples) (b) ARC4 (3 sites, 1.2×10^6 $SNR0$ samples)
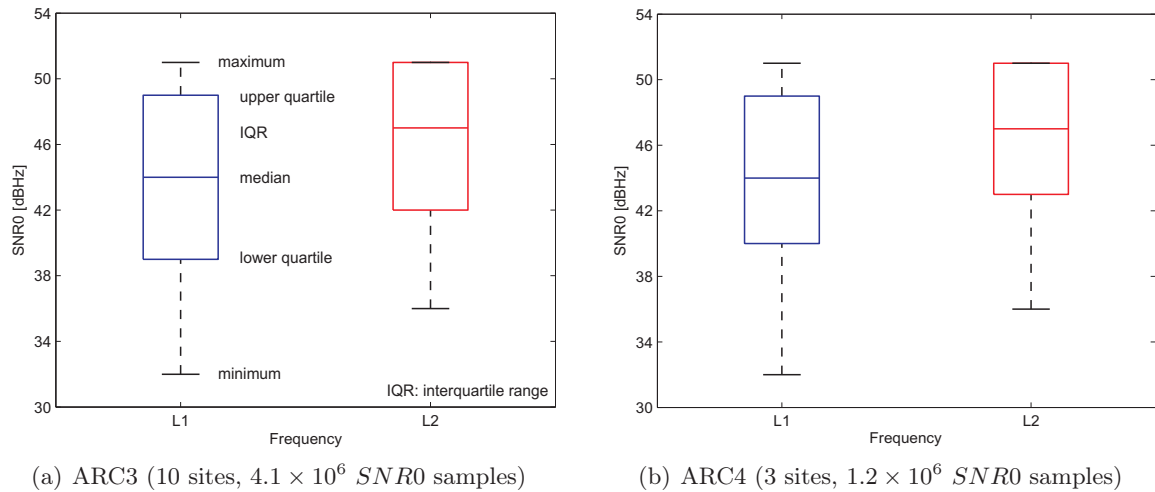
Figure 6.2: Box plots of the $SNR0$ values from the Leica ARC (DOY2004:186-193; see table 6.1)

After reliably determining the SNR extremes for each ARC, figure 6.3 compares the observation weights produced by the SNR-based EMPSNR2 and the elevation-dependent CSC2(BS), where the latter is implemented by default in the Bernese GPS Software 5.0 (Dach et al., 2007a, p. 177). For this comparison, two SA*POS*®sites, KARL (ARC1) and TAUB (ARC3), are chosen, which are located in the middle and northern parts of the investigation area, respectively, with the DWD meteorological stations KARL and WUER close by, respectively (see figure 4.1). The above-described SNR conversion, i.e., SNR [dB] $\rightarrow AMU \rightarrow SNR0$ [dBHz], is applied to the signal quality measurements from KARL, prior to computing observation weights using equation (5.12). Two representative days, 189 and 192, are considered, which are directly before and after the major rain event that occurred during days 190 and 191 (see figure 4.4(d)).

(a) L1 weights on day 189   (b) L2 weights on day 189   (c) L1 weights on day 192

(d) L1 weights on day 189   (e) L2 weights on day 189   (f) L1 weights on day 192
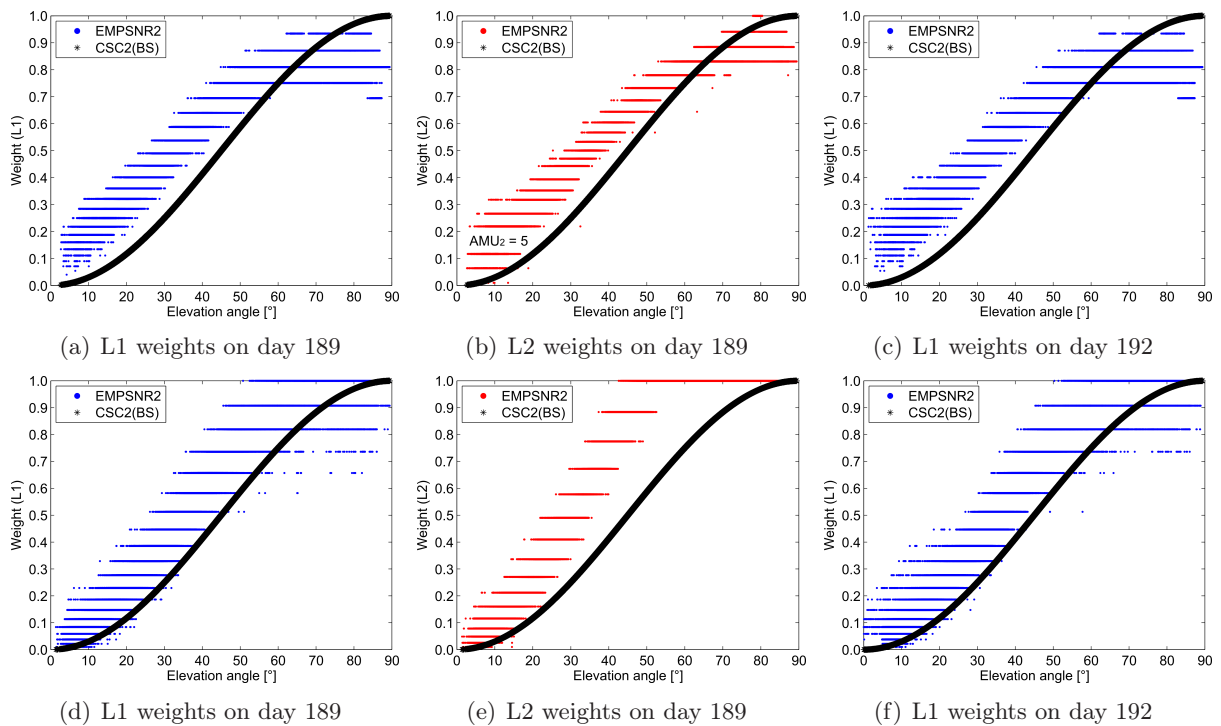
Figure 6.3: Comparison of the observation weights produced by CSC2(BS) and EMPSNR2 (upper plots: site KARL with ARC1, lower plots: site TAUB with ARC3; see tables 4.1 and 6.1)

Comparing the SNR-based weights on day 189, the ARC-dependent deviations between L1 and L2 are clearly visible. However, these differences are completely ignored when using the elevation-dependent weighting model. In general, EMPSNR2 produces higher weights than CSC2(BS) for elevation angles e of up to 70°. As e further increases, the SNR-based weights may decrease, demonstrating the fact that the best signal quality may not be necessarily achieved at the highest elevation angle. Based on the converted $SNR0$ (KARL with ARC1), the weight structure is comparable to that derived from the observed $SNR0$ (TAUB with ARC3), once again verifying the appropriateness of the applied SNR conversion. Nevertheless, the singularity occurring when converting SNR_2 into AMU_2, i.e., $AMU_2 = 5$ in equation (6.2), is obviously present in the resulting L2 weights with $SNR0 = 41$ dBHz and $w = 0.17$ (see figures 6.1(a) and 6.3(b)). Moreover, the weights shown in figure 6.3(e) exhibit similar patterns to those displayed in figure 5.5(d), which are obtained using the analytical model ANLSNR (see equation (5.10)). This can be understood by examining the associated weights illustrated in figure 5.9 for $SNR0$ between 35 and 55 dBHz. Compared to day 189, the L1 weights on day 192 are slightly nosier for $e < 30°$. This indicates that EMPSNR2 copes with variable atmospheric conditions and enables a realistic quality assessment of low-elevation observations. This advantage can be exploited when including low-elevation data to overcome poor satellite geometry, and to decorrelate station height and troposphere parameter estimates (Dach et al., 2007a, p. 247).
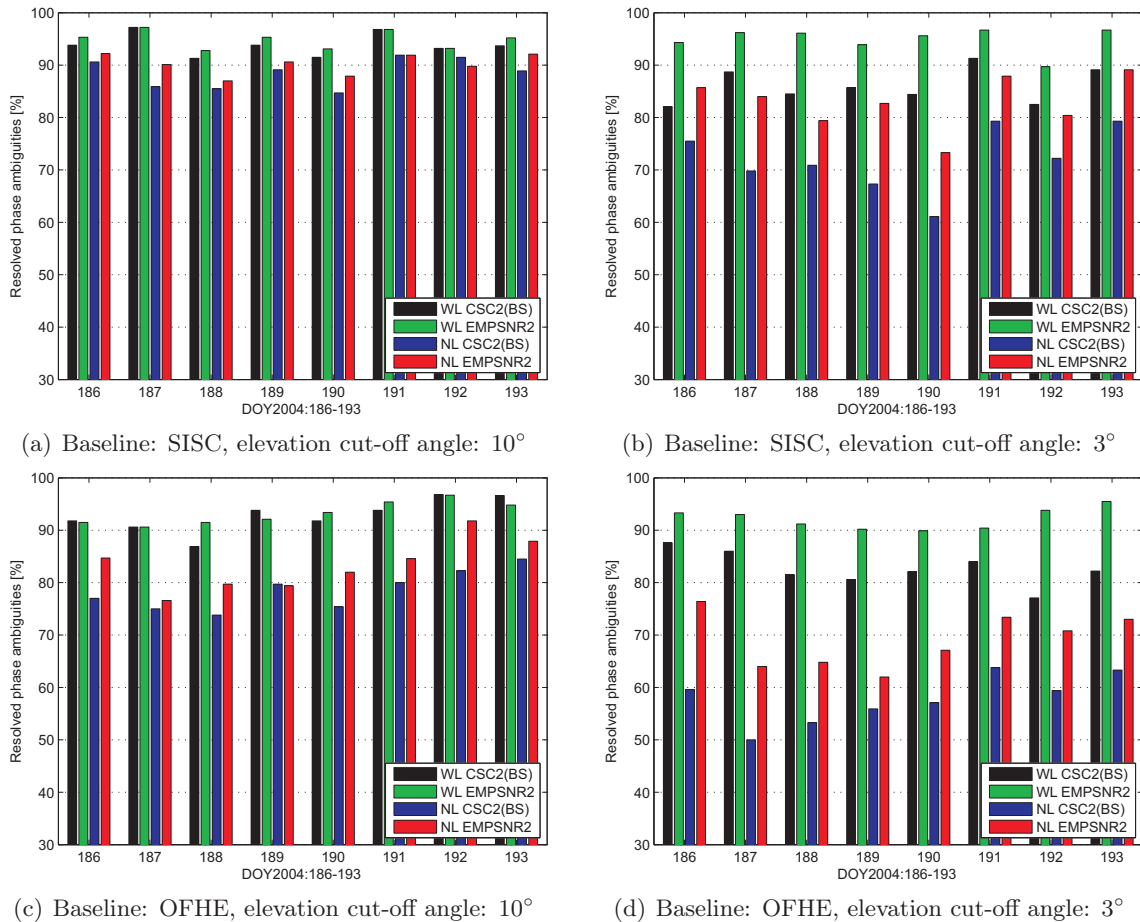
Since in this case study the information about antenna radomes is not available in the RINEX observation files, radome types are not considered in the ARC specification. Moreover, the receiver firmware version is also not taken into account, while an a posteriori check of the related station log files does not find any receiver firmware update during the investigation period of this case study. In terms of future research, model refinements within these contexts should be carried out, for example, by checking station log files and RINEX header information.

6.1.2 Effects on ambiguity resolution

Using the `SIGMA`-dependent algorithm of the Bernese GPS Software 5.0 to resolve phase ambiguities, the success rate is directly related to the a posteriori errors of the float ambiguity estimates, resulting from the initial least-squares (LS) adjustment (Dach et al., 2007a, p. 175). Since not only the parameter estimates, but also the associated accuracy measures can be improved by an advanced stochastic model, EMPSNR2 is supposed to perform better than CSC2(BS) in ambiguity resolution. Considering site multipath effects and elevation cut-off angle, figure 6.4 compares the percentage of resolved ambiguities with respect to observation weighting.

Due to the significantly larger wide-lane (WL) cycle of about 86 cm than the narrow-lane (NL) cycle of about 11 cm (see section 3.1.5), more WL ambiguities are resolved within the LC5 solutions than NL ambiguities within the LC3 evaluations. This becomes more evident as the elevation cut-off angle decreases (cf. figures 6.4(a) and (b)), and the impact of site multipath increases (cf. figures 6.4(a) and (c)). For a minimum elevation angle of 10°, the employment of EMPSNR2 only insignificantly (slightly) improves the results of WL (NL) ambiguity resolution (see figures 6.4(a) and (c)). However, for a minimum elevation angle of 3°, about 10% of the WL and NL ambiguities can be additionally resolved, if the elevation-dependent weighting model CSC2(BS) is replaced by the SNR-based EMPSNR2 (see figures 6.4(b) and (d)). As the elevation cut-off angle decreases from 10° to 3°, the daily number of ambiguities increases from about 64 to 98. This is because low-elevation GPS data are frequently contaminated by unrepairable cycle slips, such that an introduction of multiple ambiguities is necessary. Regarding the day-to-day variations in the results of NL ambiguity resolution, lower percentages of resolved ambiguities are detected on days 188 and 190, corresponding to the time periods with high precipitation (RF) measurements at the DWD meteorological sites (see figure 4.4(d)).

(a) Baseline: SISC, elevation cut-off angle: $10°$

(b) Baseline: SISC, elevation cut-off angle: $3°$

(c) Baseline: OFHE, elevation cut-off angle: $10°$

(d) Baseline: OFHE, elevation cut-off angle: $3°$

Figure 6.4: Representative examples of the results of ambiguity resolution using CSC2(BS) and EMP-SNR2 (SISC: 119.4 km, weak multipath, OFHE: 114.8 km, strong multipath; see table 4.3)

For a minimum elevation angle of $3°$, table 6.2 provides the complete results of ambiguity resolution obtained by means of different observation weighting models. Applying CSC2(BS) and EMPSNR2 to the same data set, the daily numbers of ambiguities (#AMB) are sometimes slightly different, with a maximum difference of 6 (KAST, day 190). This originates from the processing step "screening post-fit residuals" (see figure 4.2 and table 4.4). By considering all baselines, the conclusions drawn from figure 6.4 can be verified numerically. Using the SNR-based observation weighting scheme, the results of WL and NL ambiguity resolution can be enhanced by up to 16.7% (OFHE, day 192) and 23.9% (KAST, day 191), respectively. Moreover, the improvement in resolving the WL ambiguities appears to be more significant for longer baselines (cf., e.g., HLTA and SISC). On average, for GPS baseline solutions at a regional scale, an enhancement of about 10% in both WL and NL ambiguity resolution can be expected when employing EMPSNR2 instead of CSC2(BS). Considering the influence of variable atmospheric conditions, lower success rates of NL ambiguity resolution are observed on day 190 for HLTA, KAST, and SISC, as well as on days 188 and 190 for OFHE, showing an excellent agreement with the DWD *RF* measurements illustrated in figure 4.4(d). This demonstrates the contribution of such freely available surface meteorological data to a physical interpretation of GPS processing results, even though they do not have high temporal and spatial resolution. For an elevation cut-off angle of $10°$, the complete results of ambiguity resolution are presented in table D.1. The improvements achieved by applying EMPSNR2 are significantly smaller, being below 5% on average. Nevertheless, for the baselines KAST and OFHE, which are strongly affected by multipath effects, considerable increases in the NL ambiguity resolution of 8.1% and 9.5% are detected on days 186 and 192, respectively.

Table 6.2: Effects of applying different observation weighting models on the results of phase ambiguity resolution in case study 1 (elevation cut-off angle: 3°)

Weighting model	CSC2(BS) Number/Percent			EMPSNR2 Number/Percent			Improvement Percent	
HLTA	#AMB	WL	NL	#AMB	WL	NL	WL	NL
186	85	83/97.6	64/75.3	85	83/97.6	75/88.2	0.0	12.9
187	97	94/96.9	59/60.8	96	93/96.9	74/77.1	0.0	16.3
188	94	91/96.8	60/63.8	94	92/97.9	68/72.3	1.1	8.5
189	86	81/94.2	51/59.3	84	81/96.4	66/78.6	2.2	19.3
190	92	84/91.3	**50/54.3**	89	86/96.6	**57/64.0**	5.3	9.7
191	100	98/98.0	68/68.0	100	98/98.0	85/85.0	0.0	17.0
192	99	96/97.0	59/59.6	99	97/98.0	82/82.8	1.0	23.2
193	94	92/97.9	62/66.0	94	92/97.9	78/83.0	0.0	17.0
Total	747	719/96.3	473/63.3	741	722/97.4	585/78.9	1.1	15.6
KAST	#AMB	WL	NL	#AMB	WL	NL	WL	NL
186	106	100/94.3	68/64.2	105	100/95.2	81/77.1	0.9	12.9
187	106	102/96.2	68/64.2	103	96/93.2	80/77.7	−3.0	13.5
188	99	96/97.0	65/65.7	99	95/96.0	80/80.8	−1.0	15.1
189	118	114/96.6	74/62.7	116	108/93.1	90/77.6	−3.5	14.9
190	**119**	114/95.8	**66/55.5**	**113**	107/94.7	**74/65.5**	−1.1	10.0
191	109	107/98.2	71/65.1	109	107/98.2	97/89.0	0.0	**23.9**
192	109	107/98.2	67/61.5	107	103/96.3	89/83.2	−1.9	21.7
193	107	104/97.2	71/66.4	106	103/97.2	93/87.7	0.0	21.3
Total	873	844/96.7	550/63.0	858	819/95.5	684/79.7	−1.2	**16.7**
SISC	#AMB	WL	NL	#AMB	WL	NL	WL	NL
186	106	87/82.1	80/75.5	105	99/94.3	90/85.7	12.2	10.2
187	106	94/88.7	74/69.8	106	102/96.2	89/84.0	7.5	14.2
188	103	87/84.5	73/70.9	102	98/96.1	81/79.4	11.6	8.5
189	98	84/85.7	66/67.3	98	92/93.9	81/82.7	8.2	15.4
190	90	76/84.4	**55/61.1**	90	86/95.6	**66/73.3**	11.2	12.2
191	92	84/91.3	73/79.3	91	88/96.7	80/87.9	5.4	8.6
192	97	80/82.5	70/72.2	97	87/89.7	78/80.4	7.2	8.2
193	92	82/89.1	73/79.3	92	89/96.7	82/89.1	7.6	9.8
Total	784	674/86.0	564/71.9	781	741/94.9	647/82.8	**8.9**	**10.9**
OFHE	#AMB	WL	NL	#AMB	WL	NL	WL	NL
186	89	78/87.6	53/59.6	89	83/93.3	68/76.4	5.7	16.8
187	100	86/86.0	50/50.0	100	93/93.0	64/64.0	7.0	14.0
188	92	75/81.5	**49/53.3**	91	83/91.2	**59/64.8**	9.7	11.5
189	93	75/80.6	52/55.9	92	83/90.2	57/62.0	9.6	6.1
190	84	69/82.1	**48/57.1**	79	71/89.9	**53/67.1**	7.8	10.0
191	94	79/84.0	60/63.8	94	85/90.4	69/73.4	6.4	9.6
192	96	74/77.1	57/59.4	96	90/93.8	68/70.8	**16.7**	11.4
193	90	74/82.2	57/63.3	89	85/95.5	65/73.0	13.3	9.7
Total	738	610/82.7	426/57.7	730	673/92.2	503/68.9	**9.5**	**11.2**

6.1.3 Effects on troposphere parameters

The use of low-elevation (i.e., $e < 10°$) GPS data with appropriate weights may improve the performance of site-specific troposphere parameter (TRP) estimation. This plays an important role in characterising the state of the Earth's neutral atmosphere, for example, GPS water vapour monitoring is currently one of the operational techniques in GPS meteorology. To demonstrate the influence of the SNR-based weighting model EMPSNR2 on TRP evaluation, figure 6.5 compares the parameter estimates and the associated standard deviations (STD), obtained by analysing the two longer baselines SISC and OFHE with similar lengths but different multipath impact. Thereby, different elevation cut-off angles of 10° and 3° are considered.
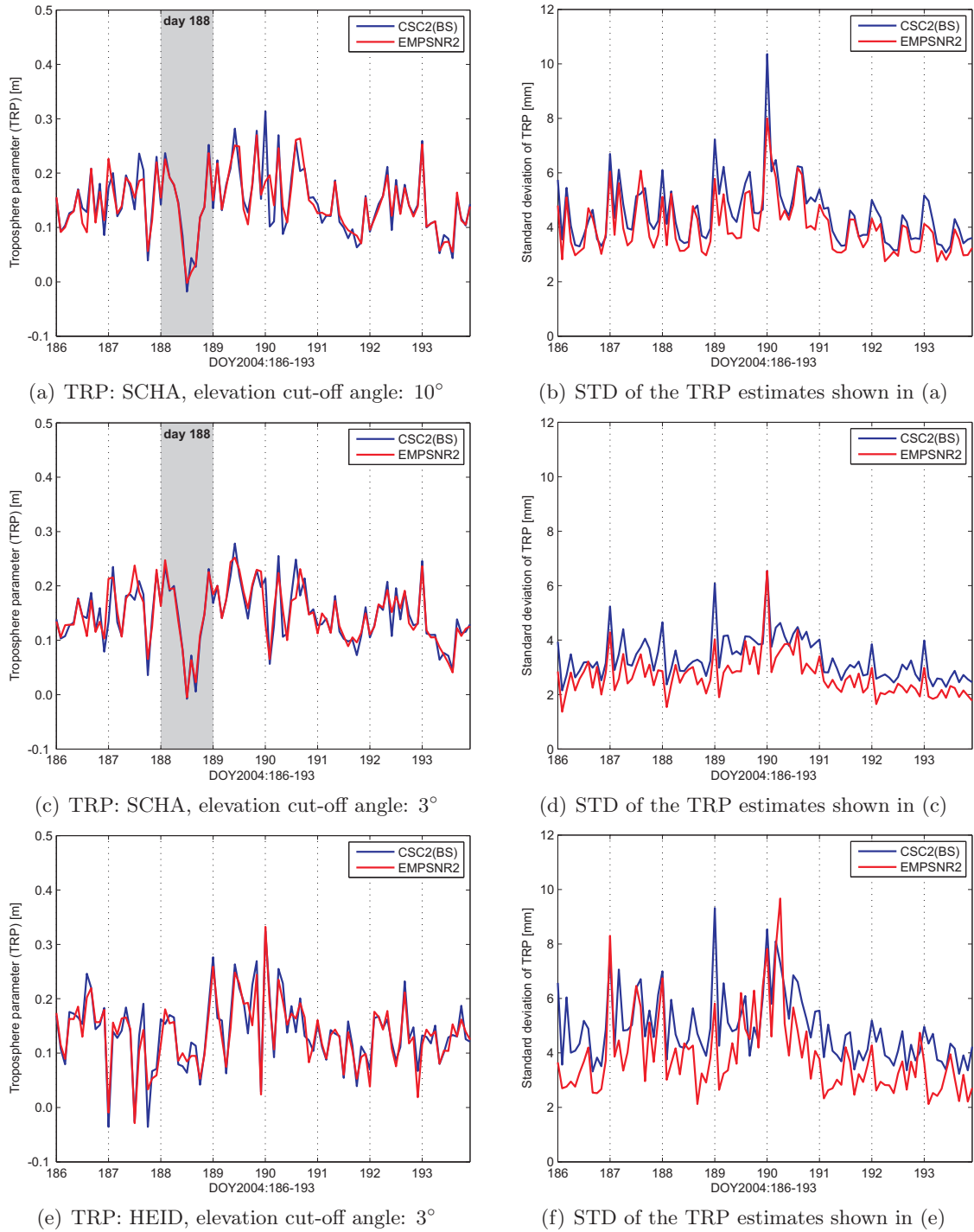
Prior to comparing the TRP estimates, the site-specific constant a priori model values (Dach et al., 2007a, p. 244, 533), for example, computed using the dry Saastamoinen model (Saastamoinen, 1973) in combination with the dry Niell mapping function (Niell, 1996), are removed. Therefore, each visualised TRP contains not only the zenith wet delay, but also the deviation of the a priori model from the reality. Specifying a time span of 2 h for GPS daily solutions (see table 4.4), a total of $12 + 1 = 13$ parameters per day per station are estimated due to the piece-wise linear parameterisation of TRP in the Bernese GPS Software 5.0 (Dach et al., 2007a, p. 246). Since the thirteenth parameter on the current day and the first parameter on the next day refer to the same time point and possess a similar precision, only the first 12 parameters resulting from a one-day session are plotted. While ΔTRP_a (ΔTRP_r) denotes the median absolute (relative) difference between the TRP obtained using EMPSNR2 and CSC2(BS), ΔSTD_a (ΔSTD_r) is the median absolute (relative) improvement in the associated standard deviations:

$$\Delta\text{TRP}_r\,[\%] = \frac{\Delta\text{TRP}_a}{\text{med}\left(\text{TRP}_{\text{CSC2(BS)},i}\right)} = \frac{\text{med}\left(\left|\text{TRP}_{\text{CSC2(BS)},i} - \text{TRP}_{\text{EMPSNR2},i}\right|\right)}{\text{med}\left(\text{TRP}_{\text{CSC2(BS)},i}\right)}, \quad (6.3)$$

$$\Delta\text{STD}_r\,[\%] = \frac{\Delta\text{STD}_a}{\text{med}\left(\text{STD}_{\text{CSC2(BS)},i}\right)} = \frac{\text{med}\left(\text{STD}_{\text{CSC2(BS)},i} - \text{STD}_{\text{EMPSNR2},i}\right)}{\text{med}\left(\text{STD}_{\text{CSC2(BS)},i}\right)}, \quad (6.4)$$

where $\text{med}(\cdot)$ denotes the median operator, and i indicates the TRP index varying from 1 to $12 \times 8\ (\text{days}) = 96$. Regarding the TRP estimates for the site SCHA, the median absolute difference ΔTRP_a amounts to about 1 cm for both elevation cut-off angles, leading to a relative difference ΔTRP_r of more than 5% (see figures 6.5(a) and (c)). The employment of EMPSNR2 significantly improves the standard deviations of TRP, resulting in ΔSTD_r of 10.6% and 19.5% for minimum elevation angles of 10° and 3°, respectively (see figures 6.5(b) and (d)). As the elevation cut-off angle decreases from 10° to 3°, the median TRP standard deviation decreases by 1.2 mm, which is mainly due to the increased data volume and redundancy by including low-elevation observations. In comparison to the SCHA-related TRP estimates, the HEID-related ones shown in figure 6.5(e) exhibit a larger parameter change of $\Delta\text{TRP}_a = 1.4$ cm, corresponding to a ΔTRP_r of about 10%. Furthermore, the use of EMPSNR2 produces a more significant quality enhancement of $\Delta\text{STD}_r = 21.7\%$ (see figure 6.5(f)). Considering the similar baseline lengths of SISC (119.4 km) and OFHE (114.8 km), a comparison between figures 6.5(d) and (f) reflects the impact of strong multipath effects on the quality of the TRP estimates.

As can be seen in figures 6.5(a) and (c), the SCHA-related TRP values depict a significant decrease on day 188. To explain this, figure 6.6 illustrates the TRP estimates together with the freely available water vapour pressure data from the DWD stations WUER and STUT, which are located relatively close to the SA*POS*®site SCHA (see figure 4.1). After applying a simple moving average filter, figure 6.6(a) visualises the smoothed TRP, which maintain the long-periodic variation pattern of the original 2-hour estimates, and appear to be more suitable

(a) TRP: SCHA, elevation cut-off angle: 10°

(b) STD of the TRP estimates shown in (a)

(c) TRP: SCHA, elevation cut-off angle: 3°

(d) STD of the TRP estimates shown in (c)

(e) TRP: HEID, elevation cut-off angle: 3°

(f) STD of the TRP estimates shown in (e)

Figure 6.5: Representative examples of the results of TRP estimation using CSC2(BS) and EMPSNR2 (SISC: 119.4 km, weak multipath, OFHE: 114.8 km, strong multipath; see table 4.3)

for a comparison with the DWD meteorological data at a lower temporal resolution of 6 h. Note that the DWD water vapour pressure data are not observations but quantities computed based on surface temperature (T) and humidity (RH) measurements (Mayer, 2006, sect. 8.3.2). As figure 6.6(b) shows, the smoothed TRP values are obviously positively correlated with the water vapour pressure data from both meteorological sites, particularly on day 188. The disagreement occurring on day 190 is probably due to an overestimation of the dry delay term using the a priori Saastamoinen model, since on this day the air pressure reaches its minimum (see figure 4.4(a)), while the water vapour pressure achieves its maximum.

(a) TRP: SCHA, elevation cut-off angle: 3°

(b) Comparison with DWD water vapour pressure
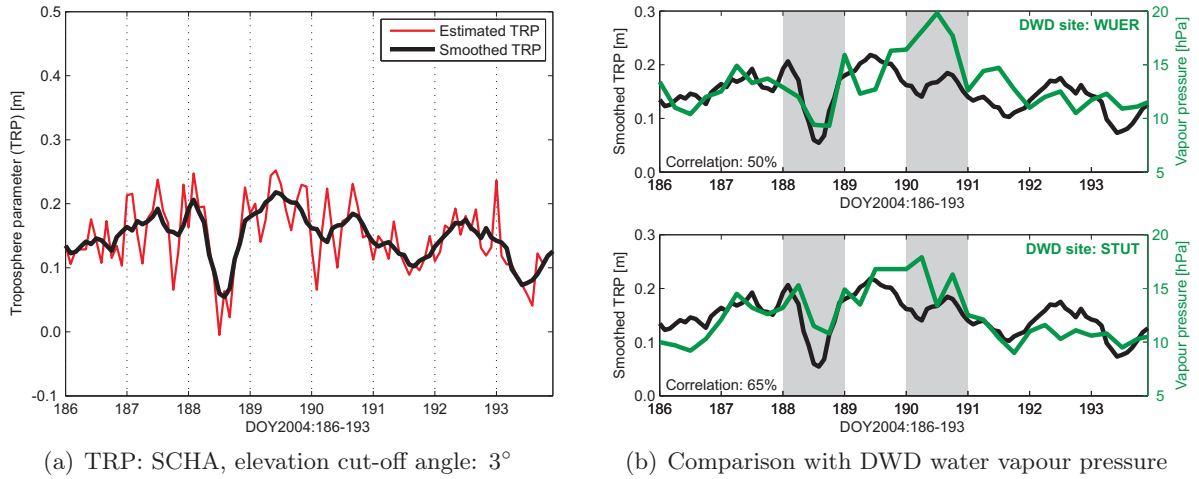
Figure 6.6: Physical interpretation of the SCHA-related TRP estimates using the freely available DWD surface water vapour pressure data (SISC: 119.4 km, weak multipath, observation weighting model: EMPSNR2; see figure 6.5(c))

Considering all analysed baselines and different elevation cut-off angles of 10° and 3°, table 6.3 provides the median absolute and relative differences, $\Delta \text{TRP}_{a/r}$ and $\Delta \text{STD}_{a/r}$, defined by equations (6.3) and (6.4), respectively. On average, the application of different observation weighting models, i.e., CSC2(BS) and EMPSNR2, results in absolute TRP deviations of up to 2.7 cm, reaching approximately 20% of the parameter estimate. Compared to the elevation-dependent CSC2(BS), the use of the SNR-based EMPSNR2 enhances the TRP precision as much as 1.4 mm absolutely and 21.7% relatively. Similar magnitudes of improvements, achieved by means of advanced stochastic models, were also reported by Jin and Park (2005) and Jin et al. (2010). Decreasing the elevation cut-off angle from 10° to 3°, the numerator of equation (6.4) ΔSTD_a increases (see table 6.3), and the denominator decreases because of the increased data volume and redundancy (cf. figures 6.5(b) and (d)). These two factors lead to rapidly increased ΔSTD_r from about 13% to 20%. Within the context of TRP estimation, more significant effects of EMPSNR2 are also observed for baselines with strong multipath impact (e.g., KAST, OFHE). Changes in TRP estimates at the centimetre level and improvements in TRP precision at the millimetre level are already significant for GNSS-based determination of atmospheric water vapour fields (Bender et al., 2008; Fuhrmann et al., 2010, sect. 8.3).

Table 6.3: Effects of using different observation weighting models on the results of the TRP estimation in case study 1 ($\Delta \text{TRP}_{a/r}$ [cm/%], $\Delta \text{STD}_{a/r}$ [mm/%]; see equations (6.3) and (6.4))

Baseline [km]	Multipath impact	Station ID	Elevation cut-off angle: 10°		Elevation cut-off angle: 3°	
			$\Delta \text{TRP}_{a/r}$	$\Delta \text{STD}_{a/r}$	$\Delta \text{TRP}_{a/r}$	$\Delta \text{STD}_{a/r}$
HLTA	weak	HLBR	1.4/11.6	1.0/12.0	1.8/13.0	1.2/20.6
63.2		TAUB	1.5/12.8	1.0/12.5	1.7/14.0	1.2/20.5
KAST	strong	KARL	**2.7/19.0**	1.3/14.3	**2.6/16.4**	**1.4**/17.4
61.4		STUT	2.7/18.8	**1.3**/14.4	2.4/14.8	1.4/16.9
SISC	weak	SIGM	0.7/4.6	0.5/10.4	0.8/5.4	0.6/19.7
119.4		SCHA	0.7/5.0	0.5/10.6	0.9/6.4	0.6/19.5
OFHE	strong	OFFE	1.4/9.7	0.9/14.5	1.3/9.6	1.0/21.7
114.8		HEID	1.4/10.3	0.9/**14.7**	1.4/9.9	1.0/**21.7**
Mean	−	−	**1.6/11.5**	**0.9/12.9**	**1.6/11.2**	**1.1/19.8**

6.1.4 Effects on coordinate estimates

After significant improvements in ambiguity resolution and TRP estimation have been detected, the effects of EMPSNR2 on site coordinate determination are initially investigated based on the median absolute coordinate difference, which is defined as

$$\Delta \text{CRD}_a \, [\text{mm}] = \text{med} \left(\left| \text{CRD}_{\text{CSC2(BS)},i} - \text{CRD}_{\text{EMPSNR2},i} \right| \right), \qquad (6.5)$$

where CRD represents a generic notation for the topocentric coordinates northing (N), easting (E), and height (H). The index i varies from 1 to 8 (days), since a daily solution results in one set of station coordinates (N, E, H). For different elevation cut-off angles of $10°$ and $3°$, table 6.4 provides ΔCRD_a only for the rover site of each processed baseline (see table 4.3), as the reference site is kept fixed to its a priori coordinates. It can be seen that the median absolute coordinate differences induced by applying different observation weighting models are below 1 mm in the horizontal components N and E, but can reach up to about 5 mm in the vertical component H. Furthermore, larger ΔCRD_a are found in the coordinate estimates of TAUB, STUT, and HEID, which coincides fairly well with the results of the TRP estimation presented in table 6.3. This indicates the well-known correlation between TRP and station height estimates on the one hand, and verifies the higher degree of effectiveness of EMPSNR2 in a strong multipath environment on the other. Using different stochastic models to analyse long-term GPS observations collected for more than 12 h, Jin et al. (2010) also found differences in baseline components of up to 3 mm, particularly in the height component.

Table 6.4: Effects of applying different observation weighting models on site coordinate estimates in case study 1 (unit: mm; see equation (6.5))

| Analysed baseline	Length [km]	Multipath impact	Station ID	Cut-off angle: $10°$			Cut-off angle: $3°$		
				ΔN_a	ΔE_a	ΔH_a	ΔN_a	ΔE_a	ΔH_a
HLTA	63.2	weak	TAUB	0.4	0.1	**3.1**	0.4	0.2	**4.1**
KAST	61.4	strong	STUT	0.4	0.9	**1.6**	0.3	0.5	**1.3**
SISC	119.4	weak	SCHA	0.2	0.1	0.9	0.2	0.1	0.5
OFHE	114.8	strong	HEID	0.3	0.2	**1.8**	0.5	0.2	**1.5**

In addition to examining the absolute coordinate differences, the repeatability of daily coordinate estimates is also analysed to evaluate the performance of the proposed SNR-based weighting model in long-term relative positioning. Considering different elevation cut-off angles and observation weighting models, table 6.5 provides the coordinate root mean square deviations (RMSD) of the northing, easting, and height components in a local topocentric system. Regarding the magnitudes of the RMSD at first, the maximum is below 2 mm for the horizontal components and 4 mm for the vertical. The small RMSD values demonstrate not only the high performance of the Bernese GPS Software 5.0, but also the appropriateness of the applied GPS data processing strategies. For both minimum elevation angles, increased multipath impact leads to larger RMSD, which is clearly visible in the horizontal components (cf., e.g., SISC and OFHE), and indicates a decreased stability in the daily coordinate estimates. For the majority of cases, decreasing the elevation cut-off angle from $10°$ to $3°$ affects the height repeatability in a positive manner. This arises from the proper use of low-elevation observations, which improve the satellite geometry and decorrelate the station height and TRP estimates. Such a systematic behaviour of the vertical RMSD depending on the minimum satellite elevation angle was also detected by Luo and Mayer (2008) in a preliminary investigation for automatic near real-time monitoring of the GPS permanent site at the Black Forest Observatory (BFO).

Table 6.5: Effects of applying different observation weighting models on site coordinate root mean square deviations (RMSD) in case study 1 (unit: mm)

Elevation cut-off angle: 10°				CSC2(BS)			EMPSNR2		
Baseline	**Length** [km]	**Multipath**	**Station**	N	E	H	N	E	H
HLTA	63.2	weak	TAUB	0.9	0.6	1.1	0.9	0.9	1.8
KAST	61.4	strong	STUT	1.4	1.1	**3.2**	1.5	1.3	**3.4**
SISC	119.4	weak	SCHA	0.8	0.7	**3.2**	0.6	0.6	**3.8**
OFHE	114.8	strong	HEID	1.3	**1.9**	**3.5**	1.5	1.8	**3.7**
Elevation cut-off angle: 3°				N	E	H	N	E	H
HLTA	63.2	weak	TAUB	1.1	0.7	2.0	1.4	0.8	2.3
KAST	61.4	strong	STUT	1.5	1.1	**2.3**	1.5	1.3	**3.7**
SISC	119.4	weak	SCHA	0.8	0.7	**3.0**	0.9	0.7	**3.2**
OFHE	114.8	strong	HEID	1.7	1.8	**3.1**	1.8	1.8	**3.5**

Comparing the coordinate RMSD with respect to observation weighting, EMPSNR2 exhibits insignificant advantages over CSC2(BS) in the horizontal components and a slight degradation in the vertical component, with a maximum of 1.4 mm (STUT, elevation cut-off angle: 3°). This can be explained by the following three facts. Firstly, although some selected sites, such as STUT and HEID, have relatively strong multipath effects, the SA*POS*®stations are on average high-quality continuously operating reference stations (CORS), which attenuates the degree of efficiency of EMPSNR2. Secondly, the use of highly redundant GPS data on a daily basis enhances the robustness of static coordinate estimates against adverse satellite geometry and low data quality. Finally, the deficiencies in tropospheric modelling cannot be simply compensated by an advanced stochastic model, and have a stronger impact when analysing long baselines and low-elevation data. To demonstrate the last named argument, examples of station height increments are shown in figure 6.7. For both observation weighting schemes, larger height variations are detected on days 188, 190, and 191 with high RH and RF measurements (see figures 4.4(c) and (d)). As expected, the SNR-based EMPSNR2 is more sensitive to variable atmospheric conditions than the elevation-dependent CSC2(BS). A comparison between figures 6.5(c) and 6.7(b) shows an obvious correlation between the TRP estimates and height increments.

(a) Site: STUT (baseline: KAST, 61.4 km)   (b) Site: SCHA (baseline: SISC, 119.4 km)
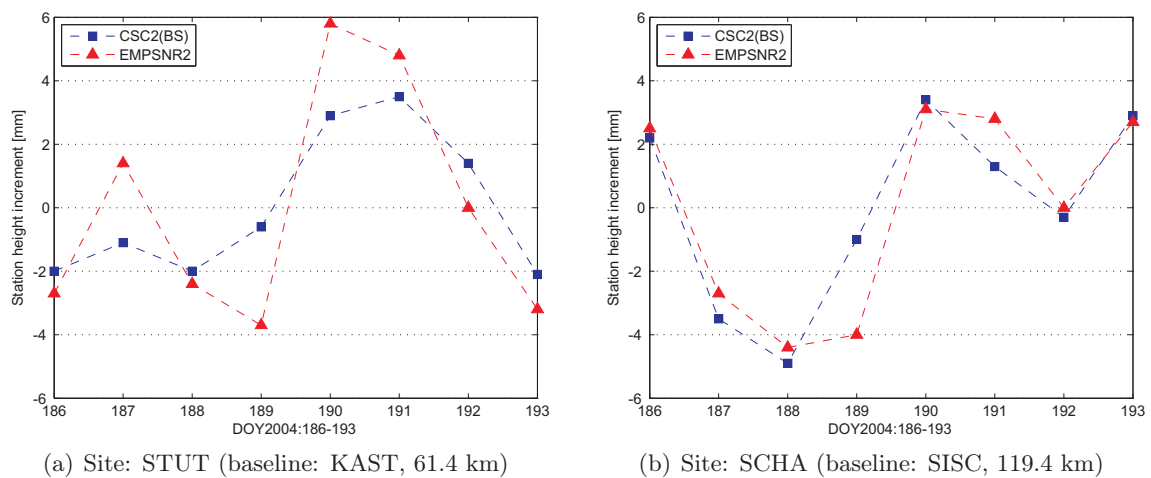
Figure 6.7: Representative examples of station height increments obtained by means of different observation weighting models (elevation cut-off angle: 3°)

In order to unveil the full impact of EMPSNR2 on site coordinate estimation, the aforementioned three facts must be taken into account when selecting and processing GPS data. In particular, the data analysis should be carried out using short-term (e.g., several hours) and low-quality observations collected under strong multipath environments. To ensure that the potential coordinate improvements are actually due to the application of EMPSNR2, the tropospheric models should remain the same as in the case study of long-term relative positioning. Nevertheless, more sophisticated modelling of GPS tropospheric delays, for example, by incorporating high-resolution meteorological data and by means of advanced mapping functions, such as GMF and VMF1, is indispensable for accurate and reliable coordinate determination.

6.2 Case study 2: short-term relative positioning

The main objective of this case study is to investigate the influence of the suggested SNR-based weighting model on site coordinate determination using short-term GPS observations. Nonetheless, to verify the improvements achieved in case study 1, additional aspects such as ambiguity resolution and TRP estimation are also considered. According to the finding from case study 1 that the effects of EMPSNR2 on parameter estimation become more obvious as the elevation cut-off angle decreases, the GPS data analysis in this case study is carried out with a minimum elevation angle of 3° and without screening post-fit residuals in order to achieve a higher degree of model efficiency (see table 4.5).

6.2.1 SNR extremes and observation weights

Based on the information about signal quality measures provided by Landau (2006b), all Trimble receivers applied in this case study deliver $SNR0$ values in dBHz directly, so that no SNR conversion is necessary. Furthermore, the RINEX observation files contain antenna radome types that must be taken into account in the specification of the antenna-receiver combination (ARC). Although only 3-hour GPS data are processed for each of the 21 consecutive days (DOY2007:161-181; see section 4.2.3), all available SNR measurements are used to find representative extremes for reliable weight computation. Table 6.6 provides the detected SNR extremes on L1 and L2 for different ARC. The Leica instruments deliver the same minimum and maximum as found in case study 1 (see table 6.1), while the $SNR0$ data from the Trimble equipment exhibit larger ranges, especially on L2 (e.g., ARCII). By examining the corresponding box plots, these boundary values are analysed for extreme outliers, defined as $SNR0$ outside the $3 \cdot \text{IQR}$ of the lower and upper quartiles (IQR: interquartile range; see figure 5.1(b)). For a sample data set from a normal distribution with $\mathcal{N}(\mu, \sigma^2)$, the 3-IQR limit corresponds approximately to $\mu \pm 5\sigma$ (Falk et al., 2002, p. 29). The results showed that the found SNR extremes given in table 6.6 are non-outliers and can be substituted into equation (5.12) to calculate the SNR-based observation weights.

Table 6.6: Antenna-receiver-specific SNR extremes used for computing the SNR-based observation weights in case study 2 ($SNR0$ in dBHz)

| ARC	Antenna	Receiver	Radome	Min/Max (L1)	Min/Max (L2)
I	TRM55971	Trimble NetR5	TZGD	22/56	10/47
II	TRM29659	Trimble 4700	TCWD	25/56	**8/52**
III	LEIAT503	Leica SR520	LEIC	32/51	36/51
IV	LEIAT303	Leica SR520	LEIC	32/51	36/51

For the selected 3-hour processing time interval, i.e., 15-18 h in GPS time (see figure 4.5), figure 6.8 compares the observation weights produced by CSC2(BS) and EMPSNR2 under different aspects. While the elevation-dependent weights exhibit a uniform behaviour, the SNR-based ones illustrate obvious variations with respect to carrier frequency, antenna-receiver combination, site-specific multipath impact, and near-ground atmospheric conditions. Furthermore, for low- and medium-elevation observations, EMPSNR2 generally provides higher weights than CSC2(BS).

Regarding the individual plots of figure 6.8, the SNR-based weights shown in figure 6.8(a) illustrate the typical characteristics of the analysed Leica ARC (see figures 6.3(d) and (e)). In spite of a relatively short observation period of 3 h, the BIBE-related $SNR0$ values cover the full ranges of [32, 51] and [36, 51] for L1 and L2, respectively, defined by the associated global extremes (see ARCIII in table 6.6). Considering the same day but another ARC, for instance, ARCII, figure 6.8(b) depicts obviously different variation patterns of the SNR-based weights, especially on L2. Substituting the L1 local minimum $SNR0_1 = 29$ dBHz and the L2 local maximum $SNR0_2 = 48$ dBHz into equation (5.12), along with the corresponding global SNR extremes given in table 6.6, the resulting minimum L1 and maximum L2 weights are equal to 0.05 and 0.85, respectively. In figure 6.8(c), the SNR-based weights are shown for the site DARM, which is strongly affected by multipath effects (see figure 4.6(c)). The weight values exhibit larger variation ranges and a decreasing tendency for L1 observations at elevation angles above 60°. For the same site DARM and day 166, on which high relative humidity (RH) and precipitation (RF) are registered at the DWD meteorological sites (see figures 4.8(c) and (d)), figure 6.8(d) depicts significant variations in the SNR-based weights. This emphasises the necessity of such a realistic observation weighting model in the presence of strong multipath effects, particularly under variable atmospheric conditions. In this case, changes in site environment, for example, surface moisture content, may considerably affect site-specific multipath characteristics, leading to substantial variations in GPS observation quality.

The larger the differences between the weights produced by CSC2(BS) and EMPSNR2, the more significant the effects on GPS parameter estimation. In comparison to CSC2(BS), the impacts of EMPSNR2 on ambiguity resolution, TRP estimation, and coordinate determination are analysed in the following sections. Thereby, special attention is paid to the evaluation of site coordinates, which is strongly related to the results of ambiguity resolution and TRP estimation.

6.2.2 Effects on ambiguity resolution

In this case study, the phase ambiguities are resolved using the same algorithm that was employed in case study 1 (i.e., `SIGMA`-dependent strategy, LC5, LC3; see table 4.5). To demonstrate the advantages of EMPSNR2 over CSC2(BS) in ambiguity resolution, figure 6.9 compares the percentages of the resolved wide-lane (WL) and narrow-lane (NL) ambiguities with respect to baseline length and multipath impact. As figure 6.9(a) shows, for the shortest baseline AFLO (32.4 km), very slight improvements in WL ambiguity resolution are visible, while the application of EMPSNR2 increases the percentages of the resolved NL ambiguities by up to 18.5% (day 172). The effect of this significant enhancement on coordinate estimation will be discussed in section 6.2.4. Regarding the longest baseline RATA (203.4 km), the results of WL and NL ambiguity resolution are improved by an average of about 5% and 9%, respectively, when utilising EMPSNR2 instead of CSC2(BS). A comparison between figures 6.9(a) and (b) indicates that the performance of ambiguity resolution degrades with increasing baseline length, which is particularly obvious when comparing the results of the NL ambiguity resolution. Moreover, it is interesting to note that the days on which fewer NL ambiguities are resolved, i.e., 163, 164, 169, and 173, correspond to the days with high precipitation (RF) measurements at the DWD sites KEMP and WUER, being located near the baseline-forming SA*POS*®stations RAVE and
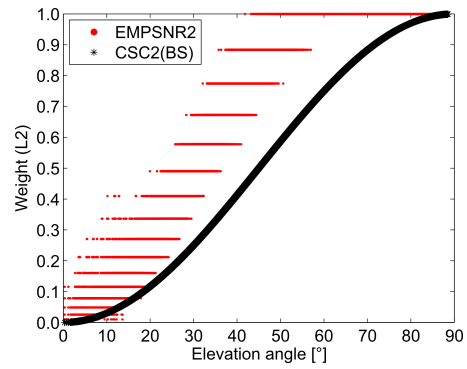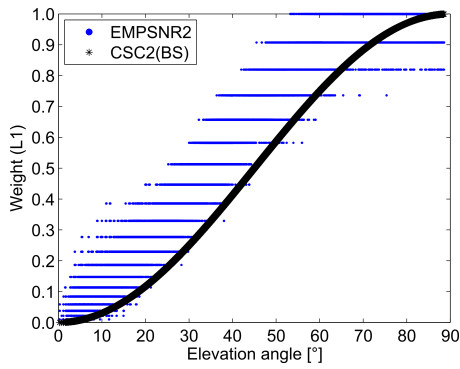
(a) Site BIBE, weak MP, ARCIII, day 165, $SNR0_{1/2}^{\min} = 32/36$ dBHz, $SNR0_{1/2}^{\max} = 51/51$ dBHz
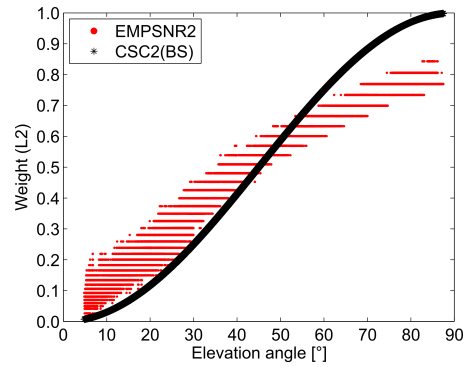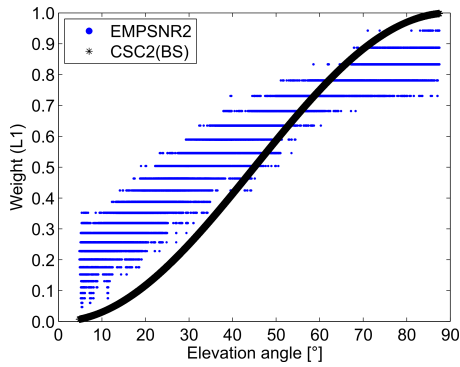
(b) Site AFBG, weak MP, ARCII, day 165, $SNR0_{1/2}^{\min} = 29/8$ dBHz, $SNR0_{1/2}^{\max} = 55/48$ dBHz
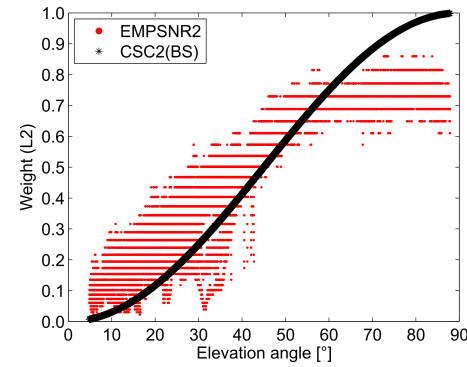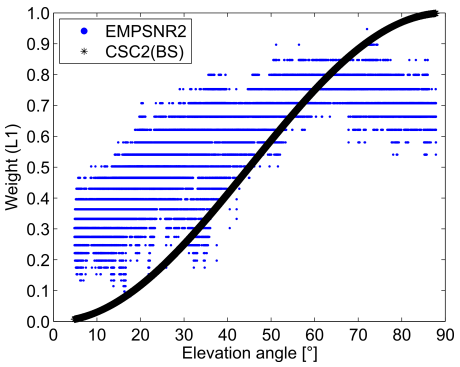
(c) Site DARM, strong MP, ARCI, day 165, $SNR0_{1/2}^{\min} = 29/12$ dBHz, $SNR0_{1/2}^{\max} = 55/44$ dBHz
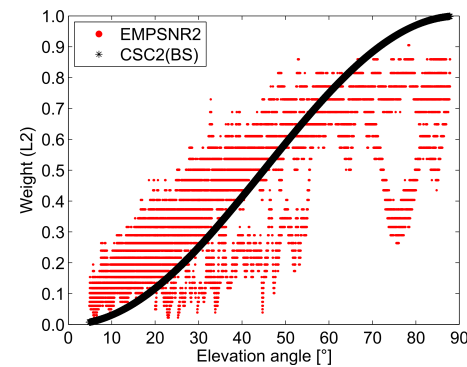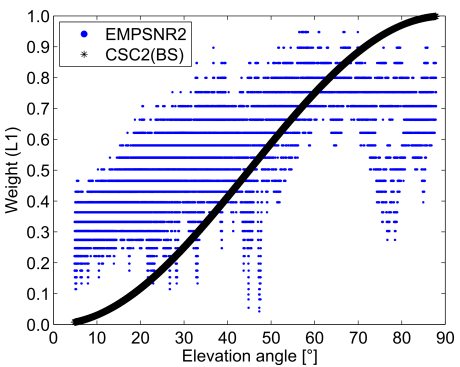
(d) Site DARM, strong MP, ARCI, day 166, $SNR0_{1/2}^{\min} = 26/12$ dBHz, $SNR0_{1/2}^{\max} = 55/45$ dBHz

Figure 6.8: Comparison of the observation weights produced by CSC2(BS) and EMPSNR2 for short-term (3 h) and high-frequency (1 Hz) GPS measurements (MP: multipath; see table 4.1 for site characteristics and table 6.6 for global SNR extremes)

TAUB, respectively (see figures 4.1 and 4.8(d)). Such day-to-day variations in the success rates of NL ambiguity resolution were also observed in case study 1 (see section 6.1.2). Comparing the baselines TAAF and HEDA, which have similar lengths, but experience different multipath effects, figures 6.9(c) and (d) depict average increases in NL ambiguity resolution of 7.4% and 5.2%, respectively, if the proposed SNR-based observation weighting model EMPSNR2 is applied in place of the elevation-dependent CSC2(BS).
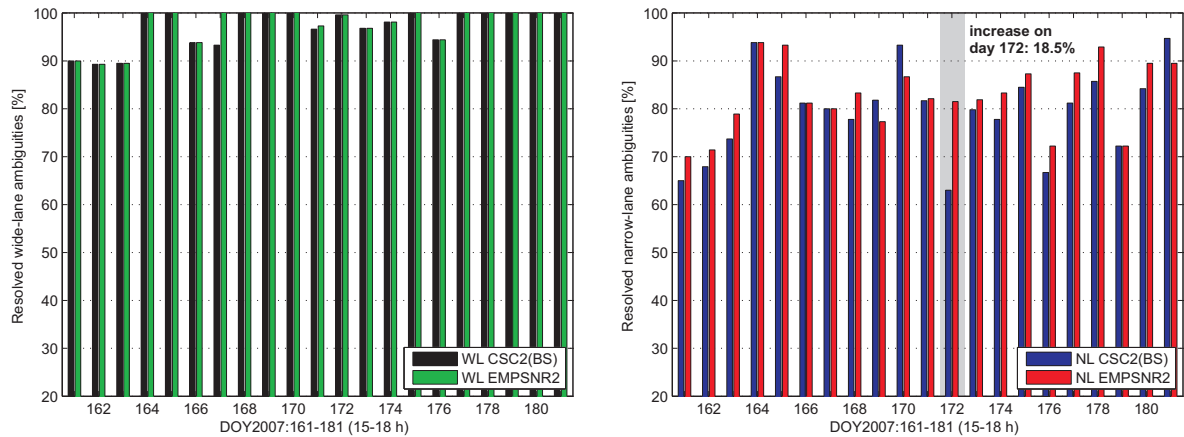
(a) AFLO: 32.4 km, weak MP (left: WL AMB resolution, right: NL AMB resolution)
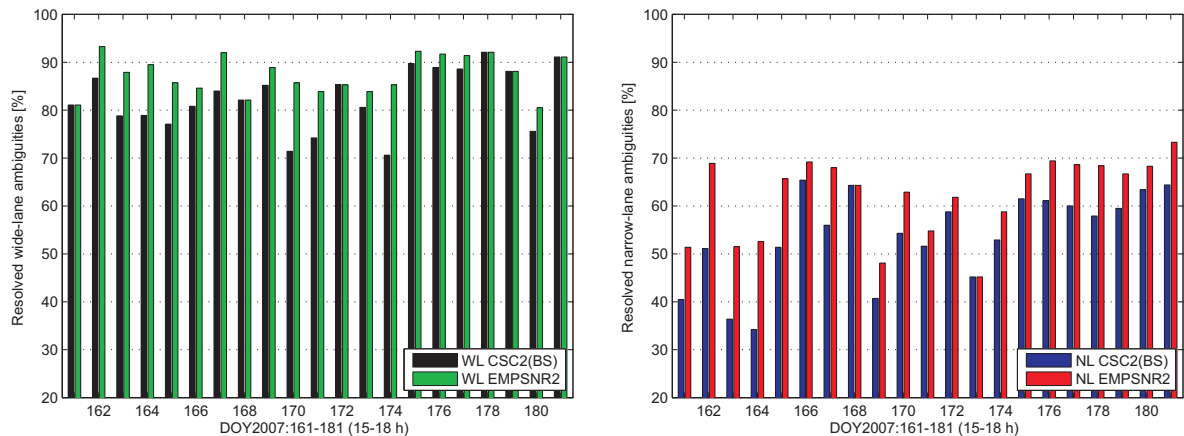
(b) RATA: 203.7 km, weak MP (left: WL AMB resolution, right: NL AMB resolution)
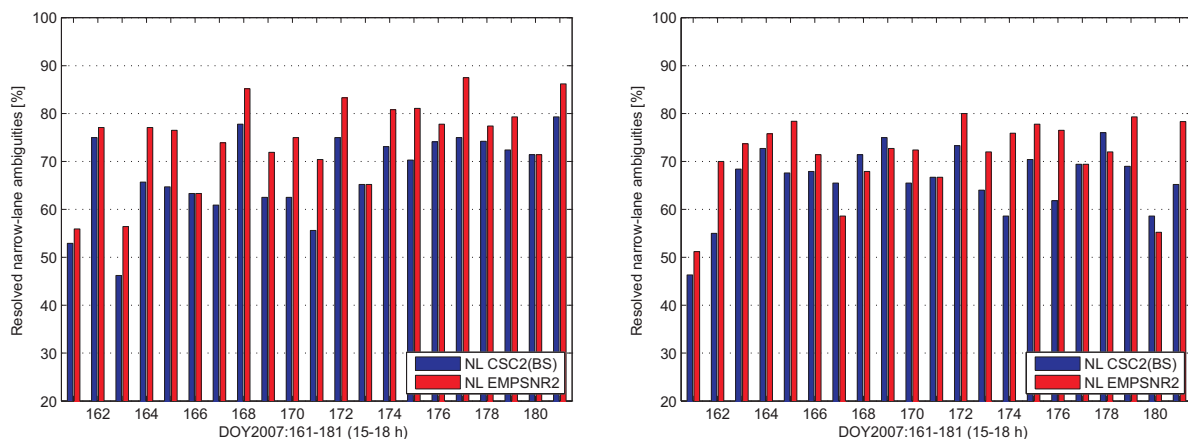
(c) TAAF: 53.7 km, weak MP, NL AMB resolution   (d) HEDA: 54.1 km, strong MP, NL AMB resolution

Figure 6.9: Representative examples of the results of ambiguity (AMB) resolution using CSC2(BS) and EMPSNR2 (elevation cut-off angle: 3°, MP: multipath; see table 4.3)

Taking all baselines analysed in this case study into consideration, table 6.7 presents the total results of ambiguity resolution using different observation weighting models. Replacing the conventional CSC2(BS) by the advanced EMPSNR2 within GPS data analysis, the average success rates of WL and NL ambiguity resolution can be improved by up to 4.9% and 8.6%, respectively. The corresponding maximum daily enhancements amount to 14.7% and 18.5%, coinciding with the respective maximum improvements of 16.7% and 23.9% found in case study 1 (see table 6.2). While EMPSNR2 leads to considerable increases in WL ambiguity resolution only for long baselines (> 100 km; e.g., RATA), significant improvements in NL ambiguity resolution are also detected for short baselines (< 40 km; e.g., AFLO). In addition to the results of ambiguity solution summarised over th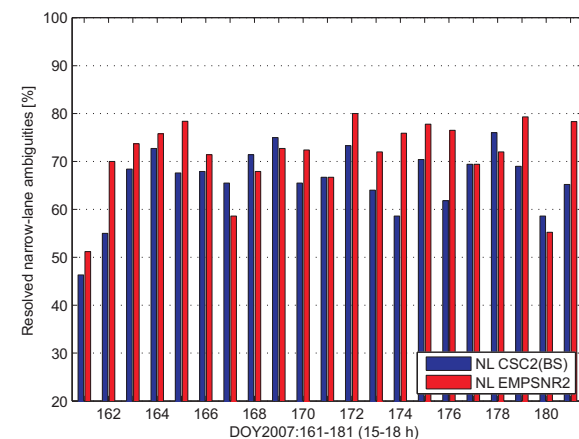e whole investigation period of 21 days, representative daily results are provided in table D.2 for AFLO and RATA, and in table D.3 for TAAF and HEDA. In table D.2, the AFLO-related daily numbers of ambiguities (#AMB) show extremely large values on days 171 and 172, while a significant improvement in NL ambiguity resolution is achieved only on day 172. This will be discussed in more detail in section 6.2.4.
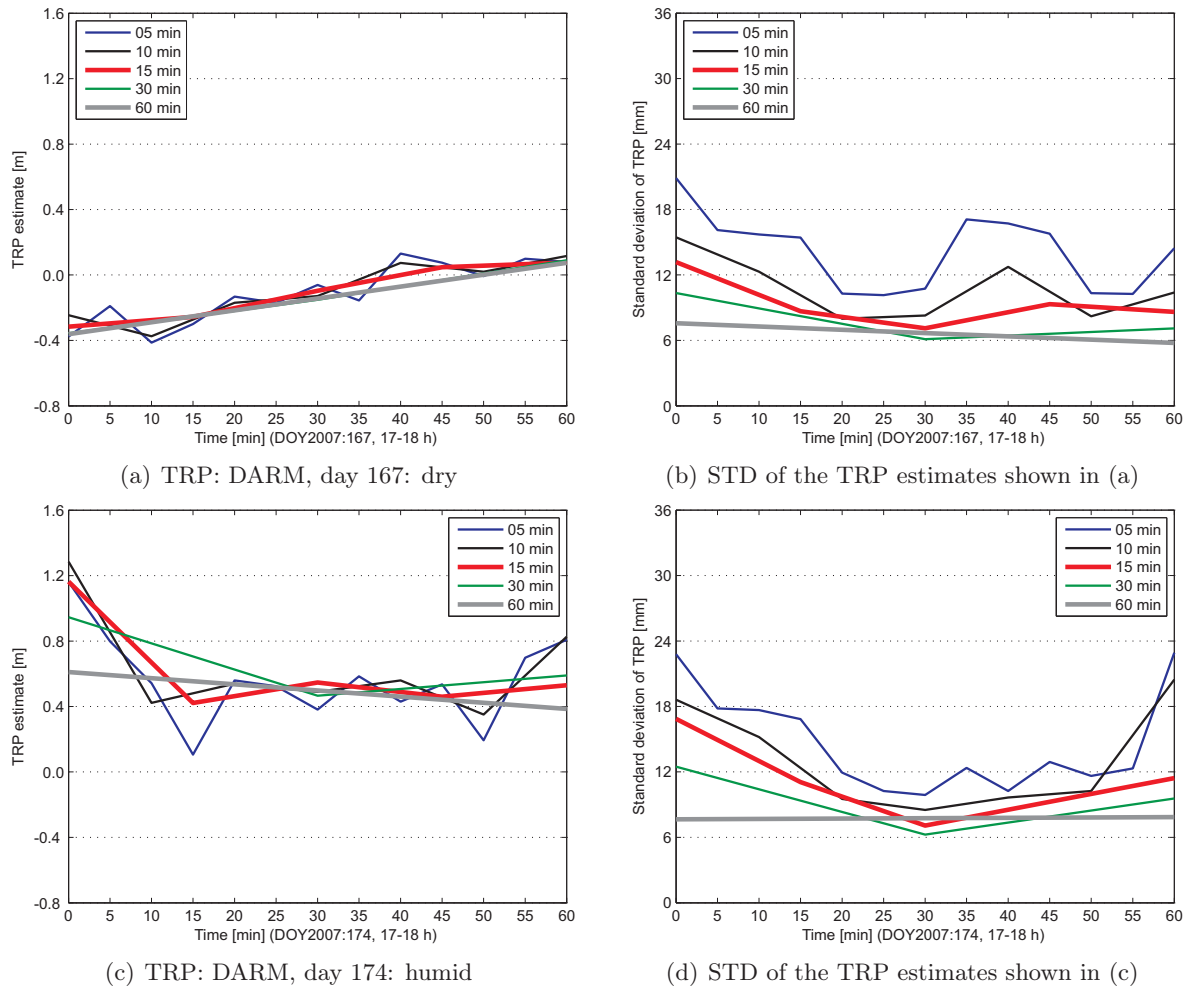
Table 6.7: Effects of applying different observation weighting models on the total results of phase ambiguity resolution in case study 2 (elevation cut-off angle: 3°)

Model and baseline	CSC2(BS) Number/Percent			EMPSNR2 Number/Percent			Improvement Total		Improvement Maximum	
	ΣAMB	WL	NL	ΣAMB	WL	NL	WL	NL	WL	NL
AFLO	**1007**	983/97.6	770/76.5	**1007**	986/97.9	828/82.2	0.3	5.7	6.7	**18.5**
SIBI	769	725/94.3	521/67.8	769	729/94.8	564/73.3	0.5	5.5	3.1	17.5
TAAF	639	608/95.1	429/67.1	639	606/94.8	476/74.5	−0.3	7.4	0.0	14.8
HEDA	661	609/92.1	435/65.8	661	611/92.4	469/71.0	0.3	5.2	6.9	17.3
RATA	735	608/82.7	397/54.0	735	644/87.6	460/62.6	**4.9**	**8.6**	**14.7**	18.4

6.2.3 Effects on troposphere parameters

Prior to analysing the effects of EMPSNR2 on site-specific troposphere parameter (TRP) estimation, figure 6.10 shows some results of the determination of an appropriate TRP time span using short-term (1 h) and high-frequency (1 Hz) GPS observations. To illustrate the worst-case scenario with respect to multipath impact, the DARM-related TRP estimates and standard deviations, obtained by specifying different time spans of 5, 10, 15, 30, and 60 min, are compared for two representative days, 167 and 174. According to the DWD surface meteorological data depicted in figure 4.8, dry atmospheric conditions prevailed on day 167, while on day 174 there was high relative humidity (RH) and significant precipitation (RF) in the northern part of the investigation area (see the DWD sites FRAN and WUER). These different near-ground atmospheric conditions are obviously reflected by the different magnitudes of the corresponding TRP values (cf. figures 6.10(a) and (c)). Using a larger time window, TRP can be more precisely estimated due to the higher observation redundancy (see figures 6.10(b) and (d)). However, at the same time, more details in the temporal variations of TRP are neglected because of the decreased parameter number. For both dry and humid atmospheric conditions, a time span of 15 min turns out to be a reasonable compromise between adequate delay characterisation and reliable parameter estimation. Within the context of GPS meteorology, such a 15-minute TRP time interval was also used by Bender et al. (2008) to achieve an optimum evaluation of the zenith tropospheric delay. Additional examples of the span determination are provided in figure C.2 to demonstrate the appropriateness of the selected TRP time window to short-term GPS relative positioning using high-frequency data.

(a) TRP: DARM, day 167: dry

(b) STD of the TRP estimates shown in (a)

(c) TRP: DARM, day 174: humid

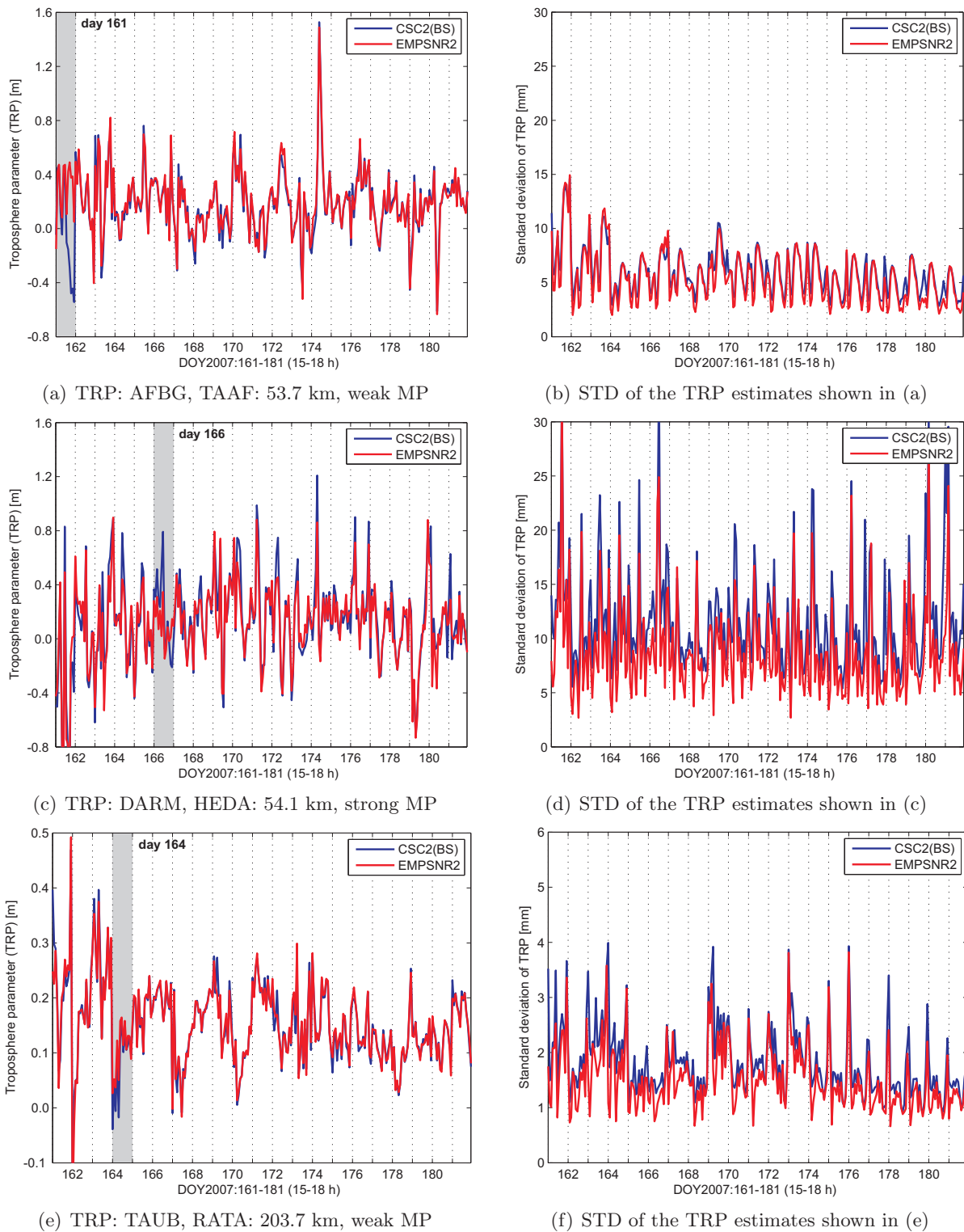(d) STD of the TRP estimates shown in (c)

Figure 6.10: Representative examples of TRP estimation using different time spans (baseline: HEDA, 54.1 km, strong multipath effects, elevation cut-off angle: 3°, observation weighting model: CSC2(BS), sampling interval: 1 s, processing time interval: 17-18 h)

Considering multipath impact and baseline length, figure 6.11 illustrates examples of the results of TRP estimation using different observation weighting schemes. A comparison between AFBG and DARM shows that strong multipath effects significantly amplify the TRP noise level and increases the median standard deviation from about 5 mm (AFBG) to 8 mm (DARM). For the site DARM, the use of different observation weighting models results in significant $\Delta TRP_{a/r}$ and $\Delta STD_{a/r}$ values of 5.1 cm/38.1% and 2.4 mm/23.7%, respectively (see equations (6.3) and (6.4)). As the baseline length increases, for example, from TAAF (53.7 km) to RATA (203.7 km), the median TRP standard deviation decreases from about 5 mm for AFBG to 1.5 mm for TAUB. Such improved TRP precision with increasing baseline length was also reported by Luo et al. (2007a, p. 67), which may be explained by the decreased correlation in the observation and parameter domains for larger separation distances.

In addition, DWD surface meteorological data are used to support the interpretation of the significant differences in the TRP estimates, which are marked in figures 6.11(a), (c), and (e). As figure 4.8(c) shows, relatively high *RH* of 77% is measured on day 161 at the DWD station FRAN, which is located close to the SA*POS*®site AFBG (see figure 4.1). Day 166 is the most humid one over the entire investigation period, which affects the SNR-based observation weights of DARM in a significant manner (see figure 6.8(d)). On day 164, a high *RH* of 82% and large *RF* of 26 mm were registered by the DWD station KEMP, which is not far from the SA*POS*®site

RAVE (see figures 4.8(c) and (d)). The correlation between the considerable deviations in the TRP estimates and the DWD surface metrological data verifies the high sensitivity of EMPSNR2 to variations in the near-ground atmospheric conditions, which takes a further step towards a realistic assessment of GPS observation quality.

(a) TRP: AFBG, TAAF: 53.7 km, weak MP

(b) STD of the TRP estimates shown in (a)

(c) TRP: DARM, HEDA: 54.1 km, strong MP

(d) STD of the TRP estimates shown in (c)

(e) TRP: TAUB, RATA: 203.7 km, weak MP

(f) STD of the TRP estimates shown in (e)

Figure 6.11: Representative examples of the results of TRP estimation using CSC2(BS) and EMPSNR2 (elevation cut-off angle: 3°, TRP time span: 15 min, MP: multipath)
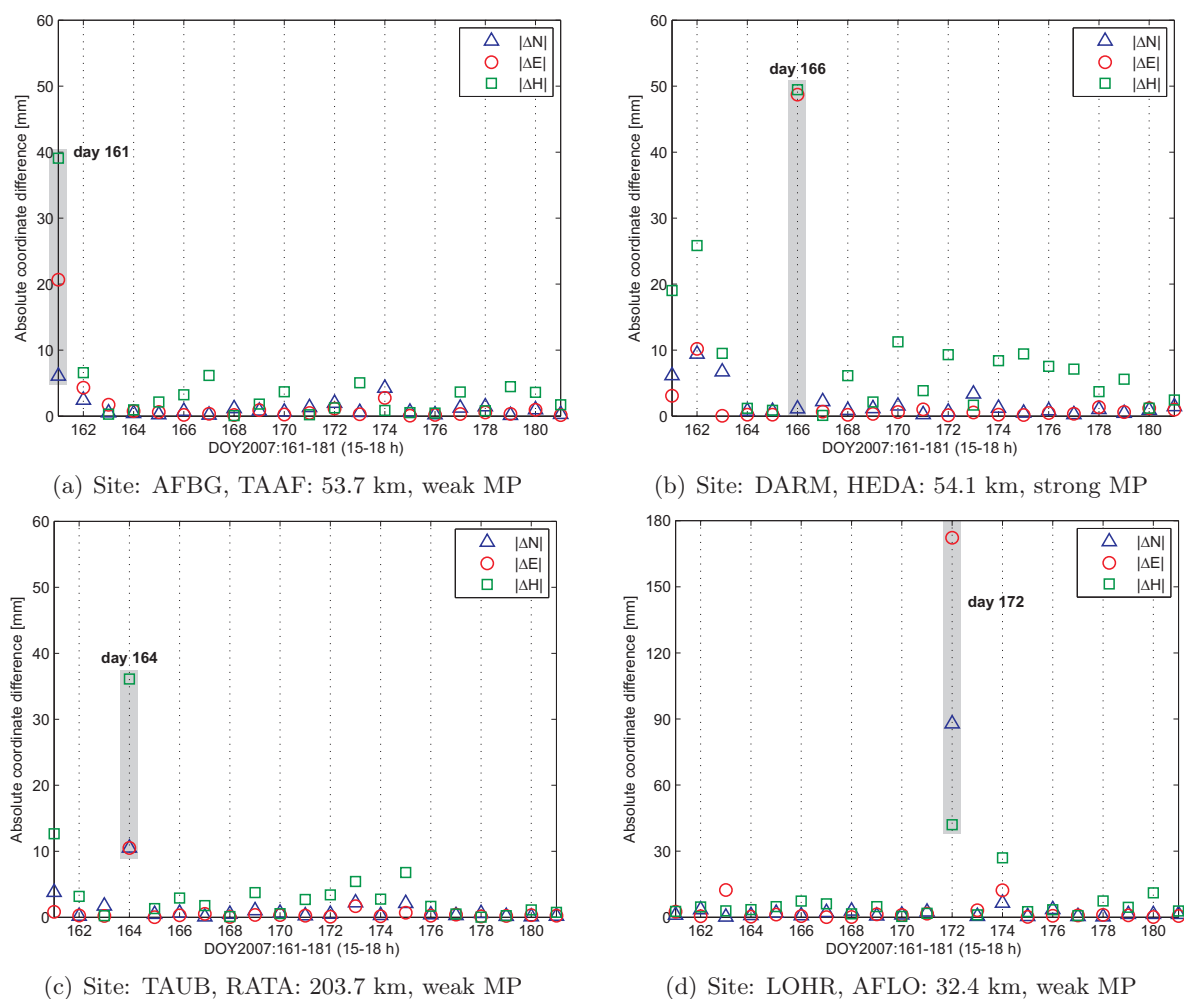
On the basis of $\Delta\text{TRP}_{a/r}$ and $\Delta\text{STD}_{a/r}$ given by equations (6.3) and (6.4), respectively, table 6.8 presents the effects of different observation weighting on the results of TRP estimation for all baselines analysed in this case study. The employment of different weighting models results in ΔTRP_a values of up to 5.2 cm, appearing to increase with increasing multipath impact and to decease with increasing baseline length. In comparison to CSC2(BS), the use of EMPSNR2 improves on average the TRP standard deviations by as much as 2.5 mm absolutely and 24.1% relatively. The enhancements in the TRP standard deviations, i.e., ΔSTD_a, are affected by multipath impact and baseline length in a similar manner as to the differences in the TRP estimates, i.e., ΔTRP_a. The mean ΔTRP_a resulting from case study 2 is nearly twice as large as that from case study 1, while the mean ΔSTD_a from both case studies are at a comparable level (cf. tables 6.3 and 6.8). Due to the strong correlation between station height and TRP estimates (Dach et al., 2007a, p. 241), significant changes in TRP may lead to considerable variations in the vertical component of a site's coordinates. This provides additional motivation for examining the effects of EMPSNR2 on station coordinate determination.

Table 6.8: Effects of applying different observation weighting models on the results of the TRP estimation in case study 2 (see equations (6.3) and (6.4))

Analysed baseline	Length [km]	Multipath impact	Station ID	Elevation cut-off angle: $3°$	
				$\Delta\text{TRP}_{a/r}$ [cm/%]	$\Delta\text{STD}_{a/r}$ [mm/%]
AFLO	32.4	weak	AFBG	4.6/19.8	1.1/13.3
			LOHR	4.5/20.2	1.1/13.4
SIBI	42.5	weak	SIGM	1.9/13.8	0.7/12.2
			BIBE	1.9/14.2	0.7/12.5
TAAF	53.7	weak	TAUB	2.3/14.0	0.5/8.2
			AFBG	2.3/13.5	0.5/8.4
HEDA	54.1	strong	HEID	**5.2/40.4**	**2.5/24.1**
			DARM	5.1/38.1	2.4/23.7
RATA	203.7	weak	RAVE	0.5/3.8	0.2/13.3
			TAUB	0.5/3.2	0.2/14.5
Mean	–	–	–	**2.9/18.1**	**1.0/14.4**

6.2.4 Effects on coordinate estimates

To verify the impact of significant changes in TRP on site coordinate estimates, figure 6.12 illustrates examples of absolute differences of topocentric coordinates determined by means of CSC2(BS) and EMPSNR2. As can be seen from figures 6.12(a), (b), and (c), cm-level coordinate changes are possible when significant deviations in the corresponding TRP estimates are present, for example, on days 161, 166, and 164 as shown in figures 6.11(a), (c), and (e), respectively. Moreover, it is interesting to see that large coordinate differences are found not only in the station height, but also in the horizontal components, particularly for site DARM, which is strongly affected by multipath effects. These considerable coordinate variations, occurring under non-ideal observational conditions such as a highly variable atmosphere and a strong multipath environment, demonstrate the realistic properties of the proposed SNR-based weighting model and its applicability to short-term GPS relative positioning using low-quality data. Compared to the other three examples, figure 6.12(d) depicts clearly larger horizontal coordinate differences. This is mainly attributed to the low data quality, caused by numerous observation gaps and short periods of measurements, as mentioned within the context of multipath analysis in section 4.2.3 (see figure 4.7(a)). Additional discussion of this phenomenon will be provided later in this section when analysing the influence of EMPSNR2 on coordinate repeatability.

(a) Site: AFBG, TAAF: 53.7 km, weak MP

(b) Site: DARM, HEDA: 54.1 km, strong MP

(c) Site: TAUB, RATA: 203.7 km, weak MP

(d) Site: LOHR, AFLO: 32.4 km, weak MP

Figure 6.12: Examples of absolute differences of topocentric coordinates estimated by means of different observation weighting models (MP: multipath; cf. figures 6.11(a), (c), and (e))

As figure 6.12 illustrates, in the presence of outliers, it is particularly appropriate to use the median absolute coordinate difference $\Delta\mathrm{CRD}_a$, given by equation (6.5), to assess the average effect of EMPSNR2 on site coordinate estimates. The resulting $\Delta\mathrm{CRD}_a$ are provided in table 6.9 and show a dominant impact on the height component, with a maximum of 6.1 mm for the site DARM. Position changes at this level are significant for studies involving highly precise and sensitive detection of recent crustal movements using CORS (Knöpfler et al., 2010). Furthermore, comparing the coordinate differences in the horizontal components, larger values are found in the northing component, which was also observed in case study 1 (see table 6.4).

Table 6.9: Effects of applying different observation weighting models on site coordinate estimates in case study 2 (unit: mm; see equation (6.5))

Analysed baseline	Length [km]	Multipath impact	Station ID	Elevation cut-off angle: $3°$		
				$\Delta\mathrm{N}_a$	$\Delta\mathrm{E}_a$	$\Delta\mathrm{H}_a$
AFLO	32.4	weak	LOHR	1.3	0.8	**3.5**
SIBI	42.5	weak	BIBE	0.5	0.5	1.0
TAAF	53.7	weak	AFBG	0.8	0.5	1.8
HEDA	54.1	strong	DARM	1.0	0.6	**6.1**
RATA	203.7	weak	TAUB	0.5	0.3	1.8

After analysing the absolute coordinate changes induced by different observation weighting, table 6.10 gives an impression of the effect of EMPSNR2 on coordinate repeatability. Thereby, the root mean square deviations (RMSD) of the daily coordinate solutions from the arithmetic mean are presented in the local topocentric system. Due to the short observation period of 3 h, the coordinate estimates from this case study exhibit cm-level repeatability, which is obviously larger than that from case study 1 using daily GPS measurements (see table 6.5). Nevertheless, the employment of EMPSNR2 seems to considerably improve both the horizontal (e.g., LOHR) and vertical (e.g., DARM) coordinate repeatability. However, degraded stability in the height component is also observed (e.g., TAUB). In the following examples, daily coordinate increments are investigated in more detail in order to provide a realistic picture of the positive impact of EMPSNR2 on coordinate repeatability.

Table 6.10: Effects of applying different observation weighting models on site coordinate root mean square deviations (RMSD) in case study 2 (unit: cm)
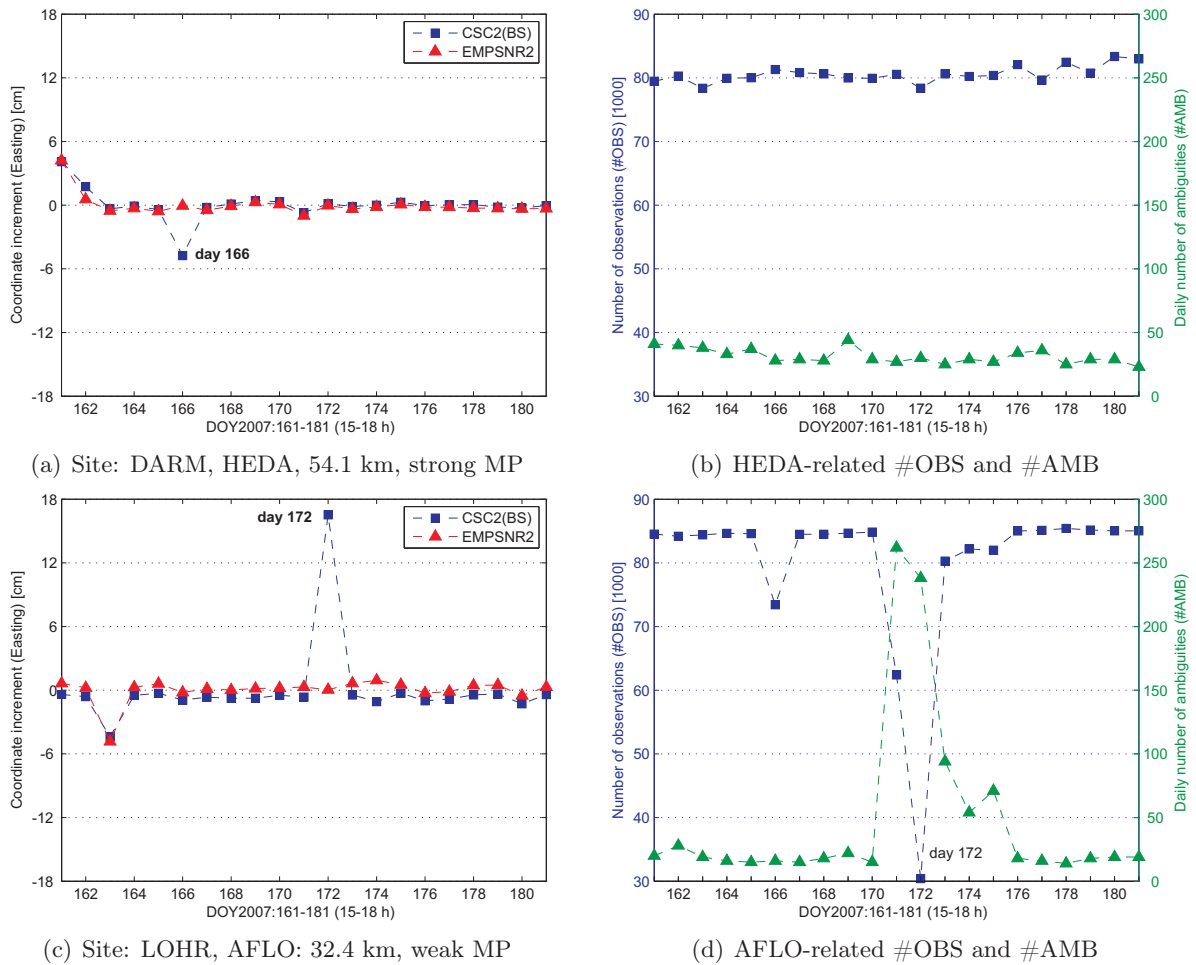
Elevation cut-off angle: 3°				CSC2(BS)			EMPSNR2		
Baseline	**Length** [km]	**Multipath**	**Station**	N	E	H	N	E	H
AFLO	32.4	weak	LOHR	**2.1**	**3.9**	1.0	**0.6**	**1.2**	1.2
SIBI	42.5	weak	BIBE	0.6	0.3	1.2	0.7	0.3	1.3
TAAF	53.7	weak	AFBG	1.3	1.0	1.6	1.3	0.9	1.5
HEDA	54.1	strong	DARM	0.8	**1.5**	**2.3**	0.9	**1.0**	**1.8**
RATA	203.7	weak	TAUB	0.6	0.3	**1.4**	0.6	0.4	**1.8**

Figure 6.13 depicts the height increments of the stations for which considerable deviations in the TRP estimates are detected in figures 6.11(a), (c), and (e). On days 161, 166, and 164 when there are large differences in the estimated TRP for AFBG, DARM, and TAUB, respectively, significant discrepancies are found in the corresponding height increments. For the site DARM, which is strongly affected by multipath effects, noticeable changes are also visible on days 161 and 162, coinciding with the large coordinate differences in figure 6.12(b). While the height increments of AFBG and DARM are enhanced by applying EMPSNR2 instead of CSC2(BS), the TAUB-related ones experience a negative impact. In particular, the height increment on day 164 increases to a similar level as seen on day 173. Considering the related DWD surface meteorological data from WUER, KONS, KEMP (see figure 4.8), humid atmosphere prevailed on days 164 and 173. This indicates that the use of EMPSNR2 does not necessarily improve coordinate repeatability, but produces more realistic and physically interpretable results.

(a) Site: AFBG, weak MP   (b) Site: DARM, strong MP   (c) Site: TAUB, weak MP
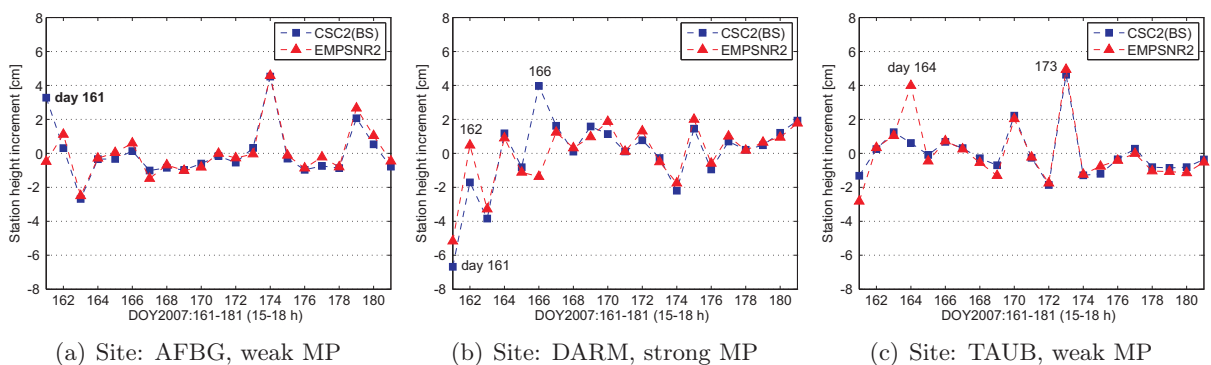
Figure 6.13: Representative examples of station height increments corresponding to the TRP estimates with significant differences shown in figures 6.11(a), (c), and (e) (MP: multipath)

In addition to the vertical component, figure 6.14 depicts examples of easting coordinate increments, along with the daily number of double-difference observations (#OBS) and daily number of phase ambiguities (#AMB). As figure 6.14 shows, the use of EMPSNR2 improves the coordinate estimates by 4.7 cm on day 166 for DARM (see figure 6.14(a)) and 16.5 cm on day 172 for LOHR (see figure 6.14(c)). This corresponds to the significant absolute coordinate differences $|\Delta E|$ illustrated in figures 6.12(b) and (d). For the baseline HEDA with strong multipath impact, both #OBS and #AMB are relatively constant over time (see figure 6.14(b)). Therefore, the DARM-related example demonstrates the fact that EMPSNR2 is capable of dealing with multipath variations induced by variable atmospheric conditions, for example, changes in the surface moisture content (day 166: high RH; see figure 4.8(c)). In contrast, the AFLO-related #OBS and #AMB exhibit strong variations on days 171 and 172, which are also visible in the LOHR-related multipath index shown in figure 4.7(a). Despite a large #AMB of 262 on day 171, there exist adequate observations with which more than 80% of the NL ambiguities are resolved (see figure 6.9(a)). However, on day 172, #AMB remains more or less the same, while #OBS is only half as much as that on day 171, resulting in the lowest success rate of NL ambiguity resolution using CSC2(BS). Under this circumstance, the employment of EMPSNR2 significantly enhances the percentage of the resolved NL ambiguities by 18.5%, leading to accurate coordinate estimates in spite of the limited data quality. Therefore, the LOHR-related example shows the applicability of EMPSNR2 to short-term and low-quality GPS data.

(a) Site: DARM, HEDA, 54.1 km, strong MP

(b) HEDA-related #OBS and #AMB

(c) Site: LOHR, AFLO: 32.4 km, weak MP

(d) AFLO-related #OBS and #AMB

Figure 6.14: Comparison of easting coordinate increments with respect to observation weighting model, daily number of double-difference observations (#OBS), and daily number of phase ambiguities (#AMB) (MP: multipath)

Based on the more detailed analysis of site coordinate increments, it becomes evident that the apparently considerable decreases in the coordinate RMSD presented in table 6.10 are mainly due to the occurrence of special cases with respect to atmospheric variability and data quality. Under normal observational conditions, a general improvement in station coordinate determination by means of EMPSNR2, however, cannot be verified through this case study. Taking the coordinate RMSD of BIBE as an example (see table 6.10), the use of EMPSNR2 instead of CSC2(BS) seems to exert only a minor influence on coordinate repeatability. In order to exploit the full potential of EMPSNR2, further case studies are necessary, particularly considering observation period, data quality, and processing technique (e.g., precise point positioning).

6.3 Concluding remarks

In comparison to the elevation-dependent observation weighting model CSC2(BS), which is implemented by default in the Bernese GPS Software 5.0, this chapter verified the efficiency of the proposed SNR-based weighting scheme EMPSNR2 in long- and short-term relative positioning. By considering baseline length, multipath impact, minimum elevation angle, and atmospheric conditions, parameter estimates such as phase ambiguities, site-specific troposphere parameters (TRP), and station coordinates were analysed with respect to observation weighting. A physical interpretation of the results was achieved by incorporating DWD surface meteorological data. The main findings from two representative case studies are summarised as follows:

- Despite the complexity induced by SNR conversion, the observation weights derived using signal quality measures reflect variations in receiver characteristics, site quality, and atmospheric conditions. Compared to CSC2(BS), EMPSNR2 produces higher weights for low- and medium-elevation data, increasing their contributions to parameter estimation.

- Using EMPSNR2 instead of CSC2(BS) to resolve double-difference phase ambiguities, an average improvement of 10% can be expected in both wide-lane (WL) and narrow-lane (NL) ambiguity resolution. While the advantages in resolving the WL ambiguities are primarily found for long baselines (e.g., > 100 km), the enhancements in resolving the NL ambiguities are also detected for shorter baselines (e.g., < 40 km).

- A switch from CSC2(BS) to EMPSNR2 may lead to cm-level (20%) changes in site-specific TRP estimates and mm-level (20%) improvements in the associated standard deviations. The degree of efficiency of EMPSNR2 seems to increase with increasing multipath impact and decreasing elevation cut-off angle, for example, from $10°$ to $3°$.

- Under normal observational conditions (i.e., calm atmosphere and weak multipath), the use of EMPSNR2 instead of CSC2(BS) results in coordinate changes of up to about 5 mm. However, when analysing short-term and low-quality GPS data, EMPSNR2 may significantly improve site coordinate estimates at the cm- or even dm-level.

The effects of EMPSNR2 on the results of parameter estimation are not independent from each other, but are mutually related. For example, improved ambiguity resolution may enhance the performance of TRP estimation, and both improvements together contribute to accurate and reliable coordinate determination. Furthermore, despite their low temporal (6 h) and spatial (6 sites) resolution, the freely available DWD surface meteorological data played an important role in the physical interpretation of the results, providing a realistic picture of the model efficiency.

Chapter 7

Residual-based Temporal Correlation Modelling

This chapter describes a residual-based approach to modelling temporal correlations of GPS observations. Section 7.1 reviews previous studies on temporal correlation modelling and their main achievements. Next, section 7.2 presents a decomposition procedure using the studentised residual, which is more suitable for temporal correlation analysis than the least-squares (LS) residual. At the preliminary stage of the residual-based temporal correlation modelling, the remaining systematic signals, caused by multipath effects for instance, are extracted via Vondrák filtering and sidereal stacking. Thereby, the determination of appropriate filter parameters and orbit repeat times, as well as statistically rigorous outlier handling, play an important role. The resulting noise component is almost free of systematic effects and can be used to study the temporal correlation properties of GPS observations. Finally, for each decomposed noise series, the best-fitting autoregressive moving average (ARMA) model is automatically identified by means of the freely available MATLAB® Toolbox ARMASA. Section 7.3 provides a deeper insight into ARMA modelling with respect to order selection and parameter estimation.

7.1 Review of previous work

As summarised in table 3.10, for modelling temporal correlations of GPS observations, several approaches have been proposed, such as autocorrelation function (ACF), variance component estimation (VCE), ARMA processes, and atmospheric turbulence theory. Analysing baselines mainly ranging between 10 and 60 km, El-Rabbany (1994, p. 34) described the temporal correlation behaviour by fitting empirical correlation functions of exponential and polynomial types to the sample ACF of double-difference phase residuals. The exponential function

$$f_{AE}(h) = \exp(-|h|/T) \qquad (7.1)$$

was found to be the best LS approximation for the ACF of GPS phase residuals. The term h is the time shift (or lag), and T denotes the unknown correlation time corresponding to the $1/e$ point, where e is Euler's number. It was concluded that GPS double-difference observations are positively correlated, where the correlation time takes values of 263, 270, and 169 s for L1, L2, and the ionosphere-free linear combination LC3, respectively. These results are generally valid for baselines of up to 100 km. Moreover, there is no particular trend for correlation time as a function of baseline length until this distance (El-Rabbany, 1994, p. 36, 89).

Howind et al. (1999) integrated the temporal correlation function given by equation (7.1) into the LS adjustment process to assess the sensitivity of the estimated site coordinates in GPS networks with long baselines (e.g., 548 km). Significant coordinate changes of up to 2 cm are possible, with the largest variations in the longitude and ellipsoidal height. Accordingly, the consideration of temporal correlations turns out to be an important issue when using GPS observations for deformation analysis. The origin of temporal correlations is attributed to the influence of the troposphere. El-Rabbany and Kleusberg (2003) presented a modified sequential LS adjustment in which temporal correlations are modelled by means of equation (7.1). For all analysed baselines, the neglect of temporal correlations has insignificant effects on parameter

estimates, but results in over-optimistic accuracy measures and a smaller size of the confidence hyperellipsoid (i.e., shorter ambiguity search time). Increasing the data sampling interval from 20 s to 10 min, the coordinate standard deviations obtained by neglecting temporal correlations approach those derived with temporal correlations considered. It was also concluded that there exists no particular relationship between correlation time and baseline length. For sampling intervals shorter than 5 min, an increase of 30% in correlation time (from 263 to 342 s) increases the coordinate standard deviations by 20-30%. Howind (2005, p. 57) suggested another empirical correlation function that consists of an exponential and a cosine oscillation component:

$$f_{JH}(h) = \begin{cases} 1, & \text{if } h = 0, \\ 0.5 \cdot \exp\left(-\frac{h}{ND_1}\right) \cos\left(\frac{2\pi \cdot h}{ND_1 \cdot P}\right), & \text{if } h \geq 1, \end{cases} \tag{7.2}$$

where ND_1 is known as the zero-crossing correlation length, and P denotes the oscillation period. While the parameter ND_1, representing the smallest lag value at which the sample ACF falls below zero, is determined numerically, the unknown period P is estimated using a LS regression on the sample ACF of detrended double-difference residuals. Applying this correlation model to relative positioning in the Antarctic GPS network, the phase observations are found to be positively correlated over time, and the correlation lengths reach about 300 s for short baselines (14 km) and 15 min for long baselines (127-433 km). Furthermore, in terms of short-baseline solutions, the extension of the GPS stochastic model by considering temporal correlations leads to insignificant changes in coordinate estimates, but to more realistic (twice as large) coordinate errors. For long-baseline solutions, both coordinate estimates and the associated accuracy measures are considerably improved by taking temporal correlations into account.

On the basis of stochastic parameters estimated by analysing raw GPS observations, Leandro and Santos (2007) developed an empirical stochastic (ESto) model to construct the variance-covariance matrix (VCM) for pseudo-range measurements. The temporal and spatial correlations are determined using sample auto- and cross-correlation functions of double-difference code observations, which are initially reduced by the approximate geometric distances between the receiver and satellite antennas in order to satisfy the stationarity assumption. The ESto model provides a good approximation of the residual autocorrelation, which decreases with decreasing satellite elevation angle. Using ESto to analyse the C/A-code data from a short baseline of 2 km, coordinate biases can be significantly reduced by up to 37 cm (71%), particularly in the height component. Moreover, in comparison to a scaled identity matrix and an empirically determined elevation-dependent variance model, ESto produces more realistic accuracy measures of site coordinate estimates.

Using high-frequency (e.g., 1 and 5 Hz) single- and double-difference residuals from zero and short baselines (e.g., 3 and 10 m), the stochastic analyses carried out by the Delft group focused on the receiver-dependent noise and correlation characteristics. Examining the correlograms of LS residual time series, Tiberius et al. (1999) reported temporal correlation lengths of about 10 s for L2 observations, while L1 measurements were found to be temporally uncorrelated. In addition, by applying different signal processing techniques, various receivers may exhibit distinctly different temporal correlation properties. Analysing zero-baseline residual time series by means of sample ACF, Borre and Tiberius (2000) showed that a GPS receiver is indeed capable of providing temporally uncorrelated observations at a sampling rate of 1 Hz. However, significant temporal correlations of 0.8-0.9 may exist between consecutive 5-Hertz observations. This is because, at high sampling rates between 5 and 10 Hz, a default tracking loop bandwidth may not be sufficiently large to provide independent measurements (Braasch and van Dierendonck, 1999). By studying the noise characteristics of seven commonly used GPS receivers, Bona (2000) found that the noise was seldom white, particularly for code observations.

Although the VCE technique has been successfully used to estimate observation variances, as well as covariances between channels (spatial correlations) and observation types (cross correlations) (Wang et al., 1998; Tiberius and Kenselaar, 2000; Satirapod et al., 2002; Amiri-Simkooei et al., 2009; Li et al., 2011), it is rarely applied to modelling temporal correlations of GPS observations. By estimating time covariances based on 1-Hertz residuals from a zero-baseline, Tiberius and Kenselaar (2003) verified the conclusions drawn by Tiberius et al. (1999), namely the absence of temporal correlations on L1 and correlation lengths of about 10-20 s on L2. However, the assessment of GPS receiver noise using zero-baselines does not necessarily provide an accurate indication of receiver performance (Langley, 1997). Analysing 1-Hertz residuals from ultra-short baselines of about 5 m, Li et al. (2008) detected significant temporal correlations for all observation types, being larger than 0.5 at a lag of 50 s.

Another mathematical approach to describe the temporal correlation behaviour of GPS observations is to fit stochastic processes to residual time series. For example, Wang et al. (2002) employed first-order autoregressive processes (AR(1)) within a stochastic assessment procedure, which accounts for the heteroscedastic, spatially and temporally correlated error structure of GPS observations. Thereby, the temporal correlation coefficients are first estimated to transform the original double-difference observations into temporally uncorrelated measurements whose VCM has a block-diagonal structure and can be obtained by means of VCE (e.g., MINQUE). The final parameter estimation is carried out using the transformed observations and the associated VCM. Applying this advanced stochastic assessment to baseline solutions, essentially random residuals are obtained for different baseline lengths of 15 m, 215 m, and 13 km. While more reliable ambiguity resolution is achieved for the short baseline of 15 m, significant changes of up to 1 cm in the height component are found for the longer baselines of 215 m and 13 km. This procedure is only suitable for short observation periods as it assumes that the AR(1) coefficients and the variances of GPS observations are time-invariant for the entire observation period. To process long-term observation data sets, Satirapod et al. (2001) suggested a segmented stochastic modelling method, which effectively deals with long observation periods and comes up with a computationally more efficient approach for VCE. The application of this advanced modelling procedure in medium-baseline (e.g., 23 and 75 km) solutions leads to more random residuals and mm-level accuracy improvements in the estimated baseline components. Borre and Tiberius (2000) also made use of AR(1) processes to describe receiver temporal correlations, where the results are strongly dependent on the observation and receiver types.

Starting from the origin of the physical correlations between GPS signals propagating through the Earth's lower atmosphere, namely turbulent irregularities, Schön and Brunner (2008a) developed a fully populated variance-covariance model based on atmospheric turbulence theory. Assuming Taylor's hypothesis of frozen turbulence (Wheelon, 2001, p. 240), temporal correlations are converted into spatial correlations with the help of wind velocity and direction. In the absence of wind, only the slowly varying satellite geometry decorrelates GPS observations. Consequently, based on the results of simulation studies, large correlation lengths of up to 3600 s are possible. The introduction of a wind vector with a moderate velocity of 4 m/s significantly changes the correlation structure and reduces the correlation length to about 600 s. Furthermore, low-elevation observations are found to be less correlated over time due to the faster changing characteristic separation distances of the lines-of-sights at low elevation angles. Employing the VCE method, Schön and Brunner (2008b) proposed the SIGMA-C model that combines the SIGMA-ϵ model (Hartinger and Brunner, 1999) with a fully populated VCM derived using atmospheric turbulence theory. Analysing GPS data from the specially designed Seewinkel test network, which consists of six exactly aligned GPS sites and provides baselines of 1 to 16 km, the SIGMA-C model produces physical correlation patterns of GPS double-difference observations that are similar to those obtained by means of sample auto- and cross-correlation functions.

Using representative model parameters and wind vectors, temporal correlations over about 300 s are reported, with a sharp drop from 100% to 50-60% at a lag of 1 epoch (1 s). In comparison to temporal correlations, only moderate spatial correlations between double-differences are detected, with maximum values smaller than 20%. In addition, the use of SIGMA-C delivers more realistic formal coordinate variances in spite of highly redundant observation data.

Focusing on the effects of physical correlations on long-baseline (e.g., about 1500 km) positioning and tropospheric zenith path delay (ZPD) estimation, Jin et al. (2010) applied the residual-based stochastic model, relying upon the classical variation covariance (equivalent to Method 3 in Satirapod et al., 2001). For long observation periods, the entire session is divided into short segments for which a time-invariant stochastic model can be assumed due to the slowly changing error characteristics over time. Comparing this residual-based stochastic model with a scaled identity matrix, differences reach about 1 cm in the troposphere parameters and as much as 3-6 mm in the baseline components, particularly in the height estimate. Furthermore, taking physical correlations into account, the baseline and ZPD estimates are closer to the reference values. By differencing observations across adjacent epochs, Petovello et al. (2009) presented a new Kalman filter formulation, which not only cancels time-correlated errors in GPS observations, but also gives full consideration to measurement noise. In both simulated and field studies, where time-correlated errors are generated and approximated by means of first-order Gauss-Markov processes, the conventional Kalman filter neglects temporal correlations and produces over-optimistic estimates of position errors. In contrast, the proposed filter algorithm delivers more realistic accuracy measures, which are closer to the actual values in the case that the magnitude of the time-correlated error is significantly (e.g., 5 times) larger than that of the measurement noise.

To summarise, although based on different modelling theories, all of the aforementioned approaches aim for accurate parameter estimates and realistic quality measures by considering temporal correlations of GPS observations in the stochastic model. The achieved encouraging results serve as valuable experiences and helpful references for the questions to be answered in this thesis. For example, while performing residual-based temporal correlation analysis using ACF and stochastic processes, the assumption of stationarity is usually made. However, its validity in practice has been rarely verified, for instance, by applying statistical tests. In the occurrence of non-stationarity, it is important to ask for the possible physical causes or error sources by considering their characteristics in the time and frequency domains. In addition, the impacts of the remaining systematic errors (e.g., multipath) on temporal correlation properties should be investigated in more detail. Instead of specifying a certain type of ARMA process with a predefined order like AR(1), the best-fitting ARMA model can be identified for a given noise time series. This enables not only a more accurate description of the temporal correlation behaviour, but also the verification of the sufficiency of AR(1) modelling. Apart from sample ACF, rigorous statistical tests are available for assessing the efficiency of the estimated ARMA models. Taking some of these aspects into account, the next section introduces a residual decomposition process for extracting stochastic noise from GPS observation residuals.

7.2 Residual decomposition

This section begins with a brief introduction to the so-called studentised residuals, serving as input data for the decomposition procedure. Subsequently, to give an overview, the entire residual decomposition process is presented, along with its contributions to the mathematical models of GPS observations. Next, the principles and key issues of the individual decomposition steps are described in more detail, where representative examples are provided.
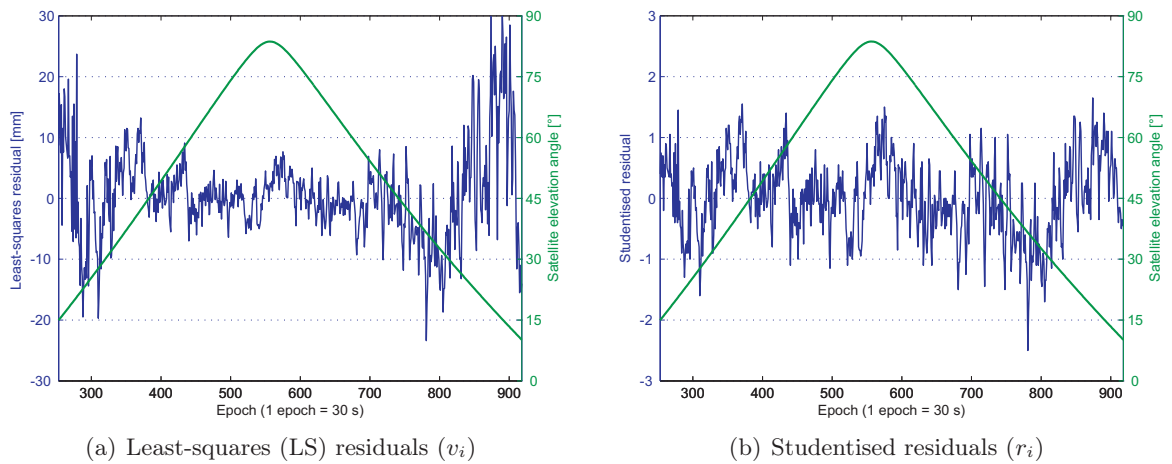
7.2.1 Studentised residuals

The ordinary LS residual vector $\boldsymbol{v} = (v_1, \ldots, v_n)^T$, for example, resulting from GPS data analysis, represents a negative estimate of the stochastic error vector $\underline{\boldsymbol{e}}$, i.e.,

$$\boldsymbol{v} = -\hat{\boldsymbol{e}} = \boldsymbol{A}\hat{\boldsymbol{x}} - \boldsymbol{l}. \tag{7.3}$$

The vector of stochastic error terms $\underline{\boldsymbol{e}}$ cannot be directly observed and is generally assumed to be normally distributed with $\underline{\boldsymbol{e}} \sim \mathcal{N}(\boldsymbol{0}, \sigma_0^2 \boldsymbol{Q_{ee}})$, where σ_0^2 is the a priori variance factor (or the variance of unit weight), and $\boldsymbol{Q_{ee}}$ is the cofactor matrix of $\underline{\boldsymbol{e}}$. For uncorrelated stochastic errors, i.e., $\boldsymbol{C_{ee}} = \sigma_0^2 \boldsymbol{Q_{ee}} = \text{diag}(\sigma_1^2, \ldots, \sigma_n^2)$, $\boldsymbol{v}$ reflects the variance function of the true model errors. Therefore, the unknown variances σ_i^2 are commonly determined by estimating the variances of the ordinary LS residuals, indicating $\sigma_i^2 = \text{Var}(v_i)$ which holds approximately in static GPS positioning (Bischoff et al., 2006). If $\underline{\boldsymbol{e}}$ follows a normal distribution, the LS residuals are also normally distributed with $\mathcal{N}(\boldsymbol{0}, \sigma_0^2 \boldsymbol{Q_{vv}})$, where $\boldsymbol{Q_{vv}}$ is the residual cofactor matrix (Heck, 1981a). GPS measurement errors, which are insufficiently described by the functional model, will distort the residuals' probability distribution and induce deviations from the assumed normality (Luo et al., 2011a). Within the context of GPS temporal correlation modelling, the LS residuals have the main disadvantage that they are commonly heteroscedastic, strongly depending on the satellite elevation angle. This is due on the one hand to the correlation between observation quality and satellite geometry, and on the other to the decreasing efficiency of the applied functional model for low-elevation measurements. To avoid the difficulties in statistical assessments caused by the heteroscedasticity of LS residuals, the so-called studentised residuals, defined as

$$r_i = \frac{v_i}{\hat{\sigma}_i} = \frac{v_i}{\hat{\sigma}_0 \cdot \sqrt{\boldsymbol{Q_{vv}}(i,i)}}, \tag{7.4}$$

are preferred for temporal correlation analysis of GPS observations, where $\hat{\sigma}_0^2$ is the a posteriori variance factor, and $\boldsymbol{Q_{vv}}(i,i)$ is the i-th diagonal element of $\boldsymbol{Q_{vv}}$ (Cook and Weisberg, 1982, p. 18; Howind, 2005, p. 39, 42). Dividing v_i by the corresponding standard deviation estimates $\hat{\sigma}_i$, the resulting r_i exhibit more homogenous variances than v_i and maintain the temporal correlation properties, since the off-diagonal elements of $\boldsymbol{Q_{vv}}$ do not appear in the residual standardisation given by equation (7.4). Along with satellite elevation angles, figure 7.1 shows examples of LS and studentised residuals, obtained from a precise point positioning (PPP) analysis using the Bernese GPS Software 5.0 (Dach et al., 2007a, p. 231, 427).

(a) Least-squares (LS) residuals (v_i)   (b) Studentised residuals (r_i)

Figure 7.1: Examples of LS and studentised residuals (SA*POS*®site: OFFE, satellite: PRN 08, DOY2008:276, elevation cut-off angle: $10°$, weighting model: $\sin^2(e)$; see equation (7.4))

The Bernese GPS Software 5.0 provides both LS (`REAL`) and normalised residuals, where the latter is defined as $v_i/\sqrt{\boldsymbol{Q_{vv}}(i,i)}$. Being different from LS residuals, normalised residuals are converted to one-way L1 carrier-phase residuals. Assuming that all observations are equally weighted, a real double-difference LC3 residual of 36 mm corresponds to a normalised one-way L1 residual of 6 mm (Dach et al., 2007a, p. 145). For reliable statistical assessments, for example, outlier detection, it is recommended to store normalised residuals when analysing low-elevation data with an elevation-dependent observation weighting model. Dividing normalised residuals by the a posteriori sigma of unit weight $\hat{\sigma}_0$, which represents the estimated sigma of one-way L1 observable at zenith, unitless studentised residuals are obtained (see equation (7.4)). Under the assumption of independent and identically distributed (iid) measurement errors, studentised residuals possess a constant variance of 1, and are thus homoscedastic (Howind, 2005, p. 39). Exhibiting strong elevation dependency, the LS residuals shown in figure 7.1(a) are heteroscedastic and range between -3 and 3 cm, while the studentised residuals displayed in figure 7.1(b) are considerably homoscedastic and mainly vary within ± 1. The homogenous variance structure is due to the elevation-dependent factor $\sqrt{\boldsymbol{Q_{vv}}(i,i)}$, which is illustrated in Fuhrmann et al. (2010, p. 52). Furthermore, as Howind (2005, p. 38, 39) showed, the use of an observation weighting model insignificantly affects LS residuals, but strongly influences studentised residuals.

From its denotation, the studentised residual may be erroneously assumed to follow the well-known Student's t-distribution. In fact, it follows Pope's τ-distribution with f degrees of freedom, where f is equal to the redundancy of a LS adjustment (i.e., $f = n - u$; Pope, 1976, p. 15; Heck, 1981b). For $f \geq 2$, according to Beckman and Trussell (1974) and Heck (1981a), there exists a rigorous relationship between a τ-distributed random variable with f degrees of freedom $\underline{\tau}_f$ and a t-distributed random variable with $f - 1$ degrees of freedom $\underline{t}_{f-1}$:

$$\underline{\tau}_f = \sqrt{\frac{f \cdot \underline{t}_{f-1}^2}{f - 1 + \underline{t}_{f-1}^2}}, \quad \underline{t}_{f-1} = \sqrt{\frac{(f - 1) \cdot \underline{\tau}_f^2}{f - \underline{\tau}_f^2}}. \tag{7.5}$$

For large degrees of freedom, i.e., $f \geq 30$, which is generally fulfilled in static GPS positioning, both the τ- and t-distributions approach the standard normal distribution $\mathcal{N}(0,1)$, where the probability density function of the τ-distribution has a lower rate of convergence (Heck, 1981a). Taking advantage of this convergence in distribution, a two-step procedure for multiple outlier detection is developed in this thesis and will be presented in section 7.2.4. An important application of studentised residuals is to test geodetic observations for outliers in combination with Pope's τ-criterion. Such a testing procedure is particularly applicable if σ_0^2 is unknown, making the use of Baarda's data-snooping impossible (Heck, 1981b).

In spite of improved homogeneity of variance, the studentised residuals of GPS observations are also affected by various systematic effects that are insufficiently considered or completely neglected within the mathematical models and remain in the LS residuals. Regarding some representative examples shown in figure 7.2, the residual time series of PRN 24 illustrates a slowly varying trend, while obvious quasi-periodic oscillations are present in the residuals of PRN 18. Such long-periodic trends are frequently detected for low-elevation satellites, while the oscillations with increasing periods at higher elevation angles reflect the characteristics of site-specific multipath effects (Bilich et al., 2008). These remaining systematic errors may introduce non-stationary signal components, significantly affecting the temporal correlation analysis by means of (empirical or sample) ACF and ARMA processes (Brockwell and Davis, 2002, p 23; Howind, 2005, p. 55; Schön and Brunner, 2008b). Therefore, relying upon the classical component model described in section 2.2.1, a residual decomposition process is first developed in order to separate the remaining systematic effects from stochastic noise.

(a) Slowly varying trend (PRN 24) (b) Quasi-periodic oscillations (PRN 18)
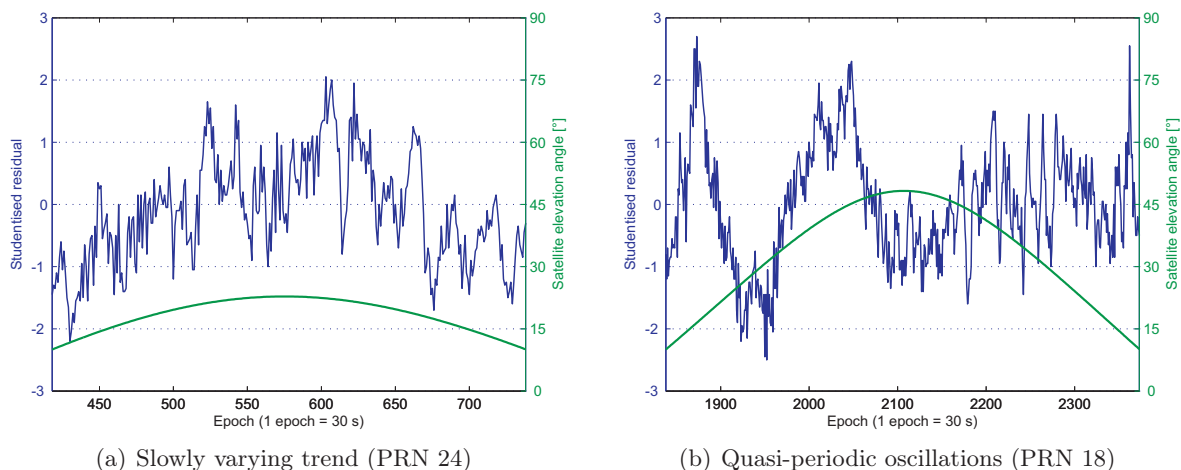
Figure 7.2: Examples of studentised residuals with significant systematic signals (SA*POS*®site: OFFE, DOY2008:276, elevation cut-off angle: $10°$, observation weighting model: $\sin^2(e)$)

7.2.2 Decomposition model

Based on the concept of the classical additive decomposition model, which subdivides a time series into a long-periodic trend, an oscillating seasonal component, and a random noise (see equation (2.21)), figure 7.3 schematically shows the residual decomposition process and its potential contributions to the mathematical models of GPS observations. The input data are time series of studentised residuals, which are available on multiple consecutive days and under almost identical satellite geometry (see section 7.2.5). The first run of the Vondrák filter produces the detrended (Vondrák) residuals (see section 7.2.3), which are subsequently used for outlier detection and repair (see section 7.2.4). The second run of the Vondrák filter on the basis of the repaired (outlier-free) studentised residuals (OFR) delivers the slowly varying and long-periodic trend component. After that, taking advantage of the daily repeating GPS satellite geometry, the site-specific effects of a quasi-periodic nature are captured by means of a sidereal stacking technique, which calculates the epoch-wise arithmetic means of the detrended residuals (DTR; Howind, 2005, p. 55). After subtracting both the trend and quasi-periodic components from the outlier-free residuals, the noise component (NCR) can be obtained, which generally represents temporally correlated coloured noise. Finally, the dependence in the noise component can be modelled by fitting appropriate ARMA processes, resulting in temporally uncorrelated white noise residuals (WNR). The decomposed systematic terms, i.e., the trend and quasi-periodic components, may contribute to refining the functional model of GPS observations, while the temporal correlations, characterised by means of ARMA estimates, should be taken into consideration in the stochastic model.

In order to verify the efficiency of the proposed residual decomposition and ARMA modelling, the statistical hypothesis tests introduced in section 2.3 are applied to the residuals after repairing outliers (OFR), detrending (DTR), sidereal stacking (NCR), and ARMA modelling (WNR). The tests for normal distribution (see section 2.3.2) are able to illustrate the effects of the remaining systematic errors on the distributional properties of GPS observables, providing additional proofs for the postulates asserted by Tiberius and Borre (1999). The trend tests (see section 2.3.3) are carried out not only to evaluate the efficiency of the detrending approach using the Vondrák filter, but also to provide valuable information for the trend modelling when performing the (non-)stationarity tests (see section 2.3.4). The unit root tests for (non-)stationarity examine the applicability of ACF and ARMA processes in more sophisticated ways than the tests for homogeneity of variances, such as the two-sample F-test, β-test, and the multi-sample Bartlett

test (Howind, 2005, p. 16, 17). The tests for uncorrelatedness (see section 2.3.5) are only applied to the residuals before and after ARMA modelling, i.e., NCR and WNR, respectively, since OFR and DTR are evidently temporally correlated due to the remaining systematic signals. Based on the results of the uncorrelatedness tests, the appropriateness of the determined ARMA models can be assessed in a statistically rigorous manner.
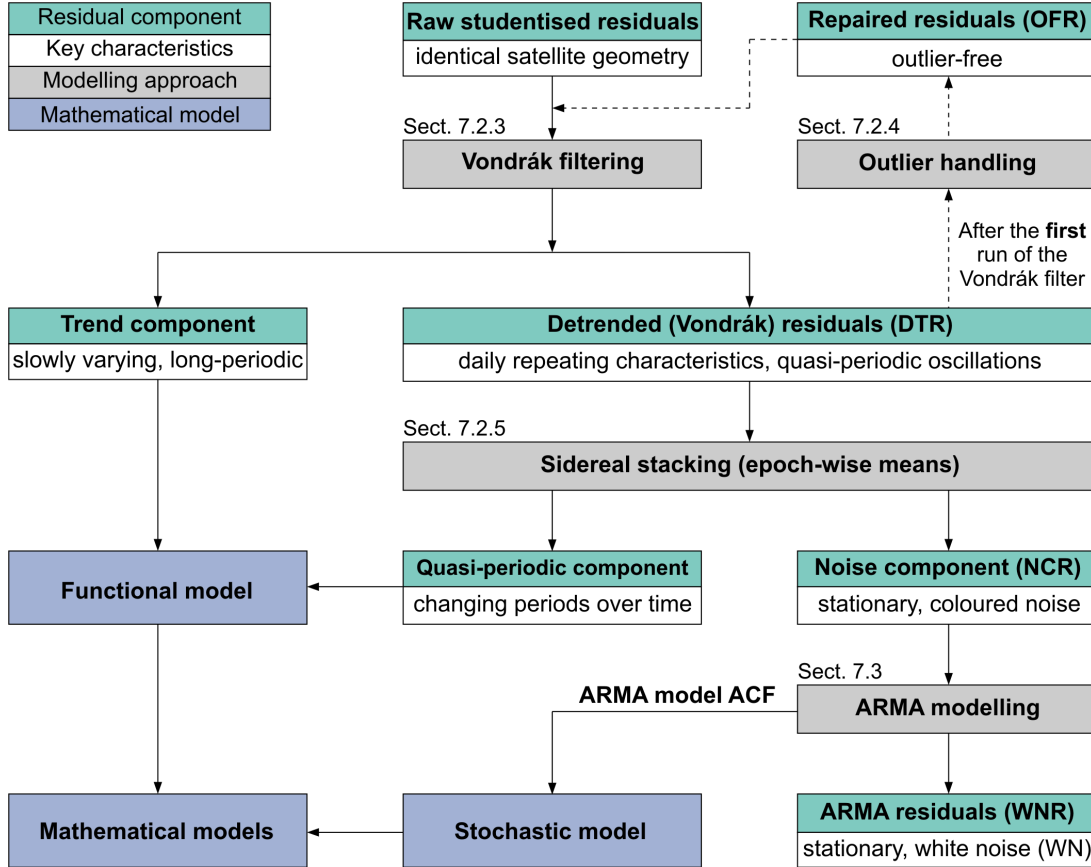
Figure 7.3: Flowchart of a residual decomposition process for analysing and modelling temporal correlations of GPS observations (ACF: autocorrelation function), after Luo (2010)

In the past, several studies have demonstrated the possibility of mitigating the remaining systematic errors by means of an improved stochastic model (Wang et al., 2002; Nahavandchi and Joodaki, 2010). Nevertheless, the proposed approach first removes the remaining systematic effects in order to fulfil the precondition of ARMA modelling. Furthermore, such a mathematically rigorous analysis procedure may construct a future temporal correlation scenario of GPS observations, where the residual systematic errors could be sufficiently considered in GPS data analysis, for example, using advanced atmospheric and multipath models.

7.2.3 Vondrák filtering

A time series of observational data can be written as (x_i, y_i), $i = 1, 2, \ldots, n$, where x_i and y_i denote the measurement epochs and the measurements, respectively. The basic idea behind the Vondrák filter is to find a compromise between absolute fitting (F) and absolute smoothing (S), which can be expressed mathematically as follows (Vondrák, 1969):

$$ Q = F + \lambda^2 S \longrightarrow \min, \quad F = \sum_{i=1}^{n} p_i \cdot (y_i' - y_i)^2, \quad S = \sum_{i=1}^{n-3} (\Delta^3 y_i')^2, \tag{7.6} $$

where y_i' is the filtered value corresponding to observation y_i, p_i is the weight of y_i, $\Delta^3 y_i'$ is the third-order difference of the filtered values calculated based on a cubic Lagrange polynomial $L_i(x)$, and λ^2 is a unitless positive coefficient that regulates the degree of filtering or the smoothness of y_i'. The smoothed curve is defined in the interval between two points (x_{i+1}, y_{i+1}') and (x_{i+2}, y_{i+2}') as $L_i(x)$, running through the four adjacent points (x_i, y_i'), (x_{i+1}, y_{i+1}'), (x_{i+2}, y_{i+2}'), and (x_{i+3}, y_{i+3}'), i.e.,

$$(\Delta^3 y_i')^2 = \int_{x_{i+1}}^{x_{i+2}} \left[L_i'''(x)\right]^2 dx = (a_i y_i' + b_i y_{i+1}' + c_i y_{i+2}' + d_i y_{i+3}')^2, \tag{7.7}$$

where the definition of the Lagrange polynomial $L_i(x)$ and the derivation of equation (7.7) are provided in Appendix B.4, along with the coefficients a_i, b_i, c_i, and d_i. To minimise the objective function Q, its first-order partial derivative with respect to y_i' is set to zero:

$$\frac{\partial Q}{\partial y_i'} = \frac{\partial F}{\partial y_i'} + \lambda^2 \frac{\partial S}{\partial y_i'} = 0, \tag{7.8}$$

where all partial derivatives have been elaborated by Vondrák (1969). The filtered values y_i' can be obtained by solving a system of n linear equations in the form

$$\boldsymbol{A} \cdot \boldsymbol{y}' = \boldsymbol{b}, \tag{7.9}$$

where $\boldsymbol{A}$ is the coefficient matrix, $\boldsymbol{y}' = (y_1', \ldots, y_n')^T$, and $\boldsymbol{b} = (b_1, \ldots, b_n)^T$ with $b_i = (p_i/\lambda^2) \cdot y_i$. While the vector $\boldsymbol{b}$ can be built up in a trivial manner, the construction of the coefficient matrix $\boldsymbol{A}$ turns out to a more complex issue. In Appendix B.5, the Vondrák coefficient matrix $\boldsymbol{A}$ and the computation of its elements are discussed in more detail.

Applying the Vondrák filter in practice, the unitless positive coefficient λ^2 must be properly specified, since it controls the degree of the compromise between the two extreme possibilities, namely absolute fitting and absolute smoothing. If $\lambda = 0$, then Q can be minimised by simply setting $y_i' = y_i$, indicating that the filtered values are identical with the measurements. This option will result in a rough curve and is known as absolute fitting. In contrast, if $\lambda \longrightarrow \infty$, then there are two conditions to be satisfied at the same time: $S = 0$ and $F \longrightarrow \min$. Under this circumstance, the use of $y_i' = y_i$ will not work, because the condition $S = 0$ will thereby not be fulfilled. However, fitting a quadratic polynomial by means of the LS algorithm satisfies both conditions simultaneously, and this option is referred to as absolute smoothing. To demonstrate the influence of λ^2 on the filter outcomes, figure 7.4 shows examples of applying the Vondrák filter with different smoothing factors ϵ, where ϵ is defined as the inverse of λ^2, i.e., $\epsilon = 1/\lambda^2$. Obviously, the smaller ϵ (larger λ), the stronger the smoothing effect. In addition, it is worth mentioning that both short- and long-periodic signals can be efficiently captured by the Vondrák filter when using appropriate smoothing factors.

In order to find the optimum value for ϵ, different methods have been proposed. Assuming that the measurement accuracy m is known, Vondrák (1969) suggested the use of the mean error $M = M(\epsilon)$, which is estimated on the basis of the Vondrák residuals $\tilde{y}_i = y_i - y_i'$ as

$$M = \left[\frac{1}{n-3} \sum_{i=1}^{n-3} p_i \cdot \tilde{y}_i^2\right]^{1/2}, \tag{7.10}$$

where $n - 3$ is the number of redundant observations. The most appropriate value of ϵ is the one for which the equation $M(\epsilon) = m$ is satisfied. By randomly sampling the observation series into a filtering and a validation series, which are denoted as $(x_{1,i}, y_{1,i})$ and $(x_{2,i}, y_{2,i})$,

(a) $\lambda = 10^2, \epsilon = 10^{-4}$ (b) $\lambda = 10^4, \epsilon = 10^{-8}$ (c) $\lambda = 10^6, \epsilon = 10^{-12}$
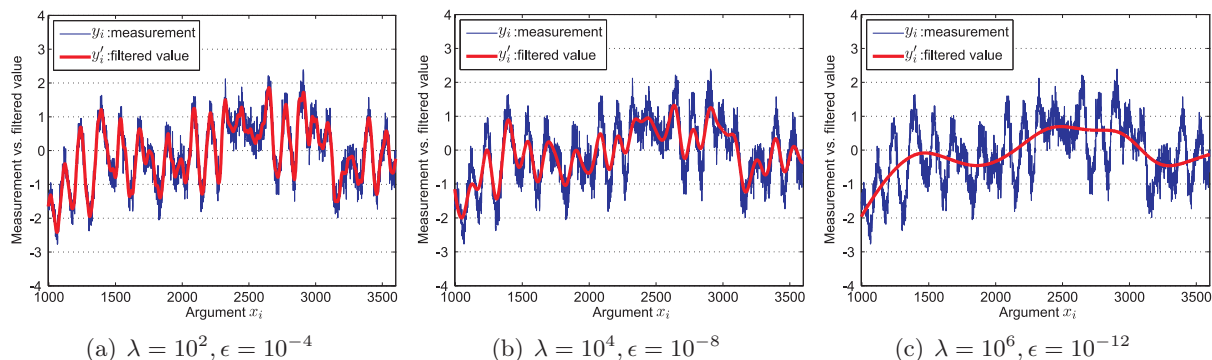
Figure 7.4: Vondrák filtering of studentised double-difference residuals with different smoothing factors (baseline: HEDA, 54.1 km, strong multipath, satellite pair: PRN 22-12, DOY2007:165)

respectively, Zheng et al. (2005) employed the cross-validation technique based on the variance of the validation series relative to the filtered values:

$$C = \frac{1}{n_2} \sum_{i=1}^{n_2} \left[y_{2,i} - f'(x_{2,i}) \right]^2, \qquad (7.11)$$

where n_2 is the length of the validation series, and $f'(x_{2,i})$ are values obtained by applying the cubic spline interpolation to the filtered values $\{y'_{1,1}, y'_{1,2}, \ldots, y'_{1,n_1}\}$ at the epoch $x_{2,i}$. Resampling the measurement data for each of the smoothing factors coming into question, the ϵ value with the smallest average C is chosen to be the optimum one. Taking advantage of the sidereal daily repeating properties of GPS multipath signals, Zheng et al. (2005) used the cross-validation Vondrák filter (CVVF) to derive multipath models for coordinate time series, obtained by processing three consecutive days of 10-Hertz GPS data from a short baseline of about 86 m. The results showed that the root mean square (RMS) of GPS positioning errors can be reduced by 20-40%. However, it should be noted that the CVVF method assumes temporally uncorrelated white noise with a Gaussian (normal) distribution. It represents an effective signal decomposer, which can be used to separate noise and signal in a data series, when the noise level is lower than the magnitude of the signal. If the noise level is higher the signal magnitude, high-frequency signals tend to be filtered out together with the noise.

Within the framework of the residual decomposition process described in section 7.2.2, the Vondrák filter is used only to capture the slowly varying and long-periodic trend component. This allows for a more physically reasonable extraction of quasi-periodic signals, for example, by means of sidereal stacking (see section 7.2.5), and avoids the significant impact of Vondrák filtering on the temporal correlation properties of the decomposed noise. Keeping these points in mind, an empirical criterion for the determination of the optimum ϵ is developed in this thesis, which maximises the similarity (or day-to-day correlation) of the detrended residual time series (DTR in figure 7.3) being available on N consecutive days:

$$R = \sum_{I=1}^{N-1} \sum_{J=I+1}^{N} \mathrm{corr}(\tilde{y}_{I,i}, \tilde{y}_{J,i}) \longrightarrow \max, \quad N > 1, \quad i = 1, \ldots, n, \qquad (7.12)$$

where $\mathrm{corr}(\cdot)$ denotes the correlation coefficient operator (e.g., using `corrcoef` in MATLAB®). Due to the actually unknown temporal correlation behaviour of the noise component, simulation studies were carried out based on representative noise and signal realisations to study the influence of ϵ on the temporal correlation properties and the applicability of the CVVF method to temporally correlated coloured noise (see section 8.1.2).

From a theoretical point of view, the Vondrák filter represents an appropriate smoothing method, since it directly treats the observations of a variable without any superfluous intermediate steps. From a practical perspective, it does not require any predefined fitting function and provides filtered values even at the two ends of a data series. In addition, being superior to the original Whittaker's method (Whittaker and Robinson, 1924, p. 303–316), the Vondrák filter is applicable to both equidistant and non-equidistant data series (Zheng and Luo, 1992; Zheng et al., 2005). Finally, the performance of the Vondrák filter is hardly restricted by non-linearities in the data, which is not the case for the smoothing algorithms based on (weighted) moving average (Vondrák, 1969; Brockwell and Davis, 2002, p. 27).

7.2.4 Outlier handling

In this thesis, outliers are defined as individual studentised residuals that are inconsistent with the statistical nature of the bulk of the data. Prior to the residual-based temporal correlation modelling, outliers should be detected and appropriately handled, since they may adversely affect the results of the Vondrák filtering, the performance of sidereal stacking, and the stationarity of the decomposed noise. Making use of the Vondrák residuals $\tilde{y}_i = y_i - y_i'$ (DTR in figure 7.3), a two-step procedure is employed, consisting of outlier identification and validation. To identify outliers in the first step, the MAD-based (median absolute deviation) criterion is used, which is also implemented in the MATLAB® Curve Fitting Toolbox™ for robust local regression. This criterion considers $\tilde{y}_i$ (and thus y_i) as an outlier if

$$|\tilde{y}_i - \text{med}(\tilde{y})| > 5MAD \quad \text{with} \quad MAD = \text{med}(|\tilde{y}_i - \text{med}(\tilde{y})|), \qquad (7.13)$$

where $\text{med}(\cdot)$ is the median operator and $\tilde{y} = \{\tilde{y}_1, \ldots, \tilde{y}_n\}$. For sample data from a normal distribution $\mathcal{N}(\mu, \sigma^2)$, it can be proved that $MAD = z_{0.75} \cdot \sigma$, where $z_{0.75} = 0.675$ is the 0.75-quantile (or upper quartile) of the standard normal distribution $\mathcal{N}(0, 1)$. Therefore, the 5-MAD criterion applied in this thesis is consistent with the commonly used 3-sigma rule for outlier detection, provided that the population can be assumed to be normal.

According to the fact that the sample variance is more sensitive to outliers than the sample mean, the F-test is undertaken in the second step to assess the influence of the identified 5-MAD outliers on the sample variance of $\tilde{y}$ (Snedecor and Cochran, 1967, p. 116; Niemeier, 2008, p. 110). Thereby, the residual data sets with and without outliers are denoted as $\tilde{y}_a$ and $\tilde{y}_b$, respectively. Since the sample variance s_a^2 is generally larger than s_b^2, the one-sided F-test for equality of variances is performed based on the F-distributed test statistic T_F

$$T_F = \frac{s_a^2}{s_b^2} = \frac{\frac{1}{n_a-1} \sum_{j=1}^{n_a} (\tilde{y}_{a,j} - \mu_a)^2}{\frac{1}{n_b-1} \sum_{k=1}^{n_b} (\tilde{y}_{b,k} - \mu_b)^2} \sim F(\nu_a, \nu_b) \qquad (7.14)$$

with $\nu_a = n_a - 1$ and $\nu_b = n_b - 1$ degrees of freedom, where n_a and n_b are the sample sizes of $\tilde{y}_a$ and $\tilde{y}_b$, respectively. The null hypothesis of equal variances $\sigma_a^2 = \sigma_b^2$, indicating an insignificant effect of the detected 5-MAD outliers, is rejected at a significance level of α if $T_F > F_{\nu_a, \nu_b; 1-\alpha}$, where $F_{\nu_a, \nu_b; 1-\alpha}$ is the $(1 - \alpha)$ quantile of the F-distribution. Since the F-test is known to be extremely sensitive to non-normality (Markowski and Markowski, 1990), it is carried out using the Vondrák residuals $\tilde{y}_i$ instead of the original studentised residuals y_i whose probability distribution may be considerably distorted by long-periodic trends. A rejection of the null hypothesis suggests the statistical significance of the outlying $\tilde{y}_i$, which are then replaced by the linearly interpolated values of the non-outlying $\tilde{y}_i$. Next, the repaired Vondrák residuals are added to the filtered values y_i' to obtain the outlier-free (or repaired) studentised residuals (OFR). After handling significant outliers by means of such a remove-repair-restore (RRR) technique, the Vondrák

filter is applied to the OFR, as changes in the residual data may lead to different smoothing factors ϵ determined using equation (7.12). The two-step approach to outlier detection has been successfully employed in residual stacking for multipath mitigation (Fuhrmann et al., 2010, p. 84) as well as in data scrubbing for distribution analysis of GPS observations (Luo et al., 2011a). More detailed statistical assessments of T_F and representative examples of outlier repair will be presented in sections 8.1.3 and 8.2.3. Figure 7.5 illustrates different effects of the identified 5-MAD outliers (black dots) on the variance of Vondrák residuals.

(a) 71 significant outliers (DOY2007:166, wet)   (b) 3 insignificant outliers (DOY2007:167, dry)
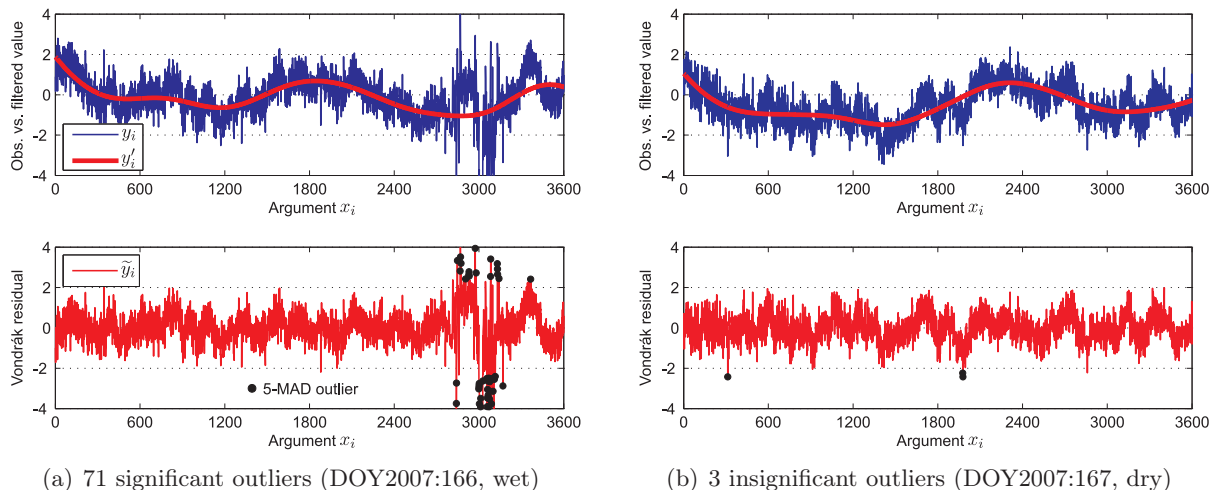
Figure 7.5: Examples of outlier detection using the 5-MAD criterion and one-sided F-test (baseline: TAAF, 53.7 km, weak multipath, satellite pair: PRN 22-12; see figure 4.8(c))

Comparing the residuals related to the same double-difference and two consecutive days, figure 7.5 depicts completely different results of outlier detection. After removing the long-periodic trends, which are sufficiently captured by the Vondrák filter in both examples, a total of 71 and 3 outlying $\tilde{y}_i$ are identified using the 5-MAD criterion for day 166 and 167, respectively. Moreover, the filtered values y_i' shown in figure 7.5(a) are hardly degraded by the outliers. Applying the F-test at a significance level of $\alpha = 1\%$, the 71 outliers lead to the rejection of the null hypothesis of equal variances, while the 3 outliers influence the Vondrák residual variance in a statistically insignificant manner. Accordingly, the 5-MAD outliers on day 166 need to be repaired. The different numbers of outliers between the two consecutive days can be explained by the different atmospheric conditions, which are particularly visible in the relative humidity (RH) measurements shown in figure 4.8(c). The number of outliers seems to be physically interpretable, and this will be discussed in more detail in sections 8.1.3 and 8.2.3.

7.2.5 Sidereal stacking

The main objective of sidereal stacking is to extract the remaining site-specific effects (e.g., multipath), which do not change significantly between consecutive days. As described in section 3.2.3, multipath effects can be subdivided into a near-field and a far-field component. The former exhibits long-periodic and non-zero mean properties, while the latter introduces short-periodic and zero mean signals. Using the Vondrák filter, the near-field multipath with a period of up to several hours (Wübbena et al., 2006a) can be effectively detected. The far-field multipath with a period of up to half an hour (Seeber, 2003, p. 317) remains in the Vondrák residuals (DTR) and can be captured during the stacking process. In general, multipath signals repeat with the daily repeating GPS satellite constellation, although variations do occur if the surface moisture content changes or the satellite orbits are considerably altered (Kim et al., 2003).

As a usual rule of thumb, the repeat time of the GPS constellation is 23 h 56 min (86160 s), indicating that the GPS satellites visible today are supposed to be visible at the same location 23 h 56 min later. A more accurate approximation of the orbit repeat time is one mean sidereal day, i.e., 23 h 56 min 4 s (86164 s). During such a period the GPS satellites complete two orbits in inertial space, and the Earth one revolution. Instead of the large-valued orbit repeat time, the term orbit repeat lag or daily advance is also used, which represents the difference between one mean solar day of 24 h (86400 s) and the orbit repeat time, amounting to approximately 236 s. In general, all GPS satellites are assumed to have the same sidereal repeat time.

Seeber et al. (1998) found that the satellite orbit repeat time is neither sidereal nor identical, but varies from satellite to satellite. The orbital period of the GPS satellites is intentionally specified to be about 4 s shorter than half a sidereal day in order to compensate for the dominant nodal drift rate ($d\Omega/dt$) of about 14.7° per year towards the west, caused by the dynamic form factor J_2 (Choi et al., 2004; Dilßner, 2007, p. 119). Therefore, it is expected that the GPS orbit repeat time is generally about 8 s shorter than one mean sidereal day. Accordingly, the orbit repeat lag is on average about 8 s larger than 236 s. Regarding the one-year satellite-specific orbit repeat periods illustrated by Dilßner (2007, p. 122), three types of signals are clearly visible. The satellite-dependent quasi-linear drifts of up to ±8 s per year are due to the resonance effects associated with the tesseral harmonics in the Earth's gravity field. Small-amplitude (< 1 s) oscillations with a period of about 14 days are produced by the lunar gravity, while large abrupt changes are attributed to satellite manoeuvres (Choi et al., 2004).

The orbit repeat time of the GPS satellites can be evaluated in different ways. Based on Kepler's third law, Choi et al. (2004) used the broadcast ephemerides to determine the orbit repeat time for each satellite. Considering the results when filtering 1-Hertz GPS position estimates, low-frequency (0.001-0.04 Hz) errors are significantly reduced. Two programs for finding the repeat periods of the GPS constellation were provided by Agnew and Larson (2007). One determines the orbit repeat time by applying Kepler's third law, and the other makes use of the aspect repeat time, representing the period over which the satellite comes closest to occupying the same topocentric place. The aspect repeat time (lag) has an average value of 86153 s (247 s) and fluctuates through the day by as much as 2.5 s at high latitudes. Moreover, the orbit and aspect repeat times can differ from each other by up to 3 s, where the aspect repeat time is usually shorter. Relying upon the autocorrelation of coordinate time series and double-difference residuals, Ragheb et al. (2007) found the optimum GPS orbit repeat time (lag) of 86154 s (246 s), providing an independent verification for the previous results. Within the context of GPS seismology, Larson et al. (2007) used 1-Hertz GPS position time series to estimate time-varying and site-dependent orbit repeat lags by maximising the peak cross-correlation or minimising the RMS difference for a range of lag values (e.g., 236-256 s). In general, the repeat lags determined using both techniques agree at the level of 1 or 2 s and are centred at about 245 s. Taking advantage of the sidereal repeatability of the GPS constellation, the orbit repeat time has been successfully used for multipath mitigation in the measurement and position domains (Choi et al., 2004; Larson et al., 2007; Ragheb et al., 2007; Zhong et al., 2010; Lau, 2012).

In this thesis, an empirical approach has been developed that enables the determination of satellite- and site-specific orbit repeat times (lags) based on GPS broadcast ephemerides. Taking satellite elevation angle as an example, the principle sketch of this empirical method is shown in figure 7.6(a). Assuming that GPS observations and (site-specific) navigation messages are available in the RINEX format on at least two consecutive days, information about satellite azimuth and elevation angle is first derived with the help of the program cf2ps (Hilla, 2002). After finding the common part of satellite geometry between the two consecutive days I and
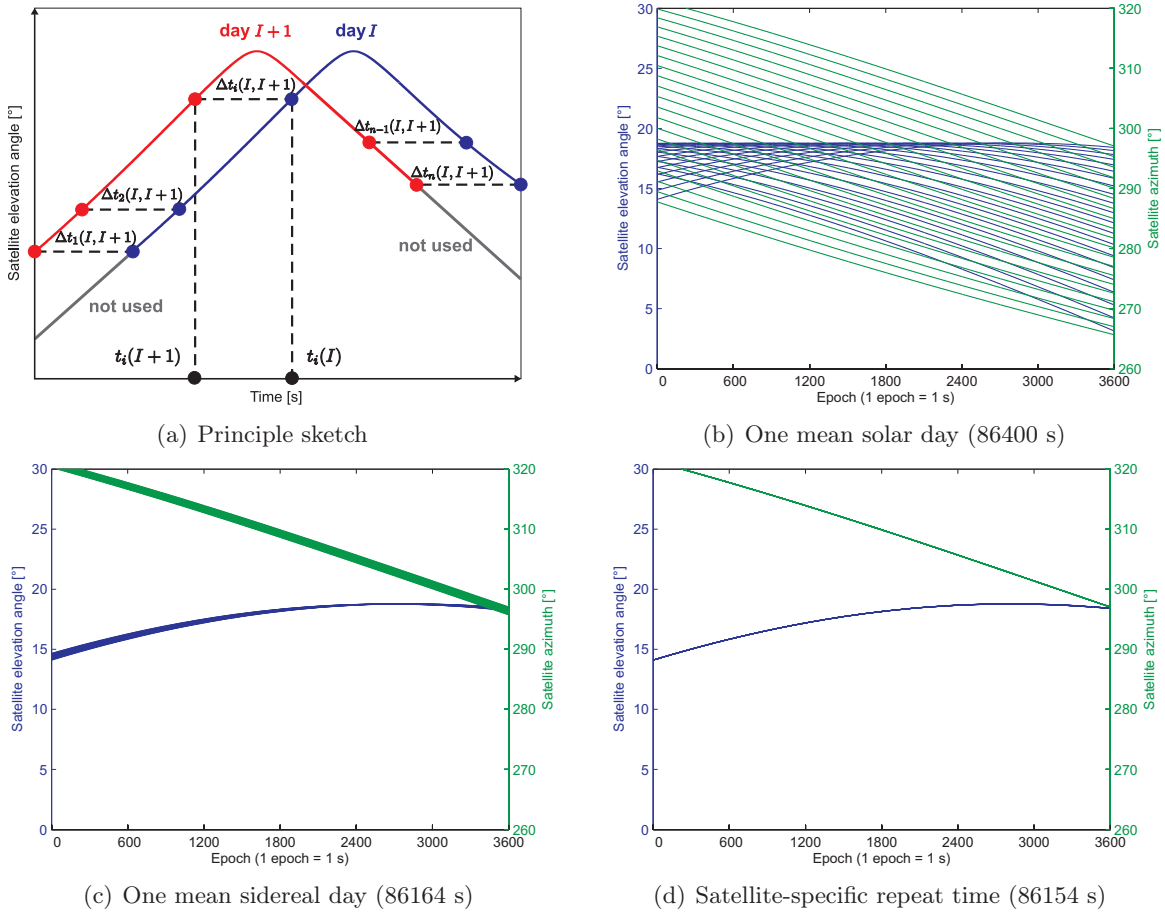
$I + 1$, the mean orbit repeat lag $\Delta t(I, I + 1)$ for a certain satellite can be computed as

$$\Delta t(I, I + 1) = \frac{1}{n} \sum_{i=1}^{n} \Delta t_i(I, I + 1) = \frac{1}{n} \sum_{i=1}^{n} \left[t_i(I) - t_i(I + 1) \right], \quad (7.15)$$

where n denotes the number of the used observations, depending on the data sampling interval. If a total of $N(N \geq 2)$ consecutive days of data are available, then the final satellite-specific orbit repeat lag Δt for the entire observation period is

$$\Delta t = \frac{1}{N - 1} \sum_{I=1}^{N-1} \Delta t(I, I + 1). \quad (7.16)$$

By considering different values for the orbit repeat time, figure 7.6 shows 1-hour satellite geometry on 21 consecutive days to demonstrate the advantage of the individually determined satellite-specific orbit repeat time. Figure 7.6(b) displays the scenario in which the sidereal repeatability of the GPS constellation or the orbit repeat lag is completely ignored. As a result, different satellite geometry prevails within the same GPS time interval on the consecutive days. This difference can be significantly reduced if one mean sidereal day of 23 h 56 min 4 s is used as the orbit repeat time (see figure 7.6(c)). Nevertheless, as figure 7.6(d) illustrates, the optimum results with respect to identical satellite geometry is achieved by means of the satellite-specific

(a) Principle sketch

(b) One mean solar day (86400 s)

(c) One mean sidereal day (86164 s)

(d) Satellite-specific repeat time (86154 s)

Figure 7.6: Empirical determination of satellite-specific orbit repeat lags and their influence on 1-hour GPS satellite geometry on 21 consecutive days (SA*POS*®site: RAVE, satellite: PRN 22, DOY2007:161-181, sampling interval: 1 s)

orbit repeat time, which is 10 s less than one mean sidereal day in this example. Section 8.1.1 will present more examples of the determined satellite-specific orbit repeat lags and the associated quality measures. Furthermore, the empirically derived lag values are verified by means of the Fortran program `orbrep.f`[1], provided by Agnew and Larson (2007).

Although the determination of satellite-specific orbit repeat times is discussed within the context of sidereal stacking, it must be considered during the course of residual data preparation. Using the satellite individual orbit repeat periods, time windows can be found in which almost identical satellite geometry prevails on multiple consecutive days (see figure 7.6(d)). Furthermore, the satellite-specific property of the orbit repeat time turns out to be an important issue when stacking residuals with a short sampling interval, for example, 1 s. Nevertheless, in the case that observation data are collected with longer sampling intervals (e.g., 30 s), it is still recommended to apply the best possible orbit repeat period (e.g., 86160 s; Ragheb et al., 2007) rather than to simply neglect it (Howind, 2005, p. 55). Under the assumption that satellite-specific orbit repeat times have been taken into account, the sidereal stacking procedure is carried out by computing the epoch-wise arithmetical means of the Vondrák residual (DTR) time series, which are available on N consecutive days:

$$s_i = \frac{1}{N} \sum_{I=1}^{N} \tilde{y}_i(I), \quad i = 1, \dots, n, \quad I = 1, \dots, N. \tag{7.17}$$

A small N (e.g., $N = 3$) may be helpful for s_i to capture short-term variations in local site environment, for example, changes in surface moisture content. In contrast, a larger N will make the stacking results less dependent on such factors, reflecting an average situation of the remaining site-specific error effects. Intuitively, the day-to-day correlation between $\tilde{y}(I)$ decreases with an increasing temporal separation distance. To achieve a better understanding, the principle of sidereal stacking is schematically shown in figure 7.7.
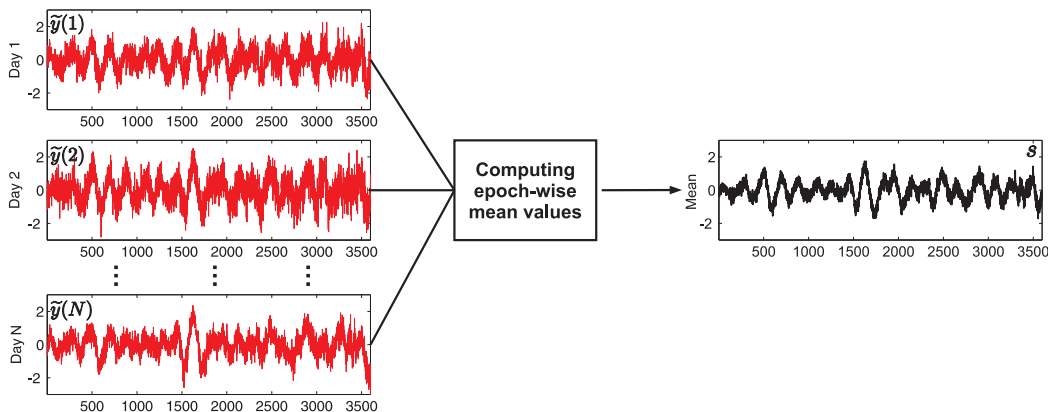

Figure 7.7: Sidereal stacking by calculating epoch-wise mean values (see equation (7.17))

After performing Vondrák filtering and sidereal stacking, the long-periodic trend y_i' (see equation (7.6)) and short-periodic oscillation s_i (see equation (7.17)) can be obtained separately. A further subtraction of s_i from the Vondrák residuals $\tilde{y}_i(I)$ results in the noise component NCR, which is supposed to be homoscedastic and temporally correlated (i.e., coloured noise). Since the remaining systematic effects have been largely reduced, the sample ACF can be conveniently used to assess the degree of the noise's temporal correlation. If it is significant, an appropriate ARMA time series model can be estimated to characterise the correlation behaviour and exploit it to predict future values.

---

[1] Available free of charge at `www.ngs.noaa.gov/gps-toolbox/Larson.htm`

7.3 ARMA modelling

ARMA modelling aims for the determination of an appropriate $ARMA(p, q)$ model as given in equation (2.42) to represent a stationary time series $\{x_1, x_2, \ldots, x_n\}$, for example, the noise component obtained from the residual decomposition process (see section 7.2.2). It involves a number of interrelated problems, such as parameter estimation (i.e., computing the coefficients $\{a_1, \ldots, a_p\}$, $\{b_1, \ldots, b_q\}$, and the white noise variance σ_Z^2), order selection (i.e., finding the optimum orders p and q), and model identification (i.e., deciding among the best-fitting AR, MA, and ARMA models). In this thesis, ARMA modelling is carried out by means of the ARMASA Toolbox[2], which is available free of charge in MATLAB$^{\circledR}$ Central and allows for an automatic identification of the best-fitting ARMA model for a given noise realisation (Broersen, 2000b). The determination of a suitable $ARMA(p, q)$ model using the ARMASA Toolbox mainly consists of two steps: order selection and model identification, schematically shown in figure 7.8.
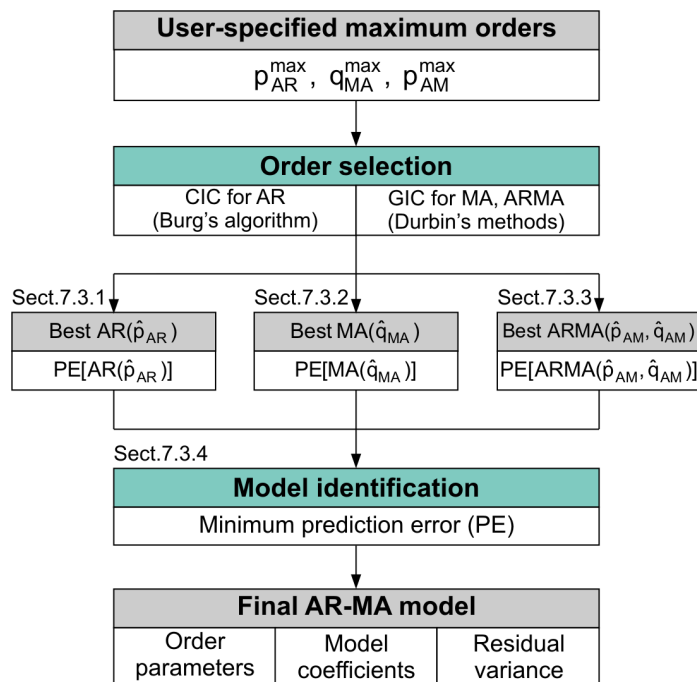
Figure 7.8: ARMA modelling using the ARMASA Toolbox, after Luo et al. (2011b)

In the first step, AR, MA, and ARMA models are computed to some user-specified maximum orders $p_{AR}^{\max}$, $q_{MA}^{\max}$, and $(p_{AM}^{\max}, p_{AM}^{\max} - 1)$, respectively. For AR estimation, Burg's maximum entropy algorithm (Burg, 1967) is applied, where the best model candidate is chosen based on the combined information criterion (CIC, see section 7.3.1; Broersen, 2000c). For MA and ARMA estimation, Durbin's first (Durbin, 1959) and second (Durbin, 1960) methods are employed, along with the generalised information criterion (GIC, see section 7.3.2; Broersen, 2000b) for order selection. In the second step, the model identification among the best-fitting AR, MA, and ARMA candidates is performed using an accuracy measure called prediction error (PE, see section 7.3.4; Broersen, 2006, p. 99). The model candidate with the minimum PE is identified as the final AR-MA(p, q) model for the given data. The notation AR-MA(p, q) is used if AR, MA, and ARMA processes are not intentionally distinguished. In this section, both the algorithms for parameter estimation and the criteria for model selection are briefly described. For a more detailed discussion of ARMA modelling, the reader is referred to the cited original articles and textbooks, for example, Brockwell and Davis (2002, chap. 5) and Broersen (2006).

---

[2]Available at www.mathworks.com/matlabcentral/fileexchange/1330

7.3.1 AR estimation

The AR process of order p defined by equation (2.43) plays an important role in time series analysis. Using the so-called Yule-Walker equations, given by

$$\boldsymbol{\Gamma}_p \cdot \boldsymbol{\alpha}_p = -\boldsymbol{\gamma}_p \quad \text{and} \quad \gamma(0) + \boldsymbol{\alpha}_p^T \cdot \boldsymbol{\gamma}_p = \sigma_Z^2, \tag{7.18}$$

the vector of AR coefficients $\boldsymbol{\alpha}_p = (a_1, \ldots, a_p)^T$ and the white noise (WN) variance σ_Z^2 can be determined based on the true covariance matrix $\boldsymbol{\Gamma}_p = [\gamma(i - j)]_{i,j=1}^p$ (cf. equation (2.37)) and the true autocovariance vector $\boldsymbol{\gamma}_p = [\gamma(1), \ldots, \gamma(p)]^T$ (Brockwell and Davis, 2002, p. 139; Broersen, 2006, p. 91). In the case of finite samples, where the true autocovariances $\gamma(h)$ are generally unknown, the biased estimates $\hat{\gamma}(h)$ (see equation (2.35)) are usually substituted for the true covariances $\gamma(h)$ into equation (7.18). The approximation of $\gamma(h)$ by $\hat{\gamma}(h)$ is accurate only if the length of the observed data is much larger than the length of the true autocovariance function (ACVF), where a short ACVF indicates uncorrelatedness at small lags (Broersen, 2006, p. 44). Accordingly, in the literature, $\hat{\gamma}(h)$ is often referred to as the asymptotically unbiased estimator for the true ACVF. The deviation from the asymptotical theory may produce severe biases in the estimated model parameters (Broersen and Wensink, 1993). In addition to the Yule-Walker solution, the AR(p) parameters can also be estimated simultaneously using the forward least-squares (LS) algorithm by minimising the residual sum of squares (RSS)

$$RSS(p) = \sum_{t=p+1}^{n} (x_t + \hat{a}_1 x_{t-1} + \cdots + \hat{a}_p x_{t-p})^2, \tag{7.19}$$

where n denotes the length of $\{x_t\}$. However, the LS method does not necessarily guarantee the stationarity and causality of the AR model estimate (see section 2.2.3; Broersen, 2006, p. 125). Causality is often required, for example, in filter design (Klees et al., 2003).

In comparison to the above-mentioned approaches, Burg's method, also known as the maximum entropy algorithm, is preferred in the practice of AR estimation, because it always produces causal models (Klees and Broersen, 2002, p. 5; Broersen, 2006, p. 126) and frequently delivers higher Gaussian likelihood than the Yule-Walker method (Brockwell and Davis, 2002, p. 406). In principle, Burg's algorithm determines each AR coefficient individually by successively minimising the corresponding sum of squares of the forward and backward residuals. According to Broersen (2006, p. 127), for a given noise time series $\{x_t\}$ with n elements, the forward (f) and backward (b) residuals of intermediate order k ($k \geq 0$) are defined as

$$f_0(t) = b_0(t) = x_t, \tag{7.20}$$

$$f_k(t) = x_t + \hat{a}_1^k x_{t-1} + \cdots + \hat{a}_k^k x_{t-k}, \tag{7.21}$$

$$b_k(t) = \hat{a}_k^k x_t + \hat{a}_{k-1}^k x_{t-1} + \cdots + x_{t-k}, \tag{7.22}$$

where $t = k + 1, \ldots, n$. If $\hat{\boldsymbol{\alpha}}^{[k]} = (\hat{a}_1^k, \hat{a}_2^k, \ldots, \hat{a}_k^k)^T$ is the vector of the estimated AR coefficients and $\tilde{\hat{\boldsymbol{\alpha}}}^{[k]} = (\hat{a}_k^k, \hat{a}_{k-1}^k, \ldots, \hat{a}_1^k)^T$ is its reversal vector, the forward and backward residuals at stage k can be written in the matrix form as

$$f_k(t) = \begin{pmatrix} x_t & x_{t-1} & \cdots & x_{t-k} \end{pmatrix} \begin{pmatrix} 1 \\ \hat{\boldsymbol{\alpha}}^{[k]} \end{pmatrix}, \tag{7.23}$$

$$b_k(t) = \begin{pmatrix} x_t & x_{t-1} & \cdots & x_{t-k} \end{pmatrix} \begin{pmatrix} \tilde{\hat{\boldsymbol{\alpha}}}^{[k]} \\ 1 \end{pmatrix}. \tag{7.24}$$

Employing the Levinson-Durbin recursion (Broersen, 2006, p. 94), which relates the coefficients of the AR$(k-1)$ model to those of the AR(k) model by

$$\hat{\boldsymbol{\alpha}}^{[k]} = \begin{pmatrix} \hat{\boldsymbol{\alpha}}^{[k-1]} + \hat{a}_k^k \cdot \tilde{\hat{\boldsymbol{\alpha}}}^{[k-1]} \\ \hat{a}_k^k \end{pmatrix}, \tag{7.25}$$

the forward and backward residuals of order k become

$$f_k(t) = f_{k-1}(t) + \hat{a}_k^k b_{k-1}(t-1), \tag{7.26}$$

$$b_k(t) = b_{k-1}(t-1) + \hat{a}_k^k f_{k-1}(t). \tag{7.27}$$

To minimise the sum of the squares of the forward and backward residuals, i.e.,

$$RSS(k) = \sum_{t=k+1}^{n} \left[f_k^2(t) + b_k^2(t) \right], \tag{7.28}$$

its derivative with respect to $\hat{a}_k^k$ is set to zero. Then, the single unknown $\hat{a}_k^k$, representing the final Burg's estimate of a_k^k, can be expressed explicitly by

$$\hat{a}_k^k = \frac{-2 \sum_{t=k+1}^{n} \left[f_{k-1}(t) \cdot b_{k-1}(t-1) \right]}{\sum_{t=k+1}^{n} \left[f_{k-1}^2(t) + b_{k-1}^2(t-1) \right]}, \tag{7.29}$$

provided that the AR$(k-1)$ model has already been estimated by means of Burg's algorithm. Considering the inequality $f_{k-1}^2(t) + b_{k-1}^2(t-1) \geq \pm 2 f_{k-1}(t) \cdot b_{k-1}(t-1)$, the estimate $\hat{a}_k^k$ will never be larger than one in absolute value. This indicates that all zeros of the AR polynomial given by equation (2.46) are outside the unit circle, and thus the determined AR(k) model is causal (Broersen, 2006, p. 128). The residual variance can be computed recursively using

$$\hat{s}_k^2 = \hat{s}_{k-1}^2 \left[1 - (\hat{a}_k^k)^2 \right], \tag{7.30}$$

where a detailed proof of equation (7.30) is provided by Brockwell and Davis (2002, p. 70). The starting values of the Levinson-Durbin recursion

$$s_0^2 = \gamma(0), \quad a_1^1 = \boldsymbol{\alpha}^{[1]} = -\frac{\gamma(1)}{s_0^2}, \quad s_1^2 = s_0^2 \left[1 - (a_1^1)^2 \right] \tag{7.31}$$

can be used to initialise Burg's successive estimation. In fact, the starting value for a_1^1 can be derived from equations (7.26)-(7.29). For finite samples, the sample variance $\hat{\gamma}(0)$ and the lagged product autocovariance $\hat{\gamma}(1)$ are substituted into equation (7.31) for $\gamma(0)$ and $\gamma(1)$, respectively. After estimating all AR models to some user-specified maximum order $p_{AR}^{\max}$, the optimum AR$(\hat{p}_{AR})$ model is selected as the one that minimises the combined information criterion

$$\text{CIC}(p) = \ln s_p^2 + \max \left(\prod_{k=0}^{p} \frac{1 + 1/(n+1-k)}{1 - 1/(n+1-k)} - 1, \quad 3 \sum_{k=0}^{p} \frac{1}{n+1-k} \right) \tag{7.32}$$

with the residual variance

$$s_p^2 = \sigma_X^2 \prod_{k=1}^{p} (1 - r_k^2), \tag{7.33}$$

where σ_X^2 denotes the process variance, and r_k is known as the reflection coefficient of order k, defined as the negative of the partial correlation at lag k (Broersen, 2006, p. 90, 96, 200). Comparing equations (7.30) and (7.33) with each other, r_k is actually identical with the AR

coefficient a_k. Applying Burg's method, all absolute values of the reflection coefficients are less than one. Therefore, the residual variance s_p^2 given by equation (7.33) tends to decrease with increasing p. To avoid over-parameterisation, the second summand of the CIC becomes larger as p increases. Moreover, the CIC takes a higher penalty factor of 3 than Akaike's information criterion (AIC) using a penalty factor of 2 (Akaike, 1973). The higher the penalty factor, the smaller the probability of overfitting (Broersen, 2006, p. 192). In Broersen (2000c), the CIC was reported to perform better than the AIC, if the candidate order is higher than $0.1n$. This advantage is of particular importance when estimating AR models for short data sets. To achieve accurate model estimates with moderate computational time, the highest candidate order for model selection with the CIC is $\min(n/2, 1000)$ in the ARMASA Toolbox. If the highest available candidate is selected, it is advisable to try higher AR candidate orders (Broersen, 2006, p. 224).

7.3.2 MA estimation

For a given noise realisation, the determination of an appropriate MA model defined by equation (2.44) is more complicated than the AR estimation. Applying the innovation algorithm, for example, described in Brockwell and Davis (2002, p. 71), the initial estimates of the MA model parameters can be computed recursively, which are then optimised within an iterative and non-linear process to maximise the Gaussian likelihood. However, the optimisation cannot be always achieved at the specified accuracy level. Furthermore, the obtained MA model is not necessarily invertible (see section 2.2.3; Klees and Broersen, 2002, p. 6). In the ARMASA Toolbox, Durbin's first method is implemented for MA estimation, since it always produces invertible MA models (Broersen, 2006, p. 136). Based on the asymptotical equivalence of $AR(\infty)$ and $MA(q)$ (Brockwell and Davis, 2002, p. 233), Durbin's algorithm makes use of a long AR process of order M ($AR(M)$) as an intermediate stage to approximate the $MA(q)$ process $B_q(r)$, i.e.,

$$C_M(r)x_t = \hat{z}_t, \quad x_t = B_q(r)z_t, \tag{7.34}$$

where $C_M(r)$ is the Mth-degree characteristic polynomial of $AR(M)$, and $B_q(r)$ is given by equation (2.47). Best results were reported in Broersen (2000a) if $M = 2\hat{p}_{AR} + q$, where $\hat{p}_{AR}$ is the optimum AR order selected by means of the CIC (see equation (7.32)). Since $\hat{z}_t \approx z_t$ holds for large M, for an arbitrary MA order q, it follows from equation (7.34) that

$$C_M(r)B_q(r) \approx 1, \quad B_q(r) \approx 1/C_M(r). \tag{7.35}$$

An estimate of B_q can be obtained by fitting an $AR(q)$ model using the Yule-Walker algorithm, if one treats the $AR(M)$ parameters $\{\hat{c}_1, \ldots, \hat{c}_M\}$ as a noise realisation (Broersen, 2006, p. 136). According to Broersen (2006, p. 224), the residual variance s_q^2 can be determined in an empirical manner by filtering the noise realisation $\{x_t\}$ with $\hat{B}_q^{-1}(r)$:

$$\hat{z}_t = \hat{B}_q^{-1}(r)x_t, \quad \hat{s}_q^2 = \frac{1}{n}\sum_{t=1}^{n}\hat{z}_t^2. \tag{7.36}$$

After determining all MA models to some user-specified maximum order $q_{MA}^{\max}$, the best-fitting $MA(\hat{q}_{MA})$ process is chosen by minimising the generalised information criterion

$$\text{GIC}(q) = \ln s_q^2 + 3\frac{q}{n}. \tag{7.37}$$

The maximum q specified in the ARMASA Toolbox is $\min(n/5, 400)$, which is lower than that for AR estimation. This is mainly due to the use of a long AR model as an intermediate stage in the MA estimation (Broersen, 2006, p. 180, 224).

7.3.3 ARMA estimation

The estimation of an ARMA(p, q) model turns out to be the most complicated step. The difficulties consist not only in the non-linearity of MA parameter estimation, but also in the separation of the process dynamics into the AR and MA components. In practice, the Hannen-Rissanen algorithm can be used to obtain preliminary model parameters by performing a high-order AR estimation and a LS linear regression (Hannen and Rissanen, 1982; Brockwell and Davis, 2002, p. 156). Next, a non-linear optimisation of the initial estimates is undertaken to maximise the Gaussian likelihood function. As mentioned before, the maximum likelihood solution does not guarantee reliable parameter determination due to the inherent convergence problem and deficiencies in producing causal and invertible models.

From a given noise sequence $\{x_t\}$, the ARMASA Toolbox determines ARMA models by means of Durbin's second method. Using Durbin's first method, the unknown residuals of an ARMA(p, q) process can be estimated by approximating a long AR(M) model:

$$C_M(r)x_t = \hat{z}_t, \quad A_p(r)x_t = B_q(r)z_t. \tag{7.38}$$

The order M is chosen to be $M = 3\hat{p}_{AR} + p + q$ (Broersen, 2000a), where $\hat{p}_{AR}$ is the order of the best-fitting AR process with the minimum CIC (see equation (7.32)). Based on the residual estimates $\{\hat{z}_t\}$, the parameters of $\hat{A}_p(r)$ and $\hat{B}_q(r)$ can be obtained by minimising

$$\sum_{t=\max(p,q)+1}^{n} \left[\hat{A}_p(r)x_t - \hat{B}_q(r)\hat{z}_t \right]^2. \tag{7.39}$$

The estimates of $A_p(r)$ and $B_q(r)$ only represent an initial approximation of the true ARMA process and do not necessarily satisfy the causality and invertibility requirements. Therefore, $\hat{A}_p(r)$ and $\hat{B}_q(r)$ are improved successively within a two-step procedure. In the first step, $\hat{A}_p(r)$ is used together with $C_M(r)$ to obtain a better estimate of $B_q(r)$ by

$$\hat{B}_q'(r) \approx C_M^{-1}(r)\hat{A}_p(r), \tag{7.40}$$

which can be easily derived from equation (7.38) by setting $\hat{z}_t \approx z_t$. In the second step, the enhanced MA estimate $\hat{B}_q'(r)$ is used to derive a better estimate of $A_p(r)$ by

$$\hat{A}_p'(r) \approx C_M(r)\hat{B}_q'(r). \tag{7.41}$$

The original method proposed by Durbin (1960) performs iterative updates of the MA and AR parameters until the estimates converge. Iteration of equations (7.40) and (7.41) will considerably improve the quality of the estimated ARMA model, if the initial AR estimate $\hat{A}_p(r)$ is very poor (Klees and Broersen, 2002, p. 7; Broersen, 2006, p. 145).

To find the best-fitting ARMA$(\hat{p}_{AM}, \hat{q}_{AM})$ model for the given noise data $\{x_t\}$, the residual variance $s_{p,q}^2$ is computed for each ARMA candidate after filtering $\{x_t\}$ with $\hat{A}_p'(r)/\hat{B}_q'(r)$ by

$$\hat{z}_t = \frac{\hat{A}_p'(r)}{\hat{B}_q'(r)}x_t, \quad \hat{s}_{p,q}^2 = \frac{1}{n}\sum_{t=1}^{n} \hat{z}_t^2. \tag{7.42}$$

The final ARMA order $(\hat{p}_{AM}, \hat{q}_{AM})$ is selected as the pair that minimises the GIC$(p + q)$ given by equation (7.37). When choosing ARMA order candidates, the ARMASA Toolbox does not consider all possible (p, q) combinations within the user-specified maximum order $p_{AM}^{\max}$, but only examines the so-called hierarchical ARMA models with $q = p - 1$. Accordingly, the highest

order candidate is ARMA$(p_{AM}^{\max}, p_{AM}^{\max} - 1)$, and the best-fitting ARMA model possesses the order $(\hat{p}_{AM}, \hat{p}_{AM} - 1)$ and the minimum GIC$(2\hat{p}_{AM} - 1)$. The special nesting of $(p, p - 1)$ is due to the fact that the hierarchical ARMA models are good discrete approximations for continuous time processes (Priestly, 1981, p. 382), and enables a significant reduction in the required computational time. Furthermore, limiting the selection candidates exclusively to ARMA$(p, p - 1)$ models reduces the loss in model quality caused by the order selection process (Broersen and de Waele, 2004). However, one disadvantage is that the true underlying ARMA process may not always be among the nested candidate models, which does not necessarily has a negative impact on the quality of model estimates (Broersen, 2006, p. 215). Using the ARMASA Toolbox, ARMA$(p, p - 1)$ models are evaluated for $p = 2, \ldots, \min(n/10, 200)$ (Broersen, 2006, p. 225).

7.3.4 AR-MA identification

Once the best-fitting AR$(\hat{p}_{AR})$, MA$(\hat{q}_{MA})$, and ARMA$(\hat{p}_{AM}, \hat{p}_{AM} - 1)$ model candidates are selected, the model identification is carried out based on the minimum squared error of the one-step prediction, simply called the prediction error (PE). Figure 7.9 illustrates the difference between the PE and residual variance, computed by equations (7.33), (7.36), and (7.42) for AR, MA and ARMA models, respectively. If the parameter estimates (i.e., $\hat{p}$, $\hat{q}$, $\hat{A}_{\hat{p}}(r)$, $\hat{B}_{\hat{q}}(r)$) and the residuals $\{\hat{z}_t\}$ are related to the same data series, for example, $\{x_t\}$, the variance of $\{\hat{z}_t\}$ is referred to as the residual variance. In contrast, the term PE is defined as the variance of the residuals, obtained by filtering the data series from the same AR-MA(p, q) process, for example, $\{x_t'\}$, which, however, has not contributed to determining the model parameters.
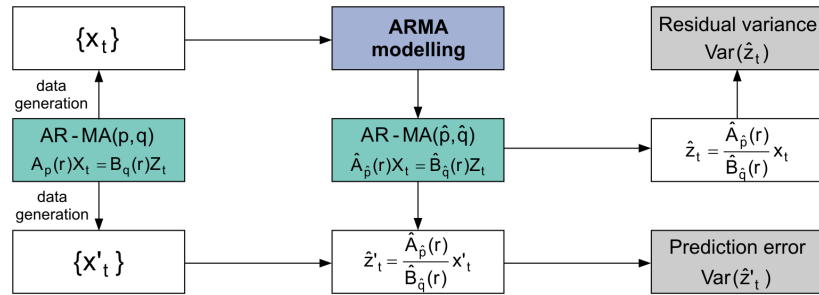
Figure 7.9: Difference between residual variance and prediction error

Note that the minimum obtainable PE is the white noise variance σ_Z^2, which occurs when the true AR-MA process and the model estimate are identical (Broersen, 2006, p. 101). For unbiased AR-MA$(\hat{p}, \hat{q})$ estimates, i.e., $\hat{p} \geq p$ and $\hat{q} \geq q$, the asymptotic expectation of the PE is

$$\mathrm{E}(PE) = \sigma_Z^2 \left(1 + \frac{\hat{p} + \hat{q}}{n} \right), \tag{7.43}$$

where n is the number of observations (Broersen, 2006, p. 129). The residual variance is always smaller than the PE due to the dependence between the data and parameter estimates (Klees and Broersen, 2002, p. 4). As a scaled version of the PE, the model error

$$ME = n \left(\frac{PE}{\sigma_Z^2} - 1 \right) \tag{7.44}$$

provides an easy measure for assessing the quality of the model estimates (Broersen, 2006, p. 102). Regarding equations (7.43) and (7.44) together, for unbiased AR-MA estimates, the asymptotic expectation of the ME does not depend on the number of observations and is equal to the sum of the selected orders, i.e., $\mathrm{E}(ME) = \hat{p} + \hat{q}$. The term $\hat{p} + \hat{q}$ is also known as the Cramér-Rao

lower bound (Stoica and Moses, 1997, p. 286) for achievable accuracy with unbiased models. According to Broersen (2000b), the PE for the best-fitting $AR(\hat{p}_{AR})$ model is

$$PE(\hat{p}_{AR}) = s_{\hat{p}_{AR}}^2 \prod_{k=1}^{\hat{p}_{AR}} \frac{1 + 1/(n+1-k)}{1 - 1/(n+1-k)}, \tag{7.45}$$

where $s_{\hat{p}_{AR}}^2$ is the associated residual variance (see equation (7.33)). For the optimum $MA(\hat{q}_{MA})$ and $ARMA(\hat{p}_{AM}, \hat{q}_{AM} = \hat{p}_{AM} - 1)$ models, the PE can be calculated using

$$PE(m) = s_m^2 \frac{1 + m/n}{1 - m/n}, \tag{7.46}$$

where the parameter m denotes the number of the estimated model coefficients, i.e., $m = \hat{q}_{MA}$ and $m = \hat{p}_{AM} + \hat{q}_{AM} = 2\hat{p}_{AM} - 1$, respectively, and s_m^2 is the residual variance of the corresponding model (see equations (7.36) and (7.42)). The best-fitting model candidate with the minimum PE is identified as the final time series model for a given noise realisation. Filtering the coloured noise with the estimated AR-MA model, the residual time series should represent a white noise sequence. Therefore, the efficiency of the AR-MA estimate in characterising the noise's temporal correlation behaviour can be assessed by testing the residuals for uncorrelatedness. To demonstrate the high performance of the ARMASA Toolbox in modelling temporal correlations of GPS observations, figure 7.10 presents the results of fitting an AR-MA model to a decomposed noise series from a PPP data analysis using the Bernese GPS Software 5.0.
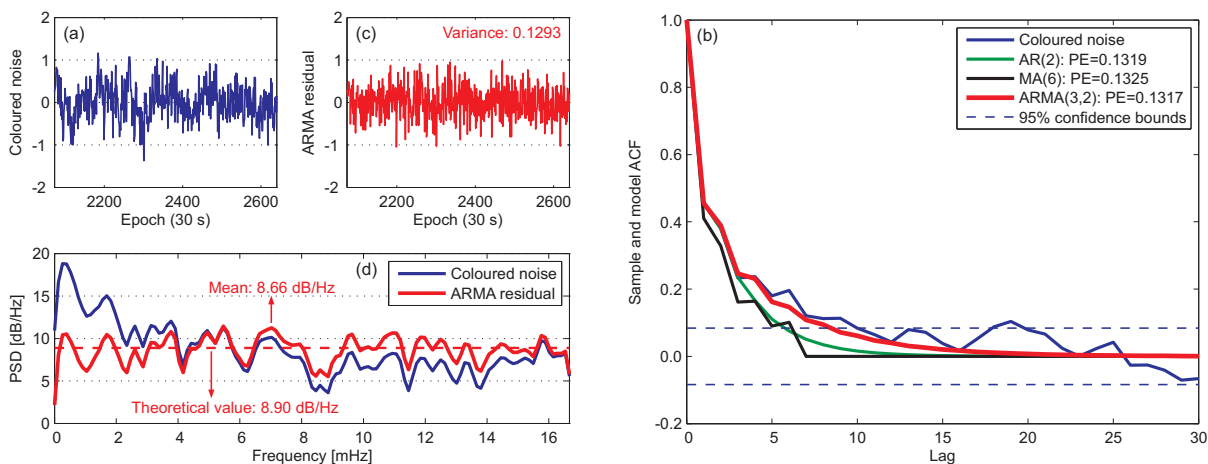
Figure 7.10: Example of ARMA modelling using the ARMASA Toolbox (a) decomposed noise series, (b) sample and model ACF, (c) ARMA residuals, (d) power spectral density (PSD) before and after ARMA modelling (SA*POS*®site: TUEB, weak multipath, satellite: PRN 32, DOY2008:275, sampling interval: 30 s)

The decomposed noise series to be analysed is shown in figure 7.10(a), and the associated sample and model ACF of the best-fitting AR, MA, and ARMA candidates are depicted in figure 7.10(b). Due to the minimum PE, the $ARMA(3,2)$ model is considered to be the most appropriate one to describe the noise's temporal correlation behaviour. This PE-based model identification can be verified by comparing the model and sample ACF curves. Obviously, the $ARMA(3,2)$ process produces the best-fitting model ACF. After filtering the coloured noise with the estimated $ARMA(3,2)$ model, the residual time series is displayed in figure 7.10(c), with a sample variance of 0.129 computed by means of equation (7.42). As expected, this residual variance is smaller than the corresponding PE of 0.1317, which is attributed to the dependence between the data and parameter estimates (see figure 7.9). To assess the efficiency of the $ARMA(3,2)$ model,

figure 7.10(d) compares the power spectral density (PSD) estimates of the coloured noise and ARMA residuals. According to the fact that a white noise process $\mathrm{WN}(0, \sigma_Z^2)$ has a constant PSD function of $\sigma_Z^2/(2\pi)$ (Brockwell and Davis, 2002, p. 118), the ARMA residuals appear to be largely uncorrelated, and the associated mean PSD is very close to the theoretical value, with a relative bias of about 3%. More results of the ARMA modelling will be presented in sections 8.1.6 and 8.2.6, along with the associated performance assessments, for example, using suitable statistical hypothesis tests (see sections 8.1.7 and 8.2.7).

7.4 Concluding remarks

Reviewing the previous studies on temporal correlations of GPS observations, there are two main deficiencies in the proposed approaches using autocorrelation functions (ACF) and first-order autoregressive (AR(1)) processes, namely statistically rigorous verification of the assumed stationarity and appropriate handling of the remaining systematic effects. In order to take these aspects into account, this chapter initially introduced a residual decomposition process, which captures the long-periodic trends and quasi-periodic oscillations with the help of Vondrák filtering and sidereal stacking, respectively. Next, the decomposed noise is described by the best-fitting autoregressive moving average (ARMA) model, determined automatically by means of the ARMASA Toolbox. The reliable performance of the suggested residual-based temporal correlation modelling is ensured by applying the studentised residuals with homogenous variances, an effective procedure for handling outliers, and a satellite-specific determination of orbit repeat times. The main advantages of such a methodically sophisticated and mathematically rigorous modelling approach are summarised as follows:

- Being largely free of the residual systematic effects, the decomposed noise is supposed to be essentially stochastic. Therefore, from a theoretical point of view, it is reasonable to characterise it in the stochastic model of GPS observations. Moreover, in the absence of systematic signals, the derived temporal correlation may provide a more realistic picture of the statistical properties of GPS measurement noise.

- The separation between long-periodic trends and quasi-periodic oscillations makes it possible to study their individual influences on the residual statistical properties, such as probability distribution, stationarity, and temporal correlation.

- The extension from AR(1) to AR-MA(p, q) processes allows for a more accurate characterisation of the noise's temporal correlation behaviour. In addition, an evaluation of the selected orders and identified model types based on representative data sets can verify the sufficiency of the commonly used AR(1) models.

- In comparison to sample and empirically fitted ACF, causal and invertible AR-MA(p, q) models determined using information criteria and statistical measures are mathematically more rigorous. They provide not only correlation information in the form of model ACF, but also establish linear relationships between observables at different epochs. This may be exploited in developing a dynamic GPS stochastic model which propagates over time.

The efficiency of residual decomposition and ARMA modelling can be visually assessed by performing continuous wavelet transforms (see section 2.4), and statistically verified by applying hypothesis tests for normality, trend, (non-)stationarity, and uncorrelatedness (see section 2.3).

Chapter 8

Results of Residual–based Temporal Correlation Modelling

Using the studentised GPS residuals from the short-term relative positioning and long-term precise point positioning (PPP) case studies (see sections 4.2.3 and 4.3.2), this chapter presents the outcome of the temporal correlation modelling described in chapter 7 with respect to satellite geometry, multipath impact, and atmospheric conditions. Prior to this, the results of computing satellite-specific orbit repeat lags, determining appropriate Vondrák filter parameters, and detecting significant residual outliers are shown. The efficiency of the proposed residual decomposition and ARMA modelling is visually assessed based on wavelet scalograms and statistically evaluated by means of hypothesis tests. Making use of the estimated ARMA models, the PPP stochastic model is extended by taking the noise's temporal correlation into account.

8.1 Case study 2: short-term relative positioning

This case study uses a subset of the residuals from the short-term relative positioning, namely 10 days (DOY2007:161-170) of 1-hour studentised double-difference residuals (SDDR) of the ionosphere-free linear combination LC3 (see table 4.5). The data sampling interval is 1 s, and the observation weighting model is the proposed SNR-based EMPSNR2 (see section 5.3). Analysing representative observational data in terms of baseline length (see table 4.3), multipath impact (see figure 4.6), and atmospheric conditions (see figure 4.8), the effects of these factors on the noise's temporal correlation properties and the results of ARMA modelling can be studied. Considering the 1-second data sampling interval, an accurate determination of satellite-specific orbit repeat lags plays an important role in residual homogenisation with regard to satellite geometry. As illustrated in figure 7.6, appropriate orbit repeat lags are essential for similar satellite-receiver geometry on multiple consecutive days.
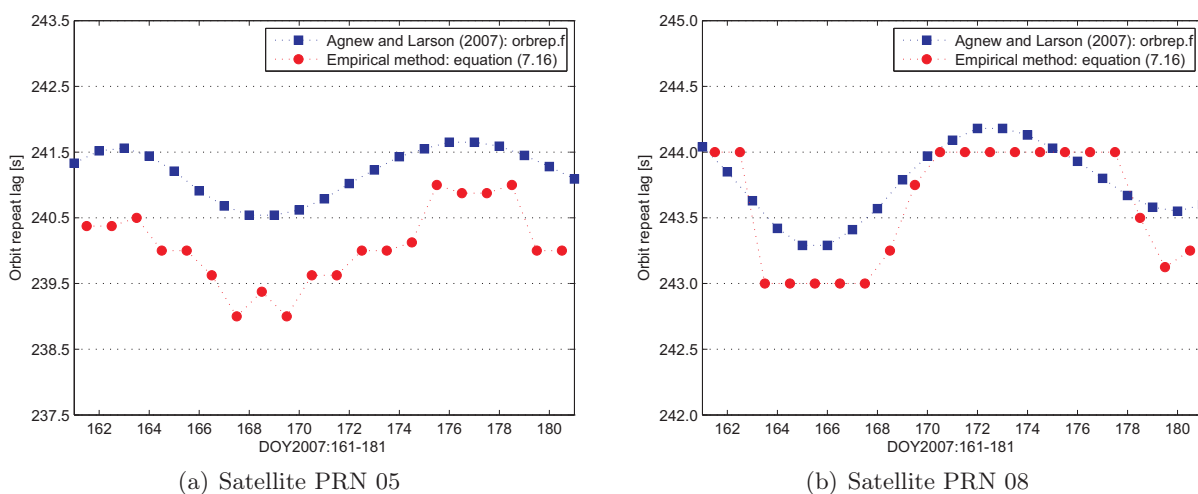
8.1.1 Satellite-specific orbit repeat lags

Having been defined in section 7.2.5, orbit repeat lag is the difference between one mean solar day (24 h = 86400 s) and the satellite orbit repeat period, amounting on average to 246 s (Ragheb et al., 2007). For each of the 8 baseline-forming SA*POS*®sites used in this case study (see table 4.1), the satellite-specific orbit repeat lags are determined by means of the empirical approach described in section 7.2.5, where the entire 21 days of 3-hour (i.e., DOY2007:161-181, 15-18 h) GPS observations and navigation messages are considered. For one satellite observed at one site, the corresponding orbit repeat lag can be computed for a maximum number of 20 times. Regarding the satellite-related mean lag values and standard deviations derived from different sites, only marginal differences are detected, which are, in most cases, less than the data sampling interval of 1 s. Therefore, the final satellite-specific orbit repeat lags and the associated standard deviations are site-averaged values. Figure 8.1 compares the empirically determined results with those obtained using the program `orbrep.f`, representing an analytical approach based on Kepler's third law (Agnew and Larson, 2007). As figure 8.1(a) shows, the orbit repeat lags vary from satellite to satellite between 240 and 263 s. The empirical and analytical results coincide fairly well with each other, exhibiting a mean difference of 0.4 s and a standard deviation

of about 1 s. Considering the analytical results as a reference, a mean difference near zero and a small standard deviation indicate the high accuracy and consistency of the empirically derived orbit repeat lags, respectively. Comparing the median standard deviations, which characterise the average precision of the lag estimates, the analytical method seems to be twice as good as the empirical one. This may be explained by the different time periods of the input navigation messages. While the empirical results are produced based on 3-hour navigation data, the program `orbrep.f` reads daily broadcast ephemeris files. In most instances, the standard deviations of the empirically determined orbit repeat lags are less than 1 s, coping with sidereal stacking applied to the 1-second residual data. Table D.4 provides the final satellite-specific orbit repeat lags, calculated by employing the empirical and analytical methods.

(a) Satellite-specific orbit repeat lags   (b) Standard deviations of the lag estimates
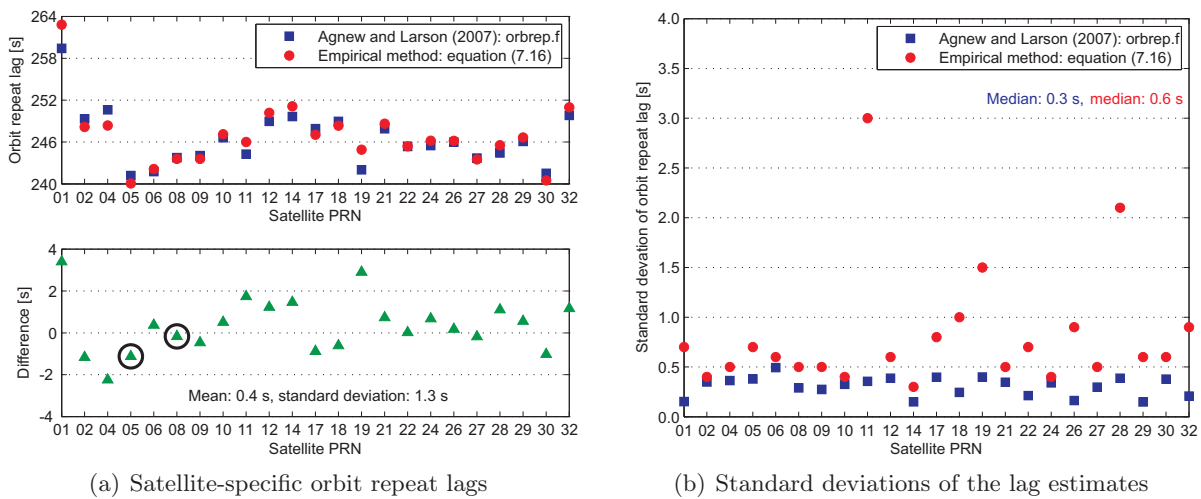
Figure 8.1: Validation of the empirically determined satellite-specific orbit repeat lags by means of the program `orbrep.f` (Agnew and Larson, 2007; PRN: pseudo random noise)

Taking two representative GPS satellites, PRN 05 and 08, as an example, figure 8.2 compares the individual orbit repeat lags derived by applying different approaches. The analytical method delivers lag values on a daily basis, indicating a total of 21 estimates for each satellite. The corresponding results shown in figure 8.2 obviously depict the small-amplitude (< 1 s) and 14-day

(a) Satellite PRN 05   (b) Satellite PRN 08

Figure 8.2: Examples of GPS satellite-specific orbit repeat lags determined using the analytical (Agnew and Larson, 2007) and empirical (see section 7.2.5) approaches (see figure 8.1(a))

periodic oscillations caused by the lunar gravity (Choi et al., 2004). Making use of the information about satellite geometry, the empirical approach provides one solution for two consecutive days, leading to a maximum number of 20 lag estimates. In spite of a short observation period of 3 h, it is interesting to observe that the empirically derived orbit repeat lags also reflect the small-amplitude oscillations, with mean biases corresponding to those displayed in figure 8.1(a). Considering the 1-second data sampling interval, integer values (in seconds) of the empirically determined orbit repeat lags are used to homogenise the residual time series for similar satellite geometry on consecutive days.

8.1.2 Vondrák filter parameters

The smoothing factor ϵ of the Vondrák filter regulates the degree of filtering or the smoothness of the filtered series (see figure 7.4). According to Vondrák (1969) and Zheng et al. (2005), ϵ can be expressed as

$$\epsilon = 1/\lambda^2 = 10^{-k}, \tag{8.1}$$

where λ^2 can be found in equation (7.6), and k is a positive integer referred to as the Vondrák filter parameter. Determining the most appropriate smoothing factor ϵ is practically equivalent to finding the best possible k. Based on the optimisation criterion given by equation (7.10), Vondrák (1969) found the optimum value of $k = 8$ when filtering a set of latitude observations at the Geodetic Observatory Pecný. Within the context of multipath mitigation, Zheng et al. (2005) applied the cross-validation Vondrák filter (CVVF) to coordinate time series, where the detected optimum k values vary between 4 and 7 for different days and coordinate components.

In this thesis, the Vondrák filter is used to capture slowly varying long-periodic trends, so that the remaining daily repeating signals of a quasi-periodic nature can be extracted in a physically more sophisticated manner, for example, by means of the sidereal stacking technique. Keeping this objective in mind, the optimum filter parameters are derived by maximising the day-to-day correlation of the Vondrák residuals and minimising the impact of Vondrák filtering on the noise's temporal correlation structure. While the former condition can be mathematically formulated by equation (7.12), the latter must be empirically assessed by simulation-based analysis due to the generally unknown noise's correlation characteristics. Each simulated time series represents the sum of a signal and a noise component. Considering that multipath effects induce both short- and long-periodic perturbations (see section 3.2.3), the signal component is generated using the multipath model

$$\delta\phi(e; \vartheta, d, \lambda) = \frac{\lambda}{2\pi} \tan^{-1} \frac{\vartheta \sin\left[4\pi \frac{d}{\lambda} \sin e\right]}{1 + \vartheta \cos\left[4\pi \frac{d}{\lambda} \sin e\right]}, \tag{8.2}$$

which primarily depends on the elevation angle e of the incident signal (Elósegui et al., 1995; King and Williams, 2009). This multipath model assumes that the incoming GPS signals are plane waves with a wavelength of λ. Furthermore, the horizontal reflector is planar and infinitely large, located at a distance of d below the GPS antenna. The parameter ϑ, ranging between 0 and 1, denotes the attenuation of the voltage amplitude of the reflected signal with respect to the direct signal. In order to construct scenarios as close to reality as possible, the elevation angles of 9 GPS satellites, observed at the SA*POS*®site Heidelberg (HEID) during a 1-hour period (DOY2007:161, 17-18 h), are incorporated into the multipath simulation. Following the parameter settings in King and Williams (2009) and Zhong et al. (2010), the reflected signal in a static multipath environment is assumed to be attenuated by a factor of $\vartheta = 0.1$. Moreover, representative reflector-antenna distances d of 0.1-3.0 m are specified to produce multipath signals with different quasi-periods. The multipath simulation is only carried out for L1 observations, indicating that $\lambda = 19$ cm (see table 3.2).

In addition to the signal part, the noise component is created using different stochastic processes, such as the Gaussian white noise (WN) process, $\{Z_t\} \sim \mathrm{WN}(0, \sigma_Z^2)$, and representative autoregressive moving average (ARMA) processes. The ARMA coefficients are specified by considering the temporal correlation properties of GPS observation noise presented in Wang et al. (2002) and Luo et al. (2012b). Following the notation of a general ARMA(p, q) process defined by equation (2.42), table 8.1 provides the model parameters of the applied noise-generating processes. Once an ARMA process is uniquely known, the associated autocorrelation function (ACF) can be derived from the model parameters using the two methods described in section 2.2.3. Figure 8.3 illustrates the model ACF of the noise-generating processes. As can be seen, the ARMA model ACF exclusively exhibit positive correlations, corresponding to the general assumption that GPS observations are positively correlated over time. In comparison to the AR(1) process, the model ACF of the ARMA$(3, 2)$ process depicts a slowly decaying temporal correlation structure, implying a longer correlation length. However, as will be demonstrated in section 8.1.6, the order of the best-fitting ARMA model identified from a given noise realisation depends on the entire correlation structure rather than on the correlation length alone.

**Table 8.1:** Model parameters of the stochastic processes employed for noise simulation

Stochstic	Model parameters according to equation (2.42)						Reference
process	a_1	a_2	a_3	b_1	b_2	σ_Z [mm]	
WN$(0, 1)$	$-$	$-$	$-$	$-$	$-$		Broersen (2006, p. 60)
AR(1)	-0.90	$-$	$-$	$-$	$-$	1.00	Wang et al. (2002)
ARMA$(3, 2)$	-0.73	-0.38	0.14	-0.33	-0.35		Luo et al. (2012b)
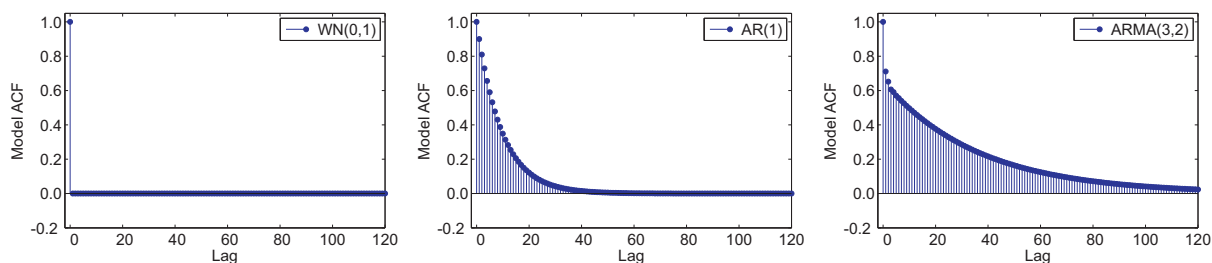
Figure 8.3: Model ACF of the noise-generating stochastic processes presented in table 8.1

For the GPS satellite PRN 18, figure 8.4 illustrates examples of simulated data series using different reflector-antenna distances ($d = 0.1, 1.5, 3.0$ m; see equation (8.2)) and noise-generating processes (see table 8.1). First of all, it can be seen that the quasi-periodic nature of the simulated multipath signal becomes less obvious as d decreases. This agrees with the theory that a near-ground antenna with a small d is primarily affected by the near-field multipath, producing slowly varying long-periodic errors. As d increases, the antenna experiences greater influence from distant reflectors, causing rapidly oscillating quasi-periodic signals (Georgiadou and Kleusberg, 1988; Wanninger, 2000, p. 23). In this multipath simulation, an upper limit of 3 m is chosen for d, which still reflects reality under certain site-specific observational conditions. For example, in order to attenuate signal shadowing and diffraction effects, the GPS antenna at the Black Forest Observatory (BFO) is installed on top of an aluminium tripod, being about 3.6 m above the ground (Luo and Mayer, 2008). Regarding the simulated noise, the positive correlations seem to amplify the process variance in a significant manner. For example, AR(1) processes have a variance of $\sigma_X^2 = \sigma_Z^2/(1 - a_1^2)$ (Brockwell and Davis, 2002, p. 18), increasing $\sigma_Z = 1$ mm by more than twice to $\sigma_X = 2.3$ mm ($a_1 = -0.9$; see table 8.1).
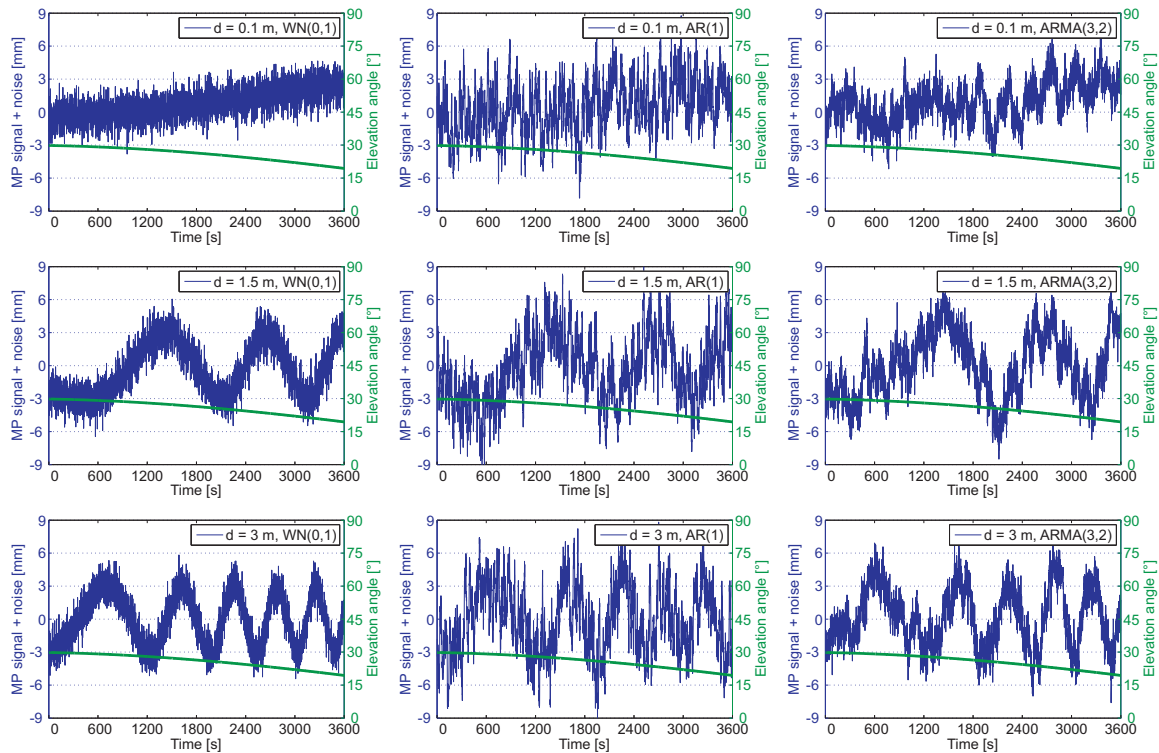
Figure 8.4: Examples of simulated data series using different reflector-antenna distances d and noise-generating stochastic processes (SA*POS*®site: HEID, satellite: PRN 18, DOY2007:161, 17-18 h, MP: multipath; see table 8.1 and equation (8.2))

In the case that the noise's temporal correlation behaviour is exactly known, for example, described by the model ACF of an ARMA process, the objective of minimising the impact of Vondrák filtering on the noise's correlation structure can be formulated by

$$\sum_{h=1}^{h_{\max}} [\hat{\rho}_{\tilde{y}}(h) - \rho_M(h)]^2 \longrightarrow \min, \quad h \in \mathbb{N}, \tag{8.3}$$

where $\hat{\rho}_{\tilde{y}}(h)$ denotes the sample ACF of the Vondrák residual time series $\tilde{y}$ at lag h, and $\rho_{\mathrm{M}}(h)$ is the model ACF of the noise-generating stochastic process. Applying this ACF-based minimum constraint, the optimum filter parameter k can be determined for each simulated data series, where $h_{\max}$ is equal to 20, 50, and 150 s for WN(0, 1), AR(1), and ARMA(3, 2), respectively (see figure 8.3). Analysing the examples shown in figure 8.4, figure 8.5 compares the results of the Vondrák filter, where the optimum k values are determined using the CVVF method (Zheng et al., 2005) and equation (8.3). If the simulated noise is WN, both approaches produce comparably large filter parameters, leading to almost identical filtered values. However, if the simulated noise exhibits strong positive correlations, the CVVF method tends to provide small k values and rough filtered series. This may be attributed to its performance degradation when the noise level is higher than the magnitude of the signal (Zheng et al., 2005). As figure 8.4 illustrates, increased noise level can be a consequence of positive temporal correlations. In comparison to CVVF, the ACF-based minimum constraint delivers larger k values, sufficiently capturing the generated multipath signals. To show the effects of the filter parameters on the noise's correlation structure, figure 8.6 compares the sample ACF of the Vondrák residuals with the model ACF of the noise-generating processes. In the case of coloured noise, i.e., AR(1) and ARMA(3, 2), the CVVF method generally eliminates the noise's autocorrelations, resulting in almost uncorrelated Vondrák residuals. In contrast, the use of equation (8.3) maintains the input noise's correlation structure, where this maintenance appears to degrade with increasing model complexity.
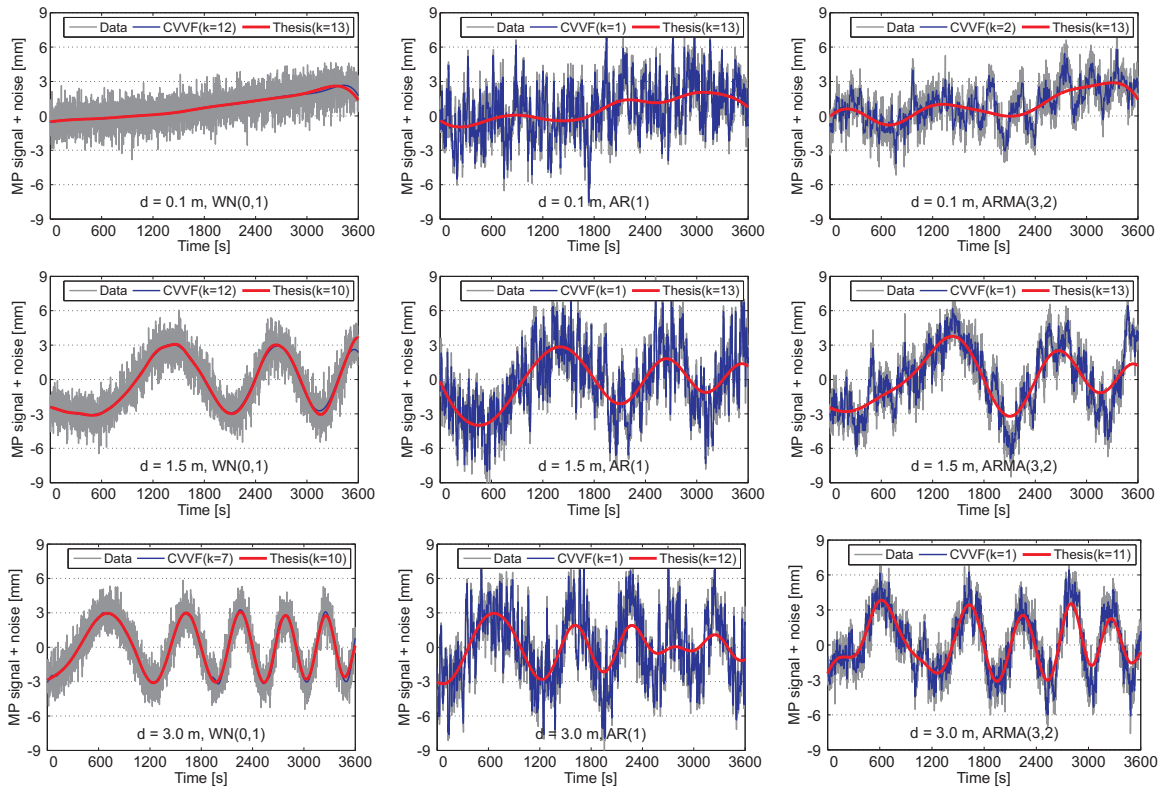
Figure 8.5: Vondrák filtering of the simulated series using filter parameters determined by means of different approaches (CVVF: Zheng et al., 2005, Thesis: equation (8.3); see figure 8.4)
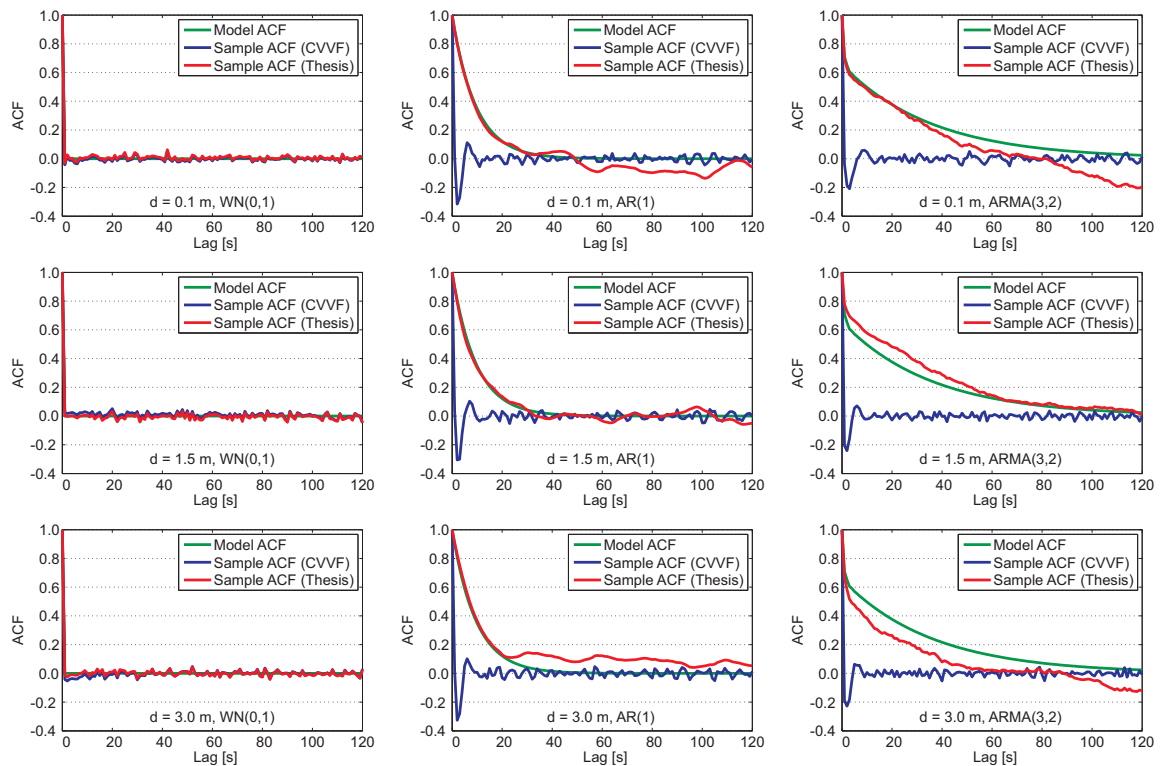

Figure 8.6: Comparison of the sample ACF of the Vondrák residuals with the model ACF of the noise-generating processes (see table 8.1 and figures 8.3, 8.4, and 8.5)

Considering all the reflector-antenna distances and GPS satellites analysed in this simulation study, figure 8.7 displays the optimum Vondrák filter parameters determined by means of equation (8.3). Figure 8.7(a) shows the satellite geometry during the 1-hour time interval. For all three noise-generating processes, the mean k value decreases as the reflector-antenna distance d increases. This is due to the increased multipath oscillations whose characterisation requires smaller filter parameters (see figure 8.4). In the case of coloured noise, i.e., AR(1) and ARMA(3, 2), illustrated in figures 8.7(c) and (d), respectively, one can easily discern that the satellite-specific filter parameters become more variable as d increases. Accordingly, for large reflector-antenna distances, differences in satellite geometry play an important role when using the Vondrák filter to capture quasi-periodic far-field multipath signals. In summary, Vondrák filtering with $k = 13$ seems to sufficiently detect long-periodic trends without significant impact on noise's temporal correlation.

(a) 1-hour satellite geometry

(b) Noise model: WN(0, 1)

(c) Noise model: AR(1)

(d) Noise model: ARMA(3, 2)
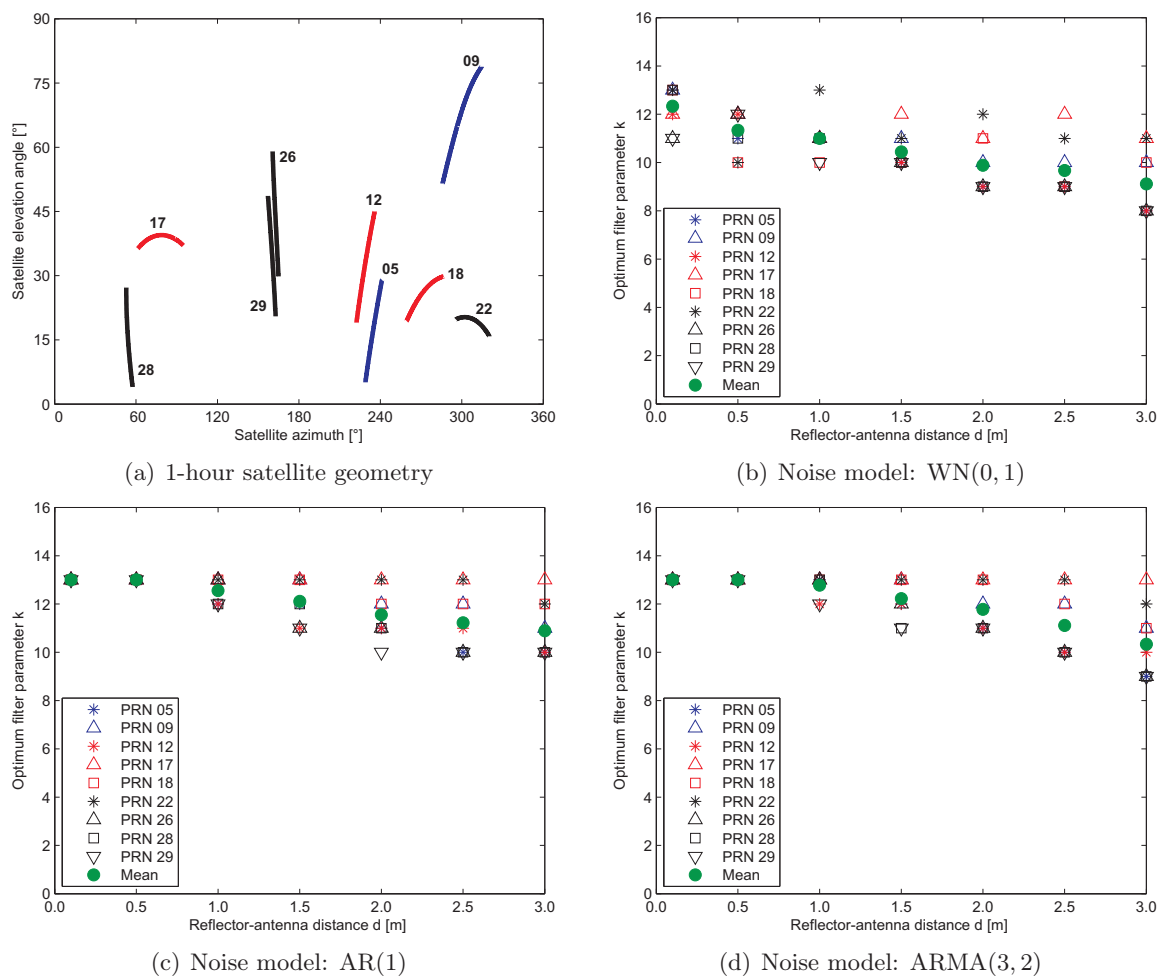
Figure 8.7: Optimum Vondrák filter parameters determined using equation (8.3) for all the analysed reflector-antenna distances and GPS satellites (site: HEID, DOY2007:161, 17-18 h)

To effectively extract the remaining daily repeating signals by means of sidereal stacking, the optimum Vondrák filter parameters are computed for each double-difference by maximising the day-to-day correlation of the Vondrák residuals (see equation (7.12)). Thereby, the candidate values for k vary from 1 to k_{max} with a step of 1, where the upper limit k_{max} is chosen to be 13 and 10 for the baselines with weak and strong multipath impact, respectively (see table 4.3). This choice is made according to the mean results presented in figure 8.7. The determined optimum k values are visualised in figure 8.8 for all the available double-differences, where k_{max} is considered, in most cases, as the best possible one. The use of smaller Vondrák filter pa-

rameters allows capturing some randomly occurring signals, for instance, induced by variable atmospheric conditions. This may improve the day-to-day similarity of the Vondrák residuals, and consequently, the performance of sidereal stacking. Taking the double-difference TAAF1718 (i.e., baseline: TAAF, satellite pair: PRN 17-18) as an example, the employment of the Vondrák filter with $k = 12$ increases the residual mean day-to-day correlation coefficient by more than 50%, from 0.30 to 0.46. Filtering the raw SDDR with the determined optimum k values, the resulting Vondrák residuals are first used for outlier detection (see figure 7.3).
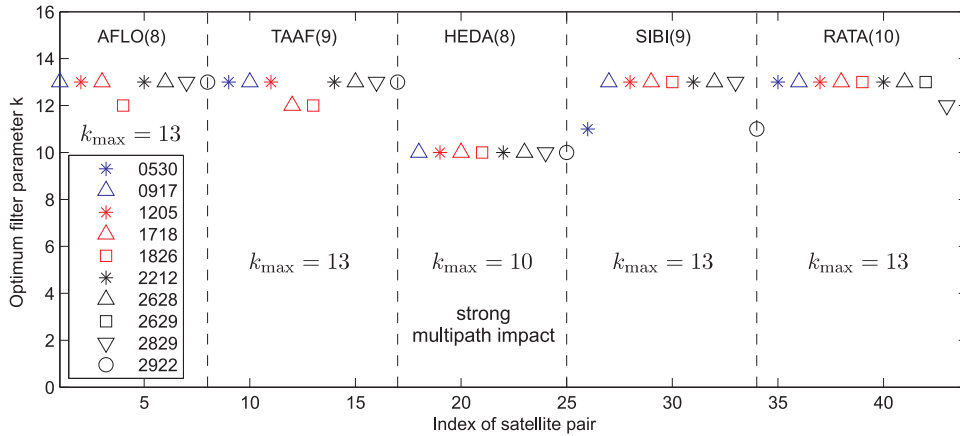
Figure 8.8: Optimum Vondrák filter parameters determined using equation (7.12) for all the available double-differences (see table 4.3 for baseline characteristics)

8.1.3 Results of outlier handling

Relying upon the Vondrák residuals, the outlier detection described in section 7.2.4 is performed in two steps: outlier identification using the 5-MAD criterion (see equation (7.13)) and outlier verification by means of the one-sided F-test (see equation (7.14)). This two-step procedure is applied to a total of 368 SDDR times series. The minimum data length is chosen to be 600 epochs (1 epoch = 1 s) by considering the correlation time of about 200 s for LC3 double-difference observations (El-Rabbany, 1994, p. 36) and the rule of thumb that the sample ACF can be reliably estimated for lags of up to a third of the sample size (Brockwell and Davis, 2002, p. 404). The results of outlier detection are shown in figure 8.9.

(a) Outlier identification

(b) Outlier verification ($\alpha = 1\%$)
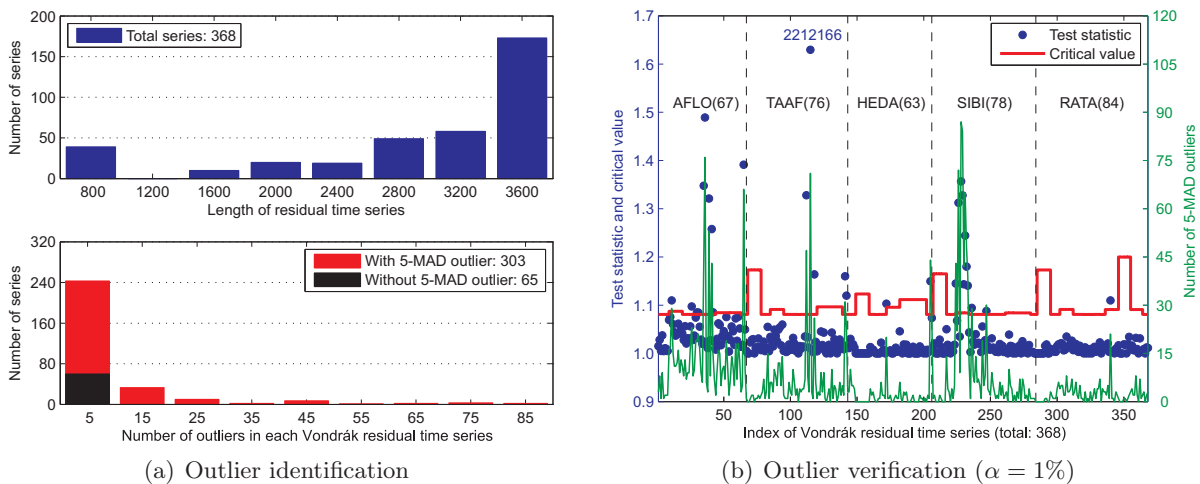
Figure 8.9: Results of the two-step procedure for outlier detection using the Vondrák residuals

As can be seen from figure 8.9(a), 5-MAD outliers exist in 303 (82%) Vondrák residual time series, where in 95% of the cases the number of outliers in a single series is less than 30. This requires a careful examination of the influence of the identified 5-MAD outliers. Figure 8.9(b) illustrates the results of outlier verification by means of the one-sided F-test at a significance level of $\alpha = 1\%$, which corresponds to the probability of committing a Type I error (see section 2.3.1). For 275 of the 303 time series with outliers, the detected 5-MAD outlying samples appear to insignificantly affect the sample variance of the Vondrák residuals. In the occurrence of significant impacts, where the test statistics are larger than the critical values, a strong positive correlation between the F-test statistic and the number of outliers is clearly visible.

In order to benefit from a large and representative residual data set, the $303 - 275 = 28$ residual time series with significant 5-MAD outliers are not simply excluded from the temporal correlation modelling, but repaired using the remove-repair-restore (RRR) technique introduced in section 7.2.4. In the remove step, the Vondrák filtered values are subtracted from the raw SDDR. In the repair step, the 5-MAD outliers are replaced by the linearly interpolated values of the non-outlying Vondrák residuals. In the restore step, the repaired Vondrák residuals are added to the filtered values, which are subtracted in the remove step. By doing so, the repaired SDDR should be free of the 5-MAD outliers, significantly affecting the sample variance of the Vondrák residuals. Taking the SDDR time series TAAF2212166 (baseline: TAAF, satellite pair: PRN 22-12, DOY2007:166) with the largest test statistic as an example (see figure 8.9(b)), figure 8.10(a) illustrates the efficiency of the RRR technique with which the significantly outlying SDDR can be sufficiently reduced. Based on the repaired SDDR (OFR in figure 7.3), the optimum Vondrák filter parameters k are determined again, and the results are identical with those shown in figure 8.8. Applying the Vondrák filter to OFR, the resulting residuals are reanalysed for outliers. As figure 8.10(b) shows, all the F-test statistics are less than the critical values, and the numbers of 5-MAD outliers are largely reduced in comparison to figure 8.9(b). These improvements verify the performance of the RRR technique, producing high-quality SDDR data for the subsequent residual decomposition and ARMA modelling.

(a) Example SDDR time series: TAAF2212166

(b) Verification after outlier repair ($\alpha = 1\%$)
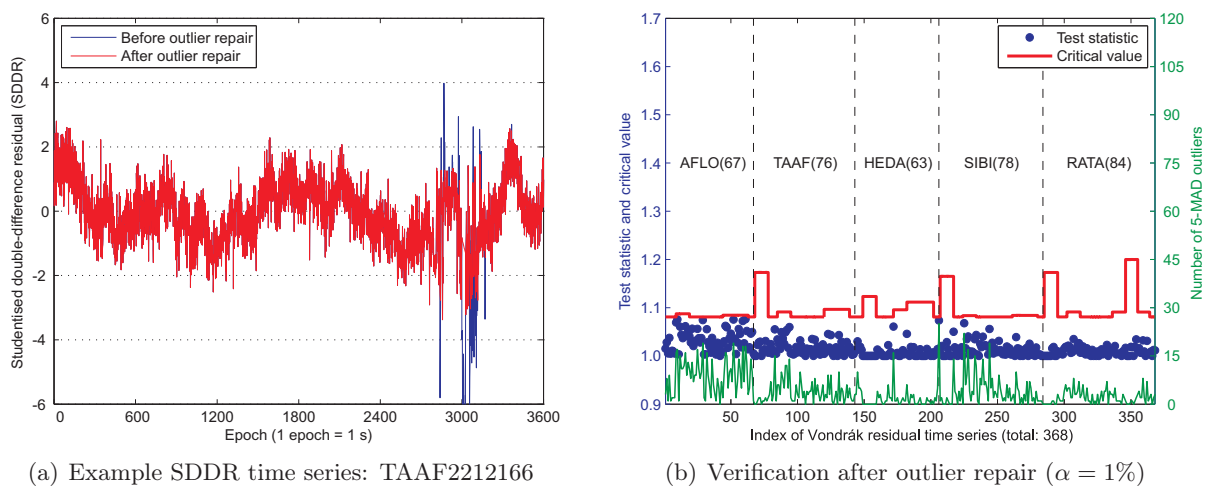
Figure 8.10: Results of the outlier repair by means of the remove-repair-restore (RRR) technique

From a theoretical point of view, the applied F-test assumes statistically independent and normally distributed samples $(\tilde{y}_{a,1}, \dots, \tilde{y}_{a,n_a})$ and $(\tilde{y}_{b,1}, \dots, \tilde{y}_{b,n_b})$ (Niemeier, 2008, p. 110). However, considering the principle of the outlier verification, both data sets $\tilde{y}_a$ and $\tilde{y}_b$ are obviously dependent, since they differ from each other only with respect to the presence of 5-MAD outliers. Furthermore, the remaining quasi-periodic signals may cause deviations from the assumed normal distribution. Therefore, under statistical aspects, a comparison between the empirical distribu-

tion of the test statistic T_F and the theoretical F-distribution will illustrate the influence of applying the F-test in violation of the theoretical assumptions. Taking the one-sided test property into account (see section 7.2.4), figure 8.11 compares the empirical cumulative distribution function (CDF) of T_F with the theoretical CDF of the F-distribution, where the degrees of freedom ν_a and ν_b are specified by considering the maximum sample size and the maximum number of outliers. As one can easily discern in figure 8.11(a), prior to outlier repair, there exist large deviations between the empirical and theoretical CDF for $T_F > 1.05$. These discrepancies are taken advantage of to assess the significance of the identified 5-MAD outliers. After repairing outliers by means of the RRR technique, as figure 8.11(b) displays, both CDF curves coincide with each other, exhibiting quantile differences less than 0.01 in most cases. To account for the correlation between the data sets $\tilde{y}_a$ and $\tilde{y}_b$, the test for comparing two correlated variances (Snedecor and Cochran, 1967, p. 195) may be applied for future research.

| (a) Before outlier repair | (b) After outlier repair |
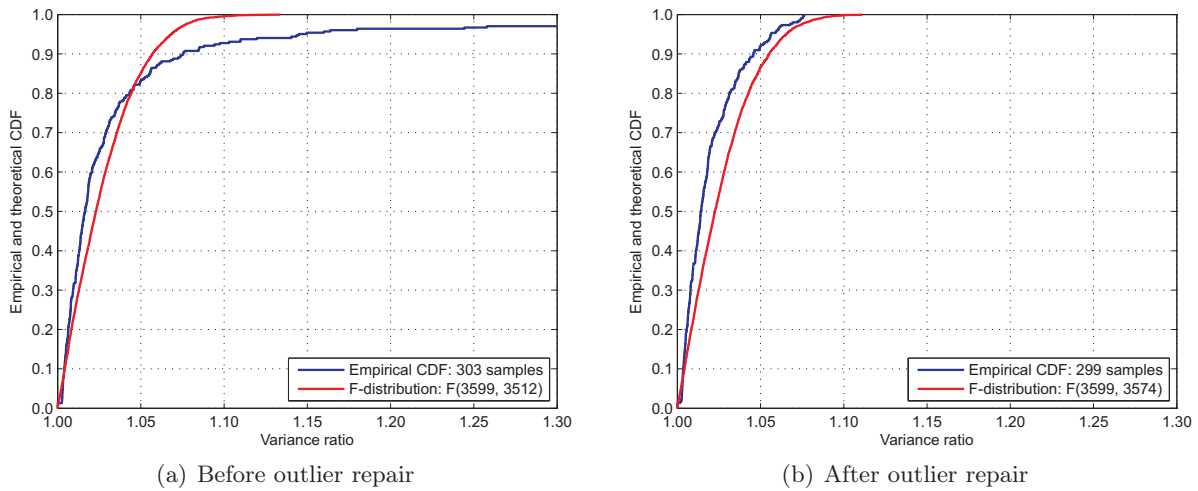
Figure 8.11: Comparison of the empirical and theoretical distributions of the F-test statistic T_F before and after outlier repair using the RRR technique (see equation (7.14))

In addition, by incorporating the DWD surface meteorological data (see figure 4.8), attempts are made to find physical factors that influence the number of outliers. Considering the comparable heights and the relatively short distance between the SA*POS*®site TAUB and the DWD station WUER (see figure 4.1(a)), figure 8.12 compares the relative humidity (RH) measurements from WUER with the daily numbers of 5-MAD outliers from the TAUB-related baselines TAAF and RATA prior to outlier repair (see table 4.3).
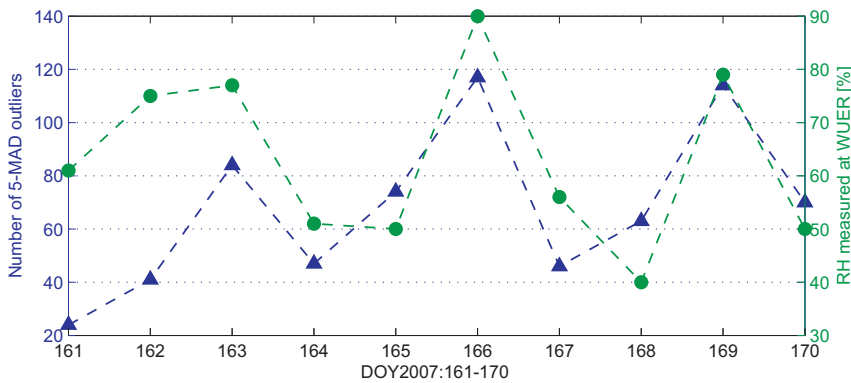
Figure 8.12: Comparison of the daily numbers of 5-MAD outliers with surface relative humidity (RH) measurements (baselines: TAAF, RATA, DWD station: WUER; see figures 4.1 and 4.8(c))

As can be clearly seen in figure 8.12, the daily numbers of 5-MAD outliers and the *RH* measurements are generally positively correlated, with a correlation coefficient of about 0.6. Such an obvious correlation indicates the strong impact of the wet atmosphere on GPS data quality and emphasises the necessity of advanced tropospheric modelling, particularly for the wet delay component. This can be achieved, for example, by incorporating representative meteorological data with a high temporal and spatial resolution into GPS data analysis, as well as by applying the state-of-the art tropospheric mapping functions, such as the GMF and VMF1 (Boehm et al., 2006a,b). In order to benefit from a larger residual data set without significant outliers, the repaired SDDR are used as input for the temporal correlation modelling, which actually begins with residual decomposition.

### 8.1.4 Results of residual decomposition

Following the data homogenisation with respect to satellite geometry and outlier repair by means of the RRR technique, the residual decomposition process described in section 7.2.2 is carried out in order to obtain stochastic noise that is largely free of the remaining systematic effects. Using the notations introduced before, OFR denotes the repaired SDDR, DTR refers to the detrended (Vondrák) residuals, and NCR represents the decomposed noise. Considering that the two baselines TAAF and HEDA have similar lengths but different multipath effects (see table 4.3), figures 8.13, 8.14, and 8.15 depict the results of Vondrák filtering, sidereal stacking, and noise extraction for the satellite pair PRN 12-05, respectively.

As figure 8.13 shows, the 10 days of site-mean elevation angles are largely consistent, reflecting the high accuracy of the empirically determined satellite-specific orbit repeat lags (see figure 8.1 and table D.4). Employing a filter parameter of $k = 13$, figure 8.13(a) illustrates the efficiency of the Vondrák filter in capturing slowly varying long-periodic trends. In spite of the similar satellite geometry on the 10 consecutive days, obvious deviations are present in the filter outcomes, which are mainly due to the different atmospheric conditions. These kinds of day-to-day deviations tend to become more significant as baseline length increases. In comparison to the TAAF-related example, figure 8.13(b) exhibits considerably larger variations in OFR, which are caused predominantly by the strong multipath impact of HEDA (see figure 4.7(a)). Furthermore, the interaction between site-specific multipath effects and variable atmospheric conditions may induce some randomly occurring and strongly deviating signals, which can be well detected by the Vondrák filter using smaller filter parameters (e.g., $k = 10$).

After removing the trend component from OFR, the resulting DTR are used for sidereal stacking to extract the daily repeating signals of a quasi-periodic nature. Comparing the 3-day DTR displayed in figure 8.14, the TAAF-related example primarily shows daily repeating effects, while the HEDA-related one clearly exhibits quasi-periodic signals with a period of several minutes. As schematically illustrated in figure 7.7, the sidereal stacking is accomplished by computing the epoch-wise arithmetical means of DTR from multiple days. Two approaches based on 10- and 3-day DTR are compared with each other. In comparison to the 3-day stacking variant, the 10-day means are not only smoother, but also slightly shifted, where the shifts are particularly observable in the presence of quasi-periodic oscillations (see figure 8.14(b)). This may arise from using the average of the two related satellite-specific orbit repeat lags as the representative value for a satellite pair. As a consequence, the decomposed noise may still contain some periodic signals, contaminating the results of the temporal correlation analysis. Subtracting the daily repeating signals from DTR results in the final stochastic noise NCR (see figure 8.15). Compared to the 10-day stacking approach, the 3-day solution enables a more accurate signal characterisation, leading to more homogenous noise with smaller variance. Moreover, the variance of the noise component seems to decrease with increasing multipath impact.

(a) SDDR: TAAF1205 ($k = 13$)   (b) SDDR: HEDA1205 ($k = 10$)
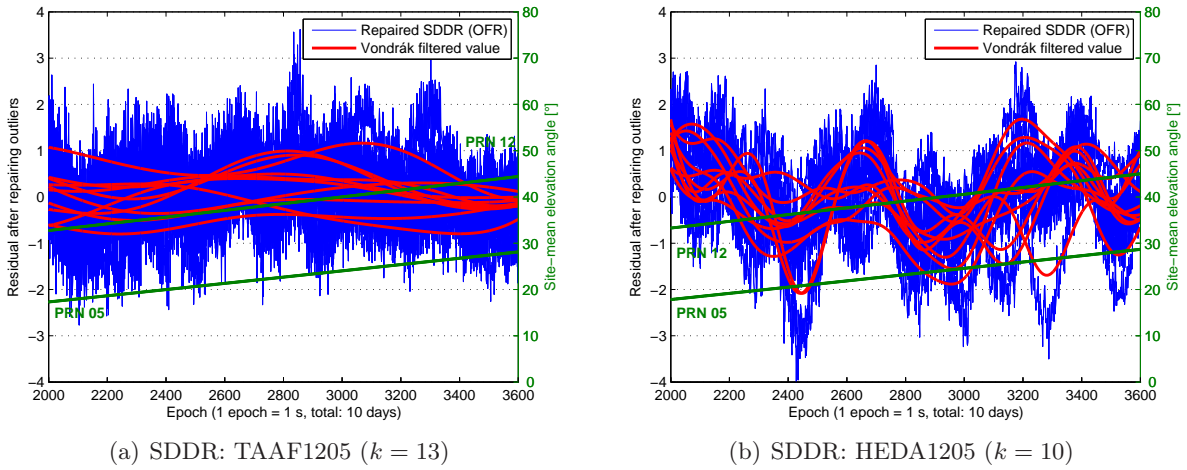
Figure 8.13: Examples of Vondrák filtering with respect to multipath impact (TAAF: 53.7 km, weak multipath, HEDA: 54.1 km, strong multipath, DOY2007:161-170; see table 4.3)



(a) SDDR: TAAF1205   (b) SDDR: HEDA1205
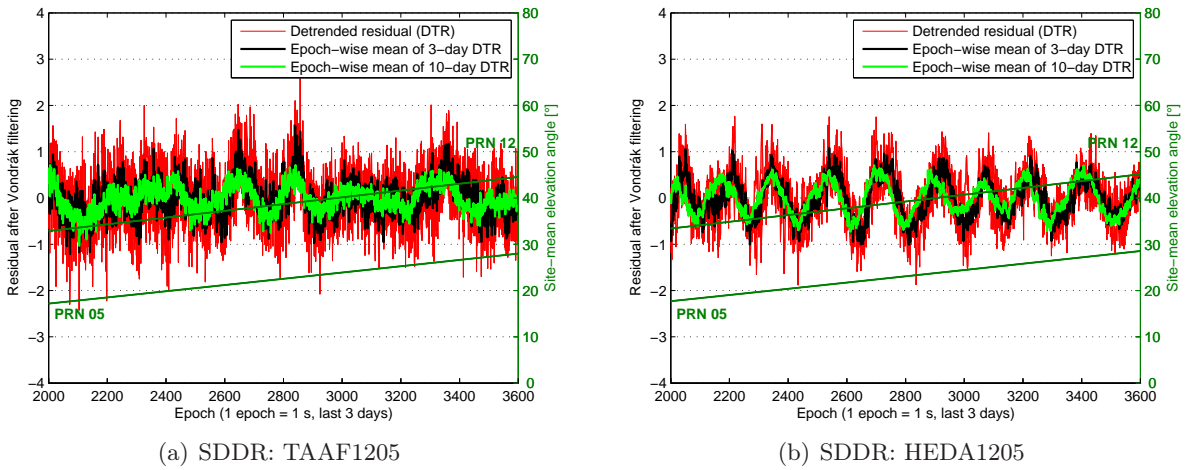
Figure 8.14: Examples of sidereal stacking using different days of DTR (DOY2007:168-170, orbit repeat lags: 250 s for PRN 12, 240 s for PRN 05, 245 s for PRN 12-05; see table D.4)

(a) SDDR: TAAF1205   (b) SDDR: HEDA1205
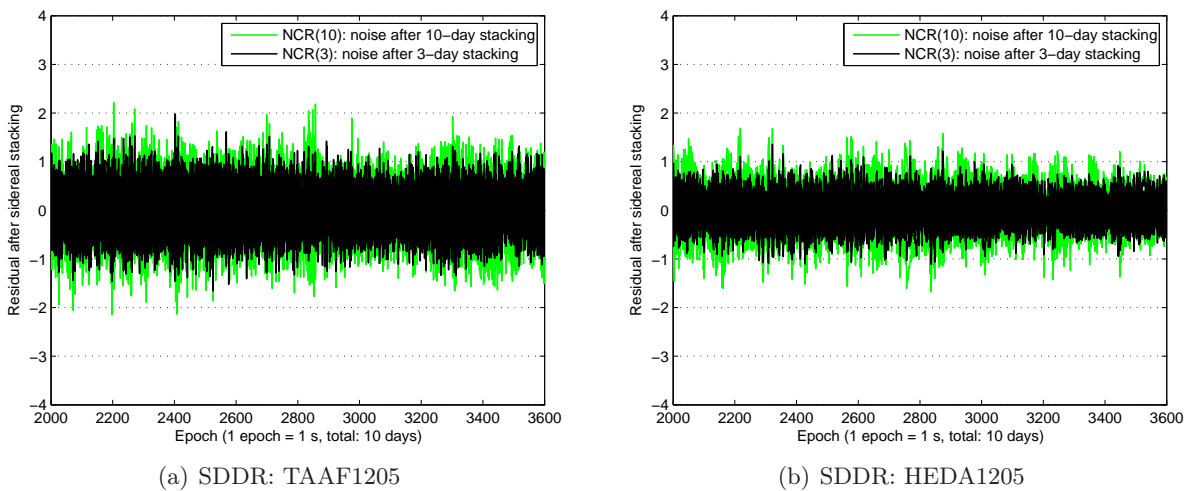
Figure 8.15: Noise after applying the 3-day and 10-day sidereal stacking (DOY2007:161-170)

To minimise the influences of the remaining systematic effects on the residual-based temporal correlation modelling, such a decomposition process is necessary prior to analysing the noise's temporal correlation properties. To demonstrate this, figure 8.16 compares the sample ACF of OFR, DTR, and NCR from the same examples used for residual decomposition. As can be seen in both plots, the remaining systematic signals in OFR and DTR significantly affect the temporal correlation structure, and consequently, the ACF-based evaluation of temporal correlation characteristics (e.g., correlation length). While figure 8.16(a) primarily illustrates the effect of long-periodic trends, figure 8.16(b) also shows the impact of quasi-periodic signals. In addition, comparing the sample ACF of NCR(3) and NCR(10) obtained after stacking 3-day and 10-day DTR, respectively, the advantages of applying a shorter stacking time interval in capturing quasi-periodic oscillations are clearly visible. Accordingly, the NCR(3) data are used for the following correlation analysis and ARMA modelling. Within this context, it is worth mentioning that observations collected over three consecutive days are often used in coordinate- and residual-level GPS sidereal filtering for multipath mitigation (Zheng et al., 2005; Ragheb et al., 2007; Zhong et al., 2010). Comparing the sample ACF of NCR(3) with respect to multipath impact, the zero-crossing correlation length (i.e., lag value for ACF being equal to zero) seems to decrease with increasing multipath, while the lag-1 correlation level (i.e., ACF value for lag being equal to one) appears to increase with increasing multipath. In order to obtain a realistic picture of the noise's temporal correlation behaviour, a detailed analysis is carried out with regard to baseline length, multipath impact, satellite geometry, and atmospheric conditions.


(a) SDDR: TAAF1205   (b) SDDR: HEDA1205
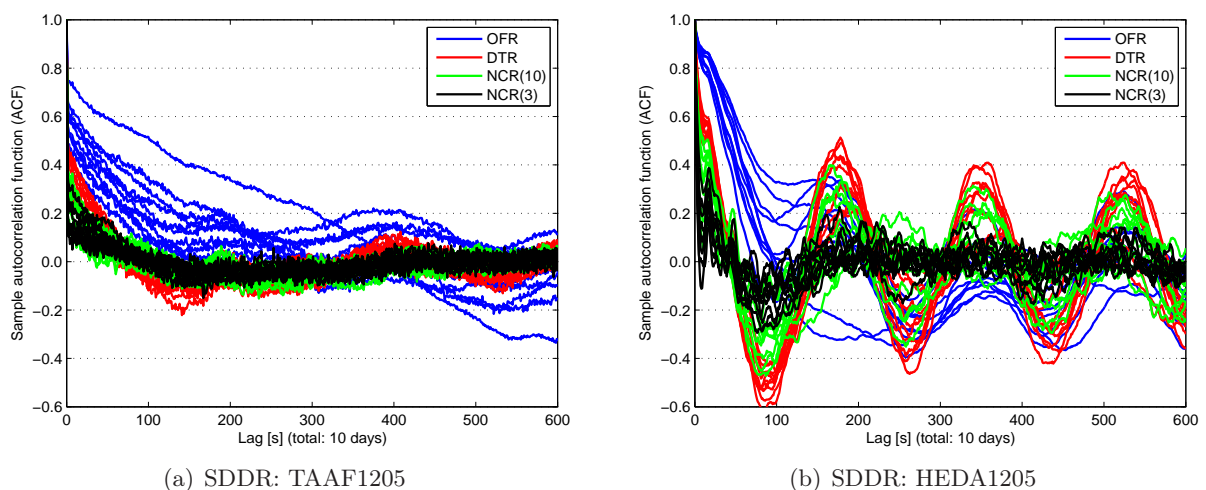
Figure 8.16: Comparison of the sample ACF of OFR, DTR, and NCR (TAAF: 53.7 km, weak multipath, HEDA: 54.1 km, strong multipath, DOY2007:161-170; see figures 8.13, 8.14, and 8.15)

8.1.5 Results of the correlation analysis

The noise's temporal correlation analysis is performed based on the two aforementioned characteristics of the sample ACF of NCR(3), namely the zero-crossing correlation length and lag-1 correlation level. The former represents the smallest lag at which the sample ACF falls below zero (see ND_1 in equation (7.2)). The latter is the autocorrelation coefficient at lag 1, which is usually of great interest for assessing correlatedness. To study the effects of baseline length and multipath impact on noise's temporal correlation, both parameters are computed baseline-wise, and the results are presented by box plots in figure 8.17. The statistical characteristics, such as arithmetical mean and 95% quantile, are derived without the extreme outliers outside the interval $[Q_{0.25} - 3 \cdot \text{IQR}, Q_{0.75} + 3 \cdot \text{IQR}]$, where $Q_{0.25}$ and $Q_{0.75}$ denote the lower and upper quartiles, respectively, and IQR is the interquartile range defined as $Q_{0.75} - Q_{0.25}$.

Comparing the HEDA-related box plots with those from other baselines, strong multipath effects seem to halve the mean correlation length from about 80 to 40 s with a decreased IQR, and to double the mean correlation level from about 0.3 to 0.6 with an increased IQR. The extreme outliers, marked by red plus signs in figure 8.17(a), can be partly found in figure 8.16(b) at small lags. Regarding the box plots of SIBI (42.5 km) and RATA (203.7 km) for instance, baseline length appears to insignificantly affect the noise's temporal correlation properties. This may be explained by the sufficient removal of the remaining distance-dependent systematic effects during the course of the residual decomposition, and coincides with the findings reported by El-Rabbany (1994, p. 89) and El-Rabbany and Kleusberg (2003).

(a) Zero-crossing correlation length   (b) Lag-1 correlation level
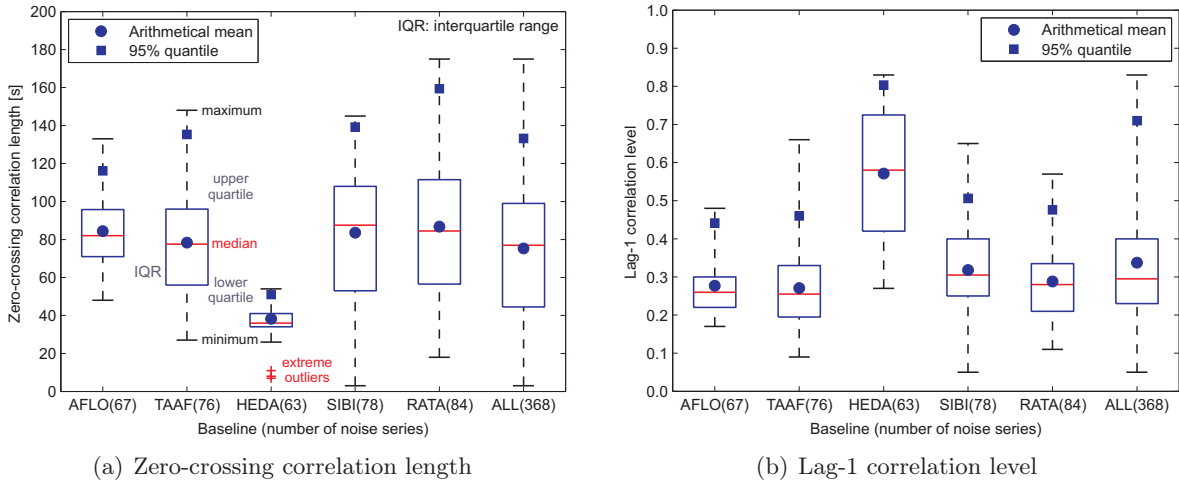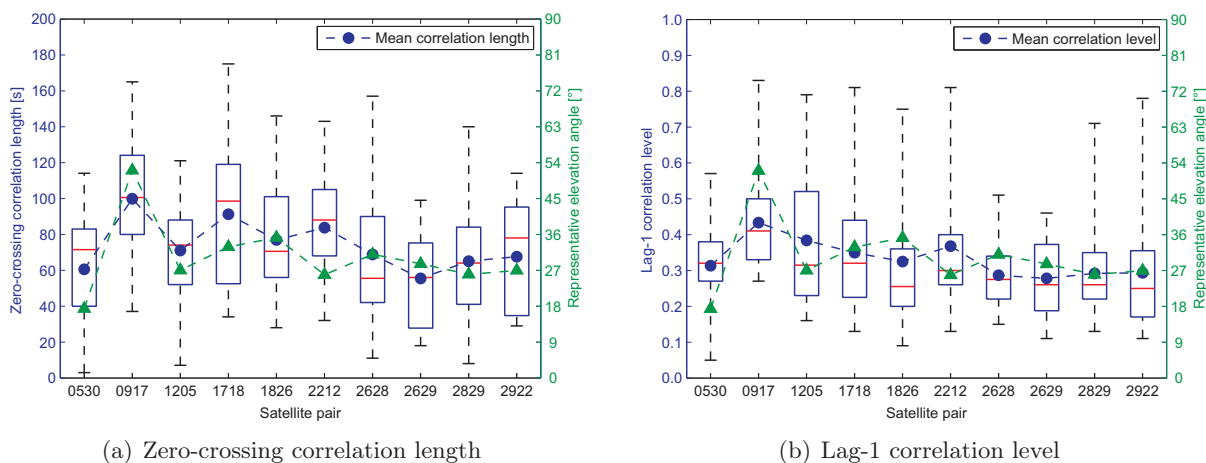
Figure 8.17: Temporal correlation characteristics with respect to baseline length and multipath impact (see table 4.3 for baseline properties, 1-hour SDDR noise, sampling interval: 1 s)

Examining the sample ACF shown in figures 8.16 and C.3, the reduction of long-periodic trends significantly impacts upon both the correlation length and level, while the removal of daily-repeating signals decreases the correlation level and the portion of negative correlations. The dominance of positive correlations in NCR(3) corresponds to the general assumption of positively correlated GPS observations. Considering all the analysed noise series, the zero-crossing correlation length and lag-1 correlation level have 95% quantiles of 133 s and 0.7, respectively. The maximum correlation length found in this case study is about 180 s (3 min). Note that the temporal correlation properties are derived from only 1-hour SDDR, and thus are not necessarily representative. Since the GPS data are dominated by low-elevation observations (see figure 4.5), the presented results may illustrate a low-correlation scenario, provided that the noise's temporal correlation decreases with decreasing satellite elevation angle.

To demonstrate the impact of satellite geometry on the noise's temporal correlation behaviour, the mean correlation characteristics are calculated for each satellite pair, where the sample sizes vary from 25 to 50. In addition, for each satellite pair, a representative elevation angle is derived as follows: On the basis of the epoch-wise 4-element means, the median elevation angle is first computed for one baseline, one satellite pair, and one day. Next, the average of all medians, which are related to the same satellite pair, but to different baselines and days, is calculated as the final representative elevation angle. Figure 8.18 depicts the mean temporal correlation characteristics with respect to satellite geometry. For different satellite pairs, there exist obvious deviations in the correlation properties, particularly in correlation length. Furthermore, it is interesting to observe that the mean correlation length and level are positively correlated with the representative elevation angle, where the correlation coefficients are larger than 0.6. This simply indicates that the noise's temporal correlation becomes on average shorter and weaker as

the satellite elevation angle decreases. Such variation patterns were also reported by Leandro and Santos (2007) while analysing geometrically reduced double-difference pseudo-ranges from small baselines. Schön and Brunner (2008a) explained the cause based on the characteristic separation distances of the lines-of-sights, which vary much faster at low elevation angles. Although the SDDR used in this case study evidently reflect the influence of satellite elevation angle on the noise's temporal correlation, a double-difference residual involves two satellites and two sites, making it difficult to find a representative measure of satellite geometry. For this reason, it seems to be more appropriate to use zero-difference residuals, for example, those obtained from precise point positioning (see section 8.2.5).

(a) Zero-crossing correlation length

(b) Lag-1 correlation level

Figure 8.18: Temporal correlation characteristics with respect to satellite geometry (see figure 8.7(a) for satellite geometry, 1-hour decomposed SDDR noise, sampling interval: 1 s)

On the basis of atmospheric turbulence theory, Schön and Brunner (2008a) showed that the correlation pattern of GPS phase observations depends not only on the changing satellite geometry, but also on the prevailing atmospheric conditions. For example, the wind speed (WS) plays a key role in decorrelation processes. Moreover, as illustrated in Fuhrmann et al. (2010, p. 92, 104), after removing the site-specific error effects by stacking, there are still signals in the GPS observation residuals that are induced by the azimuthally anisotropic tropospheric wet delays. In the light of these findings, it seems reasonable to incorporate the DWD surface meteorological data into the noise's temporal correlation analysis to enable a physical interpretation of the results. Along with the WS and RH measurements, figure 8.19 presents the mean correlation characteristics on a daily basis, where the sample sizes vary between 26 and 44. The WS data in the DWD collective standard format KL2000 are given on the Beaufort scale (B), which empirically relates wind speed to observed conditions at sea, such as foam coverage and wave shape. While a Beaufort number of 0 describes a calm sea like a mirror, a value of 12 indicates hurricane-force wind, leading to huge waves making the sea completely white with driving spray. Using the empirical formula

$$v_{10}\,[\mathrm{m/s}] = 0.836\,[\mathrm{m/s}] \cdot B^{3/2} \tag{8.4}$$

given by Stewart (2008, p. 43), the Beaufort scale B can be converted into the metric-based unit m/s, where v_{10} is the wind speed at a height of 10 m above the ground in a flat and completely open area. As figure 8.19(a) shows, temporally variable WS is predominantly observed at the northern and central four DWD sites, i.e., FRAN, WUER, KARL, and STUT, while variable RH is measured at all the six meteorological stations. To achieve the maximum temporal variability, the mean WS and RH are computed using the above-mentioned four and all the six DWD sites, respectively. The upper plot of figure 8.19(b) illustrates a moderate negative correlation of -0.4 between the daily mean zero-crossing correlation length and WS. In particular, large correlation

(a) DWD surface WS and RH measurements

(b) Mean temporal correlation characteristics
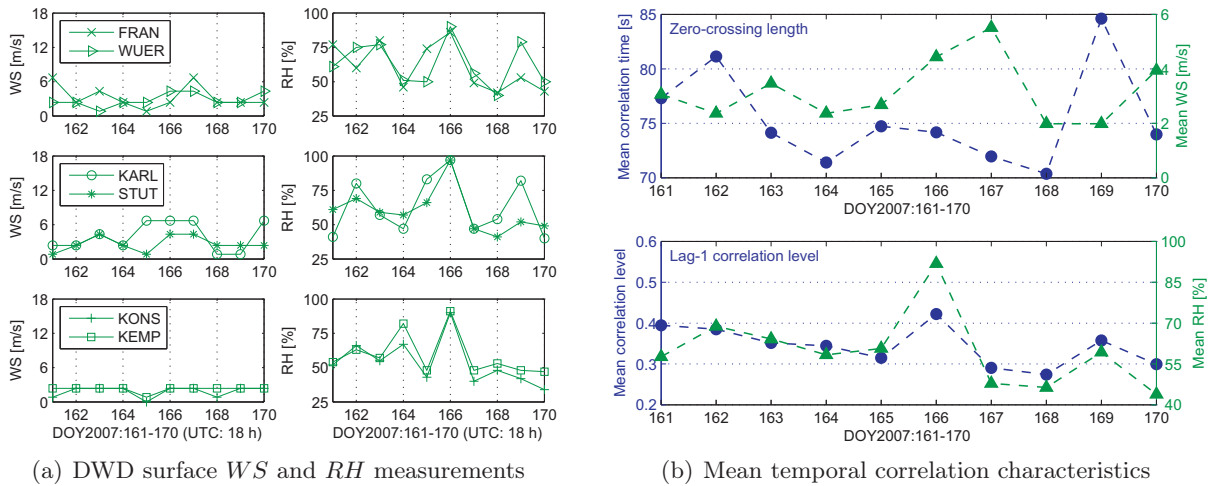
Figure 8.19: Temporal correlation characteristics with respect to atmospheric conditions (see figure 4.8 for the DWD surface meteorological data; WS: wind speed, RH: relative humidity)

lengths are found on days 162 and 169 with low WS, while a small correlation length is visible on day 167 with a high WS. In spite of the moderate correlation level, it is interesting to see that the mathematically derived correlation lengths can be physically interpreted. From the lower plot of figure 8.19(b), one can easily discern a strong positive correlation of 0.8 between the daily mean lag-1 correlation level and RH. As mentioned before, this can be explained by the remaining tropospheric wet delays and the changes in the site-specific multipath environment due to variable atmospheric conditions. To illustrate the effects of a humid atmosphere on the noise's temporal correlation structure, figure 8.20 compares the decomposed noise and the associated sample ACF for the double-difference RATA1826 on two representative days, 166 and 170, with the maximum and minimum mean RH, respectively (see figure 8.19(b)). In comparison to day 170, the noise series from day 166 is more variable and exhibits increased signal content with decreasing satellite elevation angle. As a result, the corresponding sample ACF depicts a higher lag-1 correlation level (day 166: 0.36, day 170: 0.17) and a longer zero-crossing correlation length (day 166: 137 s, day 170: 92 s). By comparing the mean correlation length and RH shown in figure 8.19(b), a weak positive correlation of 0.3 is detected.

(a) Noise time series NCR(3)

(b) Noise sample ACF
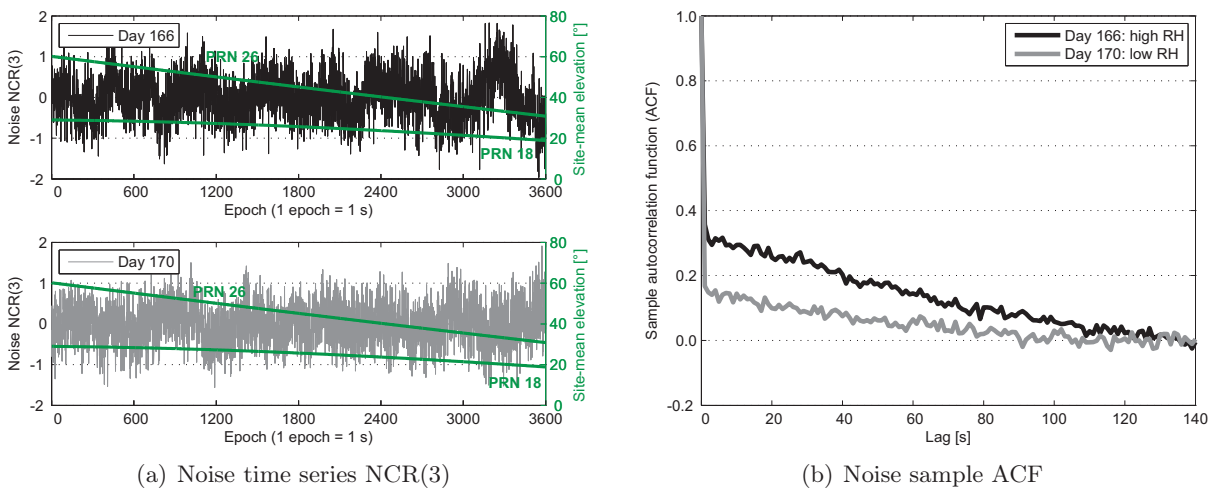
Figure 8.20: Effects of a humid atmosphere on the noise's temporal correlation (baseline: RATA, 203.7 km, weak multipath, satellite pair: PRN 18-26, DOY2007:166, 170; see figure 8.19(b))

Analysing the short-term (1 h) SDDR, being located near the observation time of the DWD surface meteorological data (see figure 4.8), the noise's temporal correlation characteristics derived in this case study are physically interpretable and sensitive to variations in atmospheric conditions. Nevertheless, additional studies are necessary in which not only more representative residuals, but also high-resolution meteorological data should be used. Moreover, forming baselines and selecting satellite tracks by paying particular attention to their orientations, the effects of satellite azimuth and wind direction on the noise's correlation properties can be investigated. For each decomposed noise series, the best-fitting ARMA model is determined, allowing for a mathematically rigorous description of the noise's temporal stochastic behaviour.
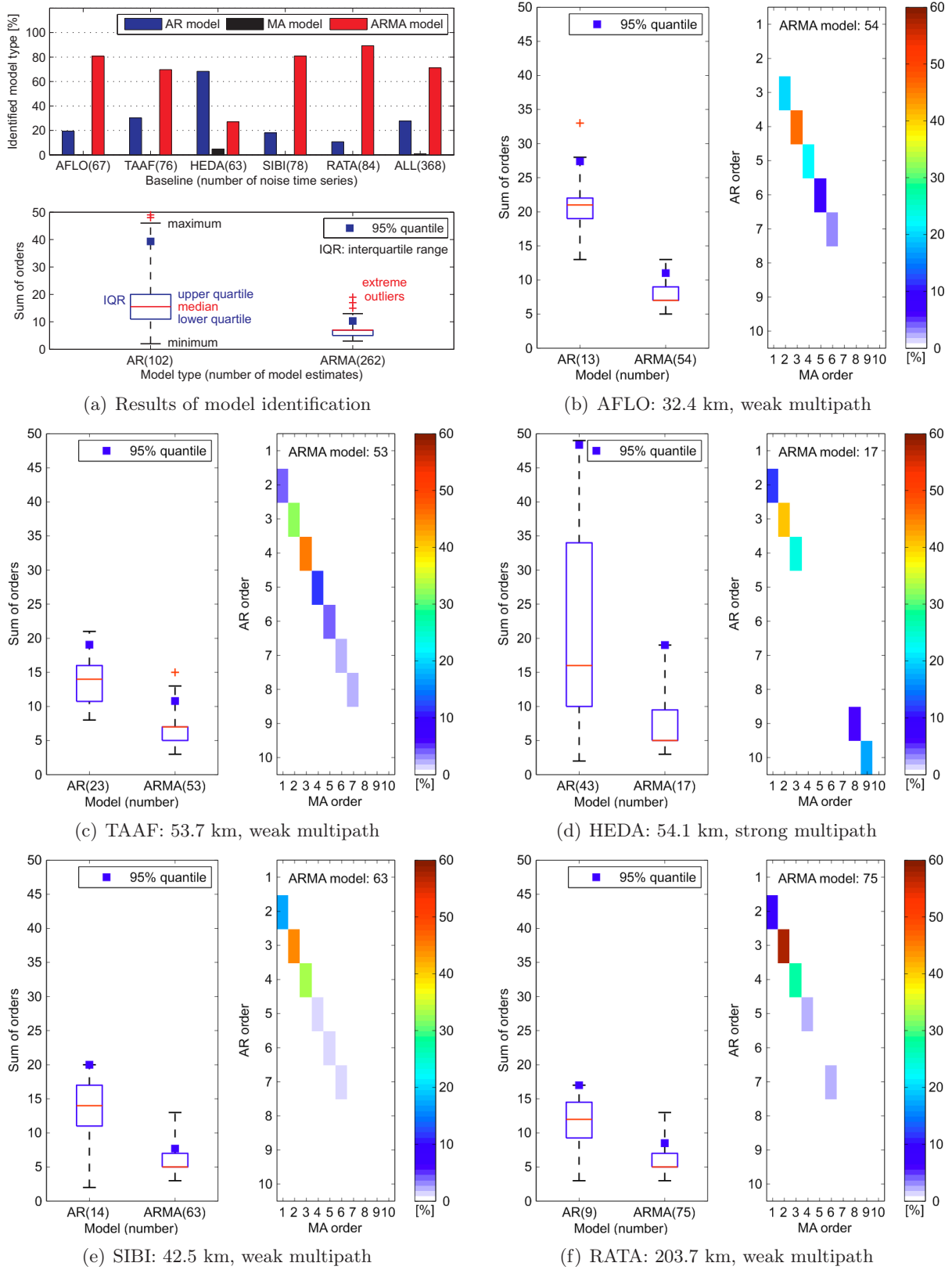
8.1.6 Results of ARMA modelling

In this thesis, ARMA modelling is carried out using the ARMASA Toolbox (Broersen, 2006, chap. 9), which enables an automatic identification of the best-fitting ARMA model for a given noise realisation (see section 7.3). Before applying this free toolkit within the residual-based temporal correlation modelling, Luo et al. (2011b) empirically evaluated its performance based on numerous simulated noise time series with representative temporal correlations, being comparable to GPS residuals. The results showed that having sufficient data is essential for unbiased model identification and parameter estimation. In the case where the data volume is about 10 times the zero-crossing correlation length, the model error estimated by means of equation (7.44) is very close to the optimum efficiency of the Cramér-Rao lower bound (see section 7.3.4). For longer data lengths, more than 80% of the identified ARMA models are unbiased, and the rate of biased model estimates increases with increasing correlation complexity. Furthermore, the use of hierarchical ARMA$(p, p-1)$ models considerably reduces the required computational time. In summary, the ARMASA Toolbox is capable of efficiently producing causal and invertible ARMA models for stationary GPS noise series of sufficient length.

The input data for ARMA modelling are the decomposed noise sequences NCR(3) (see figure 7.3). As illustrated in figures 8.16 and C.3, the noise's sample ACF values decay rapidly, which is desirable for fitting ARMA models (Brockwell and Davis, 2002, p. 403). Following the suggestions given by the ARMASA demonstration program, the maximum candidate orders $p_{AR}^{\max}$, $q_{MA}^{\max}$, and $p_{AM}^{\max}$ are chosen to be 100, 20, and 10 for the AR(p), MA(q), and ARMA$(p, p-1)$ models, respectively. Accordingly, the maximum order models are AR(100), MA(20), and ARMA(10, 9). In figure 8.21, the results of model identification and order selection are presented.

From the upper plot of figure 8.21(a) it can be seen that AR and ARMA estimates dominate the results of the model identification. In fact, only one noise series from the baseline SIBI can be considered as WN, and MA models are identified only three times for the HEDA-related data. Moreover, multipath impact seems to play an important role in model identification. If strong multipath is present (e.g., HEDA), AR models are preferred in comparison to ARMA alternatives. In contrast to multipath, baseline length insignificantly affects the model identification. Regarding the box plots of the sum of orders shown in the lower plot of figure 8.21(a), the specified maximum orders, i.e., $p_{AR}^{\max} = 100$ and $p_{AM}^{\max} = 10$, appear to be sufficient, since all the selected $\hat{p}_{AR}$ are below 50, and 99% of $\hat{p}_{AM} + \hat{q}_{AM}$ are less than $10 + 9 = 19$.

Considering the AR and ARMA model estimates for each baseline, figures 8.21(b)-(f) illustrate the box plots of the sum of orders (i.e., AR: $\hat{p}_{AR}$, ARMA: $\hat{p}_{AM} + \hat{q}_{AM} = 2\hat{p}_{AM} - 1$), as well as the relative frequency of the identified hierarchical ARMA models. For the baselines with weak multipath impact, the 95% quantiles of the AR orders vary from 17 to 27 with a IQR (interquartile range) between 3 and 6, while the 95% quantiles of the sum of the ARMA orders vary from 7 to 11 with a constant IQR of 2. This indicates the inadequacy of using AR(1)

(a) Results of model identification

(b) AFLO: 32.4 km, weak multipath

(c) TAAF: 53.7 km, weak multipath

(d) HEDA: 54.1 km, strong multipath

(e) SIBI: 42.5 km, weak multipath

(f) RATA: 203.7 km, weak multipath

Figure 8.21: Results of the model identification and order selection using the ARMASA Toolbox (1-hour decomposed SDDR noise, sampling interval: 1 s, AR: $\hat{p}_{AR}$, ARMA: $\hat{p}_{AM}+\hat{q}_{AM} = 2\hat{p}_{AM}-1$; see table 4.3 for baseline properties and section 7.3 for ARMA modelling)

processes to describe the noise's temporal correlation and the necessity of applying higher-order AR and ARMA models, even in weak multipath environments. As figure 8.21(d) displays, higher-order AR processes appear to be more applicable in the case of strong multipath impact, where the AR orders have a 95% quantile of 48 and a significantly increased IQR of 24. Regarding the associated ARMA estimates, $\hat{p}_{AM} + \hat{q}_{AM} \leq 7$ is satisfied for 13 out of 17 cases. Like the problem of polynomial fitting, higher ARMA orders allow for a more accurate characterisation or a better fit to the given noise, but do not necessarily indicate longer and stronger temporal correlations. Despite the thorough filtering and stacking procedures performed during the course of the residual decomposition, there may exist remaining systematic effects in NCR(3), which do not destroy the noise stationarity. In this case, the ARMASA Toolbox attempts to account for the residual signals by selecting higher-order time series models. This is true for the baseline HEDA with strong multipath impact, particularly under variable atmospheric conditions.
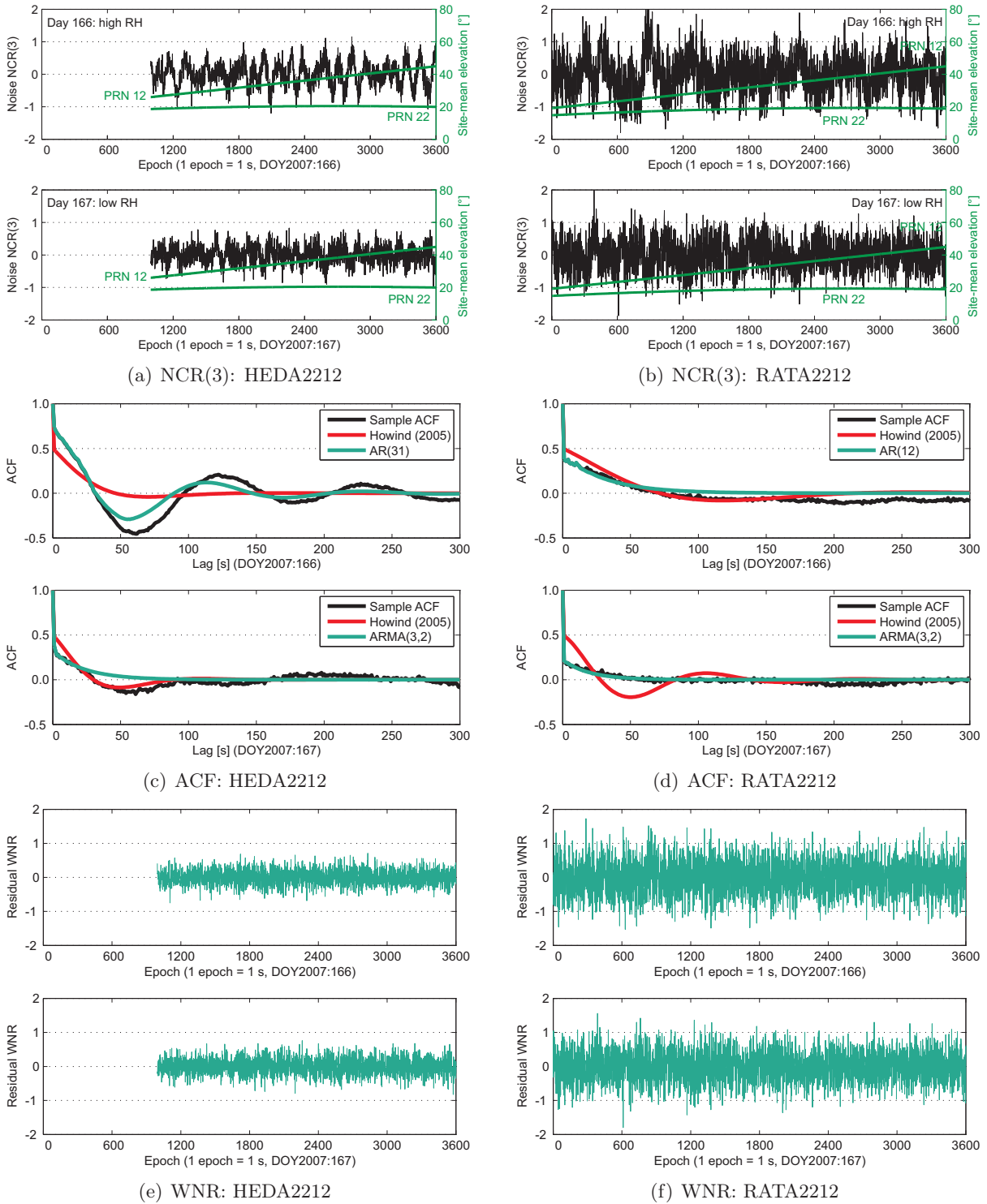
In addition to the baseline-related analysis, figure 8.22 depicts the sum of ARMA orders with respect to satellite geometry and atmospheric conditions, where the same representative elevation angles and mean WS are used, as shown in figures 8.18 and 8.19(b), respectively. Despite a weak negative correlation of -0.3 between the 95% quantiles of the sum of orders and the representative elevation angles, figure 8.22(a) suggests that the sum of orders tends to increase with decreasing satellite elevation angle. This can be understood by considering the increased residual systematic signals at low elevation angles. They are neither considered in GPS data processing nor captured during the residual decomposition, but can be handled by fitting high-order ARMA models. Comparing the 95% quantiles of the sum of orders with the mean WS, figure 8.22(b) illustrates a moderate negative correlation of -0.4. Using another completely different software called ITSM2000-V.7.1 (Brockwell and Davis, 2002, p. 395), Luo et al. (2012b) analysed the same SDDR data by means of ARIMA$(p, 1, q)$ processes. Thereby, WS exhibits a similar influence on order selection, where the remaining systematic effects are eliminated by undertaking the first-order difference instead of the residual decomposition (see section 2.2.1).

(a) Satellite geometry

(b) Wind speed (WS)
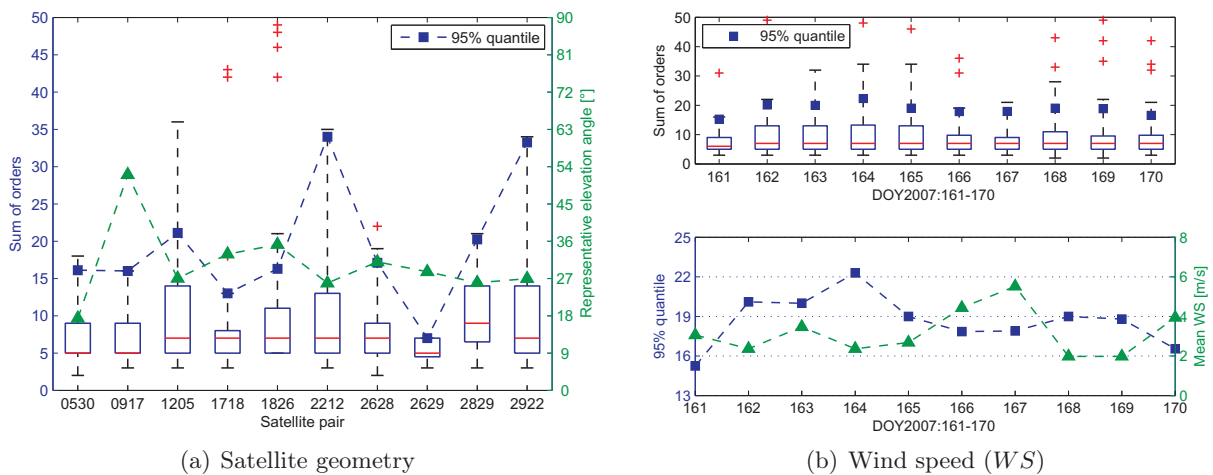
Figure 8.22: Sum of ARMA orders with respect to satellite geometry and atmospheric conditions (see figure 8.18 for representative elevation angles and figure 8.19(b) for mean WS)

Figure 8.23 illustrates examples of ARMA modelling under variable atmospheric conditions. The baselines HEDA and RATA are chosen, which are representative with respect to multipath impact and baseline length, respectively (see table 4.3). Two consecutive days, 166 and 167, are considered, for which the RH measurements at the DWD stations are significantly different (see figure 8.19(a)). The noise series displayed in figures 8.23(a) and (b) reflect the variable atmosphere, leading to deviations in the remaining systematic signals in NCR(3). As figures 8.23(c)

and (d) show, high-order AR(31) and AR(12) models are identified for day 166 and characterise the complex correlation structure, which is actually caused by the large magnitudes of the residual systematic effects. For day 167, low-order ARMA(3, 2) models appear to be adequate enough to describe the noise's correlation properties. Applying the empirical ACF given

(a) NCR(3): HEDA2212

(b) NCR(3): RATA2212

(c) ACF: HEDA2212

(d) ACF: RATA2212

(e) WNR: HEDA2212

(f) WNR: RATA2212

Figure 8.23: Examples of ARMA modelling under different atmospheric conditions (HEDA: 54.1 km, strong multipath, RATA: 203.7 km, weak multipath, satellite pair: PRN 22-12, DOY2007:166, 167; see figure 8.19(a) for *RH* measurements)

by equation (7.2) (Howind, 2005, p. 57), the results are compared with those from the ARMA modelling. In the low-valued lag areas, where strong temporal correlations are present, the estimated empirical ACF exhibit considerable deviations from the noise's sample ACF. This is attributed to the specification of a constant lag-1 correlation of 0.5 and the use of LS regression for overall minimisation. In contrast, the ARMA model ACF flexibly capture the lag-1 correlations of the noise's sample ACF and enable a more accurate fit in the presence of a damped periodicity. Such advantages of fitting ARMA models over estimating empirical ACF were also reported by Luo et al. (2012b). Filtering the coloured noise series NCR(3) with the determined ARMA models, the outcomes are called ARMA residuals (WNR in figure 7.3), visualised in figures 8.23(e) and (f). Obviously, the systematic signals remaining in NCR(3), particularly on day 166, are well absorbed by the ARMA models, resulting in homogeneous WNR. To verify the uncorrelatedness of WNR or the efficiency of ARMA modelling, the statistical tests described in section 2.3.5 are employed, of which the results will be discussed in section 8.1.7. Comparing figures 8.23(e) and (f) with each other, it is clearly visible that the HEDA-related WNR exhibit smaller variances than the RATA-related ones. This gives some motivation to undertake a more detailed analysis of the residual (or estimated WN) variances.

Figure 8.24 provides a baseline-wise presentation of the standard deviations (STD) of NCR(3) and WNR. In comparison to other baselines with weak multipath impact, the HEDA-related STD of NCR(3) are on average 0.16 smaller. After filtering NCR(3) with the identified ARMA models, the mean STD is attenuated by about 0.05, with a maximum decrease of 0.08 for HEDA. This agrees with the results of order selection shown in figure 8.21, since fitting a higher-order ARMA model generally leads to a lower estimated WN variance (Brockwell and Davis, 2002, p. 169). Therefore, the smaller variances observed in figure 8.23(e) are due to stronger multipath effects and higher ARMA orders, where the former obviously plays a dominant role.

(a) STD of NCR(3) and WNR   (b) Box plots of the STD shown in (a)
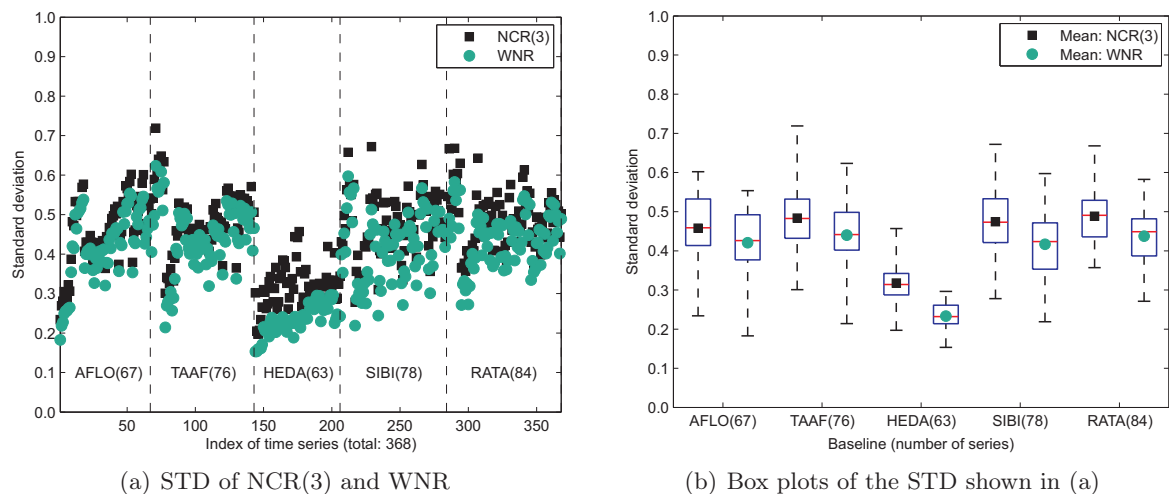
Figure 8.24: Noise standard deviations (STD) before (NCR(3)) and after (WNR) ARMA modelling (see table 4.3 for baseline properties)

Figure 8.25 depicts the STD of NCR(3) and WNR with respect to satellite geometry. In both plots, there exist strong negative correlations of about -0.9 between the mean STD and the representative elevation angles. Considering the conclusion drawn from figure 8.22(a) that higher orders are needed at low elevation angles, as well as the fact that higher-order ARMA models result in smaller estimated WN variances, the STD of WNR is supposed to decrease with decreasing elevation angle. However, as figure 8.25(a) illustrates, the STD of NCR(3) increases as the elevation angle decreases, which seems to be a more dominant factor making the STD of WNR larger than the higher ARMA orders trying to make them smaller. In addition, the daily

mean STD of WNR is found to be weakly correlated with the mean WS and RH, with correlation coefficients of 0.2 and -0.3, respectively. When employing ARMA models in forecasting applications, although not relevant for this work, the choice of arbitrarily high orders should be avoided, since the quality of the forecasts depends not only on the WN variance, but also on the errors of the estimated model parameters. These will become large for high-order ARMA models (Brockwell and Davis, 2002, p. 169).

(a) STD of NCR(3) vs. elevation angle

(b) STD of WNR vs. elevation angle
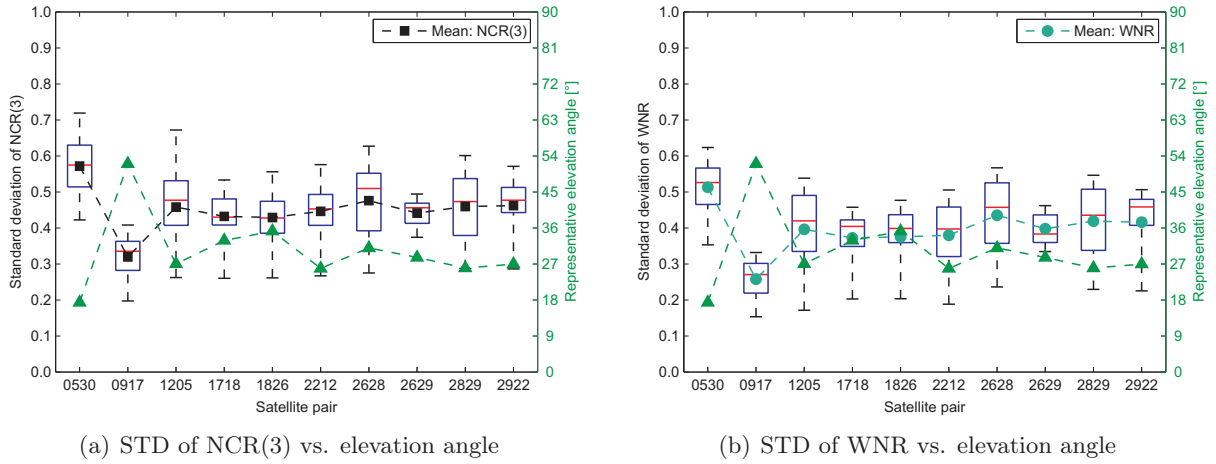
Figure 8.25: Standard deviations (STD) of NCR(3) and WNR with respect to satellite geometry (see figure 8.18 for representative elevation angles)

Assuming that the fitted time series model represents the true data-generating process, the ARMA residuals (WNR) would be realisations of a WN process. In this case, about 95% of the sample ACF of WNR should lie within the confidence bounds $\pm 1.96/\sqrt{n}$, where 1.96 is the 0.975-quantile of the standard normal distribution, and n is the data length (see section 2.2.2). Regarding the same examples used for the residual decomposition (see figure 8.16), figure 8.26 shows the sample ACF of NCR(3) and WNR, along with the model ACF of the fitted ARMA processes. For lags of up to the zero-crossing correlation length (see section 8.1.5), the sample ACF of NCR(3) can be well approximated by the ARMA model ACF. However, the noise's sample autocorrelations at large lags cannot be captured, reflecting the short-memory nature

(a) SDDR: TAAF1205

(b) SDDR: HEDA1205
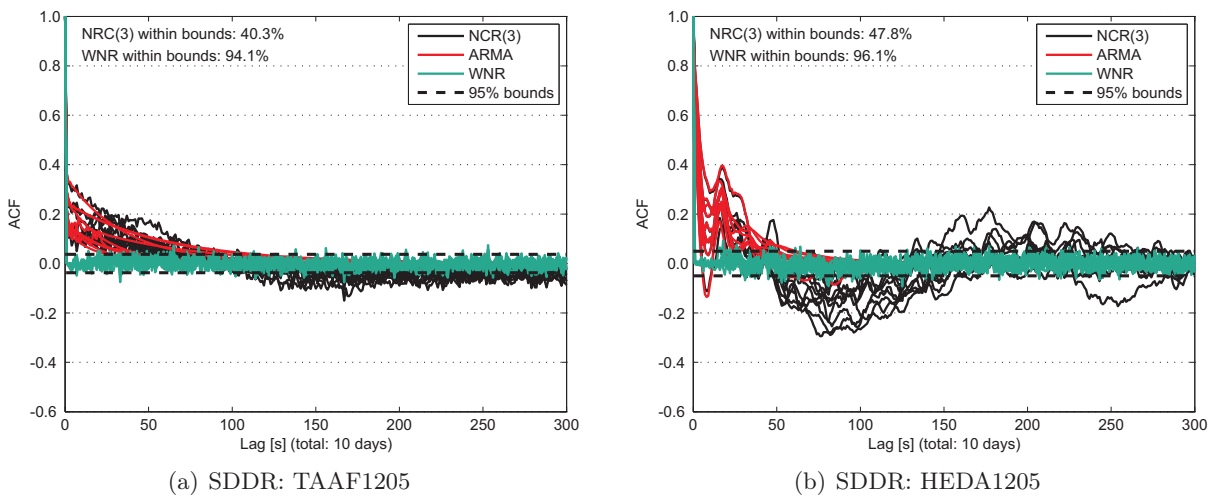
Figure 8.26: Comparison of noise's sample and ARMA model ACF (TAAF: 53.7 km, weak multipath, HEDA: 54.1 km, strong multipath, satellite pair: PRN 12-05, DOY2007:161-170)
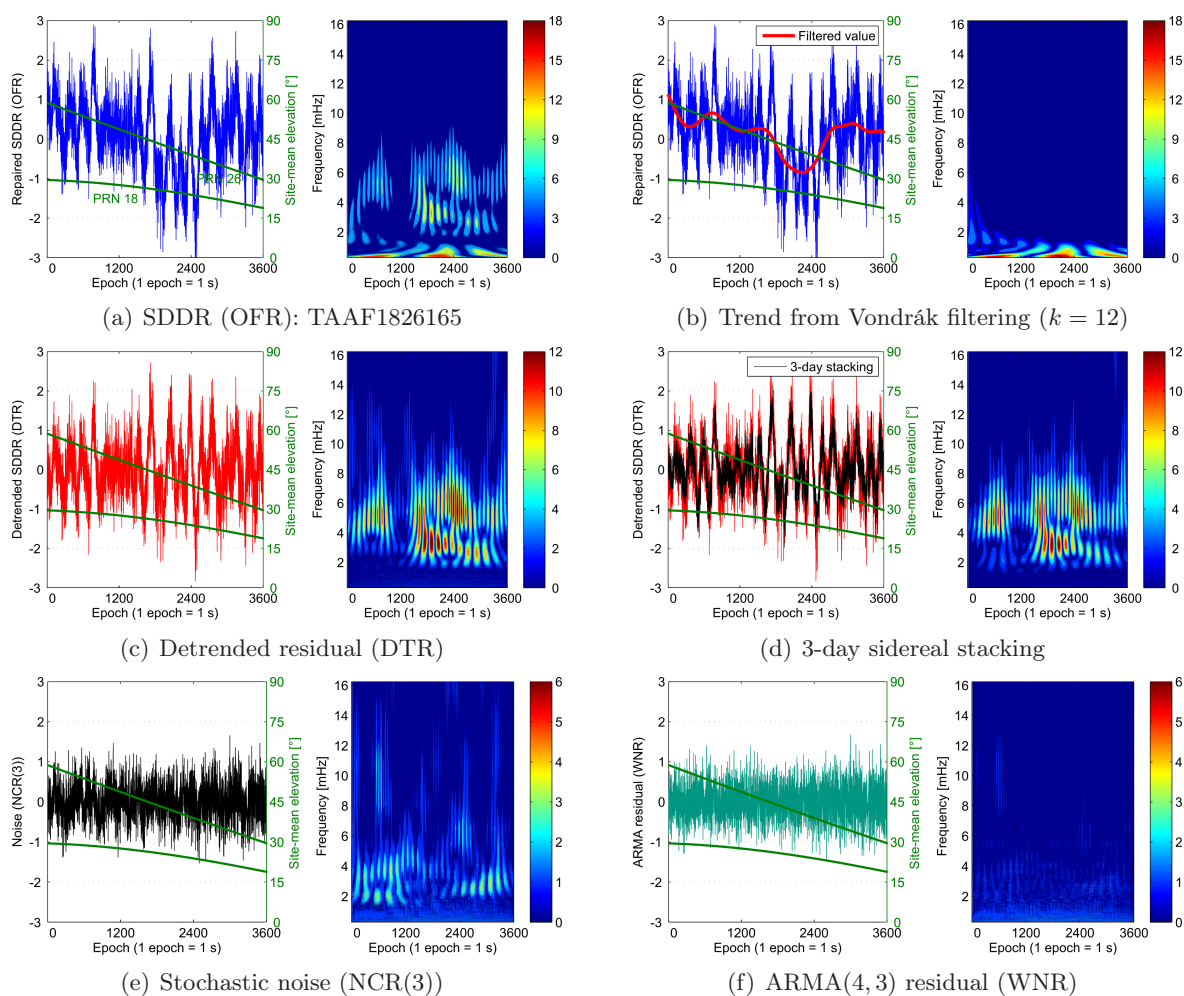
of stationary ARMA processes (Luo et al., 2012b). After filtering NCR(3) with the estimated ARMA models, the sample ACF of the resulting WNR fall within the plotted confidence intervals roughly 95% of the time. This indicates not only the uncorrelatedness of the ARMA residuals, but also the appropriateness of the identified ARMA models. Comparing the widths of the confidence intervals from both examples, the one displayed in figure 8.26(a) is slightly smaller (TAAF1205: 0.07, HEDA1205: 0.10). This is due to the longer data length of TAAF1205 (2848 epochs) in comparison to HEDA1205 (1604 epochs). Additional examples, demonstrating the efficiency of ARMA processes in modelling coloured noise, are provided in figure C.4, particularly in the presence of residual systematic signals, as shown in the upper plot of figure 8.23(a).

Although the residual-based temporal correlation modelling by means of ARMA processes represents a mathematical approach, the estimated model parameters reflect the influences of site-specific multipath effects, satellite geometry, and variable atmospheric conditions. The effectiveness of using ARMA models of moderate orders in noise characterisation also verifies the high performance of the proposed residual decomposition in detecting the remaining systematic signal components of long- and short-periodic nature. In the next section, the efficiency of the residual decomposition and ARMA modelling will be assessed by means of continuous wavelet transforms and appropriate statistical hypothesis tests.

8.1.7 Visual and statistical verification

Applying the continuous wavelet transform (CWT) to the residual components, for example, by means of the MATLAB® Wavelet Toolbox™ (MWT; see section 2.4.2), the resulting scalograms are used for the visual verification of the residual decomposition and ARMA modelling. Thereby, the real-valued Morlet wavelet $\psi_M(t) = \pi^{-1/4} e^{-t^2/2} \cos(5t)$ with a centre frequency of $F_m = 0.813$ is chosen as the mother wavelet (see figure 2.7). Substituting $F_m = 0.813$ and $\Delta t = 1$ s into equation (2.99), scales a varying between 50 and $n \cdot F_m$ with a step of 25 are found suitable for detecting signals with the minimum and maximum periods of 1 min and n s, respectively, where n denotes the data length and has a minimum of 600 in this case study (see section 8.1.3). In terms of positions b, the CWT performed using the MWT smoothly shifts the analysing wavelet over the full domain of the signal to be transformed. Considering different multipath impact, figures 8.27 and 8.28 show representative examples of wavelet scalograms. Using the real-valued Morlet wavelet $\psi_M(t)$ as the mother wavelet, the resulting wavelet coefficients $\mathscr{W}_{\psi_M}[f](a, b)$ of a signal $f(t)$ are also real numbers (see equation (2.97)). The absolute values of $\mathscr{W}_{\psi_M}[f](a, b)$ are visualised in the wavelet scalograms, illustrating the time-frequency localisation property of the CWT. The y-axis represents the pseudo-frequency, which is computed by means of equation (2.99) for each scale a. Regarding the scale limits $n \cdot F_m$ and 50, the corresponding pseudo-frequencies are $1000/n$ and 16 mHz, respectively.

As figures 8.27(a) and 8.28(a) show, the wavelet scalograms well represent the signal composition of the repaired SDDR (OFR) in both the time and frequency domains, particularly the low-frequency trends and the quasi-periodic oscillations with temporally varying frequencies. Both examples exhibit signals with short periods of several minutes, suggesting the existence of far-field multipath effects. Applying the Vondrák filter with $k = 12$ (see figure 8.8), as displayed in figure 8.27(b), the slowly varying trend component can be sufficiently detected. If a smaller filter parameter of $k = 10$ is used, the filtered curve depicted in figure 8.28(b) also contains some oscillations with a period of about 500 s. After removing the Vondrák trends, figures 8.27(c) and 8.28(c) illustrate the detrended residuals (DTR), predominantly affected by rapidly oscillating signals of a quasi-periodic nature. In the TAAF-related example (see figure 8.27(d)), the 3-day sidereal stacking sufficiently captures the short-periodic component, leading to stochastic noise (NCR(3)) that is largely free of systematic effects (see figure 8.27(e)). In contrast, as can be
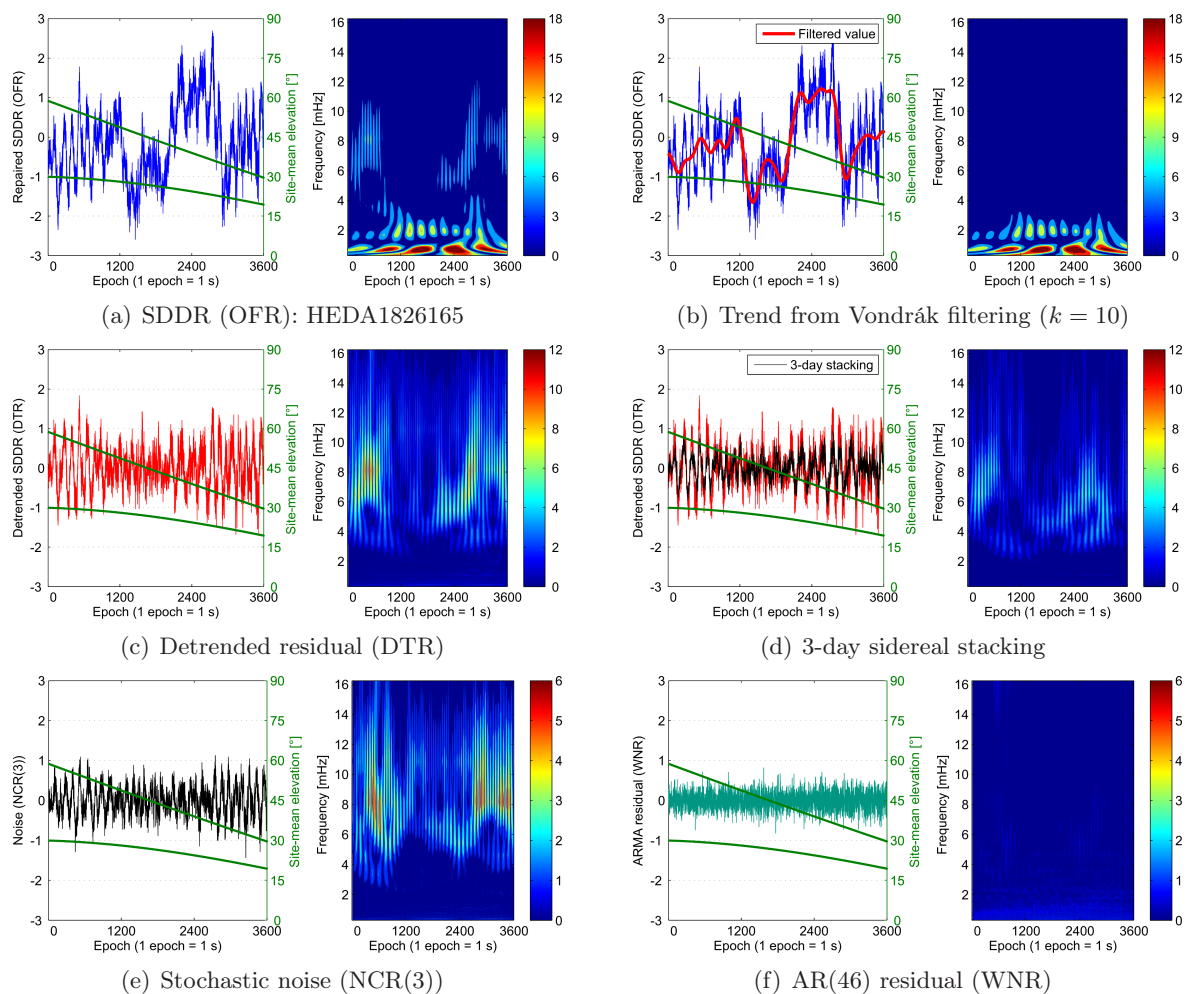
(a) SDDR (OFR): TAAF1826165

(b) Trend from Vondrák filtering ($k = 12$)

(c) Detrended residual (DTR)

(d) 3-day sidereal stacking

(e) Stochastic noise (NCR(3))

(f) ARMA(4, 3) residual (WNR)

Figure 8.27: Verification of the residual decomposition and ARMA modelling based on wavelet scalo-grams (baseline: TAAF, 53.7 km, weak multipath, satellite pair: PRN 18-26, DOY2007:165, mother wavelet: Morlet wavelet; see equation (2.94) and figure 2.7)

observed in figure 8.28(d), only a part of the quasi-periodic signals can be stacked so that some high-frequency oscillations remain in NRC(3) (see figure 8.28(e)). After filtering the noise series with the identified low-order ARMA(4, 3) and high-order AR(46) models, the scalograms of the resulting ARMA residuals (WNR) exhibit insignificant wavelet coefficients in figures 8.27(f) and 8.28(f), respectively. This indicates that the remaining systematic signals in the noise component can be handled by appropriately determined ARMA models.

In addition to wavelet scalograms, which provide a visual impression of the performance of the residual decomposition and ARMA modelling, the input OFR, as well as the outputs DTR, NRC(3), and WNR, are also statistically verified by means of different hypothesis tests for normality, trend, (non-)stationarity, and uncorrelatedness (see section 2.3). To allow for easy application of these test methods, the quantiles of the distributions of the test statistics are provided in appendix A, along with the available MATLAB® functions. Table 8.2 gives an overview of the employed statistical tests, including the associated null hypotheses $\mathcal{H}_0$, notations, and key references. In this case study, the hypothesis testing is performed at a significance level of $\alpha = 1\%$, which corresponds to the probability of committing a Type I error (see table 2.3). In the following analysis, the non-rejection rate of $\mathcal{H}_0$ is used to evaluate the validity of the tested null hypothesis, where only representative examples are discussed. For the sake of completeness, the entire test results are presented in table D.5.

Table 8.2: Overview of the statistical hypothesis tests used for the performance verification of the residual decomposition and ARMA modelling (see section 2.3 and appendix A)

Null hypothesis $\mathcal{H}_0$	Statistical test	Notation	Reference
Normal distribution	Jarque-Bera test	JB	Jarque and Bera (1987)
	Anderson-Darling test	AD	Anderson and Darling (1952)
	Lilliefors test	LF	Lilliefors (1967)
	Chi-square test	CS	Lehmann and Romano (2005, p. 590)
Trend-free (two-sided)	Cox-Stuart test	CT	Hartung et al. (2005, p. 247, 249)
	Mann-Kendall test	MK	
Non-stationarity	Augmented Dickey-Fuller test	ADF	Said and Dickey (1984)
Stationarity	KPSS[1] test	KPSS	Kwiatkowski et al. (1992)
Uncorrelatedness	Von Neumann ratio	VNR	Bingham and Nelson (1981)
	Ljung-Box portmanteau test	LB	Teusch (2006, p. 100–104)
	Kolmogorov-Smirnov test	KV	
	Cramér-von Mises test	CM	

[1] Kwiatkowski-Phillips-Schmidt-Shin

(a) SDDR (OFR): HEDA1826165

(b) Trend from Vondrák filtering ($k = 10$)

(c) Detrended residual (DTR)

(d) 3-day sidereal stacking

(e) Stochastic noise (NCR(3))

(f) AR(46) residual (WNR)

Figure 8.28: Verification of the residual decomposition and ARMA modelling based on wavelet scalograms (baseline: HEDA, 54.1 km, strong multipath, satellite pair: PRN 18-26, DOY2007:165, mother wavelet: Morlet wavelet; see equation (2.94) and figure 2.7)

As described in section 7.2.1, the studentised residual like SDDR follows Pope's τ-distribution which approaches the standard normal distribution for large degrees of freedom (Heck, 1981a). This is generally valid in static GPS positioning due to the high number of redundant observations. However, the distribution of SDDR can significantly deviate from the assumed normality due to the remaining differential atmospheric delays and generally unmodelled multipath effects. This is particularly true when analysing long-baseline GPS data collected under non-ideal observational conditions (Tiberius and Borre, 1999; Luo et al., 2011a). After Vondrák filtering and sidereal stacking, the remaining systematic signals are supposed to be largely reduced. Therefore, testing the repaired SDDR (OFR) and the decomposed noise (NCR(3)) for normality indirectly evaluates the efficiency of the suggested residual decomposition approach. Moreover, in the interest of a reliable outlier validation using the F-test statistic given by equation (7.14), it is necessary to check for the distribution of the detrended residuals (DTR), since the F-test is known to be highly sensitive to non-normality (Markowski and Markowski, 1990). If both NCR(3) and ARMA residuals (WNR) can be regarded as normal, the determined ARMA model reflects a Gaussian linear process, providing favourable properties in statistical modelling. Due to the large baseline length of RATA and the strong multipath impact of HEDA (see table 4.3), their results of the normality tests are illustrated in figure 8.29, where a total of 226957 and 163490 samples (84 and 63 data series) are considered, respectively.

To cope with the deficiencies in the GPS mathematical models, the tests for normal distribution are carried out in the composite hypothesis case, i.e., the mean and variance are estimated from data. Nevertheless, the null hypothesis that the samples are normally distributed cannot be rejected for only a small part of OFR, about 39% and 10% in the case of RATA and HEDA, respectively. Furthermore, in regional-scale GPS networks, multipath impact seems to affect the test results more significantly than baseline length. After removing the Vondrák trends (i.e., from OFR to DTR), the non-rejection rates of the normality hypothesis are increased by nearly 50%, reaching on average 84% and 68% for RATA and HEDA, respectively. This verifies not only the efficiency of Vondrák filtering, but also the appropriateness of using DTR for outlier validation. In the HEDA-related example, an additional improvement of about 15% is achieved after performing the 3-day sidereal stacking. Compared to far-field multipath, which induces rapidly oscillating quasi-periodic signals, near-field effects cause slowly varying long-periodic errors and have a more significant impact on the probability distribution of GPS phase observations (Luo et al., 2011a). As shown in figure 8.28(e), the HEDA-related noise series may still contain some systematic oscillations, which can be sufficiently handled within ARMA modelling. This increases the average non-rejection rate of $\mathcal{H}_0$ to 98% for WNR (see figure 8.29(b)), corresponding fairly well to the specified significance level of $\alpha = 1\%$. Note that the increased non-rejection of the normality hypothesis from OFR to WNR is also attributed to the decreased temporal correlation, which better fulfils the test assumption of uncorrelated samples. By incorporating DWD surface meteorological data, Luo et al. (2011a) found obvious positive correlations of about 0.5 between the test statistics and relative humidity measurements.

A favourable property of the non-parametric trend tests is that the data do not need to follow any particular distribution (see section 2.3.3). Therefore, they are especially applicable to OFR for which the normality hypothesis appears to be largely invalid (see figure 8.29). For the baselines RATA and HEDA, figure 8.30 shows the results of the trend tests. One can easily discern that more than 80% of OFR exhibit trends, which can be sufficiently captured by the Vondrák filter, resulting in predominantly trend-free DTR. A better trend removal is achieved for HEDA, which may be explained by the use of the smaller Vondrák filter parameters (see figure 8.8). The sidereal stacking primarily deals with quasi-periodic signals, and thus only insignificantly affects the trend test results. The obtained NCR(3) are largely free of long-term dependency and suitable for ARMA modelling. Filtering NCR(3) with stationary ARMA models, the resulting

WNR are also trend-free. Apart from evaluating the detrending performance, the trend tests also help accurately specify the model parameters when testing for (non-)stationarity.

(a) RATA: 203.7 km, weak multipath

(b) HEDA: 54.1 km, strong multipath
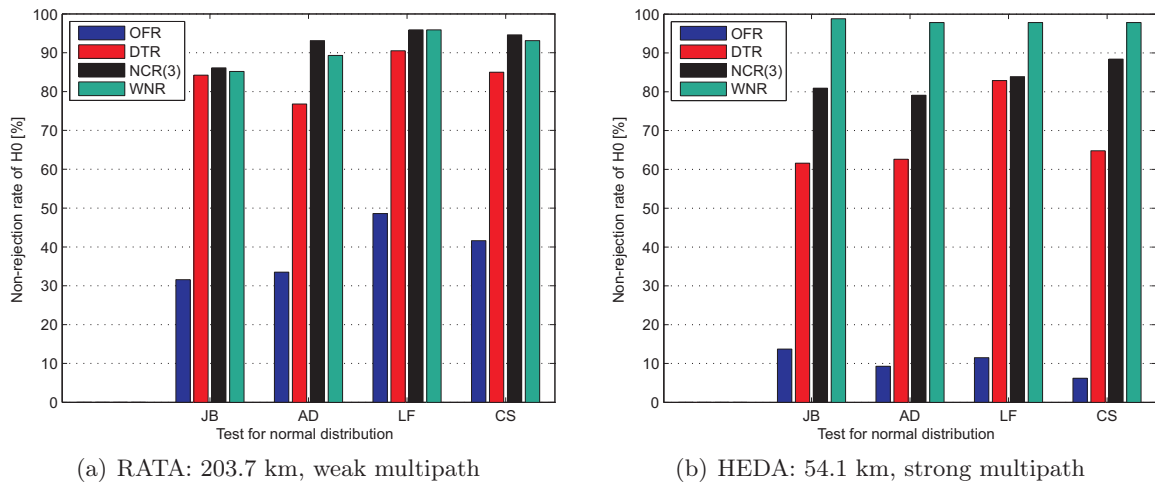
Figure 8.29: Representative results of the applied normality tests JB (Jarque-Bera test), AD (Anderson-Darling test), LF (Lilliefors test), and CS (chi-square test) ($\alpha = 1\%$; see section 2.3.2)

(a) RATA: 203.7 km, weak multipath

(b) HEDA: 54.1 km, strong multipath
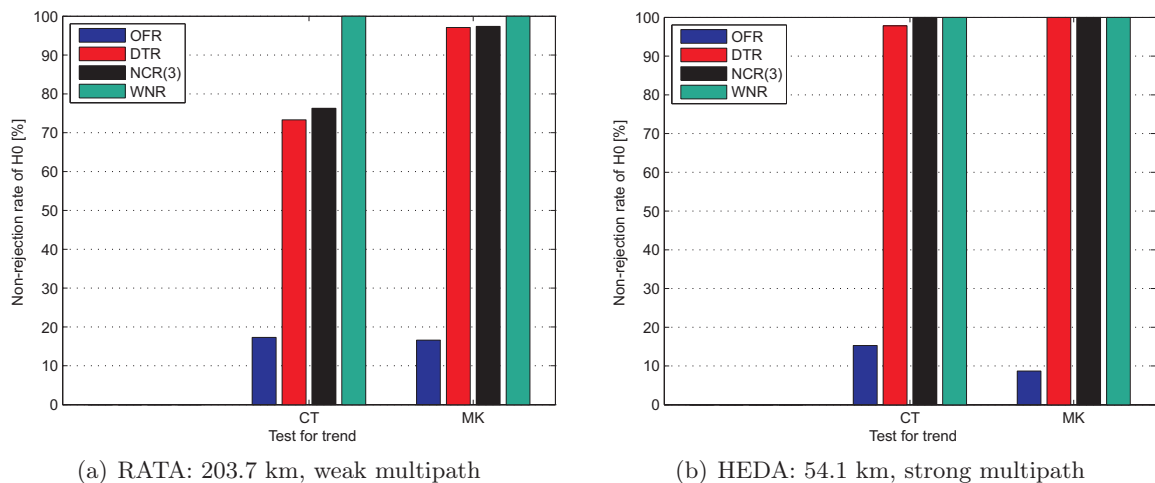
Figure 8.30: Representative results of the applied trend tests CT (Cox-Stuart test) and MK (Mann-Kendall test) ($\alpha = 1\%$; see section 2.3.3)

The temporal correlation modelling by means of ARMA processes assumes stationarity of the decomposed noise, which makes a rigorous statistical assessment of this assumption necessary. It is accomplished using the ADF and KPSS unit root tests, which specify opposite null hypotheses. While the ADF test verifies non-stationarity by looking for AR unit roots, the KPSS test checks for stationarity by searching for MA unit roots (see appendix B.2). An AR unit root suggests that the data cannot be directly described by a stationary ARMA model, whereas a MA unit root indicates that the data are overdifferenced (see section 2.3.4). For reliable test results, one has to choose appropriate regression models, i.e., c and δ in equations (2.78) and (2.81), as well as reasonable truncation lags, i.e., l in equations (2.78) and (2.84). As mentioned before, the specification of the test regression with respect to trend modelling relies upon the results of the trend tests. More precisely speaking, a linear trend is estimated only if its presence can be validated by both the CT and MK tests, since modelling a deterministic trend will decrease the power of the ADF test. For the KPSS test, a truncation lag of $\sqrt{n}$ is used, where n denotes the data length (Kwiatkowski et al., 1992). For the ADF test, the lag number is selected according

to equation (2.79) (Schwert, 1989). Note that using too large truncation lags will decrease the power of both the ADF and KPSS tests. Applying the unit root tests to the residual components from RATA and HEDA, the results are depicted in figure 8.31.

(a) RATA: 203.7 km, weak multipath   (b) HEDA: 54.1 km, strong multipath
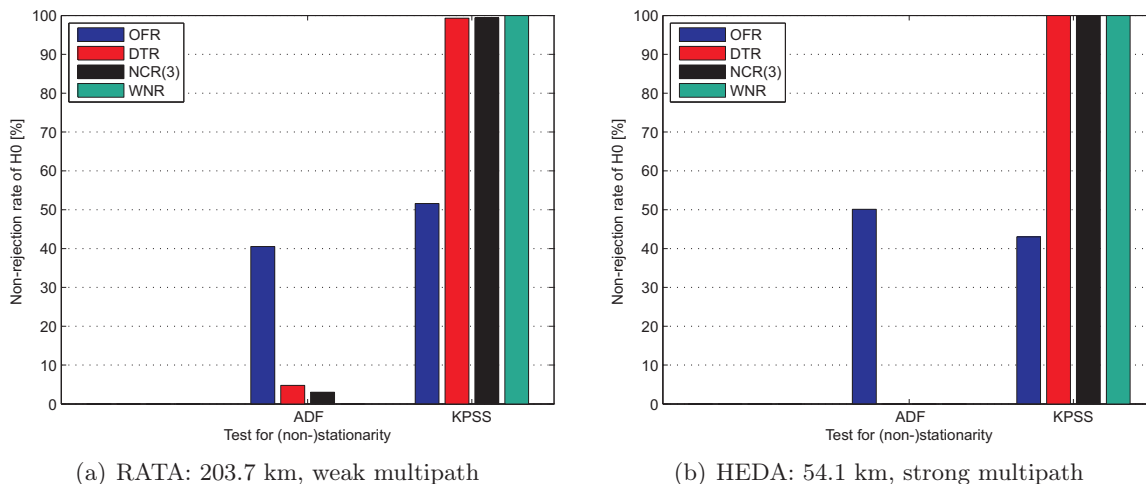
Figure 8.31: Representative results of the applied unit root tests ADF (augmented Dickey-Fuller test) and KPSS (Kwiatkowski-Phillips-Schmidt-Shin test) ($\alpha = 1\%$; see section 2.3.4)

Due to the opposite null hypotheses, the ADF and KPSS tests deliver complementary results. Regarding the OFR-related test outcomes, the sums of the ADF and KPSS non-rejection rates amount to 92% and 93% for RATA and HEDA, respectively. This demonstrates not only the internal consistency of the applied unit root tests, but also the appropriateness of the used regression models and truncation lags. The deviations from 100% can be attributed to the specified significance level of $\alpha = 1\%$ and the fact that the KPSS test tends to reject the null hypothesis too frequently for positively correlated data (Kwiatkowski et al., 1992). Since the stationarity hypothesis cannot be rejected for only about 50% of OFR, it seems inappropriate to perform ARMA modelling at this level. After removing the Vondrák trends, the resulting DTR mainly contain quasi-periodic signals and appear to largely satisfy the stationarity assumption. Nevertheless, due to the presence of systematic oscillations (see figure 8.14(b)), fitting ARMA models to DTR may suffer from selecting very high orders. The 3-day sidereal stacking sufficiently reduces the residual daily repeating effects and preserves the stationary property, making NCR(3) the most suitable data for ARMA modelling. Filtering stationary noise series with stationary ARMA models, the resulting WNR are also stationary.

The tests for uncorrelatedness introduced in section 2.3.5 assess not only the significance of noise's temporal correlation, but also the appropriateness of ARMA model estimates. Due to the remaining systematic signals, the temporal correlations in OFR and DTR are obviously significant (see figure 8.16). Therefore, the uncorrelatedness tests are only applied to NCR(3) and WNR, i.e., noise before and after ARMA modelling, respectively. According to Brockwell and Davis (2002, p. 39, 415), a truncation lag of $h = 20$ is used for the computation of the LB test statistic given by equation (2.88). Figure 8.32 presents the results of the uncorrelatedness tests for RATA and HEDA. Although the systematic signals are largely reduced during the course of the residual decomposition, all the analysed noise series exhibit statistically significant temporal correlations, which must be accounted for in the GPS stochastic model. After filtering the coloured noise with the estimated ARMA models, the resulting WNR can be regarded as being temporally uncorrelated and represent realisations of WN processes. By additionally considering the normality test results (see figure 8.29), the random variables, generating the WNR data, are independent and identically distributed (Kreiß and Neuhaus, 2006, p. 22).

(a) RATA: 203.7 km, weak multipath   (b) HEDA: 54.1 km, strong multipath
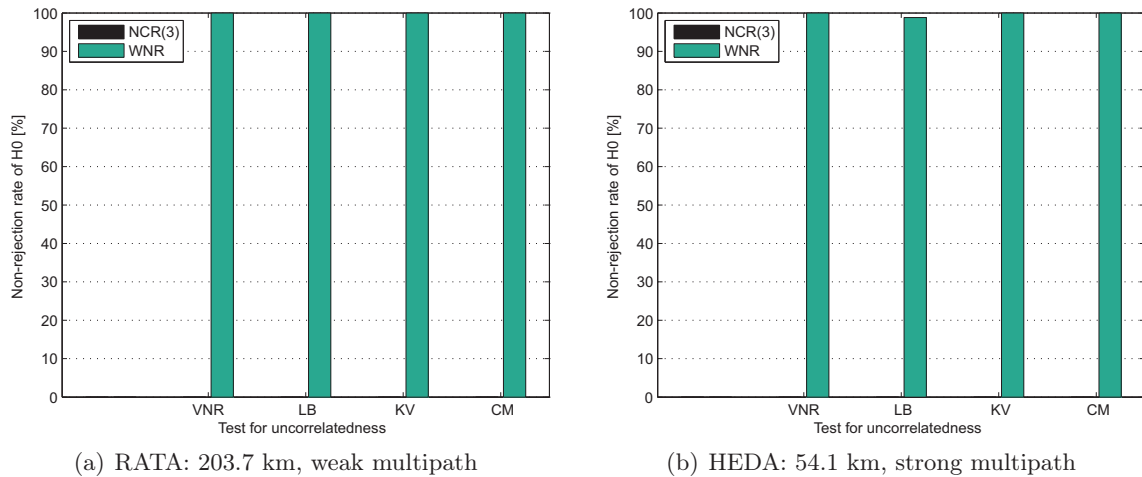
Figure 8.32: Representative results of the applied uncorrelatedness tests VNR (test based on von Neumann ratio), LB (Ljung-Box portmanteau test), KV (Kolmogorov-Smirnov test), and CM (Cramér-von Mises test) ($\alpha = 1\%$; see section 2.3.5)

Apart from verifying the performance of the residual decomposition and ARMA modelling, the hypothesis tests also contribute to a better understanding of the impacts of signal components on the residual statistical properties. In comparison to quasi-periodic oscillations induced by far-field multipath, long-periodic trends due to near-field multipth and residual atmospheric effects lead to more significant deviations of SDDR from normality and stationarity (see figures 8.29 and 8.31). Therefore, appropriate handling of the remaining systematic effects is not only in the interest of the GPS functional model, but also benefits the stochastic model.

8.2 Case study 3: long-term PPP

In addition to the 1-second SDDR from the short-term relative positioning, the temporal correlation modelling is also carried out based on 10 days (DOY2008:275-284) of 30-second studentised zero-difference residuals (SZDR) from the precise point positioning (PPP) described in section 4.3.2. Taking advantage of the simple receiver-satellite relationship in PPP, the influence of satellite geometry on the noise's temporal correlation properties can be studied more reliably. Different multipath environments are also considered within this case study to verify the related conclusions drawn from case study 2. Along with visual and statistical assessments, the results are physically interpreted by incorporating DWD surface meteorological data. Making use of the best-fitting ARMA model estimates, the PPP stochastic model is extended by taking the temporal correlation of GPS observation noise into account.

8.2.1 Unique orbit repeat lag

In case study 2, satellite-specific orbit repeat lags are accurately determined by means of the empirical approach described in section 7.2.5, where the resulting lag values vary between 240 and 263 s (see table D.4). Analysing the broadcast ephemerides of all GPS satellites from DOY1996:001 to DOY2006:120, Agnew and Larson (2007) showed a major lag variation band of 238-253 s. The data sampling interval in this case study is 30 s and is larger than these lag variation ranges, making it reasonable to use a unique orbit repeat lag for all GPS satellites. A value of 240 s seems to be a good choice, as it is closest to the optimum lag of 246 s (Ragheb et al., 2007) and results in an integer daily advance of 8 epochs (Howind, 2005, p. 55). Figure 8.33 compares the satellite geometry on 10 consecutive days, emphasising the necessity of considering the orbit repeat lag for similar satellite geometry and accurate stacking results.

(a) Orbit repeat time (lag): 86400 s (0 s)

(b) Orbit repeat time (lag): 86160 s (240 s)
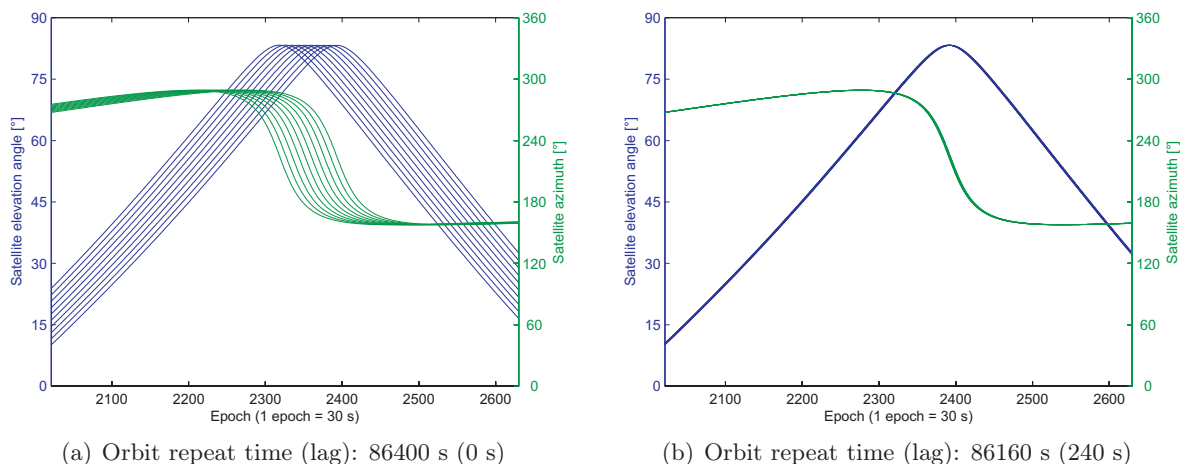
Figure 8.33: Comparison of satellite geometry using different orbit repeat lags (SA*POS*®site: TUEB, satellite: PRN 11, DOY2008:275-284, sampling interval: 30 s)

As figure 8.33(a) illustrates, the neglect of the orbit repeat lag leads to considerably different satellite geometries on multiple consecutive days, which would decrease the day-to-day similarity of the residual time series and attenuate the efficiency of the sidereal stacking technique (see section 7.2.5). If the unique lag value of 240 s (8 epochs) is considered, the satellite geometry becomes largely consistent, resulting in high day-to-day correlations of the SZDR data. In addition to the visual assessment, for the GPS satellites observed at the SA*POS*®sites TUEB and BING, the median and maximum absolute differences of the satellite elevation angle (ELV) and azimuth (AZI) between the two days DOY2008:275 and 284 are computed after accounting for the constant orbit repeat lag. The statistical characteristics can be expressed by

$$|\Delta\text{GMT}|_{\text{opt}} = \text{opt}(|\text{GMT}_{275,i} - \text{GMT}_{284,i}|), \tag{8.5}$$

where GMT denotes the geometry component (i.e., ELV, AZI), opt is the statistical operator (i.e., min, med, max), and i refers to the epoch. The complete results of the satellite geometry analysis are presented in table D.6. Taking the site TUEB and satellite PRN 11 as an example, figure 8.34 shows the ELV and AZI for the boundary days 275 and 284, as well as the associated absolute differences.

(a) Satellite geometry ELV and AZI

(b) Absolute differences $|\Delta\text{ELV}|$ and $|\Delta\text{AZI}|$
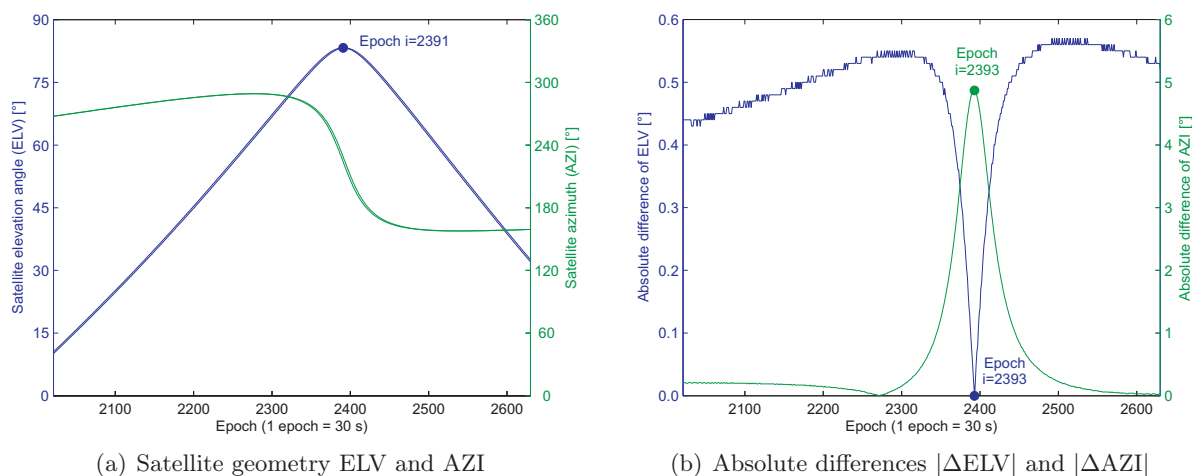
Figure 8.34: Example of satellite geometry on the boundary days to verify the appropriateness of the unique orbit repeat lag (SA*POS*®site: TUEB, satellite: PRN 11, DOY2008:275 and 284)

First of all, the minimum absolute difference of ELV, denoted as $|\Delta\text{ELV}|_{\min}$, is observed at the epoch $i = 2393$ (see figure 8.34(b)), which is very close to $i = 2391$ when the 2-day mean elevation angle attains its maximum (see figure 8.34(a)). Furthermore, it is interesting to observe that the epoch i of $|\Delta\text{ELV}|_{\min}$ coincides fairly well with that of $|\Delta\text{AZI}|_{\max}$, being equal to 2393 in this example. Regarding the entire analysis results provided in table D.6, the characteristic values $|\Delta\text{ELV}|_{\text{med}}$, $|\Delta\text{ELV}|_{\max}$, and $|\Delta\text{AZI}|_{\text{med}}$ are always below $1°$. In terms of $|\Delta\text{AZI}|_{\max}$, figure 8.34 actually depicts the worst-case scenario, with the largest $|\Delta\text{AZI}|_{\max}$ of $4.9°$. For 40 out of the 47 analysed cases (i.e., 85%), $|\Delta\text{AZI}|_{\max}$ is less than $2°$. Based on the results from the visual and numerical assessments, the unique orbit repeat lag of 240 s seems to be an appropriate choice to obtain multiple days of SZDR time series with similar satellite geometry.

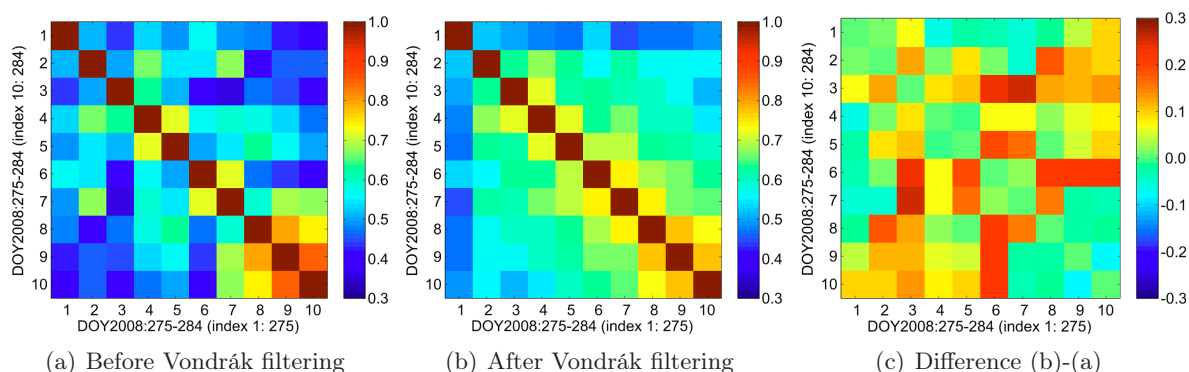### 8.2.2 Vondrák filter parameters

Considering the results achieved in section 8.1.2 and the fact that the GPS antennas at both sites TUEB and BING are installed far above the ground (see figure 4.9), $k_{\max} = 10$ is used in this case study to determine the optimum Vondrák filter parameters k, which enable an adequate trend characterisation and has a minimum impact on the noise's temporal correlation. Applying the maximum constraint on the day-to-day correlation of the Vondrák residuals given by equation (7.12), the best possible k values are derived for each zero-difference by examining the candidates $k = 1, 2, \ldots, k_{\max} = 10$. The results are displayed in figure 8.35, along with the BING-related mean day-to-day correlation coefficients before and after Vondrák filtering.

(a) Optimum k values ($k_{\max} = 10$) (b) Mean day-to-day correlation (site: BING)
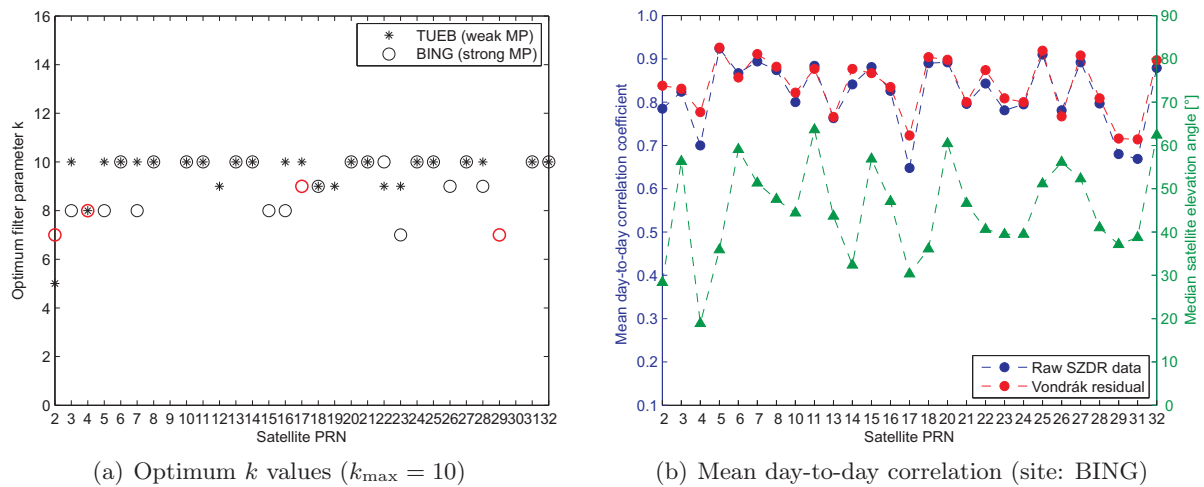
Figure 8.35: Optimum Vondrák filter parameters determined using equation (7.12) and the BING-related mean day-to-day correlation coefficients (see table 4.1 for site characteristics, red circles in (a): low-elevation satellites; MP: multipath)

In figure 8.35(a), the derived optimum filter parameters mainly range between 7 and 10, where the average seems to decrease with increasing multipath impact. This agrees with the finding from the simulation study presented in section 8.1.2 that the optimum k decreases with an increasing reflector-antenna distance, producing more far-field multipath signals. In most cases, $k = k_{\max} = 10$ is considered as the best one, resulting in the maximum daily similarity of the Vondrák residuals. For the BING-related SZDR before and after Vondrák filtering, figure 8.35(b) illustrates the mean day-to-day correlation coefficients, which fluctuate around a high level of 0.8 and exhibit an obvious positive correlation of 0.6 with the median satellite elevation angles. The degree of residual day-to-day similarity is weaker (stronger) for low-elevation (high-elevation) satellites, such as PRN 4, 17, and 29 (PRN 11, 15, and 20). This may be explained by the higher sensitivity of low-elevation data to variable atmospheric conditions. The strong daily correlation

of the raw SZDR verifies the appropriateness of the applied orbit repeat lag, while the high correlation level of the Vondrák residuals indicates the efficiency of the determined optimum filter parameters in capturing long-periodic trends. After Vondrák filtering, the mean day-to-day correlation coefficients are increased by about 0.1 for the low-elevation satellites PRN 2, 4, 17, and 29. This is due to the employment of smaller filter parameters (see the red circles in figure 8.35(a)), which are capable of capturing some randomly occurring signals of a non-daily repeating nature. To demonstrate the improved day-to-day correlation structure, figure 8.36 displays the correlation matrix, associated with the smallest k value shown in figure 8.35(a).

(a) Before Vondrák filtering   (b) After Vondrák filtering   (c) Difference (b)-(a)

Figure 8.36: Day-to-day correlation matrix before and after Vondrák filtering (site: TUEB, weak multipath, satellite: PRN 02, DOY2008:275-284, filter parameter: $k = 5$; see figure 8.35(a))

In this example, performing the Vondrák filter with $k = 5$ enhances the day-to-day correlation by up to 0.3 in both the near- and far-diagonal areas. The correlation pattern depicted in figure 8.36(b) additionally implies the applicability of the 3-day stacking approach rather than the 10-day one. The use of a shorter stacking time interval benefits from the higher day-to-day correlation level and allows for a more reliable detection of the daily repeating systematic signals. Analysing the TUEB-related raw SZDR data, the mean day-to-day correlation coefficients vary around 0.6 and illustrate a moderate positive correlation of about 0.4 with the median satellite elevation angles. For low-elevation satellites, Vondrák detrending also improves the mean day-to-day correlation coefficient by up to 0.1 (cf. figure 8.35(b)). After applying the Vondrák filter to the raw SZDR, the obtained residuals are used for outlier detection.

8.2.3 Results of outlier handling

In case study 2, low-quality GPS observations down to an elevation angle of 3° are included to exploit the potential of the SNR-based weighting model (see table 4.5). For the PPP analysis, a higher elevation cut-off angle of 10° is specified, and a sophisticated outlier detection is undertaken by screening post-fit residuals using the program `MAUPRP` (see tables 4.6 and 4.7). Therefore, it is expected that fewer outliers exist in the SZDR data set, providing a possibility to assess the performance of the proposed two-step outlier detection in confirming non-outliers (see section 7.2.4). A total of 515 Vondrák residual time series of lengths ranging between 240 and 680 epochs (1 epoch = 30 s) are investigated, with the results presented in figure 8.37. According to the 5-MAD criterion given by equation (7.13), a total of 165 (32%) Vondrák residual time series possess outliers, where, in about 95% of cases, the number of outliers is less than 7. Regarding the outcomes of the one-sided F-test for outlier verification shown in figure 8.37(b), only 2 of the 165 time series contain outliers that considerably affect the sample variance of the Vondrák residuals at a significance level of $\alpha = 1\%$. Despite the small numbers of outliers, a positive correlation between the F-test statistic T_F and number of outliers is clearly visible, indicating the high sensitivity of T_F (see equation (7.14)). For the site BING with strong multipath impact,

significantly fewer 5-MAD outliers are identified. This was also observed in the results of outlier detection from case study 2 (see the HEDA-related results in figure 8.9(b)).

(a) Outlier identification

(b) Outlier verification ($\alpha = 1\%$)
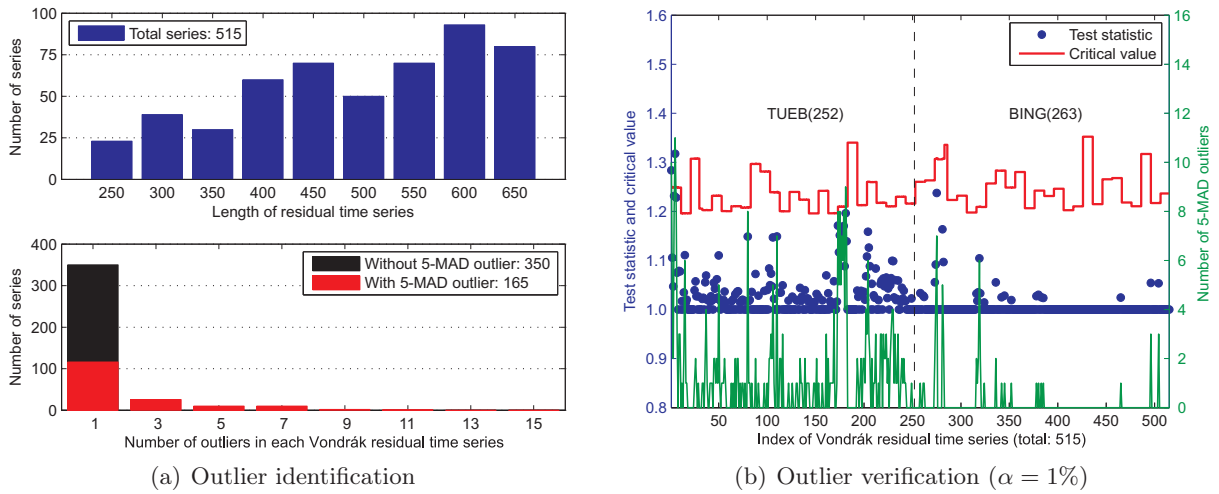
Figure 8.37: Results of the two-step procedure for outlier detection using the Vondrák residuals (see equations (7.13) and (7.14); MAD: median absolute deviation)

To verify some conclusions drawn from case study 2, figure 8.38 illustrates additional findings with regards to the distribution of the F-test statistic T_F and physical interpretation of the number of outliers. In figure 8.38(a), the empirical CDF of T_F is compared with the theoretical F-distribution, where the degrees of freedom are specified using the maximum sample size and the maximum number of outliers. In most cases, the quantile differences between the empirical and theoretical CDF are less than 0.03 and decrease, particularly for $T_F > 1.15$, after repairing the significant 5-MAD outliers by means of the remove-repair-restore (RRR) technique (see section 8.1.3). Comparing the daily numbers of outliers with the mean relative humidity (RH), averaged over the northern and central DWD meteorological stations (i.e., FRAN, WUER, KARL, STUT), a positive correlation is visible in spite of the small numbers of outliers. Therefore, it can be concluded that the proposed two-step procedure for outlier detection is also capable of dealing with the case where non-outliers are predominantly present. Furthermore, the influence of humidity on the number of outliers can be validated (cf. figure 8.12).

(a) Comparison of CDF before outlier repair

(b) Daily numbers of outliers vs. mean RH
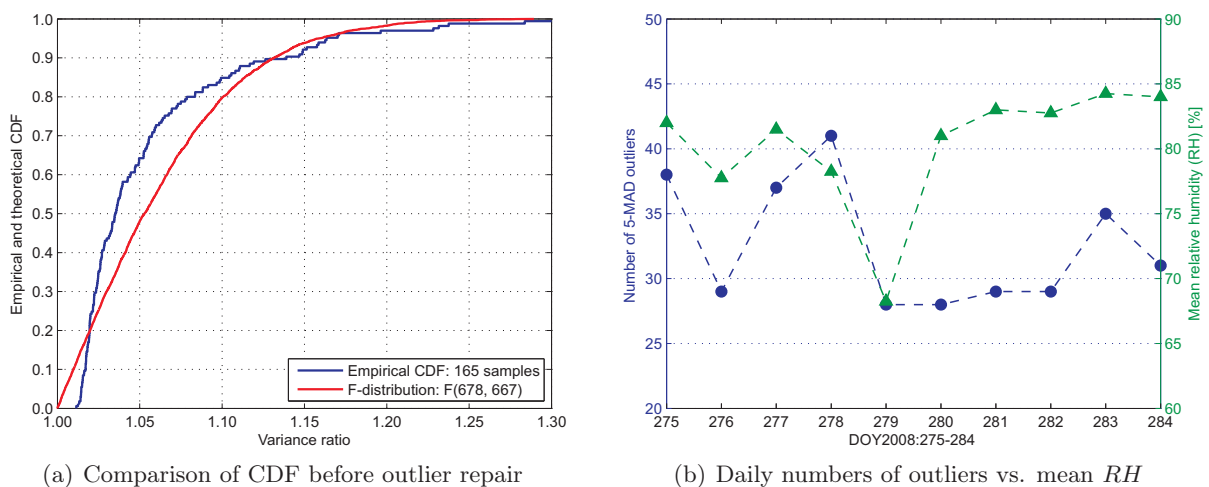
Figure 8.38: Additional results of outlier detection with respect to the distribution of T_F (see equation (7.14)) and physical interpretation of the number of outliers (see figure 4.10(c))

8.2.4 Results of residual decomposition

On the basis of the SZDR, which are homogenised with respect to satellite geometry and repaired for outliers (i.e., OFR), the residual decomposition outlined in section 7.2.2 is undertaken to remove the remaining systematic effects. The resulting stochastic noise is then used for correlation analysis and ARMA modelling. For the SZDR time series, related to the same GPS satellite PRN 11 and the sites TUEB and BING with different multipath impact, the results of Vondrák filtering, sidereal stacking, and noise extraction are depicted in figures 8.39, 8.40, and 8.41, respectively. Following the same notions, DTR denotes the detrended residuals after Vondrák filtering, and NCR refers to the decomposed noise after sidereal stacking.

Making use of OFR, the optimum Vondrák filter parameters k are again determined. However, due to the predominantly insignificant effects of the found 5-MAD outliers (see figure 8.37(b)), the obtained k values are identical to those presented in figure 8.35(a). Representative examples of Vondrák filtering of OFR are shown in figure 8.39. While the SZDR time series from TUEB primarily illustrate long-periodic trends, those from BING additionally exhibit quasi-periodic oscillations with temporally varying periods, depending on the satellite elevation angle. From both examples it can be concluded that the Vondrák filter sufficiently captures the slowly varying trends, which display not only systematic behaviour, but also day-to-day variations, particularly at low elevation angles.

After subtracting the long-periodic trends from OFR, the resulting DTR are stacked to detect the daily repeating systematic signals. Based on 3-day and 10-day DTR, the calculated epoch-wise means are compared in figure 8.40. Benefiting from the on average stronger day-to-day correlation within shorter time periods (see figure 8.36(b)), the 3-day sidereal stacking allows for a more accurate signal characterisation. This is especially visible in the TUEB-related example with a smaller mean day-to-day correlation coefficient of DTR (TUEB11: 0.5, BING11: 0.9). As observed in figure 8.14, the slight shifts of the 10-day mean curves relative to the 3-day ones are also found in this case study, particularly for satellites PRN 04, 13, 17, and 31 with larger $|\Delta\mathrm{ELV}|_\mathrm{med}$ and $|\Delta\mathrm{AZI}|_\mathrm{med}$ in table D.6. This suggests that these shifts may be attributed to remaining inconsistencies in satellite geometry, which is caused by using the average of the satellite-specific orbit repeat lags for SDDR and by applying the unique orbit repeat lag for SZDR. The removal of the stacked signals from DTR leads to the decomposed noise NCR (see figure 8.41). As expected, the 3-day stacking variant produces noise series with more homogenous variances, which is clearly visible in figure 8.41(b). Moreover, as already observed in figure 8.15, the noise variance seems to decrease with increasing multipath impact.

For both examples of the residual decomposition, figure 8.42 shows the sample ACF of OFR, DTR, and NCR to illustrate the significant impact of the remaining systematic effects on the temporal correlation structure and the efficiency of the decomposition process in signal-noise separation. While the sample ACF values of OFR in figure 8.42(a) decay slowly and suggest long-term dependency, those in figure 8.42(b) fall fairly rapidly and exhibit quasi-periodic oscillations. After Vondrák filtering, the long-term dependency in the TUEB-related OFR is largely reduced, and the quasi-periodic autocorrelation in the BING-related DTR becomes more obvious. After sidereal stacking, the noise's sample ACF in both plots depict positive correlations and decay rapidly as the lag increases, indicating short-term dependency. By comparing the noise's sample ACF with respect to multipath impact, the zero-crossing correlation length appears to decrease as multipath effects increase, which was also observed in figure 8.16. As figure 8.41(b) illustrates, the 3-day stacking approach produces more homogenous noise than the 10-day one. However, it seems to insignificantly improve the noise correlation structure when comparing the sample ACF of NCR(10) and NCR(3) in figure 8.42(b). A more significant example is presented in figure C.5

(a) SZDR: TUEB11 ($k = 10$) (b) SZDR: BING11 ($k = 10$)
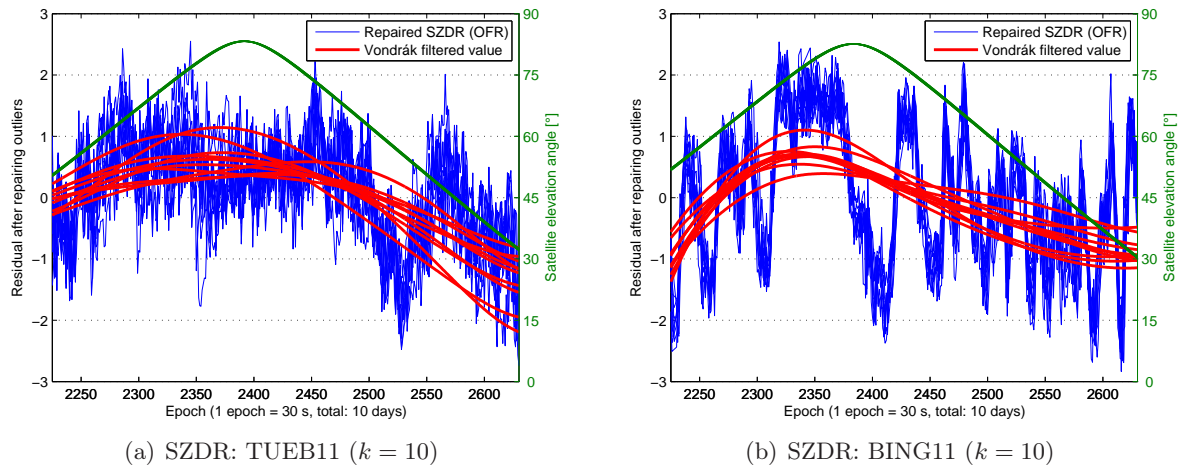
Figure 8.39: Examples of Vondrák filtering with respect to multipath impact (TUEB: weak multipath, BING: strong multipath, satellite: PRN 11, DOY2008:275-284; see table 4.1)

(a) SZDR: TUEB11 (b) SZDR: BING11
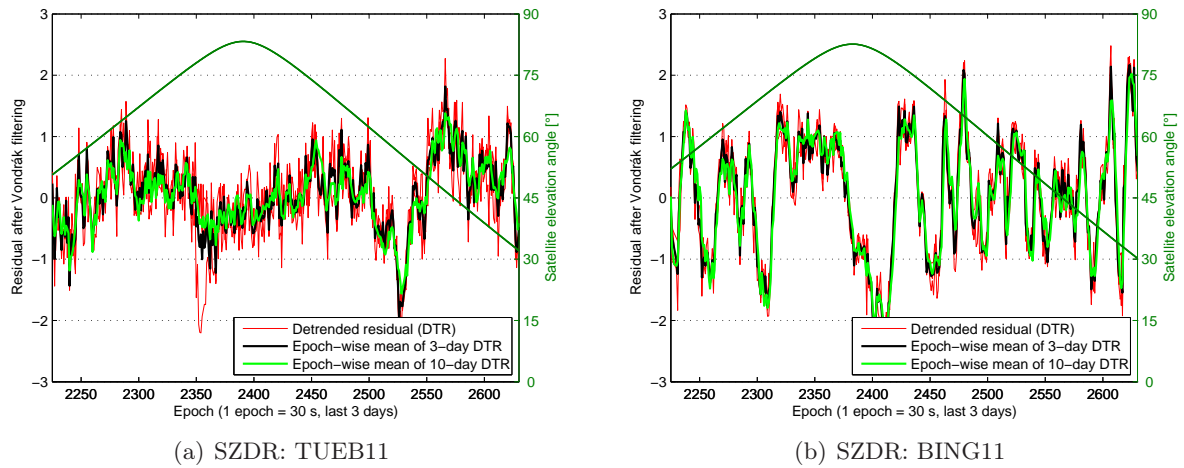
Figure 8.40: Examples of sidereal stacking using different days of DTR (DOY2008:282-284, unique orbit repeat lag: 240 s; see section 8.2.1)

(a) SZDR: TUEB11 (b) SZDR: BING11

Figure 8.41: Noise after applying the 3-day and 10-day sidereal stacking (DOY2008:275-284)

to emphasise the advantages of using a shorter stacking time period in dealing with rapid quasi-periodic oscillations at low-elevation angles. In the presence of such fluctuations with periods less than 10 epochs (5 min), stacking DTR from 3 instead of 10 consecutive days significantly enhances the noise's homoscedacity and sample ACF. A stable temporal correlation structure is a key issue for reliable correlation analysis and ARMA modelling.

(a) SZDR: TUEB11   (b) SZDR: BING11

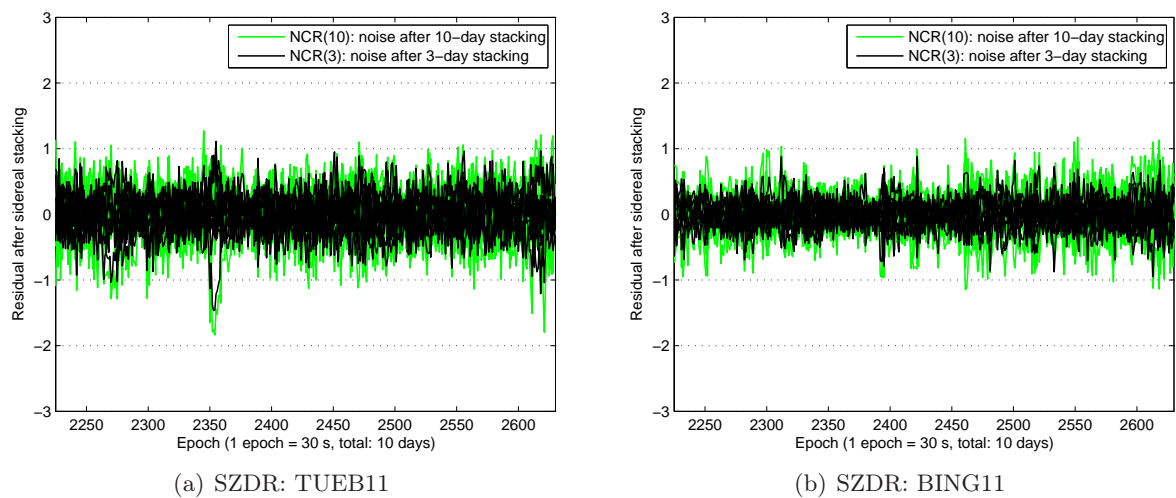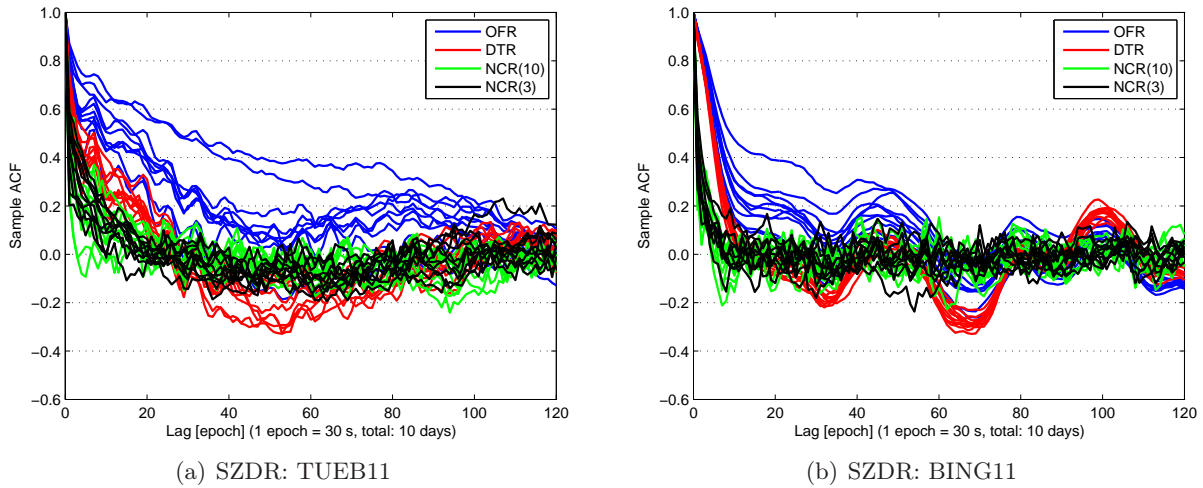**Figure 8.42:** Comparison of the sample ACF of OFR, DTR, and NCR (TUEB: weak multipath, BING: strong multipath, satellite: PRN 11, DOY2008:275-284; see figures 8.39, 8.40, and 8.41)

8.2.5 Results of the correlation analysis

Using the same characteristics of the noise's sample ACF, namely the zero-crossing correlation length and lag-1 correlation level, the temporal correlation analysis performed in this case study also considers multipath impact, satellite geometry, and atmospheric conditions. For each decomposed noise series NCR(3), both correlation characteristics are computed. Figure 8.43 presents the results with respect to multipath impact, where the arithmetic means and 95% quantiles are calculated without the extreme outliers outside the 3-IQR limits (IQR: interquartile range).

(a) Zero-crossing correlation length   (b) Lag-1 correlation level
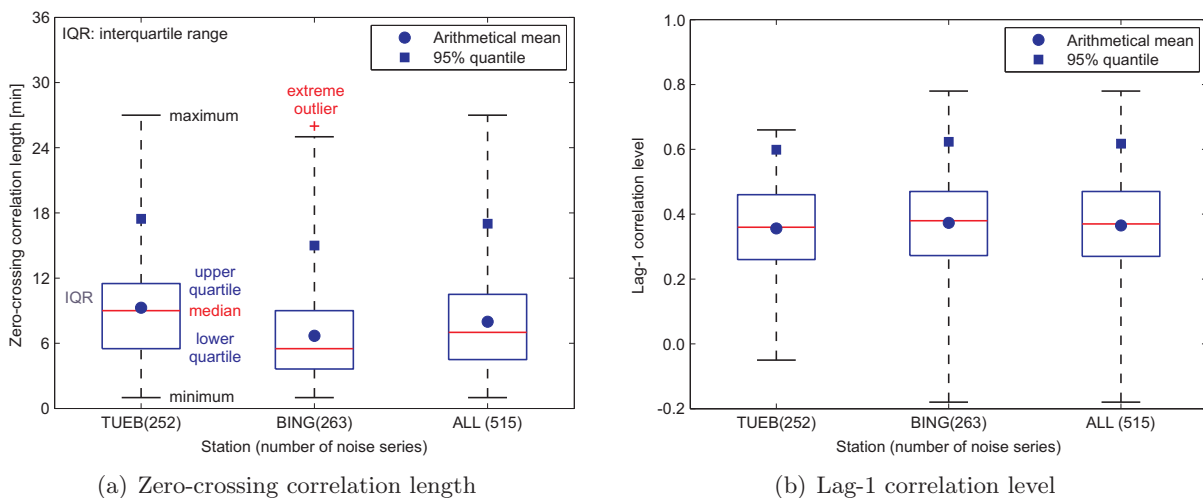
Figure 8.43: Temporal correlation characteristics with respect to multipath impact (TUEB: weak multipath, BING: strong multipath, 24-hour decomposed SZDR noise, sampling interval: 30 s)

As can be seen from figure 8.43(a), the BING-related mean zero-crossing correlation length is about 3 min (30%) shorter than the TUEB-related one. This explains the noise's correlation behaviour illustrated in figure 8.42 and verifies the conclusion drawn from case study 2 that the noise correlation length tends to decrease with increasing multipath effects (cf. figure 8.17(a)). However, as figure 8.43(b) shows, the strong multipath impact at BING only insignificantly increases the mean lag-1 correlation level by 0.02, indicating the efficiency of the 3-day sidereal stacking in capturing daily repeating quasi-periodic signals. Considering all the noise series analysed in this case study, the mean zero-crossing correlation length and lag-1 correlation level amount to 8 min and 0.37, with 95% quantiles of 17 min and 0.62, respectively.

In view of satellite geometry, the mean correlation length and level are computed for each satellite, where the sample sizes are 19 or 20. The results are visualised in figure 8.44, along with the median satellite elevation angles. For most of the analysed satellites, the noise's temporal correlation tends to become longer (shorter) and stronger (weaker) as the median satellite elevation angle increases (decreases), corresponding to the results achieved in case study 2 (cf. figure 8.18). Nevertheless, it should be noted that using SZDR on a daily basis has on the one hand the advantage in data volume and number of satellites, and on the other the disadvantage in the representativity of the median satellite elevation angles. Therefore, for future residual-based temporal correlation analysis, it is recommended to use high-frequency (e.g., 1 Hz) SZDR over a short time period (e.g., several hours).

(a) Zero-crossing correlation length (b) Lag-1 correlation level
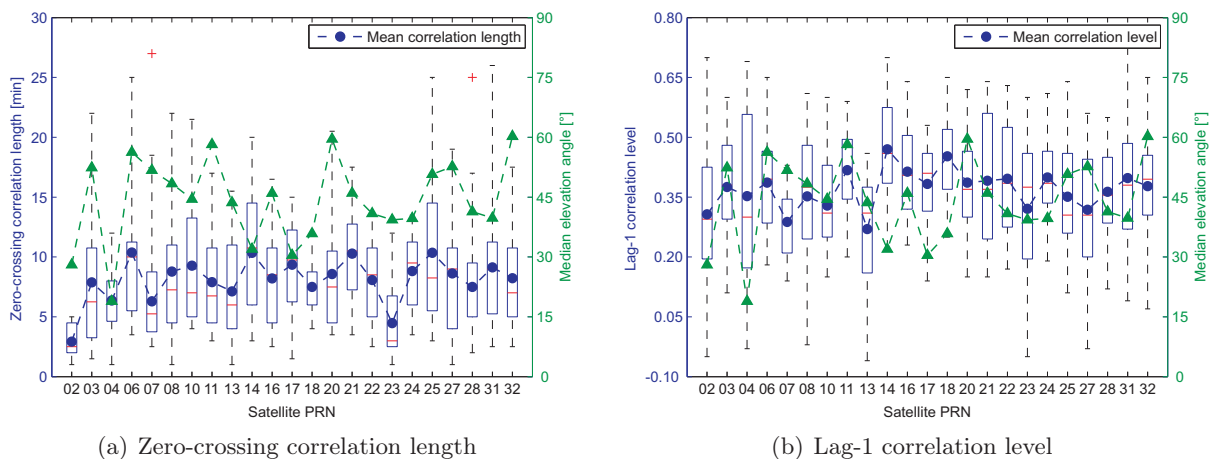
Figure 8.44: Temporal correlation characteristics with respect to satellite geometry (24-hour decomposed SZDR noise, sampling interval: 30 s)

To assess the physical interpretability of the derived temporal correlation characteristics, DWD surface meteorological data such as wind speed (WS) and relative humidity (RH) are also incorporated into this case study. Considering the locations of the SA*POS*®sites TUEB and BING, only the northern and central DWD meteorological stations, i.e., FRAN, WUER, KARL, and STUT, are taken into account (see figure 4.1). Since the temporal correlation analysis is carried out based on residuals from daily PPP solutions, the physical interpretation of the analysis results is accordingly done using daily mean WS and RH shown in figure 8.45(a). Despite a short investigation period of 10 days, there exist variable atmospheric conditions. For example, high WS and low RH prevail on day 279, while low WS and high RH are observed on day 281. Additional surface meteorological data at a higher temporal resolution of 6 h are presented in figure 4.10. After averaging the daily mean WS and RH over the four aforementioned DWD stations, the final mean WS and RH are displayed in figure 8.45(b) together with the daily mean temporal correlation characteristics, where the sample sizes range between 50 and 53.

(a) DWD surface WS and RH measurements   (b) Mean temporal correlation characteristics
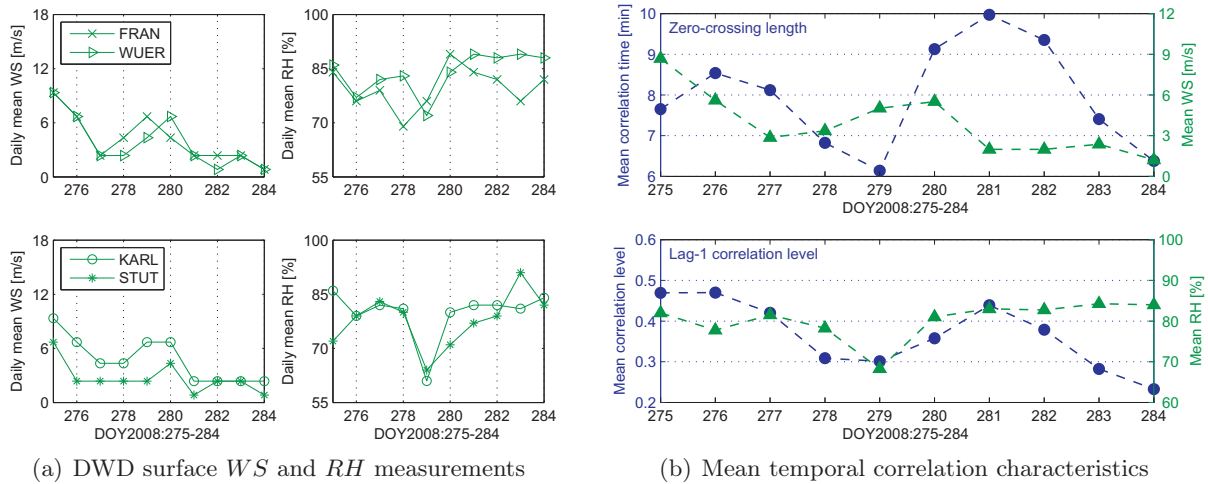
Figure 8.45: Temporal correlation characteristics with respect to atmospheric conditions (see figure 4.10 for the DWD surface meteorological data; WS: wind speed, RH: relative humidity)

From the upper plot of figure 8.45(b), one can easily discern that the daily mean zero-crossing correlation length increases (decreases) as the mean WS decreases (increases). In particular, the minimum mean correlation length is found on day 279, with a relatively large mean WS of 5 m/s and the minimum mean RH of 68%. The maximum mean correlation length appears on day 281, with a relatively small mean WS of 2 m/s and a large mean RH of 83%. The lower plot of figure 8.45(b) depicts a positive correlation between the daily mean lag-1 correlation level and the mean RH, which is particularly obvious on day 279. The large discrepancies on days 283 and 284 may be attributed to the poor representativity of the corresponding mean RH, if one regards the FRAN-related daily mean RH (see figure 8.45(a)) and the STUT-related 6-hour RH (see figure 4.10(c)). Moreover, it is found that the mean correlation length (level) increases with increasing (decreasing) mean RH (WS). To illustrate the effects of variable atmospheric conditions on the noise's temporal correlation properties, figure 8.46 compares the correlation characteristics from the two representative days 279 and 281, along with the associated noise's sample ACF. Both SA*POS*®sites and all observed GPS satellites are taken into consideration, giving a sample size of 51 for each day.

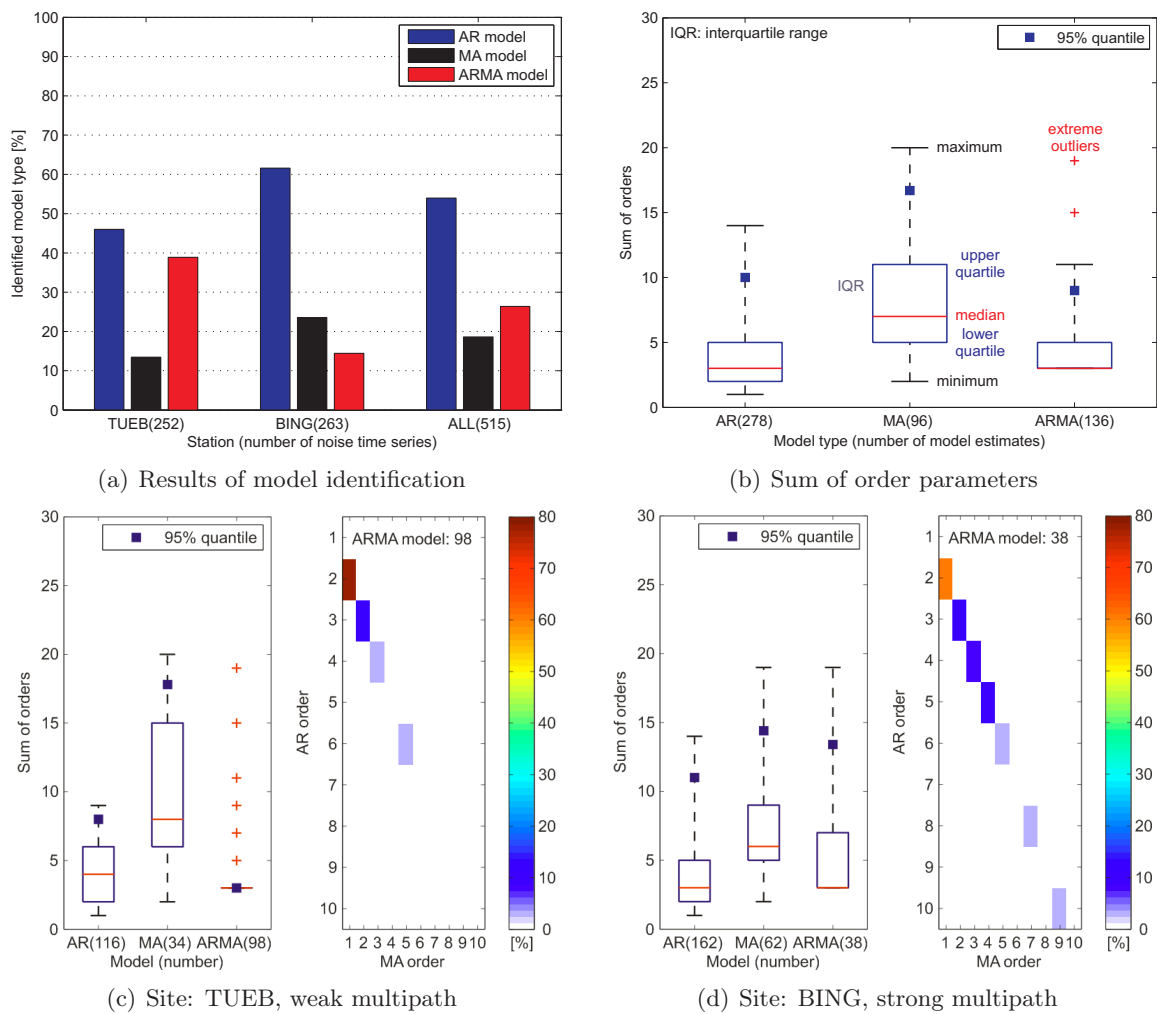(a) Temporal correlation characteristics   (b) Noise's sample ACF
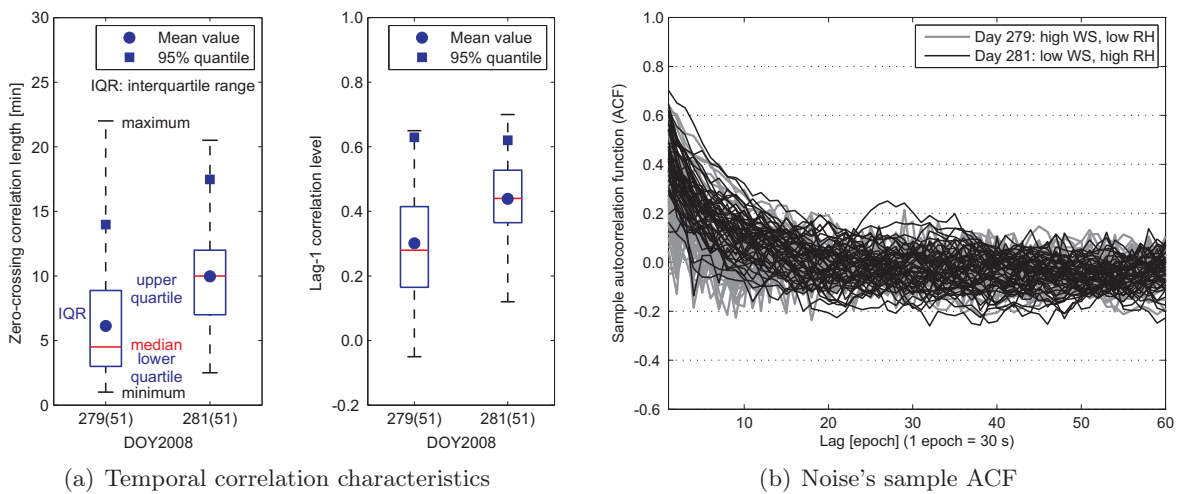
Figure 8.46: Effects of variable atmospheric conditions on the noise's temporal correlation properties (SA*POS*®sites: TUEB, weak multipath, BING, strong multipath, all GPS satellites, DOY2008:279 and 281; see figure 8.45(b) for mean WS and RH)

In addition to the increased mean correlation length and level from day 279 to 281, figure 8.46(a) also exhibits decreased interquartile ranges (IQR), indicating less variability in the determined temporal correlation characteristics. For the entire period of investigation, figure C.6 compares the IQR of the zero-crossing correlation length with the mean WS. Obviously, a positive correlation is present, suggesting that the noise's temporal correlation structure would be more heterogeneous from satellite to satellite as the wind becomes stronger. The sample ACF curves depicted in figure 8.46(b) provide not only visual supports for the conclusions drawn from the box plots, but also images of short-term dependency, which is desirable for ARMA modelling.

8.2.6 Results of ARMA modelling

The ARMASA Toolbox is also used in this case study to determine the best-fitting ARMA model for each decomposed noise series NCR(3), where the maximum orders $p_{AR}^{\max}$, $q_{MA}^{\max}$, and $p_{AM}^{\max}$ are chosen to be 100, 20, and 10, respectively. The results of the model identification and order selection are presented in figure 8.47. Fitting ARMA models to a total of 515 noise series, non-zero orders are obtained for 510 noise sequences, indicating that only about 1% of NCR(3) can be considered as white noise (WN) realisations. Regarding the identified model types shown in

(a) Results of model identification

(b) Sum of order parameters

(c) Site: TUEB, weak multipath

(d) Site: BING, strong multipath

Figure 8.47: Results of the model identification and order selection using the ARMASA Toolbox (24-hour SZDR noise, sampling interval: 30 s, AR: $\hat{p}_{AR}$, ARMA: $\hat{p}_{AM} + \hat{q}_{AM} = 2\hat{p}_{AM} - 1$, MA: $\hat{q}_{MA}$; see table 4.1 for station properties and section 7.3 for ARMA modelling)

figure 8.47(a), AR and ARMA processes appear to play a dominant role, where AR models are preferred in the case of BING, which is strongly affected by multipath effects. This agrees with the HEDA-related results illustrated in figure 8.21(a). Taking the 510 non-zero ARMA model estimates into account, figure 8.47(b) displays the box plots of the sum of orders for AR, MA, and hierarchical ARMA models (see section 7.3.3), i.e., $\hat{p}_{AR}$, $\hat{q}_{MA}$, and $\hat{p}_{AM} + \hat{q}_{AM} = 2\hat{p}_{AM} - 1$, respectively. The box plot of $\hat{p}_{AR}$ clearly demonstrates the inadequacy of using first-order AR processes (AR(1)) to describe the noise's temporal correlation behaviour. In fact, for only 30 noise series, the AR(1) model is identified as the most appropriate one. In comparison to the MA model estimates, the sums of AR and ARMA orders are less variable and exhibit smaller 95% quantiles of 10 and 9, respectively. A site-related presentation of the model identification shows that higher AR and ARMA orders are selected for the noise series from BING. This coincides with the conclusion drawn from case study 2 that in the presence of strong multipath effects, higher-order ARMA models are needed to cope with the residual systematic effects in the decomposed noise. However, in this case study, the impact of strong multipath on AR order selection is much less significant than that depicted in figure 8.21(d). This corresponds to the message sent by figure 8.43(b) that the 3-day sidereal stacking largely captures the quasi-periodic oscillations so that only marginal systematic signals remain in NCR(3). Regarding the TUEB-related results of order selection shown in figure 8.47(c), it is interesting to observe that the ARMA(2, 1) model is identified in nearly 80% of cases. In addition, the associated MA model estimates exhibit on average higher and more variable orders than the BING-related ones.

Taking advantage of a large number of satellites and the simple receiver-satellite relationship, figure 8.48(a) shows an obvious negative correlation of -0.5 between the sum of orders and the median satellite elevation angle, where the 95% quantiles are derived based on sample sizes between 17 and 20. Only considering the AR and ARMA model estimates, the negative correlation becomes more significant, with a correlation coefficient of -0.8. Although the noise series from low-elevation satellites exhibit shorter and weaker temporal correlations (see figure 8.44), higher-order ARMA models are required to deal with the more complex temporal correlation structures, caused by the increased residual systematic effects at low elevation angles.

(a) Satellite geometry   (b) Mean WS and RH
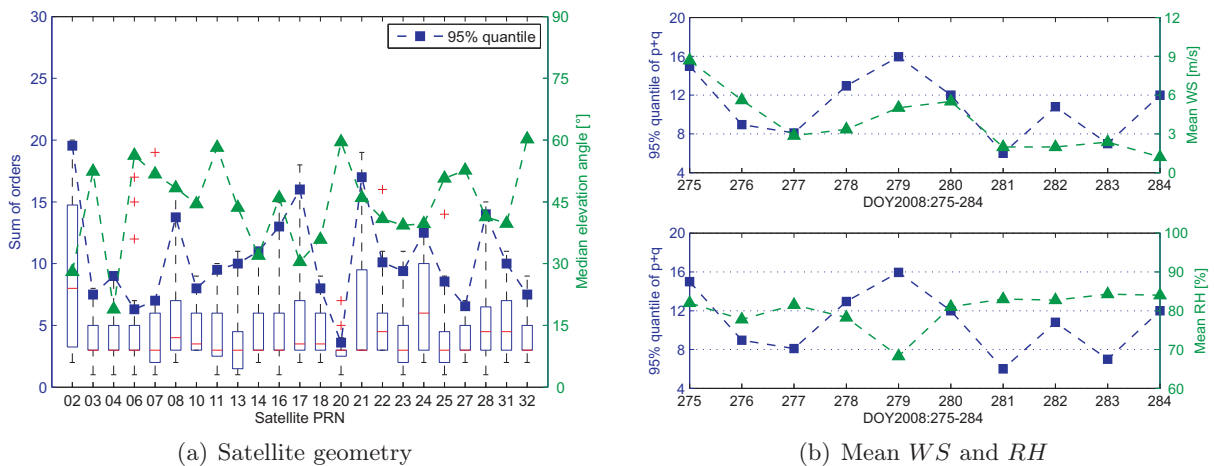
Figure 8.48: Sum of ARMA orders with respect to satellite geometry and atmospheric conditions (see figure 8.45(b) for mean wind speed WS and relative humidity RH)

In view of atmospheric conditions, figure 8.48(b) depicts higher orders on day 279 with relatively high wind speed (WS) and low relative humidity (RH). However, under such atmospheric conditions, the mean temporal correlation characteristics are supposed to be small, as illustrated in figures 8.45(b) and 8.46. Therefore, figure 8.48 demonstrates that the magnitudes of the de-

termined ARMA orders cannot be simply related to the zero-mean correlation length and lag-1 correlation level, since the order selection considers the whole temporal correlation structure rather than the two characteristic values. As figures 8.22(b) and 8.23 show, variable atmospheric conditions do affect the selected orders, but probably in both positive and negative senses.

After analysing the order parameters under different aspects, figure 8.49 provides a site-related comparison of the standard deviations (STD) of NCR(3) and WNR, i.e., noise before and after ARMA modelling, respectively. As can be seen from both plots, the noise STD become on average smaller with increasing multipath effects (TUEB vs. BING) and decreasing temporal correlations (NCR(3) vs. WNR), coinciding with the conclusions drawn from figure 8.24. However, in this case study, the magnitudes of the decreases in STD due to multipath and decorrelation are at a comparable level of about 0.03 (cf. figure 8.24). Furthermore, the BING-related box plots exhibit slightly larger IQR, indicating more variable STD.

| (a) STD of NCR(3) and WNR | (b) Box plots of the STD shown in (a) |
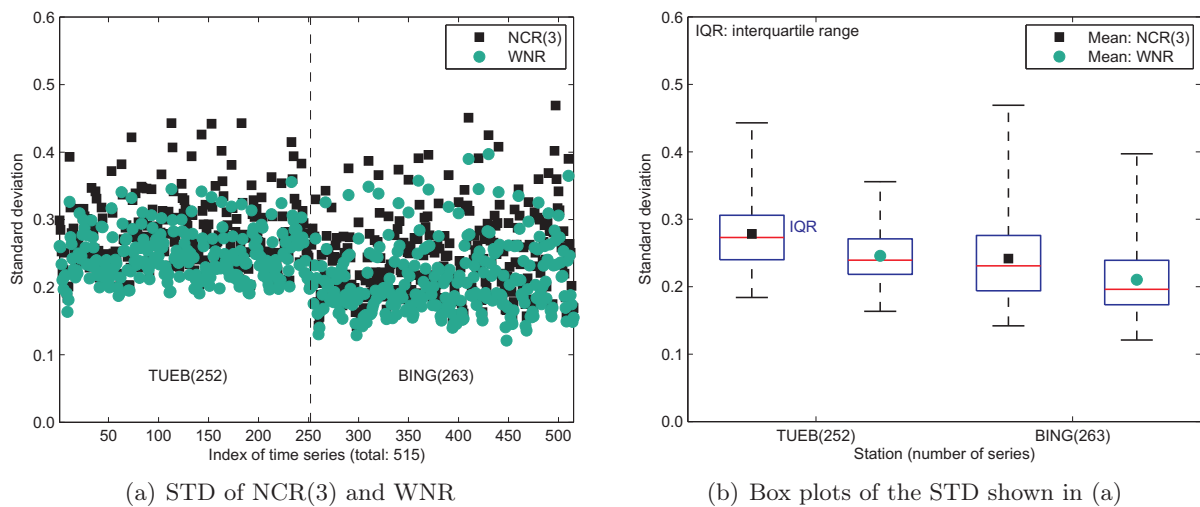
Figure 8.49: Noise standard deviations (STD) before (NCR(3)) and after (WNR) ARMA modelling (TUEB: weak multipath, BING: strong multipath; see table 4.1)

In addition to the analysis with respect to multipath impact, the mean STD of NCR(3) and WNR are investigated with regard to satellite geometry and atmospheric conditions. While the satellite-related mean STD are computed using 19 or 20 samples, the daily mean STD are obtained based on sample sizes between 50 and 53. Differing from the results achieved in the short-term relative positioning case study (see figure 8.25), the mean STD of NCR(3) and the median satellite elevation angle are weakly correlated in this case study, with a correlation coefficient of -0.2 (see figure 8.50(a)). This may arise from the use of long-term residual data, making the variability of NCR(3) less sensitive to the changing satellite geometry. Moreover, for most of the observed GPS satellites, the median elevation angles are calculated over a time period of up to about 6 h, and thus may not be representative for such an investigation. Therefore, high-frequency (e.g., 1 Hz) SZDR from short-term (e.g., several hours) PPP are strongly recommended for future residual-based temporal correlation modelling of GPS observations. Comparing the two mean STD curves, the noise level of NCR(3) turns out to be the determinant for that of WNR, which was also observed in case study 2 (see figure 8.25). The almost constant offset between the mean STD of NCR(3) and WNR amounts to about 0.03, corresponding to the average decrease in noise STD due to ARMA decorrelation (see figure 8.49). In terms of atmospheric conditions, figure 8.50(b) shows a strong positive (negative) correlation of 0.8 (-0.7) between the daily mean STD of WNR and the mean WS (RH). Such correlations were also found in case study 2, but at considerably lower levels (see section 8.1.6).

(a) Satellite geometry

(b) Mean WS and RH

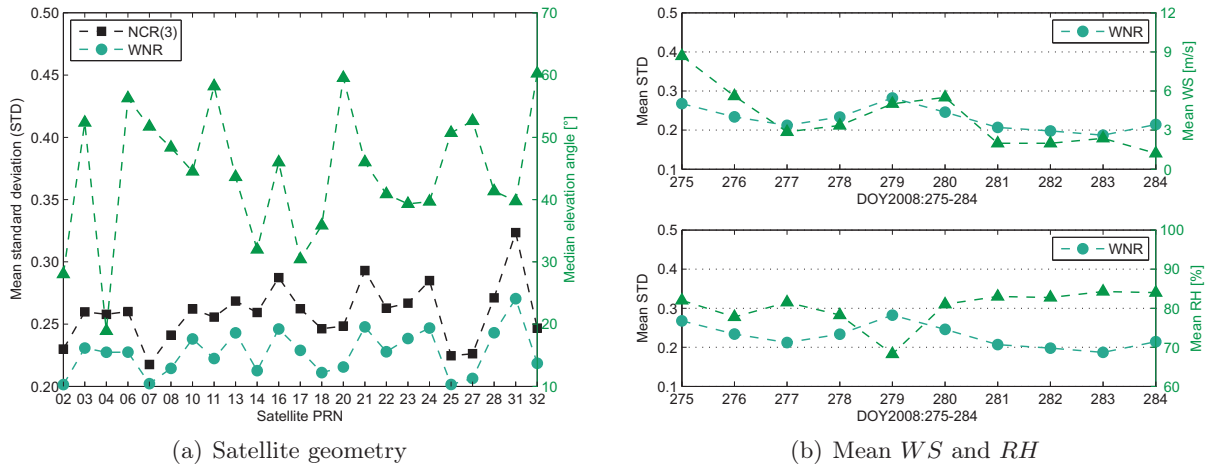**Figure 8.50:** Mean standard deviations (STD) of NCR(3) and WNR with respect to satellite geometry and atmospheric conditions (see figure 8.45(b) for mean WS and RH)

Filtering the decomposed noise NCR(3) shown in figure 8.41 with the corresponding best-fitting ARMA models, figure 8.51 demonstrates the efficiency of ARMA decorrelation. Considering the percentages of the noise's sample ACF falling into the 95% confidence bounds, the NCR(3) data exhibit significant positive correlations, where longer correlation lengths result in lower percentage values (see figure 8.51(a)). As can be seen from both examples, for lags of up to the zero-crossing point, the noise's temporal correlation properties can be sufficiently described by the ARMA model ACF. In contrast to NCR(3), the ARMA residuals (WNR) are largely uncorrelated over time, with nearly 95% of the associated sample ACF lying within the bounds. The different widths of the confidence intervals (i.e., TUEB11: 0.16, BING11: 0.19) are actually due to the different data lengths (i.e., TUEB11: 610 epochs, BING11: 416 epochs).

(a) SZDR: TUEB11

(b) SZDR: BING11
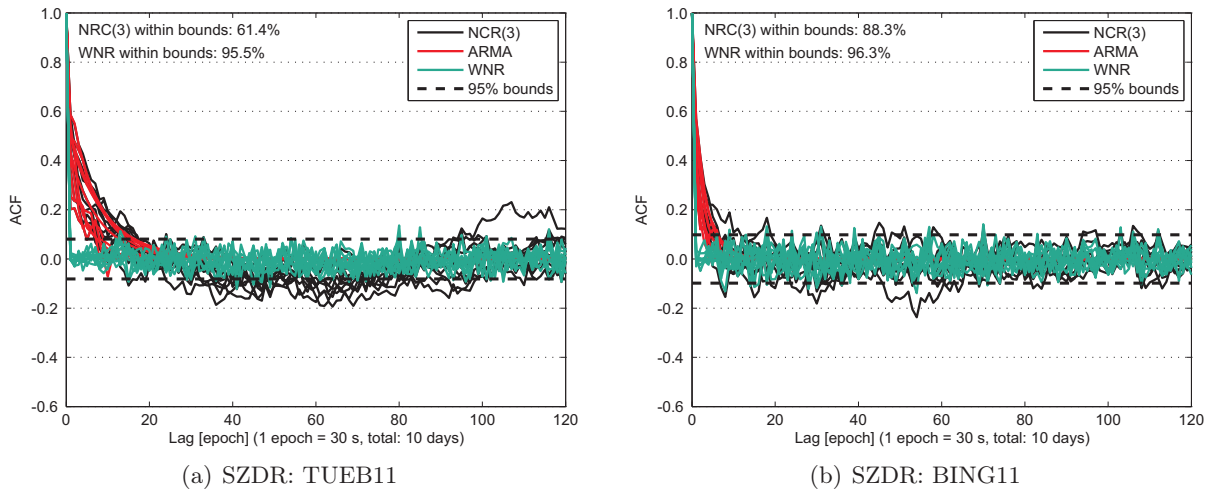
Figure 8.51: Comparison of noise's sample and ARMA model ACF (TUEB: weak multipath, BING: strong multipath, satellite: PRN 11, DOY2008:275-284)

Based on the studentised residuals of daily GPS observations, collected at a sampling interval of 30 s and analysed using the PPP technique, the results of ARMA modelling from this case study generally agree with those presented in case study 2, reflecting variations in site multipath, satellite geometry, and atmospheric conditions. This agreement also verifies the performance of the proposed residual decomposition, which produces stochastic noise being largely free of systematic effects and possessing favourable properties for ARMA modelling.

8.2.7 Visual and statistical verification

By examining the scalograms resulting from continuous wavelet transforms (CWT), the performance of the residual decomposition and ARMA modelling can be visually assessed. Considering the rapid quasi-periodic oscillations with periods less 10 epochs (i.e., 5 min, with 1 epoch = 30 s; see figure C.5), scales a ranging between 6 and $n \cdot F_m$ with a step of 3 are used to capture signals with the minimum and maximum periods of 7 and n epochs, respectively, where n denotes the data length, and F_m is the centre frequency of the applied Morlet wavelet (see figure 2.7). Substituting $F_m = 0.813$, $a = 6$, and $\Delta t = 30$ s into equation (2.99), the maximum detectable frequency amounts to 4.5 mHz. To highlight the efficiency of the proposed residual decomposition and ARMA modelling, particularly in the presence of strong multipath effects, figure 8.52 illustrates the absolute wavelet coefficients for the residual components of BING11 on day 281. This day is chosen due to the larger temporal correlation characteristics shown in figure 8.45(b). Taking advantage of the time-frequency localisation property of the CWT, the wavelet scalogram depicted in figure 8.52(a) displays the OFR signal structure, consisting of a low-frequency (long-period) trend, quasi-periodic oscillations with temporally variable frequencies, and high-frequency noise. Applying the Vondrák filter to OFR with the determined optimum filter parameter $k = 10$ (see figure 8.35(a)), the slowly varying trend is accurately detected, which can

(a) SZDR (OFR): BING11281

(b) Trend from Vondrák filtering ($k = 10$)

(c) Detrended residual (DTR)

(d) 3-day sidereal stacking

(e) Stochastic noise (NCR(3))

(f) AR(2) residual (WNR)
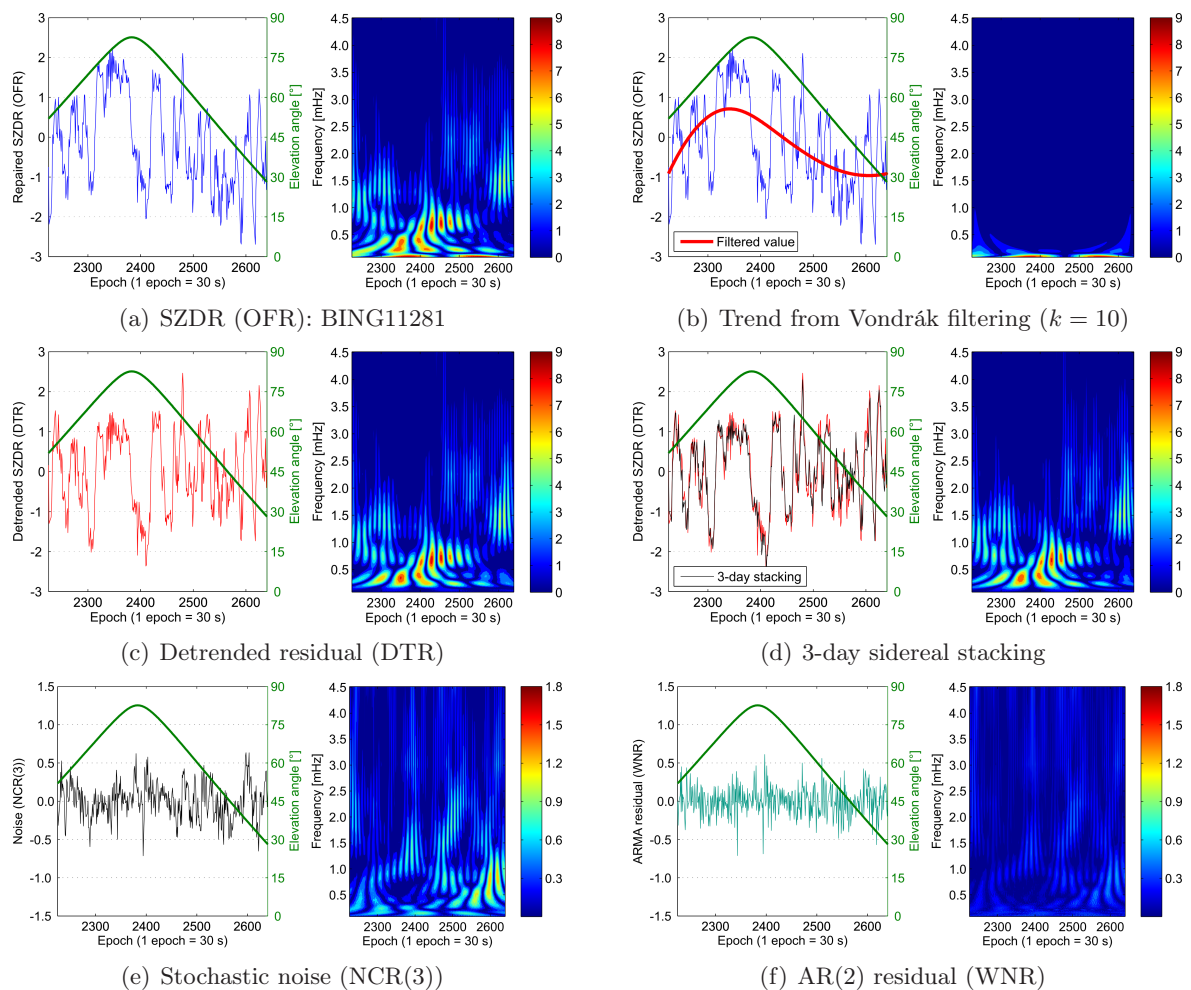
Figure 8.52: Verification of the residual decomposition and ARMA modelling based on wavelet scalograms (SAPOS®site: BING, strong multipath, satellite: PRN 11, DOY2008:281, mother wavelet: Morlet wavelet; see equation (2.94) and figure 2.7)

be seen from figure 8.52(b) in both the time and frequency domains. After removing the trend component from OFR, figure 8.52(c) mainly presents the noise and quasi-periodic oscillations whose frequencies (periods) seem to increase (decrease) with decreasing satellite elevation angle. This reflects the typical dependence of site-specific multipath effects on the satellite geometry. Considering a roof environment for instance, rapidly oscillating signals at low elevation angles suggest distant reflectors causing far-field multipath effects. Performing the 3-day sidereal stacking, the quasi-periodic signals can be sufficiently captured (see figure 8.52(d)), indirectly verifying the appropriateness of the employed unique orbit repeat lag of 240 s (see section 8.2.1). The decomposed noise shown in figure 8.52(e) still exhibits some stochastic signals of a non-daily repeating nature. They produce short-term temporal correlations, which can be well described by an AR(2) model. After filtering the noise series with the AR(2) process, figure 8.52(f) illustrates the ARMA residuals (WNR) with insignificant wavelet coefficients.

For the same day DOY2008:281 and the same satellite PRN 11, the TUEB-related wavelet scalograms of the residual components are presented in figure C.7. In the case of weak multipath effects, the efficiency of Vondrák filtering and sidereal stacking can also be verified. Since the detrended residuals DTR from TUEB have a lower mean day-to-day correlation level than those from BING (see section 8.2.2), the decomposed noise exhibits more stochastic signals in figure C.7(e), which can be sufficiently accounted for by an ARMA(2, 1) model.

Wavelet scalograms allow for a spectral investigation into the performance of the residual-based temporal correlation modelling. In addition to visual inspections, suitable hypothesis tests for normality, trend, (non-)stationarity, and uncorrelatedness are used to enable a statistical assessment of the results of the residual decomposition and ARMA modelling (see section 2.3). Instead of a significance level of $\alpha = 1\%$ applied in case study 2, $\alpha = 5\%$ is specified in this case study to verify the test performance at different significance levels. Note that a larger α value decreases the confidence in determining significance, but reduces the risk of failing to reject a false null hypothesis (or committing a Type II error), and thus indicates more statistical power. The null hypotheses ($\mathcal{H}_0$) and notations of the employed test methods can be found in table 8.2. Based on the non-rejection rates of $\mathcal{H}_0$ given in percentages, the test results are presented in bar graphs, and the corresponding numerical values are given in table D.5.

Considering different multipath impact, figure 8.53 provides a site-related presentation of the normality test results, where a total of 132979 and 124133 samples (252 and 263 data series) from TUEB and BING are used, respectively. First of all, the significant influence of strong multipath effects on the residual probability distribution can be verified. While nearly 60% of the TUEB-related OFR seem to follow a normal distribution, the normality hypothesis cannot be rejected for only about 40% of the BING-related OFR. In figure 8.53(a), it is interesting to observe that the normal distribution assumption becomes more valid during the course of the residual decomposition and decorrelation (cf. figure 8.29). In particular, the non-rejection rate of $\mathcal{H}_0$ is improved by about 20%, 10%, and 5% after Vondrák filtering, sidereal stacking, and ARMA modelling, respectively. However, regarding the BING-related test results depicted in figure 8.53(b), the performance of sidereal stacking and ARMA modelling only insignificantly (even negatively) affects the residual distributional properties. Nevertheless, the dominant enhancement of about 16% is also achieved through Vondrák detrending from OFR to DTR.

Applying the non-parametric trend tests to the residual components, the results are shown in figure 8.54. As both plots illustrate, the null hypothesis that the time series has no trend cannot be rejected for only small percentages of OFR, i.e., about 24% for TUEB and 37% for BING. However, after detrending OFR using the Vondrák filter, the non-rejection rates of $\mathcal{H}_0$ increase to about 85%, indicating the filter efficiency in trend characterisation. As expected, the removal

of quasi-periodic signals from DTR to NCR(3) insignificantly affects the trend behaviour. After filtering NCR(3) with the estimated ARMA models, the non-rejection rates of $\mathcal{H}_0$ are improved by more than 15%, which may be attributed to the favourable statistical properties of WNR, providing realisations of independent and identically distributed (iid) random variables.

(a) Site TUEB, weak multipath   (b) Site BING, strong multipath
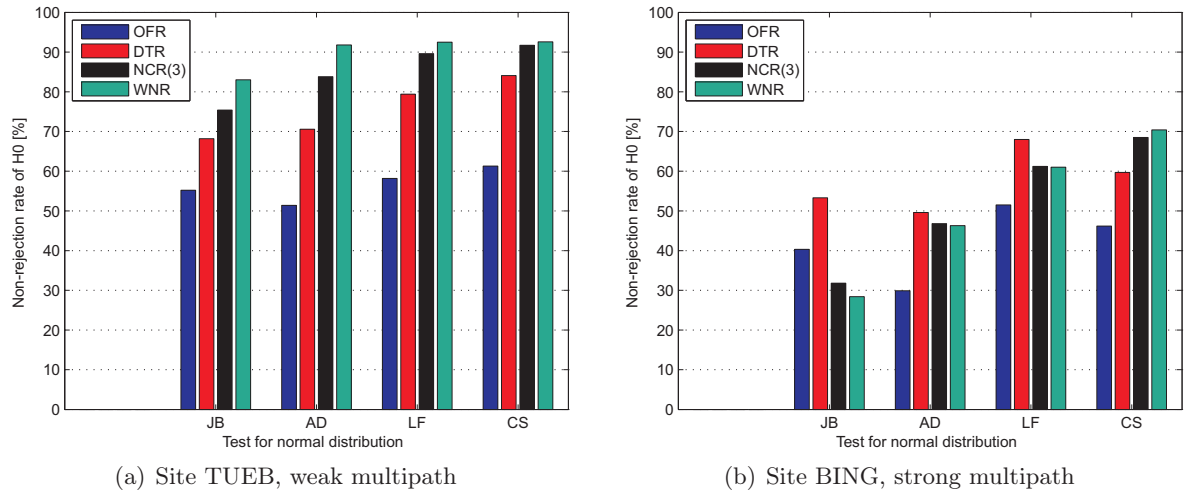
Figure 8.53: Results of the applied normality tests JB (Jarque-Bera test), AD (Anderson-Darling test), LF (Lilliefors test), and CS (chi-square test) ($\alpha = 5\%$; see section 2.3.2)

(a) Site TUEB, weak multipath   (b) Site BING, strong multipath
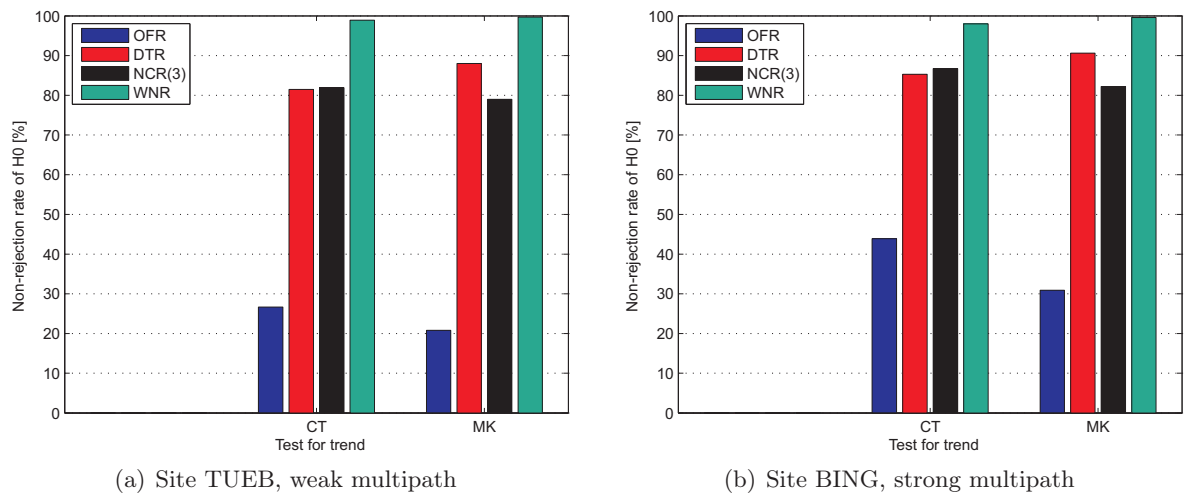
Figure 8.54: Results of the applied trend tests CT (Cox-Stuart test) and MK (Mann-Kendall test) ($\alpha = 5\%$; see section 2.3.3)

The results of the trend tests also contribute to specifying appropriate regression models for the (non-)stationarity tests. If the presence of a trend can be verified by both the CT and MK tests, a linear trend is included in the test regression, i.e., $c \neq 0$ and $\delta \neq 0$ in equations (2.78) and (2.81). The truncation lags are set in the same way as done in case study 2, i.e., using equation (2.79) for the ADF test and $\sqrt{n}$ for the KPSS test, where n denotes the time series length. Figure 8.55 depicts the results of the unit root tests, evaluating opposite null hypotheses (i.e., ADF: non-stationarity, KPSS: stationarity; see section 2.3.4). The complementary and consistent outcomes demonstrate not only the dominant role of long-periodic trends in causing non-stationarity, but also the stationarity of the noise component NCR(3) prior to ARMA modelling. By comparing the OFR-related test results, a considerably lower (higher) percentage of non-stationary (stationary) SZDR is visible for BING with strong multipath impact. This agrees

with the conclusions drawn from figure 8.39 that the OFR data from TUEB are predominantly influenced by slowly varying long-periodic trends, while those from BING are additionally affected by rapidly oscillating quasi-periodic signals, caused by far-field multipath effects.

(a) Site TUEB, weak multipath

(b) Site BING, strong multipath
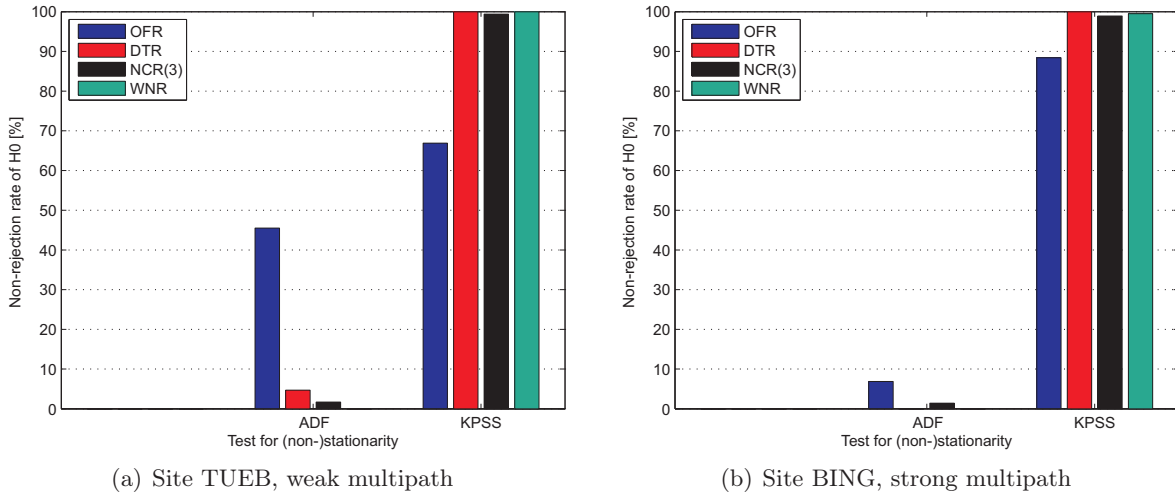
Figure 8.55: Results of the applied unit root tests ADF (augmented Dickey-Fuller test) and KPSS (Kwiatkowski-Phillips-Schmidt-Shin test) ($\alpha = 5\%$; see section 2.3.4)

To assess the significance of the noise's temporal correlation and the appropriateness of the ARMA model estimates, the noise series before and after ARMA modelling, i.e., NCR(3) and WNR, respectively, are tested for uncorrelatedness, with the results shown in figure 8.56. For the computation of the LB test statistic given by equation (2.88), a truncation lag of $h = 20$ is also applied. As can be seen from both plots, different test methods produce largely consistent results, exhibiting statistically significant temporal correlations in NCR(3). This emphasises the necessity of extending the PPP stochastic model by taking the noise's temporal correlation into consideration. After filtering the coloured noise NCR(3) with the best-fitting ARMA models, the resulting ARMA residuals WNR are almost uncorrelated. This verifies the efficiency of the identified stationary time series models in characterising the noise's temporal correlation behaviour.

(a) Site TUEB, weak multipath

(b) Site BING, strong multipath
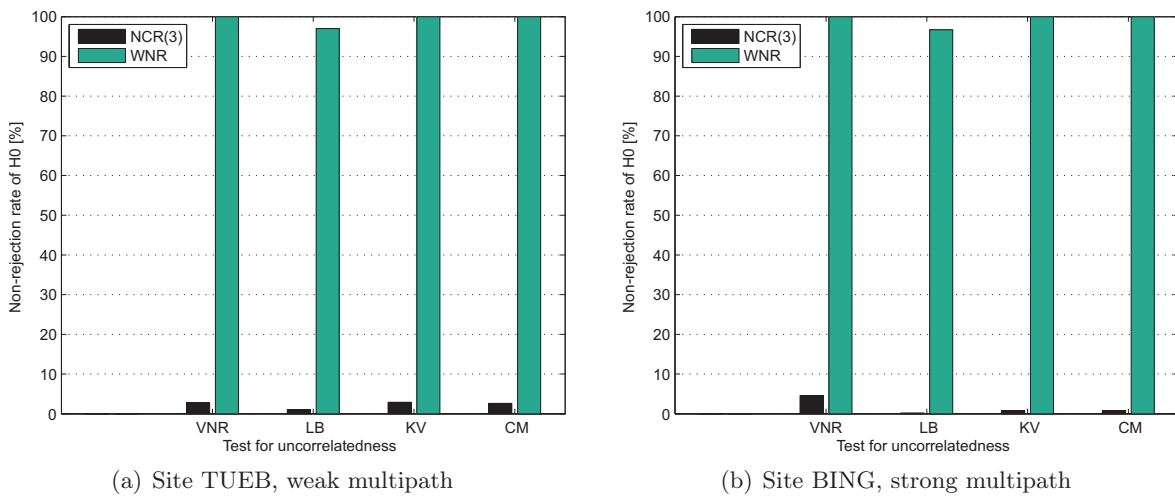
Figure 8.56: Results of the applied uncorrelatedness tests VNR (test based on von Neumann ratio), LB (Ljung-Box portmanteau test), KV (Kolmogorov-Smirnov test), and CM (Cramér-von Mises test) ($\alpha = 5\%$; see section 2.3.5)

Both the wavelet scalograms and test results obtained in this case study confirm the high performance of the residual-based temporal correlation modelling. Moreover, the impacts of the remaining systematic effects on the residual statistical properties can also be verified. While the long-periodic trends considerably distort the residual normality and stationarity, the quasi-periodic oscillations seem to induce only insignificant non-stationary components. After the appropriateness of the determined ARMA models is visually and statistically validated, the associated model ACF are used to extend the PPP stochastic model.
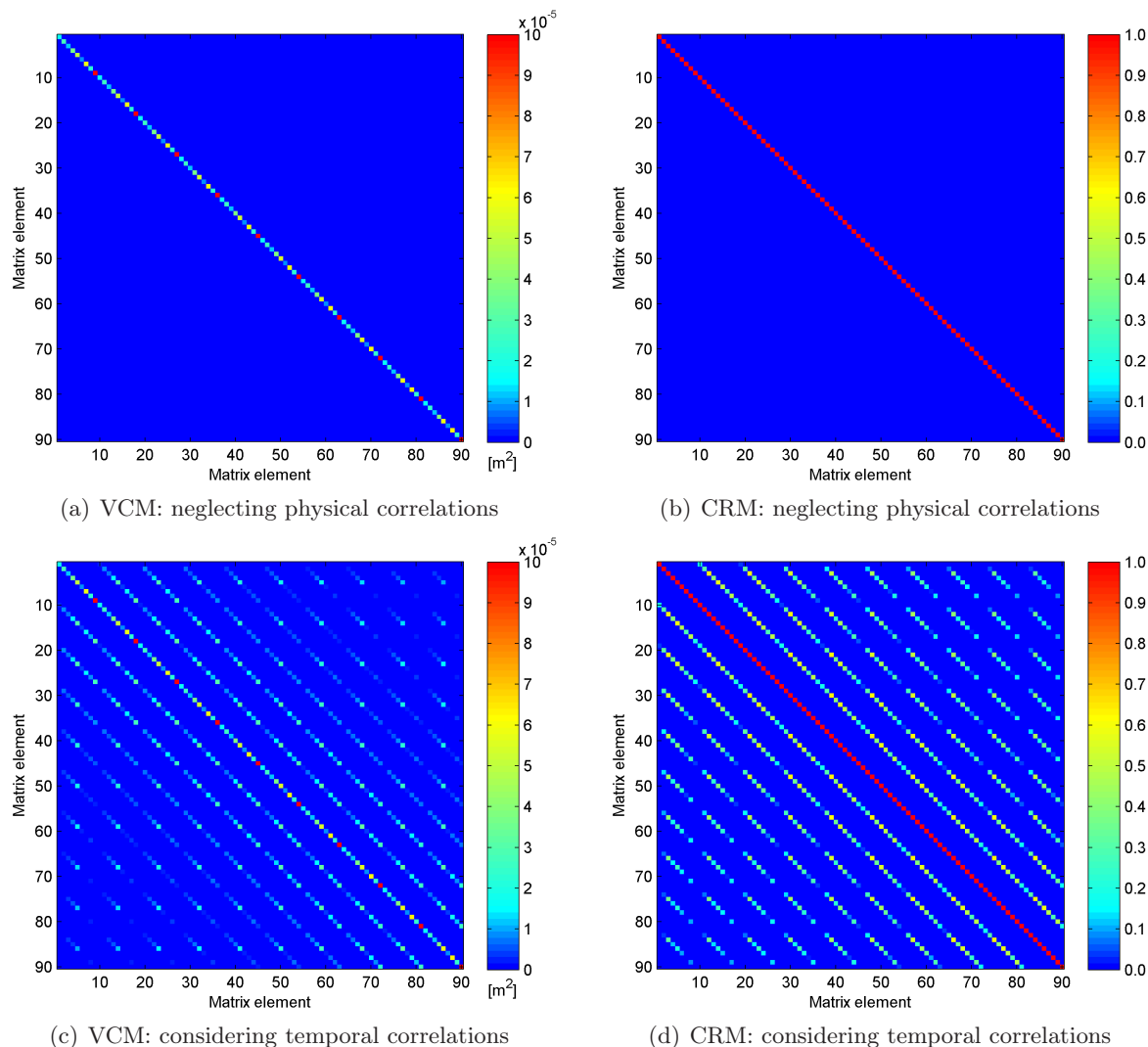
8.2.8 Extension of the PPP stochastic model

Exploiting the main property of a stationary ARMA process that its covariance function does not vary with respect to time (see equation (2.32)), the GPS stochastic model, usually expressed by a variance-covariance matrix (VCM), can be extended using the ACF of the estimated ARMA models. Taking the ionosphere-free linear combination (LC3) for a period of 10 epochs (5 min) as an example, figure 8.57 illustrates the influence of such a model extension on the structure of the VCM and the associated correlation matrix (CRM).

In this example, the variances, or the diagonal elements of the VCM, are computed using equation (3.7) in combination with the elevation-dependent observation weighting model CSC2(BS) (i.e., $\sin^2(e)$). Thereby, the L1 and L2 observations are assumed to be mutually uncorrelated and have the same a priori noise level of 1 mm in the zenith direction (Dach et al., 2007a, p. 144). For LC3 measurements at elevation angles between $10°$ and $90°$, the corresponding variances vary from $3.0 \cdot 10^{-4}$ to $8.9 \cdot 10^{-6}$ m^2. According to equation (3.27), the covariances reflecting the temporal correlation of GPS observation noise can be derived by means of

$$\sigma_{R,3}^j(t_{12}) = \sqrt{\sigma_{R,3}^j(t_1)^2 \cdot \sigma_{R,3}^j(t_2)^2} \cdot \rho_{R,3}^j(t_{12}), \tag{8.6}$$

where $\sigma_{R,3}^j(t_1)^2$ and $\sigma_{R,3}^j(t_2)^2$ are the LC3 variances for station R and satellite j at epochs t_1 and t_2, calculated depending on the satellite elevation angle. The term $\rho_{R,3}^j(t_{12})$ is the correlation coefficient at epoch difference t_{12}, provided by the ARMA model ACF (Howind, 2005, p. 59).

Neglecting the physical correlations completely, the PPP stochastic model represents a diagonal VCM (see figure 8.57(a)), and the corresponding CRM is an identity matrix (see figure 8.57(b)). Such a simple stochastic model has the advantages of easy implementation and fast computation, but the disadvantages of inaccurate parameter estimation and over-optimistic quality evaluation (Howind et al., 1999; Wang et al., 2002; Schön and Brunner, 2008b). Regarding the variances within one epoch, i.e., 9 matrix elements, significant differences are visible, indicating heterogeneous observation quality. As demonstrated in chapter 6, the proposed SNR-based weighting scheme EMPSNR2 is superior to the elevation-dependent model CSC2(BS). Therefore, it is strongly recommended to use realistic observation weights instead of an identical weight, particularly when including low-elevation (below $10°$) data collected under non-ideal observational conditions (Dach et al., 2007a, p. 144). The extension of the PPP stochastic model by accounting for the noise's temporal correlation results in considerable changes in the VCM and CRM structures. As figure 8.56 shows, the temporal correlation in the noise component NCR(3) is statistically significant, leading to covariances and correlation coefficients of up to $3.5 \cdot 10^{-5}$ m^2 and 0.63, respectively. Correlations at this level should not be simply neglected in GPS data analysis. As expected, the magnitudes of the covariances and correlations decrease as the distance from the main diagonal (or the epoch lag) increases. In fact, the VCM shown in figure 8.57(c) represents a realisation of the variance-covariance structure schematically presented in figure 3.2, where the spatial and cross correlations are still neglected.

(a) VCM: neglecting physical correlations

(b) CRM: neglecting physical correlations

(c) VCM: considering temporal correlations

(d) CRM: considering temporal correlations

Figure 8.57: Examples of PPP variance-covariance matrices (VCM) and correlation matrices (CRM) before and after considering the noise's temporal correlation (SA*POS*®site: TUEB, weak multipath, DOY2008:279, epochs: 1-10, 1 epoch = 30 s, 9 GPS satellites per epoch)

Considering the determined mean zero-crossing correlation length of about 8 min (see figure 8.43(a)), figure 8.58 displays the extended PPP stochastic model for a period of 16 epochs with respect to multipath impact and atmospheric conditions. In doing so, the sensitivity of the covariance structure can be assessed against these two factors, which strongly affect the noise's temporal correlation characteristics (see figures 8.43 and 8.45). While the SA*POS*®sites TUEB and BING are significantly different concerning multipath impact (see figure 4.9), the days DOY2008:279 and 281 are representative in view of atmospheric conditions (see figure 8.45(a)). Comparing the VCM and CRM structures shown in figures 8.58(a) and (b), it can be easily seen that the correlation length decreases with increasing multipath effects. Considering that a total of 9 satellites are observed at each epoch (1 epoch = 30 s), the covariances, covering about 120 and 70 matrix elements, exhibit correlation lengths of 7 and 4 min, respectively. These agree with the median correlation times presented in figure 8.43(a), showing that the extended stochastic model reflects the influence of site-specific multipath on the noise's temporal correlation properties. Since the correlation analysis is undertaken based on the noise's sample ACF, while the VCM extension is performed using the ARMA model ACF, this agreement indirectly verifies the efficiency of the identified ARMA models in noise characterisation.
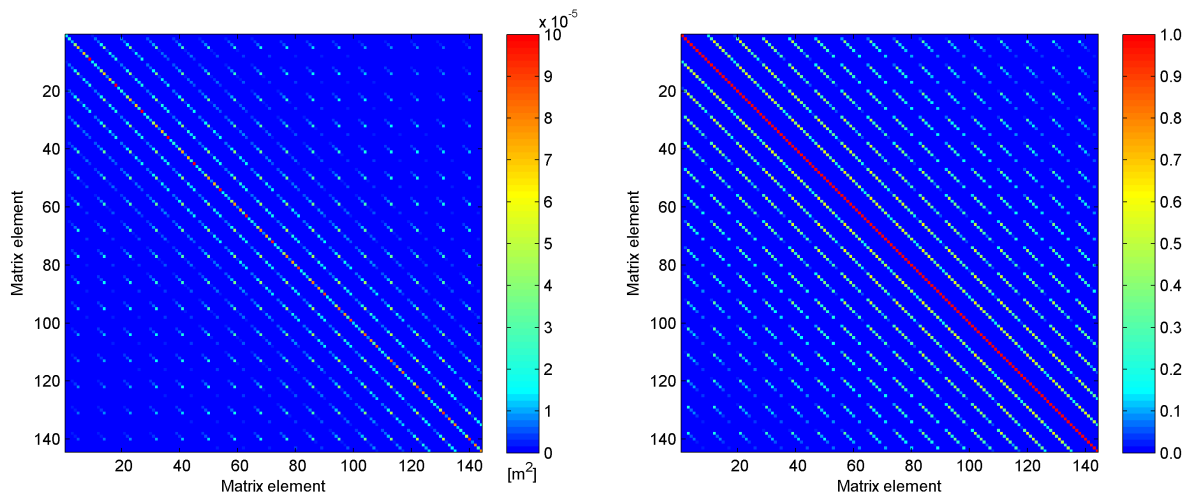
(a) VCM (left) and CRM (right) (SA*POS*®site: TUEB, weak MP, DOY2008:279, epochs: 17-32)
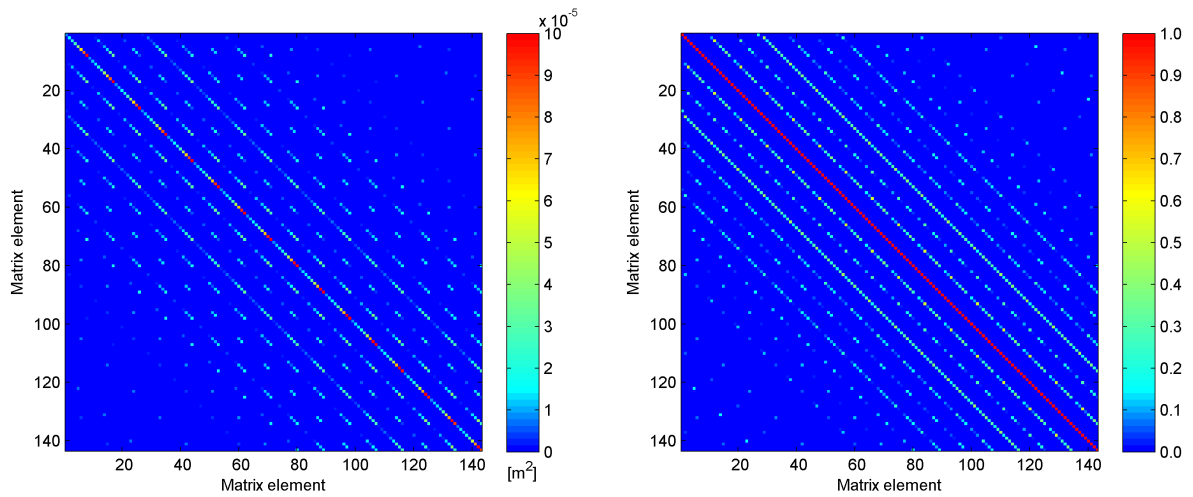
(b) VCM (left) and CRM (right) (SA*POS*®site: BING, strong MP, DOY2008:279, epochs: 17-32)
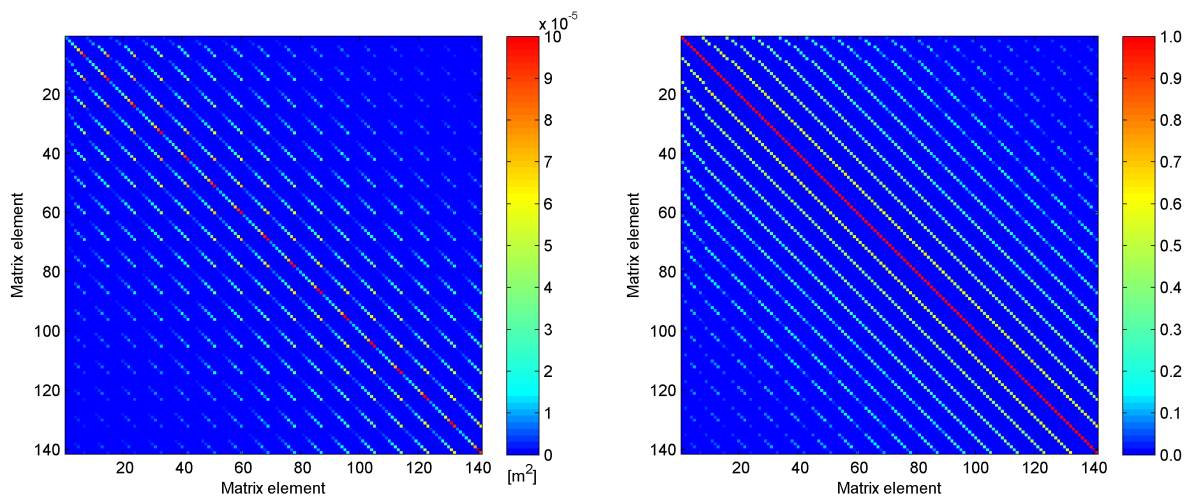
(c) VCM (left) and CRM (right) (SA*POS*®site: BING, strong MP, DOY2008:281, epochs: 1-16)

Figure 8.58: Extended PPP stochastic model with respect to multipath (MP) impact and atmospheric conditions (16 epochs, 1 epoch = 30 s, day 279: high WS and low RH, day 281: low WS and high RH; see figure 4.9 for MP and figures 4.10(c) and 8.45 for WS and RH)

As figure 8.44 shows, the noise's temporal correlation tends to increase with increasing satellite elevation angle. To minimise the impact of satellite geometry on the VCM comparison with respect to atmospheric conditions, the considered time interval is shifted from $[17, 32]$ on day 279 to $[1, 16]$ on day 281 by 16 epochs (8 epochs per day), where the unique orbit repeat lag of 240 s (8 epochs) is used (see section 8.2.1). As a consequence, the extended VCM and CRM depicted in figures 8.58(b) and (c) are related to a similar satellite geometry, and the differences between them are primarily caused by variable atmospheric conditions. Compared to day 279, on which higher wind speed (WS) and lower relative humidity (RH) prevail, considerably stronger temporal correlation can be observed in the VCM and CRM on day 281 with lower WS and higher RH, coinciding with the results illustrated in figure 8.46. In summary, the effects of variable atmospheric conditions on the temporal correlation of GPS observation noise can be accounted for by appropriately identified ARMA models. Using the ARMA model ACF to extend the PPP stochastic model, the resulting VCM and CRM also reflect atmospheric variations.

In this thesis, the extension of the GPS stochastic model is only carried out for PPP. However, it can be easily adopted to improve the VCM of double-difference observations. For example, instead of fitting empirical ACF given by equations (7.1) and (7.2), one can use the model ACF of the ARMA estimates, determined by analysing the noise component of studentised double-difference residuals. In addition to the temporal correlation information, an ARMA model provides a rigorous mathematical relationship for a sequence of random variables. This property may be taken advantage of in the future to develop a temporally propagating stochastic model, which is applicable to epoch-parameter estimation (Dach et al., 2007a, p. 149) and avoids VCM inversion in a large least-squares problem (Klees et al., 2003).

8.3 Concluding remarks

Using the studentised residuals of GPS observations from short-term relative positioning (SDDR) and long-term PPP (SZDR), this chapter presented the results of the residual-based temporal correlation modelling with respect to satellite geometry, multipath impact, and atmospheric conditions. The findings from both case studies are generally consistent and can be physically interpreted by incorporating DWD surface meteorological data. The efficiency of the residual decomposition and ARMA modelling is verified by means of continuous wavelet transforms (CWT) and statistical hypothesis tests for normality, trend, (non-)stationarity, and uncorrelatedness. The main conclusions drawn from the case studies are summarised as follows:

- To obtain multiple days of 1-second SDDR with similar satellite geometry, satellite-specific orbit repeat lags are determined using the empirical approach described in section 7.2.5. The resulting lag values vary from 240 to 263 s and agree at the 1-second level with the outcomes of the program `orbrep.f` (Agnew and Larson, 2007). For the 30-second SZDR, a unique orbit repeat lag of 240 s turns out to be applicable to all GPS satellites.

- The Vondrák filter is employed to capture long-periodic trends, where the optimum filter parameter k is derived by maximising the day-to-day correlation of the detrended residuals. The k estimates, mainly ranging between 7 and 13, decrease with increasing multipath effects. Moreover, the cross-validation Vondrák filter (CVVF) proposed by Zheng et al. (2005) filters signals, along with noise's temporal correlations.

- Applying the 5-MAD (median absolute deviation) criterion and the one-sided F-test to the Vondrák residuals, the two-step procedure for detecting multiple outliers is highly efficient in practice. The test statistic increases with the number of outliers, which is in turn posi-

tively correlated with atmospheric relative humidity. Using a remove-repair-restore (RRR) technique, the significant outliers can be sufficiently repaired, which, however, hardly affects the determination of the optimum Vondrák filter parameters.

- After properly handling outliers, the residual decomposition is performed. The slowly varying long-periodic trends can be well captured by the Vondrák filter, as well as some randomly occurring and non-daily repeating signals. The 3-day sidereal stacking enables an accurate detection of daily repeating (quasi-periodic) signals, producing homogenous coloured noise. Moreover, the remaining systematic effects significantly impact upon the residual correlation structure and should be removed prior to temporal correlation analysis.

- Making use of the zero-crossing correlation length and lag-1 correlation level of the noise's sample ACF, the correlation analysis is carried out by considering baseline length, multipath impact, satellite geometry, and atmospheric conditions. Based on 10 days of 1-hour (24-hour) SDDR (SZDR) with a sampling interval of 1 s (30 s), the determined mean correlation length and level amount to about 80 s (8 min) and 0.4 (0.4), respectively. At a regional scale, baseline length appears to marginally influence the noise's temporal correlation behaviour, while strong multipath effects may decrease the correlation length by up to 50%. Furthermore, the noise's temporal correlation becomes longer and stronger as the satellite elevation angle increases. By considering the freely available DWD surface meteorological data, the correlation characteristics tend to be larger as wind speed (WS) decreases and relative humidity (RH) increases.

- For each decomposed noise series, the best-fitting ARMA model is automatically identified using the free MATLAB$^{\circledR}$ Toolbox ARMASA (Broersen, 2006, chap. 9). The results of the model identification are dominated by AR and ARMA processes, where AR models are preferred in the presence of strong multipath effects. In the case of weak multipath, AR and ARMA models of orders of up to 22 and $(6, 5)$, respectively, seem to be adequate. In general, higher ARMA orders can be expected when analysing residuals from low-elevation satellites and strong multipath environments. The ARMA decorrelation decreases the noise standard deviation and produces white noise residuals whose standard deviation exhibits a positive (negative) correlation with WS (RH).

- Provided that the scale is properly specified, the CWT using the Morlet wavelet represents an efficient tool for visually assessing the residual decomposition and ARMA modelling. Apart from enabling a rigorous performance evaluation, the applied statistical tests show significant impacts of site-specific multipath on the residual probability distribution and strong influences of long-periodic trends on the fulfilment of normality and stationarity. Being largely free of systematic signals, the noise component still possesses statistically significant positive correlations, which must be considered in the GPS stochastic model.

- Using the ARMA model ACF, the PPP stochastic model is extended, and the resulting variance-covariance matrix (VCM) has a diagonal-dominant structure. Since the noise's temporal correlation can be sufficiently described by the estimated ARMA models, the extended VCM also reflects variations in multipath effects and atmospheric conditions.

Applying the residual-based temporal correlation modelling to different data sets, the outcomes are largely consistent, statistically valid, and physically interpretable. Nevertheless, for a reliable comparison of the noise's temporal correlation properties between relative positioning and PPP, additional investigation is required, for example, using SDDR and SZDR from GPS data analyses with widely consistent parameter settings. In order to benefit from the recent developments in

the Bernese GNSS Software, such as improved troposphere modelling by means of GMF/GPT and VMF1 (Boehm et al., 2006a,b, 2007), GPS data processing may be carried out using the new software version 5.2^1. In the interest of a more accurate physical interpretation of the results, meteorological data at high temporal and spatial resolution should be incorporated into the residual-based temporal correlation analysis. Finally, the effects of the extended stochastic model on GPS parameter estimation need more research in the future.

---

[1]More information available at `www.bernese.unibe.ch/newvers.html`

Chapter 9

Conclusions and Recommendations

9.1 Conclusions

Using the least-squares (LS) method to analyse GPS data, both the functional and stochastic models must be appropriately specified for accurate parameter estimates and realistic quality measures. In comparison to the highly developed functional model, the stochastic model applied in many GPS software products is considered to be unrealistic due to the elevation-dependent (or even identical) weighting model and the neglect of physical correlations between GPS observations. Following the specific objectives described in section 1.3, this thesis has proposed an advanced observation weighting scheme based on signal-to-noise ratio (SNR) measurements and a rigorous temporal correlation analysis using residual time series from LS evaluation. The main conclusions for the two modelling approaches presented in this work are the following:

1. Empirical SNR-based observation weighting:

The suggested SNR-based weighting model relies upon a minimum-related scaling of representative signal quality measurements and is completely independent from the formula provided by Langley (1997). It properly handles low-quality measurements of weak signals and sufficiently characterises variations in observation quality due to multipath and atmospheric effects. Following the implementation of the SNR-based weighting into the Bernese GPS Software 5.0 (Dach et al., 2007a), short- (3 h) and long-term (24 h) static relative positioning were carried out to study its effects on phase ambiguity resolution, troposphere parameter (TRP) estimation, and site coordinate determination. Compared to the commonly used elevation-dependent weighting model $\sin^2(e)$, the most important findings are summarised as follows:

- For a minimum elevation angle of 3° on a regional scale, the SNR-based weighting model improves on average the wide- and narrow-lane ambiguity resolution by 10% and the TRP standard deviation by 20%. In terms of TRP estimates, cm-level changes are possible.

- The impact of the SNR-based weighting on coordinates is normally below 5 mm. However, it may increase to several centimetres, and even more than one decimetre, when analysing short-term and low-quality data collected under non-ideal observational conditions.

2. Residual-based temporal correlation modelling:

The proposed residual-based temporal correlation modelling essentially consists of two steps, namely noise extraction through residual decomposition and noise characterisation using auto-regressive moving average (ARMA) processes. The remaining systematic effects are subdivided into long-periodic trends and quasi-periodic oscillations, which are detected by performing Vondrák filtering and sidereal stacking, respectively. The optimum Vondrák filter parameter is empirically determined by considering its influence on residual day-to-day repeatability and noise's temporal correlation. On the basis of the detrended residuals, outliers are detected in a statistically rigorous manner and can be repaired by means of a remove-repair-restore (RRR) technique. Within the context of sidereal stacking, appropriate orbit repeat lags are employed to ensure similar satellite geometry on multiple consecutive days. Once the stochastic noise is thoroughly

extracted, its temporal correlation properties are investigated based on the zero-crossing correlation length and lag-1 correlation level of the associated sample autocorrelation function (ACF). For each decomposed noise series, the best-fitting ARMA model is automatically identified using the free MATLAB® Toolbox ARMASA (Broersen, 2006, chap. 9). Both the temporal correlation characteristics and the results of ARMA modelling are analysed with respect to multipath impact, satellite geometry, and atmospheric conditions. By applying the continuous wavelet transform and statistical hypothesis tests for normality, trend, (non-)stationarity, and uncorrelatedness, the efficiency of the residual decomposition and ARMA modelling is verified. Making use of the model ACF of statistically valid ARMA estimates, the GPS stochastic model is extended by taking the noise's temporal correlation into account. This modelling approach was tested using 1-second studentised double-difference residuals (SDDR) from short-term relative positioning and 30-second studentised zero-difference residuals (SZDR) from daily precise point positioning (PPP). The most important results are summarised as follows:

- The mean zero-crossing correlation length and lag-1 correlation level determined by analysing SDDR (SZDR) are 80 s (8 min) and 0.4 (0.4), with 95% quantiles of 130 s (17 min) and 0.7 (0.6), respectively. The noise's temporal correlation decreases with increasing wind speed and increases with increasing relative humidity and satellite elevation angle. Strong multipath effects may significantly reduce the noise's correlation length.

- First-order autoregressive processes AR(1) are insufficient for noise characterisation. The model identification is dominated by AR and ARMA processes, where AR models are preferred if strong multipath is present. When analysing residuals from low-elevation satellites and severe multipath environments, higher ARMA orders are selected.

- The long-periodic trend is the most significant cause of deviations from normality and stationarity. The decomposed noise is largely stationary, fulfilling the assumption of ARMA modelling. The coloured noise can be effectively decorrelated by the ARMA estimates, and the extended PPP stochastic model reflects multipath and atmospheric variations.

9.2 Recommendations

This thesis has presented considerable positive effects of the SNR-based weighting model on static GPS relative positioning, as well as statistically significant and physically interpretable temporal correlations of GPS observations. In order to transfer the research results into practical applications, there are some topics that should be considered in the future:

SNR-based observation weighting. Benefiting from the standardisation of signal strengths in RINEX Version 3.00 (see section 5.3.1; Gurtner and Estey, 2007, p. 10), empirical SNR-based weighting models will be more applicable in practice. The proposed approach requires additional verification, for example, using PPP and representative data sets with respect to observation quality, period, and employed equipment types. In addition, the impact on the allowable a priori coordinate uncertainty should be studied (Collins and Langley, 1999, p. 29). To achieve high computational efficiency, it is strongly recommended to implement the SNR-based weighting model into GPS data processing software completely, without any auxiliary components.

Residual-based correlation modelling. Based on large amounts of residual data, the outcomes of the temporal correlation analysis should be verified and further investigated with regard to double differencing, receiver type, and wind direction. The results of ARMA modelling need to be considered in the GPS stochastic model by applying, for instance, the LS evaluation with

approximated matrix inversion (Howind et al., 1999), the modified sequential LS adjustment algorithm (El-Rabbany and Kleusberg, 2003), and the measurement transformation (decorrelation) method (Wang et al., 2002). Moreover, the development of a temporally propagating GPS stochastic model based on ARMA estimates requires more research. In the future, the unmodelled multipath effects and the remaining tropospheric delays should be handled more efficiently using robot/in-situ station calibration (Wübbena et al., 2011), modern residual stacking techniques (Fuhrmann et al., 2010, chap. 7), high-resolution meteorological data, and advanced tropospheric models (Boehm et al., 2006a,b, 2007). Additional studies on spatial and cross correlations are also necessary, which may be undertaken by means of cross-correlation functions (Leandro and Santos, 2007) and multivariate ARMA processes (Brockwell and Davis, 2002, chap. 7).

Other suggestions. To allow for a physical interpretation of the results, it is strongly advisable to incorporate surface metrological data, even though they may not have high temporal and spatial resolution. The free available MATLAB$^{\circledR}$ Toolbox ARMASA is particularly applicable in the case of large data volumes and high-order model estimation, while the ITSM2000 software package provided by Brockwell and Davis (2002, p. 395) is more appropriate for single time series analysis and simulation studies (Luo et al., 2011b, 2012b).

Applications. Considering its significant effects on site-specific troposphere parameter estimation (see sections 6.1.3 and 6.2.3), the SNR-based weighting scheme is especially deployable to high-resolution atmospheric water vapour determination. The derived numerical results of satellite orbit repeat lags, Vondrák filter parameters, and temporal correlation characteristics may be regarded as rough guides and used in other studies for the purpose of comparison. Without complex modifications, the temporal correlation modelling can be applied to residuals of GLONASS and Galileo observations. The proposed mathematical methods, such as Vondrák filtering, outlier detection, ARMA modelling, wavelet transforms, and statistical tests, are applicable to other data sets, for example, those from gravity field missions like GRACE (Gravity Recovery And Climate Experiment) and GOCE (Gravity field and steady-state Ocean Circulation Explorer).

Appendix A

Quantiles of Test Statistics

This appendix contains the right $(1-\alpha)$ and left tail (α) quantiles of the distributions of the test statistics for typical significance levels α (see section 2.3). Based on these quantiles and the test properties, for example, one- or two-sided test, the corresponding critical values can be easily derived. The tabulated values are either taken from cited references or computed using analytical approximations and empirical simulations performed in MATLAB® R2009b. The quantiles that are not available in the cited references are denoted by the string "N/A". Furthermore, in the following tables, MST/MET and REF refer to the associated MATLAB® Toolbox and reference, respectively, outlined in the description of each.

A.1 Tests for normality

Test: Jarque-Bera (JB) test
MATLAB® function: `jbtest`
REF: Jarque and Bera (1987, table 2)
MST: MATLAB® Statistics Toolbox™

Table A.1: Right tail $(1 - \alpha)$ quantiles of the distribution of the JB test statistic T_{JB} (see equation (2.69))

| Sample size n | Significance level α | | | | | |
| | 1% | | 5% | | 10% | |
	REF	MST	REF	MST	REF	MST
20	N/A	9.75	3.26	3.80	2.13	2.35
30	N/A	11.33	3.71	4.40	2.49	2.74
40	N/A	12.04	3.99	4.75	2.70	3.00
50	N/A	12.37	4.26	4.97	2.90	3.18
75	N/A	12.59	4.27	5.27	3.09	3.49
100	N/A	12.51	4.29	5.43	3.14	3.67
125	N/A	12.36	4.34	5.53	3.31	3.80
150	N/A	12.18	4.39	5.59	3.43	3.90
200	N/A	11.86	4.43	5.68	3.48	4.03
250	N/A	11.59	4.51	5.73	3.54	4.12
300	N/A	11.37	4.60	5.77	3.68	4.19
400	N/A	11.02	4.74	5.82	3.76	4.27
500	N/A	10.76	4.82	5.86	3.91	4.33
800	N/A	10.29	5.46	5.91	4.32	4.42
1000		10.11		5.93		4.46
5000		9.41		5.98		4.56
10000	N/A	9.31	5.99	5.98	4.61	4.58
100000		9.22		5.99		4.60
$\infty \to \chi^2_{2;1-\alpha}$	N/A	9.21	5.99		4.61	

Test: Chi-square (CS) test
MATLAB$^{\circledR}$ function: `chi2gof`
REF: Niemeier (2008, table A.4, p. 474)

Table A.2: Right tail $(1-\alpha)$ quantiles of the distribution of the CS test
statistic T_{CS} (see equation (2.70))

Number of bins m	Degrees of freedom $f = m - 3$	Significance level α (REF)				
		0.5%	1%	2.5%	5%	10%
10	7	20.78	18.48	16.01	14.07	12.02
11	8	21.96	20.09	17.53	15.51	13.36
12	9	23.59	21.67	19.02	16.92	14.68
13	10	25.19	23.21	20.48	18.31	15.99
14	11	26.76	24.72	21.92	19.68	17.28
15	12	28.30	26.22	23.34	21.03	18.55

Test: Lilliefors (LF) test
MATLAB$^{\circledR}$ function: `lillietest`
REF: Lilliefors (1967, table 1)
MST: MATLAB$^{\circledR}$ Statistics Toolbox$^{\text{TM}}$

Table A.3: Right tail $(1-\alpha)$ quantiles of the distribution of the LF test
statistic T_{LF} (see equation (2.71))

Sample size n	Significance level α					
	1%		5%		10%	
	REF	MST	REF	MST	REF	MST
10	0.294	0.303	0.258	0.262	0.239	0.241
11	0.284	0.292	0.249	0.252	0.230	0.231
12	0.275	0.281	0.242	0.242	0.223	0.222
13	0.268	0.271	0.234	0.233	0.214	0.215
14	0.261	0.262	0.227	0.226	0.207	0.208
15	0.257	0.254	0.220	0.219	0.201	0.201
16	0.250	0.247	0.213	0.213	0.195	0.195
17	0.245	0.240	0.206	0.207	0.189	0.190
18	0.239	0.234	0.200	0.201	0.184	0.185
19	0.235	0.229	0.195	0.197	0.179	0.181
20	0.231	0.223	0.190	0.192	0.174	0.176
25	0.203	0.201	0.180	0.173	0.165	0.159
30	0.187	0.185	0.161	0.159	0.144	0.146
$n > 30$	REF: $1.031/\sqrt{n}$		REF: $0.886/\sqrt{n}$		REF: $0.805/\sqrt{n}$	
50	0.146	0.145	0.125	0.125	0.114	0.114
100	0.103	0.104	0.089	0.089	0.081	0.082
300	0.060	0.061	0.051	0.052	0.046	0.048
500	0.046	0.047	0.040	0.040	0.036	0.037
1000	0.033	0.033	0.028	0.029	0.025	0.026
3000	0.019	0.019	0.016	0.017	0.015	0.015
5000	0.015	0.015	0.013	0.013	0.011	0.012
10000	0.010	0.011	0.009	0.009	0.008	0.008

Test: Anderson-Darling (AD) test
REF: Stephens (1986, table 4.9)

Table A.4: Right tail $(1 - \alpha)$ quantiles of the distribution of the modified AD test statistic T_{AD}^* (see equation (2.73))

Right tail quantiles	Significance level α (REF)						
	1%	**2.5%**	**5%**	**10%**	**15%**	**25%**	**50%**
$C_{AD,1-\alpha}$	1.035	0.873	0.752	0.631	0.561	0.470	0.341

A.2 Tests for trend

Test: Cox-Stuart (CT) test
REF: Hartung et al. (2005, table A.2, p. 891)
MST: MATLAB$^{\circledR}$ Statistics Toolbox$^{\text{TM}}$ (function: `binoinv`)

Table A.5: Right tail $(1 - \alpha)$ quantiles of the distribution of the CT test statistics T_{CT} and Z_{CT} (see equation (2.75))

Sample size n	Significance level α					Source
	0.5%	**1%**	**2.5%**	**5%**	**10%**	
$n < 20 : T_{CT} \sim Bin(n, 0.5), n \geq 20 : Z_{CT} \sim \mathcal{N}(0,1)$						
5	5	5	5	4	4	
6	6	6	5	5	5	
7	7	6	6	6	5	
8	7	7	7	6	6	
9	8	8	7	7	6	
10	9	9	8	8	7	
11	10	9	9	8	8	
12	10	10	9	9	8	
13	11	11	10	9	9	MST
14	12	11	11	10	9	
15	12	12	11	11	10	
16	13	13	12	11	11	
17	14	13	12	12	11	
18	14	14	13	12	12	
19	15	14	14	13	12	
$n \geq 20$	2.576	2.326	1.960	1.645	1.282	REF

If $p = 0.5$, the discrete binomial distribution $Bin(n, p)$ has a symmetric probability distribution. This can be easily demonstrated by setting $p = 0.5$ for the skewness of $Bin(n, p)$, given by

$$S_{Bin(n,p)} = (1 - 2p)/\sqrt{np(1 - p)}. \tag{A.1}$$

As is well known, a skewness of zero indicates a symmetric distribution. Taking advantage of the distributional symmetry, the left tail (α) quantile $B_{n,0.5;\alpha}$ can be expressed by

$$B_{n,0.5;\alpha} = n - B_{n,0.5;1-\alpha}, \tag{A.2}$$

where $B_{n,0.5;1-\alpha}$ denotes the corresponding right tail quantile and is directly obtainable from table A.5.

Test: Mann-Kendall (MK) test
REF: Hartung et al. (2005, table 44, p. 249; table A.2, p. 891)

Table A.6: Right tail $(1-\alpha)$ quantiles of the distribution of the MK test statistics T_{MK} (see equation (2.76)) and Z_{MK} (see equation (2.77))

Sample size n	Significance level α (REF)				
	0.5%	**1%**	**2.5%**	**5%**	**10%**
4	6	6	6	6	5
5	10	9	8	8	7
6	14	13	11	9	7
7	17	15	13	11	9
8	21	19	16	14	11
9	25	23	19	16	13
10	29	26	23	19	15
15	52	47	40	34	27
20	80	72	59	49	38
25	110	100	84	71	56
30	145	131	111	93	73
35	183	165	139	117	88
40	222	200	169	142	111
$n > 40 : Z_{MK} \sim \mathcal{N}(0,1)$					
$n>40$	2.576	2.326	1.960	1.645	1.282

A.3 Tests for stationarity

Test: augmented Dickey-Fuller (ADF) test
MATLAB® function: `adftest`
REF: Dickey (1976); Fuller (1996, table 10.A.2)
MET: MATLAB® Econometrics Toolbox™

Table A.7: Left tail (α) quantiles of the distribution of the ADF test statistic T_{ADF} (see equation (2.80))

Regression model	Sample size n	Significance level α					
		1%		**5%**		**10%**	
		REF	**MET**	**REF**	**MET**	**REF**	**MET**
Equation (2.78), $c = \delta = 0$	30	N/A	-2.643	N/A	-1.950	N/A	-1.607
	40	N/A	-2.625	N/A	-1.948	N/A	-1.610
	50	-2.62	-2.612	-1.95	-1.947	-1.61	-1.612
	75	N/A	-2.597	N/A	-1.945	N/A	-1.613
	100	-2.60	-2.590	-1.95	-1.944	-1.61	-1.614
	150	N/A	-2.581	N/A	-1.943	N/A	-1.615
	200	N/A	-2.575	N/A	-1.942	N/A	-1.616
	250	-2.58	-2.576	-1.95	-1.942	-1.62	-1.616
	300	N/A	-2.576	N/A	-1.942	N/A	-1.617
	500	-2.58	-2.570	-1.95	-1.941	-1.62	-1.616
	1000	-2.58	-2.569	-1.95	-1.942	-1.62	-1.617
	10000	-2.58	-2.566	-1.95	-1.942	-1.62	-1.618

Table A.8: Left tail (α) quantiles of the distribution of the ADF test statistic T_{ADF} (continuation of table A.7; see equation (2.80))

Regression model	Sample size n	Significance level α					
		1%		5%		10%	
		REF	**MET**	**REF**	**MET**	**REF**	**MET**
Equation (2.78), $c \neq 0, \delta = 0$	30	N/A	−3.679	N/A	−2.968	N/A	−2.623
	40	N/A	−3.612	N/A	−2.940	N/A	−2.608
	50	−3.59	−3.573	−2.93	−2.924	−2.60	−2.600
	75	N/A	−3.523	N/A	−2.901	N/A	−2.588
	100	−3.50	−3.499	−2.90	−2.890	−2.59	−2.581
	150	N/A	−3.478	N/A	−2.881	N/A	−2.577
	200	N/A	−3.462	N/A	−2.876	N/A	−2.574
	250	−3.45	−3.459	−2.88	−2.874	−2.58	−2.573
	300	N/A	−3.456	N/A	−2.871	N/A	−2.572
	500	−3.44	−3.442	−2.87	−2.868	−2.57	−2.570
	1000	−3.42	−3.438	−2.86	−2.865	−2.57	−2.569
	10000	−3.42	−3.431	−2.86	−2.861	−2.57	−2.567
Equation (2.78), $c \neq 0, \delta \neq 0$	30	N/A	−4.311	N/A	−3.574	N/A	−3.221
	40	N/A	−4.214	N/A	−3.530	N/A	−3.197
	50	−4.16	−4.155	−3.50	−3.505	−3.18	−3.183
	75	N/A	−4.088	N/A	−3.472	N/A	−3.163
	100	−4.05	−4.055	−3.45	−3.456	−3.15	−3.154
	150	N/A	−4.024	N/A	−3.441	N/A	−3.145
	200	N/A	−4.006	N/A	−3.434	N/A	−3.141
	250	−3.98	−3.998	−3.42	−3.430	−3.13	−3.138
	300	N/A	−3.991	N/A	−3.426	N/A	−3.136
	500	−3.97	−3.978	−3.42	−3.419	−3.13	−3.133
	1000	−3.96	−3.969	−3.41	−3.415	−3.13	−3.128
	10000	−3.96	−3.959	−3.41	−3.412	−3.13	−3.128

Test: Kwiatkowski-Phillips-Schmidt-Shin (KPSS) test
MATLAB$^{\circledR}$ function: `kpsstest`
REF: Kwiatkowski et al. (1992, table 1)

Table A.9: Right tail ($1 - \alpha$) quantiles of the distribution of the KPSS test statistic T_{KPSS} (see equation (2.82))

Deterministic terms		Significance level α (REF)			
		1%	2.5%	5%	10%
Equation (2.81)	$c \neq 0, \delta = 0$	0.739	0.574	0.463	0.347
	$c \neq 0, \delta \neq 0$	0.216	0.176	0.146	0.119

A.4 Tests for uncorrelatedness

Test: based on von Neumann ratio (VNR)
REF: Hart (1942); Bingham and Nelson (1981, table 2)
MST: MATLAB$^{\circledR}$ Statistics Toolbox$^{\text{TM}}$ (function: `tinv`)

Table A.10: Left tail (α) quantiles of VNR (see equation (2.85)) and right tail ($1-\alpha$) quantiles of the distribution of the modified test statistic T_{VNR} ($n \geq 15$; see equation (2.86))

Sample size n	Degrees of freedom	Significance level α (REF: $C_{n;\alpha}$, MST: $t_{n+1;1-\alpha}$)							
		1%		2.5%		5%		10%	
		REF	MST	REF	MST	REF	MST	REF	MST
5	6	0.672	–	0.831	–	1.026	–	1.314	–
10	11	0.835	–	1.012	–	1.180	–	1.390	–
15	16	0.988	2.584	1.146	2.120	1.291	1.746	1.468	1.337
20	21	1.095	2.518	1.239	2.080	1.368	1.721	1.523	1.323
25	26	1.175	2.479	N/A	2.056	1.424	1.706	N/A	1.315
30	31	1.236	2.453	N/A	2.040	1.467	1.696	N/A	1.310
35	36	1.285	2.435	N/A	2.028	1.501	1.688	N/A	1.306
40	41	1.327	2.421	N/A	2.020	1.530	1.683	N/A	1.303
45	46	1.362	2.410	N/A	2.013	1.555	1.679	N/A	1.300
50	51	1.391	2.402	N/A	2.008	1.575	1.675	N/A	1.298
55	56	1.416	2.395	N/A	2.003	1.592	1.673	N/A	1.297
60	61	1.438	2.389	N/A	2.000	1.608	1.670	N/A	1.296
70	71	N/A	2.380	N/A	1.994	N/A	1.667	N/A	1.294
80	81	N/A	2.373	N/A	1.990	N/A	1.664	N/A	1.292
90	91	N/A	2.368	N/A	1.986	N/A	1.662	N/A	1.291
100	101	N/A	2.364	N/A	1.984	N/A	1.660	N/A	1.290
150	151	N/A	2.351	N/A	1.976	N/A	1.655	N/A	1.287
200	201	N/A	2.345	N/A	1.972	N/A	1.653	N/A	1.286
300	301	N/A	2.339	N/A	1.968	N/A	1.650	N/A	1.284
400	401	N/A	2.336	N/A	1.966	N/A	1.649	N/A	1.284
600	601	N/A	2.333	N/A	1.964	N/A	1.647	N/A	1.283
800	801	N/A	2.331	N/A	1.963	N/A	1.647	N/A	1.283
1000	1001	N/A	2.330	N/A	1.962	N/A	1.646	N/A	1.282
10000	10001	N/A	2.327	N/A	1.960	N/A	1.645	N/A	1.282

Test: Ljung-Box (LB) portmanteau test
MATLAB® function: `lbqtest`
REF: Hartung et al. (2005, table A.4, p. 893)

Table A.11: Right tail ($1-\alpha$) quantiles of the distribution of the LB portmanteau test statistic T_{LB} (see equation (2.88))

Degrees of freedom (truncation lag h)	Significance level α (REF)				
	0.5%	1%	2.5%	5%	10%
10	25.19	23.21	20.48	18.31	15.99
12	28.30	26.22	23.34	21.03	18.55
14	31.32	29.14	26.12	23.68	21.06
16	34.27	32.00	28.85	26.30	23.54
18	37.16	34.81	31.53	28.87	25.99
20	40.00	37.57	34.17	31.41	28.41
22	42.80	40.29	36.78	33.92	30.81
24	45.56	42.98	39.36	36.42	33.20
26	48.29	45.64	41.92	38.89	35.56
28	50.99	48.28	44.46	41.34	37.92
30	53.67	50.89	46.98	43.77	40.26

Test: Kolmogorov-Smirnov (KV) test
REF1: Kolmogorov (1941)
REF2: Teusch (2006, table 6.2, p. 104)
MCF: MATLAB$^{®}$ Central function (`kolminv`[1])

Table A.12: Right tail $(1-\alpha)$ quantiles of the distribution of the KV test statistic T_{KV} (see equation (2.89))

Source	Significance level α				
	0.5%	**1%**	**2.5%**	**5%**	**10%**
REF1	1.73	1.63	N/A	1.35	N/A
REF2	1.731	1.628	1.480	1.358	N/A
MCF	1.731	1.628	1.480	1.358	1.224

Test: Cramér-von Mises (CM) test
REF1: Anderson and Darling (1952, table 1)
REF2: Csörgő and Faraway (1996, table 1)

Table A.13: Right tail $(1-\alpha)$ quantiles of the distribution of the CM test statistic T_{CM} (see equation (2.90))

Source	Sample size n	Significance level α			
		1%	**2.5%**	**5%**	**10%**
REF1	∞	0.7435	N/A	0.4614	0.3473
REF2	20	0.7290	0.5733	0.4578	0.3462
	50	0.7373	0.5775	0.4599	0.3468
	200	0.7415	0.5797	0.4609	0.3472
	1000	0.7426	0.5803	0.4612	0.3472
	∞	0.7435	0.5806	0.4614	0.3473

[1] Available free of charge at www.mathworks.com/matlabcentral/fileexchange/4369

Appendix B

Derivations of Equations

This appendix provides the derivations of some equations which have not been included in the main text for the sake of brevity. They may provide the reader with a better understanding of the underlying mathematical concepts and relations.

B.1 Equation (2.78): ADF regression model

In this section, the possibility of representing a general $\text{ARMA}(p,q)$ process by the regression model of the augmented Dickey-Fuller (ADF) test is mathematically illustrated. Given that an $\text{ARMA}(p,q)$ process can be well approximated by a long autoregressive process of order m ($\text{AR}(m)$; Graupe et al., 1975; Broersen, 2006, p. 142), for example, when using Durbin's methods to estimate model parameters (Durbin, 1959, 1960), it is essential to prove that a long $\text{AR}(m)$ process, given by

$$X_t = -\sum_{i=1}^{m} a_i X_{t-i} + Z_t, \quad t, m \in \mathbb{N}, \tag{B.1}$$

can be expressed by the regression model of the ADF test, i.e.,

$$X_t = \phi X_{t-1} + \sum_{j=1}^{m-1} \vartheta_j \Delta X_{t-j} + Z_t, \tag{B.2}$$

where $\{Z_t\}$ denotes a white noise (WN) process, and the terms c and δ characterising the deterministic trend are neglected (see equation (2.78)). The symbol Δ represents the lag-1 (or first-order) difference operator and is defined as $\Delta X_t = X_t - X_{t-1}$ (see equation (2.25)).

Proof of the representability of equation (B.1) using equation (B.2)

For $m = 1$, the trivial case occurs, where ϕ is equal to $-a_1$, and the second summand on the right hand side of equation (B.2) disappears. This indicates that the underlying data-generating process can be sufficiently described by an AR(1) process. In this case, equation (B.2) is known as the regression model of the standard Dickey-Fuller test (Dickey and Fuller, 1979).

For $m = 2$, adding the null term

$$N_2 = -a_2 X_{t-1} + a_2 X_{t-1} \tag{B.3}$$

to the AR(2) process

$$X_t = -a_1 X_{t-1} - a_2 X_{t-2} + Z_t, \tag{B.4}$$

it follows that

$$X_t = -(a_1 + a_2)X_{t-1} + a_2(X_{t-1} - X_{t-2}) + Z_t = \phi X_{t-1} + \vartheta_1 \Delta X_{t-1} + Z_t, \tag{B.5}$$

where $\phi = -(a_1 + a_2)$ and $\vartheta_1 = a_2$. Obviously, an AR(2) process can be expressed by the regression model of the ADF test.

For $m = 3$, adding the null terms N_2 (see equation (B.3)) and N_3 given by

$$N_3 = (-a_3 X_{t-1} + a_3 X_{t-1}) + (-a_3 X_{t-2} + a_3 X_{t-2}) \tag{B.6}$$

to the AR(3) process

$$X_t = -a_1 X_{t-1} - a_2 X_{t-2} - a_3 X_{t-3} + Z_t, \tag{B.7}$$

one obtains

$$\begin{aligned} X_t &= -(a_1 + a_2 + a_3)X_{t-1} + (a_2 + a_3)(X_{t-1} - X_{t-2}) + a_3(X_{t-2} - X_{t-3}) + Z_t \\ &= \phi X_{t-1} + \vartheta_1 \Delta X_{t-1} + \vartheta_2 \Delta X_{t-2} + Z_t, \end{aligned} \tag{B.8}$$

where $\phi = -(a_1 + a_2 + a_3)$, $\vartheta_1 = (a_2 + a_3)$, and $\vartheta_2 = a_3$. Accordingly, the proposition to be proved also holds for $m = 3$. Analogously, for an arbitrary integer AR order $m > 3$, the corresponding null term N_m can be written as

$$N_m = \sum_{j=1}^{m-1} (-a_m X_{t-j} + a_m X_{t-j}). \tag{B.9}$$

Adding all null terms $N_2, \ldots, N_m$ to the AR(m) process

$$X_t = -a_1 X_{t-1} - a_2 X_{t-2} - \cdots - a_m X_{t-m} + Z_t \tag{B.10}$$

results in

$$X_t = -\sum_{i=1}^{m} a_i X_{t-1} + \sum_{i=2}^{m} a_i \Delta X_{t-1} + \cdots + a_m \Delta X_{t-(m-1)} + Z_t, \tag{B.11}$$

which can be reformulated as

$$X_t = \phi X_{t-1} + \sum_{j=1}^{m-1} \vartheta_j \Delta X_{t-j} + Z_t, \tag{B.12}$$

where $\phi = -\sum_{i=1}^{m} a_i$ and $\vartheta_j = \sum_{i=j+1}^{m} a_i$. Comparing equations (B.10) and (B.12) with each other, the proposition that a long AR(m) process can be represented by the ADF regression model is also true for an arbitrary integer $m > 3$. Considering the approximation of an ARMA(p, q) process by a long AR(m) process, the representability of ARMA structure by the regression model of the ADF test has been proved for all natural numbers m; q.e.d.

B.2 Equation (2.81): MA unit root in the KPSS test

This section outlines the basic concept behind the stationarity tests, making use of moving averages (MA) unit roots. Furthermore, the principle of the Kwiatkowski-Phillips-Schmidt-Shin (KPSS) test and its relation to the standard Dickey-Fuller (DF) test is shown. The basic idea behind stationarity tests using MA unit roots can be explained by regarding a time series $\{Y_t\}$ that can be decomposed into a deterministic trend and an AR(1) process as

$$Y_t = c + \delta t + X_t, \quad X_t = -a_1 X_{t-1} + Z_t, \quad Z_t \sim \text{WN}(0, \sigma_Z^2). \tag{B.13}$$

Applying the lag-1 difference operator Δ to $\{Y_t\}$, it follows that

$$\Delta Y_t = Y_t - Y_{t-1} = \delta + \Delta X_t = \delta - a_1 \Delta X_{t-1} + Z_t - Z_{t-1}. \tag{B.14}$$

In fact, equation (B.14) represents an ARMA$(1,1)$ process with respect to $\{\Delta X_t\}$, i.e.,

$$\Delta X_t = -a_1 \Delta X_{t-1} + Z_t + b_1 Z_{t-1}, \tag{B.15}$$

where $b_1 = -1$. However, this ARMA$(1,1)$ process is non-invertible, since the corresponding MA characteristic equation $1 + b_1 r = 0$ has a unit root for $b_1 = -1$ (see equation (2.47)). In general, if $\{X_t\}$ is a causal and invertible ARMA(p, q) process satisfying

$$A_p(r)X_t = B_q(r)Z_t, \quad Z_t \sim \mathrm{WN}(0, \sigma_Z^2), \tag{B.16}$$

the serially differenced series $\{\Delta X_t\}$ is a non-invertible ARMA$(p, q+1)$ process with a MA polynomial of $B_q(r)(1-r)$. Therefore, testing for a MA unit root is equivalent to verifying whether the time series is overdifferenced (Brockwell and Davis, 2002, p. 196). An AR unit root in the original data suggests that the observations should be differenced before fitting an ARMA model, while a MA unit root in the lag-1 differenced data indicates that the data were overdifferenced, and they can be directly modelled by means of ARMA processes.

The KPSS test subdivides a time series $\{Y_t\}$ into a deterministic trend $c + dt$, a pure random walk $\{U_t\}$, and a stationary error $\{X_t\}$ as

$$Y_t = c + dt + U_t + X_t, \quad U_t = U_{t-1} + Z_t, \quad Z_t \sim \mathrm{WN}(0, \sigma_Z^2). \tag{B.17}$$

Applying the lag-1 difference operator Δ to $\{Y_t\}$, one obtains

$$\Delta Y_t = d + Z_t + \Delta X_t. \tag{B.18}$$

Considering $W_t = Z_t + \Delta X_t$ as the error term for ΔY_t and assuming that $\{X_t\}$ and $\{Z_t\}$ are serially and mutually uncorrelated, $\{W_t\}$ has a non-zero lag-1 autocorrelation, with all other autocorrelations being equal to zero. Therefore, $\{W_t\}$ can be expressed as a MA(1) process, i.e., $W_t = M_t + b_1 M_{t-1}$, where $\{M_t\}$ denotes a white noise process with $M_t \sim \mathrm{WN}(0, \sigma_M^2)$. Accordingly, equation (B.18) can be rewritten as

$$Y_t + a_1 Y_{t-1} = d + M_t + b_1 M_{t-1}, \tag{B.19}$$

where $a_1 = -1$. Equation (B.19) illustrates an interesting relation between the KPSS test and the standard DF test (Dickey and Fuller, 1979). The DF test verifies AR unit roots assuming the nuisance parameter $b_1 = 0$, while the KPSS test checks for MA unit roots assuming the nuisance parameter $a_1 = 0$ (Kwiatkowski et al., 1992).

B.3 Equation (2.89): Kolmogorov-Smirnov test statistic

In this section, the derivation of the test statistic of the Kolmogorov-Smirnov (KV) test for uncorrelatedness is briefly described. For a more detailed discussion of this topic with rigorous mathematical proofs, the reader is referred to Teusch (2006, p. 101). Background information about the spectral representation of a stationary time series can be found in Brockwell and Davis (2002, chap. 4) and Broersen (2006).

A stationary time series $\{X_t\}$ is a white noise (WN) process if its normalised spectral density is equal to a constant, i.e., $f_N(\lambda) = \frac{1}{2\pi}$ for all λ on the interval $[-\pi, \pi]$ (Brockwell and Davis, 2002, p. 118). According to the fact that the spectral density function of a stationary process is an even function (Brockwell and Davis, 2002, p. 113), the spectral distribution function of $\{X_t\}$

can be expressed by the integrated spectrum over the positive frequency range as

$$F_N^+(\omega) := 2 \int_0^\omega f_N(\lambda) d\lambda, \quad \omega \in [0, \pi]. \tag{B.20}$$

Under the null hypothesis of uncorrelated random variables X_t, equation (B.20) becomes

$$F_N^+(\omega) = 2 \int_0^\omega f_N(\lambda) d\lambda = 2 \int_0^\omega \frac{1}{2\pi} d\lambda = \frac{\omega}{\pi}, \quad \omega \in [0, \pi]. \tag{B.21}$$

For a zero-mean stationary time series $\{X_t\}$ with autocovariance function (ACVF) $\gamma(\cdot)$ satisfying $\sum_{h=-\infty}^{\infty} |\gamma(h)| < \infty$, the normalised spectral density function of $\{X_t\}$ is defined as

$$f_N(\lambda) = \frac{1}{2\pi \cdot \gamma(0)} \sum_{h=-\infty}^{\infty} \gamma(h) e^{-ih\lambda}, \quad -\infty < \lambda < \infty, \tag{B.22}$$

where $e^{i\lambda} = \cos \lambda + i \sin \lambda$ is Euler's formula, and $i = \sqrt{-1}$ (Brockwell and Davis, 2002, p. 112; Broersen, 2006, p. 35). Substituting the sample ACVF $\hat{\gamma}(h)$ given by equation (2.35) into equation (B.22) for the true ACVF $\gamma(h)$, a reasonable estimate of $f_N(\lambda)$ is obtained as

$$
\begin{aligned}
\hat{f}_N(\lambda) &= \frac{1}{2\pi} \sum_{h=-(n-1)}^{n-1} \frac{\hat{\gamma}(h)}{\hat{\gamma}(0)} e^{-ih\lambda} = \frac{1}{2\pi} \sum_{h=-(n-1)}^{n-1} \hat{\rho}(h) e^{-ih\lambda} \\
&= \frac{1}{2\pi} \sum_{h=-(n-1)}^{n-1} \hat{\rho}(h) \left[\cos(h\lambda) - i \sin(h\lambda) \right],
\end{aligned}
\tag{B.23}
$$

where $\hat{\rho}(h)$ is the corresponding sample ACF at lag h. Considering that $\sin(\cdot)$ is an odd function, and $\cos(\cdot)$ and $\hat{\rho}(\cdot)$ are even functions, equation (B.23) can be written as

$$\hat{f}_N(\lambda) = \frac{1}{2\pi} \left[\hat{\rho}(0) + 2 \sum_{h=1}^{n-1} \hat{\rho}(h) \cos(\lambda h) \right] = \frac{1}{2\pi} + \frac{1}{\pi} \sum_{h=1}^{n-1} \hat{\rho}(h) \cos(\lambda h). \tag{B.24}$$

Consequently, an estimate of $F_N^+(\omega)$ of a stationary time series $\{X_t\}$ can be obtained by integrating equation (B.24), i.e.,

$$\hat{F}_N^+(\omega) = 2 \int_0^\omega \hat{f}_N(\lambda) d\lambda = \frac{\omega}{\pi} + \frac{2}{\pi} \sum_{h=1}^{n-1} \hat{\rho}(h) \frac{\sin(\omega h)}{h}, \quad \omega \in [0, \pi]. \tag{B.25}$$

For large sample sizes, under the null hypothesis of uncorrelatedness, $\mathrm{E}\left[\hat{\rho}(h)\right] = \rho(h) = 0$ holds for $h \geq 1$. Accordingly, the expectation of $\hat{F}_N^+(\omega)$ is

$$\mathrm{E}\left[\hat{F}_N^+(\omega)\right] = \frac{\omega}{\pi} + \frac{2}{\pi} \sum_{h=1}^{n-1} \mathrm{E}\left[\hat{\rho}(h)\right] \frac{\sin(\omega h)}{h} = \frac{\omega}{\pi}, \quad \omega \in [0, \pi]. \tag{B.26}$$

Substituting $\omega = \pi z$ into equation (B.26), it follows that

$$\mathrm{E}\left[\hat{F}_N^+(\pi z)\right] = z, \quad z \in [0, 1]. \tag{B.27}$$

Therefore, the difference between $\hat{F}_N^+(\pi z)$ and z can be used as an indicator to assess the degree of deviation from the null hypothesis of uncorrelatedness. Based on the mathematical proofs

presented in Teusch (2006, p. 102–103), the maximum of the scaled difference

$$
\begin{aligned}
B_N(z) : \quad &= \quad \sqrt{\frac{n}{2}} \left[\hat{F}_N^+(\pi z) - z \right] = \sqrt{\frac{n}{2}} \left[z + \frac{2}{\pi} \sum_{h=1}^{n-1} \hat{\rho}(h) \frac{\sin(\pi z \cdot h)}{h} - z \right] \\
&= \quad \frac{\sqrt{2n}}{\pi} \sum_{h=1}^{n-1} \hat{\rho}(h) \frac{\sin(\pi z \cdot h)}{h}
\end{aligned}
\tag{B.28}
$$

follows asymptotically the distribution of the maximum of the Brownian bridge (Glasserman, 2004, p. 83), i.e.,

$$
Z_N := \max_{z \in [0,1]} |B_N(z)| \xrightarrow{\mathcal{D}} Z_0 := \max_{z \in [0,1]} |B_0(z)|,
\tag{B.29}
$$

where $B_0(z)$ denotes the Brownian bridge, and $\mathcal{D}$ symbolises convergence in distribution (Casella and Berger, 2002, p. 235). The random variable Z_0 follows the Kolmogorov distribution (Kolmogorov, 1933, 1941; Feller, 1948; Marsaglia et al., 2003; Teusch, 2006, p. 103–104). Accordingly, the test statistic of the KV test for uncorrelatedness is given by

$$
T_{KV} := Z_N = \max_{z \in [0,1]} |B_N(z)| = \max_{z \in [0,1]} \left| \frac{\sqrt{2n}}{\pi} \sum_{h=1}^{n-1} \hat{\rho}(h) \frac{\sin(\pi z \cdot h)}{h} \right|.
\tag{B.30}
$$

B.4 Equation (7.7): Lagrange polynomial

In numerical analysis, Lagrange polynomials are often used for the interpolation of a given set of discrete points by a polynomial, which runs exactly through the data points. In the case of the Vondrák filter, given a set of four adjacent points (x_i, y_i'), (x_{i+1}, y_{i+1}'), (x_{i+2}, y_{i+2}'), and (x_{i+3}, y_{i+3}'), the third-order interpolation polynomial in the Lagrange form $L_i(x)$ is a linear combination of the Lagrange basis polynomials $l_j(x)$, i.e.,

$$
L_i(x) := \sum_{j=i}^{i+3} l_j(x) y_j', \quad l_j(x) := \prod_{m=i, m \neq j}^{i+3} \frac{x - x_m}{x_j - x_m}.
\tag{B.31}
$$

Rewriting equation (B.31) in an explicit form, it follows that

$$
L_i(x) = l_i(x) y_i' + l_{i+1}(x) y_{i+1}' + l_{i+2}(x) y_{i+2}' + l_{i+3}(x) y_{i+3}',
\tag{B.32}
$$

where

$$
\begin{aligned}
l_i(x) &= \frac{x - x_{i+1}}{x_i - x_{i+1}} \cdot \frac{x - x_{i+2}}{x_i - x_{i+2}} \cdot \frac{x - x_{i+3}}{x_i - x_{i+3}}, & \tag{B.33} \\
l_{i+1}(x) &= \frac{x - x_i}{x_{i+1} - x_i} \cdot \frac{x - x_{i+2}}{x_{i+1} - x_{i+2}} \cdot \frac{x - x_{i+3}}{x_{i+1} - x_{i+3}}, & \tag{B.34} \\
l_{i+2}(x) &= \frac{x - x_i}{x_{i+2} - x_i} \cdot \frac{x - x_{i+1}}{x_{i+2} - x_{i+1}} \cdot \frac{x - x_{i+3}}{x_{i+2} - x_{i+3}}, & \tag{B.35} \\
l_{i+3}(x) &= \frac{x - x_i}{x_{i+3} - x_i} \cdot \frac{x - x_{i+1}}{x_{i+3} - x_{i+1}} \cdot \frac{x - x_{i+2}}{x_{i+3} - x_{i+2}}. & \tag{B.36}
\end{aligned}
$$

If $x = x_i$, all basis polynomials including $(x - x_i)$ in the numerator are equal to zero, except for $l_i(x = x_i) = 1$. As a result, it follows that $L_i(x = x_i) = l_i(x = x_i) y_i' = y_i'$. Analogously, it can be easily derived that $L_i(x = x_{i+1}) = y_{i+1}'$, $L_i(x = x_{i+2}) = y_{i+2}'$, and $L_i(x = x_{i+3}) = y_{i+3}'$, indicating that the Lagrange polynomial $L_i(x)$ actually runs through the four adjacent data

points. In accordance with equation (B.31), the third derivative of $L_i(x)$ with respect to x can be written as

$$L_i'''(x) = \sum_{j=i}^{i+3} l_j'''(x)y_j', \quad l_j'''(x) = \prod_{m=i, m \neq j}^{i+3} \frac{6}{x_j - x_m}, \tag{B.37}$$

where $L_i'''(x)$ is in fact independent from x. Therefore, the square of the third-difference of the filtered values $(\Delta^3 y_i')^2$ given by equation (7.7) can be computed by

$$\begin{aligned} (\Delta^3 y_i')^2 &= \int_{x_{i+1}}^{x_{i+2}} \left[L_i'''(x) \right]^2 dx = \left[L_i'''(x) \right]^2 (x_{i+2} - x_{i+1}) \tag{B.38} \\ &= \left[L_i'''(x)\sqrt{x_{i+2} - x_{i+1}} \right]^2 = (a_i y_i' + b_i y_{i+1}' + c_i y_{i+2}' + d_i y_{i+3}')^2, \end{aligned}$$

where

$$a_i = \frac{6\sqrt{x_{i+2} - x_{i+1}}}{(x_i - x_{i+1})(x_i - x_{i+2})(x_i - x_{i+3})}, \tag{B.39}$$

$$b_i = \frac{6\sqrt{x_{i+2} - x_{i+1}}}{(x_{i+1} - x_i)(x_{i+1} - x_{i+2})(x_{i+1} - x_{i+3})}, \tag{B.40}$$

$$c_i = \frac{6\sqrt{x_{i+2} - x_{i+1}}}{(x_{i+2} - x_i)(x_{i+2} - x_{i+1})(x_{i+2} - x_{i+3})}, \tag{B.41}$$

$$d_i = \frac{6\sqrt{x_{i+2} - x_{i+1}}}{(x_{i+3} - x_i)(x_{i+3} - x_{i+1})(x_{i+3} - x_{i+2})}. \tag{B.42}$$

The explicit presentations of $L_i(x)$ and $(\Delta^3 y_i')^2$, given by equations (B.32-36) and (B.38-42), respectively, can also be found in Vondrák (1969), but without detailed derivations. For equidistant arguments (i.e., $x_{i+1} - x_i = k, \forall i$), the coefficients a_i, b_i, c_i, d_i and $(\Delta^3 y_i')^2$ become

$$a_i = -k^{-\frac{5}{2}}, \quad b_i = 3k^{-\frac{5}{2}}, \quad c_i = -3k^{-\frac{5}{2}}, \quad d_i = k^{-\frac{5}{2}}, \tag{B.43}$$

$$(\Delta^3 y_i')^2 = k^{-5}(-y_i' + 3y_{i+1}' - 3y_{i+2}' + y_{i+3}')^2. \tag{B.44}$$

Apart from the multiplier k^{-5}, equation (B.44) represents the square of the third-difference of the filtered values originally defined by Whittaker and Robinson (1924, p. 304).

B.5 Equation (7.9): Vondrák coefficient matrix

Using equations (6) and (7) in Vondrák (1969), the elements of the Vondrák coefficient matrix $\boldsymbol{A}$ can be determined row by row. For the row index i between 4 and $n-3$, there exist seven non-zero elements in each row of $\boldsymbol{A}$. However, for the first and last three linear equations, some of the seven coefficients are equal to zero. Taking $n = 8$ as an example, the linear equation system given by equation (7.9) can be expressed as

$$\underbrace{\begin{pmatrix} X & X & X & X & 0 & 0 & 0 & 0 \\ X & X & X & X & X & 0 & 0 & 0 \\ X & X & X & X & X & X & 0 & 0 \\ X & X & X & X & X & X & X & 0 \\ 0 & X & X & X & X & X & X & X \\ 0 & 0 & X & X & X & X & X & X \\ 0 & 0 & 0 & X & X & X & X & X \\ 0 & 0 & 0 & 0 & X & X & X & X \end{pmatrix}}_{\boldsymbol{A}:8\times 8} \cdot \underbrace{\begin{pmatrix} y_1' \\ y_2' \\ y_3' \\ y_4' \\ y_5' \\ y_6' \\ y_7' \\ y_8' \end{pmatrix}}_{\boldsymbol{y}':8\times 1} = \epsilon \underbrace{\begin{pmatrix} p_1 \cdot y_1 \\ p_2 \cdot y_2 \\ p_3 \cdot y_3 \\ p_4 \cdot y_4 \\ p_5 \cdot y_5 \\ p_6 \cdot y_6 \\ p_7 \cdot y_7 \\ p_8 \cdot y_8 \end{pmatrix}}_{\boldsymbol{b}:8\times 1}, \tag{B.45}$$

where the symbol "X" in $\boldsymbol{A}$ denotes the non-zero coefficients, ϵ is the smoothing factor regulating the degree of filtering, and p_i are the weights for observations y_i. The non-zero elements in the coefficient matrix $\boldsymbol{A}$ are explicitly provided in table B.1, where the parameter values for a_i, b_i, c_i, d_i can be computed using equations (B.39-42).

Table B.1: Coefficients for the filtered values y_i' as elements in the matrix $\boldsymbol{A}$ (Vondrák, 1969)

Coeffient for	$i = 1$	$i = 2$	$i = 3$
y_1'	$\epsilon \cdot p_1 + a_1^2$	$a_1 b_1$	$a_1 c_1$
y_2'	$a_1 b_1$	$\epsilon \cdot p_2 + a_2^2 + b_1^2$	$a_2 b_2 + b_1 c_1$
y_3'	$a_1 c_1$	$a_2 b_2 + b_1 c_1$	$\epsilon \cdot p_3 + a_3^2 + b_2^2 + c_1^2$
y_4'	$a_1 d_1$	$a_2 c_2 + b_1 d_1$	$a_3 b_3 + b_2 c_2 + c_1 d_1$
y_5'	0	$a_2 d_2$	$a_3 c_3 + b_2 d_2$
y_6'	0	0	$a_3 d_3$
y_7'	0	0	0

Coeffient for	$4 \leq i \leq n - 3$		
y_{i-3}'	$a_{i-3} d_{i-3}$		
y_{i-2}'	$a_{i-2} c_{i-2} + b_{i-3} d_{i-3}$		
y_{i-1}'	$a_{i-1} b_{i-1} + b_{i-2} c_{i-2} + c_{i-3} d_{i-3}$		
y_i'	$\epsilon \cdot p_i + a_i^2 + b_{i-1}^2 + c_{i-2}^2 + d_{i-3}^2$		
y_{i+1}'	$a_i b_i + b_{i-1} c_{i-1} + c_{i-2} d_{i-2}$		
y_{i+2}'	$a_i c_i + b_{i-1} d_{i-1}$		
y_{i+3}'	$a_i d_i$		

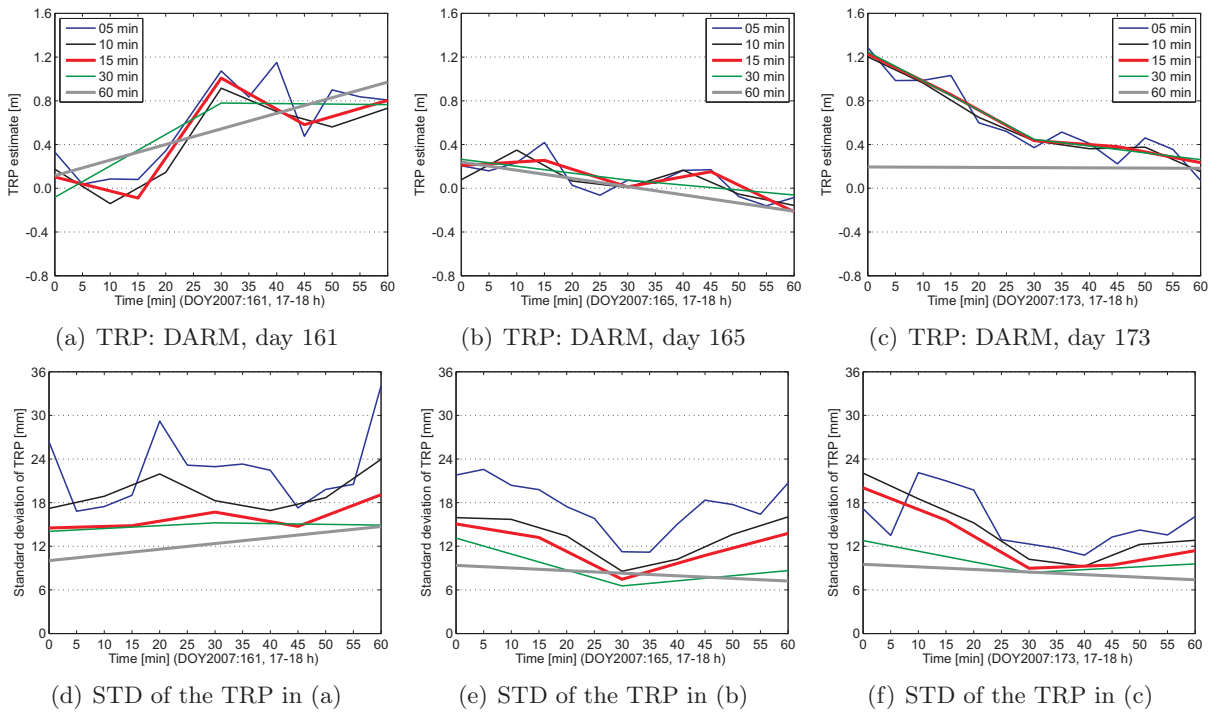| Coeffient for	$i = n - 2$	$i = n - 1$	$i = n$
y_{n-6}'	0	0	0
y_{n-5}'	$a_{n-5} d_{n-5}$	0	0
y_{n-4}'	$a_{n-4} c_{n-4} + b_{n-5} d_{n-5}$	$a_{n-4} d_{n-4}$	0
y_{n-3}'	$a_{n-3} b_{n-3} + b_{n-4} c_{n-4} + c_{n-5} d_{n-5}$	$a_{n-3} c_{n-3} + b_{n-4} d_{n-4}$	$a_{n-3} d_{n-3}$
y_{n-2}'	$\epsilon \cdot p_{n-2} + b_{n-3}^2 + c_{n-4}^2 + d_{n-5}^2$	$b_{n-3} c_{n-3} + c_{n-4} d_{n-4}$	$b_{n-3} d_{n-3}$
y_{n-1}'	$b_{n-3} c_{n-3} + c_{n-4} d_{n-4}$	$\epsilon \cdot p_{n-1} + c_{n-3}^2 + d_{n-4}^2$	$c_{n-3} d_{n-3}$
y_n'	$b_{n-3} d_{n-3}$	$c_{n-3} d_{n-3}$	$\epsilon \cdot p_n + d_{n-3}^2$

Appendix C

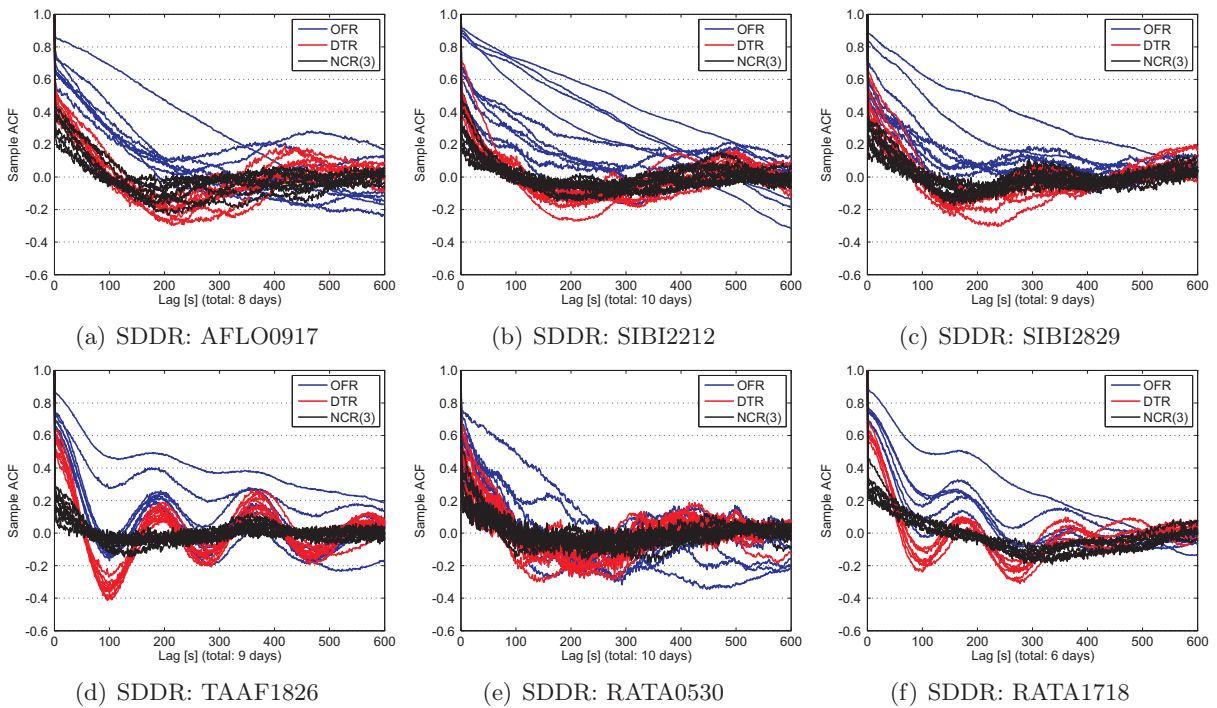# Additional Graphs
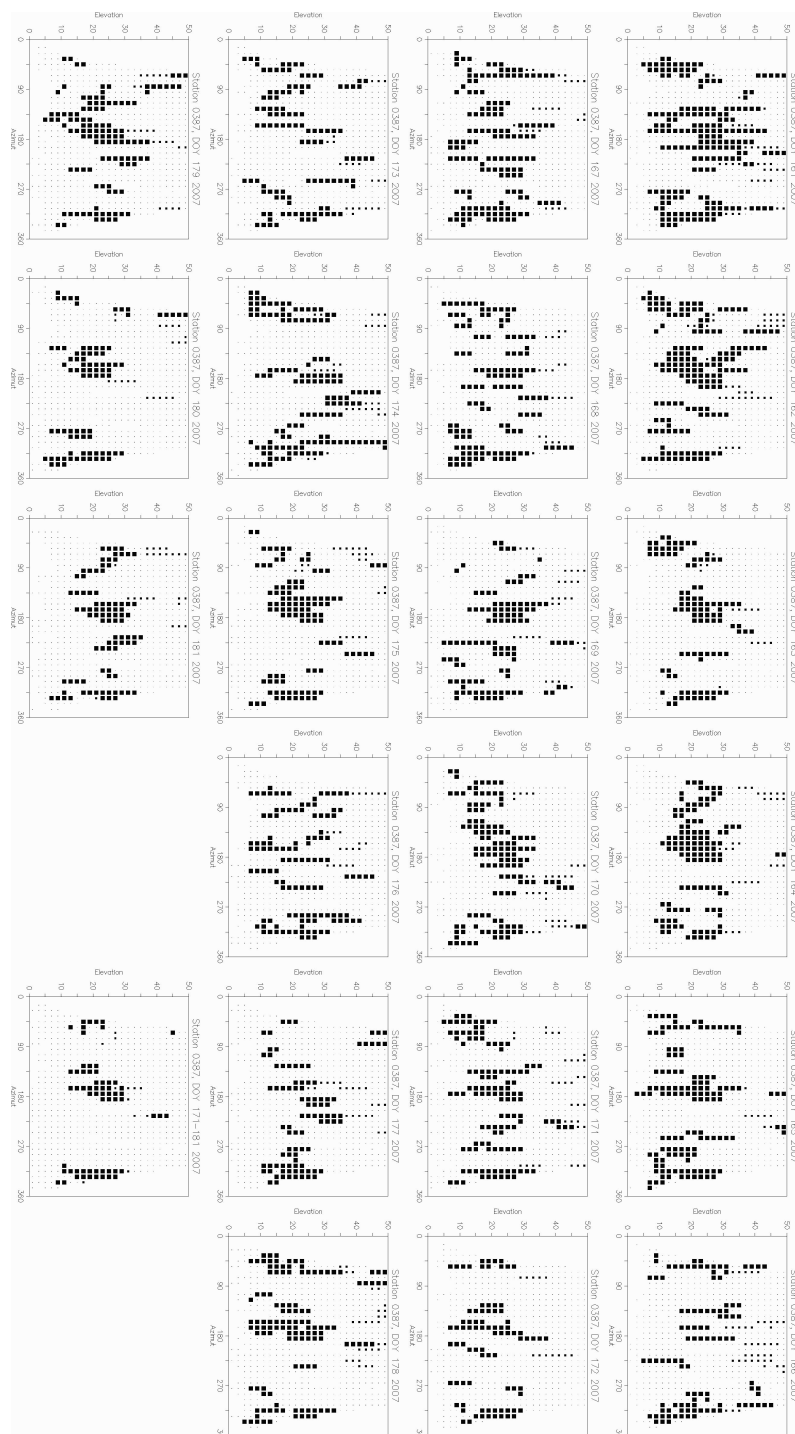
Figure C.1: Examples of daily and mean multipath plots generated using the software WaSoft/Multi-path (SA*POS*®site: HEID, strong multipath, DOY2007:161-181, sampling interval: 60 s; multipath plots provided by A. Knöpfler) [referenced in section 4.2.3]

(a) TRP: DARM, day 161   (b) TRP: DARM, day 165   (c) TRP: DARM, day 173

(d) STD of the TRP in (a)   (e) STD of the TRP in (b)   (f) STD of the TRP in (c)

Figure C.2: Examples of TRP estimation using different time spans (baseline: HEDA, 54.1 km, strong multipath, elevation cut-off angle: 3°, observation weighting model: CSC2(BS), sampling interval: 1 s, processing period: 17-18 h) [referenced in section 6.2.3]

(a) SDDR: AFLO0917   (b) SDDR: SIBI2212   (c) SDDR: SIBI2829

(d) SDDR: TAAF1826   (e) SDDR: RATA0530   (f) SDDR: RATA1718

Figure C.3: Comparison of the sample ACF of OFR (SDDR after repairing outliers), DTR (residual after Vondrák filtering), and NCR(3) (residual after 3-day sidereal stacking) (see table 4.3 for baseline characteristics) [referenced in section 8.1.5]

(a) SDDR: HEDA1718

(b) SDDR: HEDA1826
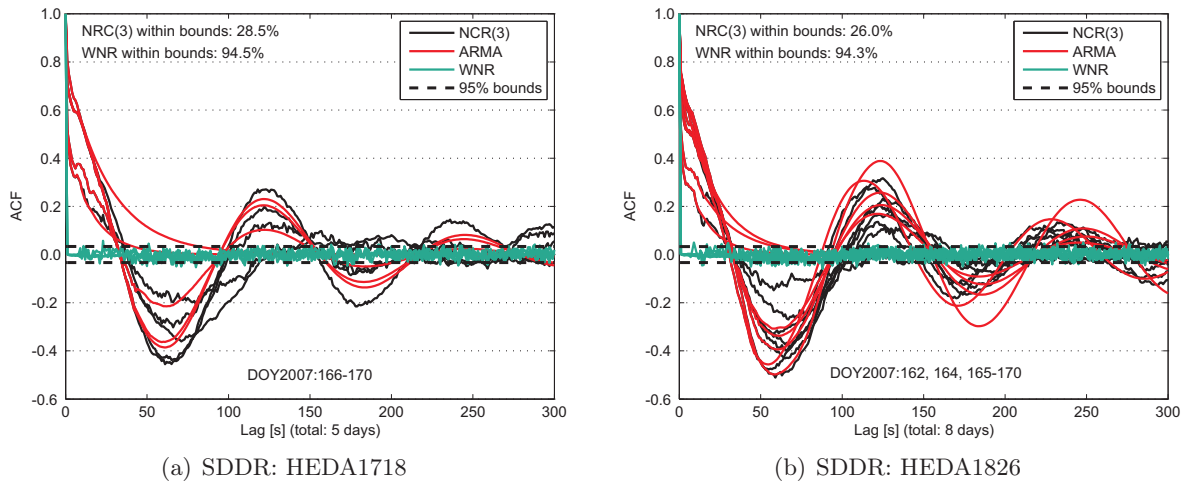
Figure C.4: Comparison of the noise's sample ACF and ARMA model ACF in the presence of strong systematic effects in NCR(3) (HEDA: 54.1 km, strong multipath, satellite pairs: PRN 17-18, 18-26) [referenced in section 8.1.6]

(a) Vondrák filtering ($k = 10$)

(b) Sidereal stacking

(c) Decomposed noise

(d) Sample ACF
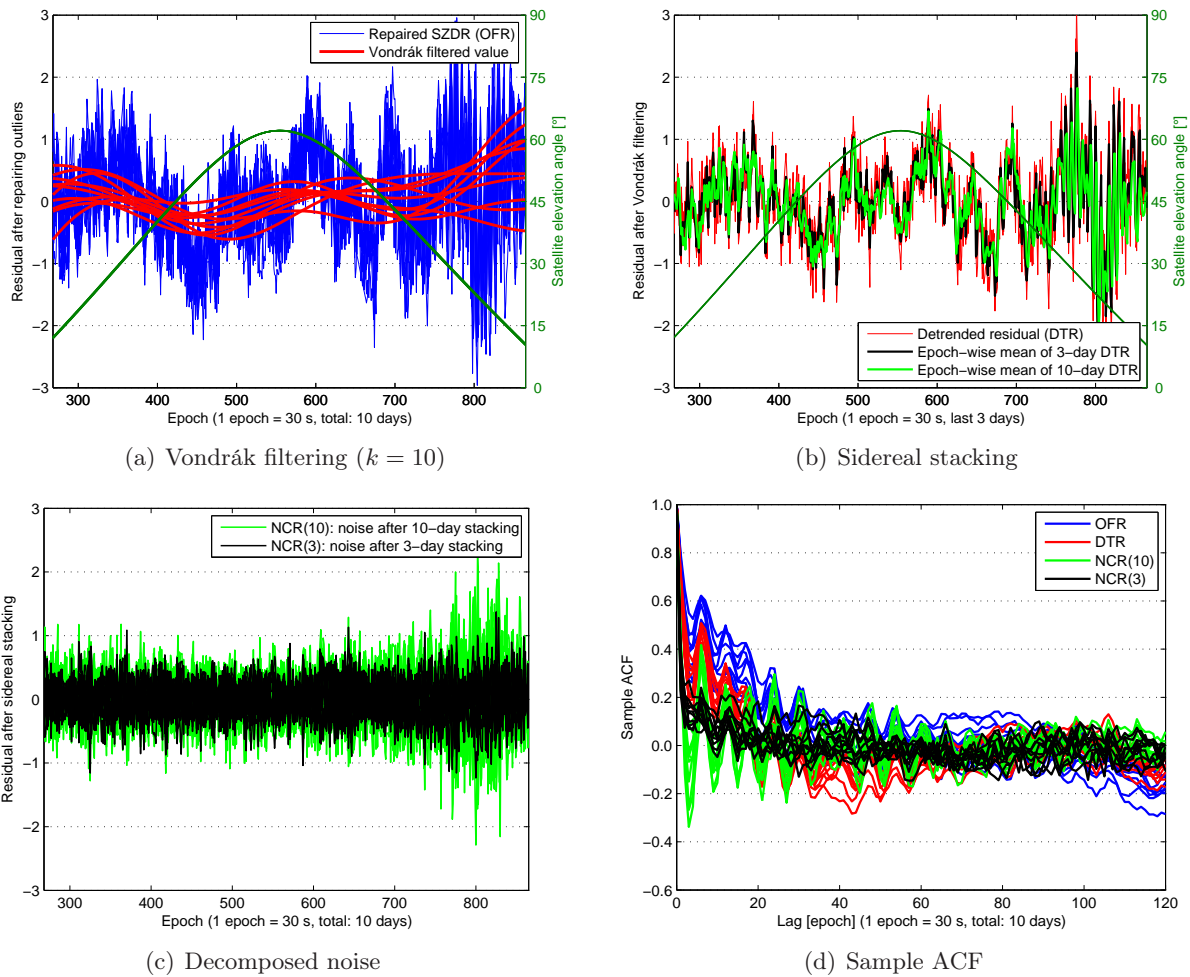
Figure C.5: Example illustrating the advantages of a shorter stacking time period (SA*POS*®site: TUEB, weak multipath, satellite: PRN 28, DOY2008:275-284) [referenced in section 8.2.4]

(a) Box plots of correlation length

(b) IQR of correlation length vs. mean WS
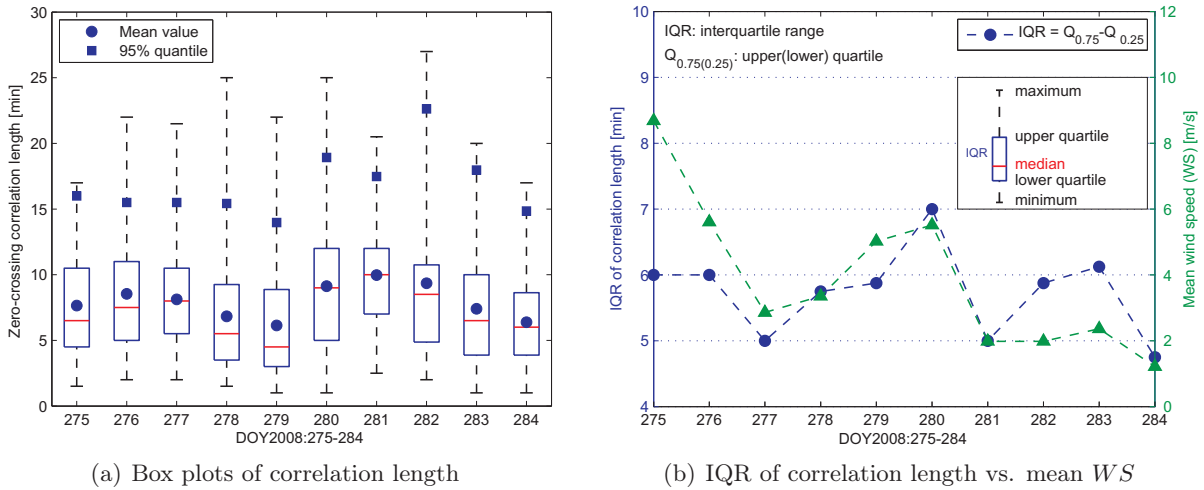
Figure C.6: Daily dispersion of the zero-crossing correlation length with respect to wind speed (WS) (SA*POS*®sites: TUEB, weak multipath, BING, strong multipath, all observed GPS satellites, DOY2008:275-284) [referenced in section 8.2.5]

(a) SZDR (OFR): TUEB11281

(b) Trend from Vondrák filtering ($k = 10$)

(c) Detrended residual (DTR)

(d) 3-day sidereal stacking

(e) Stochastic noise (NCR(3))

(f) ARMA$(2, 1)$ residual (WNR)
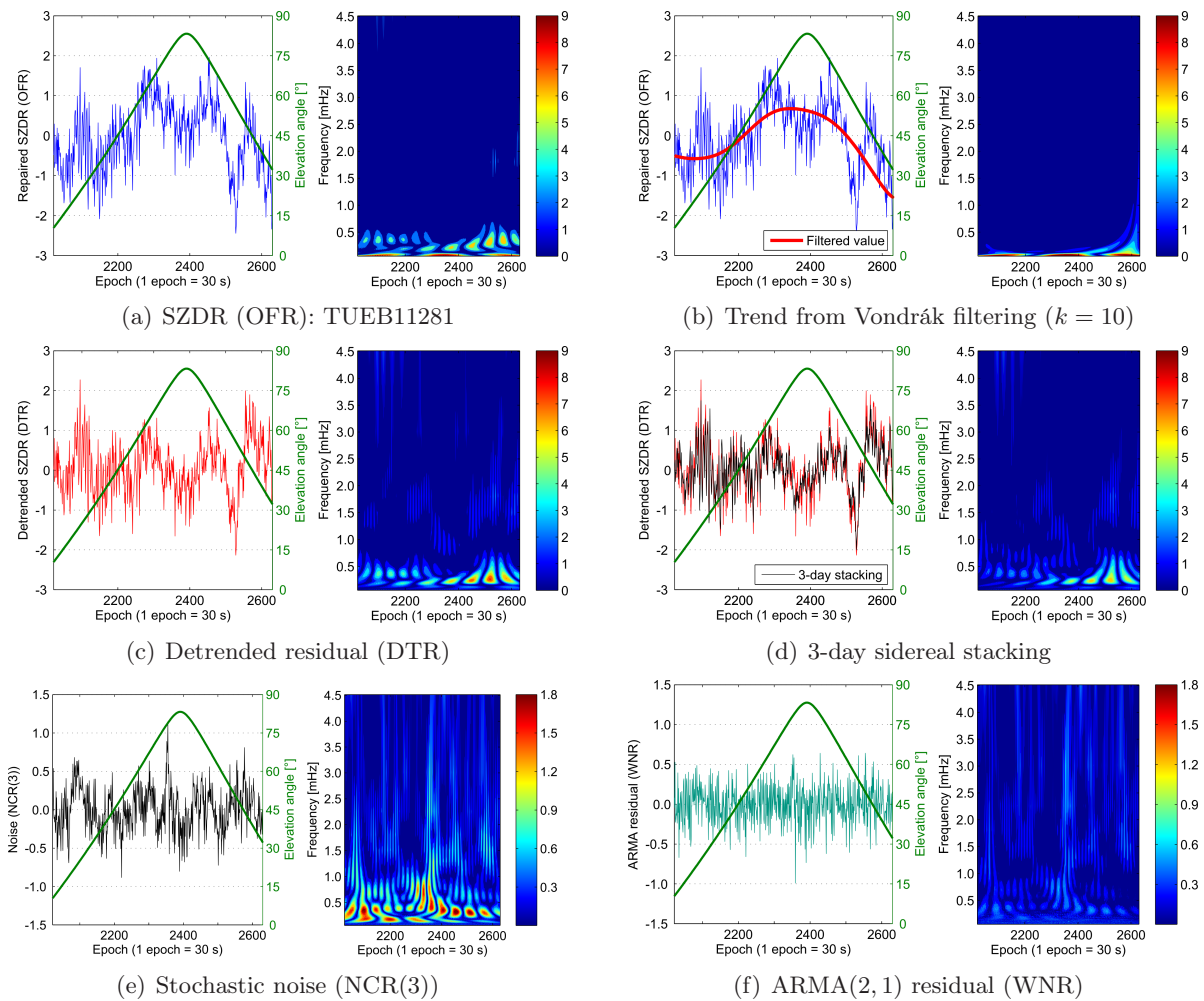
Figure C.7: Verification of the residual decomposition and ARMA modelling based on wavelet scalograms (SA*POS*®site: TUEB, weak multipath, satellite: PRN 11, DOY2008:281, mother wavelet: Morlet wavelet; see equation (2.94) and figure 2.7) [referenced in section 8.2.7]

Appendix D

Additional Tables

Table D.1: Results of ambiguity resolution using different observation weighting models in case study 1 (elevation cut-off angle: 10°) [referenced in section 6.1.2]

Weighting model	CSC2(BS)			EMPSNR2			Improvement	
	Number/Percent			Number/Percent			Percent	
HLTA	#AMB	WL	NL	#AMB	WL	NL	WL	NL
186	57	57/100.0	50/87.7	57	57/100.0	52/91.2	0.0	3.5
187	61	58/95.1	49/80.3	60	56/93.3	48/80.0	−1.8	−0.3
188	58	56/96.6	51/87.9	58	57/98.3	50/86.2	1.7	−1.7
189	56	55/98.2	47/83.9	54	53/98.1	48/88.9	−0.1	5.0
190	56	54/96.4	48/85.7	56	54/96.4	49/87.5	0.0	1.8
191	63	60/95.2	57/90.5	63	59/93.7	55/87.3	−1.5	−3.2
192	57	54/94.7	52/91.2	57	54/94.7	53/93.0	0.0	1.8
193	54	53/98.1	51/94.4	54	54/100.0	52/96.3	1.9	1.9
Total	462	447/96.8	405/87.7	459	444/96.7	407/88.7	−0.1	1.0
KAST	#AMB	WL	NL	#AMB	WL	NL	WL	NL
186	74	71/95.9	59/79.7	74	70/94.6	65/87.8	−1.3	**8.1**
187	78	76/97.4	64/82.1	78	74/94.9	65/83.3	−2.5	1.2
188	70	69/98.6	63/90.0	70	69/98.6	65/92.9	0.0	2.9
189	87	83/95.4	68/78.2	86	81/94.2	72/83.7	−1.2	5.5
190	79	75/94.9	63/79.7	76	68/89.5	63/82.9	−5.4	3.2
191	76	75/98.7	66/86.8	75	73/97.3	69/92.0	−1.4	5.2
192	73	70/95.9	64/87.7	73	71/97.3	64/87.7	1.4	0.0
193	75	73/97.3	64/85.3	75	74/98.7	66/88.0	1.4	2.7
Total	612	592/96.7	511/83.5	607	580/95.6	529/87.1	−1.1	3.6
SISC	#AMB	WL	NL	#AMB	WL	NL	WL	NL
186	64	60/93.8	58/90.6	64	61/95.3	59/92.2	1.5	1.6
187	71	69/97.2	61/85.9	71	69/97.2	64/90.1	0.0	4.2
188	69	63/91.3	59/85.5	69	64/92.8	60/87.0	1.5	1.5
189	64	60/93.8	57/89.1	64	61/95.3	58/90.6	1.5	1.5
190	59	54/91.5	50/84.7	58	54/93.1	51/87.9	1.6	3.2
191	62	60/96.8	57/91.9	62	60/96.8	57/91.9	0.0	0.0
192	59	55/93.2	54/91.5	59	55/93.2	53/89.8	0.0	−1.7
193	63	59/93.7	56/88.9	63	60/95.2	58/92.1	1.5	3.2
Total	511	480/93.9	452/88.5	510	484/94.9	460/90.2	1.0	1.7
OFHE	#AMB	WL	NL	#AMB	WL	NL	WL	NL
186	61	56/91.8	47/77.0	59	54/91.5	50/84.7	−0.3	7.7
187	64	58/90.6	48/75.0	64	58/90.6	49/76.6	0.0	1.6
188	61	53/86.9	45/73.8	59	54/91.5	47/79.7	4.6	5.9
189	64	60/93.8	51/79.7	63	58/92.1	50/79.4	−1.7	−0.3
190	61	56/91.8	46/75.4	61	57/93.4	50/82.0	1.6	6.6
191	65	61/93.8	52/80.0	65	62/95.4	55/84.6	1.6	4.6
192	62	60/96.8	51/82.3	61	59/96.7	56/91.8	−0.1	**9.5**
193	58	56/96.6	49/84.5	58	55/94.8	51/87.9	−1.8	3.4
Total	496	460/92.7	389/78.4	490	457/93.3	408/83.3	0.6	**4.9**

Table D.2: Results of ambiguity resolution using different observation weighting models in case study 2 (AFLO: 32.4 km, weak multipath, RATA: 203.7 km, weak multipath, elevation cut-off angle: 3°) [referenced in section 6.2.2]

Weighting model	CSC2(BS) Number/Percent			EMPSNR2 Number/Percent			Improvement Percent	
AFLO	#AMB	WL	NL	#AMB	WL	NL	WL	NL
161	20	18/90.0	13/65.0	20	18/90.0	14/70.0	0.0	5.0
162	28	25/89.3	19/67.9	28	25/89.3	20/71.4	0.0	3.5
163	19	17/89.5	14/73.7	19	17/89.5	15/78.9	0.0	5.2
164	16	16/100.0	15/93.8	16	16/100.0	15/93.8	0.0	0.0
165	15	15/100.0	13/86.7	15	15/100.0	14/93.3	0.0	6.6
166	16	15/93.8	13/81.2	16	15/93.8	13/81.2	0.0	0.0
167	15	14/93.3	12/80.0	15	15/100.0	12/80.0	**6.7**	0.0
168	18	18/100.0	14/77.8	18	18/100.0	15/83.3	0.0	5.5
169	22	22/100.0	18/81.8	22	22/100.0	17/77.3	0.0	−4.5
170	15	15/100.0	14/93.3	15	15/100.0	13/86.7	0.0	−6.6
171	**262**	253/96.6	214/81.7	**262**	255/97.3	215/82.1	0.7	0.4
172	**238**	237/99.6	150/63.0	**238**	237/99.6	194/81.5	0.0	**18.5**
173	94	91/96.8	75/79.8	94	91/96.8	77/81.9	0.0	2.1
174	54	53/98.1	42/77.8	54	53/98.1	45/83.3	0.0	5.5
175	71	71/100.0	60/84.5	71	71/100.0	62/87.3	0.0	2.8
176	18	17/94.4	12/66.7	18	17/94.4	13/72.2	0.0	5.5
177	16	16/100.0	13/81.2	16	16/100.0	14/87.5	0.0	6.3
178	14	14/100.0	12/85.7	14	14/100.0	13/92.9	0.0	7.2
179	18	18/100.0	13/72.2	18	18/100.0	13/72.2	0.0	0.0
180	19	19/100.0	16/84.2	19	19/100.0	17/89.5	0.0	5.3
181	19	19/100.0	18/94.7	19	19/100.0	17/89.5	0.0	−5.2
Total	1007	983/97.6	770/76.5	1007	986/97.9	828/82.2	0.3	**5.7**
RATA	#AMB	WL	NL	#AMB	WL	NL	WL	NL
161	37	30/81.1	15/40.5	37	30/81.1	19/51.4	0.0	10.9
162	45	39/86.7	23/51.1	45	42/93.3	31/68.9	6.6	17.8
163	33	26/78.8	12/36.4	33	29/87.9	17/51.5	9.1	15.1
164	38	30/78.9	13/34.2	38	34/89.5	20/52.6	10.6	**18.4**
165	35	27/77.1	18/51.4	35	30/85.7	23/65.7	8.6	14.3
166	26	21/80.8	17/65.4	26	22/84.6	18/69.2	3.8	3.8
167	25	21/84.0	14/56.0	25	23/92.0	17/68.0	8.0	12.0
168	28	23/82.1	18/64.3	28	23/82.1	18/64.3	0.0	0.0
169	27	23/85.2	11/40.7	27	24/88.9	13/48.1	3.7	7.4
170	35	25/71.4	19/54.3	35	30/85.7	22/62.9	14.3	8.6
171	31	23/74.2	16/51.6	31	26/83.9	17/54.8	9.7	3.2
172	34	29/85.3	20/58.8	34	29/85.3	21/61.8	0.0	3.0
173	31	25/80.6	14/45.2	31	26/83.9	14/45.2	3.3	0.0
174	34	24/70.6	18/52.9	34	29/85.3	20/58.8	**14.7**	5.9
175	39	35/89.7	24/61.5	39	36/92.3	26/66.7	2.6	5.2
176	36	32/88.9	22/61.1	36	33/91.7	25/69.4	2.8	8.3
177	35	31/88.6	21/60.0	35	32/91.4	24/68.6	2.8	8.6
178	38	35/92.1	22/57.9	38	35/92.1	26/68.4	0.0	10.5
179	42	37/88.1	25/59.5	42	37/88.1	28/66.7	0.0	7.2
180	41	31/75.6	26/63.4	41	33/80.5	28/68.3	4.9	4.9
181	45	41/91.1	29/64.4	45	41/91.1	33/73.3	0.0	8.9
Total	735	608/82.7	397/54.0	735	644/87.6	460/62.6	**4.9**	**8.6**

Table D.3: Results of ambiguity resolution using different observation weighting models in case study 2 (TAAF: 53.7 km, weak multipath, HEDA: 54.1 km, strong multipath, elevation cut-off angle: 3°) [referenced in section 6.2.2]

Weighting model	CSC2(BS) Number/Percent			EMPSNR2 Number/Percent			Improvement Percent	
TAAF	#AMB	WL	NL	#AMB	WL	NL	WL	NL
161	34	31/91.2	18/52.9	34	31/91.2	19/55.9	0.0	3.0
162	48	47/97.9	36/75.0	48	46/95.8	37/77.1	−2.1	2.1
163	39	37/94.9	18/46.2	39	37/94.9	22/56.4	0.0	10.2
164	35	34/97.1	23/65.7	35	34/97.1	27/77.1	0.0	11.4
165	34	32/94.1	22/64.7	34	32/94.1	26/76.5	0.0	11.8
166	30	27/90.0	19/63.3	30	27/90.0	19/63.3	0.0	0.0
167	23	22/95.7	14/60.9	23	22/95.7	17/73.9	0.0	13.0
168	27	26/96.3	21/77.8	27	26/96.3	23/85.2	0.0	7.4
169	32	31/96.9	20/62.5	32	31/96.9	23/71.9	0.0	9.4
170	32	30/93.8	20/62.5	32	29/90.6	24/75.0	−3.2	12.5
171	27	25/92.6	15/55.6	27	25/92.6	19/70.4	0.0	**14.8**
172	24	23/95.8	18/75.0	24	23/95.8	20/83.3	0.0	8.3
173	23	21/91.3	15/65.2	23	21/91.3	15/65.2	0.0	0.0
174	26	25/96.2	19/73.1	26	25/96.2	21/80.8	0.0	7.7
175	37	36/97.3	26/70.3	37	36/97.3	30/81.1	0.0	10.8
176	27	25/92.6	20/74.1	27	25/92.6	21/77.8	0.0	3.7
177	24	24/100.0	18/75.0	24	24/100.0	21/87.5	0.0	12.5
178	31	30/96.8	23/74.2	31	30/96.8	24/77.4	0.0	3.2
179	29	28/96.6	21/72.4	29	28/96.6	23/79.3	0.0	6.9
180	28	26/92.9	20/71.4	28	26/92.9	20/71.4	0.0	0.0
181	29	28/96.6	23/79.3	29	28/96.6	25/86.2	0.0	6.9
Total	639	608/95.1	429/67.1	639	606/94.8	476/74.5	−0.3	**7.4**
HEDA	#AMB	WL	NL	#AMB	WL	NL	WL	NL
161	41	37/90.2	19/46.3	41	38/92.7	21/51.2	2.5	4.9
162	40	38/95.0	22/55.0	40	38/95.0	28/70.0	0.0	15.0
163	38	34/89.5	26/68.4	38	35/92.1	28/73.7	2.6	5.3
164	33	30/90.9	24/72.7	33	30/90.9	25/75.8	0.0	3.1
165	37	34/91.9	25/67.6	37	35/94.6	29/78.4	2.7	10.8
166	28	25/89.3	19/67.9	28	24/85.7	20/71.4	−3.6	3.5
167	29	26/89.7	19/65.5	29	25/86.2	17/58.6	−3.5	−6.9
168	28	26/92.9	20/71.4	28	25/89.3	19/67.9	−3.6	−3.5
169	44	40/90.9	33/75.0	44	40/90.9	32/72.7	0.0	−2.3
170	29	27/93.1	19/65.5	29	27/93.1	21/72.4	0.0	6.9
171	27	24/88.9	18/66.7	27	24/88.9	18/66.7	0.0	0.0
172	30	29/96.7	22/73.3	30	29/96.7	24/80.0	0.0	6.7
173	25	23/92.0	16/64.0	25	23/92.0	18/72.0	0.0	8.0
174	29	27/93.1	17/58.6	29	27/93.1	22/75.9	0.0	**17.3**
175	27	26/96.3	19/70.4	27	26/96.3	21/77.8	0.0	7.4
176	34	33/97.1	21/61.8	34	33/97.1	26/76.5	0.0	14.7
177	36	34/94.4	25/69.4	36	33/91.7	25/69.4	−2.7	0.0
178	25	23/92.0	19/76.0	25	23/92.0	18/72.0	0.0	−4.0
179	29	28/96.6	20/69.0	29	28/96.6	23/79.3	0.0	10.3
180	29	25/86.2	17/58.6	29	27/93.1	16/55.2	**6.9**	−3.4
181	23	20/87.0	15/65.2	23	21/91.3	18/78.3	4.3	13.1
Total	661	609/92.1	435/65.8	661	611/92.4	469/71.0	0.3	**5.2**

Table D.4: Satellite-specific orbit repeat lags determined by means of the empirical and analytical approaches (see section 7.2.5) [referenced in section 8.1.1]

Satellite PRN	Empirical approach[1]			Analytical approach[2]			Difference
	#Value[3]	Lag [s]	STD [s][4]	#Value[3]	Lag [s]	STD [s][4]	ΔLag [s]
01	2	**262.81**	0.7		**259.41**	0.2	**3.40**
02	9	248.15	0.4		249.32	0.4	−1.17
04	17	248.36	0.5		250.61	0.4	−2.25
05	20	**240.07**	0.7		**241.19**	0.4	−1.12
06	3	242.13	0.6		241.76	0.5	0.37
08	20	243.59	0.5		243.76	0.3	−0.17
09	20	243.58	0.5		244.05	0.3	−0.47
10	20	247.12	0.4		246.61	0.3	0.51
11	20	246.00	3.0		244.27	0.4	1.73
12	20	250.18	0.6		248.96	0.4	1.22
14	20	251.11	0.3	21	249.65	0.2	1.46
17	20	247.04	0.8		247.92	0.4	−0.88
18	20	248.34	1.0		248.95	0.2	−0.61
19	12	244.91	1.5		242.01	0.4	2.90
21	12	248.63	0.5		247.90	0.3	0.73
22	20	245.39	0.7		245.37	0.2	0.02
24	7	246.18	0.4		245.51	0.3	0.67
26	20	246.16	0.9		245.98	0.2	0.18
27	15	243.51	0.5		243.69	0.3	−0.18
28	20	245.54	2.1		244.44	0.4	1.10
29	20	246.65	0.6		246.09	0.1	0.56
30	20	240.49	0.6		241.51	0.4	−1.02
32	13	250.97	0.9		249.81	0.2	1.16
Mean	−	**246.82**	**0.8**	−	**246.47**	**0.3**	**0.35**
Median	−	**246.18**	**0.6**	−	**245.98**	**0.3**	**0.37**

[1] Empirical approach: use of equations (7.15) and (7.16), input data: 21 days of 3-hour GPS observations and navigation messages (DOY2007:161-181, 15-18 h)

[2] Analytical approach: use of the free program `orbrep.f` (Agnew and Larson, 2007), input data: 21 days of 24-hour broadcast ephemeris files (DOY2007:161-181)

[3] Number of lag estimates (a maximum number of 20 for the empirical approach)

[4] Standard deviations of the determined satellite-specific orbit repeat lags

Table D.5: Results of the applied statistical tests given in terms of the non-rejection rates [%] of the null hypotheses like normal distribution, absence of trend, (non-)stationarity, and uncorrelatedness (α: significance level, MP: multipath) [referenced in sections 8.1.7 and 8.2.7]

Baseline and station		Sample size[1]	Residual component[2]	Normal distribution				Trend-free		(Non-)stationarity		Uncorrelatedness			
				JB	AD	LF	CS	CT	MK	ADF	KPSS	VNR	LB	KV	CM
	AFLO	Min: 3104	OFR	13.5	18.0	25.5	25.2	18.1	19.2	45.4	50.6	–	–	–	–
	32.4 km	Max: 3600	DTR	30.6	42.7	62.1	48.2	84.5	100.0	1.6	100.0	–	–	–	–
	Weak MP	Total: 230691	NCR(3)	28.0	51.0	65.6	52.2	97.1	98.4	0.0	100.0	0.0	0.0	0.0	0.0
			WNR	26.5	45.3	59.7	46.6	100.0	100.0	0.0	100.0	100.0	100.0	100.0	100.0
	TAAF	Min: 853	OFR	37.6	33.7	46.6	42.2	8.2	10.7	43.5	36.5	–	–	–	–
	53.7 km	Max: 3600	DTR	70.1	71.5	88.8	79.2	84.0	99.6	2.3	99.6	–	–	–	–
	Weak MP	Total: 218602	NCR(3)	58.6	73.8	87.7	78.0	94.7	99.6	0.4	99.6	0.0	0.0	0.0	0.0
			WNR	55.7	81.4	92.7	81.9	100.0	100.0	0.0	100.0	100.0	100.0	100.0	100.0
Case study 2	**HEDA**	Min: 1604	OFR	13.7	9.3	11.5	6.2	15.3	8.7	50.1	43.0	–	–	–	–
(α = 1%)	54.1 km	Max: 3600	DTR	61.6	62.6	82.9	64.8	97.8	100.0	0.0	100.0	–	–	–	–
	Strong MP	Total: 163490	NCR(3)	80.9	79.1	83.9	88.4	100.0	100.0	0.0	100.0	0.0	0.0	0.0	0.0
			WNR	98.8	97.8	97.8	97.8	100.0	100.0	0.0	100.0	100.0	98.8	100.0	100.0
	SIBI	Min: 931	OFR	28.3	21.9	32.6	29.3	16.0	11.1	48.6	46.8	–	–	–	–
	42.5 km	Max: 3600	DTR	64.0	52.7	66.1	61.6	77.2	98.6	5.9	100.0	–	–	–	–
	Weak MP	Total: 246627	NCR(3)	79.1	81.9	90.4	80.8	84.4	100.0	0.0	100.0	0.4	0.4	0.4	0.4
			WNR	75.9	91.9	91.8	93.1	100.0	100.0	0.0	100.0	100.0	100.0	100.0	100.0
	RATA	Min: 655	OFR	31.6	33.5	48.6	41.6	17.3	16.6	40.5	51.6	–	–	–	–
	203.7 km	Max: 3600	DTR	84.2	76.8	90.5	85.0	73.3	97.1	4.8	99.3	–	–	–	–
	Weak MP	Total: 226957	NCR(3)	86.1	93.1	95.9	94.6	76.3	97.4	3.0	99.4	0.0	0.0	0.0	0.0
			WNR	85.2	89.3	95.9	93.1	100.0	100.0	0.0	100.0	100.0	100.0	100.0	100.0
Case study 3	**TUEB**	Min: 255	OFR	55.2	51.4	58.2	61.3	26.7	20.8	45.5	66.9	–	–	–	–
(α = 5%)		Max: 679	DTR	68.2	70.6	79.4	84.1	81.5	88.0	4.7	100.0	–	–	–	–
	Weak MP	Total: 132979	NCR(3)	75.4	83.8	89.6	91.7	81.9	79.0	1.7	99.4	2.8	1.0	2.9	2.6
			WNR	83.0	91.8	92.5	92.6	98.9	99.7	0.0	100.0	100.0	97.0	100.0	100.0
	BING	Min: 240	OFR	40.3	29.9	51.5	46.2	43.9	30.9	6.9	88.4	–	–	–	–
		Max: 667	DTR	53.3	49.6	68.0	59.7	85.3	90.6	0.0	100.0	–	–	–	–
	Strong MP	Total: 124133	NCR(3)	31.8	46.8	61.2	68.5	86.7	82.2	1.4	98.9	4.6	0.2	0.8	0.8
			WNR	28.4	46.3	61.0	70.4	98.0	99.6	0.0	99.5	100.0	96.7	100.0	100.0

[1] Min/Max: minimum/maximum length of a single time series, Total: number of the residual samples used for hypothesis testing
[2] OFR: repaired residual, DTR: residual after Vondrák filtering, NCR(3): residual after 3-day sidereal stacking, WNR: residual after ARMA modelling

Table D.6: Analysis of satellite geometry to evaluate the appropriateness of the unique orbit repeat lag applied in case study 3 (DOY2008:275 and 284) [referenced in section 8.2.1]

SA*POS*®site and satellite PRN		Max ELV	|ΔELV|		|ΔAZI|		Epoch i for		
			med	max	med	max	Max ELV	$\|\Delta ELV\|_{min}$	$\|\Delta AZI\|_{max}$
TUEB (23)	02	35.8	0.1	0.2	0.1	0.2	1243	1434	1109
	03	84.8	0.3	0.3	0.1	3.3	1970	1968	1968
	07	72.0	0.2	0.3	0.1	1.0	168	175	165
	08	84.5	0.1	0.2	0.1	1.8	326	335	329
	10	68.1	0.2	0.3	0.1	0.6	352	330	343
	11	83.3	0.5	0.6	0.2	**4.9**	2391	2393	2393
	12	72.5	0.3	0.3	0.1	0.4	1122	1431	1122
	13	81.9	**0.7**	**0.8**	0.4	3.4	1	346	1
	14	42.1	0.1	0.2	0.1	0.1	2262	2370	2285
	16	74.2	0.3	0.4	0.1	1.3	1722	1722	1723
	17	40.4	0.4	0.6	**0.7**	0.9	814	788	794
	18	49.2	0.1	0.2	0.1	0.3	1873	1916	1866
	19	82.3	0.1	0.2	0.2	0.9	2118	2097	2110
	20	83.0	0.0	0.1	0.2	0.3	2546	2178	2552
	21	75.1	0.3	0.4	0.1	1.4	1669	1670	1668
	22	62.1	0.4	0.4	0.2	0.9	2007	2005	1998
	23	70.6	0.3	0.3	0.1	0.1	2640	2388	2511
	24	59.2	0.4	0.4	0.3	0.9	1499	1493	1485
	25	67.9	0.2	0.3	0.1	0.8	79	87	77
	27	77.5	0.1	0.2	0.1	0.7	198	222	203
	28	62.1	0.5	0.5	0.4	1.2	554	544	540
	31	55.2	**0.6**	**0.8**	**0.8**	1.6	1431	1457	1440
	32	86.8	0.0	0.1	0.2	1.0	2418	2367	2406
BING (24)	02	35.3	0.1	0.2	0.1	0.2	1250	1424	1078
	03	84.2	0.3	0.3	0.1	3.0	1961	1959	1961
	04	22.2	0.2	0.5	**0.7**	0.8	1124	1094	1095
	07	70.4	0.2	0.3	0.1	0.9	172	181	173
	08	82.6	0.1	0.2	0.1	1.3	330	340	333
	10	68.5	0.2	0.3	0.1	0.6	345	326	339
	11	82.6	0.5	0.6	0.2	**4.4**	2383	2385	2384
	13	82.9	**0.8**	**0.8**	0.3	2.3	1	337	1
	14	41.6	0.1	0.2	0.0	0.1	2268	2374	2283
	15	80.2	0.2	0.3	0.1	1.3	662	654	659
	16	74.4	0.3	0.4	0.1	1.4	1714	1713	1717
	17	39.8	0.4	0.6	**0.7**	0.9	822	794	802
	18	48.3	0.1	0.2	0.1	0.3	1883	1917	1869
	20	85.1	0.0	0.1	0.2	0.4	2543	2190	2548
	21	73.4	0.3	0.4	0.1	1.3	1673	1674	1670
	22	60.8	0.4	0.4	0.2	0.9	2012	2010	2002
	23	68.9	0.3	0.3	0.1	0.1	2640	2402	2639
	24	58.0	0.4	0.4	0.3	0.9	1505	1498	1496
	25	66.4	0.2	0.3	0.2	0.7	82	94	83
	27	75.8	0.1	0.2	0.1	0.6	203	226	214
	28	60.8	0.5	0.5	0.4	1.2	559	549	553
	29	67.7	0.7	**0.8**	0.3	0.3	1461	1736	1551
	31	56.1	**0.6**	**0.8**	**0.7**	1.6	1426	1450	1434
	32	88.9	0.0	0.1	0.2	2.7	2420	2407	2416

Bibliography

Abdi, H. and Molin, P. (2007). Lilliefors test for normality. In: N. J. Salkind (ed.), *Encyclopedia of Measurement and Statistics*, SAGE Publications, Thousand Oaks. doi:10.4135/9781412952644.

Agnew, D. C. and Larson, K. M. (2007). Finding the repeat times of the GPS constellation. *GPS Solutions*, 11(1):71–76. doi:10.1007/s10291-006-0038-4.

Akaike, H. (1973). Information theory and an extension of the maximum likelihood principle. In: B. N. Petrov and F. Csaki (eds.), Proceedings of the 2nd International Symposium on Information Theory, Tsahkadsor, Armenia, USSR, September 2-8, 1971, Akadémiai Kiadó, Budapest, pp. 267–281.

Alber, C., Ware, R., Rocken, C., and Braun, J. (2000). Obtaining single path phase delays from GPS double differences. *Geophysical Research Letters*, 27(17):2661–2664. doi:10.1029/2000GL011525.

Altamimi, Z., Sillard, P., and Boucher, C. (2002). ITRF2000: A new release of the International Terrestrial Reference Frame for earth science applications. *Journal of Geophysical Research*, 107(B10), 2214. doi:10.1029/2001JB000561.

Amante, C. and Eakins, B. W. (2009). ETOPO1 1 arc-minute global relief model: Procedures, data sources and analysis. NOAA Technical Memorandum NESDIS NGDC-24, National Geophysical Data Center, Marine Geology and Geophysics Division, Boulder, CO, USA.

Amiri-Simkooei, A. R. (2007). *Least-Squares Variance Component Estimation: Theory and GPS Applications.* PhD thesis, Delft University of Technology, Publications on Geodesy, 64, Netherlands Geodetic Commission, Delft, The Netherlands.

Amiri-Simkooei, A. R., Teunissen, P. J. G., and Tiberius, C. C. J. M. (2009). Application of least-squares variance component estimation to GPS observables. *Journal of Surveying Engineering*, 135(4):149–160. doi:10.1061/(ASCE)0733-9453(2009)135:4(149).

Amiri-Simkooei, A. R. and Tiberius, C. C. J. M. (2007). Assessing receiver noise using GPS short baseline time series. *GPS Solutions*, 11(1):21–35. doi:10.1007/s10291-006-0026-8.

Anderson, T. W. (1962). On the distribution of the two-sample Cramér-von Mises criterion. *Annals of Mathematical Statistics*, 33(3):1148–1159. doi:10.1214/aoms/1177704477.

Anderson, T. W. and Darling, D. A. (1952). Asymptotic theory of certain "goodness of fit" criteria based on stochastic processes. *Annals of Mathematical Statistics*, 23(2):193–212. doi:10.1214/aoms/1177729437.

Andrew, D. W. K. (1991). Heteroskedasticity and autocorrelation consistent covariance matrix estimation. *Econometrica*, 59(3):817–858. doi:10.2307/2938229.

Ashby, N. (2002). Relativity and the Global Positioning System. *Physics Today*, 55(5):41–47. doi:10.1063/1.1485583.

Ashjaee, J. and Lorenz, R. (1992). Precise GPS surveying after Y-code. In: Proceedings of ION GPS 1992, Albuquerque, NM, USA, September 16-18, pp. 657–659.

Ashkenazi, V. (2006). Geodesy and satellite navigation: A lighthearted look at a strange relationship. *Inside GNSS*, 1(3):44–49.

Awange, J. L. (2012). *Environmental Monitoring Using GNSS: Global Navigation Satellite Systems.* Springer-Verlag, Berlin Heidelberg.

Baltink, H. K., van der Marel, H., and van der Hoeven, A. G. A. (2002). Integrated atmospheric water vapor estimates from a regional GPS network. *Journal of Geophysical Research*, 107(D3), 4025. doi:10.1029/2000JD000094.

Bar-Sever, Y., Young, L., Stocklin, F., Heffernan, P., and Rush, J. (2004). NASA's global differential GPS system and the TDRSS augmentation service for satellites. In: Proceedings of the 2nd ESA Workshop on Satellite Navigation User Equipment Technologies, NAVITEC 2004, ESTEC, Noordwijk, The Netherlands, December 8-10.

Bassiri, S. and Hajj, G. A. (1993). Higher-order ionospheric effects on the global positioning system observables and means of modeling them. *Manuscripta Geodetica*, 18(6):280–289.

Beckman, R. J. and Trussell, H. J. (1974). The distribution of an arbitrary studentized residual and the effects of updating in multiple regression. *Journal of the American Statistical Association*, 69(345):199–201. doi:10.2307/2285524.

Bender, M., Dick, G., Ge, M., Deng, Z., Wickert, J., Kahle, H.-G., Raabe, A., and Tetzlaff, G. (2011a). Development of a GNSS water vapour tomography system using algebraic reconstruction techniques. *Advances in Space Research*, 47(10):1704–1720. doi:10.1016/j.asr.2010.05.034.

Bender, M., Dick, G., Wickert, J., Schmidt, T., Song, S., Gendt, G., Ge, M., and Rothacher, M. (2008). Validation of GPS slant delays using water vapour radiometers and weather models. *Meteorologische Zeitschrift*, 17(6):807–812. doi:10.1127/0941-2948/2008/0341.

Bender, M. and Raabe, A. (2007). Preconditions to ground-based GPS water vapour tomography. *Annales Geophysicae*, 25(8):1727–1734. doi:10.5194/angeo-25-1727-2007.

Bender, M., Stosius, R., Zus, F., Dick, G., Wickert, J., and Raabe, A. (2011b). GNSS water vapour tomography – Expected improvements by combining GPS, GLONASS and Galileo observations. *Advances in Space Research*, 47(5):886–897. doi:10.1016/j.asr.2010.09.011.

Betz, J. (2010). Link budgets. Paper presented at the Meeting of International Committee on GNSS, Working Group A: Compatibility and Interoperability, Turin, Italy, October 19, 2010.

Beutler, G., Bauersima, I., Botton, S., Gurtner, W., Rothacher, M., and Schildknecht, T. (1989). Accuracy and biases in the geodetic application of the Global Positioning System. *Manuscripta Geodaetica*, 14(1):28–35.

Beutler, G., Bauersima, I., Gurtner, W., and Rothacher, M. (1987). Correlations between simultaneous GPS double difference carrier phase observations in the multistation mode: Implementation considerations and first experience. *Manusripta Geodaetica*, 12(1):40–44.

Beutler, G., Baueršíma, I., Gurtner, W., Rothacher, M., Schildknecht, T., and Geiger, A. (1988). Atmospheric refraction and other important biases in GPS carrier phase observations. In: F. K. Brunner (ed.), *Atmospheric Effects on Geodetic Space Measurements*, School of Surveying Monograph No. 12, University of New South Wales, Kensington, Australia, pp. 15–43.

Beutler, G., Brockmann, E., Gurtner, W., Hugentobler, U., Mervart, L., Rothacher, M., and Verdun, A. (1994). Extended orbit modeling techniques at the CODE processing center of the International GPS Service for Geodynamics (IGS): Theory and initial results. *Manuscripta Geodetica*, 19(6):367–386.

Bevis, M., Businger, S., Chiswell, S., Herring, T. A., Anthes, R. A., Rocken, C., and Ware, R. H. (1994). GPS meteorology: Mapping zenith wet delays onto precipitable water. *Journal of Applied Meteorology and Climatology*, 33(3):379–386. doi:10.1175/1520-0450(1994)033<0379:GMMZWD>2.0.CO;2.

Bevis, M., Businger, S., Herring, T. A., Rocken, C., Anthes, R. A., and Ware, R. H. (1992). GPS meteorology: Remote sensing of atmospheric water vapor using the Global Positioning System. *Journal of Geophysical Research*, 97(D14):15787–15801. doi:10.1029/92JD01517.

Beyerle, G. (2009). Carrier phase wind-up in GPS reflectometry. *GPS Solutions*, 13(3):191–198. doi:10.1007/s10291-008-0112-1.

Bickel, P. J. and Doksum, K. A. (1981). An analysis of transformations revisited. *Journal of the American Statistical Association*, 76(374):296–311. doi:10.2307/2287831.

Bilich, A. and Larson, K. M. (2007). Mapping the GPS multipath environment using the signal-to-noise ratio (SNR). *Radio Science*, 42, RS6003. doi:10.1029/2007RS003652.

Bilich, A., Larson, K. M., and Axelrad, P. (2008). Modeling GPS phase multipath with SNR: Case study from the Salar de Uyuni, Boliva. *Journal of Geophysical Research*, 113, B04401. doi:10.1029/2007JB005194.

Bilich, A. L. (2006). *Improving the Precision and Accuracy of Geodetic GPS: Applications to Multipath and Seismology*. PhD thesis, University of Colorado Boulder, Boulder, USA.

Bingham, C. and Nelson, L. S. (1981). An approximation for the distribution of the von Neumann ratio. *Technometrics*, 23(3):285–288. doi:10.2307/1267792.

Bischoff, W., Heck, B., Howind, J., and Teusch, A. (2005). A procedure for testing the assumption of homoscedasticity in least squares residuals: A case study of GPS carrier-phase observations. *Journal of Geodesy*, 78(7-8):397–404. doi:10.1007/s00190-004-0390-5.

Bischoff, W., Heck, B., Howind, J., and Teusch, A. (2006). A procedure for estimating the variance function of linear models and for checking the appropriateness of estimated variances: A case study of GPS carrier-phase observations. *Journal of Geodesy*, 79(12):694–704. doi:10.1007/s00190-006-0024-1.

Bisnath, S. B. and Gao, Y. (2009). Precise point positioning: A powerful technique with a promising future. *GPS World*, 20(4):43–50.

Blewitt, G., Lavallée, D., Clarke, P., and Nurutdinov, K. (2001). A new global mode of the earth deformation: Seasonal cycle detected. *Science*, 294(5550):2342–2345. doi:10.1126/science.1065328.

Boehm, J., Heinkelmann, R., and Schuh, H. (2007). Short Note: A global model of pressure and temperature for geodetic applications. *Journal of Geodesy*, 81(10):679–683. doi:10.1007/s00190-007-0135-3.

Boehm, J., Niell, A., Tregoning, P., and Schuh, H. (2006a). Global Mapping Function (GMF): A new empirical mapping function based on numerical weather model data. *Geophysical Researches Letters*, 33, L07304. doi:10.1029/2005GL025546.

Boehm, J., Werl, B., and Schuh, H. (2006b). Troposphere mapping functions for GPS and very long baseline interferometry from European Centre for Medium-Range Weather Forecasts operational analysis data. *Journal of Geophysical Research*, 111, B02406. doi:10.1029/2005JB003629.

Bona, P. (2000). Precision, cross correlation, and time correlation of GPS phase and code observations. *GPS Solutions*, 4(2):3–13. doi:10.1007/PL00012839.

Borre, K. and Tiberius, C. (2000). Time series analysis of GPS observables. In: Proceedings of ION GPS 2000, Salt Lake City, UT, USA, September 19-22, pp. 1885–1894.

Boucher, C. and Altamimi, Z. (1992). Terrestrial Reference System and its first realizations. Veröffentlichung der Bayerischen Kommission für die internationale Erdmessung, Astronomisch-Geodätische Arbeiten, No. 52, Munich, pp. 205–213.

Box, G. E. P. and Cox, D. R. (1964). An analysis of transformations. *Journal of the Royal Statistical Society. Series B (Methodological)*, 26(2):211–252.

Box, G. E. P., Hunter, W. G., and Hunter, J. S. (1978). *Statistics for Experimenters*. John Wiley, New York.

Box, G. E. P. and Jenkins, G. M. (1976). *Time Series Analysis: Forecasting and Control*. Holden-Day, San Francisco.

Box, G. E. P., Jenkins, G. M., and Reinsel, G. C. (2008). *Time Series Analysis: Forecasting and Control*. John Wiley, Hoboken, 4th edition.

Box, G. E. P. and Pierce, D. A. (1970). Distribution of residual autocorrelations in autoregressive-integrated moving average time series models. *Journal of the American Statistical Association*, 65(332):1509–1526. doi:10.2307/2284333.

Braasch, M. S. and van Dierendonck, A. J. (1999). GPS receiver architectures and measurements. *Proceedings of the IEEE*, 87(1):48–64. doi:10.1109/5.736341.

Brockwell, P. J. and Davis, R. A. (1991). *Time Series: Theory and Methods*. Springer-Verlag, New York, 2nd edition.

Brockwell, P. J. and Davis, R. A. (2002). *Introduction to Time Series and Forecasting*. Springer-Verlag, New York, 2nd edition.

Broersen, P. M. T. (2000a). Autoregressive model orders for Durbin's MA and ARMA estimators. *IEEE Transactions on Signal Processing*, 48(8):2454–2457. doi:10.1109/78.852025.

Broersen, P. M. T. (2000b). Facts and fiction in spectral analysis. *IEEE Transactions on Instrumentation and Measurement*, 49(4):766–772. doi:10.1109/19.863921.

Broersen, P. M. T. (2000c). Finite sample criteria for autoregressive order selection. *IEEE Transactions on Signal Processing*, 48(12):3550–3558. doi:10.1109/78.887047.

Broersen, P. M. T. (2006). *Automatic Autocorrelation and Spectral Analysis*. Springer-Verlag, London.

Broersen, P. M. T. and de Waele, S. (2004). Finite sample properties of ARMA order selection. *IEEE Transactions on Instrumentation and Measurement*, 53(3):645–651. doi:10.1109/TIM.2004.827058.

Broersen, P. M. T. and Wensink, H. E. (1993). On finite sample theory for autoregressive model order selection. *IEEE Transactions on Signal Processing*, 41(1):194–204. doi:10.1109/TSP.1993.193138.

Brondeel, M. and Willems, T. (2003). Atmospheric pressure loading in GPS height estimates. *Advances in Space Research*, 31(8):1959–1964. doi:10.1016/S0273-1177(03)00157-1.

Brown, N., Geisler, I., and Troyer, L. (2006). RTK rover performance using the Master-Auxiliary Concept. *Journal of Global Positioning Systems*, 5(1-2):135–144.

Brunner, F. K., Hartinger, H., and Troyer, L. (1999). GPS signal diffraction modelling: The stochastic SIGMA-Δ model. *Journal of Geodesy*, 73(5):259–267. doi:10.1007/s001900050242.

Bulletin C43-IERS (2012). UTC time step on the 1st of July 2012. Earth Orientation Center of the International Earth Rotation and Reference Systems Service (IERS), available online at `ftp://hpiers.obspm.fr/iers/bul/bulc/bulletinc.43`, accessed on March 12, 2012.

Burg, J. P. (1967). Maximum entropy spectral analysis. In: Proceedings of the 37th Annual Meeting of the Society of Exploration Geophysicists, Oklahoma City, OK, USA, October 31, 1967; reprinted in: D. G. Childers (ed.), *Modern Spectrum Analysis*, IEEE Press, New York, 1978, pp. 34–39.

Businger, S., Chiswell, S. R., Bevis, M., Duan, J., Anthes, R. A., Rocken, C., Ware, R. H., Exner, M., VanHove, T., and Solheim, F. S. (1996). The promise of GPS in atmospheric monitoring. *Bulletin of the American Meteorological Society*, 77(1):5–18. doi:10.1175/1520-0477(1996)077<0005:TPOGIA>2.0.CO;2.

Butsch, F. and Kipka, A. (2004). Die Bedeutung des Signal- zu Rauschleistungsverhältnisses und verwandter Parameter für die Messgenauigkeit bei GPS. *Allgemeine Vermessungs-Nachrichten (AVN)*, 111(2):46–55.

Buttkus, B. (2000). *Spectral Analysis and Filter Theory in Applied Geophysics*. Springer-Verlag, Berlin Heidelberg.

Byun, S. H. and Bar-Sever, Y. E. (2009). A new type of troposphere zenith path delay product of the international GNSS service. *Journal of Geodesy*, 83(3-4):367–373. doi:10.1007/s00190-008-0288-8.

Casella, G. and Berger, R. L. (2002). *Statistical Inference*. Duxbury, Pacific Grove, 2nd edition.

Caspary, W. and Wichmann, K. (1994). *Lineare Modelle: Algebraische Grundlagen und statistische Anwendungen*. R. Oldenbourg, Munich.

Chakravarti, I. M., Roy, J., and Laha, R. G. (1967). *Handbook of Methods of Applied Statistics*, volume 1. John Wiley, New York.

Chatfield, C. (2004). *The Analysis of Time Series: An Introduction*. Chapman & Hall/CRC, Boca Raton, 6th edition.

Chatterjee, S. and Hadi, A. S. (2006). *Regression Analysis by Example*. John Wiley, Hoboken, 4th edition.

Choi, K., Bilich, A., Larson, K. M., and Axelrad, P. (2004). Modified sidereal filtering: Implications for high-rate GPS positioning. *Geophysical Research Letters*, 31, L22608. doi:10.1029/2004GL021621.

Cleveland, W. S. (1979). Robust locally weighted regression and smoothing scatterplots. *Journal of the American Statistical Association*, 74(368):829–836. doi:10.2307/2286407.

Cleveland, W. S. and Devlin, S. J. (1988). Locally weighted regression: An approach to regression analysis by local fitting. *Journal of the American Statistical Association*, 83(403):596–610. doi:10.2307/2289282.

Cocard, M., Bourgon, S., Kamali, O., and Collins, P. (2008). A systematic investigation of optimal carrier-phase combinations for modernized triple-frequency GPS. *Journal of Geodesy*, 82(9):555–564. doi:10.1007/s00190-007-0201-x.

Coifman, R. R. and Wickerhauser, M. V. (1992). Entropy-based algorithms for best basis selection. *IEEE Transactions on Information Theory*, 38(2):713–718. doi:10.1109/18.119732.

Collins, J. P. (1999). An overview of GPS inter-frequency carrier phase combinations. Geodetic Survey Division, Technical Memorandum, University of New Brunswick (UNB), New Brunswick, Canada, unpublished.

Collins, J. P. and Langley, R. B. (1999). Possible weighting schemes for GPS carrier phase observations in the presence of multipath. Department of Geodesy and Geomatics Engineering, Final contract report for the United States Army Corps of Engineers Topographic Engineering Center, No. DAAH04-96-C-0086/TCN 98151, University of New Brunswick (UNB), New Brunswick, Canada.

Collins, P. (2008). Isolating and estimating undifferenced GPS integer ambiguities. In: Proceedings of ION NTM 2008, San Diego, CA, USA, January 28-30, pp. 720–732.

Conover, W. J. (1999). *Practical Nonparametric Statistics*. John Wiley, New York, 3rd edition.

Cook, R. D. and Weisberg, S. (1982). *Residuals and Influence in Regression*. Chapman & Hall, New York.

Cox, D. R. and Stuart, A. (1955). Some quick sign tests for trend in location and dispersion. *Biometrika*, 42(1-2):80–95. doi:10.1093/biomet/42.1-2.80.

Crawley, M. J. (2007). *The R Book*. John Wiley, Chichester.

Csörgő, S. and Faraway, J. J. (1996). The exact and asymptotic distributions of Cramér-von Mises statistics. *Journal of the Royal Statistical Society. Series B (Methodological)*, 58(1):221–234.

Czopek, F. M. and Shollenberger, S. (1993). Description and performance of the GPS Block I and II L-Band antenna and link budget. In: Proceedings of ION GPS 1993, Salt Lake City, UT, USA, September 22-24, pp. 37–43.

Dach, R., Böhm, J., Lutz, S., Steigenberger, P., and Beutler, G. (2010). Evaluation of the impact of atmospheric pressure loading modeling on GNSS data analysis. *Journal of Geodesy*, 85(2):75–91. doi:10.1007/s00190-010-0417-z.

Dach, R., Hugentobler, U., Fridez, P., and Meindl, M. (2007a). Bernese GPS Software Version 5.0. Astronomical Institute, University of Bern, Stämpfli Publications AG, Bern, Switzerland.

Dach, R., Hugentobler, U., and Walser, P. (2007b). Bernese GPS Software Version 5.0 Tutorial. Astronomical Institute, University of Bern, Bern, Switzerland.

Dach, R., Schmid, R., Schmitz, M., Thaller, D., Schaer, S., Lutz, S., Steigenberger, P., Wübbena, G., and Beutler, G. (2011). Improved antenna phase center models for GLONASS. *GPS Solutions*, 15(1):49–65. doi:10.1007/s10291-010-0169-5.

Dai, L., Han, S., Wang, J., and Rizos, C. (2001). A study on GPS/GLONASS multiple reference station techniques for precise real-time carrier phase-based positioning. In: Proceedings of ION GPS 2001, Salt Lake City, UT, USA, September 11-14, pp. 392–403.

Daubechies, I. (1992). *Ten Lectures on Wavelets*. CBMS-NSF Regional Conference Series in Applied Mathematics, No. 61, Society for Industrial and Applied Mathematics, Philadelphia.

Davis, J. L., Herring, T. A., Shapiro, I. I., Rogers, A. E. E., and Elgered, G. (1985). Geodesy by radio interferometry: Effects of atmospheric modeling errors on estimates of baseline length. *Radio Science*, 20(6):1593–1607. doi:10.1029/RS020i006p01593.

De Jonge, P. J., Teunissen, P. J. G., Jonkman, N. F., and Joosten, P. (2000). The distributional dependence of the range on triple frequency GPS ambiguity resolution. In: Proceedings of ION NTM 2000, Anaheim, CA, USA, January 26-28, pp. 605–612.

Debnath, L. (2001). *Wavelet Transforms & Their Applications.* Birkhäuser, Boston.

Debnath, L. and Mikusinski, P. (2005). *Introduction to Hilbert Spaces with Applications.* Elsevier Academic Press, Burlington, 3rd edition.

Dickey, D. A. (1976). *Estimation and Hypothesis Testing in Nonstationary Time Series.* PhD thesis, Iowa State University, Ames, USA.

Dickey, D. A. and Fuller, W. A. (1979). Distribution of the estimators for autoregressive time series with a unit root. *Journal of the American Statistical Association*, 74(366):427–431. doi:10.2307/2286348.

Dilßner, F. (2007). Zum Einfluss des Antennenumfeldes auf die hochpräzise GNSS-Positionsbestimmung. Wissenschaftliche Arbeiten der Fachrichtung Geodäsie und Geoinformatik der Leibniz Universität Hannover, No. 271, Hannover, Germany.

Dixon, K. (2005). Satellite positioning systems: Efficiencies, performance and trends. *European Journal of Navigation*, 3(1):58–63.

Dixon, K. (2006). StarFire: A global SBAS for sub-decimeter precise point positioning. In: Proceedings of ION GNSS 2006, Fort Worth, TX, USA, September 26-29, pp. 2286–2296.

Dragert, H., James, T. S., and Lambert, A. (2000). Ocean loading corrections for continuous GPS: A case study at the Canadian coastal site Holberg. *Geophysical Research Letters*, 27(14):2045–2048. doi:10.1029/2000GL011536.

Durbin, J. (1959). Efficient estimation of parameters in moving average models. *Biometrika*, 46(3-4):306–316. doi:10.1093/biomet/46.3-4.306.

Durbin, J. (1960). The fitting of time series models. *Revue de l'Institut International de Statistique*, 28(3):233–243. doi:10.2307/1401322.

El-Rabbany, A. (1994). *The Effect of Physical Correlations on the Ambiguity Resolution and Accuracy Estimation in GPS Differential Positioning.* PhD thesis, Department of Geodesy and Geomatics Engineering, Technical Report, No. 170, University of New Brunswick (UNB), New Brunswick, Canada.

El-Rabbany, A. (2006). *Introduction to GPS: The Global Positioning System.* Artech House, Norwood, 2nd edition.

El-Rabbany, A. and Kleusberg, A. (2003). Effect of temporal physical correlation on accuracy estimation in GPS relative positioning. *Journal of Surveying Engineering*, 129(1):28–32. doi:10.1061/(ASCE)0733-9453(2003)129:1(28).

Elliott, G., Rothenberg, T. J., and Stock, J. H. (1996). Efficient tests for an autoregressive unit root. *Econometrica*, 64(4):813–836. doi:10.2307/2171846.

Elósegui, P., Davis, J. L., Jaldehag, R. T. K., Johansson, J. M., Niell, A. E., and Shapiro, I. I. (1995). Geodesy using the Global Positioning System: The effects of signal scattering on estimates of site position. *Journal of Geophysical Research*, 100(B6):9921–9934. doi:10.1029/95JB00868.

Elsobeiey, M. and El-Rabbany, A. (2011). Impact of second-order ionospheric delay on GPS precise point positioning. *Journal of Applied Geodesy*, 5(1):37–45. doi:10.1515/JAG.2011.004.

Estey, L. H. and Meertens, C. M. (1999). TEQC: The multi-purpose toolkit for GPS/GLONASS data. *GPS Solutions*, 3(1):42–49. doi:10.1007/PL00012778.

Euler, H.-J. and Goad, C. C. (1991). On optimal filtering of GPS dual frequency observations without using orbit information. *Bulletin Géodésique*, 65(2):130–143. doi:10.1007/BF00806368.

Falk, M., Marohn, F., and Tewes, B. (2002). *Foundations of Statistical Analyses and Applications with SAS.* Birkhäuser, Basel.

Fan, K. K. and Ding, X. L. (2006). Estimation of GPS carrier phase multipath signals based on site environment. *Journal of Global Positioning Systems*, 5(1-2):22–28.

Farrell, W. E. (1972). Deformation of the Earth by surface loads. *Reviews of Geophysics*, 10(3):761–797. doi:10.1029/RG010i003p00761.

Feller, W. (1948). On the Kolmogorov-Smirnov limit theorems for empirical distributions. *Annals of Mathematical Statistics*, 19(2):177–189. doi:10.1214/aoms/1177730243.

Feng, Y. (2008). GNSS three carrier ambiguity resolution using ionosphere-reduced virtual signals. *Journal of Geodesy*, 82(12):847–862. doi:10.1007/s00190-008-0209-x.

Ferland, R. (2006). IGSMAIL-5447: Proposed IGS05 realization. Available online at `http://igscb.jpl.nasa.gov/mail/igsmail/2006/msg00170.html`, accessed on May 6, 2011.

Fischer, B., Ruf, B., and Kuhlmann, H. (2011). Zur Auswertung von Zeitreihen in Referenzstationsnetzen am Beispiel von SA*POS*®-Stationen. *Allgemeine Vermessungs-Nachrichten (AVN)*, 118(8-9):283–292.

Fontana, R. D., Cheung, W., Novak, P. M., and Stansell, T. A. (2001). The new L2 civil signal. In: Proceedings of ION GPS 2001, Salt Lake City, UT, USA, September 11-14, pp. 617–631.

Forssell, B., Martin-Neira, M., and Harrisz, R. A. (1997). Carrier phase ambiguity resolution in GNSS-2. In: Proceedings of ION GPS 1997, Kansas City, MO, USA, September 16-19, pp. 1727–1736.

Fotopoulos, G. and Cannon, M. E. (2001). An overview of multiple-reference station methods for cm-level positioning. *GPS Solutions*, 4(3):1–10. doi:10.1007/PL00012849.

Fritsche, M., Dietrich, R., Knöfel, C., Rülke, A., Vey, S., Rothacher, M., and Steigenberger, P. (2005). Impact of higher-order ionospheric terms on GPS estimates. *Geophysical Research Letters*, 32, L23311. doi:10.1029/2005GL024342.

Fuhrmann, T., Knöpfler, A., Mayer, M., Luo, X., and Heck, B. (2010). Zur GNSS-basierten Bestimmung des atmosphärischen Wasserdampfgehalts mittels Precise Point Positioning. Schriftenreihe des Studiengangs Geodäsie und Geoinformatik, Band 2/2010, Karlsruher Institut für Technologie (KIT), KIT Scientific Publishing, Karlsruhe, Germany.

Fuller, W. A. (1996). *Introduction to Statistical Time Series.* John Wiley, Hoboken, 2nd edition.

Gao, Y. and Chen, K. (2004). Performance analysis of precise point positioning using real-time orbit and clock products. *Journal of Global Positioning Systems*, 3(1-2):95–100.

Ge, L., Han, S., and Rizos, C. (2000). Multipath mitigation of continuous GPS measurements using an adaptive filter. *GPS Solutions*, 4(2):19–30. doi:10.1007/PL00012838.

Ge, M., Gendt, G., Rothacher, M., Shi, C., and Liu, J. (2008). Resolution of GPS carrier-phase ambiguities in precise point positioning (PPP) with daily observations. *Journal of Geodesy*, 82(7):389–399. doi:10.1007/s00190-007-0187-4.

Gel, Y. R. and Gastwirth, J. L. (2008). A robust modification of the Jarque-Bera test of normality. *Economics Letters*, 99(1):30–32. doi:10.1016/j.econlet.2007.05.022.

Geng, J., Meng, X., Teferle, F. N., and Dodson, A. H. (2010). Performance of precise point positioning with ambiguity resolution for 1- to 4-hour observation periods. *Survey Review*, 42(316):155–165. doi:10.1179/003962610X12572516251682.

Geng, J., Teferle, F. N., Shi, C., Meng, X., Dodson, A. H., and Liu, J. (2009). Ambiguity resolution in precise point positioning with hourly data. *GPS Solutions*, 13(4):263–270. doi:10.1007/s10291-009-0119-2.

Georgiadou, Y. and Kleusberg, A. (1988). On carrier signal multipath effects in relative GPS positioning. *Manuscripta Geodaetica*, 13(3):172–179.

Ghoddousi-Fard, R. and Dare, P. (2006). Online GPS processing services: An initial study. *GPS Solutions*, 10(1):12–20. doi:10.1007/s10291-005-0147-5.

Gilbert, R. O. (1987). *Statistical Methods for Environmental Pollution Monitoring.* John Wiley, New York.

Glasserman, P. (2004). *Monte Carlo Methods in Financial Engineering.* Stochastic Modelling and Applied Probability, Vol. 53, Springer-Verlag, New York.

Görres, B. (2010a). Ist das GNSS-Antennenproblem gelöst? *Zeitschrift für Geodäsie, Geoinformation und Landmanagement (ZfV)*, 135(4):256–267.

Görres, B. (2010b). Vom globalen Bezugssystem bis zur Umsetzung für die Praxis. In: GNSS 2010 – Vermessung und Navigation im 21. Jahrhundert, 100. DVW-Seminar, Köln, Oktober 4-5, 2010, DVW-Schriftenreihe, Band 63/2010, Wißner-Verlag, Augsburg, Germany, pp. 39–56.

Görres, B., Campbell, J., Becker, M., and Siemes, M. (2006). Absolute calibration of GPS antennas: Laboratory results and comparison with field and robot techniques. *GPS Solutions*, 10(2):136–145. doi:10.1007/s10291-005-0015-3.

Goupillaud, P., Grossman, A., and Morlet, J. (1984). Cycle-octave and related transforms in seismic signal analysis. *Geoexploration*, 23(1):85–102. doi:10.1016/0016-7142(84)90025-5.

GPS-SPS-SS (1995). Global Positioning System Standard Positioning Service Signal Specification. United States Coast Guard, 2nd edition, June 2, 1995.

Grafarend, E. W. and Schaffrin, B. (1993). *Ausgleichungsrechnung in linearen Modellen*. BI-Wissenschaftsverlag, Mannheim.

Graupe, D., Krause, D. J., and Moore, J. B. (1975). Identification of autoregressive moving-average parameters of time series. *IEEE Transactions on Automatic Control*, 20(1):104–107. doi:10.1109/TAC.1975.1100855.

Grossmann, A. and Morlet, J. (1985). Decomposition of functions into wavelets of constant shape, and related transforms. In: L. Streit (ed.), *Mathematics and Physics, Lectures on Recent Results*, World Scientific, Singapore, pp. 135–165.

Guier, W. H. and Weiffenbach, G. C. (1997). Genesis of satellite navigation. *Johns Hopkins APL Technical Digest*, 18(2):178–181.

Gurtner, W. (2002). RINEX: The Receiver Independent Exchange Format Version 2.10. Available online at `ftp://igscb.jpl.nasa.gov/igscb/data/format/rinex210.txt`, accessed on February 23, 2011.

Gurtner, W. and Estey, L. (2007). RINEX: The Receiver Independent Exchange Format Version 3.00. Available online at `ftp://ftp.unibe.ch/aiub/rinex/rinex300.pdf`, accessed on February 23, 2011.

Haar, A. (1910). Zur Theorie der orthogonalen Funktionensysteme (Erste Mitteilung). *Mathematische Annalen*, 69(3):331–371. doi:10.1007/BF01456326.

Han, S. (1997). Quality-control issues relating to instantaneous ambiguity resolution for real-time GPS kinematic positioning. *Journal of Geodesy*, 71(6):351–361. doi:10.1007/s001900050103.

Han, S. and Rizos, C. (1999). The impact of two additional civilian GPS frequencies on ambiguity resolution strategies. In: Proceedings of the 55th Annual Meeting of The Institute of Navigation, Cambridge, MA, USA, June 27-30, 1999, pp. 315–321.

Hannen, E. J. and Rissanen, J. (1982). Recursive estimation of mixed autoregressive moving-average order. *Biometrika*, 69(1):81–94. doi:10.1093/biomet/69.1.81.

Hart, B. I. (1942). Significance levels for the ratio of the mean square successive difference to the variance. *Annals of Mathematical Statistics*, 13(4):445–447. doi:10.1214/aoms/1177731544.

Hartinger, H. and Brunner, F. K. (1999). Variances of GPS phase observations: The SIGMA-ϵ model. *GPS Solutions*, 2(4):35–43. doi:10.1007/PL00012765.

Hartung, J., Elpelt, B., and Klösener, K.-H. (2005). *Statistik: Lehr- und Handbuch der angewandten Statistik*. Oldenbourg, Munich, 14th edition.

Hatch, R., Jung, J., Enge, P., and Pervan, B. (2000). Civilian GPS: The benefits of three frequencies. *GPS Solutions*, 3(4):1–9. doi:10.1007/PL00012810.

Heck, B. (1981a). Der Einfluß einzelner Beobachtungen auf das Ergebnis einer Ausgleichung und die Suche nach Ausreißern in den Beobachtungen. *Allgemeine Vermessungs-Nachrichten (AVN)*, 88(1):17–34.

Heck, B. (1981b). Statistische Ausreißerkriterien zur Kontrolle geodätischer Beobachtungen. In: R. Conzett et al. (eds.), *Ingenieurvermessung '80*, Beiträge zum VIII. Internationalen Kurs für Ingenieurvermessung, Zurich, Switzerland, September 24-October 1, 1980, Dümmler, Bonn.

Hein, G. W., Ávila-Rodríguez, J.-Á., and Wallner, S. (2006). The DaVinci Galileo code and others. *Inside GNSS*, 1(6):62–74.

Heisenberg, W. K. (1927). On the perceptual content of quantum theoretical kinematics and mechanics. *Zeitschrift für Physik*, 43:172–198.

Heister, H., Heunecke, O., Kerraschk, T., and Pflugmacher, A. (2009). Untersuchungen zu den globalen Positionierungsdiensten von Fugro OmniSTAR - Teil I: Grundlagen und Überblick. *Zeitschrift für Geodäsie, Geoinformation und Landmanagement (ZfV)*, 134(3):131–140.

Heister, H., Heunecke, O., Kerraschk, T., and Pflugmacher, A. (2010). Untersuchungen zu den globalen Positionierungsdiensten von Fugro OmniSTAR - Teil II: Ergebnisse und Erfahrungen. *Zeitschrift für Geodäsie, Geoinformation und Landmanagement (ZfV)*, 135(1):21–31.

Hernández-Pajares, M., Juan, J. M., Sanz, J., and Orúz, R. (2007). Second-order ionospheric term in GPS: Implementation and impact on geodetic estimates. *Journal of Geophysical Research*, 112, B08417. doi:10.1029/2006JB004707.

Héroux, P. and Kouba, J. (2001). GPS precise point positioning using IGS orbit products. *Physics and Chemistry of the Earth, Part A: Solid Earth and Geodesy*, 26(6-8):573–578. doi:10.1016/S1464-1895(01)00103-X.

Herring, T. A. (1992). Modeling atmospheric delays in the analysis of space geodetic data. In: J. C. de Munck and T. A. Th. Spoelstra (eds.), Proceedings of the Symposium on Refraction of Transatmospheric Signals in Geodesy, Hague, The Netherlands, May 19-22, 1992, Netherlands Geodetic Commission, Delft, The Netherlands, pp. 157–164.

Heßelbarth, A. (2009). GNSS-Auswertung mittels Precise Point Positioning (PPP). *Zeitschrift für Geodäsie, Geoinformation und Landmanagement (ZfV)*, 134(5):278–286.

Heßelbarth, A. and Wanninger, L. (2008). Short-term stability of GNSS satellite clocks and its effects on precise point positioning. In: Proceedings of ION GNSS 2008, Savannah, GA, USA, September 16-19, pp. 1855–1863.

Heunecke, O. and Heister, H. (2010). Untersuchungen zur Genauigkeit und Verfügbarkeit der Korrekturdienste von Fugro OmniSTAR. In: GNSS 2010 – Vermessung und Navigation im 21. Jahrhundert, 100. DVW-Seminar, Köln, Oktober 4-5, 2010, DVW-Schriftenreihe, Band 63/2010, Wißner-Verlag, Augsburg, Germany, pp. 143–160.

Hilla, S. (2002). A new plotting program for Windows-based TEQC users. *GPS Solutions*, 6(3):196–200. doi:10.1007/s10291-002-0027-1.

Hipel, K. W. and McLeod, A. I. (1994). *Time Series Modelling of Water Resources and Environmental Systems*. Elsevier, Amsterdam.

Hofmann-Wellenhof, B., Lichtenegger, H., and Wasle, E. (2008). *GNSS-Global Navigation Satellite Systems: GPS, GLONASS, Galileo & more*. Springer-Verlag, Wien.

Hollander, M. and Wolfe, D. A. (1999). *Nonparametric Statistical Methods*. John Wiley, New York, 2nd edition.

Holschneider, M. (1995). *Wavelets: An Analysis Tool (Oxford Mathematical Monographs)*. Oxford University Press, New York.

Holt, C. C. (2004). Forecasting seasonals and trends by exponentially weighted moving averages. *International Journal of Forecasting*, 20(1):5–10. doi:10.1016/j.ijforecast.2003.09.015.

Hopfield, H. S. (1969). Two-quartic tropospheric refractivity profile for correcting satellite data. *Journal of Geophysical Research*, 74(18):4487–4499. doi:10.1029/JC074i018p04487.

Howind, J. (2005). Analyse des stochastischen Modells von GPS-Trägerphasenbeobachtungen. Deutsche Geodätische Kommission, No. C584, Verlag der Bayerischen Akademie der Wissenschaften, Munich.

Howind, J., Kutterer, H., and Heck, B. (1999). Impact of temporal correlations on GPS-derived relative point positions. *Journal of Geodesy*, 73(5):246–258. doi:10.1007/s001900050241.

Hyndman, R. J., Koehler, A. B., Ord, J. K., and Snyder, R. D. (2008). *Forecasting with Exponential Smoothing: The State Space Approach*. Springer-Verlag, Berlin Heidelberg.

ICD-GPS-200C (1993). Interface Control Document: NAVSTAR GPS Space Segment/Navigation user interfaces, ICD-GPS-200, Revision C. ARINC Research Corporation, El Segundo, CA, USA, October 10, 1993.

IEEE (1979). *Programs for Digital Signal Processing*. IEEE Press, New York.

IS-GPS-200E (2010). Navstar GPS Space Segment/Navigation User Interfaces. Interface Specification, IS-GPS-200, Revision E. Science Applications International Corporation GPSW SE&I, El Segundo, CA, USA, June 8, 2010.

Jarque, C. M. and Bera, A. K. (1987). A test for normality of observations and regression residuals. *International Statistical Review*, 55(2):163–172. doi:10.2307/1403192.

Jin, S. G., Luo, O., and Ren, C. (2010). Effects of physical correlations on long-distance GPS positioning and zenith tropospheric delay estimates. *Advances in Space Research*, 46(2):190–195. doi:10.1016/j.asr.2010.01.017.

Jin, S. G. and Park, P. H. (2005). A new precision improvement in zenith tropospheric delay estimation by GPS. *Current Science*, 89(6):997–1000.

Jin, S. G., Wang, J., and Park, P. H. (2005). An improvement of GPS height estimations: Stochastic modeling. *Earth, Planets and Space*, 57(4):253–259.

John, J. A. and Draper, N. R. (1980). An alternative family of transformations. *Journal of the Royal Statistical Society. Series C (Applied Statistics)*, 29(2):190–197. doi:10.2307/2986305.

Jordan, E. C. and Balmain, K. G. (1968). *Electromagnetic Waves and Radiating Systems*. Prentice Hall, Englewood Cliffs, 2nd edition.

Kaiser, G. (1994). *A Friendly Guide to Wavelets*. Birkhäuser, Boston.

Kaniuth, K. and Vetter, S. (2006). Estimating atmospheric pressure loading regression coefficients from GPS observations. *GPS Solutions*, 10(2):126–134. doi:10.1007/s10291-005-0014-4.

Kaplan, E. D. and Hegarty, C. J. (2006). *Understanding GPS: Principles and Applications*. Artech House, Norwood, 2nd edition.

Karabatić, A. (2011). Precise Point Positioning (PPP). An alternative technique for ground based GNSS troposphere monitoring. Geowissenschaftliche Mitteilungen, No. 86, Vienna University of Technology, Vienna, Austria.

Kechine, M. O., Tiberius, C. C. J. M., and van der Marel, H. (2003). Network differential GPS: Kinematic positioning with NASA's Internet-based global differential GPS. *Journal of Global Positioning Systems*, 2(2):139–143.

Kedar, S., Hajj, G. A., Wilson, B. D., and Heflin, M. B. (2003). The effect of the second-order GPS ionospheric correction on receiver positions. *Geophysical Research Letters*, 30(16), 1829. doi:10.1029/2003GL017639.

Kee, C. (1996). Wide area differential GPS. In: B. W. Parkinson and J. J. Spilker (eds.), *Global Positioning System: Theory and Applications*, Vol. 2, American Institute of Aeronautics and Astronautics, Washington D.C., USA, pp. 81–115.

Keller, W. (2004). *Wavelets in Geodesy and Geodynamics*. Walter de Gruyter, Berlin.

Kelly, J. T. (2006). PPS versus SPS: Why military applications require military GPS. *GPS World*, 17(1):28–35.

Kendall, M. (1975). *Rank Correlation Methods*. Griffin, London, 4th edition.

Kendall, M. and Ord, J. K. (1990). *Time Series*. Edward Arnold, London, 3rd edition.

Kim, D. and Langley, R. B. (2001). Quality control techniques and issues in GPS applications: Stochastic modelling and reliability testing. In: Proceedings of the 8th GNSS Workshop – 2001 International Symposium on GPS/GNSS, Jeju, Korea, November 7-9, Tutorial/Domestic Session, pp. 76–85.

Kim, D., Langley, R. B., Bond, J., and Chrzanowski, A. (2003). Local deformation monitoring using GPS in an open pit mine: Initial study. *GPS Solutions*, 7(3):176–185. doi:10.1007/s10291-003-0075-1.

King, M. A. and Williams, S. D. P. (2009). Apparent stability of GPS monumentation from short-baseline time series. *Journal of Geophysical Research*, 114, B10403. doi:10.1029/2009JB006319.

King, R. W. and Bock, Y. (2002). Documentation for the GAMIT GPS Analysis Software, Release 10.0. Massachusetts Institute of Technology (MIT), Cambridge, MA, USA.

Kirchgässner, G. and Wolters, J. (2008). *Introduction to Modern Time Series Analysis*. Springer-Verlag, Berlin Heidelberg.

Klees, R. and Broersen, P. (2002). How to handle colored observation noise in large-scale least-squares problems: Building the optimal filter. DUP Science, Delft, The Netherlands.

Klees, R., Ditmar, P., and Broersen, P. (2003). How to handle colored observation noise in large least-squares problems. *Journal of Geodesy*, 76:629–640. doi:10.1007/s00190-002-0291-4.

Knöpfler, A., Masson, F., Mayer, M., Ulrich, P., and Heck, B. (2010). GURN (GNSS Upper Rhine Graben Network) – Status and first results. In: Proceedings of FIG Congress 2010, Facing the Challenges – Building the Capacity, Sydney, Australia, April 11-16.

Koch, K.-R. (1999). *Parameter Estimation and Hypothesis Testing in Linear Models*. Springer-Verlag, Berlin Heidelberg, 2nd edition.

Kolmogorov, A. (1933). Sulla determinazione empirica di una legge di distribuzione. *Giornale dell'Instituto Italiano degli Attuari*, 4:83–91.

Kolmogorov, A. (1941). Confidence limits for an unknown distribution function. *Annals of Mathematical Statistics*, 12(4):461–463. doi:10.1214/aoms/1177731684.

Kouba, J. (2002a). Relativistic time transformations in GPS. *GPS Solutions*, 5(4):1–9. doi:10.1007/PL00012907.

Kouba, J. (2002b). Sub-daily Earth rotation parameters and the International GPS Service orbit/clock solution products. *Studia Geophysica et Geodaetica*, 46(1):9–25. doi:10.1023/A:1019894614643.

Kouba, J. (2004). Improved relativistic transformations in GPS. *GPS Solutions*, 8(3):170–180. doi:10.1007/s10291-004-0102-x.

Kouba, J. (2009). A guide to using International GNSS Service (IGS) products. Available online at `http://igscb.jpl.nasa.gov/igscb/resource/pubs/UsingIGSProductsVer21.pdf`, accessed on November 5, 2010.

Kouba, J. and Héroux, P. (2001). Precise point positioning using IGS orbit and clock products. *GPS Solutions*, 5(2):12–28. doi:10.1007/PL00012883.

Kreiß, J.-P. and Neuhaus, G. (2006). *Einführung in die Zeitreihenanalyse*. Springer-Verlag, Berlin Heidelberg.

Kwiatkowski, D., Phillips, P. C. B., Schmidt, P., and Shin, Y. (1992). Testing the null hypothesis of stationarity against the alternative of a unit root: How sure are we that economic time series have a unit root? *Journal of Econometrics*, 54:159–178. doi:10.1016/0304-4076(92)90104-Y.

Landau, H. (2006a). Conversion formulas for the SNR values from a Trimble 4000SSI receiver. Personal communication on December 15, 2006, Trimble Terrasat GmbH, Höhenkirchen-Siegertbrn, Bavaria, Germany.

Landau, H. (2006b). SNR data from the Trimble NetR5 and 4700 receivers. Personal communication on December 19, Trimble Terrasat GmbH, Höhenkirchen-Siegertbrn, Bavaria, Germany.

Langley, R. B. (1991a). The mathematics of GPS. *GPS World*, 2(7):45–50.

Langley, R. B. (1991b). The orbits of GPS satellites. *GPS World*, 2(3):50–53.

Langley, R. B. (1997). GPS receiver system noise. *GPS World*, 8(6):40–45.

Larson, K. M., Bilich, A., and Axelrad, P. (2007). Improving the precision of high-rate GPS. *Journal of Geophysical Research*, 112, B05422. doi:10.1029/2006JB004367.

Lau, L. (2012). Comparison of measurement and position domain multipath filtering techniques with the repeatable GPS orbits for static antennas. *Survey Review*, 44(324):9–16. doi:10.1179/1752270611Y.0000000003.

Lau, L. and Mok, E. (1999). Improvement of GPS relative positioning accuracy by using SNR. *Journal of Surveying Engineering*, 125(4):185–202. doi:10.1061/(ASCE)0733-9453(1999)125:4(185).

Laurichesse, D. and Mercier, F. (2007). Integer ambiguity resolution on undifferenced GPS phase measurements and its application to PPP. In: Proceedings of ION GNSS 2007, Fort Worth, TX, USA, September 25-28, pp. 839–848.

Le, A. Q. and Tiberius, C. C. J. M. (2006). Phase wind-up effects in precise point positioning with kinematic platforms. In: Proceedings of the 3rd ESA Workshop on Satellite Navigation

User Equipment Technologies, Noordwijk, The Netherlands, December 11-13, 2006.

Leandro, R. F. and Santos, M. C. (2007). Stochastic models for GPS positioning: An empirical approach. *GPS World*, 18(2):50–56.

Lehmann, E. L. and Romano, J. P. (2005). *Testing Statistical Hypotheses*. Springer-Verlag, New York, 3rd edition.

Leick, A. (1995). *GPS Satellite Surveying*. John Wiley, New York, 2nd edition.

Leick, A. (2003). *GPS Satellite Surveying*. John Wiley, Hoboken, 3rd edition.

Li, B., Shen, Y., and Lou, L. (2011). Efficient estimation of variance and covariance components: A case study for GPS stochastic model evaluation. *IEEE Transactions on Geoscience and Remote Sensing*, 49(1):203–210. doi:10.1109/TGRS.2010.2054100.

Li, B., Shen, Y., and Xu, P. (2008). Assessment of stochastic models for GPS measurements with different types of receivers. *Chinese Science Bulletin*, 53(20):3219–3225. doi:10.1007/s11434-008-0293-6.

Lilliefors, H. W. (1967). On the Kolmogorov-Smirnov test for normality with mean and variance unknown. *Journal of the American Statistical Association*, 62(318):399–402. doi:10.2307/2283970.

Liu, H., Li, X., Ge, L., Rizos, C., and Wang, F. (2011). Variable length LMS adaptive filter for carrier phase multipath mitigation. *GPS Solutions*, 15(1):29–38. doi:10.1007/s10291-010-0165-9.

Ljung, G. M. and Box, G. E. P. (1978). On a measure of lack of fit in time series models. *Biometrika*, 65(2):297–303. doi:10.1093/biomet/65.2.297.

Lo, J., El-Mowafy, A., Penna, N., and Featherstone, W. (2009). Impact of stochastic modelling on GPS height and zenith wet delay estimation. In: A. Dempster (ed.), Proceedings of the IGNSS Symposium on GPS/GNSS, Gold Coast, Queensland, Australia, December 1-3, 2009.

Luo, X. (2010). Ein Ansatz zur Residuendekomposition für die Bestimmung und Modellierung der zeitlichen Korrelationen von GNSS-Beobachtungen. In: K. Zippelt (ed.), Vernetzt und ausgeglichen - Festschrift zur Verabschiedung von Prof. Dr.-Ing. habil. Dr.-Ing. E.h. Günter Schmitt. Schriftenreihe des Studiengangs Geodäsie und Geoinformatik, Band 3/2010, KIT Scientific Publishing, Karlsruhe, Germany, pp. 221–239. doi:10.5445/KSP/1000020074.

Luo, X., Heck, B., and Awange, J. L. (2012a). Correcting GNSS a priori tropospheric zenith dry delay by incorporating regional surface meteorological data. *Advances in Space Research* (in preparation).

Luo, X. and Mayer, M. (2008). Automatisiertes GNSS-basiertes Bewegungsmonitoring am Black Forest Observatory (BFO) in Nahezu-Echtzeit. *Zeitschrift für Geodäsie, Geoinformation und Landmanagement (ZfV)*, 133(5):283–294.

Luo, X., Mayer, M., and Heck, B. (2007a). Bestimmung von hochauflösenden Wasserdampffeldern unter Berücksichtigung von GNSS-Doppeldifferenzresiduen. Schriftenreihe des Studiengangs Geodäsie und Geoinformatik, Band 2/2007, Karlsruher Institut für Technologie (KIT), KIT Scientific Publishing, Karlsruhe, Germany.

Luo, X., Mayer, M., and Heck, B. (2007b). Erweiterte Modellbildung zur Erzeugung von hochauflösenden Wasserdampffeldern. *Allgemeine Vermessungs-Nachrichten (AVN)*, 114(5):179–189.

Luo, X., Mayer, M., and Heck, B. (2007c). Quantifizierung verschiedener Einflussfaktoren in GNSS-Residuen. *Zeitschrift für Geodäsie, Geoinformatik und Landmanagement (ZfV)*, 132(2):97–107.

Luo, X., Mayer, M., and Heck, B. (2008a). Erweiterung des stochastischen Modells von GNSS-Beobachtungen unter Verwendung der Signalqualität. *Zeitschrift für Geodäsie, Geoinformatik und Landmanagement (ZfV)*, 133(2):98–107.

Luo, X., Mayer, M., and Heck, B. (2008b). Extended neutrospheric modelling for the GNSS-based determination of high-resolution atmospheric water vapour fields. *Boletim de Ciências Geodésicas*, 14(2):149–170.

Luo, X., Mayer, M., and Heck, B. (2008c). Impact of various factors on the quality of site-specific neutrospheric parameters within GNSS data processing: A case study. *Boletim de Ciências Geodésicas*, 14(4):461–481.

Luo, X., Mayer, M., and Heck, B. (2008d). Improving the stochastic model of GNSS observations by means of SNR-based weighting. In: M. G. Sideris (ed.), *Observing our Changing Earth*, Proceedings of the 2007 IAG General Assembly, Perugia, Italy, July 2-13, IAG Symposia, Vol. 133, Springer-Verlag, Berlin Heidelberg, pp. 725–734. doi:10.1007/978-3-540-85426-5_83.

Luo, X., Mayer, M., and Heck, B. (2009). Analysing the impact of data smoothing procedures on temporal correlations using examples of GPS residual time series. Poster presented at EGU General Assembly 2009, Vienna, Austria, April 19-24, 2009.

Luo, X., Mayer, M., and Heck, B. (2011a). On the probability distribution of GNSS carrier phase observations. *GPS Solutions*, 15(4):369–379. doi:10.1007/s10291-010-0196-2.

Luo, X., Mayer, M., and Heck, B. (2011b). Verification of ARMA identification for modelling temporal correlations of GNSS observations using the ARMASA toolbox. *Studia Geophysica et Geodaetica*, 55(3):537–556. doi:10.1007/s11200-011-0033-2.

Luo, X., Mayer, M., and Heck, B. (2012b). Analysing time series of GNSS residuals by means of AR(I)MA processes. In: N. Sneeuw et al. (eds.), Proceedings of the VII Hotine-Marussi Symposium on Mathematical Geodesy, Rome, Italy, July 6-10, 2009, IAG Symposia, Vol. 137, Springer-Verlag, Berlin Heidelberg, pp. 129–134. doi:10.1007/978-3-642-22078-4_19.

Lutz, S. (2009). High-resolution GPS Tomography in View of Hydrological Hazard Assessment. Geodätisch-geophysikalische Arbeiten in der Schweiz, No. 76, Schweizerische Geodätische Kommission, Zurich.

MacKinnon, J. G. (1996). Numerical distribution functions for unit root and cointegration tests. *Journal of Applied Econometrics*, 11(6):601–618. doi:10.1002/(SICI)1099-1255(199611)11:6<601::AID-JAE417>3.0.CO;2-T.

Maddala, G. S. and Kim, I.-M. (1998). *Unit Roots, Cointegration, and Structural Change.* Cambridge University Press, Cambridge.

Mader, G. L. (1992). Rapid static and kinematic Global Positioning System solutions using the ambiguity function technique. *Journal of Geophysical Research*, 97(B3):3271–3283. doi:10.1029/91JB02845.

Mader, G. L. (1999). GPS antenna calibration at the National Geodetic Survey. *GPS Solutions*, 3(1):50–58. doi:10.1007/PL00012780.

Mader, G. L. (2001). A comparison of absolute and relative GPS antenna calibrations. *GPS Solutions*, 4(4):37–40. doi:10.1007/PL00012864.

Mallat, S. (2009). *A Wavelet Tour of Signal Processing: The Sparse Way.* Academic Press, Burlington, 3rd edition.

Mallat, S. G. (1989). A theory for multiresolution signal decomposition: The wavelet representation. *IEEE Transactions on Pattern Analysis and Machine Intelligence*, 11(7):674–693. doi:10.1109/34.192463.

Mangiarotti, S., Cazenave, A., Soudarin, L., and Crétaux, J. F. (2001). Annual vertical crustal motions predicted from surface mass redistribution and observed by space geodesy. *Journal of Geophysical Research*, 106(B3):4277–4291. doi:10.1029/2000JB900347.

Manly, B. F. J. (1976). Exponential data transformations. *Journal of the Royal Statistical Society. Series D (The Statistician)*, 25(1):37–42. doi:10.2307/2988129.

Mann, H. B. (1945). Nonparametric test against trend. *Econometrica*, 13(3):245–259. doi:10.2307/1907187.

Marini, J. W. (1972). Correction of satellite tracking data for an arbitrary tropospheric profile. *Radio Science*, 7(2):223–231. doi:10.1029/RS007i002p00223.

Markowski, C. A. and Markowski, E. P. (1990). Conditions for the effectiveness of a preliminary test of variance. *The American Statistician*, 44(4):322–326. doi:10.2307/2684360.

Marmet, P. (2000). The GPS and the constant velocity of light. *Acta Scientiarum. Technology*, 22(5):1269–1279.

Marquis, W. and Riggs, J. D. (2010). Block IIR lifetimes and GPS sustainment. *GPS World*, 21(11):8–15.

Marsaglia, G., Tsang, W. W., and Wang, J. (2003). Evaluating Kolmogorov's distribution. *Journal of Statistical Software*, 8(18):1–4.

Mathews, P. M., Dehant, V., and Gipson, J. M. (1997). Tidal station displacements. *Journal of Geophysical Research*, 102(B9):20469–20477. doi:10.1029/97JB01515.

Mayer, M. (2006). Modellbildung für die Auswertung von GPS-Messungen im Bereich der Antarktischen Halbinsel. Deutsche Geodätische Kommission, No. C597, Verlag der Bayerischen Akademie der Wissenschaften, Munich.

Mayer, M., Knöpfler, A., Heck, B., Masson, F., Ulrich, P., and Ferhat, G. (2012). GURN (GNSS Upper Rhine Graben Network): Research goals and first results of a transnational geo-scientific network. In: S. C. Kenyon et al. (eds.), *Geodesy for Planet Earth*, Proceedings of the 2009 IAG Symposium, Buenos Aires, Argentina, August 31-September 4, IAG Symposia, Vol. 136, Springer-Verlag, Berlin Heidelberg, pp. 673–681. doi:10.1007/978-3-642-20338-1_83.

Mayer, M., Lindner, K., Kutterer, H., and Heck, B. (2000). Eine Strategie zur Ermittlung hochgenauer Koordinaten und Bewegungsraten im ITRF-96 unter Verwendung der Berner Software Version 4.0. In: R. Dietrich (ed.), Deutsche Beiträge zu GPS-Kampagnen des Scientific Committee on Antarctic Research (SCAR) 1995-1998, Deutsche Geodätische Kommission, No. B310, Verlag der Bayerischen Akademie der Wissenschaften, Munich, pp. 59–68.

Mayer, M., Wanninger, L., Dick, H. G., Derenbach, H., and Heck, B. (2004). Mehrwegeeinflüsse auf den SA*POS*®-Stationen Baden-Württembergs. Poster presented at the Geodetic Week 2004, Stuttgart, Germany, October 12-15, 2004.

McCarthy, D. D. and Petit, G. (2004). IERS Conventions (2003). IERS Technical Note, No. 32, Verlag des Bundesamts für Kartographie und Geodäsie, Frankfurt am Main, Germany.

McLeod, A. I. and Li, W. K. (1983). Diagnostic checking ARMA time series models using squared-residual autocorrelations. *Journal of Time Series Analysis*, 4(4):269–273. doi:10.1111/j.1467-9892.1983.tb00373.x.

Mehaffey, J. (2011). Rain, snow, clouds and GPS reception. Available online at `gpsinformation.net/gpsclouds.htm`, accessed on February 6, 2011.

Meindl, M., Schaer, S., Hugentobler, U., and Beutler, G. (2004). Tropospheric gradient estimation at CODE: Results from global solutions. *Journal of the Meteorological Society of Japan*, 82(1B):331–338. doi:10.2151/jmsj.2004.331.

Melbourne, W. G. (1985). The case for ranging in GPS based geodetic systems. In: C. Goad (ed.), Proceedings of the 1st International Symposium on Precise Positioning with the Global Positioning System, Rockville, MD, USA, April 15-19, 1985, pp. 373–386.

Menge, F., Seeber, G., Völksen, C., Wübbena, G., and Schmitz, M. (1998). Results of absolute field calibration of GPS antenna PCV. In: Proceedings of ION GPS 1998, Nashville, TN, USA, September 15-18, pp. 31–38.

Merrigan, M. J., Swift, E. R., Wong, R. F., and Saffel, J. T. (2002). A refinement to the World Geodetic System 1984 reference frame. In: Proceedings of ION GPS 2002, Portland, OR, USA, September 24-27, pp. 1519–1529.

Mireault, Y., Tétreault, P., Lahaye, F., Héroux, P., and Kouba, J. (2008). Online precise point positioning: A new, timely service from Natural Resources Canada. *GPS World*, 19(9):59–64.

Misra, P. and Enge, P. (2006). *Global Positioning System: Signals, Measurements and Performance.* Ganga-Jamuna Press, Lincoln, 2nd edition.

Moore, A. W. (2007). The International GNSS Service: Any questions? *GPS World*, 18(1):58–64.

Morland, J. and Mätzler, C. (2007). Spatial interpolation of GPS integrated water vapour measurements made in the Swiss Alps. *Meteorological Applications*, 14(1):15–26. doi:10.1002/met.2.

Morlet, J., Arens, G., Fourgeau, E., and Giard, D. (1982). Wave propagation and sampling theory. *Geophysics*, 47(2):203–236. doi:10.1190/1.1441328, 10.1190/1.1441329.

Mueller, T. M. (1994). Wide area differential GPS. *GPS World*, 5(6):36–44.

Mungan, C. E. (2006). Relativistic effects on clocks aboard GPS satellites. *The Physics Teacher*, 44(7):424–425. doi:10.1119/1.2353579.

Nabeya, S. and Tanaka, K. (1988). Asymptotic theory of a test for the constancy of regression coefficients against the random walk alternative. *The Annals of Statistics*, 16(1):218–235. doi:10.1214/aos/1176350701.

Nahavandchi, H. and Joodaki, G. (2010). Correlation analysis of multipath effects in GPS-code and carrier phase observations. *Survey Review*, 42(316):193–206. doi:10.1179/003962610X12572516251808.

Newby, S. P. (1992). *An Assessment of Empirical Models for the Prediction of the Transionospheric Propagation Delay of Radio Signals*. M.Sc.E. thesis, Department of Surveying and Engineering, Technical Report, No. 160, University of New Brunswick (UNB), New Brunswick, Canada.

Newey, W. K. and West, K. D. (1987). A simple, positive semidefinite, heteroskedasticity and autocorrelation consistent covariance matrix. *Econometrica*, 55(3):703–708. doi:10.2307/1913610.

Ng, S. and Perron, P. (1995). Unit root tests in ARMA models with data-dependent methods for the selection of the truncation lag. *Journal of the American Statistical Association*, 90(429):268–281. doi:10.2307/2291151.

Ng, S. and Perron, P. (2001). Lag length selection and the construction of unit root tests with good size and power. *Econometrica*, 69(6):1519–1554. doi:10.1111/1468-0262.00256.

Niell, A. E. (1996). Global mapping functions for the atmospheric delay at radio wavelengths. *Journal of Geophysical Research*, 101(B2):3227–3246. doi:10.1029/95JB03048.

Niell, A. E. (2000). Improved atmospheric mapping functions for VLBI and GPS. *Earth, Planets and Space*, 52(10):699–702.

Niell, A. E. (2001). Preliminary evaluation of atmospheric mapping functions based on numerical weather models. *Physics and Chemistry of the Earth, Part A: Solid Earth and Geodesy*, 26(6-8):475–480. doi:10.1016/S1464-1895(01)00087-4.

Niemeier, W. (2008). *Ausgleichungsrechnung: Statistische Auswertemethoden*. Walter de Gruyter, Berlin, 2nd edition.

NOAA/NASA/USAF (1976). U.S. Standard Atmosphere, 1976. NOAA–S/T 76–1562, U.S. Government Printing Office, Washington, D.C., USA.

Odijk, D. (2003). Ionosphere-free phase combinations for modernized GPS. *Journal of Surveying Engineering*, 129(4):165–173. doi:10.1061/(ASCE)0733-9453(2003)129:4(165).

Özlüdemir, M. T. (2004). The stochastic modeling of GPS phase observations. *Turkish Journal of Engineering and Environmental Sciences*, 28(4):223–232.

Parkinson, B. W. and Powers, S. T. (2010). The origins of GPS and the pioneers who launched the system. *GPS World*, 21(5):31–41.

Perron, P. (1988). Trends and random walks in macroeconomic time series: Further evidence from a new approach. *Journal of Economic Dynamics and Control*, 12(2-3):297–332. doi:10.1016/0165-1889(88)90043-7.

Petit, G. and Luzum, B. (2010). IERS Conventions (2010). IERS Technical Note, No. 36, Verlag des Bundesamts für Kartographie und Geodäsie, Frankfurt am Main, Germany.

Petovello, M. G., O'Keefe, K., Lachapelle, G., and Cannon, M. E. (2009). Consideration of time-correlated errors in a Kalman filter applicable to GNSS. *Journal of Geodesy*, 83(1):51–56. doi:10.1007/s00190-008-0231-z.

Petrov, L. and Boy, J.-P. (2004). Study of the atmospheric pressure loading signal in very long baseline interferometry observations. *Journal of Geophysical Research*, 109, B03405. doi:10.1029/2003JB002500.

Phillips, P. C. B. and Perron, P. (1988). Testing for a unit root in time series regression. *Biometrika*, 75(2):335–346. doi:10.1093/biomet/75.2.335.

Phillips, P. C. B. and Solo, V. (1992). Asymptotics for linear processes. *The Annals of Statistics*, 20(2):971–1001. doi:10.1214/aos/1176348666.

Phillips, P. C. B. and Xiao, Z. (1998). A primer on unit root testing. *Journal of Economic Surveys*, 12(5):423–470. doi:10.1111/1467-6419.00064.

Pireaux, S., Defraigne, P., Wauters, L., Bergeot, N., Baire, Q., and Bruyninx, C. (2010). Higher-order ionospheric effects in GPS time and frequency transfer. *GPS Solutions*, 14(3):267–277. doi:10.1007/s10291-009-0152-1.

Plackett, R. L. (1983). Karl Pearson and the chi-squared test. *International Statistical Review*, 51(1):59–72. doi:10.2307/1402731.

Pope, A. J. (1976). The statistics of residuals and the detection of outliers. NOAA Technical Report NOS 65 NGS 1, Rockville, MD, USA.

Prasad, R. and Ruggieri, M. (2005). *Applied Satellite Navigation Using GPS, GALILEO, and Augmentation Systems.* Artech House, Norwood.

Priestly, M. B. (1981). *Spectral Analysis and Time Series.* Academic Press, London.

Ragheb, A. E., Clarke, P. J., and Edwards, S. J. (2007). GPS sidereal filtering: Coordinate- and carrier-phase-level strategies. *Journal of Geodesy*, 81(5):325–335. doi:10.1007/s00190-006-0113-1.

Rao, C. R. (1970). Estimation of heteroscedastic variances in linear models. *Journal of the American Statistical Association*, 65(329):161–172. doi:10.2307/2283583.

Rao, C. R. (1971). Estimation of variance and covariance components – MINQUE theory. *Journal of Multivariate Analysis*, 1(3):257–275. doi:10.1016/0047-259X(71)90001-7.

Ray, J. (2006). GNSS Solutions: What receiver technologies exist for mitigating GNSS pseudor-ange and carrier phase multipath? *Inside GNSS*, 1(6):25–27.

Ray, J. and Griffiths, J. (2008). Overview of IGS products & analysis center modeling. Paper preseted at the IGS Analysis Center Workshop 2008, Miami Beach, FL, USA, June 2-6, 2008.

Reißmann, G. (1980). *Die Ausgleichungsrechnung: Grundlagen und Anwendungen in der Geodäsie.* VEB Verlag für Bauwesen, Berlin, 5th edition.

Rideout, W. and Coster, A. (2006). Automated GPS processing for global total electron content data. *GPS Solutions*, 10(3):219–228. doi:10.1007/s10291-006-0029-5.

Rizos, C. (2003). Network RTK research and implementation – A geodetic perspective. *Journal of Global Positioning Systems*, 1(2):144–150.

Rodrigues, E. P. (2007). Estimation of crustal vertical movements due to atmospheric loading effects by GPS observations. *Revista Brasileira de Geofísica*, 25(1):45–50. doi:10.1590/S0102-261X2007000100004.

Rost, C. (2011). Phasenmehrwegereduzierung basierend auf Signalqualitätsmessungen geodätischer GNSS-Empfänger. Deutsche Geodätische Kommission, No. C665, Verlag der Bayerischen Akademie der Wissenschaften, Munich.

Rost, C. and Wanninger, L. (2009). Carrier phase multipath mitigation based on GNSS signal quality measurements. *Journal of Applied Geodesy*, 3(2):81–87. doi:10.1515/JAG.2009.009.

Rost, C. and Wanninger, L. (2010). Carrier phase multipath corrections based on GNSS signal quality measurements to improve CORS observations. In: Proceedings of IEEE/ION PLANS 2010, Indian Wells, CA, USA, May 4-6, pp. 1162–1167.

Rothacher, M. (1992). Orbits of Satellite Systems in Space Geodesy. Geodätisch-geophysikalische Arbeiten in der Schweiz, No. 46, Schweizerische Geodätische Kommission, Zurich.

Rothacher, M. (2001). Comparison of absolute and relative antenna phase center variations. *GPS Solutions*, 4(4):55–60. doi:10.1007/PL00012867.

Saastamoinen, J. (1973). Contribution to the theory of atmospheric refraction: Part II. Refraction corrections in satellite geodesy. *Bulletin Géodésique*, 107(1):13–34. doi:10.1007/BF02522083.

Saha, K., Raju, C. S., and Parameswaran, K. (2010). A new hydrostatic mapping function for tropospheric delay estimation. *Journal of Atmospheric and Solar-Terrestrial Physics*, 72(1):125–134. doi:10.1016/j.jastp.2009.10.017.

Said, S. E. and Dickey, D. A. (1984). Testing for unit roots in autoregressive-moving average models of unknown order. *Biometrika*, 71(3):599–607. doi:10.1093/biomet/71.3.599.

Santerre, R. (1989). *GPS Satellite Sky Distribution: Impact on the Propagation of Some Important Errors in Precise Relative Positioning.* PhD thesis, Department of Surveying Engineering, Technical Report, No. 145, University of New Brunswick (UNB), New Brunswick, Canada.

Santos, M. C., Vaníček, P., and Langley, R. B. (1997). Effect of mathematical correlation on GPS network computation. *Journal of Surveying Engineering*, 123(3):101–112. doi:10.1061/(ASCE)0733-9453(1997)123:3(101).

Satirapod, C. and Luansang, M. (2008). Comparing stochastic model used in GPS precise point positioning technique. *Survey Review*, 40(308):188–194. doi:10.1179/003962608X290988.

Satirapod, C. and Rizos, C. (2005). Multipath mitigation by wavelet analysis for GPS base station applications. *Survey Review*, 38(295):2–10. doi:10.1179/003962605791521699.

Satirapod, C. and Wang, J. (2000). Comparing the quality indicators of GPS carrier phase observations. *Geomatics Research Australasia*, 73:75–92.

Satirapod, C., Wang, J., and Rizos, C. (2001). A new stochastic modelling procedure for precise static GPS positioning. *Zeitschrift für Vermessungswesen (ZfV)*, 126(6):365–372.

Satirapod, C., Wang, J., and Rizos, C. (2002). A simplified MINQUE procedure for the estimation of variance-covariance components of GPS observables. *Survey Review*, 36(286):582–590. doi:10.1179/003962602791482920.

Savitzky, A. and Golay, M. J. E. (1964). Smoothing and differentiation of data by simplified least squares procedures. *Analytical Chemistry*, 36(8):1627–1639. doi:10.1021/ac60214a047.

Schmid, R. (2010). How to use IGS antenna phase center corrections. GPS World Tech Talk Blog, February 3, 2010.

Schmid, R. and Rothacher, M. (2003). Estimation of elevation-dependent satellite antenna phase center variations of GPS satellites. *Journal of Geodesy*, 77(7-8):440–446. doi:10.1007/s00190-003-0339-0.

Schmid, R., Rothacher, M., Thaller, D., and Steigenberger, P. (2005). Absolute phase center corrections of satellite and receiver antennas: Impact on global GPS solutions and estimation of azimuthal phase center variations of the satellite antenna. *GPS Solutions*, 9(4):283–293. doi:10.1007/s10291-005-0134-x.

Schmid, R., Steigenberger, P., Gendt, G., Ge, M., and Rothacher, M. (2007). Generation of a consistent absolute phase-center correction model for GPS receiver and satellite antennas. *Journal of Geodesy*, 81(12):781–798. doi:10.1007/s00190-007-0148-y.

Schön, S. (2010). Differentielle GNSS Systeme – Code- und Phasenlösungen. In: GNSS 2010 – Vermessung und Navigation im 21. Jahrhundert, 100. DVW-Seminar, Köln, Oktober 4-5, 2010, DVW-Schriftenreihe, Band 63/2010, Wißner-Verlag, Augsburg, Germany, pp. 15–38.

Schön, S. and Brunner, F. K. (2008a). Atmospheric turbulence theory applied to GPS carrier-phase data. *Journal of Geodesy*, 82(1):47–57. doi:10.1007/s00190-007-0156-y.

Schön, S. and Brunner, F. K. (2008b). A proposal for modelling physical correlations of GPS phase observations. *Journal of Geodesy*, 82(10):601–612. doi:10.1007/s00190-008-0211-3.

Schuh, H., Estermann, G., Crétaux, J.-F., Bergé-Nguyen, M., and van Dam, T. (2004). Investigation of hydrological and atmospheric loading by space geodetic techniques. In: C. Hwang et al. (eds.), *Satellite Altimetry for Geodesy, Geophysics and Oceanography*, Proceedings of the International Workshop on Satellite Altimetry, Wuhan, China, September 8-13, 2002, IAG Symposia, Vol. 126, Springer-Verlag, Berlin Heidelberg, pp. 123–132.

Schwert, G. W. (1989). Tests for unit roots: A Monte Carlo investigation. *Journal of Business and Economic Statistics*, 7(2):147–159. doi:10.2307/1391432.

Seeber, G. (2003). *Satellite Geodesy.* Walter de Gruyter, Berlin, 2nd edition.

Seeber, G., Menge, F., Völksen, C., Wübbena, G., and Schmitz, M. (1998). Precise GPS positioning improvements by reducing antenna and site dependent effects. In: F.K. Brunner (ed.), *Advances in Positioning and Reference Frames*, Proceedings of the 1997 IAG Scientific Assembly, Rio de Janeiro, Brazil, September 3-9, IAG Symposia, Vol. 118, Springer-Verlag, Berlin Heidelberg, pp. 237–244.

Shenoi, B. A. (2006). *Introduction to Digital Signal Processing and Filter Design.* John Wiley, Hoboken.

Snedecor, G. W. and Cochran, W. G. (1967). *Statistical Methods.* Iowa State University Press, Ames, 6th edition.

Souza, E. M. and Monico, J. F. G. (2004). Wavelet shrinkage: High frequency multipath reduction from GPS relative positioning. *GPS Solutions*, 8(3):152–159. doi:10.1007/s10291-004-0100-z.

Springer, T. and Dach, R. (2010). GPS, GLONASS, and more: Multiple constellation processing in the International GNSS Service. *GPS World*, 21(6):48–58.

Steigenberger, P. (2009). Reprocessing of a Global GPS Network. Deutsche Geodätische Kommission, No. C640, Verlag der Bayerischen Akademie der Wissenschaften, Munich.

Steigenberger, P., Boehm, J., and Tesmer, V. (2009). Comparison of GMF/GPT with VMF1/ECMWF and implications for atmospheric loading. *Journal of Geodesy*, 83(10):943–951. doi:10.1007/s00190-009-0311-8.

Stephens, M. A. (1974). EDF statistics for goodness of fit and some comparisons. *Journal of the American Statistical Association*, 69(347):730–737. doi:10.2307/2286009.

Stephens, M. A. (1986). Test based on EDF statistics. In: R. D'Agostino and M. A. Stephens (eds.), *Goodness-of-fit Techniques. Statistics: A Series of Textbooks and Monographs*, Vol. 68, Marcel Dekker, New York.

Stewart, R. H. (2008). *Introduction to Physical Oceanography.* Department of Oceanography, Texas A & M University.

Stock, J. H. (1994). Units roots, structural breaks and trends. In: R. F. Engle and D. L. McFadden (eds.), *Handbook of Econometrics*, Vol. 4, North Holland.

Stoica, P. and Moses, R. L. (1997). *Introduction to Spectral Analysis.* Prentice Hall, Upper Saddle River.

Stronk, M. and Wegener, V. (2005). SA*POS*®–A satellite positioning service of the German State Survey. *GeoInformatics*, 8:40–43.

Sun, H.-P., Ducarme, B., and Dehant, V. (1995). Effect of the atmospheric pressure on surface displacements. *Journal of Geodesy*, 70(3):131–139. doi:10.1007/BF00943688.

Talbot, N. (1988). Optimal weighting of GPS carrier phase observations based on the signal-to-noise ratio. In: Proceedings of the International Symposium on Global Positioning Systems, Gold Coast, Queensland, Australia, October 17-19, 1988, pp. 4.1–4.17.

Tetewsky, A. K. and Mullen, F. E. (1997). Carrier phase wrap-up induced by rotating GPS antennas. *GPS World*, 8(2):51–57.

Tétreault, P., Kouba, J., Héroux, P., and Legree, P. (2005). CSRS-PPP: An internet service for GPS user access to the Canadian Spatial Reference Frame. *Geomatica*, 59(1):17–28.

Teunissen, P., Joosten, P., and Tiberius, C. (2002). A comparison of TCAR, CIR and LAMBDA GNSS ambiguity resolution. In: Proceedings of ION GPS 2002, Portland, OR, USA, September 24-27, pp. 2799–2808.

Teunissen, P. J. G. (1995). The least-squares ambiguity decorrelation adjustment: A method for fast GPS integer ambiguity estimation. *Journal of Geodesy*, 70(1-2):65–82. doi:10.1007/BF00863419.

Teunissen, P. J. G. (1998). Quality control and GPS. In: P. J. G. Teunissen and A. Kleusberg (eds.), *GPS for Geodesy*, chapter 7, Springer-Verlag, Berlin, 2nd edition.

Teunissen, P. J. G. (2000). The success rate and precision of GPS ambiguities. *Journal of Geodesy*, 74(3-4):321–326. doi:10.1007/s001900050289.

Teunissen, P. J. G. and Amiri-Simkooei, A. R. (2008). Least-squares variance component estimation. *Journal of Geodesy*, 82(2):65–82. doi:10.1007/s00190-007-0157-x.

Teunissen, P. J. G., Jonkman, N. F., and Tiberius, C. C. J. M. (1998). Weighting GPS dual frequency observations: Bearing the cross of cross-correlation. *GPS Solutions*, 2(2):28–37. doi:10.1007/PL00000033.

Teunissen, P. J. G. and Kleusberg, A. (1998). *GPS for Geodesy*. Springer-Verlag, Berlin, 2nd edition.

Teusch, A. (2006). Einführung in die Spektral- und Zeitreihenanalyse mit Beispielen aus der Geodäsie. Deutsche Geodätische Kommission, No. A120, Verlag der Bayerischen Akademie der Wissenschaften, Munich.

Tiberius, C. and Borre, K. (1999). Probability distribution of GPS code and phase data. *Zeitschrift für Vermessungswesen (ZfV)*, 124(8):264–273.

Tiberius, C., Jonkman, N., and Kenselaar, F. (1999). The stochastics of GPS observables. *GPS World*, 10(2):49–54.

Tiberius, C. and Kenselaar, F. (2003). Variance component estimation and precise GPS positioning: Case study. *Journal of Surveying Engineering*, 129(1):11–18. doi:10.1061/(ASCE)0733-9453(2003)129:1(11).

Tiberius, C. C. J. M. and Kenselaar, F. (2000). Estimation of the stochastic model for GPS code and phase observables. *Survey Review*, 35(277):441–454. doi:10.1179/003962600791520686.

Torge, W. (2001). *Geodesy*. Walter de Gruyter, Berlin, 3rd edition.

Torrence, C. and Compo, G. P. (1998). A practical guide to wavelet analysis. *Bulletin of the American Meteorological Society*, 79(1):61–78. doi:10.1175/1520-0477(1998)079<0061:APGTWA>2.0.CO;2.

Trauth, M. H. (2007). *MATLAB® Recipes for Earth Sciences*. Springer-Verlag, Berlin Heidelberg, 2nd edition.

Tregoning, P. and van Dam, T. (2005). Atmospheric pressure loading corrections applied to GPS data at the observation level. *Geophysical Research Letters*, 32, L22310. doi:10.1029/2005GL024104.

Tregoning, P., Watson, C., Ramillien, G., McQueen, H., and Zhang, J. (2009). Detecting hydrologic deformation using GRACE and GPS. *Geophysical Research Letters*, 36, L15401. 10.1029/2009GL038718.

Trimble (1999). SNR conversions. Mail from Trimble support on July 13, 1999, available online at `http://gauss.gge.unb.ca/papers.pdf/SNR.memo.pdf`, accessed on June 8, 2012.

Troller, M. (2004). GPS based Determination of the Integrated and Spatially Distributed Water Vapor in the Troposphere. Geodätisch-geophysikalische Arbeiten in der Schweiz, No. 67, Schweizerische Geodätische Kommission, Zurich.

Troller, M., Geiger, A., Brockmann, E., and Kahle, H.-G. (2006). Determination of the spatial and temporal variation of tropospheric water vapour using CGPS networks. *Geophysical Journal International*, 167(2):509–520. doi:10.1111/j.1365-246X.2006.03101.x.

van Dam, T. M., Blewitt, G., and Heflin, M. B. (1994). Atmospheric pressure loading effects on Global Positioning System coordinate determinations. *Journal of Geophysical Research*, 99(B12):23939–23950. doi:10.1029/94JB02122.

Velleman, P. F. and Hoaglin, D. C. (1981). *Applications, Basics, and Computing of Exploratory Data Analysis*. Duxbury Press, Boston.

Vollath, U., Birnbach, S., Landau, H., Fraile-Ordoñez, J. M., and Martin-Neira, M. (1998). Analysis of three carrier ambiguity resolution (TCAR) technique for precise relative positioning in GNSS-2. In: Proceedings of ION GPS 1998, Nashville, TN, September 15-18, pp. 417–426.

von Neumann, J. (1941). Distribution of the ratio of the mean square successive difference to the variance. *Annals of Mathematical Statistics*, 12(4):367–395. doi:10.1214/aoms/1177731677.

von Neumann, J. (1942). A further remark concerning the distribution of the ratio of the mean square successive difference to the variance. *Annals of Mathematical Statistics*, 13(1):86–88.

doi:10.1214/aoms/1177731645.

Vondrák, J. (1969). A contribution to the problem of smoothing observational data. *Bulletin of the Astronomical Institute of Czechoslovakia*, 20(6):349–355.

Wang, J., Satirapod, C., and Rizos, C. (2002). Stochastic assessment of GPS carrier phase measurements for precise static relative positioning. *Journal of Geodesy*, 76(2):95–104. doi:10.1007/s00190-001-0225-6.

Wang, J., Stewart, M. P., and Tsakiri, M. (1998). Stochastic modeling for static GPS baseline data processing. *Journal of Surveying Engineering*, 124(4):171–181. doi:10.1061/(ASCE)0733-9453(1998)124:4(171).

Wanninger, L. (2000). Präzise Positionierung in regionalen GPS-Referenzstationsnetzen. Deutsche Geodätische Kommission, No. C508, Verlag der Bayerischen Akademie der Wissenschaften, Munich.

Wanninger, L. (2002). Virtual reference stations for centimeter-level kinematic positioning. In: Proceedings of ION GPS 2002, Portland, OR, USA, September 24-27, pp. 1400–1407.

Wanninger, L. (2003). Virtual reference stations (VRS). *GPS Solutions*, 7(2):143–144. doi:10.1007/s10291-003-0060-8.

Wanninger, L. (2004). Introduction to network RTK. IAG Working Group 4.5.1: Network RTK (2003-2007), available online at `www.wasoft.de/e/iagwg451/intro/introduction.html`, accessed on September 7, 2011.

Wanninger, L. (2006). Netz-RTK. In: GPS und Galileo – Methoden, Lösungen und neueste Entwicklungen, 66. DVW-Seminar, Darmstadt, Februar 21-22, 2006, DVW-Schriftenreihe, Band 49/2006, Wißner-Verlag, Augsburg, Germany, pp. 59–69.

Wanninger, L. and Heßelbarth, A. (2009). GNSS Precise Point Positioning und seine Anwendung in der Hydrographie. In: Hydrographie – Neue Methoden von der Erfassung zum Produkt, 89. DVW-Seminar, Hamburg, Oktober 6-7, 2009, DVW-Schriftenreihe, Band 58/2009, Wißner-Verlag, Augsburg, Germany, pp. 3–18.

Wanninger, L. and May, M. (2000). Carrier phase multipath calibration of GPS reference stations. In: Proceedings of ION GPS 2000, Salt Lake City, UT, USA, September 19-22, pp. 132–144.

Wanninger, L. and Wildt, S. (1997). Identifikation von Mehrwegeeinflüssen in GPS-Referenzstationsbeobachtungen. *Allgemeine Vermessungs-Nachrichten (AVN)*, 104(1):12–15.

Ward, P. W., Betz, J. W., and Hegarty, C. J. (2006). Interference, multipath, and scintillation. In: E. D. Kaplan and C. J. Hegarty (eds.), *Understanding GPS: Principle and Applications*, chapter 6, Artech House, Norwood, 2nd edition.

Ware, R., Alber, C., Rocken, C., and Solheim, F. (1997). Sensing integrated water vapor along GPS ray paths. *Geophysical Research Letters*, 24(4):417–420. doi:10.1029/97GL00080.

Watson, C., Tregoning, P., and Coleman, R. (2006). Impact of solid Earth tide models on GPS coordinate and tropospheric time series. *Geophysical Research Letters*, 33, L08306. doi:10.1029/2005GL025538.

Weinbach, U., Raziq, N., and Collier, P. (2009). Mitigation of periodic GPS multipath errors using a normalised least mean square adaptive filter. *Journal of Spatial Science*, 54(1):1–13. doi:10.1080/14498596.2009.9635162.

Wheelon, A. D. (2001). *Electromagnetic Scintillation I. Geometrical Optics*. Cambridge University Press, Cambridge.

Whittaker, E. T. and Robinson, G. (1924). *The Calculus of Observations: A Treatise on Numerical Mathematics*. Blackie and Son, London.

Wieser, A. (2007). GNSS solutions: How important is GNSS observation weighting? *Inside GNSS*, 2(1):26–28.

Wieser, A. and Brunner, F. K. (2000). An extended weight model for GPS phase observations. *Earth, Planets and Space*, 52(10):777–782.

Wieser, A. and Brunner, F. K. (2002). Short static GPS sessions: Robust estimation results. *GPS Solutions*, 5(3):70–79. doi:10.1007/PL00012901.

Wildt, S. (2007). *Mehrwegeausbreitung bei GNSS-gestützter Positionsbestimmung.* PhD thesis, Fakultät für Forst-, Geo- und Hydrowissenschaften der TU Dresden, Dresden, Germany.

Williams, S. D. P. and Penna, N. T. (2011). Non-tidal ocean loading effects on geodetic GPS heights. *Geophysical Research Letters*, 38, L09314. doi:10.1029/2011GL046940.

Witchayangkoon, B. (2000). *Elements of GPS Precise Point Positioning.* PhD thesis, Department of Spatial Information Science and Engineering, University of Maine, Orono, USA.

Woods, A. (2006). *Medium-Range Weather Prediction: The European Approach. The Story of the European Centre for Medium-Range Weather Forecasts.* Springer-Verlag, New York.

Wu, J., Gao, J., Li, M., and Wang, Y. (2009). Wavelet transform for GPS carrier phase multipath mitigation. In: Proceedings of the 1st International Conference on Information Science and Engineering, Nanjing, China, December 26-28, 2009, pp. 1019–1022. doi:10.1109/ICISE.2009.1344.

Wu, J. T., Wu, S. C., Hajj, G. A., Bertiger, W. I., and Lichten, S. M. (1993). Effects of antenna orientation on GPS carrier phase. *Manuscripta Geodetica*, 18:91–98.

Wübbena, G. (1985). Software developments for geodetic positioning with GPS using TI 4100 code and carrier measurements. In: C. Goad (ed.), Proceedings of the 1st International Symposium on Precise Positioning with the Global Positioning System, Rockville, MD, USA, April 15-19, 1985, pp. 403–412.

Wübbena, G., Schmitz, M., and Bagge, A. (2005). PPP-RTK: Precise point positioning using state-space representation in RTK networks. In: Proceedings of ION GNSS 2005, Long Beach, CA, USA, September 13-16, pp. 2584–2594.

Wübbena, G., Schmitz, M., and Boettcher, G. (2006a). Near-field effects on GNSS sites: Analysis using absolute robot calibrations and procedures to determine corrections. In: Proceeding of the IGS Workshop – Perspectives and Visions for 2010 and beyond, May 8-12, 2006, ESOC, Darmstadt, Germany.

Wübbena, G., Schmitz, M., Boettcher, G., and Schumann, C. (2006b). Absolute GNSS antenna calibration with a robot: Repeatability of phase variations, calibration of GLONASS and determination of carrier-to-noise pattern. In: Proceeding of the IGS Workshop – Perspectives and Visions for 2010 and beyond, May 8-12, 2006, ESOC, Darmstadt, Germany.

Wübbena, G., Schmitz, M., and Matzke, N. (2011). On GNSS in-situ station calibration of near-field multipath. Paper submitted to the International Symposium on GNSS, Space-based and Ground-based Augmentation Systems and Applications, Brussels, Belgium, November 29-30, 2010.

Wübbena, G., Schmitz, M., Menge, F., Böder, V., and Seeber, G. (2000). Automated absolute field calibration of GPS antennas in real-time. In: Proceedings of ION GPS 2000, Salt Lake City, UT, USA, September 19-22, pp. 2512–2522.

Xia, L. and Liu, J. (2001). Approach for multipath reduction using wavelet algorithm. In: Proceedings of ION GPS 2001, Salt Lake City, UT, USA, September 11-14, pp. 2134–2143.

Xu, G. (2007). *GPS: Theory, Algorithms and Applications.* Springer-Verlag, Berlin Heidelberg, 2nd edition.

Yeo, I.-K. and Johnson, R. A. (2000). A new family of power transformations to improve normality or symmetry. *Biometrika*, 87(4):954–959. doi:10.1093/biomet/87.4.954.

Young, L. C. (1941). On randomness in ordered sequences. *Annals of Mathematical Statistics*, 12(3):293–300. doi:10.1214/aoms/1177731711.

Zeimetz, P. and Kuhlmann, H. (2006). Systematic effects in absolute chamber calibration of GPS antennas. *Geomatica*, 60(3):267–274.

Zeimetz, P. and Kuhlmann, H. (2008). On the accuracy of absolute GNSS antenna calibration and the conception of a new anechoic chamber. In: Proceedings of FIG Working Week 2008 – Integrating Generations, Stockholm, Sweden, June 14-19.

Zheng, D. and Luo, S. (1992). Contribution of time series analysis to data processing of astronomical observations in China. *Statistica Sinica*, 2(2):605–618.

Zheng, D. W., Zhong, P., Ding, X. L., and Chen, W. (2005). Filtering GPS time-series using a Vondrak filter and cross-validation. *Journal of Geodesy*, 79(6-7):363–369. doi:10.1007/s00190-005-0474-x.

Zhong, P., Ding, X., Yuan, L., Xu, Y., Kwok, K., and Chen, Y. (2010). Sidereal filtering based on single differences for mitigating GPS multipath effects on short baselines. *Journal of Geodesy*, 84(2):145–158. doi:10.1007/s00190-009-0352-z.

Zhong, P., Ding, X. L., Zheng, D. W., Chen, W., and Huang, D. F. (2008). Adaptive wavelet transform based on cross-validation method and its application to GPS multipath mitigation. *GPS Solutions*, 12(2):109–117. doi:10.1007/s10291-007-0071-y.

Zhu, Q., Zhao, Z., Lin, L., and Wu, Z. (2010). Accuracy improvement of zenith tropospheric delay estimation based on GPS precise point positioning algorithm. *Geo-Spatial Information Science*, 13(4):306–310. doi:10.1007/s11806-010-0400-0.

Zhu, S. Y. and Groten, E. (1988). Relativistic effects in GPS. In: E. Groten and R. Strauß (eds.), *GPS-Techniques Applied to Geodesy and Surveying*, Proceedings of the International GPS-Workshop, Darmstadt, Germany, April 10-13, 1988, Lectures Notes in Earth Sciences, Vol. 19, Springer-Verlag, Berlin Heidelberg, pp. 41–46. doi:10.1007/BFb0011322.

Zhu, S. Y., Massmann, F.-H., Yu, Y., and Reigber, C. (2003). Satellite antenna phase center´ offsets and scale errors in GPS solutions. *Journal of Geodesy*, 76(11-12):668–672. doi:10.1007/s00190-002-0294-1.

Zumberge, J. F., Heflin, M. B., Jefferson, D. C., Watkins, M. M., and Webb, F. H. (1997). Precise point positioning for the efficient and robust analysis of GPS data from large networks. *Journal of Geophysical Research*, 102(B3):5005–5017. doi:10.1029/96JB03860.

Index

Acronyms

AC	analysis centre
ACF	autocorrelation function
ACVF	autocovariance function
AD	Anderson-Darling
ADF	augmented Dickey-Fuller
AFM	ambiguity function method
AIC	Akaike's information criterion
ALS	adaptive least-squares
AMB	phase ambiguity
AMU	arbitrary manufacturer unit
APC	antenna phase centre
APL	atmospheric pressure loading
AR	autoregressive
ARC	antenna-receiver combination
ARIMA	autoregressive integrated moving average
ARMA	autoregressive moving average
ARP	antenna reference point
AS	anti-spoofing
ATT	atmospheric turbulence theory
AZI	satellite azimuth
BFO	Black Forest Observatory
BIPM	International Bureau of Weights and Measures
BLUE	best linear unbiased estimator
BP	Box-Pierce
C/A	coarse/acquisition
CALMS	Combined AFM and LSM Method with SNR weighting
CCF	cross-correlation function
CDF	cumulative distribution function
CDMA	code division multiple access
CET	Central European Time
CIC	combined information criterion
CIR	cascade integer resolution
CM	Cramér-von Mises
CNR	carrier-to-noise ratio
CODE	Centre for Orbit Determination in Europe
COM	centre of mass
CORS	continuously operating reference station
CRD	site coordinate
CRM	correlation matrix
Cs	caesium
CS	chi-square
CSC	cosecant
CSRS	Canadian Spatial Reference System
CT	Cox-Stuart
CVVF	cross-validation Vondrák filter
CWT	continuous wavelet transform

DCB	differential code bias
DF	Dickey-Fuller
DOW	day of week
DTR	detrended residual (after Vondrák filtering)
DWD	German Meteorological Service
DWT	discrete wavelet transform
EAM	empirical averaging method
ECMWF	European Centre for Medium-Range Weather Forecasts
ELV	satellite elevation angle
EOP	Earth Orientation Parameters
ESOC	European Space Operations Centre
ETRS	European Terrestrial Reference System
FFT	fast Fourier transform
FKP	area correction parameters
FOC	full operational capability
FWT	fast wavelet transform
GDGPS	Global Differential GPS
GFZ	German Research Centre for Geosciences
GIC	generalised information criterion
GIK	Geodetic Institute of KIT
GMF	global mapping function
GNSS	Global Navigation Satellite Systems
GOCE	Gravity field and steady-state Ocean Circulation Explorer
GPS	Global Positioning System
GPST	GPS time
GPT	global pressure and temperature model
GRACE	Gravity Recovery And Climate Experiment
GW	GPS week
HOW	hand-over word
IAC	Information-Analytical Centre
ICRF	International Celestial Reference Frame
IERS	International Earth Rotation and Reference Systems Service
IGS	International GNSS Service
IID (iid)	independent and identically distributed
IMF	isobaric mapping function
INS	inertial navigation system
IOC	initial operational capability
IQR	interquartile range
IRA	isotropic receiver antenna
ITRF	International Terrestrial Reference Frame
JB	Jarque-Bera
JD	Julian date
JPL	Jet Propulsion Laboratory
KIT	Karlsruhe Institute of Technology
KPSS	Kwiatkowski-Phillips-Schmidt-Shin
KS	Kolmogorov-Smirnov (test for normailty)
KV	Kolmogorov-Smirnov (test for uncorrelatedness)
LAMBDA	least-squares ambiguity decorrelation adjustment
LB	Ljung-Box

LC	linear combination of GPS observations
LC3	ionosphere-free linear combination
LC4	geometry-free linear combination
LC5	wide-lane linear combination
LC6	Melbourne-Wübbena linear combination
LF	Lilliefors
LNA	low noise amplifier
LS	least-squares
LSM	least-squares method
LUE	linear unbiased estimator
MA	moving average
MAC	master-auxiliary concept
MAD	median absolute deviation
MBOC	multiplexing binary offset carrier
MCS	master control station
ME	model error
MEDLL	multipath estimating delay lock loop
MET	MATLAB$^{®}$ Econometrics Toolbox^{TM}
MF	mapping function
MINQUE	minimum norm quadratic unbiased estimation
MK	Mann-Kendall
ML	maximum likelihood
MP	multipath
MPI	multipath index
MSE	mean squared error
MST	MATLAB$^{®}$ Statistics Toolbox^{TM}
MWT	MATLAB$^{®}$ Wavelet Toolbox^{TM}
NANU	notice advisory to NAVSTAR users
NCEP	National Centres for Environmental Prediction
NCR	noise component residual (after sidereal stacking)
NGS	National Geodetic Survey
NL	narrow-lane
NMF	Niell mapping function
NOAA	National Oceanic and Atmospheric Administration
NTS	navigation technology satellite
NWM	numerical weather model
OFR	outlier-free residual (after outlier repair)
OLS	ordinary least-squares
PACF	partial autocorrelation function
PCO	phase centre offset
PCV	phase centre variation
PDF	probability density function
PE	prediction error
PP	Phillips-Perron
ppb	parts per billion
PPK	post-processed kinematic
ppm	parts per million
PPP	precise point positioning
PRN	pseudo random noise

PSD	power spectral density
Rb	rubidium
RES	residual
RF	rain fall (precipitation)
RH	relative humidity
RINEX	Receiver Independent Exchange Format
RMSD	root mean square deviation
RRR	remove-repair-restore
RSS	residual sum of squares
RTK	real time kinematic
SA	selective availability
SA*POS*®	Satellite Positioning Service of the German State Survey
SBL	Spatial Bureau on Loading
SDDR	studentised double-difference residual
SNC	signal-to-noise count
SNR	signal-to-noise ratio
SNR0	signal-to-noise power density ratio
SPD	slant path delay
SPP	single point positioning
STD	standard deviation
STDATM	standard atmosphere
SVN	satellite vehicle number
SZDR	studentised zero-difference residual
TAI	Temps Atomique International
TCAR	three carrier ambiguity resolution
TEC	total electron content
TECU	total electron content unit
TRP	troposphere parameter
TSA	time series analysis
UMP	uniformly most powerful
UPD	uncalibrated phase delay
URG	Upper Rhine Graben
USNO	United States Naval Observatory
UTC	Coordinated Universal Time
VCE	variance component estimation
VCM	variance-covariance matrix
VLBI	very long baseline interferometry
VMF	Vienna mapping function
VNR	von Neumann ratio
VRS	virtual reference station
WFT	windowed Fourier transform
WGS84	World Geodetic System 1984
WL	wide-lane
WLSE	weighted least-squares estimator
WN	white noise
WNR	white noise residual (after ARMA modelling)
ZDD	zenith dry delay
ZPD	zenith path delay
ZWD	zenith wet delay

Curriculum Vitae

Personal Information

Name	Xiaoguang Luo
Date of birth	January 2, 1981
Place of birth	Baoji, Shaanxi, P.R. China
Nationality	Chinese
Visa status	German permanent residency
Marital status	Single

Education

09/1987 - 08/1993	Dongrenbao Primary School in Baoji
09/1993 - 08/1996	Beiya Middle School in Baoji
09/1996 - 08/1999	Baoji High School in Baoji
07.07.1999	National Higher Education Entrance Examination

Higher Education

09/1999 - 08/2000	Geodesy and Geoinformatics, Tongji University, Shanghai, China
09/2000 - 08/2001	Intensive German courses, Tongji University, Shanghai, China
10/2001 - 06/2006	Geodesy and Geoinformatics, University of Karlsruhe, Germany
Diploma thesis	Bestimmung von hochauflösenden Wasserdampffeldern unter Berücksichtigung von GNSS-Doppeldifferenzresiduen
	(Determination of high-resolution atmospheric water vapour fields by considering GNSS double-difference residuals)
20.06.2006	Academic degree: Dipl.-Ing.
07/2006 - 03/2007	Scholarship as per the Federal State Law on Graduate Funding (LGFG)

Employment

04/2007 - 11/2011	Research assistant at the Geodetic Institute (GIK) of the University of Karlsruhe (TH)/Karlsruhe Institute of Technology (KIT)

Research Interests

GNSS troposphere modelling (e.g., GNSS meteorology)

Site-specific GNSS error modelling (e.g., multipath effects)

Statistical properties of GNSS observations (e.g., distribution, correlations)

Statistical test methods and time series analysis (e.g., AR(I)MA processes)

Acknowledgements

Although this dissertation represents an individual work, it would not have been written without the sincere help and support from many people. It is a pleasure to express my gratitude to all those who made this thesis possible. Because of them, my graduate experience has become one that I will never forget and forever appreciate.

In the first place, I owe my deepest gratitude to my supervisor, Prof. Dr.-Ing. habil. Dr. h.c. B. Heck, who introduced me into the exciting world of research. He gave me not only the freedom and courage to explore on my own, but also the guidance and sympathy to overcome difficult situations. His thorough corrections to my papers have considerably improved my writing skills, and his valuable suggestions to the first version of this work are gratefully acknowledged. I have been very fortunate to have such a competent, patient, and sympathetic supervisor. I would also like to thank Prof. Dr.-Ing. habil. H. Kutterer for the acceptance of co-supervising my PhD, as well as constructive discussions and valuable comments.

All of my colleagues at GIK (Geodetic Institute) and IPF (Institute of Photogrammetry and Remote Sensing) are deeply acknowledged for their contribution to an enjoyable working atmosphere. I would like to extend a special gratitude to the GNSS group headed by Dr.-Ing. M. Mayer for a great deal of support and insightful discussions, helping me enrich my ideas and knowledge. Many thanks also go to Dipl.-Ing. A. Knöpfler and Dipl.-Ing. T. Fuhrmann for performing site quality assessments and providing PPP residuals, respectively. I benefited much from the outstanding works done by Dr.-Ing. J. Howind (Howind, 2005) and Dipl.-Math. A. Teusch (Teusch, 2006). I am very delighted to thank Dr. K. Fleming for proofreading my thesis.

Furthermore, I am very grateful to the German Research Foundation (DFG) for supporting the project "Extending the stochastic model of GPS observations by modelling physical correlations". The former University of Karlsruhe (TH) (now Karlsruhe Institute of Technology, KIT) is acknowledged for granting me the Scholarship in Accordance with the Law on Graduate Funding from the Federal State of Baden-Württemberg (LGFG). In addition, I appreciate the financial support from the German Academic Exchange Service (DAAD) within the framework of the PROBRAL program with the Laboratory of Space Geodesy (LAGE) at the Federal University of Paraná (UFPR), Curitiba, Brazil. For the successful collaboration and the unforgettable experiences in Brazil, I owe my sincere thanks to Prof. Dr. C. P. Krueger and her colleagues at LAGE. I am also grateful to Department 51 of the State Agency for Spatial Information and Rural Development (LGL) Baden-Württemberg for preparing the GPS data and absolute antenna calibration values. Dr.-Ing. H. Landau from Trimble Terrasat GmbH, Höhenkirchen, Germany, is deeply acknowledged for providing the information about receiver-dependent signal quality measures. Moreover, I sincerely appreciate the high-quality undergraduate courses and the excellent German courses at the Tongji University, Shanghai, China.

Through these busy years, many friends have helped me stay sane and overcome setbacks. I greatly appreciate their friendship and deeply thank them for believing in me. In particular, I would like to mention Dipl.-Ing. M. G. Licht and Dipl.-Ing. T. Gering who introduced me to their hospitable families, making my integration into a new country much sooner and easier. Family Licht is sincerely acknowledged for the family-like relations and the amazing Christmas celebrations. I would like thank family Gering for my first home-baked and extremely delicious birthday cake. Finally, I would like to express my sincerest appreciation and gratitude to my whole family, who have been a constant source of love, concern, support, and strength. This dissertation is dedicated to my dear parents, Qin Zhu and Xijun Luo, who gave their only child a fighting heart, a thinking mind, and an enjoyable life.